UNIVERSITAT POLITÈCNICA DE CATALUNYA BARCELONATECH

A double-porosity formulation for the THM behaviour of bentonite-based materials

Ramon Barboza de Vasconcelos

A DOUBLE-POROSITY FORMULATION FOR THE THM BEHAVIOUR OF BENTONITE-BASED MATERIALS

Ramon Barboza de Vasconcelos

A thesis submitted in partial fulfilment of the
requirements for the degree of
Doctor of Philosophy

Department of Civil and Environmental Engineering
Section of Geotechnical Engineering and Geosciences
Technical University of Catalonia
BARCELONATECH

Supervisors:
Antonio Gens Solé
Jean Vaunat

Barcelona
April 2021

Soli Deo Gloria.

Aos meus pais, Jaime e Cleonide,

Por todo amor sacrificial, apoio incondicional e incessantes orações.

In memoriam:

Prof. Ivaldo Dário da Silva Pontes Filho (1955-2016)

ABSTRACT

The thermo-hydro-mechanical (THM) behaviour of expansive clays has been extensively studied in the last decades due to the potential use of bentonites as components of engineered barrier systems (EBS) in deep geological repositories for high-level and long-lived radioactive wastes. Since the early post closure period, the EBS is subjected to changes in temperature, moisture content and stresses due to the coupled THM processes expected to occur in such an environment. The different structural levels found in unsaturated expansive clays requires the use of constitutive models that considers the explicit distinction of these pore-structure levels in their mathematical formulation in order to reproduce the development of the fabric of bentonite materials subjected to the complex THM paths taking place during the lifetime of a nuclear waste repository. A coupled THM formulation that represents the expansive soil as two overlapped but distinct structural media has been developed in the framework of classical and generalized plasticity theories. In such a double-structure approach, the THM behaviour of the expansive soil is characterized by constitutive laws formulated to account for the relevant processes affecting each porous medium and for the interaction mechanisms relating the deformation and the saturation states of the active clay particles to the structural arrangement of the clay aggregates and to the water potential in the larger interconnected pores. In addition, the mechanical response of the porous medium to any THM loading is intrinsically related to the compressibility of the clay minerals. The irreversible changes in the soil fabric are attributed to the loading-collapse (LC) mechanism and to the micro-macro structural coupling (β-mechanism). Thermal effects are incorporated in the double structure formulation in this Thesis as well as the required modifications in the stress integration process. The resultant mathematical formulation has been implemented in a finite element code (CODE_BRIGHT) able to solve, in a fully coupled way, the system of partial differential equations arising from the governing equations (balance equations). An explicit and robust integration scheme with automatic sub-stepping and error control has been employed to update the stress tensor and the internal (history) variables. The capabilities of the implemented double-porosity model to predict the expected response of expansive clays under isothermal and non-isothermal scenarios have been checked by the performance of constitutive analyses following a number of prescribed THM paths under confined and unconfined conditions. In addition, sensitivity analyses have been carried out in order to verify the dependence of the local expansive response on the initial conditions and on the sequence of load application. Special attention has been placed on the role played by the pore-water mass transfer between the two pore-structure levels in the development of the swelling potential of the expansive porous medium. The performance of the model in reproducing the actual THM behaviour of laboratory-scale tests has also been examined by means of the modelling of the hydration of two heated columns made of granular bentonite materials, selected as potential buffer materials in the construction of engineered barriers. The comparison between the available experimental data and the model results has shown the ability of the current double-porosity model to capture the main observed features of the THM behaviour of the expansive material when subjected to complex loading paths.

RESUMEN

El comportamiento termo-hidro-mecánico (THM) de las arcillas expansivas ha sido ampliamente estudiado en las últimas décadas debido al uso potencial de bentonitas en barreras de ingeniería (EB) en depósitos geológicos profundos para desechos radiactivos de alta actividad y de larga vida. Desde la post-clausura del repositorio, la EB está sometida a cambios de temperatura, contenido de humedad y tensiones a causa de los procesos acoplados THM que se espera que ocurran en dicho entorno. Los diferentes niveles estructurales presentes en las arcillas expansivas no saturadas requieren el uso de modelos constitutivos que consideren en su formulación matemática la distinción explícita de los distintos tipos de poros a fin de reproducir la evolución estructural de los materiales bentoníticos bajo las complejas trayectorias de cargas THM que tienen lugar durante la vida de un repositorio de residuos nucleares. Se ha desarrollado una formulación THM acoplada, en el marco teórico de la plasticidad clásica y generalizada, que describe el suelo expansivo como dos medios estructurales superpuestos pero distintos. Este planteamiento de modelo de doble porosidad considera que el comportamiento THM del suelo expansivo es descrito por leyes constitutivas que tienen en cuenta los procesos relevantes en cada medio poroso y los mecanismos de interacción que relacionan la deformación y el estado de saturación de las partículas de arcilla activas con la disposición estructural de los agregados de arcilla y con el potencial de agua en los macro poros. Además, la respuesta mecánica del medio poroso bajo cualquier carga THM está intrínsecamente relacionada con la compresibilidad de los minerales de arcilla. Los cambios estructurales irreversibles se atribuyen al mecanismo de carga-colapso (LC) y al acoplamiento estructural micro-macro (mecanismo β). Los efectos térmicos han sido incorporados a la formulación matemática del modelo de doble estructura, que ha sido implementada en un código de elementos finitos (CODE_BRIGHT) capaz de resolver, de forma totalmente acoplada, el sistema de ecuaciones diferenciales parciales que se originan de las ecuaciones de balance. Se ha empleado un esquema robusto de integración explícito con control automático del incremento de integración y del error para actualizar el tensor de tensiones y las variables de historia. La capacidad del modelo de doble porosidad para predecir la respuesta esperada de las arcillas expansivas en escenarios isotermos y no isotermos se ha comprobado mediante la realización de análisis constitutivos siguiendo trayectorias THM prescritas tanto a volumen constante cuanto en condiciones no confinadas. Además, se han realizado análisis de sensibilidad para verificar la dependencia de la respuesta expansiva de las condiciones iniciales y de la secuencia de aplicación de cargas. Se ha prestado especial atención al papel que desempeña la transferencia de agua entre los dos niveles de poros en el desarrollo del potencial de hinchamiento del medio poroso expansivo. También se ha examinado el desempeño del modelo en la reproducción del comportamiento THM en ensayos a escala de laboratorio mediante la simulación del calentamiento e hidratación de dos columnas de materiales granulares de bentonita seleccionados como potenciales materiales de sellado en la construcción de barreras de ingeniería. La comparación entre los datos experimentales disponibles y los resultados del modelo ha demostrado la capacidad de la presente formulación de doble porosidad de simular los principales aspectos observados en el comportamiento del material expansivo cuando está sometido a trayectorias THM complejas.

AGRADECIMIENTOS

En primero lugar, agradezco a Dios por el don de la vida y por todos los recursos que Su bondadosa providencia me ha proporcionado a lo largo de estos años. Sin el aliento y consuelo que encuentro en las páginas de las Santas Escrituras, no hubiera llegado tan lejos; y sin la certeza de la veracidad de Sus palabras y promesas, no hubiera encontrado propósito en mi existencia.

Agradezco a los profesores Antonio Gens Solé y Jean Vaunat por la dirección de esta tesis y por ayudarme a desarrollar un trabajo de investigación con la calidad y el rigor requeridos, a través de preguntas, observaciones y comentarios siempre pertinentes. También por creer en mi trabajo, por la paciencia y constancia requeridas tantas veces en esa laboriosa tarea de formar una nueva generación de investigadores y por la disposición en aclarar mis dudas y en compartir sus conocimientos teóricos y prácticos. Haber trabajado con ellos ha sido, para mí, una experiencia grata, agradable y enriquecedora.

Agradezco también a los profesores del Departamento de Ingeniería del Terreno que, directa e indirectamente, han contribuido para el desarrollo de esta tesis al transmitir parte de su vasto conocimiento en suelos no saturados, modelos constitutivos y modelación numérica.

A Samuel Amorim, Analice Lima y María Teresa Zandarín por la inestimable ayuda proporcionada antes de mi llegada a España y durante aquellos primeros días (ya tan lejanos) de adaptación a una tierra y cultura extranjeras. Sin su ayuda, ánimo y amistad, dicho proceso hubiera sido mucho más difícil. Mis sinceros agradecimientos también a Sergio Samat, Andrés Idiart, Abel Jacinto, Olga Mavrouli, Mauricio Tapias, Daniel Tarragó, Mariana Rodriguez, Rodrigo Gómez, María Teresa Yubero, Anna Ramon, Claudia Alvarado, Miquel de Francisco, Arisleidy Mesa y a tantos otros compañeros de lucha, quienes proporcionaron agradables conversaciones durante las pausas para comer y que contribuyeron activamente para que mi estancia en la UPC fuera (y siga siendo) una experiencia inolvidable. Quiero expresar también mi gratitud a Benoit Garitte por sus valiosas instrucciones en la modelación en CODE_BRIGHT y a Daniel Ruiz por las productivas conversaciones y por su colaboración en los trabajos que permitieron el desarrollo del modelo de doble porosidad tratado en esta tesis. También quiero agradecer a los compañeros de despacho con los que tuve el privilegio de compartir largas horas y agradables conversaciones. A ellos, desde estas líneas, les dedico mi cariño por todo lo vivido en estos años.

Aprovecho también para agradecer al personal del Programa de Doctorado en Ingeniería del Terreno y del servicio administrativo e informático (Óscar Rubio, Eva Martínez, Albert Marques) y al personal del CIMNE (Mari Carmen, Irene Latorre, Valentín Catalán) por realizar las diversas gestiones siempre con un trato cordial y amable.

A todos mis queridos hermanos en Cristo (en Barcelona) que, con sus vidas y ejemplos, me han enseñado, en la práctica, lo que es “llorar con los que lloran” y “alegrarse con los que se alegran”. En especial, agradezco por el apoyo, ánimo y oraciones de mis hermanos Javier Malpica, Michaela Severin, Francisco Rubio, Javier Julve y Mario Peláez. Gracias por ayudarme a llevar mis cargas en las horas más difíciles. También quiero expresar mi cariño a los Rovira Tehe y a los Pareja Munevar por “adoptarme” como si fuera un miembro más de sus familias.

A Alexandre Tissot y a Anna, su pareja, por la amistad a mí dedicada y por las apasionantes conversaciones sobre “castells”, cómics y cinema.

De manera muy especial, a mi familia y amigos en Brasil, quienes siempre han estado presentes, aunque físicamente lejos, y que nunca han dejado de creer en mi victoria aun cuando mi ánimo desfallecía. A mis padres y hermanos que, con lágrimass, me despidieron cuando tomé aquel vuelo de camino a España y que, con gran alegría, celebran conmigo el término de esta etapa en mi vida. A mi madre, que nunca ha dejado de interceder por mí en sus oraciones.

A los profesores Ivaldo Pontes Filho (*in memoriam*), Leonardo Guimarães y Lícia Costa, por la confianza en mí depositada al iniciarme en el ámbito científico y por incentivar la continuidad de mi formación profesional a través de mis estudios de doctorado.

Finalmente, y no por ello menos importante, quiero agradecer el apoyo económico recibido durante estos años a EURATOM que, a través de CIMNE (UPC), ha hecho posible el desarrollo del trabajo de investigación que culminó con la elaboración de esta tesis.

A todos, muchas gracias.

CONTENTS

LIST OF FIGURES

LIST OF TABLES

1. BACKGROUND, MOTIVATION AND OBJECTIVES

1.1. BACKGROUND

The use of nuclear power in many countries is a direct consequence of the growing energy demand necessary in all human activities, the production limitations and the regulations in the exploitation of natural resources. It has been made possible by the technological advances of the last century allied to a deeper scientific knowledge of the atomic structure. Nevertheless, the production of nuclear electricity requires the management of radioactive wastes in order to prevent these by-products from constituting a threat to human safety and a source of environmental contamination. Since the radioactive waste from the nuclear power generation processes may emit radiation for hundreds or even for thousands of years (Hoffmann, 2005), it is crucial to search for a definite solution to store such radioactive materials that fulfills, at least, the requirements listed below:

- isolation from the external environment throughout the entire period of radioactive decay, ensuring the long-term protection of humans and the biosphere from the effects of radiation (OECD NEA, 1995; IAEA, 2003; Altofer, 2010);
- low cost of operation and maintenance of facilities in order to provide adequate insulation and physical integrity of the repository during its lifetime;
- low social and environmental risks caused by the common human activities or by local natural disasters (such as earthquakes, floods, landslides, etc.) (IAEA, 2003);
- restricted access to humans, reducing the risk from inadvertent or intentional human intrusion (IAEA, 1995, 2003; Sellin and Leupin, 2013) or mitigating the threat to all regional life in case of wars.

In that sense, the construction of repositories in deep geological media is one of the preferred and safest options for the disposal of high-level and long-lived radioactive wastes (IAEA, 2003;

Bernier *et al.*, 2007). In Figure 1-1 a typical deep geological disposal with its surface and underground facilities, access galleries/tunnels and waste storage niches is illustrated.

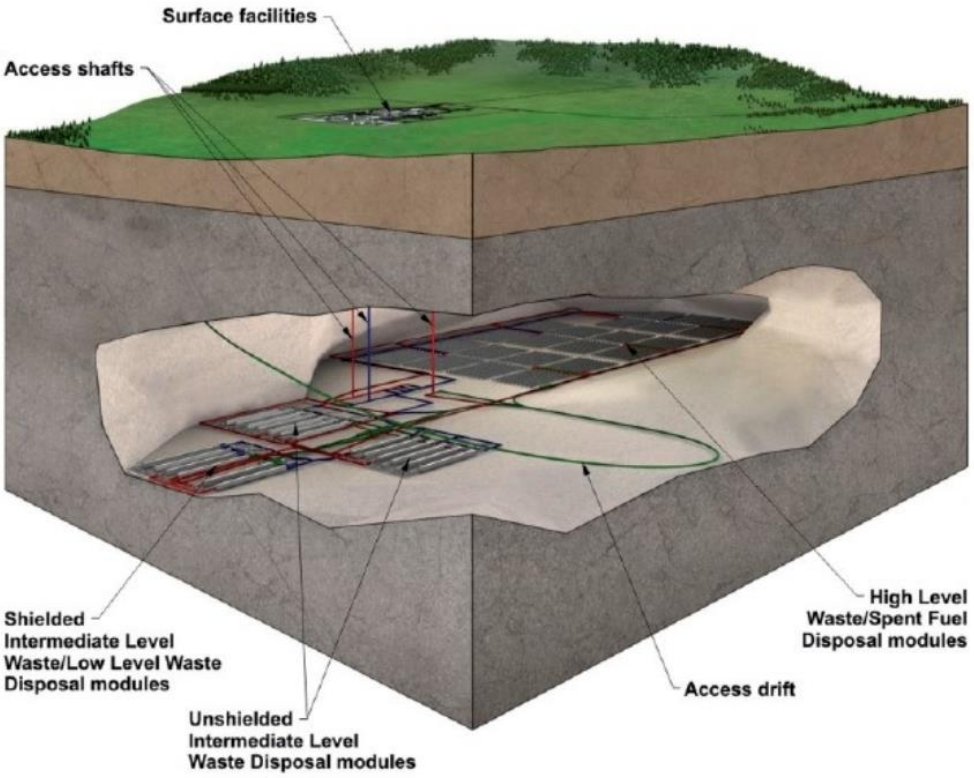

Figure 1-1: Schematic representation of a typical underground nuclear waste repository (NDA, 2011).

These underground repositories are usually arranged in horizontal and/or vertical niches constructed from access galleries excavated in the rock formation. The long-term safety design for deep disposals of radioactive wastes is based on the existence of multiple natural and artificial barriers. The spent nuclear fuel and the long-lived high-level radioactive wastes are emplaced in excavated niches inside metallic canisters, which constitute the first engineered barrier isolating these materials from the surrounding environment. The deep rock formation is considered as a geological barrier. In many conceptual programs for deep geological disposal, an expansive clay buffer (commonly a bentonite-based material) is used as a protecting and isolating barrier between the waste canisters and the surrounding host rock (Horseman and McEwen, 1996; Hökmark, 2004). These bentonite buffers represent an additional restraint to the movement of radionuclides from the radioactive waste towards the external environment (Hoffmann, 2005), especially when the physical barrier provided by the canister fails, either due to a design failure or due to the metal corrosion process over time. The low water mobility inside bentonite-based materials would minimize the risk of environmental contamination by the release and transport of radionuclides. Furthermore, the high self-sealing capacity of bentonites under wetting paths tends to improve the isolation of the nuclear waste (Pusch, 1982) by the closure of gaps and fissures inside the buffers and around the rock formation openings.

The characterization of the physico-chemical and engineering properties of deep rock formations and sealing barrier materials have become an essential part of the research tasks promoted by several energy agencies in charge of nuclear waste management around the world.

Intensive testing and monitoring programmes at different scales (field and laboratory scales), divided in several work packages, have been scheduled and carried out in collaboration with many research centers (including UPC-BarcelonaTech), have generated a large amount of technical reports, PhD theses and scientific papers that can be found in the literature. Furthermore, these experimental data have also provided enough information for the verification and validation of mathematical models able to reproduce the most relevant chemical-thermo-hydro-mechanical processes observed experimentally and expected to take place throughout the lifetime of a nuclear waste repository (Villar *et al.*, 2012b).

The development and the progressive enhancement of existing numerical codes and constitutive models for unsaturated clayey soils have enabled the suitable modelling of the swelling potential of expansive clays when submitted to changes in their moisture content under both free and confined conditions. In fact, the classical formulation of the ***B**arcelona **B**asic **M**odel* (BBM) – originally implemented for describing the collapsible behaviour of unsaturated soils of low activity (Alonso *et al.*, 1990) – served as a mathematical bases to develop the expansive model (***B**arcelona **Ex**pansive **M**odel*, BExM) described in Alonso *et al.* (1999). The main feature of such a mathematical formulation was the explicit consideration of two distinct families of pores within the material as well as the mechanical coupling between them in accordance to the theoretical basis stated by Gens and Alonso (1992). The double structure model developed by Sánchez (2004) and reported in Sánchez *et al.* (2005, 2008) is another example of a mechanical constitutive model that considers the existence of these two dominant and overlapping pore structural levels. It is important to mention that this latter model, formulated in the framework of a generalized plasticity (Sánchez, 2004), has been successfully used in the modelling of compacted bentonite-based materials wetted under isothermal (Van Geet *et al.*, 2009; Gens *et al.*, 2011) and non-isothermal conditions (Sánchez and Gens, 2006; Sánchez *et al.*, 2008). Other recent multi-porosity formulations with mechanical and/or hydraulic constitutive laws for each structural level are found in the literature, as the ones proposed in Mašín (2013), Wang and Wei (2015), Dieudonné *et al.* (2017), Ghiadistri *et al.* (2018), for instance.

The present PhD Thesis is the result of the research work carried out as part of the Doctoral Programme in Geotechnical Engineering of UPC-BarcelonaTech, which mainly consisted in the development and the numerical implementation of a double-porosity formulation into a finite element code (CODE_BRIGHT) capable of reproducing the thermo-hydro-mechanical (THM) behaviour of expansive soils. The accumulated experience of the UPC Geotechnical Group in dealing with this kind of complex constitutive models contributed to a better understanding of the mechanisms governing the behaviour of unsaturated active clays and to the development of robust numerical formulations able to reproduce many of the relevant features observed experimentally. The modelling tasks carried out during the development of this research – using both single- and double-porosity models (as the BBM, the BExM and the model developed in this document) – were performed in the context of the engineered barrier systems (EBS) for nuclear waste disposals. Several technical reports, papers and publications in congresses resulted from such numerical analyses, as for instance, Czaikowski *et al.* (2012), Gaus *et al.* (2014a, 2014b), Vasconcelos *et al.* (2014, 2019), Garitte *et al.* (2015), Vasconcelos and Gens (2015) and Gens and Vasconcelos (2019). Although some of such modelling performances also took into account the THM behaviour of the argillaceous rock surrounding the *in-situ* full-scale HE-E test (Gaus, 2011), however, the current research has been devoted to reproduce the

response of expansive clays (bentonites) subjected to high thermal gradients. This research has been funded by the European Atomic Energy Community's Seventh Framework Programme through the "Long-Term Performance of Engineered Barrier Systems (PEBS) Project" (2010-2014) and by the Euratom Research and Training Programme 2014-2018 through the "Bentonite Mechanical Evolution (BEACON) Project".

1.2. MOTIVATION AND OBJECTIVES OF THIS PhD THESIS

In the framework of the engineered barriers for nuclear waste disposal systems, it is commonly accepted that the early post-closure period is one of the most critical stages during the lifetime of a radioactive waste repository (Villar *et al.*, 2012b). The high heat generation by the radioactive decay of the wastes within the metal canister during the first years after its emplacement can compromise the stability and isolation specifications for the underground repository design. Johnson *et al.* (2002) estimated the temperature evolution by the thermal properties of the high-level nuclear wastes, the bentonite materials and the host rock (Opalinus Clay) and found that the maximum temperature around the canister could reach values as high as 150°C. The initial drier state of the bentonite buffers induces the occurrence of high temperatures close to the heat emitting source. The magnitude of the thermal gradient within the engineered barrier could affect its re-saturation process and compromise the desirable sealing capacity of such materials as becoming saturated with the natural water uptake from the surrounding geological formation. In order to investigate the impact of the thermal loading on the swelling properties and the re-saturation process of bentonite-based materials, some large-scale heating experiments have been carried out along the past decades, as the *in-situ* FEBEX test and the almost full-scale "mock-up" test (ENRESA, 2000; Huertas *et al.*, 2005). In such a context, a 1:2 scale heating test with natural hydration of the EBS was launched (in June, 2011) at the Mont Terri Underground Research Laboratory (Switzerland) in a 50-m long non-lined horizontal tunnel of 1.3 m diameter excavated in the Opalinus Clay formation (Gaus, 2011; Teodori and Gaus, 2011). This *in-situ* test (known as the HE-E experiment), composed by two independently and fully symmetric 4-m long heated sections, aimed to provide a good quality experimental database for the calibration and validation of THM constitutive models during the early re-saturation of the EBS, when the thermal gradient within the buffers is still high (Gaus, 2011; Villar *et al.*, 2016). The performance of two heating-hydration tests by the CIEMAT laboratory (Madrid, Spain) using the same granular bentonite materials employed in the field scale test has provided additional information about the THM processes taking place inside the barriers. The controlled conditions found in laboratory scale tests reduce many uncertain factors and their effects on the material response. Consequently, such tests are specially helpful for calibrating model parameters and validating the performance of existing constitutive models.

Since the assessment of a nuclear waste repository design is strongly dependent on the behaviour of the EBS, then the capability of a constitutive formulation to predict the main THM processes taking place at the different stages of a nuclear waste disposal is a matter of crucial importance. In that sense, one of the main goals of this Thesis has been the development of a fully-coupled THM mathematical formulation that considers:

- the existence of different pore structure domains in the porous medium. As mentioned in the previous section, the peculiar behaviour of the expansive clays (as bentonites) in comparison to other clayey soils can be properly explained if such a pore structure distinction is taken into account. A double-porosity formulation would be able to reproduce the structural evolution observed in this kind of material when submitted to subsequent wetting-drying cycles. Moreover, such a structural differentiation would permit a more precise evaluation of the effects caused by a clay fabric evolution, distinguishing between those processes affected by the fraction of large pores (as the mass flux of liquid water and vapour) from those related to the fraction of smaller pores (as the swelling of clay particles).

- the existence of structural coupling and mass transfer mechanisms among the distinct pore levels. Such structural interactions would relate the irreversible changes in the soil fabric to the physico-chemical processes occurring at the particle level (Gens and Alonso, 1992) and would explain the dependence of the deformation response of expansive clays with time (Alonso and Navarro, 2005).

- the thermal impact on the hydro-mechanical properties and the deformation behaviour of the expansive material. As indicated before, the changes in temperature play a central role in the performance of a clay barrier, since such thermal loadings not only affect the physical properties of the pore-water and cause water phase changes, but they could also induce significant changes in the water retention capacity of large and small pores and affect the swelling potential of such materials.

- the numerical robustness required to include (if necessary) new variables and/or constitutive laws to the ones considered in the current formulation. This is a desirable feature to keep in mind when developing and implementing a constitutive model, since it allows the continuous enhancement of existing formulations.

The implementation of the resultant double-porosity model (DPM) in CODE_BRIGHT (Olivella *et al.*, 1996) has allowed the performance of numerical simulations under isothermal and non-isothermal conditions. Therefore, the additional objectives of this research work have also been the following ones:

- The identification of those model parameters that could have a significant impact on the material response when submitted to THM loadings under distinct confinement conditions. For such a purpose, a series of constitutive analyses and parametric sensitivity studies have been performed in order to evaluate the general model potentialities and limitations.
- The calibration of some model parameters for the granular bentonite materials used in the HE-E experiment by back-analyses and comparison to the experimental data from the two aforementioned heating-hydration tests carried out by CIEMAT (Villar *et al.*, 2012b; 2016).
- The assessment of the model capability to reproduce satisfactorily a boundary value problem (the hydration of the heated columns of bentonite-based materials) and to predict the final state of the bentonite columns under near-saturated conditions.

1.3. THESIS TERMINOLOGY

Experimental evidences have shown that natural and compacted expansive clays usually possess different levels of pores (Romero, 1999; Lloret *et al.*, 2003; Hoffmann, 2005; Laird, 2006; Hoffmann *et al.*, 2007; Samper *et al.*, 2008), resulting in soil fabrics as the ones illustrated in Figure 1-2(a). Due to that and to the need to describe the factors that affect their swelling potential, distinguishing among the processes that take place at particle level and those ones that affect the soil structure, the following terminology is introduced and it will be employed hereafter:

- *Clay layer* or *elementary layer* – the basic structural "brick" of clay mineral crystals, composed by an aluminum octahedral sheet between two silica tetrahedral sheets, as in the case of smectites, vermiculites and illites (Mitchell, 1993).
- *Clay particle* or *clay platelet* – a pack of several elementary layers fastened together by Van der Waals forces, containing up to four layers of crystalline water in the interlayer pore space (Mašín and Khalili, 2016).
- *Clay aggregate* – the unit of the compacted double porosity medium, obtained by the assemblage of several clay particles (Gens and Alonso, 1992; Mašín and Khalili, 2016).
- *Micro-pores* – the voids within a clay particle (intra-particle pores) or a clay aggregate (intra-aggregate pores); consequently, both the interlayer pore space and the inter-particle voids are included (Lloret and Villar, 2007).
- *Macro-pores* – the voids among clay aggregates and other grains present in a soil (inter-aggregate pores) (Gens and Alonso, 1992).
- *Microstructure* or *microstructural level/medium* – the internal structure of individual clay platelets and aggregates of active clays and their vicinity, where the physico-chemical interactions are the prevalent phenomena governing the swelling/shrinkage of such clay minerals (Gens and Alonso, 1992; Alonso *et al.*, 2005; Wang and Wei, 2015).
- *Macrostructure* or *macrostructural level/medium* – the arrangement of clay aggregates and other soil grains with macro-pores among them, representing the macroscopic soil skeleton (Gens and Alonso, 1992; Sánchez *et al.*, 2005; Wang and Wei, 2015).

A simplified representation of the vicinity of a typical expansive clay aggregate is depicted in Figure 1-2(b). This conceptual structure represents the basic framework on which the theoretical features of the double structure model described in this Thesis will be addressed (see **Chapter 3** and **Chapter 4**).

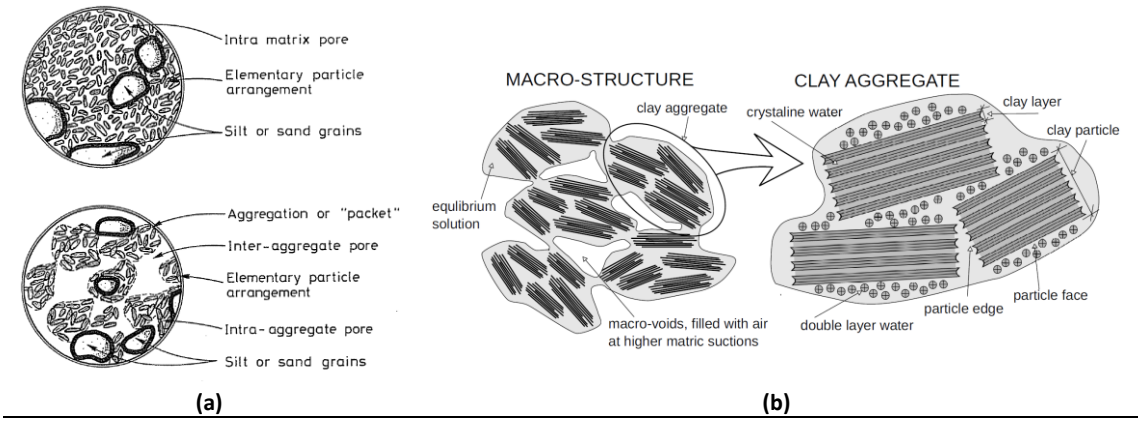

Figure 1-2: **(a)** Typical soil fabrics found in expansive clays (after Gens and Alonso, 1992); **(b)** Schematic representation of an aggregation of active clays (Mašín and Khalili, 2016).

1.4. THESIS LAYOUT

This document consists of the current introductory chapter and of nine more chapters (including the list of references) and one appendix (Appendix A), organized as follows:

- A second chapter, named as "Thermo-hydro-mechanical behaviour of expansive clays: literature review", in which the main environmental conditions and the constitutive and geotechnical properties controlling the shrinkage/swelling potential of active clays are described. The dependence of the swelling response of such clays on the changes in the water content in each pore structural level and on temperature changes is discussed. Furthermore, the main THM properties that justify the potential use of bentonites in engineered barrier systems are also listed. Special attention is given to the bentonite-based materials studied in some of the most relevant bentonite characterization projects, as the MX-80 bentonite. Finally, an overview of the main features, numerical performance and issues of the constitutive models characterized by a double pore-structure approach and developed by the UPC Geotechnical Group are given at the end of that chapter.

- The third chapter, "Double-Porosity Model (DPM) formulation I: Basic concepts, relationships and governing equations", as indicated by its title, deals with the fundamental ingredients to build a robust and fully-coupled double-porosity formulation capable of reproducing most of the observable responses of expansive clays due to changes in their water content under isothermal and non-isothermal conditions. In that sense, the basic geotechnical properties and relationships and the main THM constitutive equations to be taken into account at each structural level are defined in that chapter. The chapter ends with a short description of the finite element code (CODE_BRIGHT) used to implement the stress-strain constitutive law for the double-porosity model considered in this document.

- In the fourth chapter, entitled as "Double-Porosity Model (DPM) formulation II: Stress-strain constitutive laws in a thermo-elastoplasticity framework", the stress and the strain variables at both structural media are defined and the fully-coupled THM formulation of the double-porosity model is developed mathematically. The mechanical

interaction between the volumetric and elastic behaviour of the active clay particles and the elasto-plastic response of the soil skeleton as well as the existence of a water mass exchange between micro- and macro-pores are also considered.

- In the fifth chapter, titled as "Double-Porosity Model (DPM) formulation III: Explicit integration of the stress tensor and the double-porosity formulation in the context of a finite element approach", the main features related to the implementation of the mathematical formulation in CODE_BRIGHT are presented. The algorithm for integrating the stress tensor using an explicit, incremental method (the Modified Euler scheme) with automatic load stepping algorithm and error control is described in detail together with its main ingredients, that is, the trial step, the intersection with the current yield surface, the elastoplastic integration and the drift correction subroutines.

- The sixth chapter, named as "Application of the Double-Porosity Model to stress paths under isothermal conditions: constitutive and sensitivity analyses", the isothermal response of a cubic element of expansive material is modelled under different and controlled loading and confinement conditions. The main purpose of such numerical analyses is to check the model capabilities and limitations and to better understand the local swelling/shrinkage behaviour of the material and its dependence on some model parameters and boundary conditions.

- In the seventh chapter, termed as "Application of the Double-Porosity Model to stress paths under non-isothermal conditions: constitutive and sensitivity analyses", similar numerical modellings to the ones discussed in **Chapter 6** are performed but in this case, a heating episode precedes the controlled changes of water content in macro-pores. In that sense, the local thermal effects on both structural levels as well as the thermally-induced processes expected to occur inside an engineered barrier submitted to thermal loadings are taken in account.

- In the eighth chapter, "Application of the Double-Porosity Model to laboratory-scale heating-hydration experiments", the model predictions from the simulations of the hydration of the two heated bentonite columns by CIEMAT (Villar et al., 2012b, 2016) are compared to the available data and evaluated in the light of the main conclusions obtained from the analyses performed in **Chapter 6** and **Chapter 7**. Thermally-induced processes as the pore-water phase changes and the diffusive water vapour transport are also considered in the assessment and interpretation of the experimental data and the model results.

- Finally, in the last chapter of this document (**Chapter 9**), the main conclusions obtained from this Thesis and some suggestions for further research works are presented.

The list of the all quoted references in the Thesis is found at the end of this document (**Chapter 10**). Appendix A contains the mathematical description of the algorithm (Pegasus Algorithm) used to find the intersection with the yield surface during the performance of the trial step of the stress point algorithm implemented in CODE_BRIGHT.

1.5. PUBLICATIONS AND ACTIVITIES PERFORMED DURING THE PhD RESEARCH

The publications and research activities carried out during the development of this PhD, all of them related to the modelling of bentonite barriers by means of single- and double-porosity models, are listed below.

PUBLICATIONS IN JOURNALS

Gaus, I., Wieczorek, K., Schuster, K., Garitte, B., Senger, R., **Vasconcelos, R.** and Mayor, J.C. (2014). EBS behaviour immediately after repository closure in a clay host rock: HE-E experiment (Mont Terri URL). In: Clays in Natural and Engineered Barriers for Radioactive Waste Confinement. Geological Society, London, Special Publications, 400. 71-91.

CONFERENCE PROCEEDINGS

Vasconcelos, R. and Gens, A. (2015). Modelling infiltration tests on pelletized bentonite under non-isothermal conditions. In: Proceedings of the XIII International Conference on Computational Plasticity (COMPLAS XIII) – Fundamentals and Applications. September 1-3, 2015. Barcelona, Spain. 661-666.

Vasconcelos, R., Gens, A., Vaunat, J., Ruiz, D.F. and Villar, M.V. (2019). Modelling a heating-hydration bentonite-based column test using a double porosity approach. In: Proceedings of the XV International Conference on Computational Plasticity (COMPLAS XV). September 3-5, 2019. Barcelona, Spain.

KEYNOTE LECTURES

Gens, A., **Vasconcelos, R.B.** and Olivella, S. (2020). Towards higher temperatures in nuclear waste repositories. In: Proceedings of the 2nd International Conference on Energy Geotechnics. E3S Web of Conferences 205, 01001 (ICEGT -2020). DOI: https://doi.org/10.1051/e3sconf/202020501001

POSTERS

Garitte, B., Gens, A., **Vasconcelos, R.B.**, Vaunat, J., Gaus, I. (2015). The HE-E experiment (Mont Terri): modelling a large in situ heating test. In: Proceedings of the 6th International Conference – Clays in Natural and Engineered Barriers for Radioactive Waste Confinement. March 23-26, 2015. Brussels, Belgium. 532-533.

Gens, A., **Vasconcelos, R.B.**, Villar, M.V., Mayor, J.C. and Martín, P.L. (2015). Column tests on pellets-based barrier material: analysis and interpretation. In: Proceedings of the 6th International Conference – Clays in Natural and Engineered Barriers for Radioactive Waste Confinement. March 23-26, 2015. Brussels, Belgium. 558-559.

TECHNICAL REPORTS

Gaus, I., Garitte, B., Senger, R., Gens, A., **Vasconcelos, R.**, Garcia-Sineriz, J.-L., Trick, T., Wieczorek, K., Czaikowski, O., Schuster, K., Mayor, J.C., Velasco, M., Kuhlmann, U. and Villar, M.V. (2014). The HE-E Experiment: Layout, interpretation and THM modelling. NAGRA Arbeitsbericht NAB 14-53. NAGRA, Wettingen, Switzerland.

Gens, A. and **Vasconcelos, R.** (2018). HE-E Experiment: Modelling of the HE-E test – 1st Modelling Phase. Technical Note TN 2018-51 – Mont Terri Project (Phase 23).

Gens, A. and **Vasconcelos, R.** (2019). HE-E Experiment: Modelling of the HE-E test. Mont Terri Project TN 2019-43 – Mont Terri Project (Phase 24). Barcelona, Spain.

Vasconcelos, R., Pinyol, N., Alonso, E.E. and Gens, A. (2014). Modelling and interpretation of the EB experiment hydration & Interpretation of the final state of the EB experiment barrier. PEBS Deliverable D3.1-1 and D3.1-2.

Vasconcelos, R. (2011). Contribution to: "Long term performance of engineered barrier systems (PEBS). Mont Terri HE-E experiment: detailed design report. NAGRA Arbeitsbericht NAB 11-01. Gaus, I. (Ed.)."

Vasconcelos, R. (2012). Contribution to: "Design and predictive modelling of the HE-E test. PEBS Deliverable D3.2-1. NAB 12-003. Czaikowski, O., Garitte, B., Gaus, I., Gens, A., Kuhlman, U. and Wieczorek, K. (Eds.)."

UPC SEMINARS

Vasconcelos, R.B. (2015). Modelación del comportamiento hidromecánicos de una barrera expansiva de bentonita. In: Seminari de Recerca en Geotècnia (UPC). Marzo 10, 2015. Barcelona, España.

COURSES AND MEETINGS

BEACON (Bentonite Mechanical Evolution) – WP3/WP5 Annual Meeting (2018). January, 16-17. UPC BarcelonTech. Barcelona, Spain.

BEACON (Bentonite Mechanical Evolution) Training Course (2018). Hydromechanical behaviour of bentonite: constitutive and numerical modelling. January, 17-19. UPC BarcelonTech. Barcelona, Spain.

2. THERMO-HYDRO-MECHANICAL (THM) BEHAVIOUR OF EXPANSIVE CLAYS: LITERATURE REVIEW

2.1. INTRODUCTION

The most remarkable and distinctive feature of expansive soils is their proneness to exhibit significant changes in volume due to water content variations. In other words, these soils expand when the moisture content rises and shrink when they are dried. Changes in water content in the near-surface zone are mainly related to seasonal variations, to alterations in the surface drainage and in the vegetation coverage conditions or due to the local supply/removal of water to/from the ground induced by human activities (Johnson and Stroman, 1976; Jones and Jefferson, 2012). Expansive clays can also be easily identified by the shrinking and cracking of the ground surface after long dry periods in arid environments. This class of soils has a notable clay fraction content, whose mineralogy is the main property that responds for their differentiated volumetric behaviour in comparison to other clayey soils when their water content changes (collapsible soils, for instance). The presence of clay minerals, such as montmorillonite, vermiculite, etc., grants the swelling potential to moderate and high expansive soils. The term “swelling potential” will be used hereafter to designate both the percent swell (swelling deformation) and the swelling pressure observed or measured in such soils. The swell-shrink behaviour of clay-rich soils is enabled by the mechanical, geological and environmental conditions prevailing during the genesis and the geological history of such materials (Skempton, 1953; Gens and Alonso, 1992; Wyoming Multi-Hazard Mitigation Plan, 2014). Moreover, the actual volume change experienced by a mass of expansive soil also depends on the changes in environmental variables affecting the water content within the pores and on the magnitude of the mechanical loads applied by neighboring structures, as illustrated in Figure 2-1.

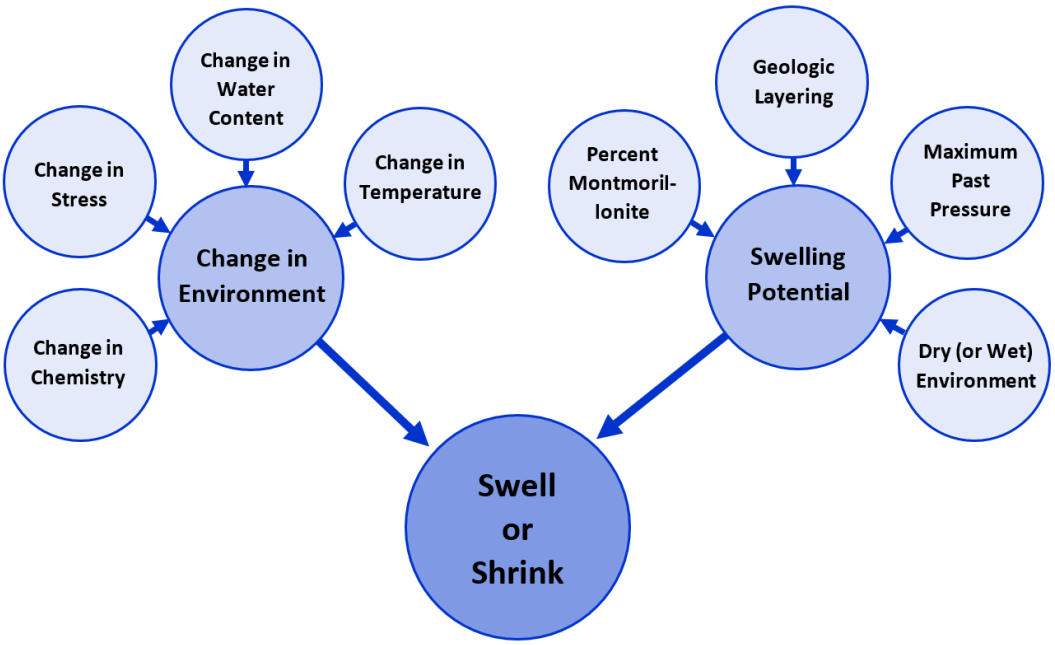

Figure 2-1: Intrinsic and environmental conditions controlling the in-situ swelling potential of expansive soils (Wyoming multi-hazard mitigation Plan, 2014).

Expansive soils are found in many parts of the world, particularly in arid and semi-arid areas (Salas and Serratosa, 1957; Fredlund *et al.*, 2012), wherein the evaporation rate is higher than the annual rainfall, which usually leads to a moisture deficiency in the soil. Consequently, those soils are subjected to seasonal cycles of strong drying and wetting paths due to natural environmental conditions. On the other hand, engineering issues due to the expansiveness of clayey soils in humid climates are limited to those regions that contain high-plasticity clays. The global distribution of expansive soils depends on geology, climate, hydrology, geomorphology and vegetation (Jones and Jefferson, 2012).

Differential heave due to the variation in soil water content causes damage to structures built or founded on expansive clays, especially in light buildings and pavements (Holtz and Gibbs, 1956; Jennings and Kerrich, 1962; Johnson, 1969). It is reported that, in many countries, the engineering problems associated with swelling-shrinking soils may exceed the combined damages from natural disasters, which represents an important source of enormous annual costs in such nations (Holtz, 1959; Jones and Holtz, 1973; Nelson and Miller, 1992; Driscoll and Crilly, 2000; Jones and Jefferson, 2012). As a consequence, a great number of studies concerned with the identification and characterization (Bain, 1971; Warkentin, 1972; Dakshanamurthy and Raman, 1973; Fredlund, 1975; Sridharan and Prakash, 2000), heave or the soil subsidence estimates (Fredlund *et al.*, 1980; Yoshida *et al.*, 1983; Walsh *et al.*, 2009; Vanapalli, 2012) and the main engineering issues associated with expansive soils (Simmons, 1991; Stavridakis, 2006; Elarabi, 2010; Houston et al., 2011) have been carried out throughout the past decades. These studies have focused mainly on the understanding of the physico-chemical processes that take place at clay particle level when the water content in the soil changes and on quantification or prediction of the induced volume changes. Furthermore, several engineering designs and treatment approaches to minimize the social and economic impacts generated by the overall

and the differential heave in constructions founded on swelling clays are also documented in the literature (Johnson and Stroman, 1976; Jeyapalan *et al.*, 1981; Tessema, 1984; Ardani, 1992).

Despite the problematic swelling-shrinkage behaviour of such clayey soils due to the temporal and/or spatial moisture variations, the in-depth understanding of the main phenomenological aspects and conditions that characterize their hydro-mechanical (HM) response has attracted the attention of the scientific community for the potential use of these materials as component of sealing barriers in radioactive waste disposal designs. A review of the most relevant features related to the swelling mechanisms, the properties affecting the swelling potential and the desirable engineering properties of bentonite-based materials subjected to non-isothermal conditions is briefly discussed in the following sections.

2.2. SWELLING BEHAVIOUR OF BENTONITE-BASED MATERIALS

Bentonites, a highly plastic clay originated by the chemical weathering of volcanic ash or glass, are largely composed by montmorillonite (Clem and Doehler, 1961; Johnson and Stroman, 1976), whose content (in weight) may reach values superior to 75%. The percentual proportion of montmorillonite contained in several bentonite-based materials proposed to be used as engineered buffers around high-level radioactive waste (HLRW) storage sites is shown in Table 2-1. Depending on the prevailing exchangeable cation attached to the bentonite particle surface, these swelling clays are classified as sodium-, calcium-, magnesium- or lithium-bentonites (Ravindra Reddy et al., 2017) whose exchangeable ions are Na^+, Ca^{2+}, Mg^{2+} or Li^+, respectively. However, most industry and engineering applications of bentonites employs Na- and Ca-bentonites since sodium and calcium are the most common exchangeable cations found in nature (Wayllace, 2008). Calcium-type bentonites are the most abundant natural bentonites (Johnson and Stroman, 1976). Nevertheless, sodium-bentonites, as the Wyoming bentonite, also termed as MX-80 bentonite in the literature, are more employed in geotechnical applications than calcium bentonites due to their high swelling potential and low hydraulic conductivity (Clem and Doehler, 1961; Mesri and Olson, 1971; Alther, 1987; Reschke and Haug, 1991; Villar and Lloret, 2007a). These geotechnical requirements together with a high radionuclide adsorption and a high heat transfer capacity provide the necessary long-term stability for a barrier system (Rizzi et al., 2012; Schanz and Al-Badran, 2014) in deep geological disposals. In such environments, bentonite-based materials are usually disposed as highly compacted blocks or as granular filling material, in pelletized form or mixed with non-expansive materials. Bentonites are also used in other engineering applications (as barriers in landfill and geosynthetic clay liners, for example) in which the high specific surface is a desirable property, especially for those situations in which the solid-liquid-chemical species interaction determines the efficiency of the chosen engineering solution.

Table 2-1: Montmorillonite content of some commercial bentonites.

Bentonite Type	% Montmorillonite (weight)	Origin	References
MX-80	75 - 92	Wyoming (US)	Pusch (1982); Duplay *et al.* (2002); Tang *et al*. (2008); Seiphoori *et al*. (2014); Bennett (2014)
FEBEX	89 - 95	Andalusia (ES)	ENRESA (2000); Villar (2002); Lloret and Villar (2007)
Volclay MX-80	85 - 95	-	Melamed and Pitkänen (1996); Komine *et al.* (2009)
Calcigel	50 - > 70	Bavaria (DE)	Agus (2005); Svensson *et al.* (2011)

The swelling potential of bentonites is tightly related to some "internal" and "external" factors (Schanz and Al-Badran, 2014). The internal factors are the ones that govern the physico-chemical interactions occurring at particle level while the external factors include those features that affect the arrangement of soil particles. As internal factors, it can be mentioned the clay mineralogy, the specific surface area (SSA) of individual clay particles, the cation exchange capacity (CEC) and the pore fluid nature, which is related to the type and to the concentration of chemical species/ions present in it. On the other hand, the dry density, the moisture content, the compaction procedures (for compacted soils), the stress history and the loading paths are the major external factors that influence the swelling behaviour of such materials.

2.2.1. SWELLING/SHRINKAGE BEHAVIOUR AT MICROSTRUCTURAL LEVEL

The swelling or the shrinkage mechanism of natural and compacted active soils can be explained through the physico-chemical processes occurring at nano- and micro-scale levels. Therefore, it is crucial to highlight the factors controlling the swelling potential of individual clay particles of the smectite group, a class of clay minerals with the largest specific surface areas (see the next section). This property, in conjunction to the net negative surface charge common to all clay minerals, leads to a high affinity of such materials to attract a large amount of ions present in the soil in order to compensate the surface charge deficit. The hydration of these ions by the pore-water molecules and the development of water layers due to the ionic concentration and its distribution near the clay particle surface are the main cause of the local volumetric expansion, which in turn, leads to a general tendency of the whole soil to swell. The nature of the prevalent ion in the soil solution also determines the magnitude of swelling, since the type of the exchangeable cation controls the amount of water that a clay mineral can imbibe. Many geotechnical properties of fine-grained soils depend on the development of surface forces (related to the SSA and the type of the dominant cation around the particle surface) and, due to that, such properties can be used as an indicator of the swelling potential of a clayey soil.

Although the shrinkage mechanism and the processes that occur during the drying of an expansive clay (as crack openings and tensile stresses developed during episodes of intense drying) cannot be explained satisfactorily by the phenomena driving the swelling mechanism, however, the factors that affect the swelling potential of a soil also influence on its response when it dries. In that sense, and taking into account that only a small and limited portion of the

engineered barrier system around the heat source is expected to suffer an intense drying during the lifetime of the deep HLRW repository, a special attention will be devoted to describe the swelling response (during wetting) of active clays. Therefore, in the following sections, only the main factors that govern the swelling mechanism at microstructural level, as well as the mechanism itself, will be presented.

2.2.1.1. CLAY MINERALOGY

The major aspect that confers the remarkable expansiveness to swelling clays is the amount and type of the dominant expansive clay mineral present in the soil (Johnson and Stroman, 1976; Gens and Alonso, 1992). Montmorillonite, a smectite mineral characterized by its high swelling potential, is one of the main mineral components of expansive soils, as bentonites for instance (as shown in Table 2-1). Chemically, this clay mineral is a hydrated aluminum silicate that also contains alkali and alkaline-earth metals in its chemical composition (Clem and Doehler, 1961). Structurally, an elementary layer of montmorillonite is made of an aluminum octahedral sheet between two silica tetrahedral sheets (Mitchell, 1993). Montmorillonite platelets are constituted by the assemblage of several elementary layers separated by layers of crystalline water of varying thickness (Johnson, 1969; Rizzi et al., 2012), as illustrated in Figure 2-2. A typical montmorillonite particle has a plate-shaped configuration with an average diameter in the range of 1000 Å – 10000 Å, i.e., 0.1 – 1.0 μm and an interlayer thickness, also termed as basal distance (d_{001}), in dry conditions, around 10 Å (van Olphen, 1963a; Pinto, 2000; Forouzan, 2016). However, different shapes and sizes are also reported in the literature, depending on the experimental techniques employed for evaluating them (see West, 1952; Kahn, 1963; Arnott, 1965; Jonas and Oliver, 1967; Schramm and Kwak, 1982; Nadeau, 1985; Mitchell, 1993; Ravindra Reddy *et al.*, 2017).

Adjacent structural layers of montmorillonite are kept together by Van der Waals forces and by exchangeable cations (Pinto, 2000; Arifin, 2008). These bonds are weak enough to allow water molecules or other polar cationic fluids to infiltrate between clay layers (Mitchell, 1993; Arifin, 2008; Forouzan, 2016), which leads to an increase of the basal distance and, consequently, the expansion of the clay particle. As in other clay minerals, montmorillonite lattices have a net negative charge distributed on their surface due to the partial isomorphic substitution of lower for higher valence cations as Al^{3+} for Si^{4+} (in the tetrahedral structure) and Mg^{2+} or Fe^{2+} for Al^{3+} (Pinto, 2000; Wayllace, 2008). Consequently, cations and water molecules (behaving as electrical dipoles) are attracted to the layer/particle surfaces in order to balance their charge deficit (Bennett, 2014).

As mentioned previously, montmorillonite is composed of several to hundred structural units depending on the water content and the type of exchangeable cation (Pusch *et al.*, 1990; Mitchell, 1993; Saiyouri *et al.*, 2004). Moreover, Saiyouri *et al.* (2004) also reported that the number of elementary layers in a montmorillonite platelet is dependent on the compaction conditions, especially at high suction values (higher than 3 MPa, in that experimental study).

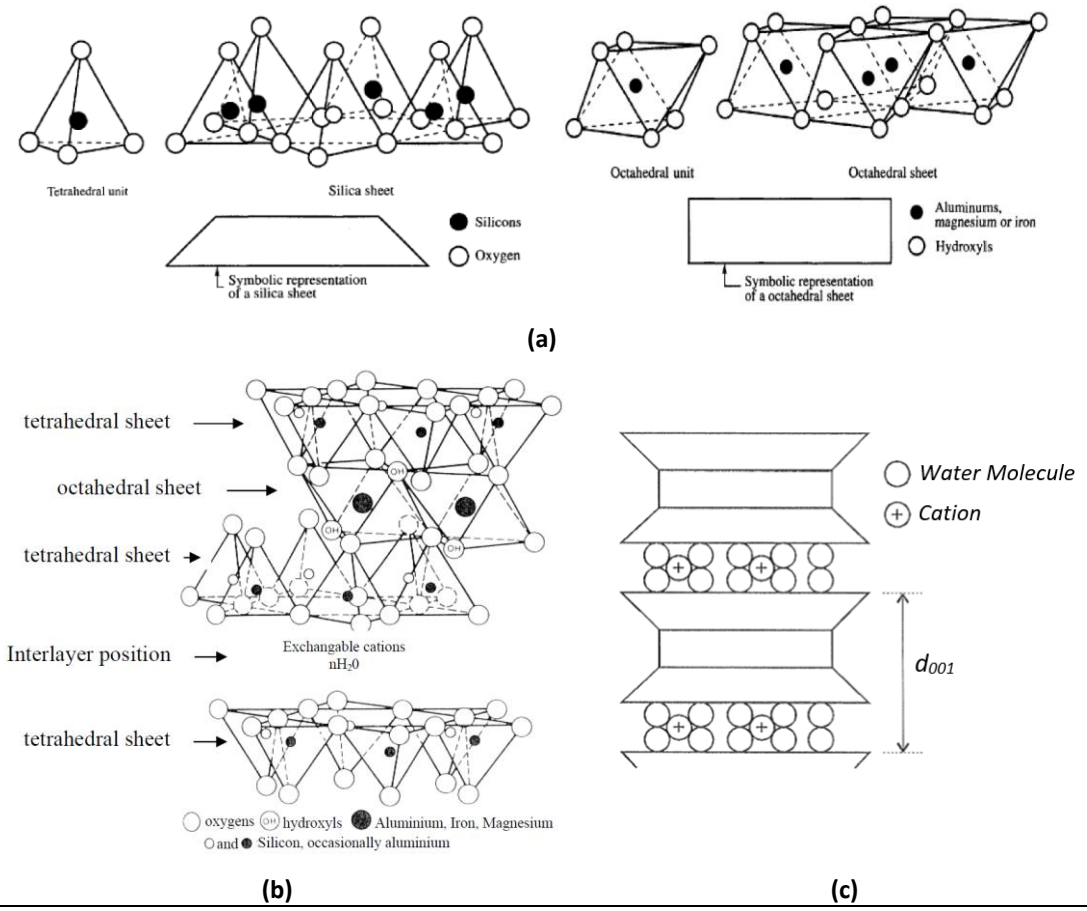

Figure 2-2: **(a)** Basic structural units in mineral clays (after Murthy, 2002); **(b)** structural representation of the montmorillonite mineral (Mitchell, 1993); **(c)** schematic representation of a smectite-group clay with water molecules in the inter-lamellar space (Pinto, 2000).

2.2.1.2. SPECIFIC SURFACE AREA (SSA)

Another intrinsic characteristic of montmorillonites that explains their remarkable behaviour in presence of water is their high specific surface area. The specific surface of a clay particle is defined as its total (external + internal) surface area per unit of mass, which is usually expressed in m^2/g. Furthermore, it increases as the particle size decreases (Rieke, 1982). Typical values for the specific surface of the main clay minerals are given in Table 2-2 (from Mitchell, 1993). Since smectites and vermicullites are considered as the smallest clay minerals, then the SSA is higher in such clay groups (in comparison to the other common pure clays). Moreover, a wide range of values for the SSA of clay minerals is found in the literature, as shown in Table 2-2. Such differences are a consequence of the methodology employed to estimate this physical property once some techniques only measure the external surface area (as the sorption of gas – BET – method or the calorimetric method) while others also take into account the internal surface of clay particles (as the EGME adsorption method). For more information on the methods for evaluating the SSA of the smallest particles in a soil, their advantages and limitations and the comparison of specific surface data from different techniques see, for instance, Mooney *et al.* (1952), Sears (1956), Heilman *et al.* (1965), Ross (1978), Mulla *et al.* (1985), Kellomäki *et al.* (1987), Heng and Fong (1991), Santamarina *et al.* (2002), Yukselen and Kaya (2006), Arnepalli *et al.* (2008), Macht *et al.* (2011) and Khorshidi *et al.* (2017).

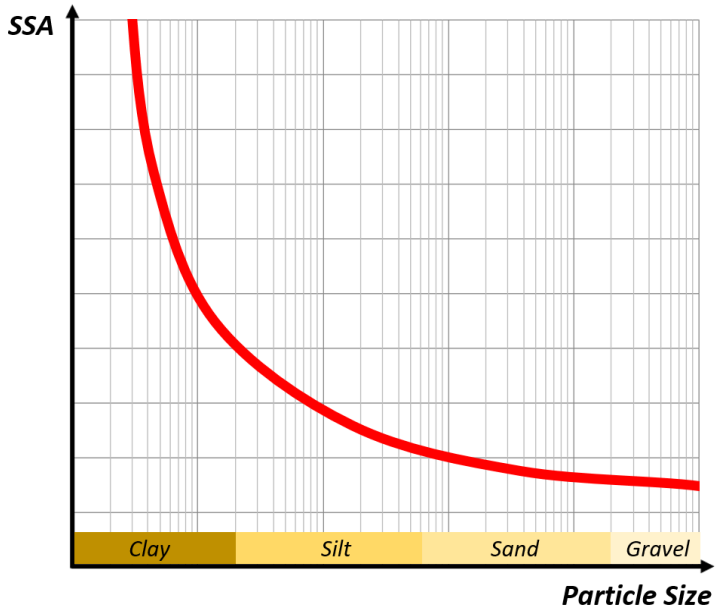

Figure 2-3: Relationship between the specific surface area and the size of a soil particle.

Table 2-2: SSA of common clay minerals in fine-grained soils (after Mitchell, 1993).

Clay Mineral	Structure	External SSA (m^2/g)	Internal SSA (m^2/g)
Halloysite	1:1	10-20	-
Kaolinite	1:1	35-70	-
Smectite	2:1	50-120	700-850
Illite	2:1	65-100	-
Vermicullite	2:1	40-80	800-900
Chlorite	2:1:1	10-40	-

Note that the amount of internal surface area is negligible for non-expansive clay minerals (as kaolinites) whereas expansive minerals (as smectites and vermicullites) have a great deal of internal as well as external surface. In the case of expansive minerals, the accounting for the internal interlayer surfaces is crucial for quantifying properly the interaction processes at the liquid-solid interface as, for instance, the amount of water molecules required to hydrate all the unbalanced charges in the immediate vicinity of a clay particle, which in turn reflects on its total swelling. Experimental data from the literature for the SSA of montmorillonite-rich clays vary in the range of 150-800 m^2/g.

2.2.1.3. EXCHANGEABLE CATION AND CATION EXCHANGE CAPACITY (CEC)

Negative charges on clay particles are usually balanced by positive ions dissolved in soil aqueous solution. Since such unbalanced charges are distributed on the particle surface (interlayer and external surfaces), then the sorption capacity of chemical species in a soil solution is intimately related to the (total) specific surface area of the clay minerals. In that sense, the higher the

specific surface, the higher the amount of ions/molecules attracted to the clay surface due to the higher unbalanced negative charges. Some of these positive ions attracted by the net negative charges of a clay particle (exchangeable ions) can be exchanged by other ions present in the soil (van Olphen, 1963a). As the total number of cations surrounding a clay mineral increases with its specific surface, thus the amount of exchangeable cations also changes in the same proportion. The nature and the concentration of the predominant exchangeable ions have a large impact on clay behaviour and on its physical properties (Clem and Doehler, 1961; Pinto, 2000).

The cation exchange capacity (CEC), given in meq./100g, is defined as the total sum of exchangeable cations absorbed (in miliequivalents), at a given pH, required to balance the charge deficit of one hundred grams of dry clay (Oweis and Khera, 1998). This property is an indication of the potential of a clay in retaining chemical species, a desirable feature (related to the high specific surface) in geotechnical applications in which the solid-liquid-chemical species interaction determines the efficiency of an engineering solution (as the retardation of contaminant flows in landfill sealants, for example). The usual values for the CEC of common clay minerals together with their specific surface area are given in Table 2-3. These values evidence the straight relation between both mineral properties. On the hand, the CEC of the main exchangeable cations present in some bentonite-based materials used for the containment and isolation of radioactive waste in deep geological disposals is shown in Table 2-4.

Table 2-3: Cation exchange capacity for common clay minerals.

Mineral	**Specific Surface (m^2/g)**	**CEC (meq./100g)**
Kaolinite	10-20	3-10
Illite	80-100	20-30
Montmorillonite	800	80-120
Chrolite	80	20-30

Table 2-4: CEC and Chemical composition of some commercial bentonites (after Mašín and Khalili, 2016).

Bentonite	**Dominant exch. cation**	**CEC (meq./100g)**	**Na (meq./100g)**	**Ca (meq./100g)**	**Mg (meq./100g)**
MX-80	Na	88	67	8	5
FEBEX	Ca	111	25	47	36
Kunigel-V1	Na	73	41	29	3
Volclay	Na	101	57	29	13

As mentioned before, bentonites have been selected for engineered barriers because of their high retention capacity of radionuclides (a consequence of their mineralogy and their large SSA), their high swelling potential to close gaps and preferential flux paths during saturation and their lower liquid mobility among other advisable properties. The low liquid permeability of such materials, especially when compacted at higher dry densities (which leads to a reduction of porosity), contributes to further restrain the flux of chemical species as contaminants and radionuclides through the porous medium. It is important to remark that the CEC also serves for

indicating the shrink-swell capacity of a clayey soil. In other words, the higher the CEC, the higher the water adsorption potential (both related to a high SSA) and, consequently, the higher the soil swelling potential (Forouzan, 2016).

2.2.1.4. CLAY-ION-WATER INTERACTION AND CLAY HYDRATION

The type and amount of clay minerals, pore fluids and exchangeable cations influence the amount of water that may be attracted and held between clay platelets (Johnson and Stroman, 1976). In expansive clay minerals, as montmorillonite, the hydration of exchangeable ions and the clay mineral surfaces is the main electro-chemical mechanism controlling the soil-water retention capacity at low humidity conditions (van Olphen, 1963a; Pusch, 1982; Arifin, 2008; Rizzi et al., 2012), for suctions ranging from 20 MPa to 550 MPa (Wayllace, 2008). From a dry state, as the water content in the immediate vicinity of clay particles increases, water molecules are absorbed between the elementary clay layers in order to hydrate the exchangeable cations. These water molecules, due to their electrical dipole structure, are oriented in relation to the clay particles and the exchangeable cations (Pinto, 2000). During the interlayer cation hydration, discrete layers of water molecules (hydrate layers) are successively introduced between the surfaces of adjacent clay unit layers (Arifin, 2008; Wayllace, 2008; Bennett, 2014). The increase of the ionic radii of the hydrated cations (see Table 2-5) results in the increase in the basal distances, which in turn, tends to generate an overall volumetric expansion of the soil mass, as illustrated in Figure 2-4. This type of swelling mechanism related to the hydration of exchangeable cations and the clay mineral surfaces is referred to as the *crystalline swelling* (Laird, 2006; Arifin, 2008).

The number of hydrate layers at fully saturated conditions is dependent on the type of the dominant interlayer cation (Pusch *et al.*, 1990; Arifin, 2008). Furthermore, the magnitude of the basal spacing due to the crystalline swelling tends to decrease with increasing the cation valence (Laird, 2006). The number of water layers and the corresponding basal distances of a montmorillonite during the hydration process of four different exchangeable cations are shown in Table 2-6, as reported in Pusch *et al.* (1990). Note that up to three layers of water molecules may be found in the inter-lamellar spacing when the prevailing cations are Na^+ and Mg^{2+}. Saiyouri *et al.* (2004) reported the development of up to four hydrate layers between elementary clay units during the saturation process of a sodium bentonite (MX-80). In fact, the highest swelling capacity among the montmorillonite group occurs for the sodium-type bentonites (Arifin, 2008), as confirmed by the data in Table 2-6.

Table 2-5: Radii of dehydrated and fully hydrated exchangeable cations (after Bennett, 2014).

Exchangeable Cation	Unhydrated Radius (Å)	Hydrated Radius (Å)
Mg^{2+}	0.66	18.0
Ca^{2+}	0.99	9.60
Na^{+}	0.97	7.90
K^{+}	1.33	5.30

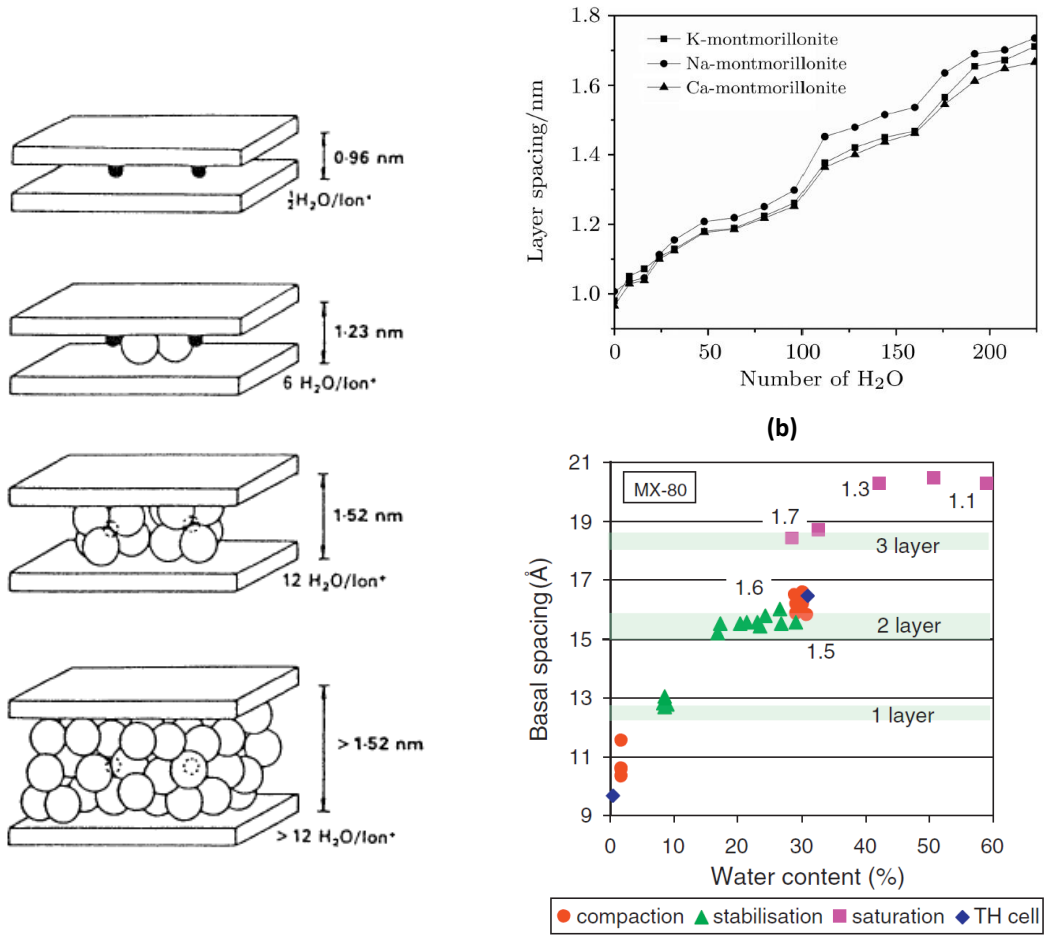

Figure 2-4: **(a)** Schematic representation of the swelling process with the increase in the number of water molecules in the inter-lamellar space (Grauer, 1990); increase in the basal distance with **(b)** the number of water molecules (Tao *et al.*, 2010) and **(c)** the water content (Villar *et al.*, 2012a).

Table 2-6.: Thickness (in angstroms) and complete hydrate layers for different exchangeable cation in a montmorillonitic soil (after Pusch *et al.*, 1990).

	d001 (Å)			
Exch. Cation	**0-hydrated layer**	**1st hydrated layer**	**2nd hydrated layer**	**3rd hydrated layer**
Mg^{2+}	9.52	12.52	15.55	18.60
Ca^{2+}	9.61	12.50	15.25	-
Na^{+}	9.62	12.65	15.88	19.36
K^{+}	10.08	12.50	16.23	-

As the moisture content increases and the surface hydration becomes less significant, water molecules and exchangeable ions (attracted to the external platelet surface) tend to diffuse away from the clay particles towards equilibrium positions (Lambe and Whitman, 1979; Arifin, 2008; Bennett, 2014) as the result of a combination between the electrostatic Coulomb forces and the Brownian motion (Bennett, 2014). The region around the clay particle in which the cations or counter-ions in aqueous solution are disposed is termed the diffuse double layer (DDL). Cation concentration drops with the distance from the clay surface and its distribution in the vicinity of a clay particle is depicted in Figure 2-5. The thickness of the DDL depends on the

type of exchangeable ion and its concentration in the soil solution (Wayllace, 2008; Forouzan, 2016). Therefore, a thicker DDL is expected to develop between the external surfaces of adjacent clay particles when the dominant cation has a lower valence (Forouzan, 2016) and the concentration of such ions is lower (Mitchell and Soga, 2005). However, the DDL can also develop between elementary layers of Na-montmorillonite once it has been observed that the hydration process can induce the breakage of larger clay particles into smaller ones and even into elementary layers (Pusch, 2001b; Laird, 2006). In that sense, sodium-type bentonites have higher swelling potential in comparison to calcium bentonites. This type of clay-water interaction, also termed as the *double layer swelling* or the *osmotic swelling*, is a result of the repulsion caused by the overlapping of interacting double layers (Pusch *et al.*, 1990; Mitchell, 1993; Delage *et al.*, 2006; Laird, 2006; Arifin, 2008) and it becomes relevant when the soil is close to its full saturation (Wayllace, 2008). The Gouy-Chapman double layer theory can explain the development of the DDL in expansive materials (Wayllace, 2008) and consequently, it can be used to estimate the swelling pressure of bentonite-based materials (van Olphen, 1963a; Mitchell, 1993).

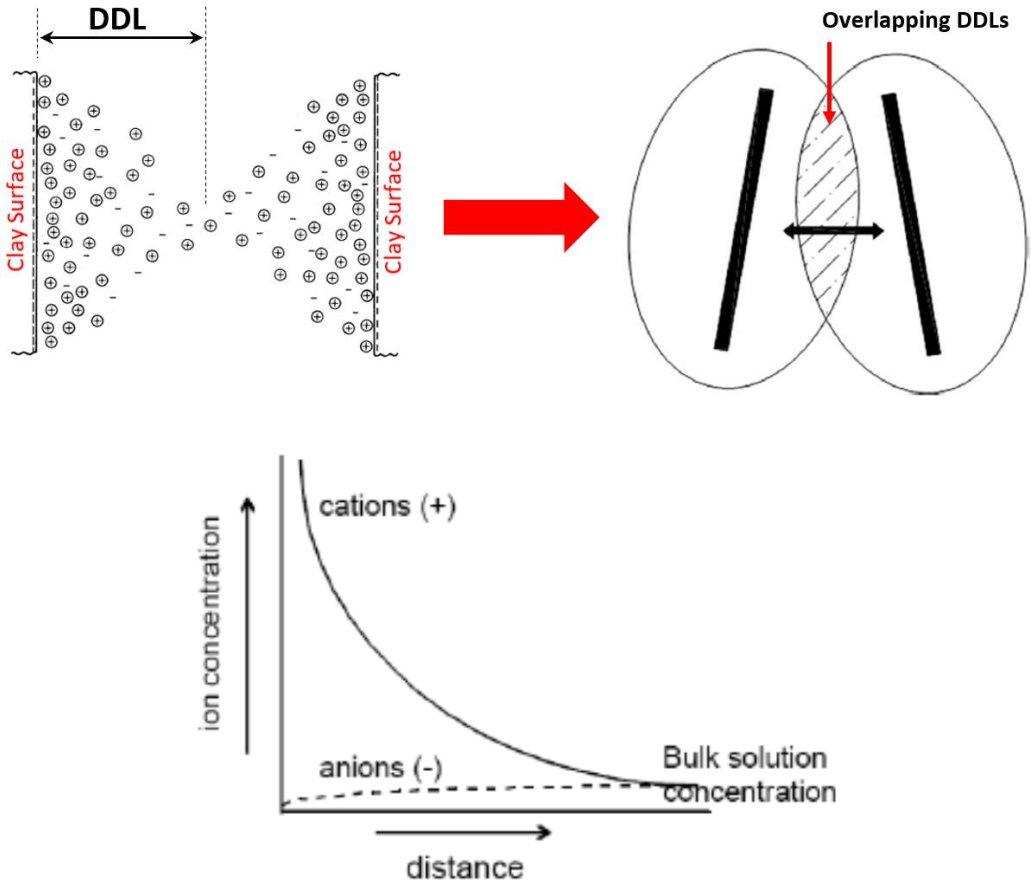

Figure 2-5: Distribution of ions around adjacent clay particles with a schematic representation of their interacting and overlapping diffuse double layers (DDL) and the resultant repulsion mechanism between them (up) (after Bayesteh and Mirghasemi, 2015) and ionic concentration with the distance from the clay surface (down) (after Mitchell, 1993).

The innermost layer of the DDL, which is tightly adhered to the external surface of clay particles, is the so-called *adsorbed water*. The amount of adsorbed water in the double layer, with respect to the total volume of water-saturated pores, varies strongly with the type of clay mineral, as shown by the data in Table 2-7. According to these experimental data, adsorbed moisture

content is higher for montmorillonite soils. For comparison purposes, the relative thicknesses of the adsorbed water layer developed around typical sodium-montmorillonite and kaolinite particles are illustrated in Figure 2-6. Consequently, montmorillonitic clays are much more active, plastic, deformable and prone to expand when moisture content increases in comparison to kaolinite-rich soils. In an air-dried mass of clayey soil, the water content is high enough to form a very thin film of water surrounding the soil particles, what is termed as hygroscopic water (Caputo, 1996). This type of soil-water can be completely removed by oven drying (usually, at temperatures higher than100°C). Its amount in the porous medium depends primarily on the clay mineralogy. Since the hygroscopic water is found around the soil particles (and not filling pores), it is expected that the hygroscopic moisture content is higher for montmorillonite soils. Again, the higher specific surface area of montmorillonites is the crucial physical property that governs the clay-water interaction, which in turn determines the characteristic behaviour of bentonites in contact with water (in liquid or in vapour form).

Table 2-7: Volume of adsorbed water in 1nm thick DDL for saturated clays at a void ratio of 2.5 (Quigley and Fernandez, 1989).

Clay Mineral	Specific Surface (m^2/g)	Volume of adsorbed water in double layer (% pore volume)
Kaolinite	20	2
Illite	100	9
Montmorillonite	800	70

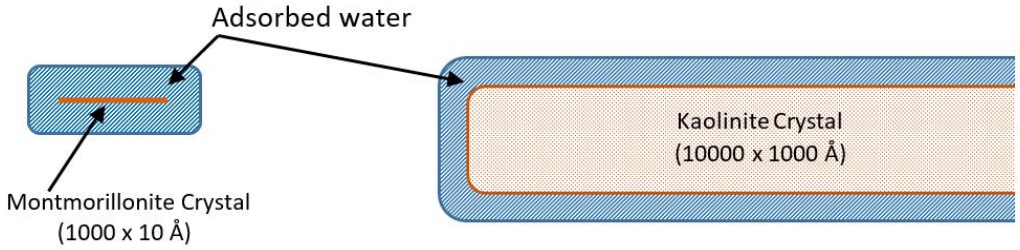

Figure 2-6: Relative sizes of adsorbed water layers in Na-montimorillonite and Na-kaolinte (after Lambe, 1958).

For low values of relative humidity, the water content of an expansive clay is enough to form an interconnected film of liquid water around the external surface of clay platelets or aggregates and around other soil particles (Cases *et al.*, 1992). As the hydration process continues, micro-pores are gradually saturated (Cases *et al.*, 1992; Jacinto *et al.*, 2012). Close to the full saturation of the expansive clay, the larger pores (macro-pores) are also filled with the so-called free water (Rizzi *et al.*, 2012). This type of soil water percolates through the pores of a soil and its movement is governed by hydraulic laws as the well-known Darcy's law. The water content in a mass of unsaturated soil is described by the soil-water retention curve (Lloret *et al.*, 2003; Villar and Lloret, 2004) which, in turn, depends on the pore size distribution. Because the free water in a compacted sample is usually found in large pores, its amount depends on the initial dry density, which is affected by the compaction conditions – see **Section 2.3** and **Section 2.4.1** for a more detailed discussion on this matter. On the other hand, it is commonly assumed that compaction procedures do not affect the evolution of micro-porosity when the expansive clay is far enough from its saturated state (Delage *et al.*, 2006). Moreover, experimental evidences have shown

that water in compacted expansive soils are found mainly into the micro-pores for high suction values (Romero *et al.*, 1999), hydrating the clay mineral surface and the exchangeable cations in the interlayer space. Therefore, in compacted specimens of active clays (as compacted bentonite samples), the amount of water retained in micro-pores do not depend on the dry density but on the SSA and the clay mineralogy (Jacinto *et al.*, 2012), and micro-pores tend to be saturated before macro-pores when a hydration process (from a dry state) takes place.

2.2.2. SWELLING BEHAVIOUR AT MACROSTRUCTURAL LEVEL

The magnitude of the interactive forces at particle level and the volumetric response of expansive clay minerals to changes in water content can be quantified indirectly by means of some soil properties measured in laboratory tests. In some engineering applications, laboratory activities are required to evaluate geotechnical properties as an indicator of the swelling potential of a clay, as the soil consistency limits, the soil plasticity and the clay activity. In other situations, swelling tests are carried out to quantify the swelling potential of a clay as a previous and essential requirement for analyzing the design of any geotechnical structure. The swelling potential can be estimated by hydrating the expansive clay at constant load (free swell, unconfined) conditions or at constant volume (isochoric, confined) conditions. These two types of laboratory tests may be implemented in one-dimensional, usually the vertical direction in oedometer apparatus, or in three-dimensional configurations (Jones and Jefferson, 2012). Typical oedometer test curves for an initial unsaturated expansive clay are shown Figure 2-7, in which the wetting path ($A \rightarrow B$) occurs at a constant token pressure (at left) or at confined conditions (at right). When in contact with water or electrolyte solutions, the swelling potential of an expansive soil is evidenced by an increase in the sample volume in unrestrained conditions or by the development of swelling pressure under constrained conditions. In the following sections, the main features of those experimental procedures are described.

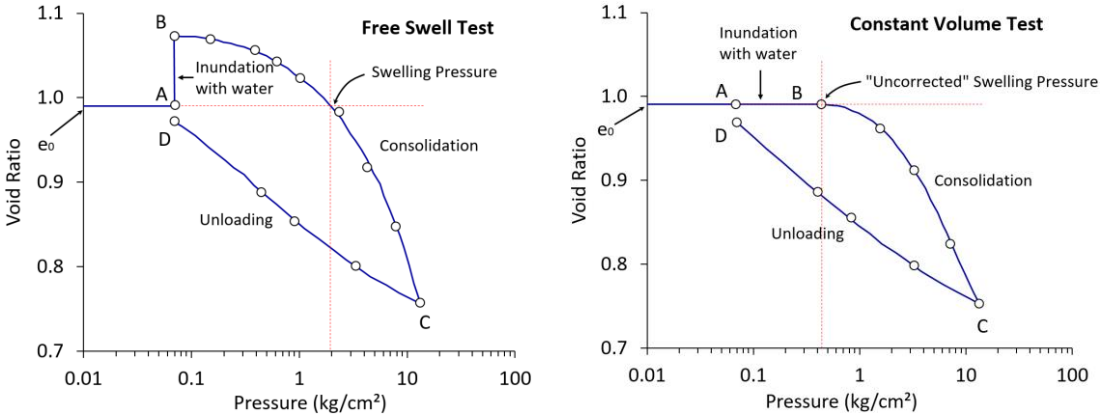

Figure 2-7: Typical consolidation responses from expansive soils wetted under unconfined (left) and confined (right) conditions (after Fredlund, 1969).

It is important to mention that the swelling behaviour depends on the changes in the clay fabric (Gens and Alonso, 1992; Jones and Jefferson, 2012). The effects of the sampling disturbance should be emphasized when measuring swelling deformations or pressures from undisturbed samples and comparing such values with the ones obtained from remolded/compacted samples.

Moreover, the laboratory method used for estimating the swelling properties of an expansive clay specimen has a significant impact on the measured data, as widely reported in the literature and illustrated in Figure 2-8. Some authors (Brackley, 1975; Justo *et al.*, 1984) attributed the discrepancies in the estimates of swelling potential to the differences in the stress paths followed by the experimental procedure selected to measure them.

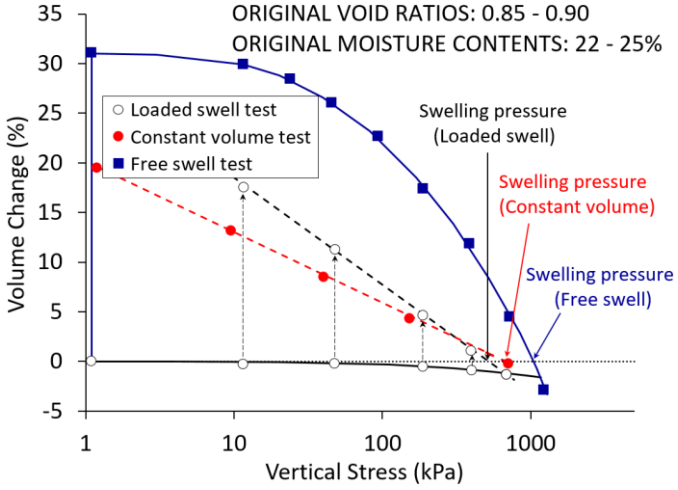

Figure 2-8: Influence of the swelling test procedure on the assessment of the swelling pressure (after Brackley, 1975).

As discussed in the previous sections, the swelling of expansive clays also depends on the type and amount of clay fraction. The initial dry density, the water content, the water chemistry, the applied loads and the confining pressure also play a crucial role on the development and amount of swelling deformations (heave) and swelling pressures. Sridharan *et al.* (1986a) and Jayalath *et al.* (2016) also pointed out the relevance of some procedural factors on the measured data from swelling pressure tests, such as the method employed for determining the swelling potential, the size and shape of a clay sample and the lateral friction between the sample and the oedometer cell.

2.2.2.1. PLASTICITY, ATTERBERG INDEXES AND CLAY ACTIVITY

Empirical relationships between some index parameters and the expansive characteristics of a clay are widely reported in the literature (Reeve *et al.*, 1980; Holtz and Kovacs, 1981; Oloo *et al.*, 1987). A remarkable engineering property of all clayey soils is their capacity of deforming continuously (without cracking) under a finite force, maintaining its deformed shape after the removal of the applied force (Andrade *et al.*, 2011). That property is defined as the soil plasticity (Perkins, 1995), which depends primarily on the water content and the nature of the clay fraction (Andrade *et al.*, 2011). In Geotechnical Engineering practice, the water content of a (remolded) cohesive soil defines the states of consistency of that soil (solid, semi-solid, plastic, liquid). The consistency limits, also termed as the Atterberg limits, are the most widely employed geotechnical indexes for the identification, classification, description and prediction of behaviour of fine-grained soils (Gorączko and Olchawa, 2017). Soil plasticity is then defined over a range of moisture content delimited by two Atterberg limits: the lower plastic limit (the plastic limit, PL) and the upper plastic limit (the liquid limit, LL), as shown in Figure 2-9. The plastic limit

is the lowest water content at which a soil can be molded without cracking (Bain, 1971; Andrade et al., 2011; Gorączko and Olchawa, 2017) while the liquid limit corresponds to the boundary between plastic and liquid consistency, at which the soil starts behaving like a viscous fluid (Bain, 1971; de Jong *et al.*, 1990; Dolinar *et al.*, 2007; Polidori, 2007; Andrade *et al.*, 2011). The plasticity index (PI), defined by the difference between the liquid limit and the plastic limit, $\mathrm{PI} = \mathrm{LL} - \mathrm{PL}$, indicates the range of water content over which the soil behaves plastically (Bain, 1971; Pinto, 2000). The several regions defining the states of consistence in fine-grained soils as function of their water content are indicated in Figure 2-9 while typical values of Atterberg indexes for some montmorillonitic clays are given in Table 2-8.

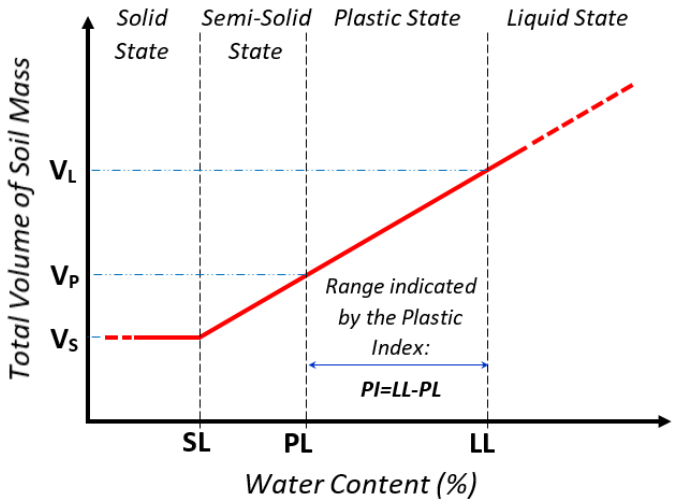

Figure 2-9: States of consistency in a fine-grained soil.

Table 2-8: Atterberg limits of montmorillonite minerals (Lambe and Whitman, 1979).

Exchangeable Cation	Liquid Limit (LL) (%)	Plastic Limit (PL) (%)	Retraction Limit (%)	Plasticity Index (PI) (%)
Na	710	54	9.9	656
K	660	98	9.3	562
Ca	510	81	10.5	429
Mg	410	60	14.7	350
Fe	290	75	10.3	215

As the swelling potential of a clay increases with the liquid limit, this Atterberg index provides a convenient indicator of the swelling potential of such soils (Johnson and Stroman, 1976; Lutenegger and Cerato, 2001). Since these soil properties depend on the amount of water a clayey soil can imbibe (Jones and Jefferson, 2012), it is expected the existence of a correlation between the liquid limit and those parameters/properties controlling the volume of water in saturated clays, as the clay fraction, the SSA, the type of exchangeable cation and the DDL thickness. In general, the liquid limit of a soil increases with the specific surface area (SSA) of the soil particles (Rieke, 1982; Sridharan *et al.*, 1986b; Lutenegger and Cerato, 2001; Olchawa and Gorączko, 2012). As clay particles are the smallest components in a soil, it may be concluded that the liquid limit of a soil tends to rise with its clay fraction. Moreover, the existence of a linear relationship between the liquid limit and the specific surface area has been reported for many fine-grained soils. Nevertheless, this linear dependence seems not to be so evident in

other natural clays, as in some rich-montmorillonite soils, as reported in Sridharan *et al.* (1986b). Results from other experimental studies (Muhunthan, 1991; Lutenegger and Cerato, 2001; Olchawa and Gorączko, 2012) suggested alternative, non-linear correlations between these two soil properties. Nevertheless, it is important to mention that any attempt to establish such a relation should take in account other variables as the clay content in the soil, the mineralogical composition, the cation exchange capacity and the surface charge (Sridharan *et al.*, 1986b). Figure 2-10 compiles some experimental relationships between the liquid limit (LL) and the specific surface area (SSA) from the literature.

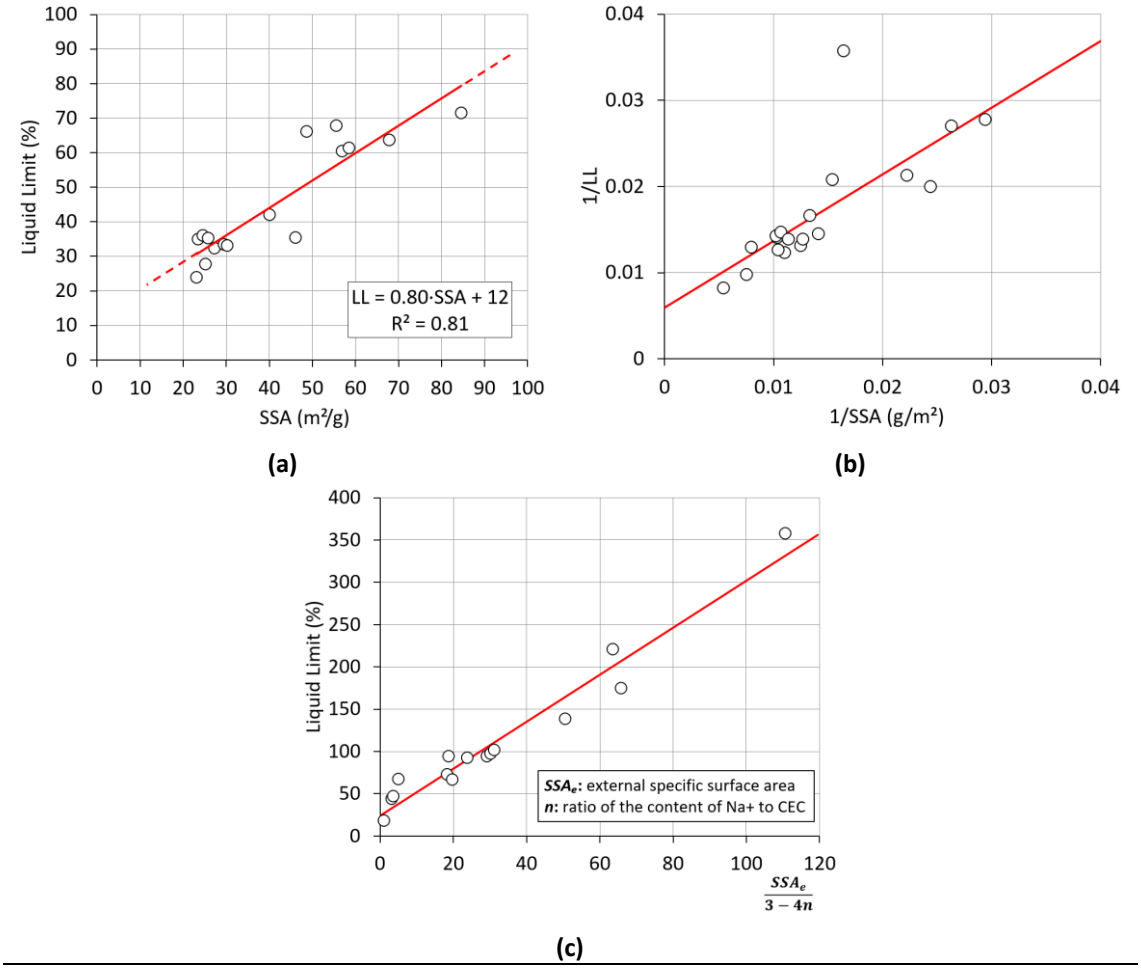

Figure 2-10: Empirical relationships between the liquid limit (LL) and the specific surface area (SSA) of expansive clays, as report in **(a)** Cerato (2001); **(b)** Muhunthan (1991); **(c)** Olchawa and Gorgczko (2012).

Sridharan *et al.* (1986b) investigated the influence of some compositional factors on the liquid limit of seven natural montmorillonite soils from India and concluded that the liquid limit of such soils was not related to their clay content or to their specific surface area (as plotted in Figure 2-11(a) and Figure 2-11(b)). A poor correlation between the liquid limit and the cation exchange capacity was also observed (Figure 2-11(c)). However, the factor that seemed to show a significant correlation with the liquid limit was the electrical double layer thickness, affected essentially by the amount of exchangeable sodium ions present in such montmorillonite soils (Figure 2-11d)). As reported in the literature (Sridharan and Rao, 1975), the thickness of the diffuse double layer and the amount of interlayer water are the main mechanisms controlling the liquid limit of swelling clays, both greatly dependent on the type of cation attracted to the clay surface. Among the most common exchangeable/interlayer cations present in clays, the sodium ions are the ones that give the largest basal distance at full saturation conditions (as

discussed in **Section 2.2.1.4**), the thickest diffuse double layer and in turn the highest liquid limit (see Figure 2-12). That dependence of the double layer thickness on the concentration of sodium cations is a consequence of their smaller size and valence (in comparison to other usual adsorbed ions) and their greater hydration energy. Thus, such ions are not strongly held by the clay particle and can be easily dissociated from the particle surface in presence of water, contributing significantly to the double layer thickness (Sridharan *et al.*, 1986b).

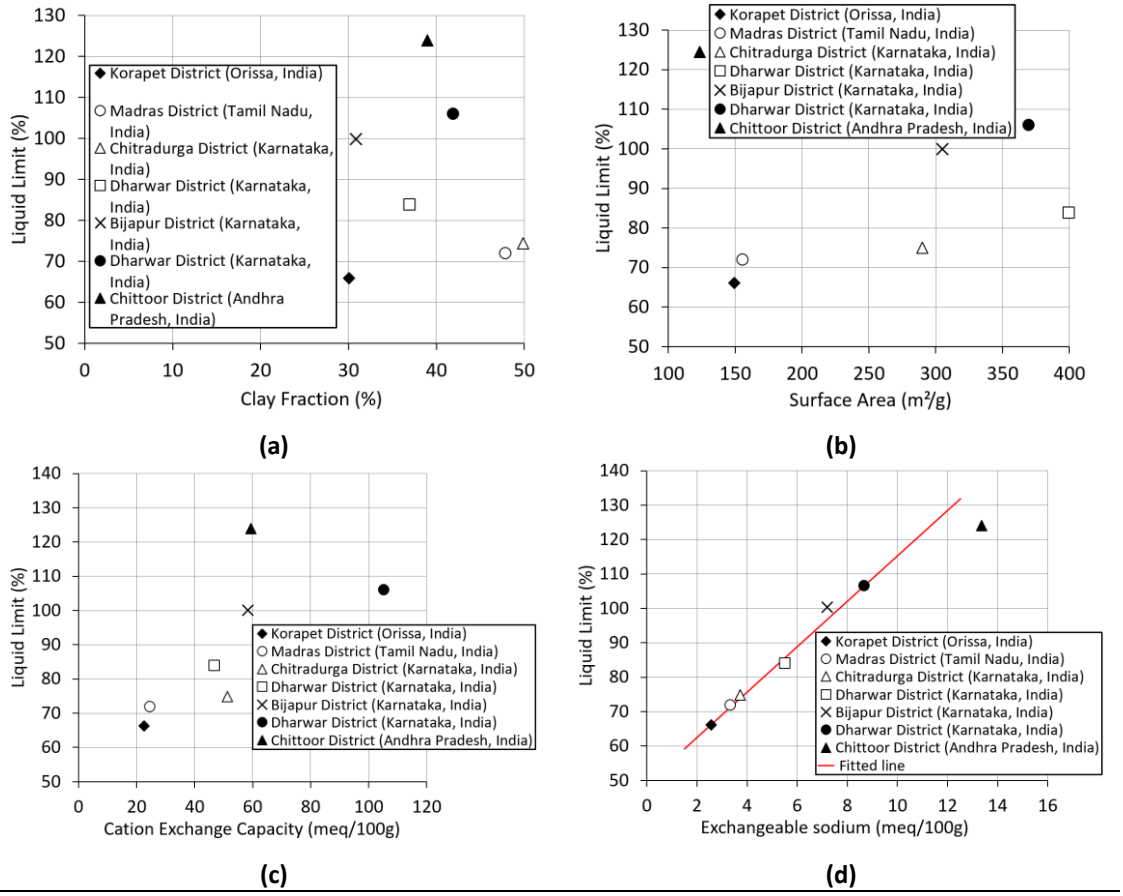

Figure 2-11: **(a)** Liquid limit versus clay fraction; **(b)** liquid limit versus SSA; **(c)** liquid limit versus CEC; **(d)** liquid limit versus exchangeable sodium ions for seven montmorillonitic soils from India (after Sridharan *et al.*, 1986b).

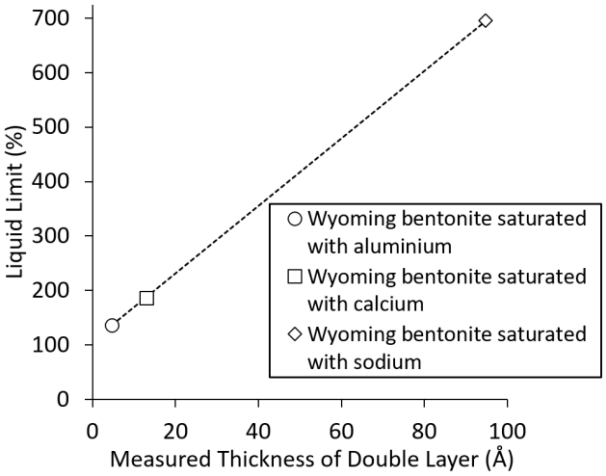

Figure 2-12: Liquid limit versus measured thickness of the DDL for a montmorillonite clay saturated with sodium, calcium and aluminium (from Krebs *et al.*, 1960).

In humid regions, the plasticity index (PI) is commonly used as an indicator of the expansive potential of clay-rich soils. As mentioned before, the PI gives the size of the plastic region of fine-grained soils. In that sense, the higher this geotechnical index, the more plastic the soil is and, consequently, the higher its swell expansion or swelling pressure. This conclusion is based on the strong correlation between the PI (related to the amount of adsorbed water) and the specific surface area (Dakshanamurthy and Raman, 1973). Therefore, higher values of PI are evaluated for montmorillonites (due to their smaller size) and, consequently, higher swelling potential are measured in clays of such a group.

In order to characterize (at least, in a qualitative way) clayey soils in terms of their swelling/shrinkage potential, some classification systems have been proposed by several authors (Holtz and Gibbs, 1956; Seed *et al.*, 1962; Snethen *et al.*, 1977; Chen, 1988; Sridharan and Prakash, 2000) with the PI of the fine-grained fraction of the soil as one of the main parameters to take into account (Jones and Jefferson, 2012). The classification of a soil, in terms of PI values, into very high, high, medium and low degrees of susceptibility to expand when the moisture content changes is given in Table 2-9, whose data are a compilation from some tables found in the literature. This table also presents the swelling classification proposed by the Building Research Establishment Digest 240 (BRE, 1993) in which a modified plasticity index (PI') is used to estimate the "real" plasticity of a soil, taking into account the whole soil sample (particle size < 425 μm) and not only its finest fraction (< 2.0 μm) (Jones and Jefferson, 2012).

Table 2-9: Classification for swelling potential of clays by the plasticity index (PI) (Sridharan and Prakash, 2000; Jones and Jefferson, 2012).

Degree of expansion	PI (%)				PI'(%)*
	Holtz and Gibbs (1956)	Chen (1988)	IS 1498 (1970)	BRE (1993)**	BRE (1993)**
Low	< 20	0-15	< 12	< 18	< 20
Medium	12-34	10-35	12-23	12-32	20-40
High	23-45	20-55	23-32	22-48	40-60
Very high	> 32	> 35	> 32	> 35	> 60

* Calculated as $PI' = PI \times \frac{(\%<425\mu m)}{100\%}$

** As indicated in Jones and Jefferson (2012). Those criteria also consider the particle size as an input parameter.

In some of those classification methods, besides the plasticity index, the particle size distribution of a clayey soil is also taken into account in order to indicate its potential to shrink or swell. Furthermore, both information can be combined through the concept of an index property, the soil activity (A_s), defined by Skempton (1953) as the ratio of the plasticity index to the clay fraction content, that is,

$$A_s = \frac{PI}{(\%\ soil\ particle < 2\mu m)} \tag{2-1}$$

The value of this rate catalogues clayey soils into three groups, according to their activity, as follows (Skempton, 1953)

i. Inactive clays (as kaolinite-rich clays): $A_s < 0.75$

ii. Normal clays (as illite-rich clays): $0.75 < A_s < 1.25$

iii. Active clays (as montmorillonite clays): $A_s > 1.25$

in such a way that the swelling potential of a clayey soil increases with the clay activity index, A_s. If the experimental PI for a clay is plotted against the clay fraction content, the clay activity index represents the slope of the straight line (through the origin) that is fitted to such points (as illustrated in Figure 2-13 for four clayey soils). Typical activity values for the commonly occurring clay minerals are given in Table 2-10 while the theoretical clay activity lines for the three main groups of clay minerals are plotted in Figure 2-13. As it can be noted, montmorillonites have the high activity values, with the sodium-montmorillonite, considered as the most expansive clay mineral (as discussed in previous sections), as also the most active clay mineral. It is known that the clay activity depends on the amount of adsorbed water (Lambe and Whitman, 1979), which in turn, is a function of the specific surface area and the clay content in a soil. Consequently, the clay activity is dependent on the clay mineralogy, as can be clearly noted from the experimental data in Table 2-10. Skempton (1953) also reported that the environmental conditions operating during the weathering and the deposition (in fresh or salt water) processes, in the case of transported clays, and the geological history of a clay stratum influence the clay activity.

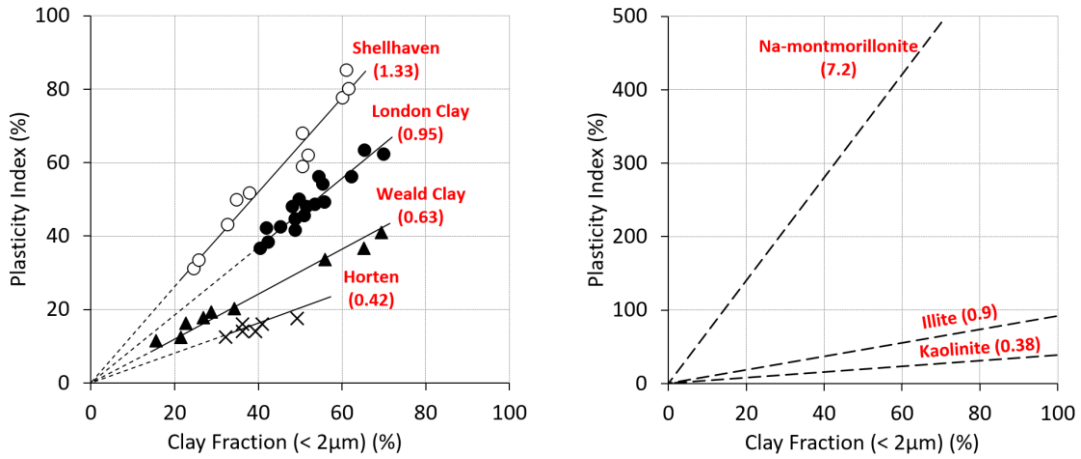

Figure 2-13: Relation between the plasticity index and the clay fraction in soils. Numbers in parentheses indicate the clay activity (after Lambe and Whitman, 1979).

Table 2-10: Clay activity of some clay minerals (from Skempton, 1953).

Clay Mineral	Clay Activity	References
Kaolinite	0.33 / 0.46	Northey (1950) / Samuels (1950)
Illite	0.90	Northey (1950)
Ca-montmorillonite	1.5	Samuels (1950)
Na-montmorillonite	7.2	Samuels (1950)

Many attempts to correlate the soil consistency limits, the clay particle size, the clay activity, the soil water content, etc., with the swell potential of clays have generated graphical schemes employed around the world to characterize an expansive soil, as the ones illustrated in Figure 2-14. Although such empirical correlations constitute a simple and useful way for estimating the

shrink-swell potential of a clay formation, it is important to keep in mind that the Atterberg limits (and the properties defined from them, as the PI and the clay activity) are determined in homogeneous water-soil mixtures from remolded soil samples. Therefore, they do not provide quantitative information about the original soil structure nor about the thickness of the adsorbed water layer around a clay particle (Lambe and Whitman, 1979). As a consequence, the index parameters and the empirical correlations arising from them cannot accurately predict the shrink-swell properties of an *in-situ* soil (Jones and Jefferson, 2012) and due to this, only should be used for classification and characterization purposes. The actual volumetric behaviour of a natural expansive clay when the moisture content changes is highly dependent on its structure, fabric and initial water content.

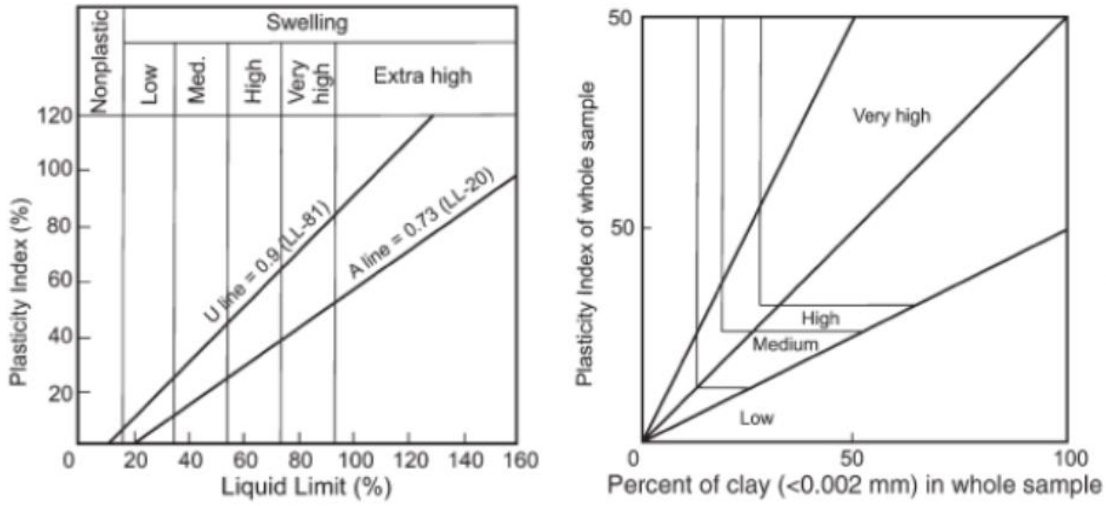

Figure 2-14: Relation between the plasticity index and the clay fraction in soils. Numbers in parentheses indicate the clay activity (after Lambe and Whitman, 1979).

2.2.2.2. THE CONSTANT LOADING METHODS: THE FREE SWELL AND THE LOADED SWELL TESTS

Also referred to as swelling strain test, this type of laboratory test measures the deformation arising from the wetting of a clayey soil specimen subjected to a predetermined loading. Although swelling strain tests may be linear (1-D) or volumetric (3-D), the most usual procedure to determine the swelling potential of expansive clays is through the one-dimensional oedometer tests (Shuai, 1996; Jones and Jefferson, 2012). This testing method is widely employed for geotechnical engineers due to its operational simplicity and to the ease of interpreting the measured data (Jayalath *et al.*, 2016).

Swelling strain tests can be performed at free swell conditions, in which the soil sample is flooded with water at a nominal pressure (usually a very low load), at the *in-situ* vertical overburden pressure or at the structural loading and allowed to develop its full swelling potential under that design loading (Sridharan *et al.*, 1986a; Shuai, 1996; ASTM D4546-08). This method is also known as the *swell-consolidation* or *swell-load method* (Nagaraj *et al.*, 2009) because a subsequent conventional consolidation procedure is applied to the soil sample in order to restore its pre-swelling volume (see Figure 2-7(a) and Figure 2-15(a)). In Figure 2-15(b),

a three-dimensional plot of the stress path followed in this laboratory procedure is shown. The swelling pressure is then defined as the pressure required to bring back the swollen sample to its original volume before the flooding with water. This swelling test provides the upper bound values for the swell and the swelling pressure of a soil (Sridharan *et al.*, 1986a; Nagaraj *et al.*, 2009). This could be a consequence of the higher energy required to expel the water absorbed during wetting (El Sayed and Rabbaa, 1986). A considerable amount of that absorbed water serves to widen the diffuse double layer thickness, increasing the inter-particle distances due to the equilibrium between the inter-particle electrical forces and the external applied loads (see **Section 2.7.1**). Therefore, higher swell is induced by this type of oedometer swelling test, which results in a higher swelling pressure in comparison to other laboratory swelling methods. The *free swell method* has the advantage that only a single specimen is required to determine the (maximum) swelling potential of an expansive clay, but it is a time-consuming test (Nagaraj *et al.*, 2009). Nevertheless, this method cannot reproduce accurately the *in-situ* stress path history of an expansive soil (Shuai, 1996). Moreover, the wetting-induced swelling followed by a reduction in the sample volume due to consolidation incorporates some hysteresis into the determination of the *in-situ* swelling pressure (Shuai, 1996; Jones and Jefferson, 2012).

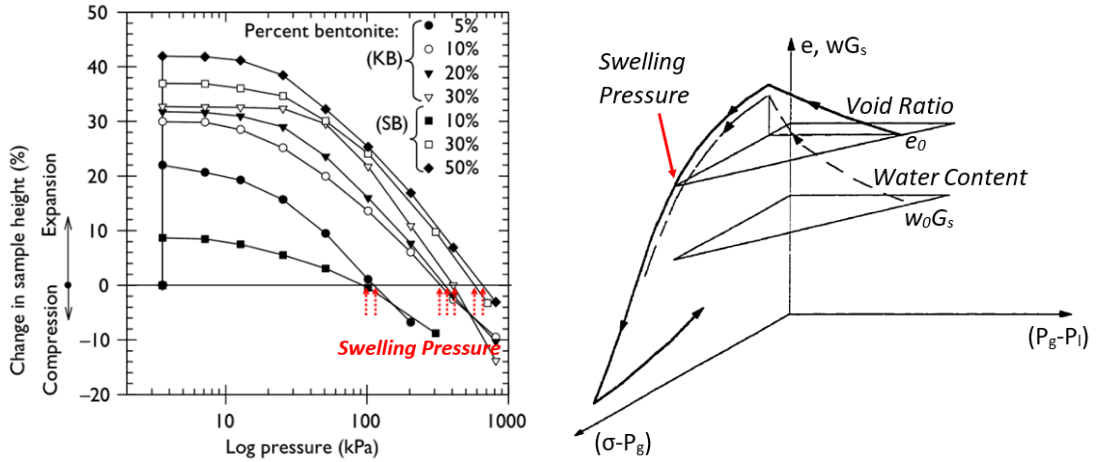

Figure 2-15: **(a)** Typical results obtained from a swell-consolidation test (Hashim and Muntohar, 2006); **(b)** Stress paths in the σ_{net}: s: e space followed during a swell-consolidation from test (after Shuai, 1996).

The wetting-induced swell or collapse under different loading conditions is also a common laboratory practice in which three or more identical dry soil samples are tested in one-dimensional consolidation apparatus. Each of those specimens is loaded to a (different) target vertical stress and when equilibrium condition is reached, inundation with water takes place under the applied vertical loading. As a consequence, "free" swell (or collapse) is measured under several constant vertical stresses. The final volume changes (or swell ratios) at full saturation are plotted against the logarithm of the corresponding applied loadings, and as a result, a straight trend line through such final equilibrium positions is determined (Sridharan *et al.*, 1986a; Nagaraj *et al.*, 2009), as the one depicted in Figure 2-16(a). In the literature, this standard laboratory method is referred to as *the method of equilibrium void ratios for different consolidation loads* (Sridharan *et al.*, 1986a) or simply as *the loaded swell oedometer test* (Shuai, 1996). A typical 3-D stress path followed during such a testing procedure is shown in Figure 2-16(b). The swelling pressure, in this case, is defined as the load that would be applied to the sample in order to prevent any volume change on saturation. The swelling pressure can be estimated from the measured data by the intersection between that plotted line representing

the equilibrium positions and the null volume change line (the horizontal line through the starting point) (Sridharan *et al.*, 1986a). This laboratory swell procedure, unlike the *free swell method*, can properly represent the normal sequence of loadings experienced by the soil in the field (Brackley, 1975; El Sayed and Rabbaa, 1986; Sridharan *et al.*, 1986a; Shuai, 1996). In comparison to other laboratory methods for evaluating the swelling potential of expansive clays, this procedure provides the lower bound for the swelling pressure (Sridharan *et al.*, 1986a). Nevertheless, it requires at least three or more clay samples at identical initial conditions, which constitutes a quite difficult and time-consuming task (Sridharan *et al.*, 1986a; Shuai, 1996; Nagaraj *et al.*, 2009).

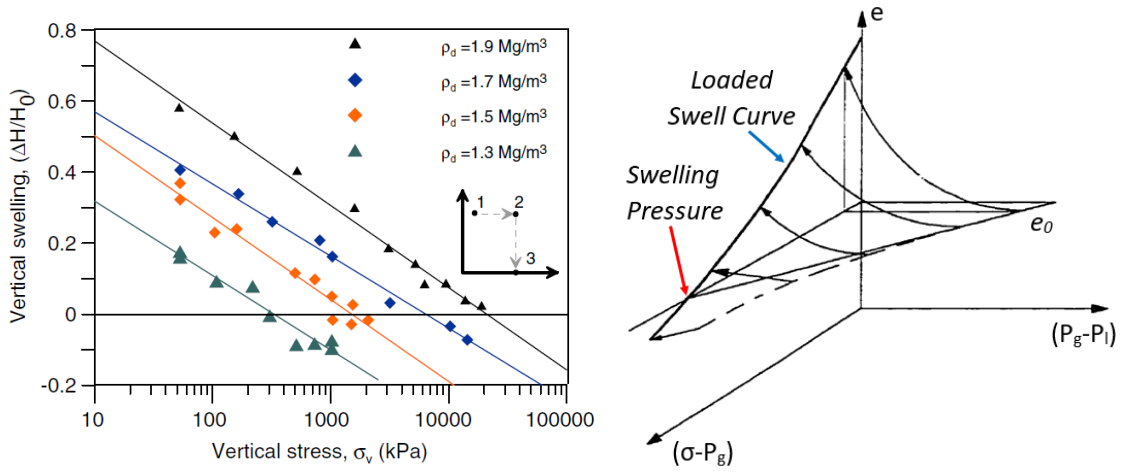

Figure 2-16: **(a)** Typical results obtained from a loaded swell oedometer test (Hoffmann *et al.*, 2007); **(b)** Stress paths in the σ_{net}: s: e space followed during a loaded swell test (after Shuai, 1996).

Some variants of the constant loading oedometer tests have been developed to estimate the wetting-induced strains and the swelling pressure of an expansive soil, as *the double oedometer test method* (Jennings and Knight, 1957; Jennings *et al.*, 1973), *the direct model method* (Jennings, 1969) and *the Chinese method* (Shuai, 1996; Feng *et al.*, 1998). In all these swelling strain methods, the swelling potential is strongly affected by the disturbance experienced by the soil during sampling or by the elasto-plastic deformations developed due to the load applied prior to the flooding of the clay specimen (Shuai, 1996).

2.2.2.3. THE CONSTANT VOLUME METHODS

The testing procedure followed during the wetting at constant volume consists, basically, in applying a certain external load to a soil specimen in order to prevent any expansion when it is in contact with water in liquid form or in vapour form. The minimum imposed stress (on saturation) for which that purpose is achieved is defined as the swelling pressure (Salas and Serratosa, 1957; Johnson and Stroman, 1976; Sridharan *et al.*, 1986a; Shuai, 1996; Vanapalli and Lu, 2012). In practical terms, a sequence of several small loads is applied while the sample is being saturated so that the tendency for swelling as suction decreases is counterbalanced during the entire wetting path (Sridharan *et al.*, 1986a). The swelling pressure is given by the loading for which the stress path crosses the null-volume change line (see Figure 2-17(a)). This

standardized method for determining the swelling pressure is known as *the constant volume method* or *the zero-swell method* (Sridharan *et al.*, 1986a; Nagaraj *et al.*, 2009) or, simply, as *swelling pressure test* (Alonso *et al.*, 2005). Again, one-dimensional oedometer tests are the most popular laboratory techniques carried out for measuring the swelling pressure at isochoric conditions. Once the soil specimen is fully saturated and there is no further volumetric deformation induced by wetting, the swollen sample is usually loaded and unloaded, following a conventional consolidation test (Shuai, 1996), as depicted in Figure 2-7(b) and in Figure 2-17(b), so that compressibility and yield properties at saturation can be estimated.

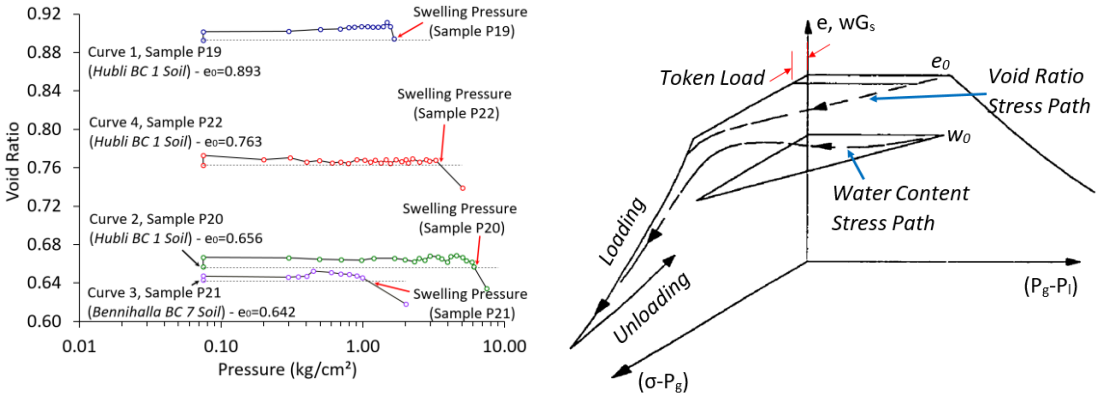

(a) **(b)**

Figure 2-17: **(a)** Typical results obtained from a swelling pressure test (modified, after Sridharan *et al.*, 1986a); **(b)** Stress paths in the σ_{net}: s: e space followed in an oedometer test under isochoric conditions (after Shuai, 1996).

The performance of a swelling pressure test is relatively rapid and it only requires a single undisturbed or remolded specimen (Sridharan *et al.*, 1986a). Moreover, it does not introduce hysteresis into the estimation of the *in-situ* state, since the sample volume remains almost constant during the saturation process. However, the determination of swelling pressures by this laboratory procedure is more sensitive to changes in the soil structure (Jones and Jefferson, 2012). In fact, the swelling pressure under confined conditions measured from disturbed samples is somewhat lower than its actual value obtained from undisturbed samples. Moreover, the conventional procedure for obtaining the swelling pressure through the constant volume method does not account for the compressibility of the oedometer apparatus and the increase in the soil compressibility due to sampling disturbances (Fredlund, 1969; Shuai, 1996; Vanapalli and Lu, 2012). In order to solve this experimental drawback, Fredlund *et al.* (1980) proposed an empirical procedure for correcting the measured swelling pressure by means of a modified Casagrande graphical method, as illustrated in Figure 2-18.

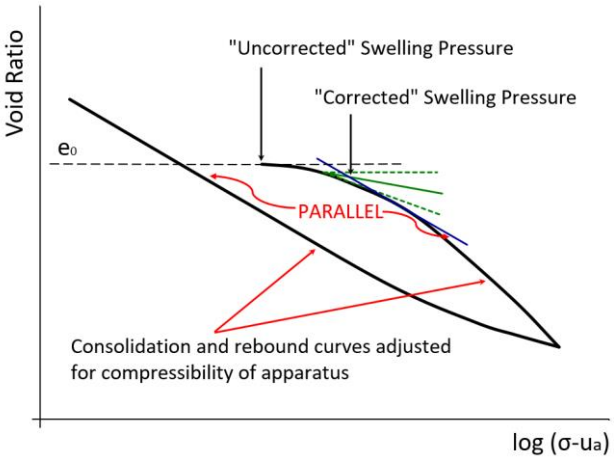

Figure 2-18: Construction procedure proposed by Fredlund *et al.* (1980) to correct the measured swelling pressure (obtained under confined conditions) accounting for the effects of sampling disturbances (from Fredlund *et al.*, 1989).

2.2.2.4. THE INITIAL DRY DENSITY AND WATER CONTENT

The swelling pressure arises as a natural response to the wetting of an initially unsaturated expansive clay when its volumetric expansion is restrained. Due to that, it is expected that the more compacted an expansive soil mass the higher the pressures developed when that material is wetted in presence of structural/geometrical elements that restrict its tendency to swell. In a confined (constant volume) swelling test, the design of the oedometer cell/loading chamber constitutes a geometrical constraint to the sample expansion, while the main structural constraint is related to the specimen porosity. In fact, many researchers have found empirical laws relating the swelling properties of expansive clay samples (measured in oedometer-based laboratory procedures as the ones described previously) to their initial dry density or void ratio (Villar, 2002; Wang *et al.*, 2012; Schanz and Al-Badran, 2014). In fact, the initial placement condition is one of the main factors controlling the swelling behaviour of expansive clays upon wetting in such a way that the higher the initial dry density the higher the magnitude of the swelling strains and pressures (Nagaraj *et al.*, 2009; Wang *et al.*, 2012). The reason for this lies in the fact that, in a denser soil specimen, a high swelling pressure (under confined conditions) is generated as a result of the lower volume of pore space available for a soil sample develops its full swelling potential when saturated (Jayalath *et al.*, 2016).

Some correlations between the swelling pressure and the dry density for bentonite-based materials chosen to be used as seals and/or buffers in deep geological HLRW repositories are plotted in Figure 2-19(a) (Dixon *et al.*, 1996; Villar, 2002; Imbert and Villar, 2006; Karnland *et al.*, 2008; Wang *et al.*, 2012). In accordance to the experimental evidences reported by several authors (Villar, 2002; Hoffmann *et al.*, 2007; Schanz and Al-Baldran, 2014), it can be established that the swelling pressure of compacted bentonite materials increases exponentially with dry density. It is important to emphasize that the values of the swelling pressure and the swelling strains measured experimentally are strongly dependent on the laboratory procedure used for that task, as depicted in Figure 2-19(b). This is a consequence of the different stress paths followed by each testing method (Hoffmann *et al.*, 2007), which may lead to important differences in the clay fabric at the end of the experimental programme.

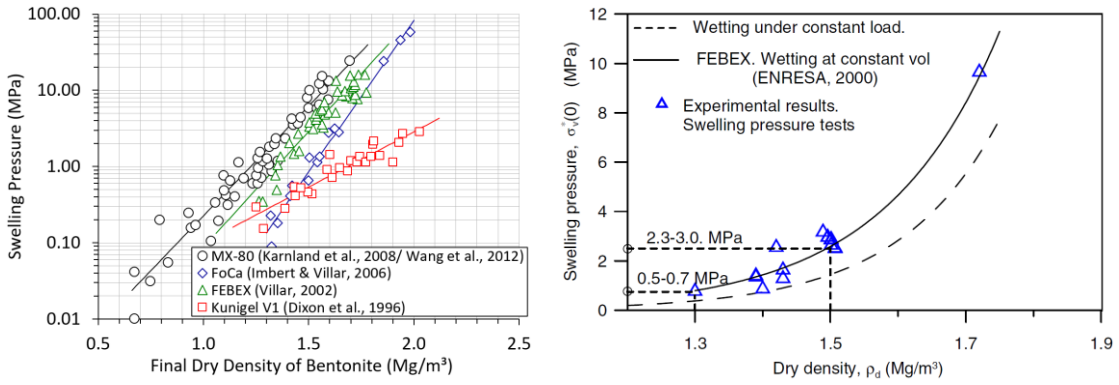

Figure 2-19: **(a)** Variation of swelling pressure with dry density of several bentonites (Wang *et al.*, 2012); **(b)** exponential correlation between swelling pressure and dry density of FEBEX bentonite materials (Hoffmann *et al.*, 2007).

Another external factor that affects the swelling response of undisturbed natural and compacted expansive materials is their initial moisture content. Several researches have concluded that, for a constant dry density, the swelling potential decreases as the initial water content increases (Jayalath *et al.*, 2016) – as illustrated in Figure 2-20 – and this tendency is more pronounced at higher densities (Lambe, 1960a). It means that a reduction in suction from a higher initial value leads to a larger expansion of the sample or to the development of high swelling pressures at constant volume conditions (Gens and Alonso, 1992). The excessive swelling strains or pressures of drier soil specimens during wetting are a consequence of the larger deficit of water in pores (micro and macro) and as a result of that, a larger amount of water must be imbibed to promote the full expansion of clay minerals (Jayalath *et al.*, 2016). On the other hand, swelling clay samples that are closer to their saturation tend to develop low volumetric expansions or less significant swelling pressures when wetted once the expansive minerals have already partially developed their full swelling potential because of the higher initial moisture content of the soil specimens.

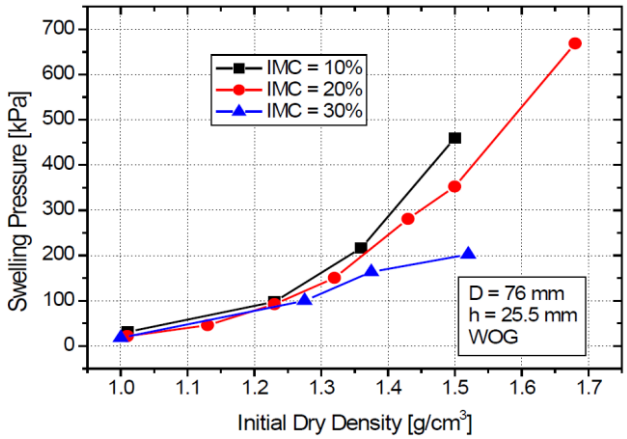

Figure 2-20: Swelling pressure development in samples compacted at several dry densities and with distinct initial water contents (Jayalath *et al.*, 2016).

2.2.2.5. CLAY STRUCTURE

Clay particle arrangements are affected by the nature of the adsorbed exchangeable cations, the pH of the soil solution, the molding water content and the method and energy of compaction (Lambe and Whitman, 1979; Abdullah *et al.*, 1999; Pinto, 2000). In undisturbed samples from clay sediments, clay platelets are structurally found in flocculated (edge-to-face contacts, as shown in Figure 2-21(a) and Figure 2-21(b)) and dispersed (face-to-face aggregation of particles, see Figure 2-21(c)) associations, depending on the nature of the net electrical forces between adjacent particles during the deposition process (Pinto, 2000; Ashoka, 2006). In saline and acidic soil solutions, clay particle edges exhibit a net positive charge (Abdullah *et al.*, 1999). In such environments, the positive charged edges are attracted to the negatively charged particle faces. Moreover, the presence of salts tends to reduce the repulsive forces between the clay particles. As a consequence, the net inter-particle attractive forces (related to the Van der Waals forces) lead to the formation of a flocculated clay structure (Lambe and Whitman, 1979; Forouzan, 2016). On the other hand, when the repulsive forces (due to the overlapping diffuse double layers) between particles are prevalent, a dispersed clay arrangement is developed (Lambe and Whitman, 1979; Forouzan, 2016). Remolding and compaction (at increasing water contents) activities as well as the application of several cycles of swelling and shrinkage (wetting-drying cycles) tend to cause a destruction of large aggregates and the disorientation of the structural elements (as the edge-to-face contacts) (Basma *et al.*, 1996; Pinto, 2000; Ashoka, 2006). Consequently, such procedures induce a reorientation of the clay particles towards a more dispersed structural configuration.

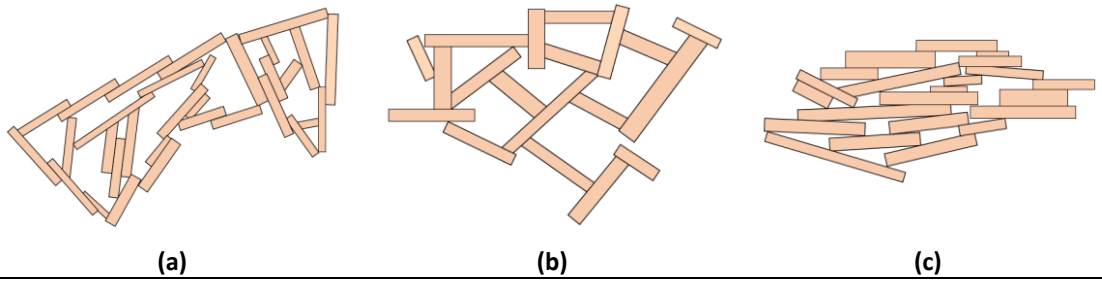

Figure 2-21: Schematic representation of clay particle arrangements (after Lambe and Whitman, 1979) for undisturbed samples from **(a)** salt water and **(b)** fresh water deposits and for **(c)** remolded samples.

The swelling potential of an expansive clay is closely related to its structure (Basma *et al.*, 1996; Abdullah *et al.*, 1999). Due to the high void ratio of edge-to-face aggregations (and consequently, the large amount of water that such clay structures can imbibe), a flocculated clay structure is prone to expand and shear more than the same clay in a dispersed configuration (Abdullah *et al.*, 1999; Forouzan, 2016). Consequently, those physico-chemical factors that contribute to the development of a flocculated structure also increase the swelling potential of a clay. Moreover, a clay with a predominant flocculated fabric is more permeable and less compressible than a clayey soil with an oriented structure.

2.2.2.6. PROCEDURAL FACTORS

Only a limited amount of research studies has been devoted to deal with the influence of the procedural factors (in laboratory practices) on the swelling behaviour of clayey soils. Procedural factors can be defined as those features intrinsically related to the laboratory testing procedure, the test apparatus and the specimen preparation. Factors such as sample size, lateral friction, level of sample disturbance, compaction and loading procedures and compressibility of oedometer cells are some of the procedural factors to take in account when testing swelling clays in laboratory (Fredlund, 1969; Elsharief *et al.*, 2014; Jayalath *et al.*, 2016).

In order to analyze the effects of the specimen size (diameter and height) on the measured swelling pressure in oedometer apparatus, Jayalath *et al.* (2016) carried out a series of swelling pressure tests on remolded samples of an expansive soil from Australia. The experimental procedure consisted of performing three swelling tests on samples with a height of 18.5 mm and with different ring diameters (50 mm, 63 mm, 76 mm). Two additional specimens with a ring diameter of 50 mm and sampling heights of 25.5 mm and 38.0 mm were also tested. The average dry density of all those samples was in the range of 1.30-1.36 g/cm^3, with an initial moisture content of 25%. The experimental response of such swelling pressure tests are given in Figure 2-22. From them, it can be noted that the measured swelling pressure tends to increase with the decrease in the sample diameter (see Figure 2-22(a)) and with the increase in the specimen height (as shown in Figure 2-22(b)). Jayalath *et al.* (2016) related the dependence of the swelling potential of the clay (expressed in the experimental findings by the vertical swelling pressure) on the sample dimensions to the fact that the tendency of the soil specimen to swell vertically is enhanced when the lateral sample movement is reduced, that is, when the ring diameter is decreased.

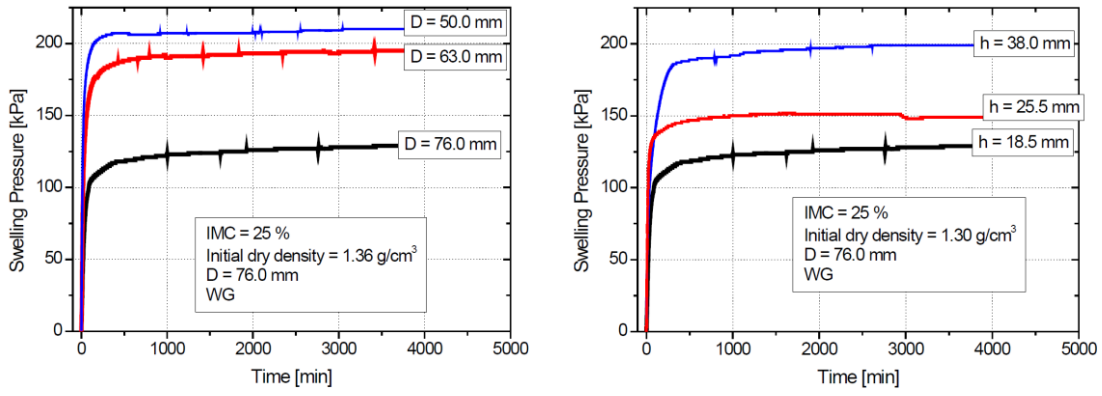

Figure 2-22: **(**Swelling pressure development at different **(a)** cell diameters (for a sample height of 18.5 mm); **(b)** sample heights (for a cell diameter of 76.0 mm). Grease was applied on the inner surface of the cells (Jayalath *et al.*, 2016).

Jayalath *et al.* (2016) also examined the influence of the sample ring friction on the swelling pressure development through the performance of several tests using a lubricant applied on the inner surface of the oedometer cell. The experimental measurement of swelling pressure with reduction of the lateral friction by the application of grease (WG) is plotted in Figure 2-23. As a general conclusion, higher swelling pressure was measured when the lateral friction between

the soil sample and the apparatus wall was reduced. The usage of lubricant reduces the lateral friction and, therefore, it leads to an increase in the susceptibility of the soil sample to expand vertically, which in turn, leads to an increase in the swelling pressure. Consequently, the development of significant frictional stresses (when any lubricant is not applied around the inner perimeter of the test apparatus, as in WOG in Figure 2-23) underestimates the measured swelling pressures.

The method of compaction also plays a crucial role in the swelling characteristics of remolded, compacted expansive soils (Jeyapalan *et al.*, 1981; Attom, 1997; Attom *et al.*, 2006). On the one hand, undisturbed samples of clayey soils tend to develop higher swelling pressure and swell strain when hydrated in comparison to remolded samples with similar initial density and water content. As discussed previously, such a result is a clear evidence of the dependence of swelling properties on the clay structure and its evolution (destruction of the original arrangements found in the clay deposit) due to disturbances arising from sampling, transportation, trimming and remolding. On the other hand, the method of compaction (dynamic, static or kneading remolding) employed in laboratory on specimens of disturbed clays generates different soil structure configurations, which is reflected in differences in the measured swelling properties. Attom *et al.* (2006) found that clayey soil samples compacted by the dynamic impact type tend to give the highest swelling pressure and volumetric expansion while the lowest values are obtained for specimens prepared by the kneading compaction technique, as shown in Figure 2-24. Statically compacted clay samples give intermediate values of swelling properties when compared to the measurements from the other two methods of remolding.

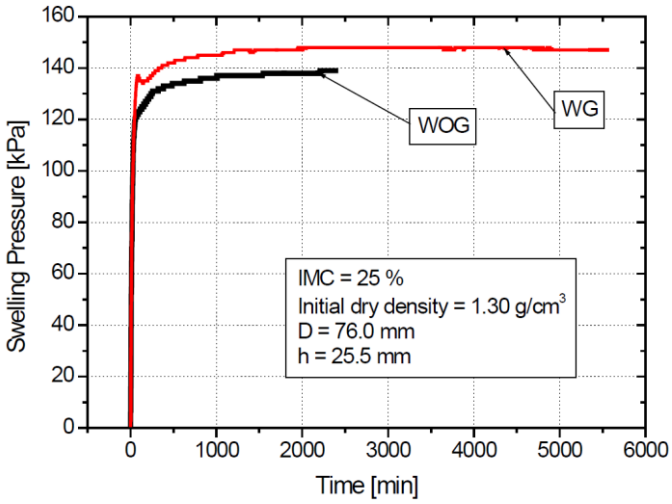

Figure 2-23: Swelling pressure development with (WG) and without (WOG) the application of grease on the inner surface of the oedometer cell (with a diameter of 76.0 mm and a height of 25.5 mm) (Jayalath *et al.*, 2016).

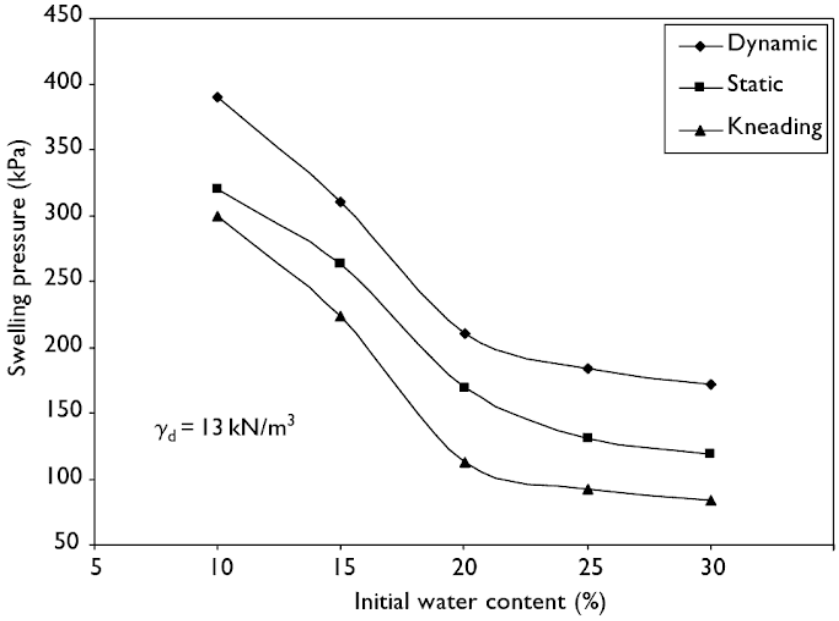

Figure 2-24: The effect of the remolding procedure on the swelling measured at distinct initial water contents for a clayey soil in Jordan (Attom *et al.*, 2006).

Compressibility characteristics and corrections for the oedometer apparatus should be evaluated and implemented to the data from swelling pressure tests in order to provide a corrected prediction of the swelling behaviour of expansive soils. In fact, the measured swelling pressure is underestimated if such corrections are not applied (Fredlund, 1969). Moreover, the effect of the sampling disturbance on the swelling properties can be considered by the empirical construction procedure by Fredlund *et al.* (1980) mentioned in **Section 2.2.2.3**. Such a correction in the swelling pressure is necessary since the compressibility of a soil tends to increase with the sampling disturbance (Shuai, 1996; Vanapalli and Lu, 2012) and, consequently, the measured laboratory data are usually lower than *in-situ* values when no correction is taken into account. As a general conclusion, it can be highlighted that the swelling pressure is not a well-defined material property (Hoffmann *et al.*, 2007) but its value is strongly dependent on the initial state of the expansive specimen, the operational procedures carried out in laboratory and the stress path followed during the hydration test.

2.3. THE PORE SIZE DISTRIBUTION (PSD) AND THE DOUBLE-POROSITY APPROACH FOR EXPANSIVE SOILS

Because the swelling pressure is intrinsically related to the dry density of an expansive soil (as discussed in **Section 2.2.2.4**), the pore size distribution and the changes in porosity induced by thermo-hydro-mechanical (THM) loadings must be taken into account in order to understand and predict properly the swelling capacity of active clays. Furthermore, the magnitude and the evolution of the hydraulic conductivity of bentonite-based materials play a central role in the performance of engineered barriers and such a soil property depends fundamentally on the shape, size and distribution of pores.

The soil fabric, together with the main physico-chemical factors already mentioned in **Section 2.2.1**, give the main conceptual basis for the development or extension of constitutive models that explicitly incorporate the effects of particle-level phenomena in their mathematical formulation. In fact, natural and compacted active soils tend to show two main fabric types, one of them characterized by the arrangement of elementary clay particles composing a clayey matrix, while the other one is made up of aggregates of clay particles that tend to form a three-dimensional structure with large inter-aggregate pores (Gens and Alonso, 1992). A schematic representation of such clay fabrics and a pair of micrographs (obtained by the electron microscopy technique) of compacted bentonite samples are given in Figure 2-25. Moreover, it is possible to distinct, at least, two families of pores in both types of structural configurations (Romero, 1999; Lloret *et al.*, 2003; Hoffmann *et al.*, 2007). The micro-porosity is constituted by the pore spaces inside elementary clay particles (intra-particle or inter-layer pores) together with the voids into individual clay aggregates (intra-aggregate or inter-particle pores). The other family of pores, the macro-porosity, encompasses the bigger voids among aggregates and other non-active soil particles.

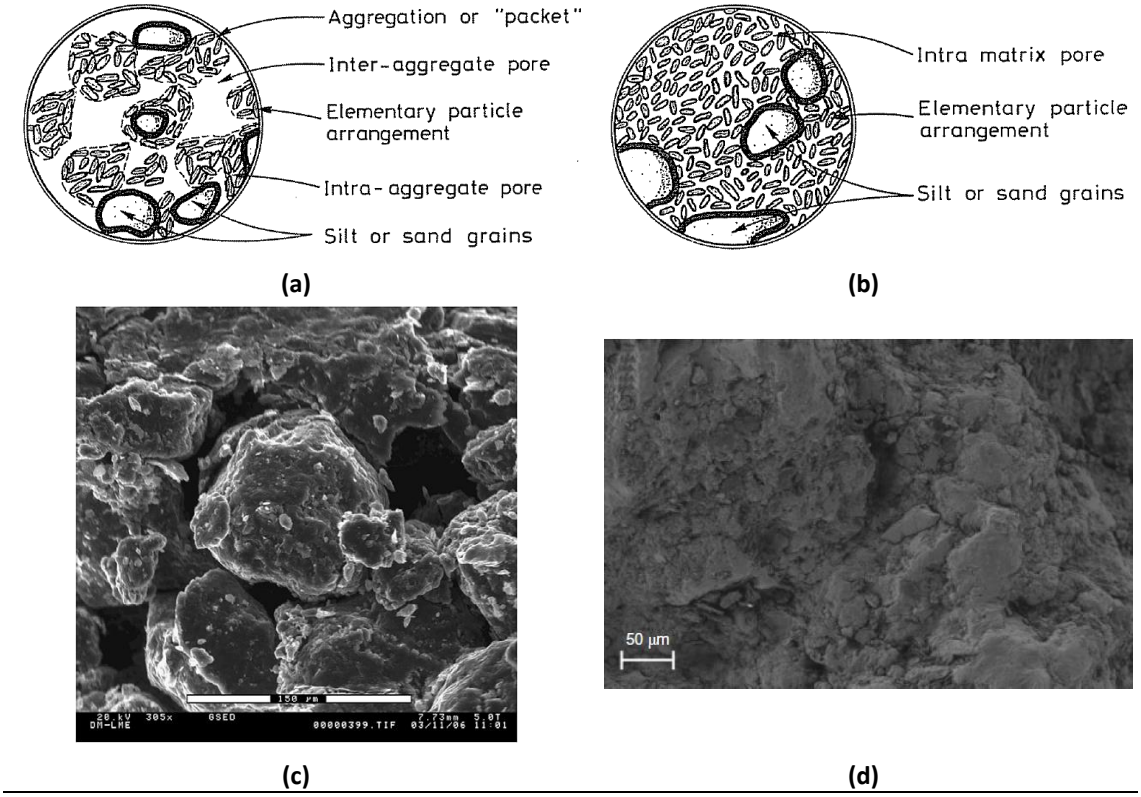

Figure 2-25: **(a)** Microfabric of a clay predominantly constituted of clay aggregates with larger pores among them (Gens and Alonso, 1992); **(b)** microfabric of a soil composed mainly by elementary clay particles (Gens and Alonso, 1992); **(c)** micrograph of FEBEX bentonite compacted at dry density of 1.40 Mg/m^3 (Lloret and Villar, 2007); **(d)** micrograph of MX-80 compacted at dry density of 1.80 Mg/m^3 after wetting/drying cycles (Seiphoori *et al.*, 2014).

The pore size distribution (PSD) of an expansive soil is obtained by the experimental technique known as mercury intrusion porosimetry (MIP). Typical PSD curves for expansive soils are shown in Figure 2-26. These curves have been obtained from porosimetry studies performed on a bentonite-pelletized mixture compacted to different values of dry densities (from 1.35 Mg/m^3 to 1.70 Mg/m^3), as reported in Hoffmann *et al.* (2007). The bimodal PSD is a clear evidence of the presence of two classes of pores in the internal structure of active soils. Nevertheless, the quantification of the volume occupied by micro-pores through the MIP technique is limited by the mercury capacity to intrude into such smaller pore spaces. In fact, this technique cannot

quantify the intra-particle pore mode in compacted clays, in which the size of such smaller pores usually varies in the range of 0.2 and 2 nm (Lloret and Villar, 2007). Intra-particle porosity is usually estimated through electron microscopy techniques. However, the most significant soil structure changes due to hydro-mechanical loadings occur predominantly at inter-particle and inter-aggregate pore levels.

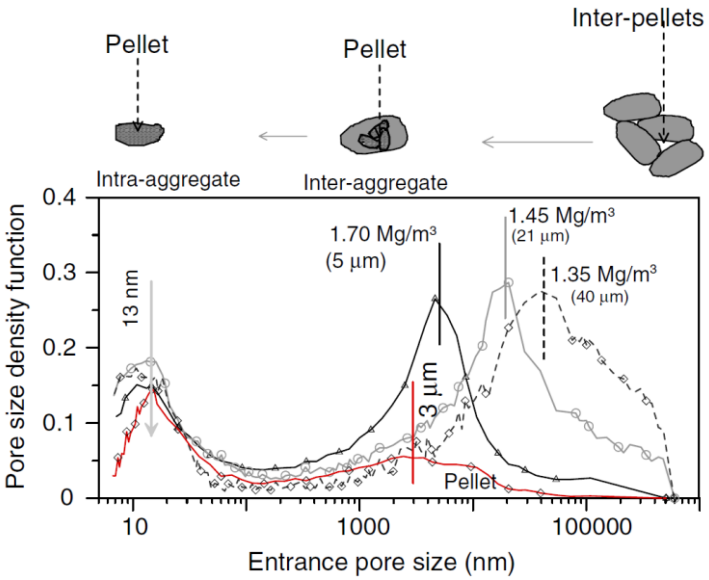

Figure 2-26: Pore size distribution of compacted samples made of a granular mixture of FEBEX bentonite pellets at several dry densities (Hoffmann *et al.*, 2007).

Mechanical loadings imposed on a soil sample during the compaction procedures generate a denser internal porous structure by the reduction of the volume of macro-pores without relevant changes in micro-porosity (Gens and Alonso, 1992; Lloret *et al.*, 2003; Hoffmann *et al.*, 2007; Lloret and Villar, 2007). This fact is confirmed by MIP results as the ones reproduced in Figure 2-26 and Figure 2-27(a). Such experimental evidences prove that the application of a mechanical loading under constant water content (representing the compaction effort) tends to affect mainly macro-porosity, once the increase in the compaction effort usually leads to the closure of macro-pores. The non-dependence of micro-porosity on the compaction effort is more recognizable in dry samples or in specimens compacted at low water content conditions (Delage *et al.*, 2006). In these conditions, the compacted soil structure is similar to the one shown in Figure 2-25(c), in which the generation and evolution of larger pores during compaction is more evident.

On the other hand, the wetting or drying of an active clay not only affects the evolution of its macro-porosity but also produces significant changes in micro-porosity. The wetting of an expansive soil tends to generate an increase in micro-porosity due to the swelling of active minerals and clay aggregates, as more water molecules are available to fill up the intra-particle and the intra-aggregate voids as suction decreases. Consequently, macro-porosity tends to decrease during wetting, mainly when the expansive material is close to its full-saturation state (Wang *et al.*, 2013; Wang and Wei, 2015), as indicated in Figure 2-27b). Under isochoric conditions, the swelling mechanism can lead to the total occlusion of inter-aggregate pores (Lloret and Villar, 2007), which results in a monomodal PSD function with no clear distinction of a multi-porosity structure in the saturated sample of active clay. In such conditions, the final

state of the soil fabric is similar to the one shown in Figure 2-25(d), although the procedure followed to cause the closure of larger pores is quite different in both situations. However, the bimodal PSD can be recovered by a subsequent dehydration of the expansive soil (Romero *et al.*, 2011), which leads to the generation of larger voids among clay aggregates due to the shrinkage of clay particles.

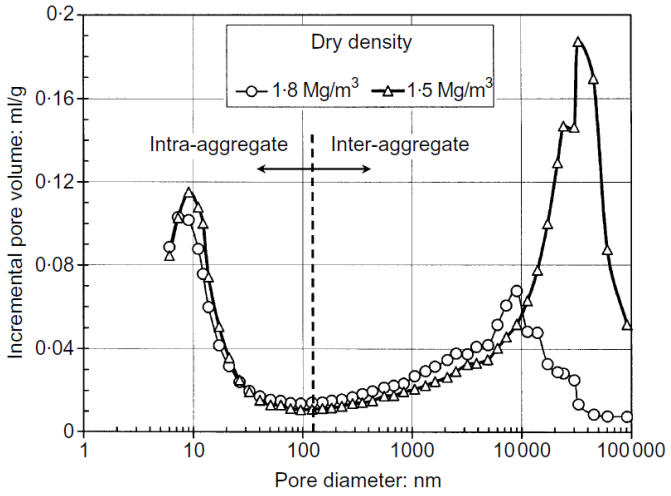

(a)

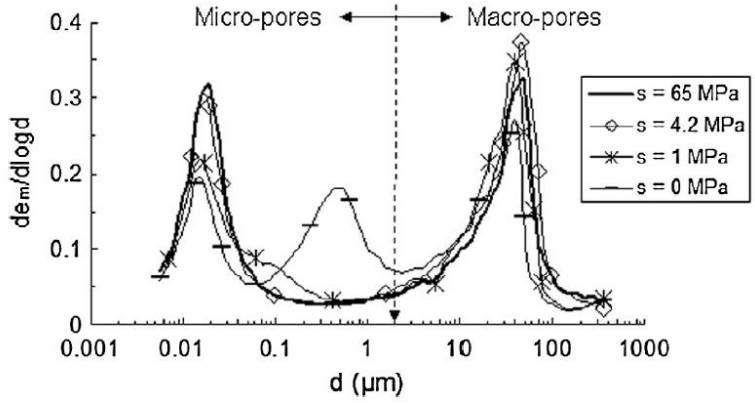

(b)

Figure 2-27**(a)** Effect of the compaction effort on the pore size distribution of compacted samples of FEBEX bentonite (Lloret *et al.*, 2003); **(b)** development of the pore size distribution of compacted MX-80 bentonite/sand mixtures under wetting path (Wang *et al.*, 2013).

The deformation response of microstructure (clay particles and aggregates) to changes in the water content of micro-pores is usually described as purely volumetric and elastic (Gens and Alonso, 1992; Alonso *et al.*, 1999; Sánchez *et al.*, 2005; Wang and Wei, 2015). Such changes in the microstructural saturation state alter the physico-chemical balance of forces at particle level, which is manifested by the expansion or shrinkage of clay particles and aggregates in drying or wetting processes, respectively (see **Section 2.7.1**). The changes in the amount of microstructural water are driven by local differences in the chemical potential of the water filling both families of pores (Alonso and Navarro, 2005). This water transfer mechanism that links both structural pore levels is briefly addressed in following sections (see **Section 2.4.3** and **Section 3.6**) and constitutes an essential ingredient for describing mathematically the deformation behaviour of microstructure to changes in the local hydro-mechanical loadings. On the other hand, irreversible changes in the clay fabric, as the ones generated by the compaction

procedure, occur in response to changes in the external hydro-mechanical loadings and usually induce structural collapses. Such structural changes affect mainly the size and distribution of larger pores and may be predicted by concepts and models commonly used to describe the elastoplastic behaviour of unsaturated non-expansive soils, as the classical *Barcelona Basic Model* (Alonso *et al.*, 1990). Furthermore, and depending on the structural stability of macro-voids, a rearrangement of the granular-like skeleton can also take place as microstructure expands or shrinks. This interaction between both pore levels makes evident the highly complex nature of expansive soils and emphasizes the harsh task of developing a consistent mathematical formulation to predict the behaviour of active clays without treating each structural medium separately.

Taking into account the distinct deformation behaviour of each structural level and making use of the theoretical concepts of the double porosity theory (Aifantis, 1980), Gens and Alonso (1992) settled the general framework for the development of constitutive models that suitably reproduce the experimental response of non-saturated swelling clays. In this general approach, the expansive soil is treated as two distinct and overlapping porous media (microstructure and macrostructure), each of them defined by their own set of stress-small strain constitutive laws and global porosities. Additionally, the interaction between these two basic structural levels is achieved by the definition of a mechanical coupling mechanism relating the generation of plastic deformations of macrostructure in response to the deformation behaviour of microstructure. In that sense, the deformations experienced by the expansive porous medium (as a whole) is split into a component associated with the microstructural elastic (and volumetric) strains and another component related to the expansion or contraction of macro-pores. Such an additive decomposition of the strain tensor constitutes the mathematical basis for the development and implementation of a general framework able to simulate the behaviour of unsaturated swelling clays. The *Barcelona Expansive Model* (BExM), described in Alonso *et al.* (1999), and the double-structure model developed by Sánchez (2004) and reported in Sánchez *et al.* (2005) are only two examples of mechanical constitutive models that incorporate the double-porosity approach by Gens and Alonso (1992) in their mathematical formulations. A brief description of the main features of these numerical models based on the double-porosity theory is presented in **Section 2.7.2**.

Despite the assumption that deformations of individual expansive clay aggregates are essentially elastic, the hydration-induced breakage of larger aggregates with unstable internal structure into smaller ones also occurs (Wang and Wei, 2015). Even in such a particular situation, the hypothesis of reversibility of microstructural strains remains, once each larger unstable aggregate can be considered as a cluster of smaller stable ones. Moreover, the complex internal fabric of individual clay aggregates is not explicitly modelled in many constitutive formulations, as those derived from the double-porosity theory, which includes the THM model developed in this Thesis. Rather, a modelling simplification is employed, taking the expansive aggregates as porous discrete bodies.

2.4. THE ROLE AND STATE OF WATER IN EXPANSIVE SOILS

The existence of two scales of porosity in expansive clays leads to the need to also define distinct types of water, since its role and participation in the hydraulic processes that take place during wetting or drying paths depend on the pore size in which that water is found. The soil-water inside the larger pores is defined as the "macrostructural water" (bulk water) while the "microstructural water" refers to the water attracted to the clay mineral surfaces and to the portion of water confined in the inter-lamellar spaces. Furthermore, it is reported in the literature that the interlayer water exhibits some physical and chemical properties quite different from those of the bulk water (Martin, 1962; Low, 1976; Sposito and Prost, 1982; Rizzi *et al.*, 2012), such as the water density, for example.

The macrostructural water, also termed as the soil "*free water*", is the amount of water in pores that participates in the advective-diffusive mass fluxes. The water movement through macro-pores is due to gradients in macrostructural water content and potentials. The macrostructural water content of a clayey soil is dependent on the initial dry density (Bradbury and Baeyens, 2002), which in turn, is affected by the compaction effort applied during the sample compaction. In non-saturated media, the macrostructural water potential is associated essentially with the cohesive and adhesive capillary forces that define the matric component of the macrostructural suction in expansive soils. The water content and the water potential are related through the soil-water retention curve, commonly described by the empirical van Genuchten relationship (van Genuchten, 1980). In expansive clays, the hydraulic constitutive relationship representing the state of the water in macro-pores can be evaluated by defining a water retention curve for the soil skeleton (macrostructure). It is also important to highlight the hydro-mechanical coupling between the macrostructural water flow and the development of swelling strains in active clays. In these expansive soils, water conductivity through macro-pores tends to reduce as they become saturated, especially when the wetting path is carried out in confined conditions. Such a decrease in water permeability is a consequence of the progressive collapse of macro-pores and the occlusion of some preferential percolation paths as the expansive material swells.

On the other hand, the amount of water found in micro-pores is assumed not to contribute to the water mass flow through the porous medium, since that type of water is strongly adhered to the clay particle surface by electro-chemical forces. Due to that, in problems related to the movement of water in soil, the microstructural water can be accounted for as part of the solid phase. However, the state of the water in micro-pores should not be neglected in deformation analyses of moderate to high expansive soils. As it has been mentioned previously, the swelling potential of such active clays can be explained by the large amount of water that can be inserted into the inter-layer spaces of a clay particle. The potential energy of microstructural water (that is, the microstructural suction) is related to the hydration of exchangeable cations at dry or lower water content conditions and to the development of the diffuse double layers at almost saturated conditions (Jacinto *et al.*, 2012; Rizzi *et al.*, 2012). In the multi-porosity approach developed by Alonso *et al.* (1999) to reproduce the deformation response of swelling clays, the microstructure is assumed to be saturated. However, a more general double-structure framework should contemplate the non-saturated state of microstructure and the existence of

local mass exchange processes between both structural media in order to allow the transfer of water from macro- to micro-pores and vice versa. In such conditions, it becomes necessary to establish a correlation between the microstructural water potential and the state of saturation of micro-pores by means of a water retention capacity law for microstructure.

In the following section, a general description of the main theoretical features associated with the water retention capacity of expansive soils is presented while the mathematical formulation of a modified van Genuchten law is briefly described in **Section 3.8.2.2**. The issue of the mass exchange of water between macrostructure and microstructure due to differences in their water potentials is discussed in **Section 2.4.3** and in **Section 3.6**.

2.4.1. THE WATER RETENTION CURVE: THEORETICAL ASPECTS

The soil-water retention capacity is assumed to be dependent on the type, fabric and mineralogy of the soil considered (Rizzi *et al.*, 2012). In the case of expansive clays, it also depends on the complex physico-chemical interactions at particle level involving the microstructural water, the clay layers and the exchangeable cations present in the inter-lamellar space (Jacinto *et al.*, 2012). Moreover, the shape of this curve is affected by the confinement conditions in which hydration or dehydration takes place. Typical water retention curves from compacted expansive samples following wetting/drying paths under confined (full lines) and unconfined (dashed lines) conditions are given in Figure 2-28. Those retention capacity curves were obtained from FEBEX bentonite samples compacted with their hygroscopic water content (of around 14%) at initial dry densities varying between 1.60 g/cm^3 and 1.75 g/cm^3 and in the temperature range of 22°C and 60°C (Villar and LLoret, 2004; Lloret *et al.*, 2004). These experimental results illustrate the impact of the strain state and the initial compaction conditions of soil samples on the amount of water retained in them (Lloret and Villar, 2007). For the same initial dry density, the amount of water stored in pores is usually higher for unconfined samples than for those that swell under isochoric conditions (Villar, 2002). The hydration under free swell conditions allows the expansive clays to fully develop their swelling potential, which leads to a significant increment of pore volume and, consequently, to a higher water retention capacity near saturation. In the case of confined samples, the increasing of the initial dry density leads to a reduction in their water retention capacity at lower suction values (see Figure 2-29). In fact, the increase in dry density implies a reduction in porosity and in the water content that can be retained in the inter-aggregate (large) pores, where the main mechanism of water retention is capillarity (Romero *et al.*, 1999; Jacinto *et al.*, 2012).

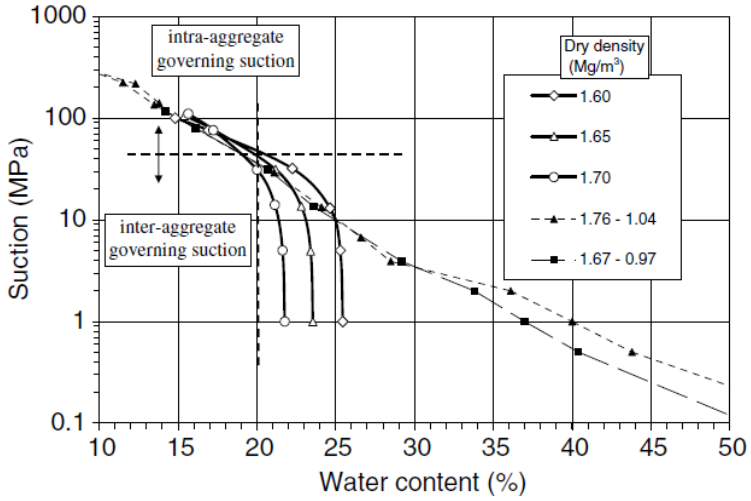

Figure 2-28: Effect of the dry density on the water retention capacity of FEBEX bentonite samples wetted under unconfined and confined conditions (Lloret and Villar, 2007).

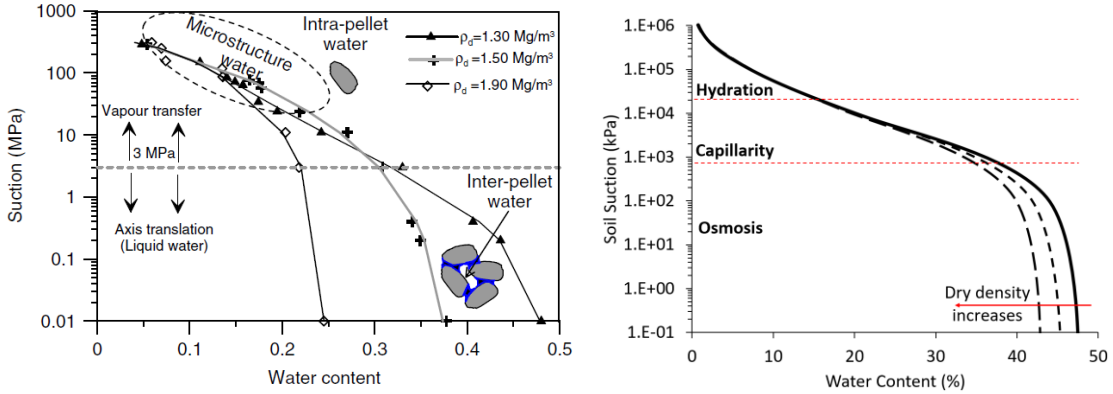

Figure 2-29: **(a)** Experimental water retention curves for FEBEX pellet mixtures at distinct dry densities obtained during wetting at isochoric conditions (Hoffmann *et al.*, 2007). The transition between the capillarity and the hydration of clay surface zones was defined at a suction value of 3 MPa; **(b)** representation of a typical water retention capacity curve for a highly plastic clay in which the water retention mechanism related to the development of the DDL close to the clay saturation (osmotic water adsorption zone) is also shown (after Wayllace, 2008).

It can be observed, in Figure 2-28 and Figure 2-29, a zone in which the volume of water stored in pores is not affected by the dry density of the expansive soil samples with suction ranging from 20 MPa to 550 MPa (Wayllace, 2008). Such a portion of the retention curves is mainly related to the water content in micro-pores and depends on the specific surface area and the mineralogical composition of the clay particle (Romero *et al.*, 1999; Yahia-Aissa *et al.*, 2001; Jacinto *et al.*, 2012). Consequently, the hydration of the clay mineral surface and the hydration of the exchangeable interlayer ions are the predominant water adsorption mechanisms controlling the quantity of water in active clays at low gravimetric water contents (Mitchell, 1993; Wayllace, 2008; Jacinto *et al.*, 2012). Such experimental data reveal the existence of two water retention zones in compacted unsaturated bentonites (Romero *et al.*, 1999), each of them associated to a distinct family of pores. Nevertheless, a third water adsorption regime – the osmotic water adsorption – becomes the predominant mechanism governing the water retention capacity of almost-saturated expansive soils, when the suction values are below 800

kPa (Wayllace, 2008). It arises from the differences between the dissolved ionic concentration in the bulk and in the interlayer pore water.

In unsaturated expansive clays, the capillary forces propel the absorption of water by the soil system, providing the amount of water required to start the wetting process at particle level with the hydration of the external surface of individual particles and aggregates. Microstructural wetting occurs when water molecules migrate from the external surface of clay particles to the voids between elementary clay layers in order to promote the hydration of cations in the inter-lamellar pores. As discussed in previous sections, the progressive adsorption of water into the mineral inter-layers leads to the formation of one, two, three or four discrete molecular layers of water and to a cumulative increase in the mineral basal spacing, characterizing the clay mineral swelling with no significant changes in the global volume of soil (Jacinto *et al.*, 2012). As more water is supplied locally to the porous medium, an inter-connected film of bulk water develops outside the clay aggregates and other mineral particles in the soil (Rizzi *et al.*, 2012) forming water "bridges" between the large pores filled with air (Villar, 2004). If the hydration process continues, the additional water provided to the soil increases the saturation state of macro-pores, which leads to the enlargement of the radii of pore-water menisci and to the reduction of the matric suction (Wayllace, 2008). During this hydration stage, the amount of water stored in the expansive soil is strongly dependent on pore geometric features, such as the macrostructural pore volume and the pore size distribution (Wayllace, 2008; Dieudonné *et al.*, 2017). When the active clay is close to its fully saturated state, the osmotic water adsorption drives the migration of water molecules from free water-saturated macro-pores (where the ion concentration is lower) to the space between clay particles, enhancing the development of the diffuse double layer and leading to a substantial increment in the soil swelling potential (Jacinto *et al.*, 2012; Rizzi *et al.*, 2012). If the saturation of the swelling clay is performed under constant volume conditions, an appreciable reduction of macro-porosity can occur in response to the increase in the intra-aggregate pore volume due to the microstructural swelling. Such a wetting-induced microstructural evolution could have a remarkable impact on the soil water retention capacity, as its capillary water retention capacity would be reduced (or neglected) if such a material were submitted to a subsequent drying-wetting cycle.

On the other hand, macro-pores are usually dried before micro-pores during the drying of a saturated swelling soil. As capillarity is the water retention mechanism driving the saturation state of macro-pores, it can be concluded that the changes in the soil density play a crucial role during the initial stages of dehydration, when suction is still small. In fact, an increase in the initial dry density of an expansive clay implies not only a decrease in the macrostructural pore volume, but also a reduction in the size of these pores (Dieudonné *et al.*, 2017). Consequently, such a pore size reduction leads to an increment of the macrostructural air-entry pressure measured along the main drying path (Della Vecchia *et al.*, 2015). As the expansive soil dries, the pore water phase becomes discontinuous in the largest pores and liquid water can be only found into the smallest macro-pores, where the capillary forces are strong enough to retain it. At very low water content conditions, all macro-pores are essentially emptied and the remaining water stored in the soil system is found in micro-pores. In such conditions, the moisture content in larger pores are due to the presence of water molecules in vapour phase. A gradient in the relative humidity arises from the unbalanced water potential (i.e., matric suction) between macro and microstructural media. In a drying path, such a local relative humidity gradient leads

to the migration of water molecules through vapour phase (Rizzi *et al.*, 2012) from micro- to macro-pores. This water mass transfer induces dehydration of microstructure, starting by drying the inter-particle voids and finally, leading to desorption of the inter-layer pores if the desaturation process continues. However, a great amount of energy is associated with the removal of water from the interlayer space. In order to remove most of the adsorbed water without producing any important structural changes in expansive clays, it is necessary to submit the soil sample to an oven drying procedure, in which temperature usually ranges between 100°C and 110°C (Basma *et al.*, 1994; Caputo, 1996; Kabubo *et al.*, 2017b). An isothermal laboratory procedure to reach such high suctions at which microstructure becomes unsaturated consists in imposing the vapour equilibrium between the pore-water potential of the dry soil and a reference atmosphere (imposed by a salt solution) with a known potential (Hoffmann, 2005; Rizzi *et al.*, 2012). This laboratory technique allows to apply suction values as high as 400 MPa (Rizzi *et al.*, 2012). van Olphen (1963b) estimated the pressure value necessary to remove the fourth, third, second and first water layer in the interlayer space for a calcium montmorillonite as being equal to 20 MPa, 125 MPa, 250 MPa and 600 MPa, respectively. The bulk shrinkage of an expansive soil when following a drying path is a consequence of the combined effects of an increase in capillary forces among clay aggregates and other soil particles (in the range of suctions for which capillarity prevails) and of the desaturation at particle level as micro-pores become drier.

The experimental determination of the soil-water characteristic curve of confined swelling clays shows a hysteretic water retention behaviour under cyclic variations of water content (ENRESA, 2000; Villar and Lloret, 2004; Lloret and Villar, 2007; Wayllace, 2008; Rizzi *et al.*, 2012; Seiphoori *et al.*, 2014). In Figure 2-30 , the measured retention curves of compacted calcium- (left) and sodium- (right) bentonites are given, in which the hysteresis effect on the wetting-drying paths under constant volume conditions is quite evident. The water retention curves of the Ca-Mg-bentonite (FEBEX bentonite) shown in Figure 2-30(a) were obtained following a wetting/drying path in confined samples with dry densities ranging from 1.58 to 1.75 Mg/m^3 (ENRESA, 2000). The hysteretic water retention behaviour of the compacted Na-bentonite (MX-80 bentonite) observed in Figure 2-30(b) was determined by performing successive wetting and drying cycles in MX-80 samples compacted at an initial dry density of 1.80 Mg/m^3 (Seiphoori *et al.*, 2014). Such significant and irreversible changes in retention curves when the expansive material is submitted to cyclic variations of suction suggest the evolution of its fabric during the wetting/drying cycles, which has a direct impact on its water retention capacity.

It is important to mention that the soil-water retention curves can also be expressed in terms of the degree of saturation (instead of the gravimetric water content), as displayed in Figure 2.30. In many geotechnical applications for which the basic volumetric relationships are more convenient, as the implementation of a mathematical formulation in a finite element code (see **Section 3.10**) for predicting the THM behaviour of expansive clays discussed in the next chapters, suction is given as a function of the degree of saturation. The degree of saturation of an unsaturated soil (S_l) is related to its gravimetric water content (w) by means of the following expression:

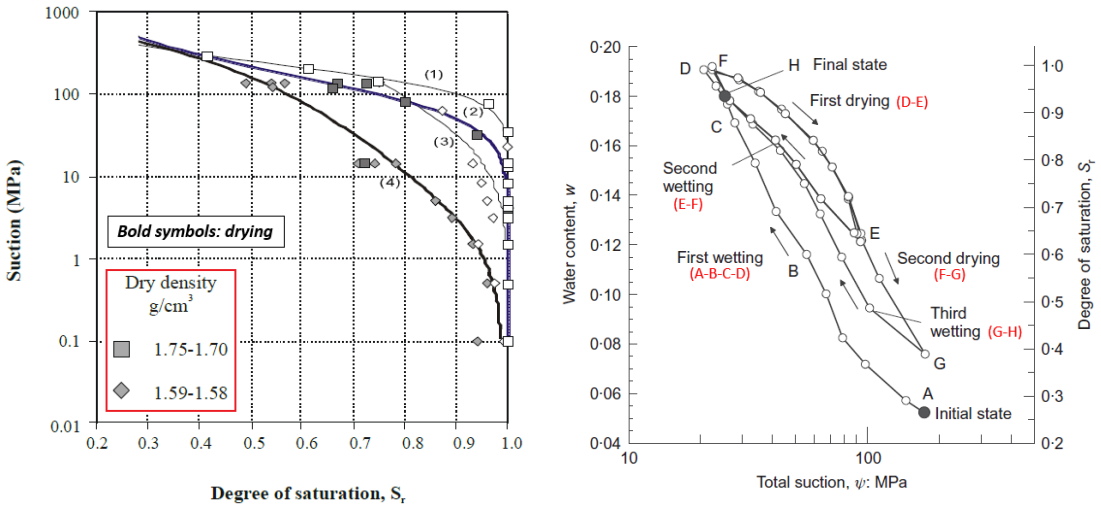

(a) **(b)**

Figure 2-30: Hysteresis of the water retention curves during cyclic changes in suction for: **(a)** compacted samples of FEBEX bentonite at different densities (ENRESA, 2000); **(b)** an MX-80 granular bentonite compacted at a dry density of 1.80 Mg/m^3 (Seiphoori *et al.*, 2014).

$$S_l = \frac{w\rho_s}{e\rho_w} \tag{2-2}$$

where e is the void ratio and ρ_s and ρ_w are the solid particle and the water densities, respectively. Nevertheless, it has been reported that this expression may relate the amount of pore-water retained in some expansive clays close to their full saturation to values of degree of saturation higher than 1.0 (Jacinto *et al.*, 2012). Such an unexpected prediction arises when it is assumed that the adsorbed water (in micro-pores) and the bulk water (in macro-pores) have the same physico-chemical properties. In fact, the drawback of using Equation (2-2) to estimate the saturation state of highly active clays from their total water content comes from not considering the denser state of the microstructural water.

2.4.2. THE MICROSTRUCTURAL WATER DENSITY

Several experimental studies suggested that the water adsorbed in the inter-layer and in the intra-aggregate pores of compacted expansive clays has a density higher than the conventional value of 1.0 Mg/m^3 (Martin, 1962; Low, 1979; Derjaguin *et al.*, 1986; Pusch *et al.*, 1990; Villar and Lloret, 2004; Fernández and Rivas, 2005; Hoffmann, 2005). Moreover, the density of the inter-layer water is not constant but increases as the free water content decreases (as displayed in Figure 2-31(a)) as well as the volume of macro-pores (see Figure 2-31(b)) and that behaviour is more prominent in sodium-type montmorillonites (Martin, 1962; Villar and Lloret, 2004; Jacinto *et al.*, 2012; Rizzi *et al.*, 2012). Another evidence of that change in the adsorbed water density is observed from the unrealistic values for the degree of saturation (greater than 1.0), obtained from the total mass of water stored in highly expansive soils near saturation, when no distinction is made in the density of pore-water according to type of pores where it is retained.

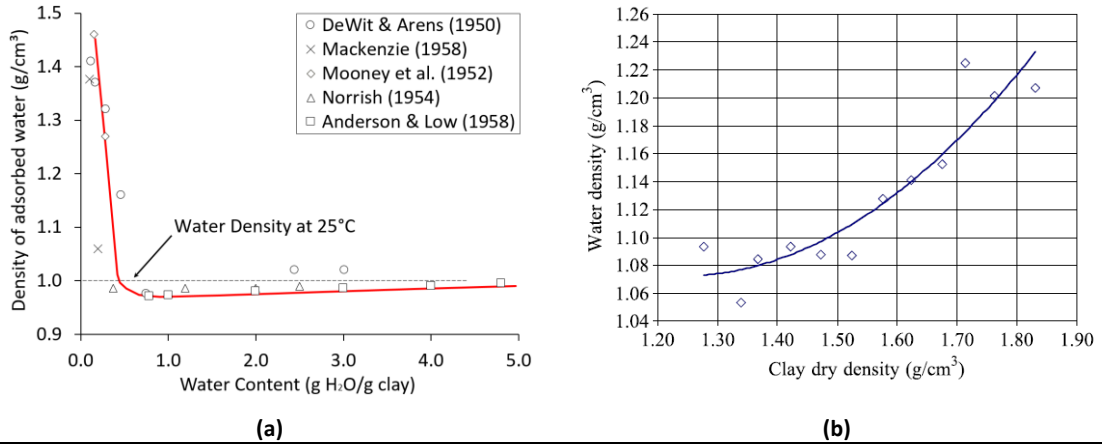

Figure 2-31: **(a)** Dependence of the adsorbed water density (a) on the water content in a Na-montmorillonite (after Martin, 1962); **(b)** on the dry density of compacted FEBEX bentonite samples (Villar, 2002).

In order to overcome the issue associated with Equation (2-2) in calculating the degree of saturation of almost saturated clays, Jacinto *et al.* (2012) proposed a method that estimates an average density for pore-water taking into account the different types of water present in a swelling clay. In such a correction procedure, the amount of water in pores is split into the portion of water in the inter-layer pores and the water held in the rest of pores (the bulk water and the water attached on the external clay particle surfaces). The average water density (ρ_w, in Equation (2-2)) is determined as a function of the gravimetric content and the density for each one of those types of pore-water. The inter-layer water content and the water density are dependent on the hydration state found in the inter-lamellar space. It means that such microstructural properties depend on the inter-layer specific surface area of the clay minerals and the type of exchangeable cation in the interlayer space. The amount of water adsorbed on the external surface of the clay aggregates depends on the type of clay mineral and on the relative humidity in the soil. In the development of their water density correction procedure, Jacinto *et al.* (2012) assumed that the amount of free water could be negligible in highly compacted clays at confined conditions. Furthermore, they adopted the same density value for the bulk water and for the water adsorbed on the external surface of the clay particles. The assumption of a changing average density for microstructural water with the hydration state of microstructure, as proposed in Jacinto *et al.* (2012), seems to solve the drawback of finding unrealistic degrees of saturation for the water retention capacity of bentonite-based materials when expressed in terms of degree of saturation (see Figure 2-32).

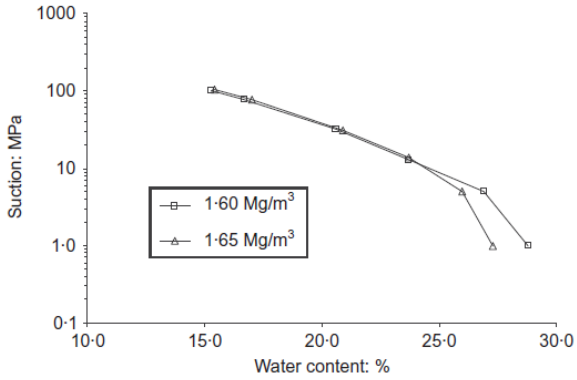

(a)

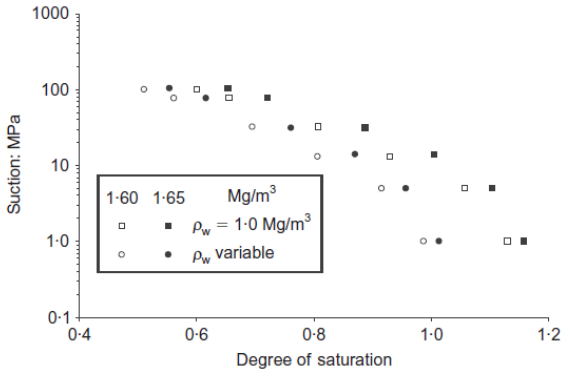

(b)

Figure 2-32: **(a)** Suction against gravimetric water content curves for compacted FEBEX bentonite samples at different dry densities (from Lloret *et al.*, 2004); **(b)** Suction against degree of saturation curves determined by means of the conventional and the "corrected" values for the adsorbed water density (Jacinto *et al.*, 2012).

2.4.3. THE MICRO-MACRO WATER EXCHANGE: THEORETICAL ASPECTS

The mass exchange of water between micro- and macro-pores in an expansive clay is the mechanism governing the saturation state of micro-pores. This mass transfer process is related to the existence of a local potential energy gradient between the microstructural water and the bulk water (in macro-pores). On the one hand, macrostructural water potential is mainly related to the capillary effects and to the saline concentration in macro pore-water. Both the tension forces that appear on the menisci formed by the water-air interface and the saline concentration of the free water are affected by the soil density state (Rizzi *et al.,* 2012). On the other hand, microstructural water potential is associated with the hydration forces of exchangeable cations and the forces arising from the water-clay particle interactions (Wayllace, 2008). Water molecules can be transferred from macro- to micro-pores and vice-versa, depending on the magnitude of the potential energy in each type of pore-water found in the clay. However, such a water mass transfer process must not be interpreted as a type of advective flux, as the water mass flux described by Darcy's law, but should be taken as a local change in the pore-water phase (Alonso and Navarro, 2005). In fact, in many geotechnical problems, as the movement of fluid phases through the porous medium, micro pore-water is generally accounted for as part of the solid phase, since it is strongly adhered to the soil particle surfaces and does not participate in such fluid transport processes (Habibagahi, 1977; Navarro and Alonso, 2001).

In the last decades, some researches have related the long-term deformations (expansion or compression) of clays to the local hydration or dehydration of the soil microstructure (de Jong, 1968; Mitchell, 1993; Navarro and Alonso, 2001). In that sense, Alonso and Navarro (2005) suggested that the secondary consolidation of plastic clays would be treated as a consolidation process at microstructural level, relating such a time-dependent process to the local dehydration of microstructure due to pore-water mass transfer from micro- to macro-pores. It has also been stated that the micro-macro water exchange rate depends on the deformation state of the aggregates of clay particles (microstructure), reducing as the microstructural void ratio also decreases (see Figure 2-33). It is also reported that the rate at which pore-water is exchanged between both structural levels is dependent on the shape, size, permeability and stiffness of the clay particles and aggregates (Alonso and Navarro, 2005).

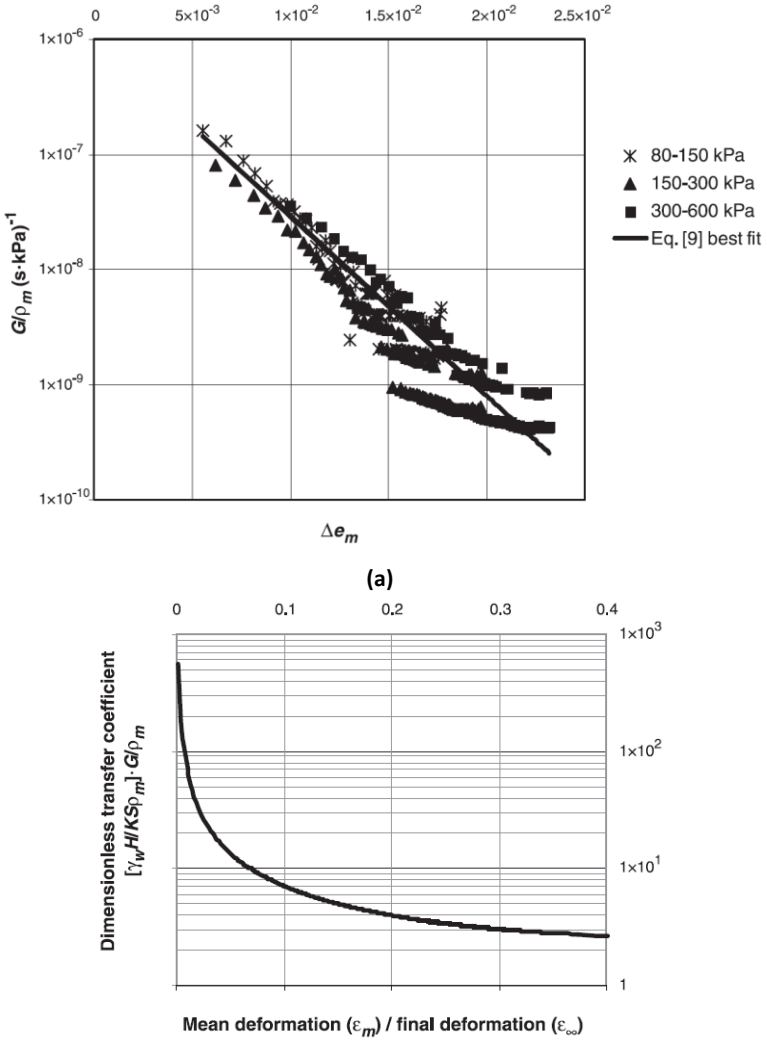

Figure 2-33: **(a)** Experimental decrease of the micro-macro water transfer coefficient (**G** in these plots) with the microstructural strains developed under several loading steps and **(b)** predicted reduction in the water transfer coefficient during the microstructural consolidation process of a clay from Galicia, Spain (Alonso and Navarro, 2005). In these plots, ρ_m is the density of microstructural water, ***H*** is the layer thickness of the clay, ***K*** is the layer permeability and **S** is its specific surface area.

The experimental characterization of the hydro-mechanical behaviour of a mixture of FEBEX pellets performed by Hoffmann (2005) has provided an insight into the hydration process of

expansive granular materials and the impact of the type of water transfer mechanism on their deformation response. In such a research program, the hydration of individual pellets in compacted samples under confined and unconfined conditions was accomplished by flooding the macro-pores with liquid water or by means of the water vapour transfer from the inter- to the intra-aggregate voids. Wetting by injecting liquid water first saturates the macro voids due to the higher permeability to water at that structural level. The hydration of the expansive pellets due to the local differences in the water potential between inter- and intra-aggregate pores starts after the quasi-saturation of macro-pores. In this type of wetting procedure, initial structural collapses can be observed due to the weakness of the inter-aggregate forces as macro-pores become saturated, while the trend to swell only appears when the re-saturation of micro-pores (due to the water uptake from macro-pores) takes place. Hoffmann (2005) also noted that the macrostructural water content in confined samples increased proportionally to the injection pressure of water when wetting was performed with liquid water. Nevertheless, the final water content in micro-pores was not affected by the magnitude of the injection pressure gradient during the water-flooding of the expansive samples. It is because the hydration process of micro-pores depends on the local differences in the potential energy of the water in micro- and macro-pores and not necessarily on the amount of bulk water present in the quasi-saturated macro voids. When the expansive samples were saturated by means of the vapour transfer procedure, the water mass exchange between the two scales of porosity was slower and the re-saturation process was basically uniform at both pore levels. Such a hydration technique enables the (quasi) local balance of the water potential in micro- and macro-pores. Consequently, the occurrence of macrostructural collapses during hydration is drastically reduced in this situation and a marked trend for the soil to swell, as micro-pores are re-saturated, is usually observed from the beginning of the wetting path. Therefore, the deformation response of an expansive clay as it hydrates is highly dependent on the wetting procedure employed to provide water to micro-pores, which affects the sequence of microstructural re-saturation (whether it occurs after or simultaneously to the saturation of macro voids).

2.4.4. HYDRAULIC CONDUCTIVITY

The hydraulic conductivity is one of the most crucial soil properties that is intrinsically related to all those hydro-mechanical processes governing the transport and the changes in the amount of water stored in pores. Furthermore, it also related to the development of the stresses and deformations generated in a mass of soil due to changes in external loadings. Consequently, it is not possible to have a suitable understanding of the constitutive behaviour of a volume of soil without considering such a soil property. In fact, any research about the feasibility of using expansive clays in engineered barriers and seals must include a detailed characterization of the hydraulic conductivity in such materials and its evolution with the changes in the environmental variables (as suction and temperature, for example) and porosity.

The saturated permeability is controlled by the soil fabric, characterized by its dry density, and usually expressed as a function of porosity (Hoffmann *et al.*, 2007). Consequently, permeability is lower in fine-grained soils, as clays. Moreover, it reduces with the increase in the compaction effort required to produce a denser soil skeleton. In unsaturated porous media, water

conductivity increases with the pore-water content due to the development of an interconnected liquid water phase throughout the large pores. In non-isothermal problems, water permeability also depends on temperature, once those thermal changes can induce structural rearrangements affecting the pore size distribution in addition to altering some physical properties and the phase of the permeating fluid – see **Section 2.5**.

Bentonites as compacted blocks or as pellet mixtures are described as materials with a very low permeability and a high swelling potential when hydrated. Such a combination of geotechnical properties makes their use in engineered barriers for radioactive waste disposals as a logical and advisable option. Many investigations were carried out along the last decades in order to relate some expected phenomena that take place during the re-saturation of a confined barrier to changes in the water flux conditions. In that sense, the experimental characterization performed by Pintado (1999), Villar (1999; 2002), Hoffmann (2005), Karland *et al.* (2008) among others provided an extensive database on the hydraulic behaviour of bentonite-based materials and its dependence on the dry density, the water content and the chemical composition of pore-water and temperature. Consequently, several empirical relationships have been obtained for modelling the hydraulic permeability of such materials under isothermal and non-isothermal conditions, as the ones proposed in Villar (2002). The experimental saturated hydraulic conductivity for several confined granulated mixtures with FEBEX bentonite pellets (left) and MX-80 bentonite pellets (right) as a function of dry density of the compacted samples are illustrated in Figure 2-34. These experimental measurements corroborate the expected decrease of water permeability with as dry density of compacted samples increases due to the reduction in their initial porosity.

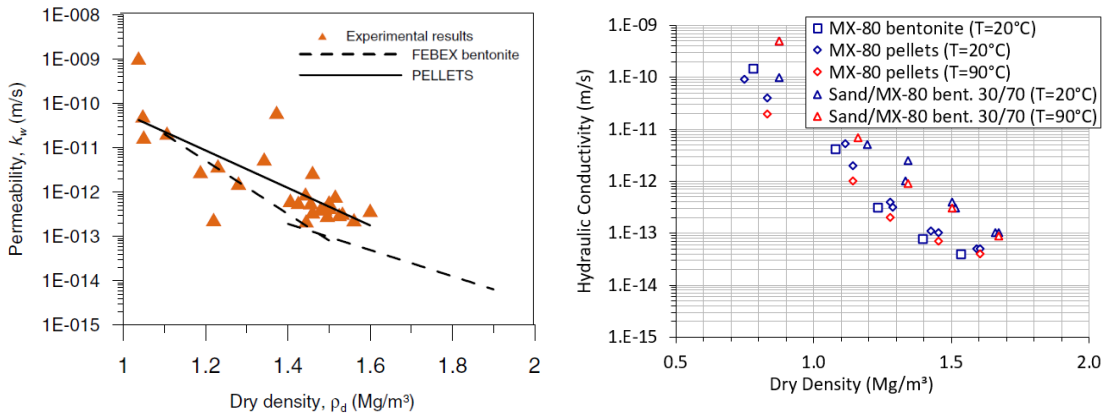

Figure 2-34: Saturated water permeability of **(a)** FEBEX bentonite pellet mixtures (Hoffmann *et al.*, 2007) and **(b)** MX-80 bentonite mixtures (modified from Karnland *et al.*, 2008) compacted at different dry densities.

The experimental development of the unsaturated hydraulic conductivity of two distinct expansive soils (bentonites) following a saturation procedure under isochoric conditions are displayed in Figure 2-35. The water permeability dependence on suction registered in Figure 2-35(a) was determined using the instantaneous profile method (Watson, 1966; Daniel, 1982) on compacted samples of a Chinese bentonite (known as GMZ bentonite) for a dry density of 1.70 Mg/m^3 (Ye *et al.*, 2009). The experimental data shown in Figure 2-35(b) were obtained from fast infiltration tests performed on samples of FEBEX bentonite pellets compacted at an average dry density of 1.30 Mg/m^3, in which the inflow and outflow water volumes were monitored

(Hoffmann, 2005; Hoffmann *et al.*, 2007). In both cases, it can be noted an initial decay in permeability values as the water content increases. Such a drop in the hydraulic conductivity, even in several orders of magnitude as in the case of the FEBEX bentonite samples (Figure 2-35(b)), can be explained in terms of the fabric evolution of the expansive clays due to changes in their pore-water content. At the beginning of the infiltration tests, the flux of water occurs through the initial network of large pores. After that initial water infiltration stage, bentonite aggregates start to swell, which leads to a progressive clogging of the inter-aggregate voids and to a reduction of soil permeability. In the case of the FEBEX bentonite pellets, the fast water-filling of macro-pores generated a weakening of the inter-aggregate contact forces, which in turn induced a drastic collapse of the initially open (and unstable) soil fabric, producing a sharp drop in permeability until reaching values close to saturated conditions (Hoffmann *et al.*, 2007), as plotted in Figure 2-35(b). However, for more stable clay fabrics, the invasion of macro-porosity due to the microstructure expansion does not produce any drastic changes in the water permeability and a typical and gradual increase of hydraulic conductivity as the expansive clay approaches its saturation can be observed (Ye *et al.*, 2009), as illustrated in Figure 2-35(a). Data provided by such water infiltration tests allow to calibrate and model the unsaturated water conductivity and its dependence on the degree of saturation. In fact, a dimensionless factor, termed as the relative permeability (see **Section 3.8.2.1**) and defined as a function of the degree of saturation, is multiplied to the saturated hydraulic conductivity to obtain the influence of the de-saturation of pores in the mass flux of water through the soil.

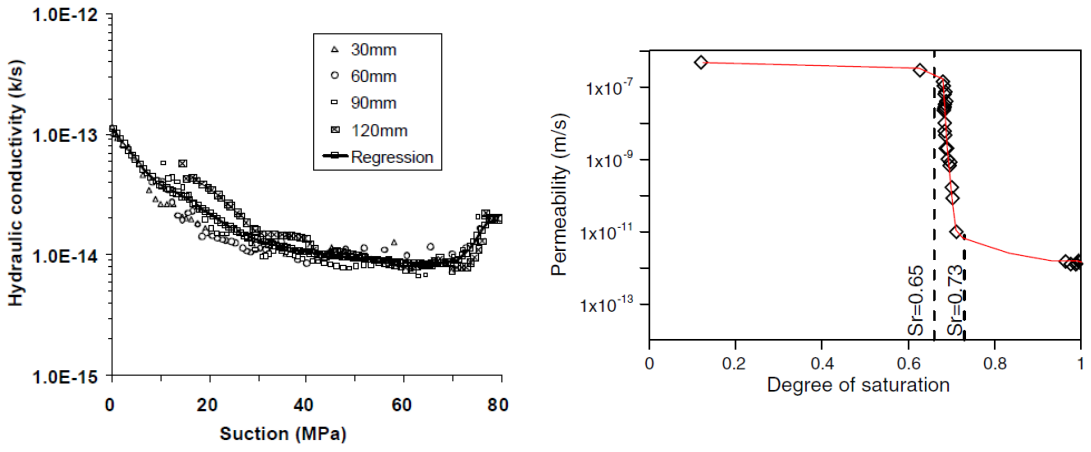

Figure 2-35: Evolution of water conductivity following a wetting path until the saturation of **(a)** compacted samples of the GMZ bentonite (Ye *et al.*, 2009) **(b)** FEBEX bentonite pellet mixtures (Hoffmann *et al.*, 2007).

The dependence of the water-saturated permeability of compacted expansive clays (bentonites) on environmental variables, as temperature and the chemical composition of pore-water, was also investigated and the conclusions of such researches are collected in several publications (Karnland *et al.*, 1992; Pusch, 2001a; Mata and Ledesma, 2003; Villar *et al.*, 2003; Villar and Lloret, 2004). The influence of thermal changes on the hydraulic conductivity of expansive soils is briefly described in **Section 2.5**. The apparent increase of water conductivity observed in experimental percolation tests using saline water may be related to the osmotic shrinkage of clay aggregates (Lloret and Villar, 2007) due to the salt concentration gradient between the permeant water (filling macro-pores) and the microstructural water (inside the aggregates). Therefore, such an increase of water conductivity with the salinity of macrostructural water is a consequence of the increment in the inter-aggregate porosity.

2.5. THERMAL IMPACT ON THE BEHAVIOUR OF EXPANSIVE CLAYS

It is well-known that thermal loadings produce significant changes in some soil engineering properties, altering the mechanical response and the water retention capacity and the flux conditions in a mass of soil, sometimes in an irreversible way. Many publications are devoted to deal with the temperature effects on inter-particle forces, pore-water pressures (Campanella and Mitchell, 1968; Baldi *et al.*, 1988), swelling potential (Yong *et al.*, 1962; Mitchell, 1993; Wang *et al.*, 2008), consolidation and creep of a mass of soil (Mitchell and Campanella, 1963; Paaswell, 1967; Delage *et al.*, 2000; Cui *et al.*, 2009), soil strength and compressibility (Joshi *et al.*, 1994), flow conditions (Habibagahi, 1977; Cho *et al.*, 1999), etc. The impact of non-isothermal loadings due to seasonal temperature variations is limited to the most superficial zones in the soil depth where the phenomena of evapotranspiration, vapour condensation and freezing/melting processes of pore-water usually take place. However, important thermal changes can also occur in a mass of soil around natural or man-built heat sources. This is the case of those applications where the porous medium is used as a natural thermal isolation system or as a buffer/backfill material for a nuclear waste disposal in deep underground repositories, as well as surrounding buried high-voltage cables, the machineries of enhanced petroleum extraction and geothermal structures (Baldi *et al.*, 1988). In the context of engineered barrier systems (EBS) for isolating the biosphere from undesirable and dangerous wastes, the use of expansive clays (bentonites) as seal/barrier is not only due to their high adsorption capacity and lower water conductivity (as discussed in previous sections) but also due to their excellent thermal properties. In fact, the bentonite-based materials must act as a "thermal bridge" between the sources of heat inside the EBS and the host rock, avoiding the occurrence of high temperature gradients that could compromise the integrity of the canister and the barrier itself. In other words, the bentonite buffer must rapidly dissipate the heat produced by the radioactive decay of the nuclear waste inside the canister and by the hydration of cementitious materials in the EBS (IAEA, 1984; Pusch *et al.*, 2012; NDA, 2016) in order to ensure that the maximum allowable temperature is not exceeded.

Despite the fact that, nowadays, the application of bentonites in engineered barriers motivates many researches for characterizing the thermal properties and response of expansive soils, the first relevant studies on the thermal behaviour of such materials aimed to evaluate the heating impact on their geomechanical and swelling properties (Aylmore *et al.*, 1969; Chandrasekharan *et al.*, 1969; Post and Paduana, 1969). Consequently, it was noted that the performance of a preheating procedure on expansive soils tends to minimize their swelling potential due to the improvement of their strength (Jeyapalan *et al.*, 1981; Joshi *et al.*, 1994). Depending on the type of thermal stabilization used to strengthen the soil (heat treatment or freezing stabilization) and on the magnitude of the applied thermal loading, the effects of the thermal treatment can be temporary or permanent. It is reported that the imposition of prolonged and very high thermal gradients on samples of compacted bentonites tends to generate irreversible structural changes that not only affect their subsequent swelling response, but also even change the mineralogical composition of the post-heated materials (Shepard, 1998; Kabubo *et al.*, 2017a). In fact, the experimental study carried out by Wang *et al.* (2008) on the swelling behaviour of two commercial expansive clays when heated to temperatures in the range 400 – 600°C found that

their swelling potential was reduced drastically as temperature increased. The oven-heating of a black cotton soil (an expansive clay from Kenya) to temperatures ranging between 200°C and 1200˚C conducted by Kabubo *et al.* (2017a) also confirmed such changes in the swelling response, with the clay showing a non-plastic behaviour at temperatures close to 700°C. Furthermore, it was also observed the occurrence of irreversible compositional changes as the vanishing of the clay fraction and the sudden appearance of the gravel fraction (due to the thermal-induced aggregation of fine-grained particles) when temperature surpassed 600°C. Such interesting findings are crucial to restrict the temperature development around a canister containing heat-emitting residues to maximum values that do not compromise the envisaged safety and the engineering and operational requirements for the bentonite barrier (IAEA, 1984).

During the lifetime of a repository for heat-generating waste, some thermal processes are expected to occur in its immediate vicinity. Some of them are intrinsically related to the heat release from the radioactive waste and its subsequent transfer through the surrounding materials (backfill material and host rock), while other ones are induced by the existence of a thermal gradient. The most relevant thermal processes that take place in the near-field of an engineered barrier system are listed below:

- the heat transfer through the canister, the engineered barrier and the host rock by conduction (mainly) and convection due to the natural or thermally-induced movement of liquid water and water vapour; heat transfer by radiation may be considered negligible after backfilling (IAEA, 1984);
- the vaporization of pore-water (generation of water vapour) in the central portion of the engineered barrier (hotter zones) and the subsequent vapour transport by the vapour diffusion mechanism;
- the condensation of the water vapour (coming from the hotter regions of the barrier) at zones close to the host rock (colder zones), where temperature is low enough to allow the occurrence of such physical process;
- the thermal expansion of the engineered barrier components and the host rock as a result of the increase in temperature due to the heat release and transfer from the metallic container to the rock;
- the differential thermal expansion of the several components of the solid structure of the porous media and the pore-water contained in it;
- the contribution of the condensation of vapour (coming from the inner portions of the barrier) to the development of swelling strains and pressures close to the barrier-rock interface;
- the shrinkage of the buffers in the vicinity of the heater due to strong pore-water vaporization;
- thermally-induced alterations of the properties of the waste isolation system, which could accelerate the occurrence of some physico-chemical processes, as the container corrosion, the nuclear waste dissolution and the transport of radionuclides (IAEA, 1984).

In all the situations and processes mentioned before, the deformation behaviour of the porous medium to natural or imposed thermal loadings mostly depends on its mineralogy, granulometry and fabric as well as its pore-water content. Moreover, the heat propagation/dissipation through a porous medium is determined by the thermal conductivity of its constituents, which in turn also depends on the soil nature and structure and on the pore-saturation state (see **Section 2.5.1.1**). In the next sections, a brief description of the soil properties related to the thermal processes taking place inside an engineered barrier is presented (**Section 2.5.1**). The main effects of moderate and intense heating on the physico-chemical properties of pore-water and on the evolution of the clay mineralogy are listed in **Section 2.5.2** and **Section 2.5.3**, respectively. In additon, the most relevant thermal effects on the soil response in general, and on the thermal behaviour of expansive clays in particular, are addressed in **Section 2.5.4** and **Section 2.5.5**.

2.5.1. THERMAL PROPERTIES

The amount of heat energy stored in and transported through a mass of soil is governed by its thermal properties (Farouki, 1981; Abu-Hamdeh, 2003; Villar, 2004). In any thermal analysis in soils or rocks, the determination of these thermal properties and their dependence on the physical composition of such geotechnical media are crucial to predict the influence of temperature and heat flux on the development (in space and time) of the THM response of those materials. In the context of clay barriers for high-level nuclear wastes, the specifications for the repository design variables – as the type and configuration of the barrier components, the separation between the canister and the host rock and between individual (and consecutive) canisters – require the thermal characterization of the barrier materials once their thermal properties control the heat dissipation and condition the effectiveness of the EBS itself. Moreover, the experimental determination of the thermal properties of bentonite materials under changing environmental conditions provide a useful database for the calibration of theoretical and empirical laws able to predict the thermal response of the barrier system during its operational lifetime.

The main properties required to thermally characterize a porous medium are: the thermal conductivity, the heat capacity (or the specific heat) and the thermal expansion coefficient. A brief description of such properties is given in the following sections. In clayey materials, such properties are affected by the water content and the density of the soil (Abu-Hamdeh, 2003; Villar, 2004). Furthermore, laboratory measurements carried out on compacted bentonites also found a temperature dependence of those soil properties (ENRESA, 2000; Xu *et al.*, 2019).

2.5.1.1. THERMAL CONDUCTIVITY

The thermal conductivity accounts for the capacity of a soil to conduct a certain amount of heat when subjected to temperature gradients. Therefore, such a thermal property is the main

parameter controlling the dissipation of the heat generated in the canister through the barrier system to the host rock (Knutsson, 1983).

The thermal conductivity of a volume of soil is dependent on the thermal conductivity of the different phases found in it. Consequently, the pore-water content exerts a direct influence on the thermal conductivity of the soil. Since the thermal conductivity of the free water is higher than the thermal conductivity of the air phase, the soil thermal conductivity increases with the water content for a given density (Villar, 2004). Nevertheless, such a dependence is not linear for fine-grained soils, but tends to exhibit a pronounced increase when the soil water content is high enough to start filling macro-voids, as clearly shown in Figure 2-36(a). The thermal conductivity of the solid phase depends solely on the mineral composition of the soil particles, whose thermal conductivity is usually higher than the thermal conductivity of pore-water. Consequently, the significant differences in the measured thermal conductivity of bentonites at similar dry densities and water contents are related to the differences in their mineralogical composition (content and type of accessory minerals) as well as to the content of quartz and other minerals mixed with bentonite particles (Villar, 2004; Tang *et al.*, 2008; Xu *et al.*, 2019).

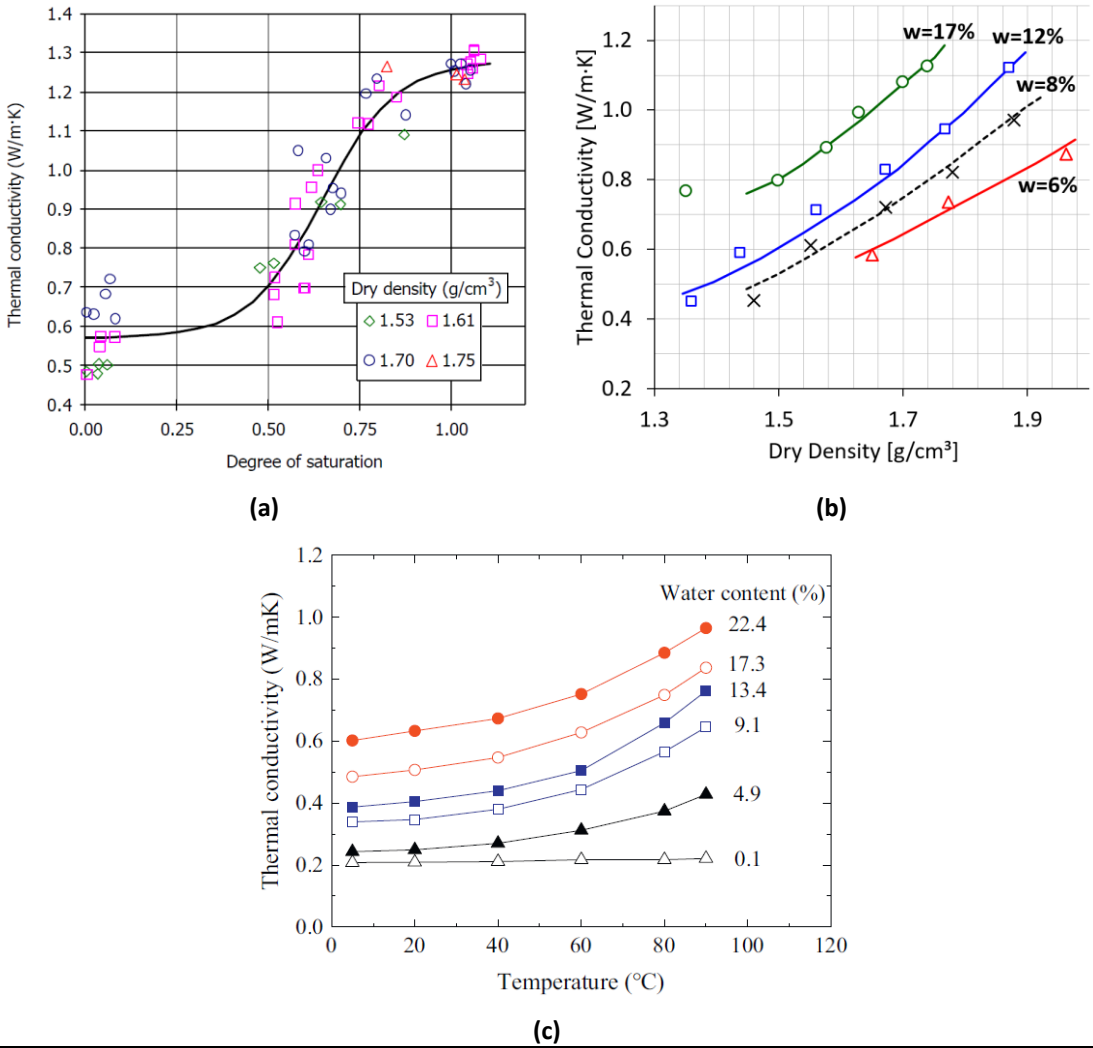

Figure 2-36: Thermal conductivity of bentonites as a function of: **(a)** the degree of saturation (Villar, 2002); **(b)** the dry density, at several water contents (from Beziat *et al.*, 1988) and **(c)** temperature (Xu *et al.*, 2019).

Experimental evidences show that the thermal conductivity tends to increase with the dry density of the soil (see Figure 2-36(b)). Such an increase is due to the reduction in porosity (macro-porosity, in compacted expansive clays) generated by the higher compaction energy required to obtain a denser material. On the one hand, the densification process reduces the space in a soil available for water or air and increases the solid content in the soil samples. On the other hand, the compaction effort applied on an unsaturated soil tends to expel the air phase from pores, leading to a mechanically-induced re-saturation of those pores. Consequently, and for a given water content, the thermal conductivity also increases with increasing dry densities, as illustrated in Figure 2-36(b).

Although the temperature dependence of thermal conductivity of compacted bentonites has not been studied as extensively as its dependence on water content and dry density, however, the few researches regarding this topic have shown a tendency of such a thermal property increases as temperature rises (Knutsson, 1983; Beziat *et al.*, 1988; Börgesson *et al.*, 1994; Xu *et al.*, 2019). These thermal conductivity changes due to temperature tend to be more noticeable for higher water contents, as shown in Figure 2-36(c). Moreover, the rate of thermal conductivity increase enhances at higher temperatures. This temperature dependence can be understood if the heat transfer in an unsaturated porous media is considered as a contribution of two heat transfer mechanisms. The first of these mechanisms is the heat conduction through the different soil components (solid, pore-water and pore-air) while the second one accounts for the heat transferred by the movement of water vapour due to temperature gradients in the soil pores (Sakaguchi *et al.*, 2007). This latter mechanism is termed as the heat latent transfer and it is related to the evaporation and condensation processes that take place at the menisci of the water "bridges" and at the water films surrounding the soil particles and to the vapour diffusion through the pores filled with air (Sakaguchi *et al.*, 2007). A schematic representation of the heat flux through an unsaturated porous medium under temperature gradients is shown in Figure 2-37. The transfer of latent heat is the main cause for the increase in the thermal conductivity with temperature, once a rise in temperature facilitates the generation of vapour and increases the water fluidity (Hiraiwa and Kasubuchi, 2000; Sakaguchi *et al.*, 2007; Smits *et al.*, 2013). Furthermore, such an increase in temperature tends to induce a reduction of the volume of water bridges (that also act as thermal bridges) at each particle contact point, leading to a decrease in the local heat conduction mechanism (Sakaguchi *et al.*, 2007). The relevance of the latent heat transmission in the heat flux process in unsaturated soils depends on the development of enough water bridges throughout the porous medium in order to promote the evaporation/condensation at those liquid-islands and the continuity of the air phase for the vapour migration. Therefore, the role played by the heat latent mechanism in the propagation of heat through a soil subjected to temperature gradients is less significant in dry and dense soils (Xu *et al.*, 2019). Consequently, the temperature dependence of the thermal conductivity is enhanced by decreasing the dry density and increasing the pore-water content (Xu *et al.*, 2019).

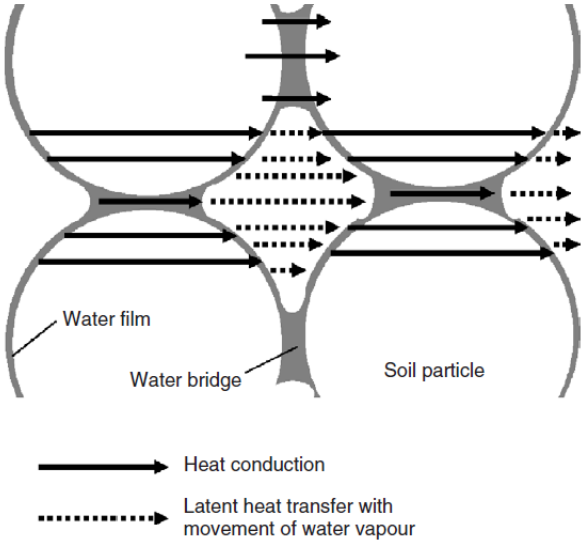

Figure 2-37: Representation of the heat conduction and the latent heat transfer due to the vapour diffusion in an unsaturated porous medium (Sakaguchi *et al.*, 2007).

A last but not least important aspect to mention is that the thermal conductivity parameter plotted in Figure 2-36(d) is, in fact, the apparent or effective thermal conductivity of the soil (Hiraiwa and Kasubuchi, 2000; Xu *et al.*, 2019) since it also implicitly accounts for the vapour diffusion induced by the temperature gradient. In other words, such a thermal parameter relates both heat transfer mechanisms to the temperature gradients according to Fourier's law (see **Section 3.8.1**). However, those heat transfer mechanisms may be decoupled in such a way that Fourier's law only takes into account the heat conduction through the distinct soil components and phases. In such a situation, the heat flux component related to the vapour diffusion is accounted for separately (see **Section 3.7.4** and **Section 3.8.2.3**). Thus, the thermal conductivity parameter does not depend on temperature, but only on the dry density (porosity) and the water content (degree of saturation). In **Section 3.8.1** an alternative expression for determining the thermal conductivity of a soil is used, which is defined in terms of the dry and the saturated thermal conductivities (see Equation (3-93)). Such a convenient choice reflects the heat flux under oven-dry and saturated conditions, when the temperature dependence of thermal conductivity and, consequently, the contribution of the latent heat transmission to the thermal flux can be considered insignificantly small (Hiraiwa and Kasubuchi, 2000).

2.5.1.2. HEAT CAPACITY AND SPECIFIC HEAT

By definition, the heat capacity accounts for the heat energy that must be absorbed by a mass of fluid or a body in order to produce a unit temperature rise while the specific heat is the amount of heat per unit mass required to generate that temperature change. Being the soil a highly heterogeneous and multi-species medium, its heat capacity is calculated from the sum of the heat capacities of its different constituents. Nevertheless, in many thermal approaches in unsaturated media, the heat capacity of the air phase can be neglected due to its negligible mass. A theoretical estimate for the specific heat of an unsaturated soil (c) is given as follows (Abu-Hamdeh, 2003):

$$c = \frac{\rho_d}{\rho}(c_s + wc_w) = \frac{c_s + wc_w}{1 + w} \qquad (2\text{-}3)$$

where ρ and ρ_d are the bulk and the dry densities of the soil, respectively; w is the soil-water content; c_s and c_w are the specific heat of the soil particles and the pore-water, respectively. Note that the relationship $\rho_d = \frac{\rho}{1+w}$ was considered in Equation (2-3). Hence, the dependence of the soil specific heat (c) on its water content (w) and dry density (ρ_d) is quite evident from this expression.

The experimental determination of heat capacities (or specific heat capacities) has shown that the values obtained from soil samples with some moisture content are typically higher than those ones evaluated from dry samples (Fernández, 2011; Wieczorek *et al.*, 2011). This is a consequence of the higher heat capacity of pore-water. Therefore, and at a given bulk density, the heat capacity (and the specific heat) of a soil increases with increasing its water content (Knutsson, 1983; Abu-Hamdeh, 2003), as displayed in Figure 2-38(a). Clayey soils are expected to exhibit larger specific heat values than other soils due to the higher capacity of clays in retaining water. Moreover, the heat capacity of a soil also increases with increasing its dry density because the reduction of porosity caused by the larger compaction effort enhances the contact between soil particles and increases the mass of the solid phase per unit volume (Abu-Hamdeh, 2003). A temperature dependence of these thermal properties was also observed in laboratory measurements, as shown in Figure 2-38(b), in which the specific heats of several dry bentonite-based materials at temperatures ranging from 20˚C to 105˚C were estimated (Wieczorek *et al.*, 2011). Such experimental results indicated an increase of the specific heat of the dry samples with increasing temperatures. Although the theoretical approach given in Equation (2-3) does not include any explicit temperature-dependent term, however, it is assumed that the specific heat of the soil minerals (c_s) is not constant but increases with temperature. Such a temperature dependence is usually given by means of empirical algebraic expressions (Skauge *et al.*, 1983). Some empirical correlations between the specific heat of some clay minerals and temperature for the range of temperatures expected to occur inside an engineered barrier for nuclear waste repositories are plotted in Figure 2-39.

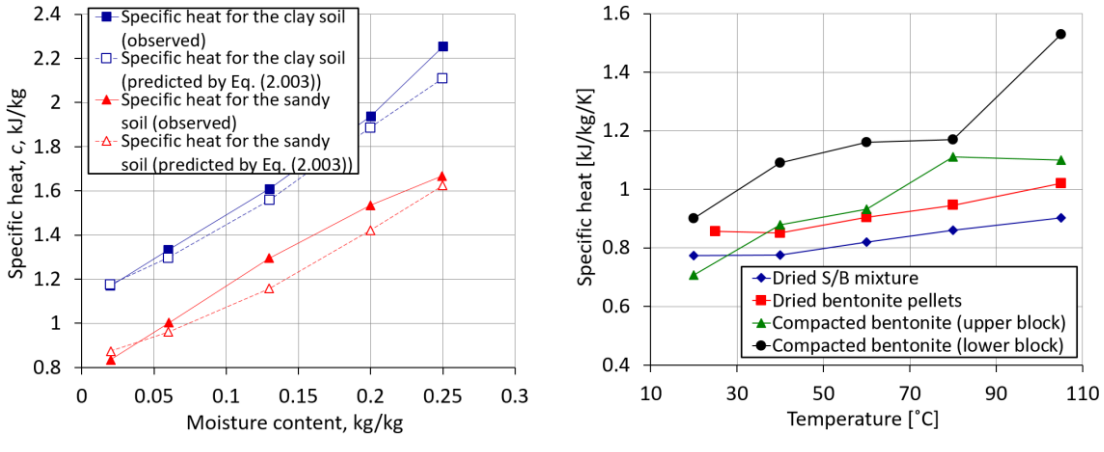

(a) **(b)**

Figure 2-38: **(a)** Specific heat as a function of the water content in a sandy soil with dry density of 1.30 Mg/m^3 (from Abu-Hamdeh, 2003); **(b)** Specific heat as a function of temperature for bentonite-based materials at dry conditions (from Wieczorek *et al.*, 2011).

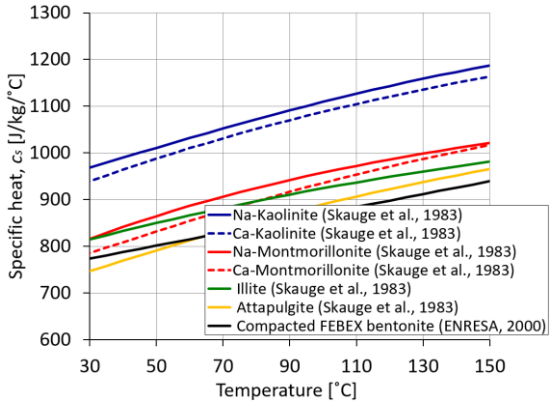

Empirical relationships for clay minerals: ***Skauge et al. (1983)***

$$c_s = f(T) = a + bT + cT^2 + dT^{-1} + eT^{-2} \quad [\frac{J}{g \cdot K}]$$

CLAY	*a* [J/g/K]	*b* (× 10^3) [J/g/K^2]	*c* (× 10^6) [J/g/K^3]	*d* [J/g]	*e* (× 10^{-4}) [J·K/g]
Na-kaolinite	6.816	-6.609	2.916	-1856	18.48
Ca-kaolinite	2.804	-1.321	0.450	-581.1	3.78
Na-montmorillonite	2.535	-1.894	1.042	-391.1	0.452
Ca-montmorillonite	5.320	-4.869	2.170	-1431	13.44
Illite	3.055	-2.437	1.312	-663.3	5.20
Attapulgite	6.613	-7.023	3.312	-1783	16.91

Empirical relationship for FEBEX bentonite (45°C – 150°C): ***Huertas et al. (2000)***

$$c_s = f(T) = 732.5 + 1.38T \quad [\frac{J}{kg \cdot °C}]$$

Figure 2-39: Empirical dependence of the specific heat of several clay minerals on temperature (from Skauge *et al.*, 1983) plotted with the temperature-dependent specific heat for the FEBEX bentonite (ENRESA, 2000).

2.5.1.3. THERMAL EXPANSION COEFFICIENTS

The existence of a heat-emitting source in a mass of soil generates a temperature gradient around the heat source. Consequently, a heat flux takes place in order to dissipate the thermal energy accumulated around the heat element towards zones far from that source (as mentioned in **Section 2.5.1.1**). Part of that heat energy is absorbed by the solid particles and fluids in the porous medium as the heat propagation takes place (see **Section 2.5.1.2**), which leads to a local increase of temperature. Thermal strains (characterized by volume changes of the soil constituents) appear in response to such temperature changes. The thermal processes related to the transport and the storage of heat in the porous medium also occur, although in a reverse direction, when the thermal source in the vicinity of a mass of soil is a heat-consuming source. In such a situation, the porous medium experiences a freezing process, instead of heating, that induces a volumetric contraction due to the local decrease in temperature. It is important to note that thermal stresses can develop due to any restriction imposed on the tendency of the soil to expand/contract when submitted to temperature changes.

The coefficient of thermal expansion is a material property that accounts for the changes in length or volume experienced by a substance when temperature is changed. The linear coefficient of thermal expansion (α_l) accounts for the thermal strains along one dimension of a solid particle while the volumetric coefficient of thermal expansion (α_v) reflects the changes in all the dimensions of a material due to heating or freezing. For materials in which the thermal expansion is isotropic, $\alpha_v \approx 3\alpha_l$ (Callister and Rethwisch, 2008). The thermal expansion (or contraction) is then a macroscopic indication of an increase (or a decrease) in the average interatomic separation.

In saturated and unsaturated soils, the thermal volume changes arise from the combined effect of the thermal expansion of the solid particles, the thermal expansion of each type of fluid in pores and from the complex interactions and processes taking place at the heated mineral-water system. On the one hand, the thermal expansion coefficient for the soil particles (α_s) is only dependent on their mineralogical composition. It is commonly assumed that the solid particles

and aggregates of a soil expand isotropically under temperature variations. Nevertheless, the few experimental measurements on the directional thermal expansion coefficients of some layered minerals showed anisotropy in their thermal response (Megaw, 1933; Hidnert and Dickson, 1945; McKinstry, 1965). McKinstry (1965) used the X-ray method to measure the directional thermal expansion in clay particles and found that the coefficients of thermal expansion perpendicular to the package of mineral layers were slightly higher than the values measured in the plane of those parallel platelets. On the other hand, the coefficient of volumetric thermal expansion for the free pore-water (α_w) is a physical parameter dependent on temperature (see Figure 2-40(a)). For the sake of simplicity, it is commonly assumed that the water in the large pores has the same thermal behaviour of the pure water at atmospheric pressure conditions. As the thermal expansion coefficient of pore-water is almost two orders of magnitude higher than the soil particles (Wang *et al.*, 2014) and since the compressibility of the pore-air phase (in unsaturated soils) is higher than the pore-water, the volumetric thermal expansion of water controls the non-isothermal response of saturated and unsaturated soils. Nevertheless, for clays in general and expansive clays in particular, the denser state of the adsorbed water in comparison to the bulk pore-water and the different nature of the water-mineral interacting forces acting at the clay particle level suggest that the thermal expansion coefficient for this type of water is not the same as the free water. Heating tests performed on clays with lower water contents and at elevated effective pressures indicated that the thermal expansion of their pore-water is significantly lower than that of the free water, especially in the range of high temperatures (Baldi *et al.*, 1988). Adopting a purely phenomenological approach, Baldi *et al.* (1988) proposed an effective thermal expansion coefficient for the water in micro-pores that depends on temperature and on the magnitude of the pressure bonding pore-water to the mineral surfaces (see Figure 2-40(b)). This bonding pressure was assumed to decrease exponentially with the distance between the water molecule and the clay surface. Using their effective thermal expansion coefficient for the adsorbed water, they could predict suitably not only the sign but also the magnitude of the experimental thermal strains measured by heating two over-consolidated clays (Pontida silty clay and Boom clay) under constant load conditions.

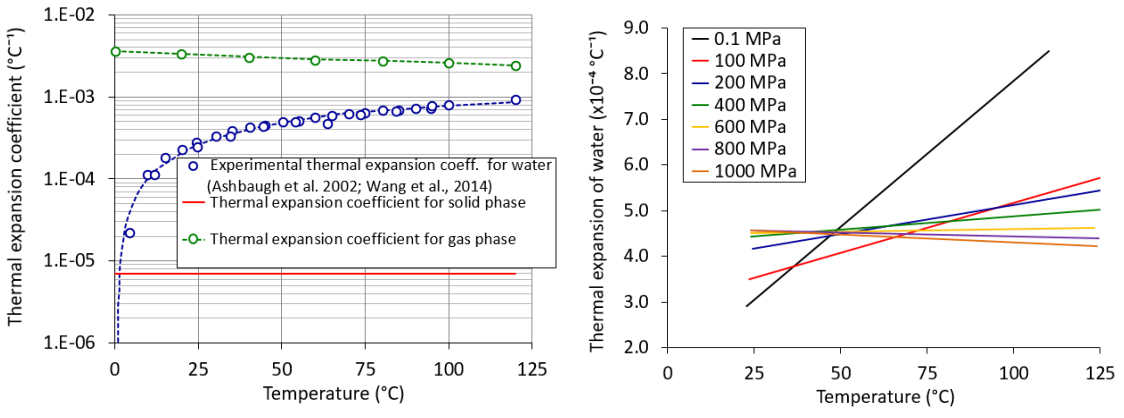

Figure 2-40: **(a)** Coefficient of thermal expansion of (pure) water, air and clay mineral as a function of temperature (after Wang *et al.*, 2014); **(b)** coefficient of thermal expansion of the adsorbed water as a function of temperature and pressure, p (after Baldi *et al.*, 1988).

The skeletal thermal expansion coefficient (α_{sk}) accounts for the elastic volumetric expansion/contraction of the solid phase of a soil due to changes in temperature, without considering the irreversible structural changes induced by a thermal loading (Khalili *et al.*, 2010). The experimental comparison between the thermal expansion of several crystalline rocks and

the individual values for their mineral constituents by Walsh (1973) found that the thermal expansion coefficient of the solid skeleton was approximately equal to the thermal expansion coefficient of the solid grains, that is, $\alpha_{sk} \approx \alpha_s$. Strictly speaking, such an approximation is only valid for rigid and monomineralic rocks with lower porosity (Palciauskas and Domenico, 1982). However, Campanella and Mitchell (1968) assumed that the condition for the whole soil porous matrix experiencing the same thermal volumetric expansion undergone in the solid particles is that all the soil grains are in mineral-to-mineral contact. Under such a hypothesis, Khalili *et al.* (2010) concluded that the thermal expansion of the porous solid skeleton is not affected by the size of pores or by its porosity, being the development of void ratio independent of temperature when the soil is not susceptible to any irreversible thermally-induced structural rearrangement as a thermal collapse (see Figure 2-41). This approximation is used to simplify and introduce the thermal influence on the mathematical formulation for predicting the THM response of expansive clays, as discussed in **Section 4.2.5**

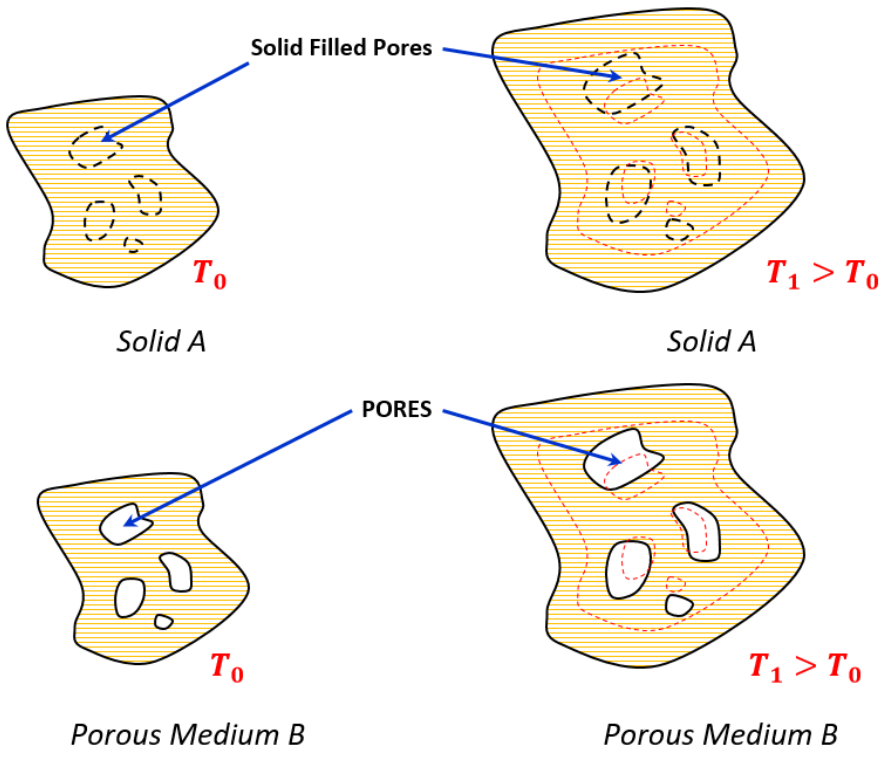

Figure 2-41: Increment in temperature of two identical, isotropic, stress-free and free to expand media: the homogeneous solid body "A" and the porous medium "B" (after Khalili *et al.*, 2010). In such conditions, the two media suffer the same thermal expansion and the void ratio (in medium "B") is independent of temperature.

It is important to emphasize that the differences in the thermal volumetric response of the distinct soil constituents, and especially, between the solid phase and the pore-water, together with the drainage conditions found in a volume of soil dictate its overall deformation response in presence of thermal loadings. The greater thermal expansion coefficient of the free water in comparison to the coefficient of thermal expansion of the mineral solids results in the development of pore pressures in saturated pores when temperature is increased (Campanella and Mitchell, 1968). The development of this excess of pore pressures due to temperature changes is more evident in low water permeability media, such as clays. In such circumstances, the dissipation of the thermally-induced pore pressures occurs when water is drained out from the saturated pores, which results in the thermal consolidation of the porous medium

(Campanella and Mitchell, 1968; Delage *et al.*, 2000; Shetty *et al.*, 2019). However, when temperature is decreased, the differential thermal expansion between the soil grains and water gives rise to a tension in pore-water, which induces the flow of water into the pores (Campanella and Mitchell, 1968). In unsaturated porous media, the expansion/contraction of pore-water accompanying temperature variations affects the saturation state of pores, which in turn, alters the effective stress distribution due to changes in the matric suction. Consequently, the thermal expansion/contraction process of soil structure depends on the volumetric strains of the soil grains but also on the thermal response of pore-water. The experimental measurements of the thermal expansion on samples of compacted clays subjected to heating-cooling cycles revealed that the thermal strains in the first heating path were usually higher than the strains measured during the subsequent thermal cycles (Campanella and Mitchell, 1968; ENRESA, 2000), see Figure 2-42(a). Moreover, an accumulation of irreversible thermal strains was observed at the end of each thermal cycle. Once the strains observed throughout the cooling stage only depend on the reversible thermal response of the clay structure (Hueckel and Baldi, 1990), thermal structural collapse evolves during heating in order to enable the soil structure to sustain the stress state at higher temperature (Campanella and Mitchell, 1968; Hueckel and Baldi, 1990). Therefore, the coefficient of thermal expansion for the clayey structure (α_{st}) accounts for the structural volume changes caused by a change in temperature (Campanella and Mitchell, 1968; Shetty *et al.*, 2019). This thermal expansion coefficient can be estimated from the slope of experimental curves relating the soil thermal strains to temperature, as the ones displayed in Figure 2-42(b). However, the determination of the thermal dilation coefficient α_{st} is not a simple task due to the practical difficulties of establishing the initiation and the amount of structural changes in the mass of soil due only to the thermal loading (Shetty *et al.*, 2019). Furthermore, the thermal strains in clayey soils are dependent on over-consolidation ratio (OCR), clay water content, thermo-mechanical stress path and thermal stress history (Delage *et al.*, 2000; Shetty *et al.*, 2019). A more detailed discussion about the complex and unusual thermal volumetric behaviour of saturated and unsaturated clays is presented in **Section 2.5.4** and **Section 2.5.5**.

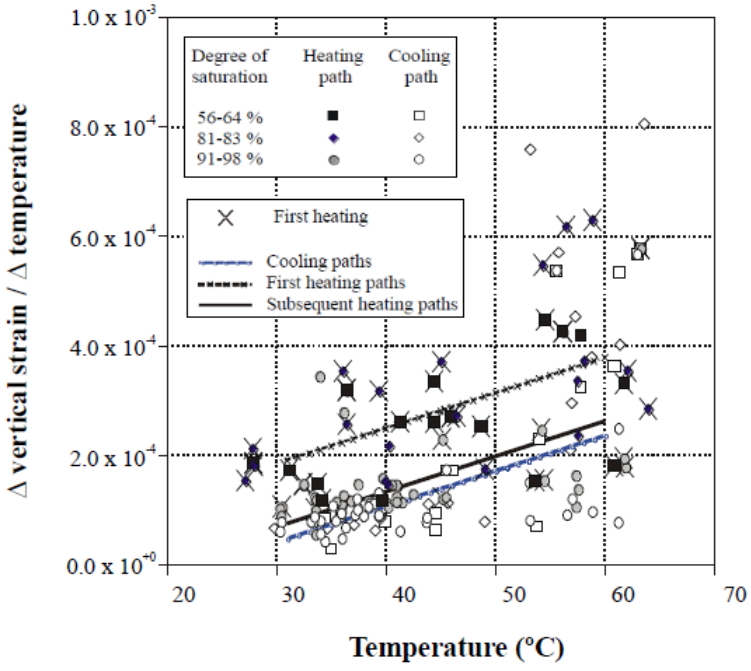

Figure 2-42: Linear thermal expansion of a compacted bentonite sample as a function of temperature during heating-cooling cycles (ENRESA, 2000).

2.5.2. THERMAL EFFECTS ON THE STATE AND PROPERTIES OF PORE-WATER

As the presence of water in pores affects both the soil response to changes in loading conditions and its own constitutive properties, any thermal problem must be studied by defining the thermal impact not only on the soil mineralogy (**Section 2.5.3**) but also on the water state and on its physico-chemical properties. It is well-known that an increase in temperature generates a decrease in the bulk water density and in its viscosity (Arifin, 2008; Rizzi *et al.*, 2012). In fact, the increase in water permeability with temperature observed in several experimental tests performed on clayey soils has been attributed to the decrease of water viscosity (Habibagahi, 1977; Pusch *et al.*, 1990; Towhata *et al.*, 1993; Cho *et al.*, 1999; Romero *et al.*, 2003; Lloret and Villar, 2004). In unsaturated porous media, the water vapour pressure increases with temperature while the surface tension of water decreases when temperature rises (Arifin, 2008; Rizzi *et al.*, 2012). Consequently, the matric component of suction is also decreased with temperature rising, since the surface tension of water is intrinsically related to the development of capillary forces in unsaturated soils (Arifin, 2008).

In expansive clays, temperature variations have a direct impact on the physico-chemical clay-water interactions. Firstly, the dielectric constant of water decreases as temperature increases (Malmberg and Maryott, 1956; Pitzer, 1983; Arifin, 2008). This temperature dependence of the dielectric constant also affects the double-layer thickness and the surface potential of clay. According to the diffuse double layer theory, the decrease of the dielectric constant of water would induce a decrease in the thickness of the diffuse double layer and an increase in the surface potential of clay (Mitchell, 1993). However, the theoretical expression for the thickness of the diffuse double layer also predicts that an increase in temperature should lead to an increase in the double-layer thickness (Morin and Silva, 1984). However, the impact of temperature variations on the thickness of the double layer is a matter with no clear conclusions, since some authors deduced that it should decrease when temperature rises (Lambe, 1960b; Paaswell, 1967; Habibagahi, 1977) while others concluded that it should increase with heating (Yong *et al.*, 1962; Morin and Silva, 1984). Mitchell (1993) suggested that the changes in the double-layer thickness (and consequently, in the swelling potential of an expansive clay) caused by an increase in temperature is counterbalanced by the thermally-induced decrease in the dielectric constant of pore-water (Delage *et al.*, 2000; Arifin, 2008). Secondly, temperature variations also influence the salt solubility of the soil solution in such a way that an increase in temperature leads to an increase in the solubility of saline solution in pore-water. The osmotic suction is affected by the saline concentration in pore-water. Therefore, when a sample of expansive clay with saline water in its pores is heated, the total suction of the salt solution usually increases with temperature and such an increase tendency is clearer for suctions higher than 1 MPa (Arifin, 2008).

The heat of expansive clays tends to enhance the transfer of water molecules from the inter-layer space to the external surface of heated clay particles (Carlsson, 1986; Arifin, 2008). Consequently, the amount of water found in the inter-lamellar pores is reduced and the amount of pore-water external to the clay elementary layers is increased as temperature rises. This is in agreement with the conclusions made by Paaswell (1967), who attributed the reduction in the number of absorbed water molecules in the clay-water system to the greater thermal agitation

state of water molecules in the inter-layer space, which in turn, facilitates their migration out of the clay elementary layers.

2.5.3. THERMAL EFFECTS ON CLAY MINERALOGY

The more appreciable effect of applying elevated temperatures to a mass of soil is the possibility of changing its properties and particle size distribution with the formation of granules and brick-like material (Kabubo *et al.*, 2017a, 2017b) due to the thermally-induce aggregation and fusion of the fine-grained particles. In clayey soils, such thermal loadings tend to reduce the compressibility, the plasticity index and the water-clay attractiveness while the soil permeability is increased due to its desiccation and cracking. In expansive clays, heating also tends to cause a decrease in their swelling potential, cohesiveness and water retention capacity and an increase in their strength (Arifin, 2008; Wang *et al.*, 2008; Kabubo *et al.*, 2017a, 2017b). If temperatures are sufficiently high and the heat exposure time is long enough, these thermal changes are irreversible, resulting in a harder, non-plastic and non-expansive soil due to partial or total destruction of the original clay crystalline structure and the formation of particles in the range of gravel fraction.

Two thermally-induced chemical processes that can take place when a bentonite material is exposed to very high temperatures (as in a clay barrier surrounding a container of radioactive wastes) are the smectite-to-illite transformation and the thermal cementation (Arifin, 2008). The thermal process in which smectite mineral is converted into a more stable silicate material is known as smectite illitization. This thermo-chemical process depends on the range of temperature and the exposure time during heating and on the pore-water chemistry, especially the concentration of potassium cation in the soil aqueous solution. On the other hand, heating of expansive bentonites can enhance the precipitation of cementing agents or the formation of physico-chemical bonding between the clay particles and aggregates. The thermo-chemical processes associated with the mineralogical and structural evolution of expansive clays are beyond the scope of this Thesis, useful information about this matter can be found in Oscarson and Dixon (1989), Pytte and Reynolds (1989), Whitney (1990), Inoue *et al.* (1992), Pusch *et al.* (1998), Pusch (2000), Karnland and Birgersson (2006), Wersin *et al.* (2007), Pusch *et al.* (2010), Wilson and Bond (2016), among others.

2.5.4. THERMAL EFFECTS ON THE HM BEHAVIOUR OF SATURATED CLAYS

The extensive experimental investigation of the thermal effects on saturated fine-grained soils revealed that their thermal response is strongly dependent on the mineralogical composition, on the clay fabric, on the thermal behaviour of water and on the drainage conditions (Campanella and Mitchell, 1968; Rizzi *et al.*, 2012). Furthermore, in the range of temperatures usually considered in such studies (from 5 to 100˚C), the increase in temperature is accompanied by a larger thermal expansion of pore-water, which induces, at some extent, an increment of the pore-water pressures due to the poor drainage conditions of such materials.

When the thermal loading is performed without allowing the dissipation of the generated excess of pore pressures (undrained conditions), temperature increments causes proportional (and significant) increases in pore pressures, which in turn, lead to a decrease in the effective stress. On the other hand, when the clay samples are cooled under undrained conditions, the pore-water pressure also decreases and the effective stress increases during the decreasing of temperature. The performance of sequential heating-cooling cycles in undrained tests on some saturated clays also showed the occurrence of a residual pore pressure after each thermal cycle and the observation of a temperature-pore pressure hysteretic behaviour (Campanella and Mitchell, 1968), as shown in Figure 2-43(a). Campanella and Mitchell (1968) attributed that pore pressure-temperature hysteresis to changes in the clay compressibility during rebound and recompression (see Figure 2-43(b)).

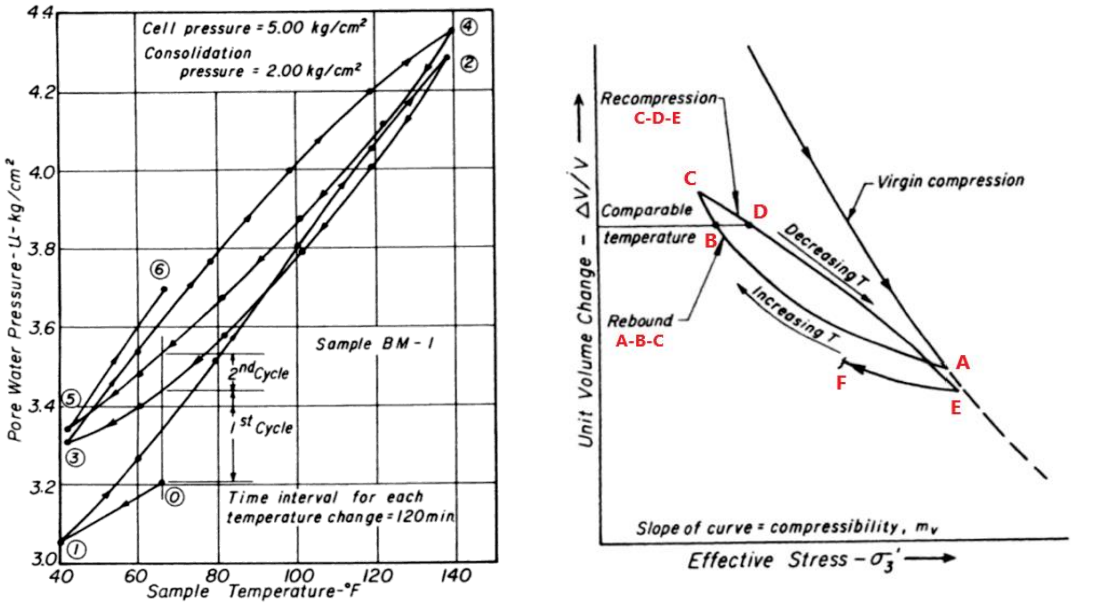

Figure 2-43: **(a)** Effect of heating-cooling cycles on the evolution of pore pressure in a saturated clay (Campanella and Mitchell, 1968); **(b)** relationship between the thermally-induced volumetric strains and the effective stress under undrained conditions (after Campanella and Mitchell, 1968).

When temperature changes occur at drained conditions, the dissipation of the thermally-induced excess of pore pressures gives rise to a thermal consolidation of normally consolidated clay samples. Such a characteristic thermal collapse of the saturated clay structure can be explained by the weakening of the inter-particle bond strength caused by the increase in temperature (Campanella and Mitchell, 1968). On the other hand, the thermal volumetric response of a saturated clay to increases in temperature when submitted to sequential thermal cycles is strongly dependent on the previous thermo-mechanical loadings. It is widely reported that the over-consolidation ratio (OCR) of a clay sample has a significant effect on the nature of the thermal deformations, as clearly shown in Figure 2-44(a). In fact, the experimental thermal volumetric change behaviour in drained conditions confirmed that over-consolidated clays (OCR>1) react to a temperature increase by expanding (at least during the first stages of heating), as any material when heated, while normally consolidated clays (OCR=1) suffer a thermal plastic contraction (Campanella and Mitchell, 1968; Delage *et al.*, 2004; Rizzi *et al.*, 2012). Furthermore, such a contractive behaviour becomes predominant as the OCR decreases

(Delage *et al.*, 2000). The initial volumetric expansion observed in over-consolidated clays is a result of the thermal undrained expansion of pore-water and soil minerals. During this first heating stage, saturated over-consolidated clays behave thermo-elastically, since the soil structure can carry the decrease in effective stresses without collapsing (Campanella and Mitchell, 1968; Baldi *et al.*, 1988). This assertion can be confirmed from the experimental thermal volume changes measured in saturated samples of Boom Clay (at several values of OCR) under a heating-cooling path, as displayed in Figure 2-44(a). Since it is commonly assumed that cooling generates elastic deformation only (Hueckel and Baldi, 1990), the "parallelism" between the curves of cooling and those ones representing the initial heating phase of over-consolidated clays suggests that the increase in temperature occurs without any structural rearrangements (Delage *et al.*, 2000). However, as temperature keeps rising, clay structure becomes unstable under the thermally-induced effective stresses and an irreversible thermal collapse of structure takes place. It is reported that the temperature at which the transition from thermal expansion to thermal contraction increases with the OCR values (Baldi *et al.*, 1988; Towhata *et al.*, 1993; Delage *et al.*, 2000). From this point on, the plastic contraction induces a thermal hardening of the porous medium. However, such a strain hardening is equivalent to a mechanical consolidation at constant, elevated temperature. Delage *et al.* (2000) reported that the performance of drained heating tests on a Boom Clay sample (at OCR=2) showed that the time required to reach the thermal equilibrium after the application of an increment in temperature is much less than the time for dissipating the pore pressures generated by such a thermal loading. Consequently, the amount of water drained as increasing temperature was insignificant compared to the amount of pore-water expelled after the temperature stabilization (see Figure 2-44(b)). Therefore, the dissipation of the excess of pore-water generated during each heating step occurs under constant temperature similarly to an isothermal consolidation test. The performance of isotropic compression tests at different temperatures also showed that the thermal strain hardening is more significant at low temperatures (Cui *et al.*, 2000; Delage *et al.*, 2004). Moreover, a clear tendency of decreasing the yield pressure as temperature increases was also observed, which is known as the thermal softening of the yield surface (Hueckel and Baldi, 1990). The application of a thermal heating-cooling cycle on normally consolidated clays induces significant structural changes evidenced by the over-consolidated behaviour of the soil to subsequent increases in temperature as a result of the thermal strain hardening occurred during the first heating episode (Campanella and Mitchell, 1968; Rizzi *et al.*, 2012).

The pioneering study by Campanella and Mitchell (1968) set up the conceptual basis to develop several thermo-mechanical formulations (Schiffmann, 1971; Derski and Kowalski, 1979; Hueckel and Borsetto, 1990; Hueckel and Pellegrini, 1996; Cui *et al.*, 2000; Hamidi *et al.*, 2015, 2017) for modelling the main features of the experimental response of saturated clays to heating (Paaswell, 1967; Campanella and Mitchell, 1968; Yong *et al.*, 1969; Habibagahi, 1977; Morin and Silva, 1984; Demars and Charles, 1982; Baldi *et al.*, 1988; Del Olmo *et al.*, 1996; Bernier *et al.*, 1997; Delage *et al.*, 2000; Sultan *et al.*, 2010). In that sense, the combination of a suitable modified thermo-plasticity theory and the concept of critical state model (Schofield and Wroth, 1968) allowed to develop consistent and incremental elasto-plastic formulations that incorporate an explicit dependence on temperature. Thermo-mechanical models, as the ones developed by Hueckel and Borsetto (1990) and by Cui *et al.* (2000), incorporated successfully in their formulations the main features observed in remolded clays under non-isothermal conditions, as the variation of the elastic domain with temperature, the thermoplastic consolidation and its dependence on the thermo-mechanical loading history. Furthermore, the

anisotropic elastoplastic response of saturated natural clays to thermo-mechanical loadings and the progressive destruction of clay anisotropy under increasing isotropic stresses was studied by Del Olmo *et al.* (1996) and modelled by the rotational kinematic hardening thermo-plastic approach by Hueckel and Pellegrini (1996). The thermo-mechanical behavior of structured saturated clays at higher temperatures has been also investigated recently by means of constitutive formulations that take in account the effects of clay structure and temperature on the position of the normal consolidation line, as the ones proposed by Hamidi *et al.* (2015, 2017).

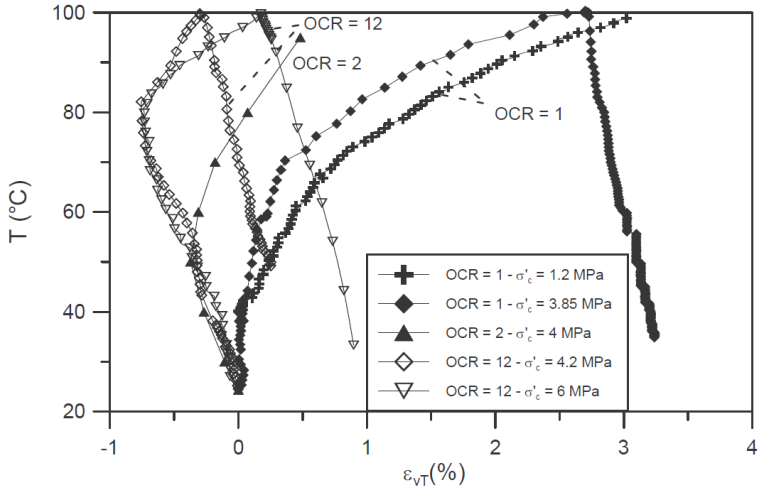

(a)

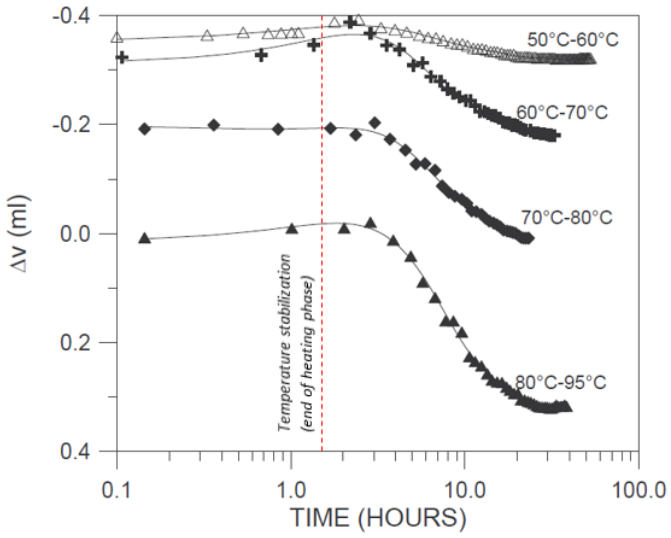

(b)

Figure 2-44: **(a)** Thermally-induced strains developed during a heating-cooling cycle on samples of Boom Clay at different OCR values (Delage *et al.*, 2004); **(b)** thermal consolidation of an over-consolidated Boom Clay sample (OCR=2) at high temperatures (after Delage *et al.*, 2000).

2.5.5. THERMAL EFFECTS ON THE HM BEHAVIOUR OF UNSATURATED CLAYS

The thermal impact on the hydro-mechanical behaviour of unsaturated fine-grained soils in general and expansive clays in particular is mainly related to the changes in their water retention capacity, to phase change (vaporization and condensation) and the processes associated with it and to the development of thermally-induced irreversible changes in the soil skeleton. The

interactions between thermal, water retention and mechanical processes that take place during a thermal loading compel that the evaluation of the thermal effects on a partially saturated porous medium must be considered in a fully coupled way.

As discussed previously, the thermal volumetric changes of water in non-saturated pores leads to changes in the volumetric water content as a consequence of the differential thermal expansion of the partially soil constituents. This change in the saturation state of pores generates suction variations, leading to a thermally-induced hydration or dehydration of pores. On the other hand, the increase of temperature also enhances the generation of vapour (vaporization), which causes a local drying of the soil. Consequently, pore-water vapour diffuses towards zones far from the heat source where it condensates, giving rise to a local wetting of pores. Besides the changes in the properties and the physical state of water retained in pores during a thermal loading, another important feature to take into account in non-isothermal problems is the thermal impact on the water retention capacity itself. The experimental investigation of the thermal effects on the water retention capacity of compacted samples of the plastic Boom Clay (Romero *et al.*, 2001), the FEBEX bentonite (Villar and Lloret, 2004), the MX-80 bentonite (Tang and Cui, 2005) and a Calcigel bentonite (Arifin, 2008), at temperatures between 20˚C and 80˚C, found that, at a constant water content, the total suction decreases with increasing temperature. Experimental suction characteristic curves for the compacted samples of MX-80 bentonite (Tang and Cui, 2005) at different temperatures are plotted in Figure 2-45. The reduction in the water retention capacity of unsaturated clays as temperature rises has been mainly associated with the heating-induced decrease in the matric suction (due to hydration and capillary forces), as an increase in temperatures reduces the surface tension of pore-water (Romero *et al.*, 2001) and the amount of water in the inter-layer space (Arifin, 2008). However, Romero *et al.* (2001) and Villar and Lloret (2004) also attributed this temperature-dependent behaviour of the water characteristic curve to irreversible thermally-induced changes in the fabric and the pore-water chemistry of the clay. The thermal effects on the hydraulic properties of clays indirectly affect the effective stress state and the deformation response of the mass of soil to the applied thermal loading (François and Laloui, 2008) due to changes in the matric suction. In addition, the movement of liquid water through the porous medium also depends on its viscosity, which decreases as temperature increases, and on the available porosity for the advective flux of water, which is affected by the stresses and suction variations due to temperature changes (Gens *et al.*, 1998). Furthermore, thermally-induced changes in the saturation state of pores also affects the temperature field due to the changes in heat flux conditions, as discussed in **Section 2.5.1.1**.

The deformation behaviour of unsaturated clays to thermal loadings is strongly dependent on the thermal effects generated on the water retention capacity of the soil. As discussed in the previous section, the development and intensity of the elastic (dilation) and plastic (contraction) components of the thermally-induced strains during heating are dependent on the OCR. Both the current stress state and the pre-consolidation pressure are affected by the suction variations caused by temperature changes. In general, and as mentioned before, an increase in temperature under constant mechanical loads leads to a thermal softening of the yield surface. However, such a heating episode could induce a significant drying of pores. Therefore, this suction increase would induce an increase in the pre-consolidation pressure and a consequent change in the soil volumetric response under the same thermal loading. In other words, the

thermally-induced drying of pores can generate an increase in OCR, causing a decrease in the thermal collapse tendency of the unsaturated clay (François and Laloui, 2008). Thus, two opposite tendencies on the evolution of the yield surface may occur during heating (see Figure 2-46): a thermal softening as temperature increases (Hueckel and Baldi, 1990) and a suction hardening with increasing suction (Alonso *et al.*, 1990; Bagherieh *et al.*, 2009).

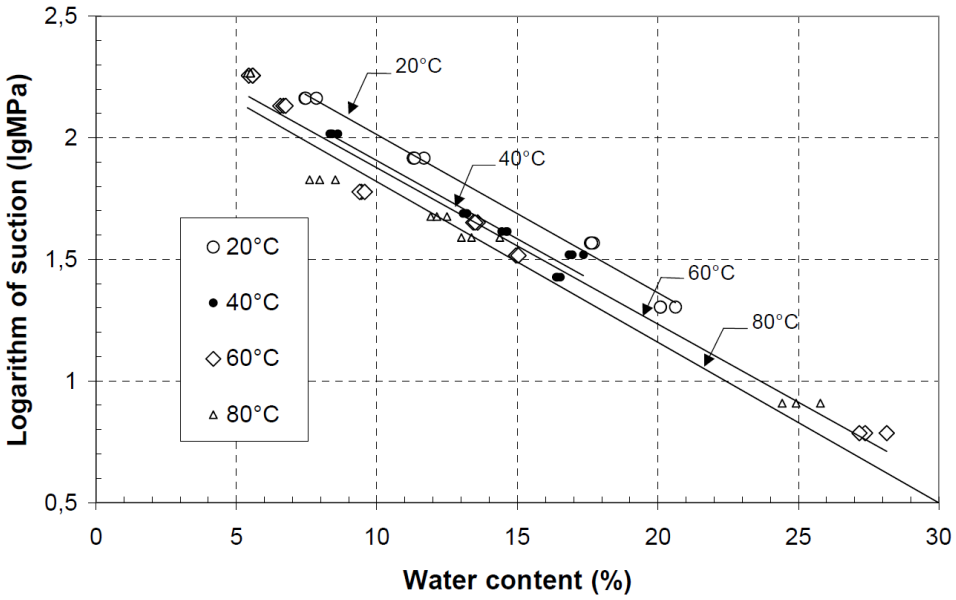

Figure 2-45: Experimental water retention curves at isochoric conditions and different temperatures for samples of MX-80 bentonite with dry densities in the range of 1.65-1.70 g/cm^3 (Tang and Cui, 2005).

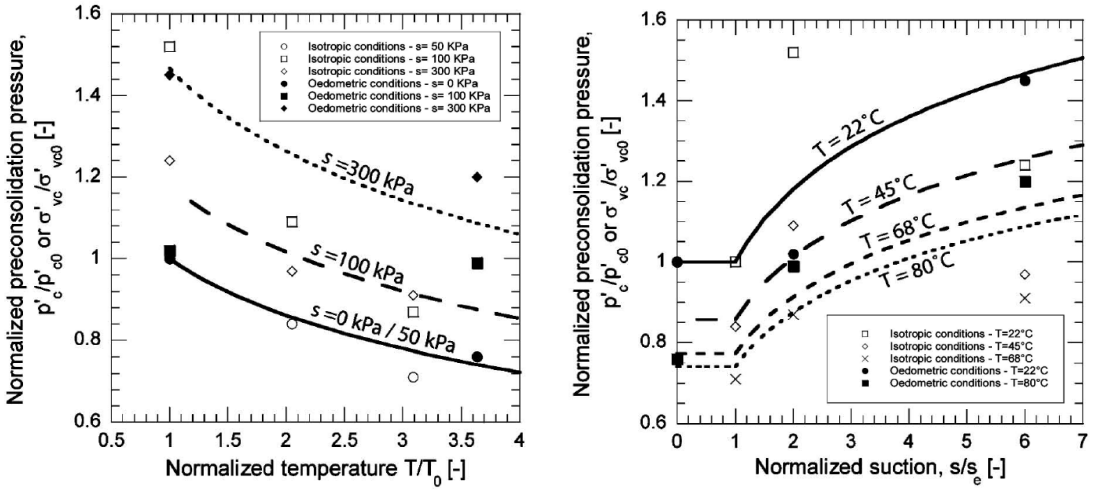

Figure 2-46: Evolution of the pre-consolidation pressure of a sandy silt with **(a)** temperature, at several constant suctions; **(b)** suction, at several constant temperatures (Salager *et al.*, 2008).

In order to reproduce the main experimental features observed in laboratory tests on unsaturated soils under non-isothermal conditions (Wiebe *et al.*, 1998; Romero *et al.*, 2003; Salager *et al.*, 2008), some THM formulations for low-plasticity soils were developed throughout the past decades. The earliest of such THM models was proposed by Gens (1995) by joining the elasto-plastic approach for unsaturated soils by Alonso *et al.* (1990) to the thermo-plastic formulation for saturated soils by Hueckel and Borsetto (1990) in a general and consistent

constitutive framework (François and Laloui, 2008). The resultant thermo-elastoplastic model, an extension of the *Barcelona Basic Model* (Alonso *et al.*, 1990) and hereafter referred to as the BBM model, belongs to the family of modified Cam-Clay models and considers two independent stress variables to model the unsaturated behaviour: the net stress and the matric suction. Consequently, the plastic yield surface of the BBM not only depends on stresses (and history variables) but also on matric suction and temperature. The thermal effect on the size of the elastic domain was included in the BBM formulation by Gens (1995) through the temperature dependence of the pre-consolidation net stress for saturated conditions (p_0^*) – the hardening parameter of BBM – and of the shear strength (p_s) according to the expressions shown in **Section 4.4.1.1**. The thermal effects on the retention curve is usually included in a constitutive formulation by relating the increase in temperature to a decrease of the air-entry pressure (François and Laloui, 2008). A relationship between the air-entry suction and the temperature-dependent surface tension was included in the BBM formulation by Olivella and Gens (2000). The suction hardening of the yield surface was already considered in the original BBM formulation (Alonso *et al.*, 1990) through the dependence of the soil compressibility on suction. A brief description of the main features of this thermo-elastoplastic model is given in **Section 4.4.1**. A detailed description of the original and the extended constitutive formulations of the BBM and the modelling performance of this thermo-elastoplastic formulation can be found in Alonso *et al.* (1990), Gens (1995), Sánchez and Gens (2006). Another constitutive model for saturated and unsaturated soils under thermal loads is the ACMEG-TS (***A**dvanced **C**onstitutive **M**odel in **E**nvironmental **G**eomechanics – **T**hermal and **S**uction effects*) framework developed by François and Laloui (2008). This THM formulation uses the concept of generalized effective stress by Bishop (1959), instead of the couple of stress state variables commonly used for describing the stress-strain relationship in unsaturated soils (Fredlund *et al.*, 2012). As a consequence, a direct dependence of the mechanical response on the thermal, hydraulic and mechanical loads is ensured. Another distinctive aspect of the ACMEG-TS model (in comparison to the BBM model) is the assumption that the apparent pre-consolidation pressure (the hardening parameter of the model) not only depends on the volumetric plastic strain but also on suction and temperature. This means that the pre-consolidation pressure also determines the onset of thermal and hydric collapses. Moreover, the mechanical constitutive part of the model (stress-strain relationship) is interconnected with the hydraulic constitutive model in such a way that the mechanical and thermal states can also modify the air-entry suction value in the water retention curve (François and Laloui, 2008). In this THM model, the desaturation process is taken as a yielding phenomenon, which requires the definition of a hydric yield limit (the air-entry suction for initially saturated soils) that depends on the degree of saturation, the volumetric plastic strain and temperature. The hysteresis in the water retention curve (under re-wetting) is also considered and modelled as a plastic process. A wetting-drying cycle activates two successive hydric yield limits that delimit the size of the water retention hysteresis. For a detailed insight of the constitutive formulation of the ACMEG-TS model and its capabilities in predicting the thermo-elastoplastic response of saturated and unsaturated soils, see François *et al.* (2007), François and Laloui (2008), Sanavia *et al.* (2014) and Papafotiou *et al.* (2017), for instance. Other thermo-elastoplastic formulations for modelling the saturated and unsaturated responses of clays have been developed throughout the past decade. Interested readers are referred to Mašin and Khalili (2012), Tourchi and Hamidi (2015) and Thatcher *et al.* (2016) for further details.

Although both the BBM and the ACMEG-TS models have reproduced quite well the THM responses of compacted low and moderate plastic soils, however, they are not able to predict satisfactorily the behaviour of highly plastic clays, especially the features related directly or indirectly to the volumetric deformation of micro-pores (Sánchez and Gens, 2006; François and Laloui, 2008). The existence of different families of pores in an expansive clay, fully or partially saturated by water with different physico-chemical properties, and subjected to forces of different nature and intensities in addition to the complex hydro-mechanical interactions among these structural levels require that the deformation behaviour of such materials be approached by multi-porosity models. In other words, the swelling response of active clays to THM loadings cannot be properly predicted by means of constitutive formulations developed for reproducing the behaviour of non-expansive, single-porosity unsaturated soils. In fact, the hydro-mechanical response of swelling clays to temperature changes is more related to the thermal impact caused on the water-clay system (micro-scale) than the thermal effects on the free water and the soil skeleton (macro-scale). In **Section 2.7.2** a brief description of a family of constitutive double-porosity models that has been used to model the hydro-mechanical behaviour of bentonite-based materials under isothermal and non-isothermal conditions is given.

Concerning the temperature dependence of the swelling potential in expansive clays, the experimental observations on compacted samples of FEBEX bentonite showed that an increase in temperature resulted in decreasing the swelling strain under constant loading (Villar and Lloret, 2004; Romero *et al.*, 2005). Furthermore, Villar and Lloret (2004) measured the axial deformations of several compacted specimens under different vertical loads (as shown in Figure 2-47(a)) when wetted at temperatures between 30˚C and 80˚C and found that the decrease in the swelling strains at higher temperatures was more evident for those samples under lower vertical stresses. Moreover, from the linear experimental correlations between the axial swelling, temperature and vertical stresses shown in Figure 2-47(a), it can be noted that the swelling potential would vanish at temperatures superior to 100˚C. On the other hand, the temperature dependence of swelling pressure has not reached a consensus yet, since both tendencies of decreasing and increasing in the swelling pressure when temperature rises have been reported. An increase in temperature resulted in a decrease in the swelling pressure of some *Ca*-bentonites (as FEBEX bentonite) submitted to temperatures in the range 20-130˚C, as reported in Pusch *et al.* (1990), Villar and Lloret (2004) and Villar *et al.* (2010) and as displayed in Figure 2-47(b). The decrease in swelling potential with temperature increasing was related to the reduction of the hydration forces between clay elementary layers as a result of the reduction in the number of water molecule layers in the inter-lamellar space. Since the crystalline swelling (Laird, 2006) is the prevailing swelling mechanism in calcium-type bentonites (Pusch *et al.*, 1990), the swelling pressure in such materials tends to decrease at higher temperatures. Villar and Lloret (2004) also associated such a reduction in swelling capacity to the thermally-induced migration of water from micro-pores (inter-layer and intra-aggregate pores) to macro-pores (inter-aggregate voids). However, Pusch *et al.* (1990) found that the heating of a sodium-type bentonite, at temperatures varying between 20°C and 130°C, induced an increase in its swelling pressure. This behaviour was associated with the increase in the double layer repulsion of adjacent particles. In fact, the osmotic swelling (Laird, 2006) is the main process controlling the swelling potential in this type of bentonites (Pusch *et al.*, 1990). Moreover, the molecular dynamics simulations carried out by Akinwunmi *et al.* (2019) on a sodium smectite clay, at three different dry densities and for temperatures ranging from 150K to 600K, predicted a gradual increase in swelling pressures with increasing temperature (see Figure 2-48). They ascribed the

increase of swelling pressures to the thermal motion of the inter-layer water molecules and counter ions at elevated temperatures and found that such an increase was more evident at high dry densities.

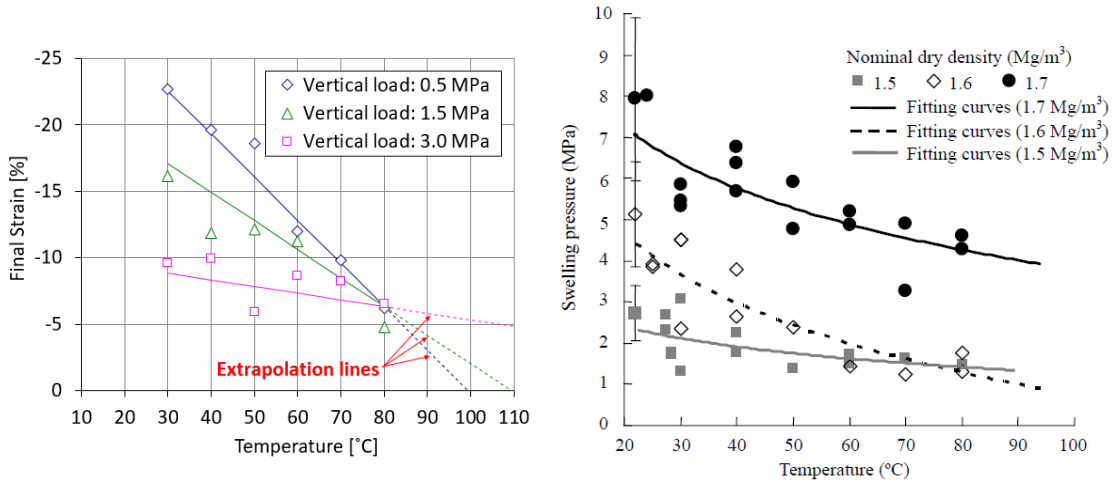

(a) **(b)**

Figure 2-47: **(a)** Final vertical swelling strains of compacted samples of FEBEX bentonite at dry density of 1.60 Mg/m^3 under different vertical loads and temperatures (modified from Villar and Lloret, 2004); **(b)** swelling pressure evolution with temperature for saturated samples of FEBEX bentonite at different dry densities (Villar *et al.*, 2010).

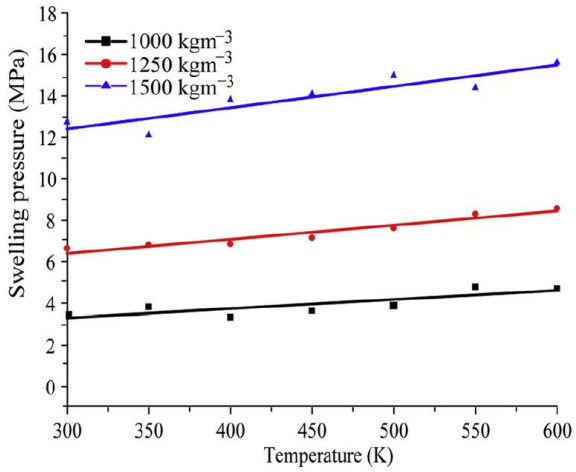

Figure 2-48: Swelling pressure of a sodium smectite clay as a function of temperature (ranging from 300K to 600K) at several dry densities and evaluated by means of molecular dynamics simulations (Akinwunmi *et al.*, 2019).

Although the chemical composition of sodium and calcium bentonites seems to influence the dominant swelling mechanism (crystalline or osmotic swelling) and their swelling behavior under increasing thermal loadings, however, some apparently contradictory findings on bentonites with similar mineralogical composition suggest that other factors should be taken in conjunction with clay mineralogy. The experimental heating carried out by Cho *et al.* (2000) and Bag and Rabbani (2017) on calcium-type bentonites submitted to temperatures varying between 20˚C and 90˚C concluded that heating enhanced the swelling pressure of such materials. In both experimental studies, the increase in swelling pressures due to heating was attributed to an increase in the osmotic pressure (due to the reduction of the double-layer thickness) and in the pore-water pressure (due to the differential expansion of pore-water and the clay skeleton),

which counteracted the thermally-induced decrease in hydration pressure. On the other hand, Pusch *et al.* (2003) conducted a heating test programme in which exposed some highly compressed samples of MX-80 pellets (a sodium bentonite) to a moderate heating (22˚C-65˚C) and to a thermal treatment by percolating hot water vapour (at temperatures between 110˚C and 150˚C). In both situations, the swelling pressures observed were lower than the values obtained at room temperature conditions. Such a drop in swelling pressures at higher temperatures was attributed to the thermal stresses that disintegrated the very dense grains and exposed a larger inter-lamellar surface area to extensive hydration (Pusch *et al.*, 2003). Moreover, for the samples exposed to the hot vapour treatment, the microstructural investigation indicated the occurrence of cementation by precipitation of silica released by the hot vapour. This thermally-induced cementation caused an additional decrease in swelling pressures at elevated temperatures (Pusch *et al.*, 2003).

Thus, the dependence of swelling pressure on temperature has been mainly attributed to changes in the dielectric constant and surface potential of the pore-water and in the electric potential of the diffuse double layer (Pusch *et al.*, 1990; Cho *et al.*, 2000; Ye *et al.*, 2013; Tripathy *et al.*, 2015; Bag and Rabbani, 2017), to the diffusion of ions (Yong *et al.*, 1962), to the cement formation or the dissolution of montmorillonite (Pusch *et al.*, 2003; Ye *et al.*, 2014), to the thermally-induced water transfer between intra-layer and inter-particle pores (Villar and Lloret, 2004; Villar *et al.*, 2010), to changes in the chemical composition, salinity or pH of the soil solution (Herbert *et al.*, 2008; Ye *et al.*, 2014), etc. From all this, it can be concluded that the development of swelling pressures embraces several temperature-dependent properties and physico-chemical processes that have opposite influence on the swelling capacity of clays. The assessment of the thermal impact on the swelling potential is crucial for clays used as buffer or backfill material in engineered barriers for radioactive waste repositories. In fact, the performance and the integrity of the barrier system are strongly dependent on the evolution of the swelling properties of the bentonite barrier as heat is released from the radioactive decay in the canister.

2.6. THE USE OF BENTONITE-BASED MATERIALS IN ENGINEERED BARRIERS

As other clayey porous media, bentonite-based materials are characterized by their very low water permeability. That is a desirable property for an engineered barrier system since it is expected the release of radionuclides in such nuclear waste disposals. Consequently, a potential risk of radionuclide transport towards the external environment due to the hydrogeological cell established between the barrier and the host rock exists. The low water mobility inside the buffer minimizes the risk of environmental contamination. Furthermore, the self-sealing capacity of bentonites due to their high swelling potential ensures the isolation of the nuclear waste (Pusch, 1982) since all the preferred paths for the flux of water and/or vapour can be closed satisfactorily when the barrier becomes saturated. Other remarkable properties that justify the choice of expansive clays – as compacted bentonite-based materials or as mixtures of bentonite powder with quartz sand or crushed rock – as candidates to form engineered barriers

in nuclear waste disposals are (Wheelwright *et al.*, 1981; IAEA, 1984; Savage *et al.*, 1999; Hoffmann, 2005; Sellin and Leupin, 2013; NDA, 2014):

- the high retention capacity of corrosive chemical species and radionuclides due to the high specific surface of such materialS. This property is crucial in the long-term performance of the engineered barrier system (EBS), when the canister corrosion takes place in an almost saturated barrier.
- the thermal conductivity and its changes as the water content in the buffer increases after the repository closure. The thermal conductivity of the buffer controls the dissipation of the heat generated by the radioactive decay. Consequently, it governs the temperature evolution, its distribution in the vicinity of the canister and the heat transport through the clay to the rock as the barrier is saturated due to the migration of water from the rock to the clay.
- sufficient mechanical strength to allow emplacement as preformed units and to provide resistance to applied mechanical forces, besides providing mechanical support for the waste container.
- the ability to deform plastically when subjected to external forces, which should minimize the emergence of preferred paths for groundwater migration as a consequence of a more brittle mechanical behaviour of the backfill.
- the low economic cost of extraction, transportation and production of the components for an engineered barrier system when such natural materials are employed.

In the following sections, a brief description of the main properties, the fabrication procedure, the initial status and other relevant characteristics of bentonite-based materials used in recent clay barrier systems are pointed out. Nevertheless, a special attention is devoted to the expansive materials employed as buffers in the *in-situ* HE-E experiment (see **Section 2.6.4.5**).

2.6.1. AS COMPACTED BLOCKS

The use of compacted bentonite bricks as buffers in multi-barrier systems is often considered as a suitable choice for the isolation of high-level radioactive waste (HLRW). Besides the main requirements for a clay barrier listed in the previous section, compacted bentonite blocks also provide an excellent mechanical stability for the barrier system, acting as a mechanical support for horizontal canisters (as in the EB test – see **Section 2.6.4.2**) and preventing large movements of the metallic container (canister sinking) inside the barrier. Nevertheless, bentonite blocks must be installed manually at their as-planned position in the excavated niche, surrounding the metallic canister. Depending on the engineered barrier design, the emplacement operations of bentonite blocks, the canister and the barrier monitoring system (if it is required) demand the development of a detailed sequence of installation to be followed in order to guarantee the correct emplacement and alignment of each component of the barrier system and to minimize the presence of construction gaps. Some precautions must also be taken regarding the packing, handling, transporting and storage tasks of bentonite blocks in order to avoid impact damage

during their handling and transport and any deterioration due to their exposure to environments of high humidity (ENRESA, 2000). Moreover, if the bentonite barrier is composed uniquely by compacted blocks, the use of expansive granular material could be required for filling the gap between the installed barrier and the surrounding host rock (Dixon *et al.*, 2011). Two examples of conceptual bentonite barriers made of compacted blocks are shown in Figure 2-49. Two typical cross sections of the barrier of compacted blocks used in the full-scale hydration test carried out in the underground research laboratory (URL) managed by NAGRA at Grimsel (Switzerland), as part of the FEBEX Project (see **Section 2.6.4.1**) are illustrated in Figure 2-49(a) together with the shapes and dimensions of such bentonite blocks. The layout of a portion of the large-scale *in-situ* test of the Swedish disposal concept (the "Prototype Repository" test) conducted at the underground Äspö Hard Rock Laboratory and managed by SKB (Swedish Agency for Radioactive Waste Disposal) is shown in Figure 2-49(b). The compacted blocks placed in the backfilled tunnel and the compacted bentonite rings and cylinders around the vertical canister are made of MX-80 sodium bentonite. The construction gap filling was made using a bentonite-granulated material (pellets) so that the project requirements related to the swelling and hydraulic properties of the constructed engineered barrier could be fulfilled (Dixon *et al.*, 2011).

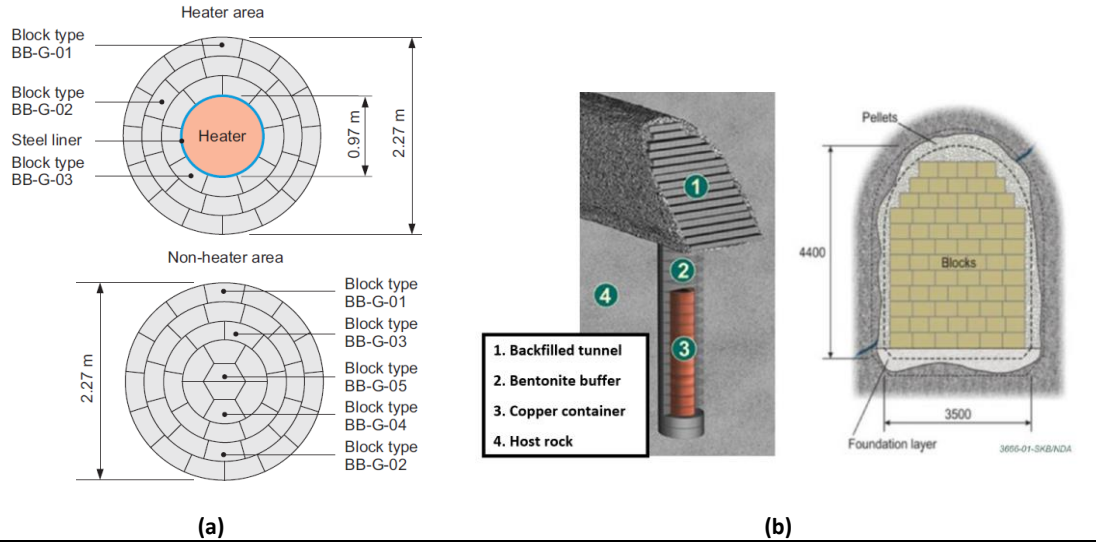

Figure 2-49: **(a)** Geometry of the clay barrier made of compacted blocks of FEBEX bentonite used in the Grimsel Test site (Lanyon and Gaus, 2016); **(b)** conceptual design for the Prototype Repository test in which compacted blocks of MX-80 bentonite are used to fill the access tunnel and the vertical holes around the canisters(NDA, 2016).

Bentonite blocks are obtained from granulated bentonite material compacted at its hygroscopic water content by means of uniaxial or isostatic compaction techniques until reaching a desirable and specified dry density. Consequently, the manufactured blocks usually have a low initial water content and a high unconfined compressive strength. Depending on the geometry of the barrier, different shapes and dimensions can be defined for the compacted blocks. In such conditions, the design and fabrication of molds would be necessary (ENRESA, 2000). Each bentonite block fabricated to the *in-situ* FEBEX test had an initial water content ranging from 12.5% to 15.5% and dry densities close to 1.70 Mg/m^3 (ENRESA, 2000). The bed of compacted bentonite blocks on which the canister of the large-scale EB experiment lied down (see **Section 2.6.4.2**) was manufactured for the FEBEX test and had an average dry density of 1.69 Mg/m^3 and a water content of 14.4% (Villar *et al.*, 2014a). The comprehensive laboratory characterization programme performed on compacted samples of FEBEX bentonite at different water contents,

dry densities and temperatures generated an extensive dataset and several empirical correlations relating such variables to changes in those thermal properties affecting the heat transport in a clay barrier (as Figure 2-36(a) and Figure 2-45(a), for example). The bentonite bricks made of sodium MX-80 bentonite emplaced to hold the heater system in the *in-situ* HE-E test (see **Section 2.6.4.5**) had a dry density of 1.8 Mg/m^3 and an average water content of 10.3% (Gaus, 2011; Teodori and Gaus, 2011). The laboratory thermal characterization of the MX-80 blocks carried out at the Geotechnical Laboratory of GRS in Braunschweig (Germany) found that temperature changes (in the range 20 – 105˚C) would not cause any significant variation in the thermal conductivity and the specific heat during the early post-closure period, when saturation changes can still be disregarded (Wieczorek *et al.*, 2011). However, as the bentonite blocks re-saturates by water uptake from the surrounding geological formation, such thermal properties exhibit a marked dependence on the pore-water content and the material becomes more sensitive to temperature increments. At as-emplaced saturation conditions, the measured thermal properties for the compacted MX-80 blocks were averaged as 1.1 W/m·K (thermal conductivity), 1.4 J/g/K (specific heat at 20˚C) and 2.0 J/g/K (specific heat at 105˚C). On the other hand, the average thermal conductivity of dry samples was 0.8 W/m·K with a specific heat capacity ranging between 0.8 J/g/K (at 20˚C) and 1.3 J/g/K (at 105˚C). Those thermal parameters were obtained by correlating the changes suffered in the electric resistivity of a double spiral-shaped sensor placed between two small samples of the same compacted block. The pair of small samples and the heating sensor were kept together by means of a clamping device (Wieczorek *et al.*, 2011). The measurement of the thermal conductivity of saturated samples of MX-80 bentonites with bulk densities between 1.96 Mg/m^3 and 2.17 Mg/m^3 found values in the range 1.35 – 1.45 W/m·K using the Transient Hot Strip Method (Knutsson, 1983). For additional and detailed information related to the production, the use and the THM characterization of bentonite compacted blocks as buffer material in engineered barrier systems, consult ENRESA (2000), Huertas *et al.* (2005), Sánchez and Gens (2006), NDA (2016), among others.

2.6.2. AS HIGH DENSITY GRANULES (PELLETS)

The advantages of using bentonite pellets as a backfill material in engineered barriers are commonly related to the handling, transportation, storage and emplacement operations, the lower generation of debris and suspended powder during the construction procedures and the *in-situ* material compaction by gravity fall (Hoffmann, 2005). Moreover, the use of bentonite pellets minimizes the gaps inside the barrier system and in the rock-buffer interface, improving the thermal, hydraulic, mechanical and chemical transfer properties between the barrier and the surrounding bedrock (Marjavaara *et al.*, 2013). However, the emplacement of such materials into a very limited or difficult working space may generate segregation, which could lead to a significant heterogeneity in the spatial distribution of dry density and the occurrence of preferential paths for the transport of fluids and chemical species through the inter-pellet voids.

The fabrication procedure followed to obtain bentonite pellets usually generates a very high dry density material with a very low water content (Hoffmann *et al.*, 2007). For example, the FEBEX bentonite pellets emplaced in the *in-situ* EB experiment (see **Section 2.6.4.2**) had a bulk density of individual pellets close to 2.00 Mg/m^3 and an initial water content oscillating between 3% and 4% (Hoffmann, 2005). In the case of the MX-80 bentonite pellets, employed as the granular fill

in the *in-situ* heating-hydration HE-E test (see **Section 2.6.4.5**), the initial dry density of granules varied in the range 1.97 – 2.11 Mg/m^3 (Molinero *et al.*, 2017) with initial water contents around 5 – 6% (Plötze and Weber, 2007; Villar *et al.*, 2012b). The manufacturing of high-density pellets consists in pre-heating a mass of bentonite powder so that a drier and more compressible material can be produced (Hoffmann, 2005). This pre-heated material is compacted by means of a roller press and crushed in granules with several grain size distributions. The grain size distribution curves of the as-emplaced bentonite pellets used in the experimental tests mentioned previously are shown in Figure 2-50.

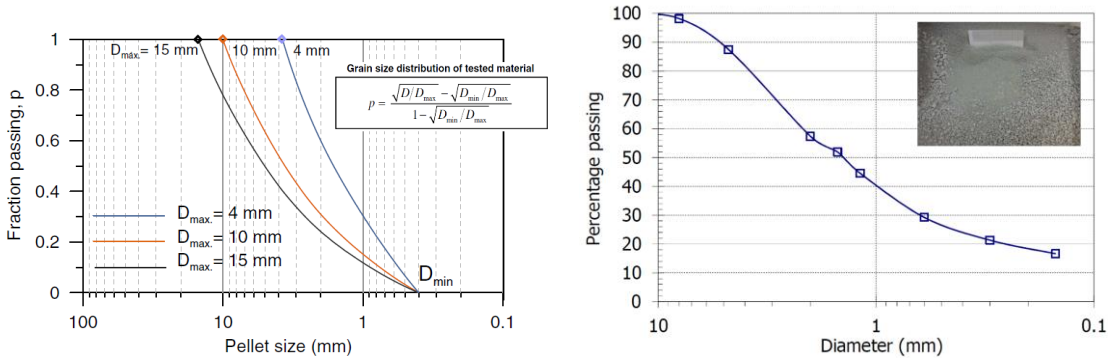

Figure 2-50: Grain size distribution for a granular mixture of **(a)** FEBEX bentonite pellets used in the EB test (Hoffmann *et al.*, 2007); **(b)** MX-80 bentonite pellets emplaced in one section of the HE-E experiment (after Villar *et al.*, 2012b).

The fabrication process of high-density pellets generates an intermediate family of pores between the intra-aggregate pores (micro-porosity) and the large inter-pellet voids (macro-pores). This third pore level (meso-porosity) is associated with the voids between clay aggregates inside an individual pellet (see Figure 2-51). However, for the sake of simplicity and without losing the robustness required for a multi-porosity formulation, the high complexity of the internal structure of this type of expansive materials is reduced in such a way that both the inter- and the intra-aggregate porosities found inside a pellet are accounted for as being micro-porosity.

The superficial thermal conductivity of the MX-80 pellets sent to CIEMAT (***C**entro de **I**nvestigaciones **E**nergéticas, **M**edio**A**mbientales y **T**ecnológicas*, in Madrid, Spain) from the HE-E test site was determined at room temperature by the transient hot wire method. The dry specific heat capacity was obtained at several temperatures ranging from 22˚C to 298˚C (Villar *et al.*, 2012b). The measured thermal conductivity of the as-received mass of pellets was 0.12 W/m·K while the specific heat values ranged between 0.64 J/g/K (at 22˚C) and 0.97 J/g/K (at 115˚C) (Fernández, 2011). Other useful information related to the properties of bentonite pellets and their use as buffer materials in projects of great scientific and academic relevance are found in Hoffmann (2005), Hoffmann *et al.* (2007) and Molinero *et al.* (2017).

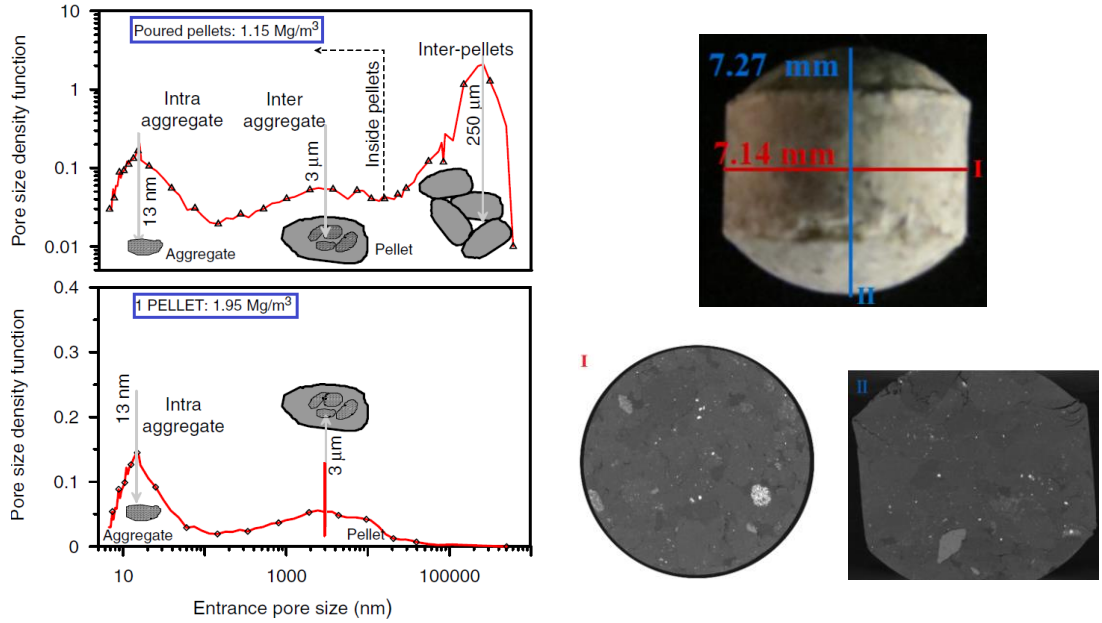

Figure 2-51: **(a)** Pore size distribution for a granular mixture of pellets (up) and for an individual pellet (down) of FEBEX bentonite (Hoffmann *et al.*, 2007); **(b)** X-ray microtomography through horizontal and vertical sections of an MX-80 bentonite pellet at its initial state (from Molinero *et al.*, 2017).

2.6.3. MIXED WITH COARSE MATERIALS

Another attractive choice for the expansive granular filling material in engineered barriers is the mixture of pure bentonite (commonly as powder) with sand or crushed *in-situ* geological materials. Besides the advantages already mentioned in **Section 2.6.2** of using granulated bentonite-based materials as engineered backfilling for radioactive waste disposals, the sand-bentonite mixture produces an increase in the thermal conductivity and in the mechanical strength of the resultant material (Cui, 2017). When crushed *in-situ* excavated material is used as the coarse element in the mixture, the chemical compatibility between the emplaced barrier and the surrounding geological environment is enhanced (Cui, 2017).

Several laboratory investigations were carried out along the past decades in order to evaluate the impact of the proportion (in dry mass) of bentonite and sand on the behaviour of the granular mixture and to determine a suitable proportion that could optimize the sealing properties required for its use as bentonite barriers for nuclear waste repositories. In that sense, the research results from the GRS laboratory (Braunschweig, Germany) during the "SB Project" ("**S**elf-sealing **B**arriers of Clay/Mineral in a Clay Repository") constitute an important benchmark in understanding the THM response of such mixtures under representative *in-situ* conditions. In fact, the experimental findings from such research investigations provided enough knowledge that allowed the selection of the type and the mass proportion of bentonite and sand in the mixture used as the backfill material in one section of the HE-E test (see **Section 2.6.4.5**). The most relevant conclusions of such studies are reported in Rothfuchs *et al.* (2012). The reduction of the bentonite content tends to cause a decrease in the water content of the wet mixture, in the liquid and plastic limits and in the swelling pressure and an increase in the bulk density of the mixture and in its water and gas permeabilities (Rothfuchs *et al.*, 2012; Manca, 2015). In this

type of granular fill, the sand particles are partially or totally covered by bentonite particles (Colmenares, 2002), as shown in Figure 2-52(a), and most of the water stored in pores is found in the bentonite fraction because the sand grains cannot adsorb water (Cui, 2017). In contrast, higher bentonite contents generate a buffering effect during the compaction of the sand-bentonite (S/B) mixture, inhibiting the development of denser mixtures (Rothfuchs *et al.*, 2012). The particle density of a S/B mixture ($\rho_{s,mix}$) can be estimated by means of a weighted average of the particle densities of sand ($\rho_{s,S}$) and bentonite ($\rho_{s,B}$) as follows

$$\rho_{s,mix} = \frac{1}{\frac{r_S}{\rho_{s,S}} + \frac{r_B}{\rho_{s,B}}} \tag{2-4}$$

where r_S and r_B are the ratio of sand and bentonite, respectively, in the S/B mixture. For the granular S/B mixture used as backfill material in one section of the *in-situ* HE-E test, the proportion of 65% of quartz sand and 35% of a crushed and sieved Na-bentonite, both with a grain spectrum of 0.5 – 1.8mm (see Figure 2-52(b)), resulted in a material with a dry density of the solid grains ($\rho_{s,mix}$) of 2.71 Mg/m^3 (Villar *et al.*, 2012b). The as-emplaced initial water content of the mixture was about 4% (Gaus, 2011; Villar *et al.*, 2012b). A thermal conductivity value of 0.33 W/m·K was measured for this S/B mixture in its as-delivered state and at room temperature conditions (Villar *et al.*, 2012b). Wieczorek *et al.* (2011) measured thermal conductivity values between 0.30 W/m·K (at 20°C) and 0.44 W/m·K (at 105°C) for the S/B mixture at its as-received water content. Furthermore, an average value around 0.31 W/m·K was measured for the thermal conductivity of this granular mixture at dry conditions. Such measurements were obtained by using the "Hot Disk Thermal Constants Analyser". The specific heat capacity provided by the CIEMAT laboratory for the dry mixture varied between 0.74 J/g/K (at 22˚C) and 0.90 J/g/K (at 115˚C) (Fernández, 2011). Similar values were also obtained by the GRS laboratory: 0.77 J/g/K (at 20°C) and 0.90 J/g/K (at 105°C) (Wieczorek *et al.*, 2011). For additional information on the main geotechnical properties and THM behaviour of sand/bentonite mixtures, see Colmenares (2002), Rothfuchs *et al.* (2012) and Manca (2015).

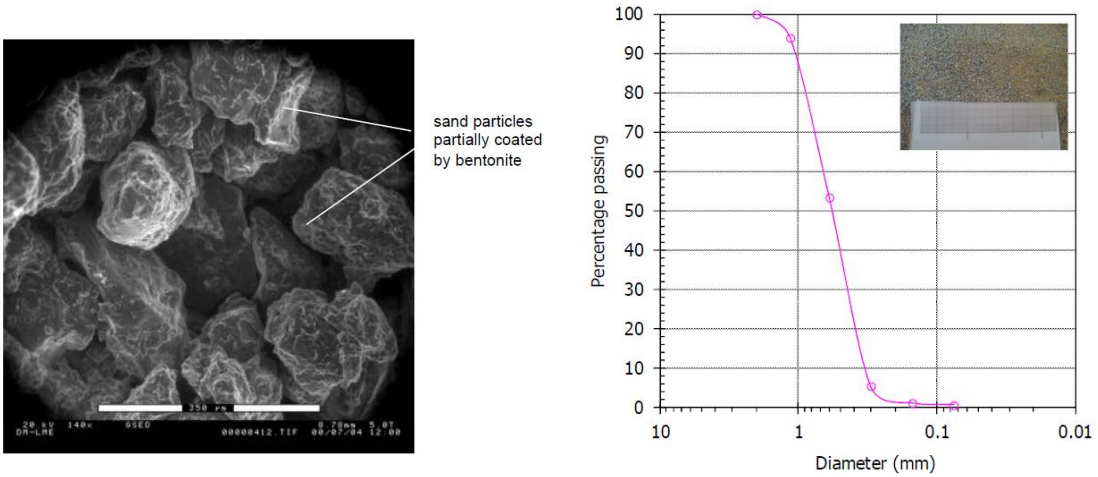

(a) **(b)**

Figure 2-52: **(a)** Micrograph of a compacted S/B mixture showing sand particles partially covered by bentonite powder (Colmenares, 2002); **(b)** Grain size distribution for the granular S/B mixture emplaced in one section of the HE-E experiment (after Villar *et al.*, 2012b).

2.6.4. THE ENGINEERED BENTONITE BARRIER CONCEPT IN THE "EU SCENARIO"

In Figure 2-53, some conceptual designs of engineered barrier sections in nuclear waste disposals proposed by research projects in which a real scale test has been performed at underground laboratories are shown. Note that bentonite buffers may be composed by compacted blocks only (Figure 2-53(a)) or by compacted blocks (on which the canister rests) with bentonite pelletized material (Figure 2-53(b)) or powder bentonite mixed with other granular coarse materials (Figure 2-53(c)) filling up the void zone between the host rock wall and the metallic container.

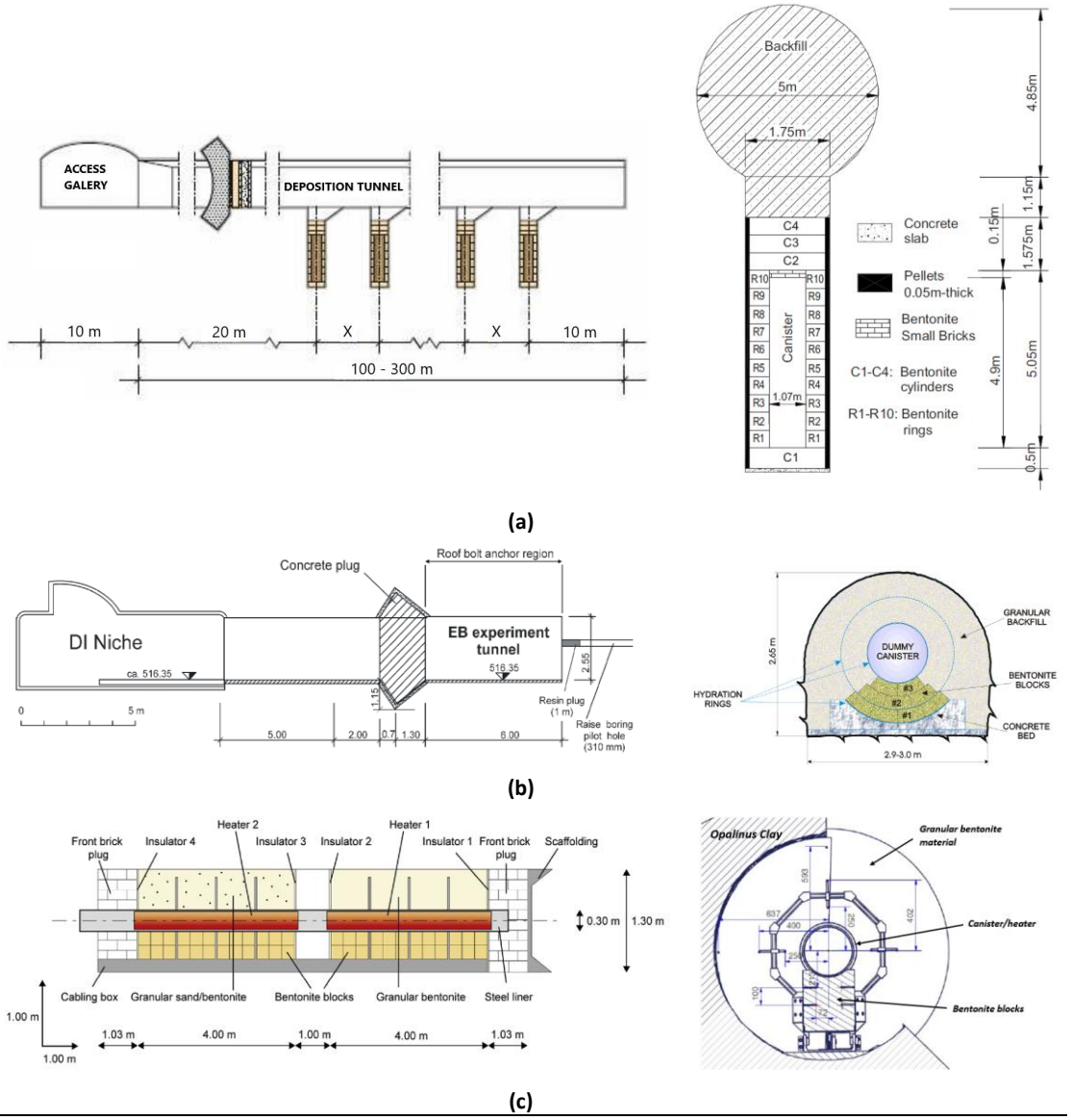

Figure 2-53: Layout of the longitudinal (left) and cross (right) sections, showing the dimensions and the barrier components of the multi-barrier system for **(a)** the KBS-3 system (Swedish repository concept – SKB; **(b)** the EB Experiment (Spanish repository concept – ENRESA/AITEMIN/NAGRA); **(c)** the HE-E experiment (Swiss repository concept – NAGRA/GRS).

In the European Union (EU) scenario, many relevant research programmes associated with the high-level and/or long-lived radioactive waste disposals have been conducted by several energy

and management agencies throughout the past three decades. In the next sections, some of the most relevant investigation projects and/or large-scale experiments carried out are briefly described.

2.6.4.1. THE FEBEX PROJECT

The ***F**ull-scale **E**ngineered **B**arriers **EX**periment* (FEBEX) was a two-phase project – **FEBEX I** (1996-1999) and **FEBEX II** (2000-2004) – managed by the Spanish agency ENRESA and performed for the purpose of studying the behaviour of the near-field components for a high level radioactive waste repository in crystalline rock. In that sense, the experimental tasks consisted of: an *in-situ* full-scale test, performed under natural conditions at the Grimsel Test Site (Switzerland); an almost real-scale "mock-up" test, performed at CIEMAT facilities in Madrid (Spain); and a series of laboratory tests in order to determine parameters and evaluate the thermo-hydro-mechanical, the thermo-hydro-geochemical and the gas generation behaviour (Huertas *et al.*, 2005). In the two large-scale heating-hydration tests, the increase in temperature was simulated by heaters placed horizontally and surrounded by a bentonite barrier, while the re-saturation process of the barrier was natural in the *in situ* test and controlled in the mock-up test (Lloret and Villar, 2007). The clay barrier was composed by compacted blocks of a calcium montmorillonite extracted from the Cortijo de Archidona deposit, in the zone of Serrata de Níjar (Almería, Spain), the so-called "FEBEX bentonite". Partial dismantling of the *in situ* test was carried out in 2002, with the removal of one heater (of the two initial heaters). The other heater was left running until the late 2014, when the dismantling activities of this second heater started. The mock-up test is still running, after more than 20 years since its beginning. More information about the FEBEX Project (since its beginning until the present), the *in situ* operations, the large-scale tests, the laboratory studies, the modelling performances, etc., can be found in a large amount of scientific and technical publications, as for instance, in ENRESA (2000), Lloret *et al.* (2004), Huertas *et al.* (2005), Villar *et al.* (2005; 2018), Villar (2006), Sánchez and Gens (2006), Lloret and Villar (2007), Villar and Lloret (2007b) and Gens *et al.* (2018). For further details, the reader can also consult the Grimsel Test Site webpage (http://www.grimsel.com/).

2.6.4.2. THE EB EXPERIMENT

The ***E**ngineered **B**arrier* (EB) Experiment, carried out by ENRESA with the contribution of the Swiss agency NAGRA, was a long running experiment that started in 2000 and was incorporated in 2010 into the PEBS Project (*Long-term **P**erformance of **E**ngineered **B**arrier **S**ystems*) (2010-2014). This experiment consisted in an isothermal artificial hydration of a bentonite barrier composed of compacted blocks and granular pellets made of the same expansive clay (FEBEX bentonite), performed in the underground research laboratory (URL) of Mont Terri (Switzerland), inside a horizontal gallery drilled in an impervious clay shale (Opalinus Clay). A steel dummy canister (simulating the nuclear waste canister) was placed on the top of a lower supporting bed of compacted bentonite blocks and the remaining space between the canister, the compacted blocks and the horizontal gallery in which the experiment has been performed

was filled with FEBEX bentonite pellets (see Figure 2-53(b)). The forced hydration of the isolating/sealing barrier was launched in order to reduce the test duration to a reasonable period of time (due to the very low permeability of the host rock). Besides the real scale experiment, the engineered barrier project also included a laboratory experimental programme in order to characterize the hydro-mechanical properties of the emplaced granular bentonite material. A full dismantling operation of the experiment, together with the extraction of samples for laboratory testing, was accomplished during the autumn and winter of 2012 (Schuster *et al.*, 2014). For an insight of the EB experiment (construction, instrumentation, artificial hydration system, dismantling, post-mortem sampling and testing) and the laboratory activities carried out within the scope of the engineered barrier project and the hydro-mechanical modelling tasks performed as a consequence of such experimental tests, see AITEMIN (2001; 2012), Hoffmann (2005), Alonso and Hoffmann (2007), Hoffmann *et al.* (2007), Palacios *et al.* (2013) and Villar *et al.* (2014a).

2.6.4.3. THE RESEAL PROJECT

The RESEAL Project, coordinated by the Belgian agency SCK-CEN in collaboration with other European agencies/organizations (including UPC), aimed to demonstrate the feasibility of bentonite seals in avoiding preferential pathways for water, gas and radionuclide migration along the seal/host rock interface and through the excavated damage zone (EDZ) (Gens *et al.*, 2009a). The main project activities, which started in 1996 and lasted until 2007, were focused on the performance of two sealing experiments in the HADES URL in Mol (Belgium): the borehole and the shaft sealing experiments, both of them carried out in galleries excavated in a deep and plastic clay formation (Boom Clay). The borehole sealing experiment aimed at sealing a 25 cm diameter horizontal borehole in the Boom Clay by means of pre-compacted blocks of two bentonites – namely the Serrata and the *Fo*urges-*Ca*haignes (FoCa) clays – subject to natural and artificial hydration (Van Geet *et al.*, 2009). The large-scale shaft sealing test consisted in the installation, the closing and the subsequent forced hydration of a bentonite seal, composed by FoCa clay pellets and powder mixed at a weight ratio of 50/50 (Dereeper and Volckaert, 2002), in a 2.2 m diameter vertical shaft (excavated manually in 1984) located in the surroundings of the HADES URL. The clay seal had a height of about 2.2 m, in which the lower portion of the seal (the first 60 cm) was heavily compacted; from this level up, the sealing material was installed without further compaction (Van Geet *et al.*, 2009). Detailed information about the construction of the bentonite seals, the monitoring programme for evaluating the response of the installed seals and the host rock as the hydration test was carried out, the performance of permeability, radionuclide migration and gas breakthrough tests (in the borehole seal experiment), besides the modelling tasks and the main conclusions of the RESEAL Project can be found in Volckaert *et al.* (2000), Van Geet *et al.* (2007; 2009), Gens *et al.* (2009a; 2011) among others.

2.6.4.4. THE TIMODAZ PROJECT

The ***T**hermal **IM**pact **O**n the **DA**maged **Z**one* (TIMODAZ) *Project*, was a four-year research project (2006-2010) coordinated by the Belgian organization ESV EURIDICE GIE and co-funded by the

European Commission (EC). In such a project participated several European radioactive waste management agencies and nuclear research institutes with the scientific support of other research institutions (including the research Centre CIMNE-UPC), universities, industrial partners and consultancy companies. The main objective of that project was to evaluate the combined effect of the EDZ evolution and the thermal impact on clay host rocks in the vicinity of a radioactive waste repository. For such a purpose, laboratory and *in-situ* thermal experiments were designed and carried out for three types of deep clay formations: the Boom Clay (Mol, Belgium), the Opalinus Clay (Mont Terri, Switzerland) and the Callovo-Oxfordian Argillite (Meuse, France). The THM behaviour of the selected clays was characterized by means of small-scale tests under controlled temperature/stresses/pore pressure conditions while the excavation process and the thermal loading impact on the process of localization and/or fracturing were simulated through middle- to large-scale tests on hollow cylinder samples. In addition, *in-situ* heating experiments were performed in different underground laboratories within the TIMODAZ Project, being the small-scale ATLAS heater test and the large-scale PRACLAY heater experiment, both carried out in the HADES URL (Mol, Belgium) and the small-scale SE-H (self-sealing with heating) experiment in the Mont Terri URL (Switzerland) the most prominent experimental prototypes. Other relevant activities and tasks carried out during the TIMODAZ Project, the main experimental/modelling achievements regarding the THM characterization, the behaviour of the selected clay formations and the current state of the *in-situ* heating experiments are reported in Bastiaens *et al.* (2003), Charlier *et al.* (2010) or on the project website (http://www.timodaz.eu/).

2.6.4.5. THE HE-E EXPERIMENT

The HE-E experiment is a full-scale heating test with natural re-saturation of the bentonite barrier at high temperatures (around 140°C). The performance of this *in-situ* heating experiment constituted one of the main objectives of the PEBS Project (2010-2014). The experiment started on June 28th, 2011 and it is still running so far. The experiment is located at the Mont Terri URL (Switzerland) in a 50-m long non-lined horizontal microtunnel (MT) of 1.3 m diameter excavated in the Opalinus Clay formation. The section of the MT in which the HE-E experiment is running is the same section in which the Ventilation (VE) Test (Mayor *et al.*, 2005; Mayor and Velasco, 2008) was carried out from December 2001 to June 2010 (Gaus, 2011). This MT section has a length of 10 m and it is divided in two independently heated sections (identified as NAGRA Section and GRS Section) of 4 m length each, in which the heaters (one per section) were placed (see Figure 2-54). Compacted bentonite blocks with average dry density of 1.81 Mg/m^3 and initial water content of 10.3%, made of sodium bentonite MX-80 from Wyoming (Plötze and Weber, 2007), support the canister in both heated sections. The void zone between the host rock, the compacted bentonite blocks and the heaters is filled up with granular bentonite-based materials. The NAGRA Section is filled with MX-80 bentonite pellets whose average as-emplaced dry density and water content values are 1.46 Mg/m^3 and 5.9%, respectively. The GRS Section is filled with a S/B mixture with 65% of sand and 35% of sodium bentonite GELCLAY WH2, with an average dry density of 1.50 Mg/m^3 and an as-emplaced water content around 4%. The bentonite material used in the mixture has a similar composition of the MX-80 bentonite (Villar *et al.*, 2012b). The test sections are isolated from the external environment by two concrete plugs while a third concrete barrier separates the two sections, as illustrated in Figure 2-54.

Furthermore, a thermal insulation and a vapour barrier were also constructed at both ends of each heater element (Gaus *et al.*, 2014b).

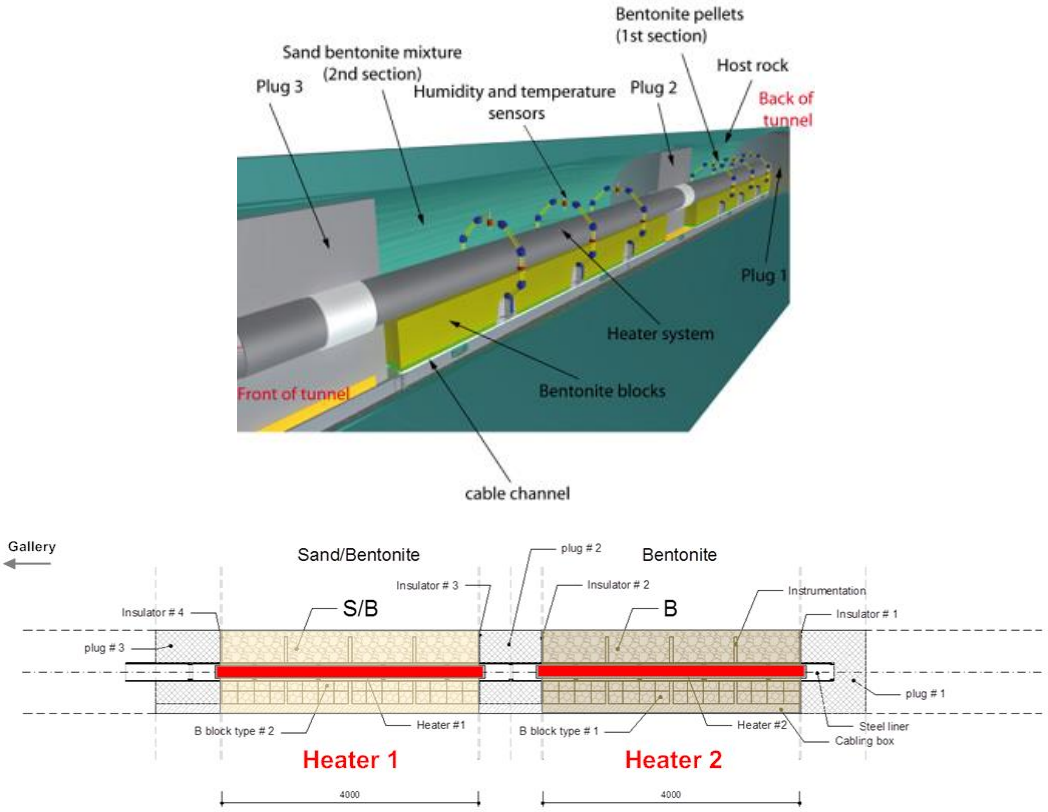

Figure 2-54: Schematic layout of the in-situ HE-E experiment and the different components of each heated section. Heater 1 is emplaced into the GRS Section; heater 2 is located in the NAGRA Section (after Gaus, 2011).

The heating strategy consisted in gradually increasing the heater temperature until reaching a target value of 140°C, on both canister surfaces, in June 2012 (one year after the beginning of heating). Heater temperature has been held unchanged since then. Both 4-m long heaters were designed to work independently and the heater system can operate by either power or temperature control (Gaus, 2011). Temperature evolution around the HE-E experiment site is monitored through a system of temperature sensors installed on the heater surface, inside the bentonite buffers and in the surrounding host rock.

One of the main objectives of the HE-E heating test is to provide a large experimental database required for the calibration and validation tasks of the existing numerical models. This data collection has been recorded by a set of sensors arranged in three zones:

- Inside the bentonite barrier: thermo-couple sensors of temperature and relative humidity were installed before the emplacement of the granular materials (see Figure 2-55) along three cross sections (per heated section) and at different positions – near the heater (C), at half-distance (M) and close to the buffer-host rock interface (H).
- In the Opalinus Clay, close to the MT surface and up to a distance of 2 m inside the host rock, where the impacts of the activities carried out inside the MT on the THM behaviour of the host rock are more appreciable. Temperature, humidity, hydraulic pressure and

displacement are monitored by sensors distributed along several cross instrumented sections (as shown in Figure 2-56), most of them installed for monitoring the Ventilation (VE) Test (2001-2010).

- In the host rock at larger distances from the MT wall, where the hydraulic overpressures due to the thermal pulse are expected to occur (Czaikowski *et al.*, 2012). Four instrumented boreholes drilled from the so-called "Gallery 98" (two of them perforated during the VE Test) have been used for monitoring the pore pressure response at far field (see Figure 2-57). Furthermore, pore pressure data available before the beginning of the heating experiment were used to evaluate the extension of the depressurization zone around the underground galleries, which served to reproduce the initial hydraulic conditions in the vicinity of the HE-E experiment site.

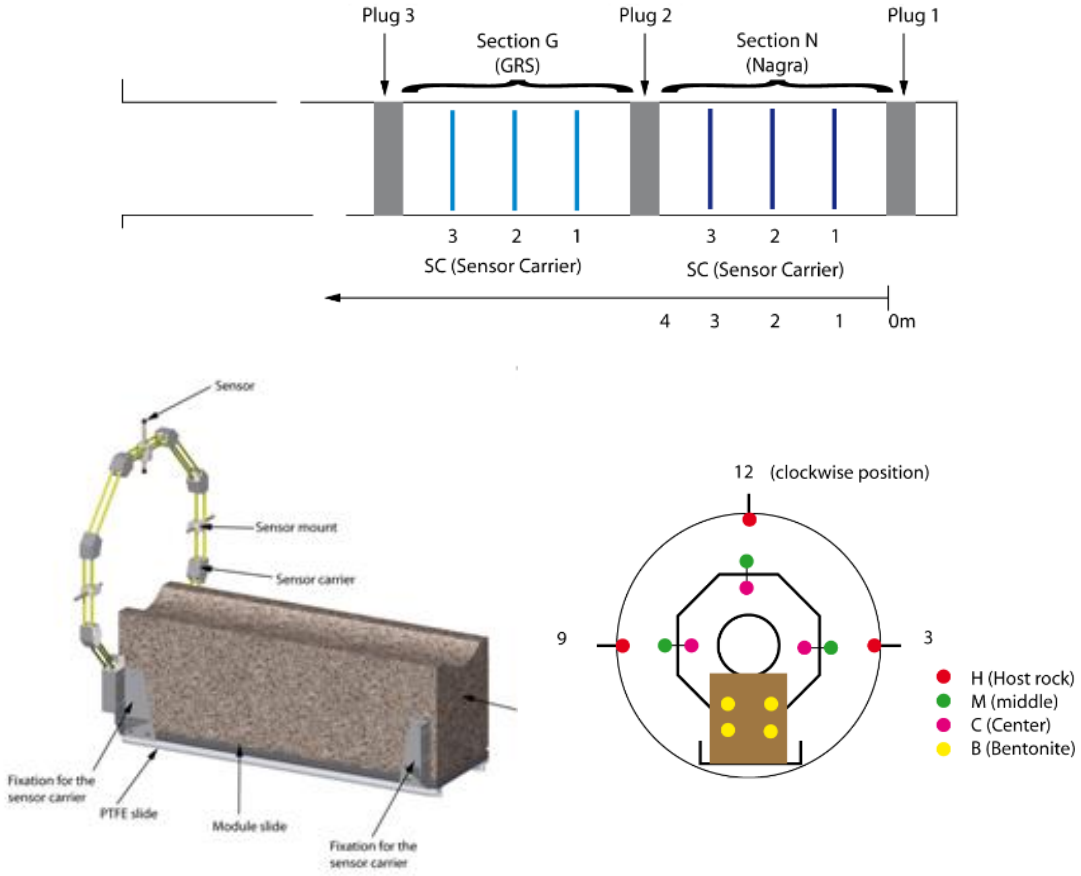

Figure 2-55: Location of the instrumented sections inside the barriers (up), layout of the structural support for the instrumentation within the barrier and around the heaters (down, in the left corner) and sensor locations along each cross section (down, in the right corner) (Gaus, 2011).

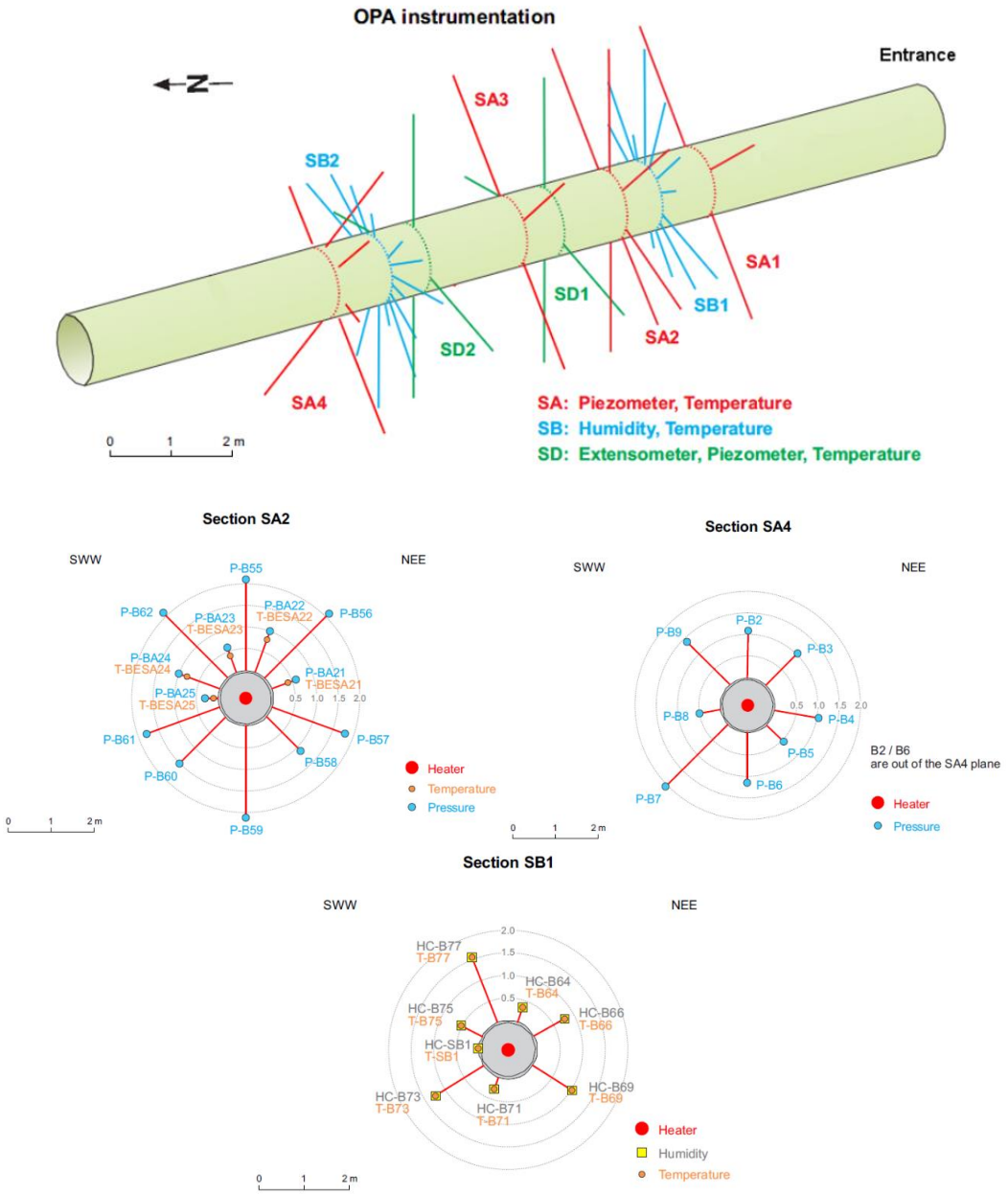

Figure 2-56: Layout of the instrumented cross sections in the Opalinus Clay (host rock) around the microtunnel (MT) (up) and distribution of sensors for monitoring the evolution of pore-water pressure, temperature and relative humidity in the host rock along three instrumented sections: SA2, SA4 and SB1 (down) (Teodori and Gaus, 2011).

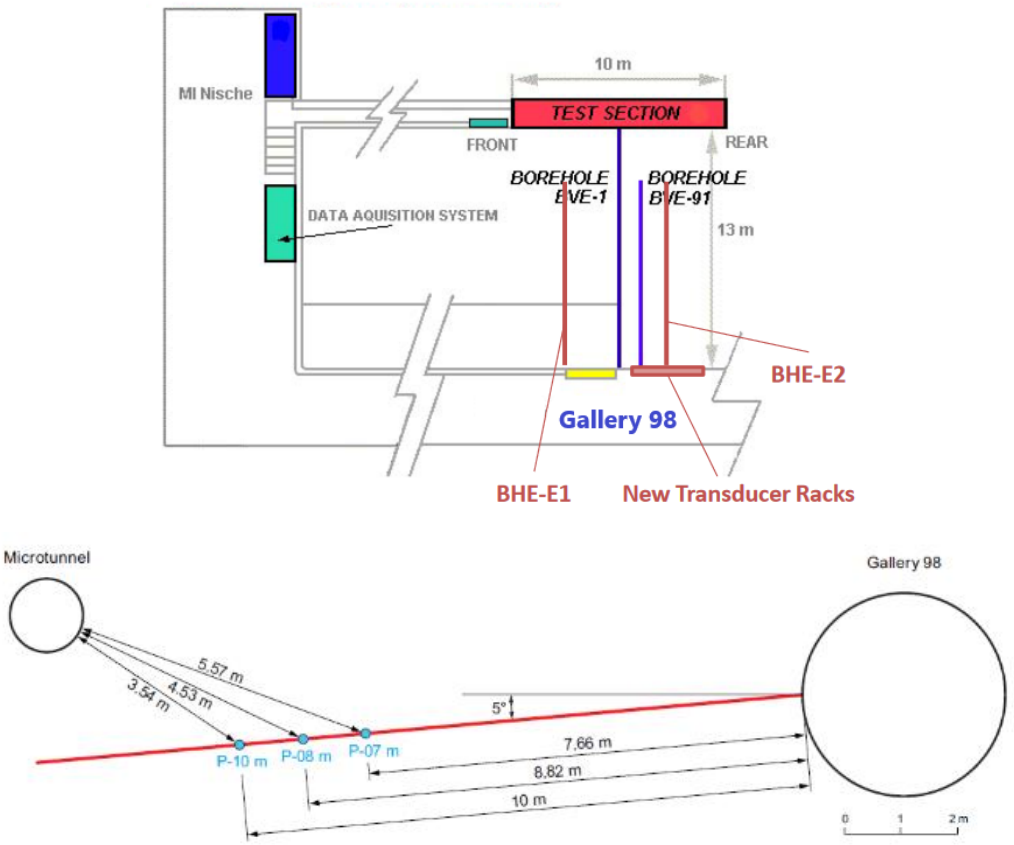

Figure 2-57: Layout of the instrumentation for measuring pore pressure in the far field of the HE-E test (test section), showing the location of boreholes (BVE-1, BVE-91, BHE-E1 and BHE-E2) (up) containing pore pressure sensors (down) for the borehole BVE-91 (Teodori and Gaus, 2011).

It is important to mention that no significant swelling pressures are expected to develop during the experiment as a consequence of the lower re-saturation rates of the barriers (Gaus, 2011). Due to that, no measurements of swelling pressures were considered during the design phase. More detailed information about the field conditions in the surroundings of the experiment site before and after the previous VE Test, the instrumentation layout in the host rock and inside the bentonite barriers, the monitoring programme (for the VE and the HE-E tests) and the operational and modelling tasks carried out for the HE-E experiment can be found in Thury and Bossart (1999), Mayor *et al.* (2005), Mayor and Velasco (2008), Gaus (2011), Teodori and Gaus (2011) and Gaus *et al.* (2014a; 2014b).

The performance of two laboratory tests, one for each granular bentonite-based material used in the *in-situ* heating test, has allowed a better characterization of the thermo-hydraulic properties of such filling materials at known and controlled boundary conditions. Furthermore, they have also enhanced the knowledge concerning the non-isothermal hydration of bentonite buffers (provided by the *in-situ* test) due to the isolation, identification and quantification of the thermo-hydraulic (TH) processes that take place during the barrier re-saturation. Both laboratory tests were carried out in the CIEMAT laboratory (Madrid, Spain) and the materials used to construct the 50-cm long bentonite columns, each of them with an inner diameter of 7 cm (as illustrated in Figure 2-58), were brought directly from the Mont Terri test site (Villar *et al.*, 2012b). The as-received water contents of the granular bentonite materials were similar to

their initial emplacement values: 6.4% for the pellets and 3.6% for the sand-bentonite mixture. The heating of the bentonite cells has been performed by means of a plane stainless steel heater placed at the bottom of the cells. A cooling chamber located on the top of the cells allows the circulation and the injection of water (at laboratory temperature) into the granular bentonite materials. The evolution of temperature and relative humidity inside the columns during the test was monitored by means of thermo-couple sensors installed at three different levels (10 cm, 22 cm and 40 cm from the heater element approximately).

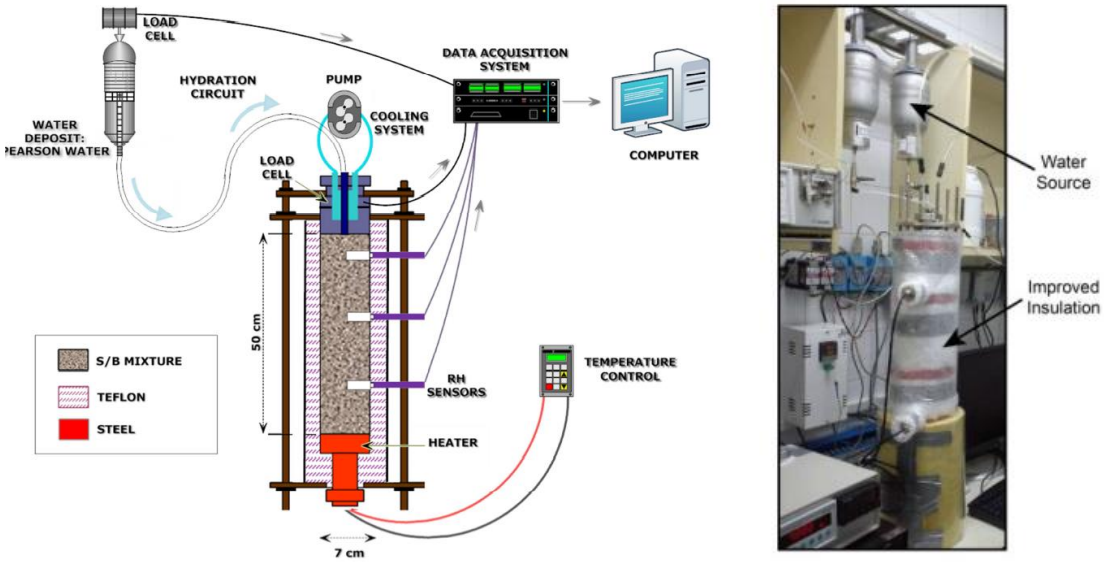

Figure 2-58: Experimental setup for the heating-infiltration tests (left) and one of the bentonite cells (the column of bentonite pellets) during operation and wrapped with the insulation material (after Villar *et al.*, 2012b).

The laboratory heating of both cells started in November, 2011. The infiltration of water under a thermal gradient inside the cells (at a heater temperature of 140˚C) started around 4,000 hours since the beginning of heating in the column containing the S/B mixture while it took around 5,000 hours (June 2012) to initiate the hydration of the cell with pellets (Villar *et al.*, 2014b). The cell with the S/B mixture was dismantling in February, 2015 (Villar *et al.*, 2016) while the heating-hydration of the column made of bentonite pellets keeps still running. The numerical modelling of these infiltration tests at high temperatures using the double porosity approach proposed and detailed throughout the next three chapters is discussed in **Chapter 8**. For more information about the experimental procedures carried out previously and during the fabrication of the bentonite columns, the main features and data observed during the performance of the heating-infiltration tests as well as the dismantling of the S/B cell and the current state of the column of pellets, see Villar *et al.* (2012b; 2015b; 2016) and Iglesias *et al.* (2018).

2.7. MODELLING THE EXPANSIVE BEHAVIOUR OF UNSATURATED CLAYS

2.7.1. SWELLING AND SHRINKAGE MECHANISMS FROM AN EFFECTIVE STRESS STANDPOINT

The distinctive volumetric behaviour of expansive clays subjected to changes in their moisture conditions can be explained by the unbalanced stress state at particle scale between the inter-particle physico-chemical stresses (σ_m^{R-A}) and the external effective stresses (σ_m) transferred by the clay structure (Lambe, 1960a). The physico-chemical stresses arise from the electrical interactions between negative-charged clay particles and the dissolved ions within and around these particles. They are transferred through the interacting diffuse double layers and the internal crystalline water layers acting at face-to-face contacts (Măsin and Khalili, 2016). Therefore, the amount of water in the diffuse double layer and in the inter-lamellar space determines the magnitude of the volumetric expansion/contraction, as discussed in previous sections (see **Section 2.2.1.4**). Eventually, due to the electrical charges of the chemical species present in the adsorbed water and on the clay particle surface, attractive (London van der Waals) and repulsive (interacting diffuse double layers) forces develop and, depending on the net electrical forces (difference between repulsive and attractive forces), the space between adjacent particles can increase or decrease (Lambe, 1960a). Under zero net stress conditions, the amount of water imbibed by the inter-particle space (and consequently, the volumetric expansion/contraction) is solely controlled by these net electrical forces. The net repulsive pressure (σ_m^{R-A}) tends to increase with decreasing the inter-particle spacing (as in an unconfined drying path) and to decrease with the increase of the double layer thickness (as in a wetting path under free swell conditions) (Lambe, 1960a). If the amount of free pore-water present in the soil is high enough, the double diffuse layer between clay particles would expand until reaching the equilibrium between repulsive and attractive forces. In such conditions, the full disaggregation of particle packages can occur (Laird, 2006) with clay behaving as a slurry upon flooding.

Nevertheless, in most geotechnical situations, the total free swell/shrink potential of active clays is limited through the application of external loadings or due to the presence of physical elements that restrain the volumetric deformations. Assuming that the prevailing assembly of clay particles is characterized by a face-to-face configuration (as the one shown in Figure 2-21(c)) loaded perpendicularly to the clay surfaces, the average distance between interacting particles changes in order to reach a new static equilibrium configuration in response to the variations in the applied (or induced) effective stress state ($\Delta\sigma_m$). On the other hand, a change in the double layer thickness induces a change in the net electrical inter-particle pressure ($\Delta\sigma_m^{R-A}$). In a simplified (and general) form, this is expressed as

$$\Delta\sigma_m = \Delta\sigma_m^{R-A} \tag{2-5}$$

In other words, changes in the effective stress in clays with a like-dispersed structure generates equal stress changes within the clay-water system. Such changes in the inter-particle pressures are evidenced, in a macrostructural scale, by the volumetric expansion/contraction of the soil

or by an increase/decrease in the swelling pressure. In such conditions, the effective stress principle by Terzaghi (1936) that states that a volume changes occur when the effective stress acting on the soil mass changes, is satisfied (Lambe, 1960a; Măsin and Khalili, 2016). In unsaturated soils, this principle is formulated in terms of a couple of stress variables (see **Section 3.3**), usually the net stress and the matric suction, whose variations are correlated to the volumetric behaviour at partially saturated conditions (Fredlund *et al.*, 2012). Thus, during the drying process of a clay sample, the water vaporization causes an increase in the effective stress acting on the clay particles due to the increase of suction (negative pore-water pressure). The increase in the effective pressure induces a migration of water from the inter-particle space to the exterior air-water menisci, where it evaporates (Lambe, 1960a). This process leads to a reduction in the diffuse double layer thickness and, consequently, it results in a local contraction at particle level. The shrinkage process continues until a new equilibrium state between external and internal forces acting on the clay-water system is achieved (see Figure 2-59(a), down). Moreover, the volumetric contraction of clays is dependent on the initial water content, the degree of saturation and the magnitude of the water content changes (Lambe, 1960a). On the other hand, the swelling of expansive clays can be related to a decrease in the effective stress, caused by the reduction of suction. Due to the hydric deficiency of the double layer, such an effective stress decrease promotes the imbibition of free water from the external air-water interfaces by the water-clay system, which leads to an increment in the double layer thickness (Lambe, 1960a). Consequently, the clay swelling proceeds until the net repulsive pressure between interacting clay particles is in equilibrium with any applied effective stress (see Figure 2-59(a), up). As mentioned in previous sections, the swelling behaviour of clays is related to their mineralogical composition (**Section 2.2.2.1**), their initial water content and dry density (**Section 2.2.2.4**), the arrangement and orientation of particles in natural and compacted clays (**Section 2.2.2.5**) and to the confining pressure imposed during wetting (**Section 2.2.2.2**). In addition, the swelling potential is also dependent on the chemical composition and properties of the pore-fluid (Abdullah *et al.*, 1999; Lloret *et al.*, 2004; Estabragh *et al.*, 2013) and on the time required for the soil to fully develop its swelling potential as water molecules is absorbed into the inter-particle space (Lambe, 1960a).

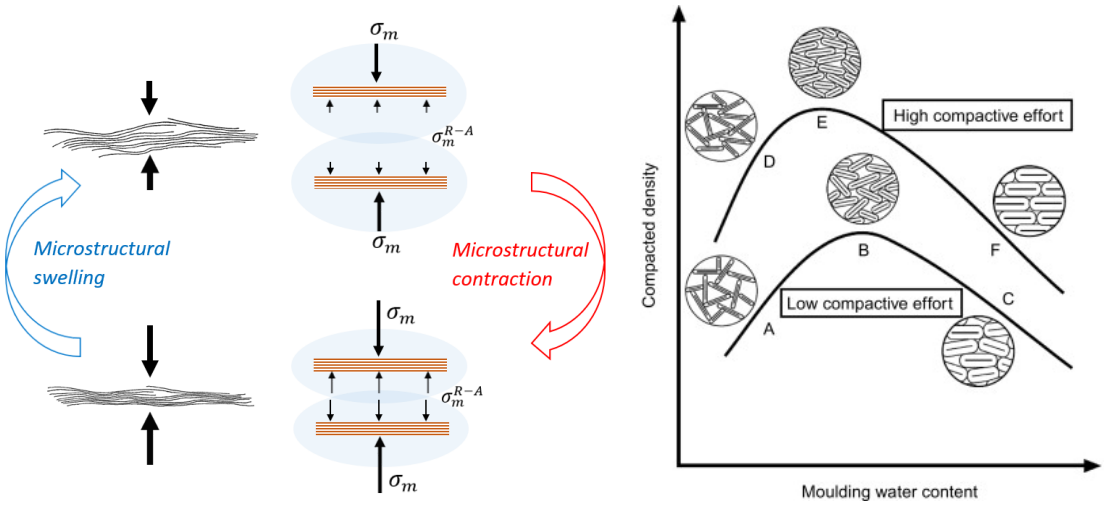

Figure 2-59: **(a)** Conception of microstructural swelling/contraction from the balance between "external" effective stresses and "internal" net electrical pressures acting on "parallel" clay particles; **(b)** dependence of the remolded clay fabric on the water content and the compaction effort (Wagner, 2013).

Although the deformation response of swelling clays has been described in terms of changes in their effective stress, it is important to highlight that the magnitude of swelling or shrinkage of such soils under a given effective stress change is, in fact, controlled by their physico-chemical characteristics arising from the large specific surface area of the elementary particles (Lambe, 1960a). In addition, and due to the nature of the physico-chemical forces between interacting clay particles, it is assumed that the deformations of an assembly of clay particles (forming a clay aggregate) are volumetric and reversible. This assumption constitutes the phenomenological basis for the development of double porosity formulations to model the swelling response of unsaturated expansive clays under isothermal and non-isothermal conditions, as the ones described in the following section (**Section 2.7.2**). Furthermore, the additional hypothesis of a saturated clay matrix made of parallel assembly of particles has been assumed in those constitutive formulations in order to satisfy Terzaghi's effective stress principle (Yang *et al.*, 1998). Nevertheless, Măsin and Khalili (2016) also demonstrated the validity of the effective stress principle to predict the elastic volumetric deformation of saturated clay aggregates formed by a system of particles in both face-to-face (dispersed) and edge-to-face (flocculated) configurations as long as the overall dry density of particles would not exceed 2.2 Mg/m^3. In such a study, experimental data from the literature on the unconfined water retention curves, the swelling pressures, the mechanical unloading at saturation, the compression at different suctions and the wetting under constant loads of several compacted bentonite samples were analysed. A unique relationship between the aggregate void ratio and the mean Terzaghi's effective stress for both variable suction and total stress was achieved, thus validating the use of the effective stress principle to also estimate the volumetric expansion/contraction of the clay aggregates (Măsin and Khalili, 2016). However, it is important to emphasize that the remolding and the compaction procedures destruct the original structural arrangement of clay particles in a soil. For a given compaction energy, the compaction wet of optimum tends to generate an oriented (dispersed) clay fabric and for a given molding water content, the increase in the compaction effort tends to reorient the clay particles towards a dispersed structural arrangement (see Figure 2-59(b)). Consequently, the effective stress principle can be assumed as valid to predict the microstructural volumetric response of remolded and compacted samples of expansive clays.

2.7.2. THE BARCELONA EXPANSIVE MODEL (BExM) AND THE DOUBLE POROSITY APPROACH FOR GENERALIZED STRESS STATES

The **B**arcelona **Ex**pansive **M**odel (BExM) was one of the earliest elasto-plastic models for describing properly the swelling-shrinkage behaviour of expansive clays during wetting-drying cycles. This constitutive model was conceived as an enhancement of the original BBM (for non-plastic and moderate expansive unsaturated soils) by the consideration of a double pore structure in the soil, according to the conceptual basis for expansive clays presented in Gens and Alonso (1992). In that sense, microstructure accounts for the clay matrix and the inter-layer and inter-particle voids (micro-pores) while macrostructure refers to the arrangement of soil particles and aggregates and the relatively large pores between them (Gens and Alonso, 1992; Gens *et al.*, 2011). The swelling and shrinkage behaviour of active clay minerals is associated with the microstructural level while the major structural rearrangement of pore space is related to the behaviour of macrostructure (Yang *et al.*, 1998; Alonso *et al.*, 1999; Wang and Wei, 2015).

The interaction between these two overlapping media is established by means of a mechanical coupling mechanism that accounts for the structural changes at macrostructure in response to the deformation behaviour of the microstructure (Sánchez and Gens, 2006).

In the original mathematical formulation of the BExM model as described in Alonso *et al.* (1999), the mechanical behaviour of microstructure is elastic and volumetric and micro-pores remain saturated. It is assumed the "parallelism" of interacting clay particles and, consequently, the effective stress concept – as discussed in the previous section – is used to describe the volumetric deformation of saturated particles and aggregates. Therefore, changes in microstructural volumetric strains are related only to changes in the net mean stress (dp) and/or in the matric suction (ds), i.e., to changes in the effective mean stress, $d(p+s)$. The locus of the current effective mean stress state acting on microstructure corresponds to a curve in the $p{:}\,s$ space, termed as the neutral loading line (NL) by Gens and Alonso (1992), for which no microstructural volumetric strains occur if the stress path moves on it, that is, $d(p+s)=0$. The neutral line divides at each instant the zone of microstructural swelling, $d(p+s)<0$, from the zone of microstructural shrinkage, $d(p+s)>0$, as illustrated in Figure 2-60(a). On the other hand, the mechanical behaviour of the soil skeleton (macrostructure) is described by means of the elasto-plastic BBM model (Alonso *et al.*, 1990). Consequently, the mathematical formulation for the macrostructural part of the model inherits the same features of the BBM model, as the use of two independent stress state variables, the extension of the concept of critical state to the unsaturated conditions and the dependence of the yield surface on the stress level, the matric suction and the history variables. In addition to the plastic mechanism related to the loading and collapse (LC) of macrostructure already implemented in the original BBM formulation, Alonso *et al.* (1999) also defined two additional hardening processes, both of them coupled to the LC plastic mechanism and arising from the macrostructural irreversible changes due to the swelling or shrinkage of microstructure. The first of those plastic mechanisms is related to the plastic strains generated by the shrinkage of microstructure (**S**uction **I**ncrease – **SI** locus), as the macrostructural collapse experienced by a marked open soil skeleton (loose macrostructure) under low suction conditions when submitted to a drying path (Alonso *et al.*, 1995), for instance. The second additional plastic mechanism accounts for the structural rearrangement in the soil skeleton due to the swelling of microstructure (**S**uction **D**ecrease – **SD** locus). This is the case of the accumulated swelling strains observed at the end of the first wetting-drying cycle in dense macrostructures or the structural collapse of open macrostructures at relatively high confining pressures during the final stages of wetting (Alonso *et al.*, 1995). These micro-macro interaction mechanisms are given by two curves in the $p{:}\,s$ space that bound an elastic region around the current NL locus, as displayed in Figure 2-60(a). Alonso *et al.* (1999) also postulated a unidirectional coupling among the three yield surfaces (LC, SI and SD) so that the activation of the SD or the SI mechanisms leads to a change in the LC position, but the activation of LC does not cause any movement of SI and SD. Gens and Alonso (1992) suggested that the magnitude of the plastic strains induced by the deformation state of microstructure is proportional to the microstructural volumetric strains. Furthermore, it also depends on the degree of openness of macrostructure, represented by the ratio between the current net mean stress (p) and the pre-consolidation net mean stress at the current suction (p_0). Consequently, a pair of micro-macro interaction functions have been defined: one related to microstructural swelling paths (SD) and the other one associated with microstructural shrinkage paths (SI). Typical shapes for the pair of micro-macro interaction functions are displayed in Figure 2-60(b) together with some observed/expected responses from sequential

wetting-drying cycles due to the structural coupling between both media. Different expressions for the micro-macro interaction functions have been proposed in the literature (Yang *et al.*, 1998; Alonso *et al.*, 1999; Alonso *et al.*, 2005; Sánchez *et al.*, 2005; Gens *et al.*, 2011).

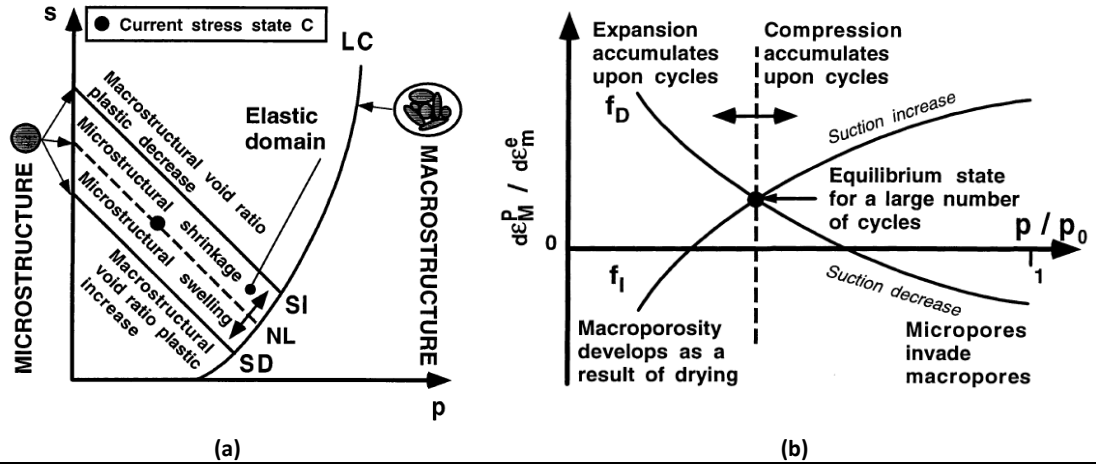

Figure 2-60: Main constitutive aspects of the BExM: **(a)** yield loci in the p: s plane; **(b)** micro-macro interaction functions and some typical structural changes due to the mechanical coupling between both media (Alonso *et al.*, 1999).

Although the original formulation of the BExM model (and its posterior enhanced versions) has predicted satisfactorily most essential features observed in expansive clays (Yang *et al.*, 1998; Alonso *et al.*, 1999, 2005; Vasconcelos *et al.*, 2014), some practical drawbacks limit, however, its implementation into current geotechnical applications. The major of them is the large number of parameters required to model the microstructural behaviour and the micro-macro coupling processes in addition to the difficulty of estimating such parameters from conventional laboratory tests (Wang and Wei, 2015). In that sense, Alonso *et al.* (2005) postulated some numerical simplifications into the original BExM formulation (Alonso *et al.*, 1999) and suggested a laboratory procedure to derive the microstructural compressibility and the model parameters for the micro-macro interaction functions. Despite that, the experimental determination of such parameters remains a difficult and subjective task. Furthermore, the issue of defining the onset of the non-reversible strains associated with the mechanical coupling between microstructure and macrostructure led to the formulation of a double porosity approach in terms of a generalized stress state in the context of the generalized plasticity theory (Sánchez, 2004; Sánchez *et al.*, 2005).

One of the major advantages of using a generalized plasticity model is that the explicit definition of a yielding function shape for the plastic mechanisms associated with the micro-macro interaction is not required anymore. In this double porosity framework developed by Sánchez *et al.* (2005) the nature (swelling/compression) of the microstructural deformation is defined by means of a pair of directional vectors ($\widehat{\boldsymbol{n}}_C = \frac{\partial F_{NL}}{\partial \widehat{\boldsymbol{\sigma}}}$ and $\widehat{\boldsymbol{n}}_S = \frac{\partial F_{NL}}{\partial \widehat{\boldsymbol{\sigma}}}$) respect to the neutral loading line (F_{NL}) in the p: s space, as illustrated in Figure 2-61(a). Thus, for a given generalized effective stress state ($\widehat{\boldsymbol{\sigma}}$) and a given elastic generalized effective stress increment ($\dot{\widehat{\boldsymbol{\sigma}}}^e$), microstructure shrinks when $\widehat{\boldsymbol{n}}_C^T \cdot \dot{\widehat{\boldsymbol{\sigma}}}^e > 0$ while it swells when $\widehat{\boldsymbol{n}}_S^T \cdot \dot{\widehat{\boldsymbol{\sigma}}}^e > 0$. The conditions $\widehat{\boldsymbol{n}}_C^T \cdot \dot{\widehat{\boldsymbol{\sigma}}}^e = 0$ or $\widehat{\boldsymbol{n}}_S^T \cdot \dot{\widehat{\boldsymbol{\sigma}}}^e = 0$ represent a loading scenario in which no microstructural deformation occurs (stress paths moving along the neutral line). As in the original BExM formulation, the macrostructural

packing of the soil particles and aggregates affects the magnitude of the irreversible strains induced by the microstructural deformations. Such plastic deformations also move the LC yield curve to the right (closing macrostructure) or to the left (opening macrostructure) of its current position in the p: s space. Sánchez *et al.* (2005) also used the concept of "image point", as the projection of the current stress state on the BBM yield surface (as shown in Figure 2-61(b)), to determine the plastic flow direction for generalized stress states. For a detailed explanation of the main relevant features of the generalized plasticity theory, the mathematical formulation and implementation into a finite element code and the numerical applications of this double porosity model, see Sánchez (2004), Sánchez *et al.* (2005, 2008) and Gens *et al.* (2011).

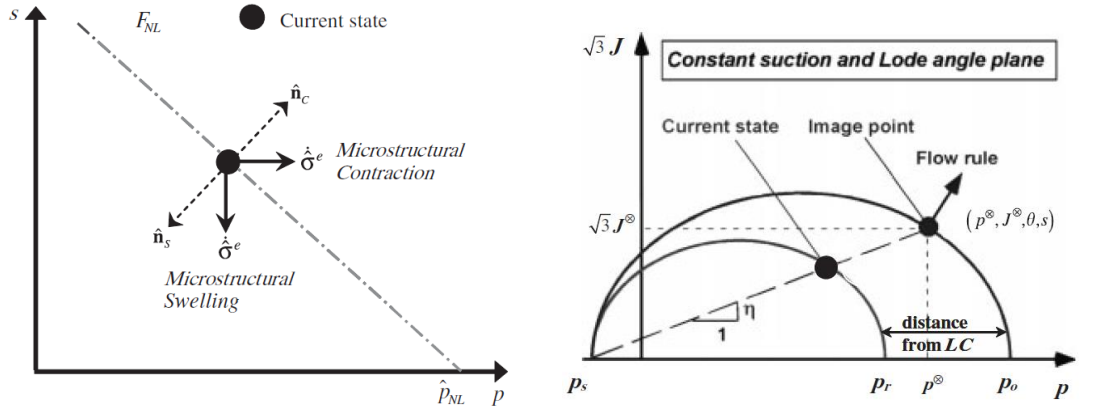

(a) **(b)**

Figure 2-61: **(a)** Definition of microstructural swelling and contraction directions in the p: *s* plane and **(b)** definition of the plastic flow direction in the context of the generalized plasticity theory (Sánchez *et al.*, 2005).

It is important to emphasize that both the original BExM (Alonso *et al.*, 1999; 2005) and the double-porosity approach in generalized stress conditions (Sánchez *et al.*, 2005) consider the saturation of microstructure during the hydro-mechanical loading/unloading process. Although the exchange of water between micro-pores and macro-pores (due to differences in the total water potential between both media) was considered in Sánchez (2004) and Sánchez and Gens (2006) when modelling the re-saturation of a bentonite barrier under non-isothermal conditions, however, such a mass transfer process did not change the saturation state of micro-pores. The hydraulic micro-macro coupling was also considered in Gens *et al.* (2011), who used a mathematical formulation with a similar mechanical part as the one in Sánchez *et al.* (2005) to predict the development of the swelling pressure of compacted mixtures of bentonite powder and pellets. Due to the initial state of those materials (usually at very high suctions) and to the experimental evidences of the increase of swelling pressures as a result of the notable development of micro-porosity as microstructure hydrates, Gens *et al.* (2011) assumed the non-saturation of micro-pores, which also required the definition of a hydraulic constitutive law for the microstructural level. Furthermore, the original BExM model is only able to reproduce the response of expansive clays under isothermal conditions, as the temperature-dependent processes have not been included in its mathematical formulation. On the other hand, the double porosity approach by Sánchez *et al.* (2005) accounts for the thermal problem but without distinguishing the thermal effects on each structural level or considering the thermal interactions between both media.

2.7.3. THE DOUBLE-POROSITY MODEL (DPM) PROPOSED IN THIS THESIS

A new proposal for improving the existing double structure formulations (BExM) has been developed in order to reproduce the THM response of double-porosity materials subjected to significant thermo-hydraulic loadings. The main ingredients of the THM constitutive formulation and the most relevant features of its implementation in a finite element code (CODE_BRIGHT) are discussed in detail in the next chapters (**Chapter 3** to **Chapter 5**).

Like the mathematical formulations mentioned in the previous section, this new THM double-porosity approach is built on the main conceptual features proposed by Gens and Alonso (1992). In that sense, the expansive soil is considered explicitly as two interacting porous media (microstructure and macrostructure), each of them defined separately by a set of variables and stress-small strain constitutive laws but interconnected by structural coupling processes relating their deformation behaviour. The mechanical behaviour of microstructure is approached by an elastic constitutive law that relates the microstructural effective pressure to the volumetric deformations experienced by this structural level due to the changes in the complex physico-chemical phenomena that take place in the water-clay particle system. Macrostructure is described in the framework of elasto-plasticity models for non-expansive unsaturated soils (in this case, the BBM formulation). The mechanical micro-macro coupling is defined in the context of generalized plasticity theory (as in Sánchez *et al.*, 2005) and the structural changes occurring in the soil skeleton due to the deformation response of microstructure are accounted for by means of a two interaction functions. Furthermore, the hydraulic micro-macro coupling is also considered (as in Sánchez (2004) and Gens *et al.* (2011)) by the inclusion of a water mass transfer mechanism between micro-pores and macro-pores. In that sense, a set of hydraulic variables and constitutive equations have been also defined in order to describe the hydraulic behaviour of microstructure in response to changes in the environmental variables. Consequently, and as in Gens *et al.* (2011), the de-saturation of micro-pores is also contemplated by the double-porosity approach proposed in this Thesis. Additionally, some enhancements (in comparison to the previous versions of the BExM and to the double-structure approach by Sánchez *et al.* (2005) and Gens *et al.* (2011)) have been incorporated in this new double-porosity constitutive formulation. The most relevant (besides the ones already mentioned before) are:

- A consistent relationship for the elastic parameters of microstructure and macrostructure. In that sense, macrostructural elastic response is defined in terms of the current compressibility of microstructure (clay particles or aggregates).
- Different density states for the bulk water and the pore-water in micro-pores. A microstructural density function is defined in order to contemplate the high-density state of the intra-aggregate water.
- Hydraulic non-equilibrium between microstructure and macrostructure. A water retention curve is defined for each structural level, which also allows to correlate the water potential in micro-pores to their saturation state. Hydraulic equilibrium is achieved through the water transfer mechanism between micro- and macro-pores.
- The development of swelling pressures or swelling strains in wetting paths after the saturation of macro-pores. It is a consequence of the additional swelling potential

provided by the full saturation of the initially unsaturated micro-pores, when the saturation of micro-pores occurs after the saturation of macro-pores (as in a wetting by liquid water).

- Thermal effects on the hydro-mechanical properties and constitutive laws. Both the thermal expansion/contraction of microstructure and soil skeleton (macrostructure) are considered as well as the thermal impact on the water retention capacity and the dependence of the thermal flux conditions on the soil water content. Water phase changes are also included in the THM formulation.

Some of the practical issues found in the original BExM formulation (Alonso *et al.*, 1999) and in its subsequent improved versions (already mentioned before) remain in the double-porosity approach developed in this Thesis. Among them, it can be mentioned the large amount of model parameters required for describing the microstructural behaviour and its interaction with macrostructure besides the remaining difficulty of estimating them from conventional laboratory tests. Moreover, some assumptions were made during the development of the constitutive formulation discussed in this document, as the local equilibrium between microstructural and macrostructural air pressures, the negligible role of the osmotic suction on the retention curves and the non-generation of irreversible structural changes due to the thermal strains of the microstructure (see **Chapter 3** and **Chapter 4** for more details). However, and despite all these hypotheses, the first numerical performances using a similar formulation for isothermal conditions (see Ruiz (2020)) have demonstrated the model capabilities in reproducing satisfactorily the response of expansive clays under changing environmental conditions.

3. DOUBLE POROSITY FORMULATION: BASIC CONCEPTS AND RELATIONSHIPS, AND GOVERNING EQUATIONS

3.1. INTRODUCTION

The main goal of a multi-porosity approach is to establish a mathematical, fully coupled formulation that relates the observable deformation behaviour in expansive clays to the impact caused by the changes in the thermo-hydro-mechanical (THM) loads in each structural pore level. In such a task, model robustness and mathematical simplicity are two desirable requirements. Consequently, a special effort is made in the definition and the convenient choice of model variables and parameters with a physical meaning that can be easily determined by current experimental tests. Regarding the number of input parameters, user's experience dictates that the lesser the better. However, the number of parameters required in a mathematical formulation increases with the model complexity and with the number of coupled processes considered. Additionally, it is also sought that new improvements in the numerical code can be easily incorporated as the understanding of the main physico-chemical processes governing the behavior of the porous medium is enhanced.

Keeping these requirements in mind, the first step for the implementation of a multi-porosity model is to define the medium as a material composed by different and overlapping structural levels (Sánchez *et al.*, 2005) and to postulate the governing equations that describe the main features in each level and the coupling mechanisms that control the interaction among them. In this sense, the double-porosity theory developed for analyzing coupled THM problems and presented in this Thesis considers the soil (the expansive clay) as a continuum composed by two basic structural levels: a microstructure medium and a macrostructure medium. Microstructure is conceived as the assemblage of active clay particles inside a clay aggregate and the intra-aggregate pores (micro-pores). The macrostructure medium is associated with the macroscopic soil skeleton formed by the arrangement of clay aggregates and other soil grains and the inter-aggregate voids among them (macro-pores). Strictly speaking, macrostructure is a virtual (not a

real) porous material defined for mathematical purposes while the microstructural medium (individual clay aggregates) is an idealization of a real geotechnical material (Gesto, 2014). A schematic representation of this simplified/idealized double-porosity medium is illustrated in Figure 3-1.

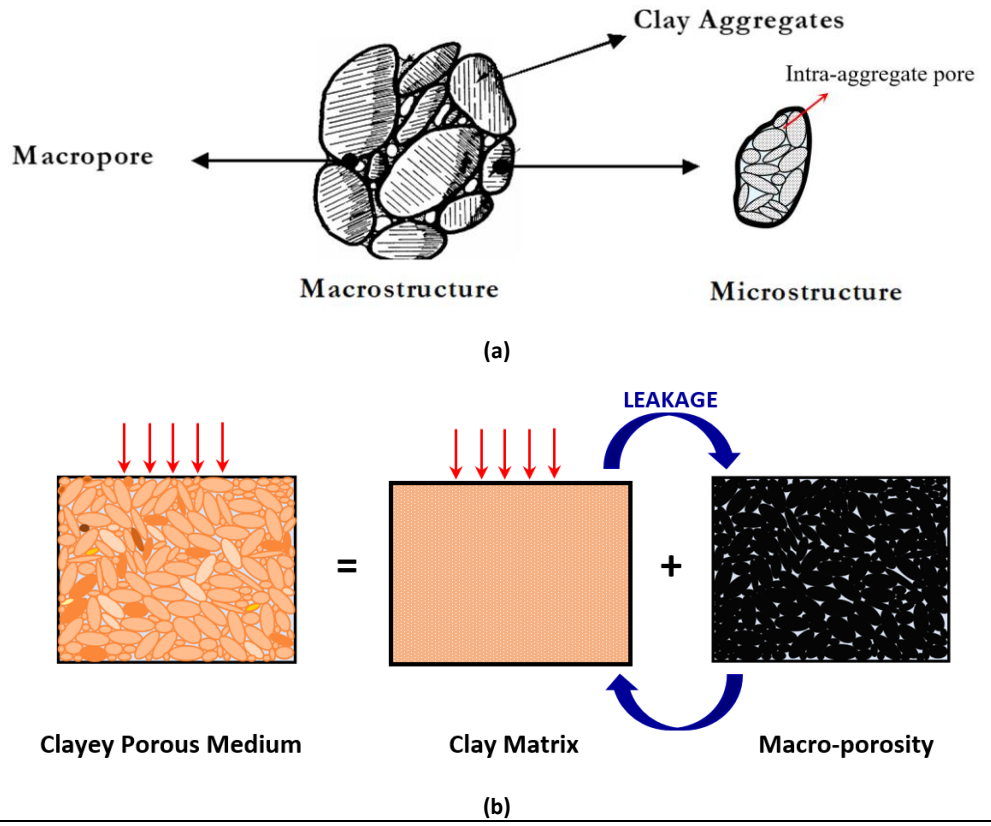

Figure 3-1: Schematic representation of **(a)** the two structural pore levels; **(b)** double-porosity concepts (after Sánchez *et al.*, 2005).

The behavior of the expansive soil is obtained as the contribution of these two overlapping media, each of them described by their own set of constitutive laws and material parameters. Porosity, fluid pressures, degree of saturation, liquid densities and other properties are defined for each structure level. As a consequence, different fluid pressures can be present in each class of pores, which generates a gradient in the potential energies between micro-structural and macrostructural pore-water. Interaction between these continuous media is given by a leakage term that controls the fluid (water and gas) mass transfer from one structural level to the other (Sánchez, 2004).

In the next sections of this chapter, a brief description of the main ingredients required to implement the double-porosity model is given, that is, the basic and useful relationships among different geotechnical variables and the concept of stresses and strains in the framework of a multi-porosity approach and in the context of the multi-mechanism plasticity. Additionally, the balance equations to be solved when performing THM analyses are also described.

3.2. PHASE DIAGRAM AND BASIC RELATIONSHIPS

An unsaturated soil is a mixture of several phases. In order to define some basic volume-mass relationships commonly used in geotechnical problems, it is useful to depict the phase diagram that shows all the phases (solid, liquid and/or gas) present in the soil. In Figure 3-2, two phase diagrams representing a soil element as a double-porosity medium are shown, one of them associated with the volume occupied by each phase at each structural level (Figure 3-2(a)) and the other one associated with mass quantities (Figure 3-2(b)). Variables defined with the sub-index "*m*" are related to the microstructure medium (solid particles and micro-pores) while sub-index "*M*" refers to variables defined for the macrostructure. Variables defined for the soil (the whole porous medium) are not labeled with a subscript.

From the phase diagram, an immediate conclusion is that the volume of voids in the soil (V_p) is the summation between the volume occupied by macro-pores (V_{pM}) and micro-pores (V_{pm}). The actual microstructure volume (V_m) accounts for the volume of the intra-aggregate (micro) pores and the volume occupied by the solid phase (V_s). Porosities (ϕ and ϕ_m) and void ratios (e and e_m) for the two "true" geotechnical media (expansive soil and clay aggregate) are defined as

$$\phi = \frac{V_p}{V} \tag{3-1}$$

$$\phi_m = \frac{V_{pm}}{V_m} \tag{3-2}$$

$$e = \frac{V_p}{V_s} = \frac{V_p}{V - V_p} = \frac{\phi}{1 - \phi} \tag{3-3}$$

$$e_m = \frac{V_{pm}}{V_s} = \frac{V_{pm}}{V_m - V_{pm}} = \frac{\phi_m}{1 - \phi_m} \tag{3-4}$$

Two additional porosity variables arise from the concepts shown above and need to be introduced in order to define the "natural" additive decomposition of total porosity (ϕ), which is given by

$$\phi = \frac{V_p}{V} = \frac{V_{pm}}{V} + \frac{V_{pM}}{V} = \bar{\phi}_m + \bar{\phi}_M \tag{3-5}$$

where $\bar{\phi}_m$ and $\bar{\phi}_M$ are defined as the "marked" porosity associated with microstructure and macrostructure, respectively. Although these variables are not porosities, according to the classical definition of this geotechnical variable, they are necessary and helpful to the mathematical formulation of a double-porosity model. In fact, they can be defined as micro- and macro-pore volume fractions (Ruiz, 2020). Therefore, these "marked" porosities will be referred to as "micro-pore volume fraction" ($\bar{\phi}_m$) and "macro-pore volume fraction" ($\bar{\phi}_M$) while the "constitutive" micro-porosity (ϕ_m) will be termed as the "aggregate porosity" or simply "micro-porosity" from now on. The aggregate porosity can be evaluated in terms of the macro- and micro-pore volume fractions as follows:

$$\phi_m = \frac{V_{pm}}{V_m} = \frac{V_{pm}}{V}\frac{V}{V_m} = \frac{V_{pm}}{V}\left(\frac{V}{V - V_{pM}}\right) = \frac{\overline{\phi}_m}{1 - \overline{\phi}_M} \tag{3-6}$$

Volume by phases and structural media:

$V_{pm} = V_{lm} + V_{gm}$ $\quad V_{pM} = V_{lM} + V_{gM}$

$V_m = V_s + V_{pm}$ $\quad V = V_m + V_{pM} = V_s + V_p$

Total Volume: $V = V_s + V_{lm} + V_{lM} + V_{gm} + V_{gM}$

"Marked" Porosities: $\bar{\phi}_m = \frac{V_{pm}}{V}$ $\quad \bar{\phi}_M = \frac{V_{pM}}{V}$

"True" Porosities: $\phi_m = \frac{V_{pm}}{V_m}$ $\quad \phi = \frac{V_{pm}+V_{pM}}{V}$

Degree of Saturation: $S_{lm} = \frac{V_{lm}}{V_{pm}}$ $\quad S_{lM} = \frac{V_{lM}}{V_{pM}}$

$S_{gm} = \frac{V_{gm}}{V_{pm}}$ $\quad S_{gM} = \frac{V_{gM}}{V_{pM}}$

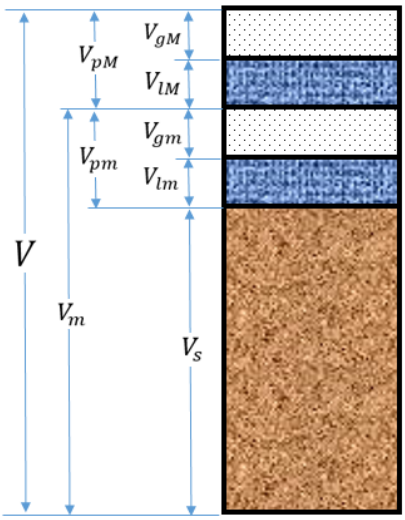

(a)

Total Mass for each species:

$m^s = \rho_s(1 - \phi)V$

$m^w = m_m^w + m_M^w$

$m^a = m_m^a + m_M^a$

Total Mass: $m = m^s + m^w + m^a$

Total Mass for each species at each medium:

$m_m^w = m_{lm}^w + m_{gm}^w$

$m_M^w = m_{lM}^w + m_{gM}^w$

$m_m^a = m_{lm}^a + m_{gm}^a$

$m_M^a = m_{lM}^a + m_{gM}^a$

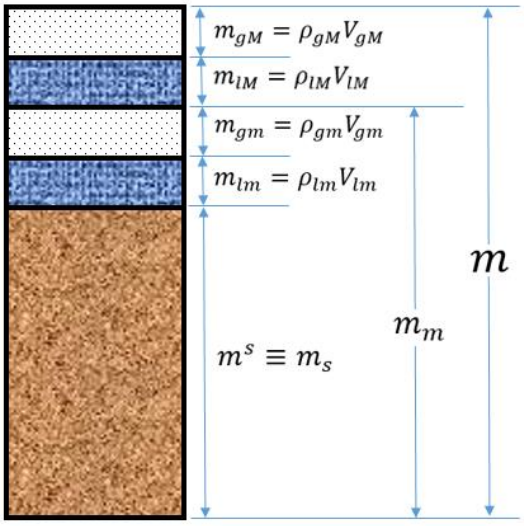

$$m_m = m^s + m_m^w + m_m^a = m^s + m_{lm} + m_{gm}$$
$$m = m_m + m_M^w + m_M^a = m_m + m_{lM} + m_{gM}$$

(b)

Figure 3-2: Phase diagram relating **(a)** volumes and **(b)** mass of species at each structural level.

Other basic volumetric relationship derived from the phase diagram is the definition of the degree of saturation for the fluid phases in the porous medium. In a double-porosity approach, it is necessary to determine this variable for each fluid phase in each medium, in addition to the classical concept of degree of saturation for a whole soil. Thus,

$$S_{\alpha\beta} = \frac{V_{\alpha\beta}}{V_{p\beta}} \tag{3-7}$$

where $S_{\alpha\beta}$ is the degree of saturation of the α-phase (subscript "l" for liquid phase and "g" for gas phase) in the β-porous medium (microstructure, macrostructure or soil) whereas $V_{\alpha\beta}$ denotes the fraction of the volume of voids ($V_{p\beta}$) occupied by the fluid species in the corresponding structural level.

A compositional approach is used for describing the porous medium (Olivella *et al.*, 1994). Consequently, a multi-species formulation is adopted to express mathematically the main THM phenomena that take place in the soil mass. In this approach, the solid phase is composed by the mineral species; the liquid phase contains pore-water and dissolved air whereas the gas phase is composed by dry air and water vapour (see Figure 3-3). Some typical parameters and relationships found in mathematical formulations for single-porosity models need to be extended in order to define their analogous variables/relations at each structural medium when a double-structure model is considered. Two of those parameters are the partial density ($\theta^{\gamma}_{\alpha\beta}$) and the mass fraction ($\omega^{\gamma}_{\alpha\beta}$) for each species (superscript "w" for water and "a" for air) in each fluid phase (subscript α) contained in each structural medium (subscript β), defined as

$$\theta^{\gamma}_{\alpha\beta} = \frac{m^{\gamma}_{\alpha\beta}}{V_{\alpha\beta}} \tag{3-8}$$

$$\omega^{\gamma}_{\alpha\beta} = \frac{m^{\gamma}_{\alpha\beta}}{m_{\alpha\beta}} \tag{3-9}$$

where $m^{\gamma}_{\alpha\beta}$ and $m_{\alpha\beta}$ are the mass of "γ" species and the total mass of "α" phase at the β-structural level, respectively. These two variables are related to each other through the following relationship:

$$\theta^{\gamma}_{\alpha\beta} = \frac{m^{\gamma}_{\alpha\beta}}{V_{\alpha\beta}} = \frac{m^{\gamma}_{\alpha\beta}}{m_{\alpha\beta}} \cdot \frac{m_{\alpha\beta}}{V_{\alpha\beta}} = \omega^{\gamma}_{\alpha\beta} \cdot \rho_{\alpha\beta} \tag{3-10}$$

where $\rho_{\alpha\beta}$ is the local density for the fluid phase in each structural medium. A local density is also defined for the solid phase ($\rho_s = \frac{m_s}{V_s}$). The total mass of a fluid in each structural level ($m_{\alpha\beta}$) is then given by

$$m_{\alpha\beta} = m^{w}_{\alpha\beta} + m^{a}_{\alpha\beta} \tag{3-11}$$

On the other hand, the bulk density ($\tilde{\rho}$) is evaluated taking as reference the whole soil volume. This variable is determined for each species ($\tilde{\rho}^{\gamma}$), for each species in each porous medium ($\tilde{\rho}^{\gamma}_{\beta}$) and for each species in a phase within a specific structural medium ($\tilde{\rho}^{\gamma}_{\alpha\beta}$) according to the following expressions:

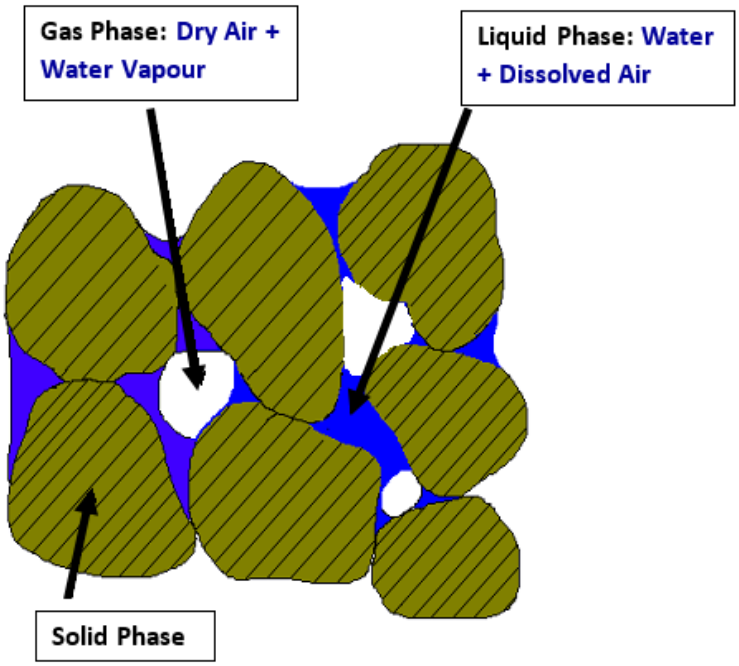

Figure 3-3: Schematic representation of a partially saturated porous medium.

$$\tilde{\rho}^{\gamma} = \frac{m^{\gamma}}{V} \tag{3-12}$$

$$\tilde{\rho}_{\beta}^{\gamma} = \frac{m_{\beta}^{\gamma}}{V} \tag{3-13}$$

$$\tilde{\rho}_{\alpha\beta}^{\gamma} = \frac{m_{\alpha\beta}^{\gamma}}{V} \tag{3-14}$$

The bulk densities can also be expressed in terms of porosities and saturation variables by means of some useful relationships as

$$\tilde{\rho}_{\alpha\beta}^{\gamma} = \frac{m_{\alpha\beta}^{\gamma}}{V} = \frac{m_{\alpha\beta}^{\gamma}}{V_{\alpha\beta}} \cdot \frac{V_{\alpha\beta}}{V_{p\beta}} \cdot \frac{V_{p\beta}}{V} = \theta_{\alpha\beta}^{\gamma} \cdot S_{\alpha\beta} \cdot \bar{\phi}_{\beta} \tag{3-15}$$

and

$$\tilde{\rho}_{\beta}^{\gamma} = \tilde{\rho}_{l\beta}^{\gamma} + \tilde{\rho}_{g\beta}^{\gamma} = \left(\theta_{l\beta}^{\gamma} S_{l\beta} + \theta_{g\beta}^{\gamma} S_{g\beta}\right) \cdot \bar{\phi}_{\beta} \tag{3-16}$$

If it is assumed that the void spaces are filled exclusively by the species water and air, the global density for each fluid phase in each structural level ($\tilde{\rho}_{\alpha\beta}$) is given by

$$\tilde{\rho}_{\alpha\beta} = \tilde{\rho}_{\alpha\beta}^{w} + \tilde{\rho}_{\alpha\beta}^{a} = \left(\theta_{\alpha\beta}^{w} + \theta_{\alpha\beta}^{a}\right) \cdot S_{\alpha\beta}\bar{\phi}_{\beta} = \rho_{\alpha\beta} \cdot S_{\alpha\beta} \cdot \bar{\phi}_{\beta} \tag{3-17}$$

in which the following relationships (derived from the definitions shown previously) have been used to link global and local densities

$$\theta_{\alpha\beta}^{w} + \theta_{\alpha\beta}^{a} = \left(\omega_{\alpha\beta}^{w} + \omega_{\alpha\beta}^{a}\right) \cdot \rho_{\alpha\beta} = \rho_{\alpha\beta} \tag{3-18}$$

$$\omega_{\alpha\beta}^{w} + \omega_{\alpha\beta}^{a} = 1 \tag{3-19}$$

The bulk density for the species water ($\tilde{\rho}^{w}$) and air ($\tilde{\rho}^{a}$) in the soil, in the context of a double-porosity approach, can be determined as

$$\begin{aligned}\tilde{\rho}^{w} &= \tilde{\rho}_{m}^{w} + \tilde{\rho}_{M}^{w} \\ &= \left(\theta_{lm}^{w} S_{lm} + \theta_{gm}^{w} S_{gm}\right) \cdot \bar{\phi}_{m} + \left(\theta_{lM}^{w} S_{lM} + \theta_{gM}^{w} S_{gM}\right) \cdot \bar{\phi}_{M}\end{aligned} \tag{3-20}$$

$$\begin{aligned}\tilde{\rho}^{a} &= \tilde{\rho}_{m}^{a} + \tilde{\rho}_{M}^{a} \\ &= \left(\theta_{lm}^{a} S_{lm} + \theta_{gm}^{a} S_{gm}\right) \cdot \bar{\phi}_{m} + \left(\theta_{lM}^{a} S_{lM} + \theta_{gM}^{a} S_{gM}\right) \cdot \bar{\phi}_{M}\end{aligned} \tag{3-21}$$

while the global densities for the liquid ($\tilde{\rho}_{l}$)and the gas ($\tilde{\rho}_{g}$) phases are, respectively, evaluated as

$$\tilde{\rho}_{l} = \tilde{\rho}_{lm} + \tilde{\rho}_{lM} = \rho_{lm} \cdot S_{lm} \cdot \bar{\phi}_{m} + \rho_{lM} \cdot S_{lM} \cdot \bar{\phi}_{M} \tag{3-22}$$

$$\tilde{\rho}_{g} = \tilde{\rho}_{gm} + \tilde{\rho}_{gM} = \rho_{gm} \cdot S_{gm} \cdot \bar{\phi}_{m} + \rho_{gM} \cdot S_{gM} \cdot \bar{\phi}_{M} \tag{3-23}$$

The bulk density for the solid phase is expressed by

$$\tilde{\rho}^{s} = \frac{m_{s}}{V} = \frac{m_{s}}{V_{s}} \cdot \frac{V_{s}}{V} = \rho_{s} \cdot (1 - \phi) \tag{3-24}$$

Taking into account the density concepts and the expressions presented above, the global density for the whole soil ($\tilde{\rho}$) can be determined by adding the bulk densities of the species in the soil mass, which leads to

$$\begin{aligned}\tilde{\rho} &= \tilde{\rho}^{s} + \tilde{\rho}^{w} + \tilde{\rho}^{a} \\ &= \rho_{s} \cdot (1 - \phi) + \left(\rho_{lm} S_{lm} + \rho_{gm} S_{gm}\right) \cdot \bar{\phi}_{m} \\ &\qquad + \left(\rho_{lM} S_{lM} + \rho_{gM} S_{gM}\right) \cdot \bar{\phi}_{M}\end{aligned} \tag{3-25}$$

The same expression would be found if the bulk soil density was obtained from the global densities of each phase, that is, $\tilde{\rho} = \tilde{\rho}^{s} + \tilde{\rho}_{l} + \tilde{\rho}_{g}$.

3.3. TOTAL, NET AND CONSTITUTIVE STRESSES

The stress concept in Soil Mechanics requires the definition of a total stress ($\boldsymbol{\sigma}_{t}$) as the total load per unit surface for the whole porous medium and an effective (constitutive) stress ($\boldsymbol{\sigma}$) defined as the amount of the applied loading that generates deformations in the soil or changes

in its shearing resistance (Terzaghi, 1936; Lambe and Whitman, 1979). To deal with non-saturated soil problems, it is also necessary to define a net stress tensor ($\hat{\boldsymbol{\sigma}}$) as the amount of the applied stress that exceeds the pore air pressure (Bishop, 1959). This latter stress variable combined with the matric suction are the two independent stress state variables most commonly used to describe the shear strength and the volume change behavior of unsaturated soils (Fredlund *et al.*, 2012).

One of the hypotheses adopted for the formulation of a double-porosity model is that the different concepts of stress in the soil (total, constitutive and net stresses) refer to the stresses acting on the macrostructural medium. In addition to this, it is also assumed that the total stress tensor of each structural medium ($\boldsymbol{\sigma}_{t,\beta}$) corresponds to the total stress applied to the whole soil ($\boldsymbol{\sigma}_t$), that is,

$$\boldsymbol{\sigma}_{t,\beta} = \boldsymbol{\sigma}_t \tag{3-26}$$

The net and the effective stresses acting on each medium (denoted by $\hat{\boldsymbol{\sigma}}_\beta$ and $\boldsymbol{\sigma}_\beta$, respectively) are defined, in a tensorial notation, as

$$\hat{\boldsymbol{\sigma}}_\beta = \boldsymbol{\sigma}_t - P_{g\beta}\mathbf{I} \tag{3-27}$$

$$\boldsymbol{\sigma}_\beta = \hat{\boldsymbol{\sigma}}_\beta + \chi_\beta \cdot \left(P_{g\beta} - P_{l\beta}\right)\mathbf{I} = \boldsymbol{\sigma}_t + \left(\chi_\beta \cdot \left(P_{g\beta} - P_{l\beta}\right) - P_{g\beta}\right)\mathbf{I} \tag{3-28}$$

where χ_β is a soil property, also known as the Bishop coefficient or the effective stress parameter, which takes a value ranging from 0 (for completely dry state) to 1 (for fully saturated state); $P_{g\beta}$ and $P_{l\beta}$ are, respectively, the gas and the liquid pressures in pores for each structural level and $\mathbf{I}$ is the identity tensor. The term $\left(P_{g\beta} - P_{l\beta}\right)$ is the relevant water potential (s_β) of the porous medium β. It is assumed that $s_\beta > 0$ when the porous material is unsaturated. When the porous medium is fully saturated with air (that is, it is completely dry), $\chi_\beta = 0$, and the net stress, given by Equation (3-27), can be interpreted as the effective stress acting on the particle contacts of this medium. When the porous skeleton becomes saturated by liquid species (water, for example) the original expression of effective stresses for saturated media proposed by Terzaghi (1936), $\boldsymbol{\sigma}_\beta = \boldsymbol{\sigma}_t - P_{l\beta}\mathbf{I}$, is recovered. The stress state between these two limiting situations is described by means of any two independent stress state variables for unsaturated conditions as the net stress (Equation (3-27)) and the matric suction, for example. Equation (3-28) is able to estimate the effective stress state in such conditions. The contribution of suction to the effective stress is controlled by the effective stress parameter whose value is dependent on many geotechnical variables, as the soil stress history, the soil structure and the hydraulic hysteresis, among others (Nikooee *et al.*, 2011). In many mathematical formulations for unsaturated soils, the effective stress parameter is taken as a function of the water degree of saturation. In **Section 3.3.2**, a liquid saturation-dependent function for this parameter is discussed.

The expressions for the total, the net and the constitutive stresses acting on a volume of soil, on an individual aggregate (microstructural porous medium) and on a packing of aggregates

(macrostructural medium) are given in Table 3-1. It is convenient to mention that all the stress expressions in this document are defined in accordance with the Soil Mechanics criterion in which compressive loadings are assigned positive quantities.

Table 3-1: Definition of stresses for the soil, the micro and the macro porous media.

Stresses in the soil (tensorial notation)	
Total stress ($\boldsymbol{\sigma}_t$):	$\boldsymbol{\sigma}_t$
Net stress ($\widehat{\boldsymbol{\sigma}}$):	$\widehat{\boldsymbol{\sigma}} = \boldsymbol{\sigma}_t - P_g\mathbf{I}$
Effective stress ($\boldsymbol{\sigma}$):	$\boldsymbol{\sigma} = \left(\boldsymbol{\sigma}_t - P_g\mathbf{I}\right) + \chi \cdot \left(P_g - P_l\right)\mathbf{I} = \boldsymbol{\sigma}_t + \left(\chi \cdot \left(P_g - P_l\right) - P_g\right)\mathbf{I}$
Stresses in the microstructural medium (tensorial notation)	
Total stress ($\boldsymbol{\sigma}_{t,m}$):	$\boldsymbol{\sigma}_{t,m} \equiv \boldsymbol{\sigma}_t$
Net stress ($\widehat{\boldsymbol{\sigma}}_m$):	$\widehat{\boldsymbol{\sigma}}_m = \boldsymbol{\sigma}_t - P_{gm}\mathbf{I}$
Effective stress ($\boldsymbol{\sigma}_m$):	$\boldsymbol{\sigma}_m = \boldsymbol{\sigma}_t + \left(\chi_m \cdot \left(P_{gm} - P_{lm}\right) - P_{gm}\right)\mathbf{I}$
Stresses in the macrostructural medium (tensorial notation)	
Total stress ($\boldsymbol{\sigma}_{t,M}$):	$\boldsymbol{\sigma}_{t,M} \equiv \boldsymbol{\sigma}_t$
Net stress ($\widehat{\boldsymbol{\sigma}}_M$):	$\widehat{\boldsymbol{\sigma}}_M = \boldsymbol{\sigma}_t - P_{gM}\mathbf{I} \equiv \widehat{\boldsymbol{\sigma}}$
Effective stress ($\boldsymbol{\sigma}_M$):	$\boldsymbol{\sigma}_M = \boldsymbol{\sigma}_t + \left(\chi_M \cdot \left(P_{gM} - P_{lM}\right) - P_{gM}\right)\mathbf{I} \equiv \boldsymbol{\sigma}$

Due to material or constitutive non-linearities found in many engineering problems, it is more convenient to describe the mechanical behavior of a continuum in terms of stress increments or stress rates. Therefore, the equations arising from (3-27) and (3-28) are given by

$$\dot{\widehat{\boldsymbol{\sigma}}}_\beta = \dot{\boldsymbol{\sigma}}_t - \dot{P}_{g\beta}\mathbf{I} \tag{3-29}$$

$$\dot{\boldsymbol{\sigma}}_\beta = \dot{\boldsymbol{\sigma}}_t + \left(\dot{\chi}_\beta \cdot \left(P_{g\beta} - P_{l\beta}\right) + \chi_\beta \cdot \left(\dot{P}_{g\beta} - \dot{P}_{l\beta}\right) - \dot{P}_{g\beta}\right)\mathbf{I} \tag{3-30}$$

where $\dot{\boldsymbol{\sigma}}_t$, $\dot{P}_{l\beta}$, $\dot{P}_{g\beta}$ represent the infinitesimal rates of the total stress, the pore-liquid pressure (when water is the liquid species in pores) and the pore-gas pressure, respectively. $\dot{\chi}_\beta$ is the incremental form of the effective stress parameter (a general expression for $\dot{\chi}_\beta$ is given in **Section 4.2.3**).

The expressions for the microstructural and the macrostructural effective stresses presented in the Table 3-1 can be combined in order to obtain an alternative expression for the micro constitutive stress, given by

$$\boldsymbol{\sigma}_m = \boldsymbol{\sigma} + \left(\left(\chi_m \cdot \left(P_{gm} - P_{lm}\right) - P_{gm}\right) - \left(\chi_M \cdot \left(P_{gM} - P_{lM}\right) - P_{gM}\right)\right)\mathbf{I} \tag{3-31}$$

which will be useful to formulate the mechanical stress-strain law of the double-porosity model to be developed in the next chapter. Such an expression relates explicitly the mechanical behavior of expansive clays not only to the changes in the environmental variables, but also to the physico-chemical processes that take place at aggregate level (Gens and Alonso, 1992; Sánchez *et al.*, 2005).

It is also important to mention that a more general definition of effective stress for a non-saturated soil takes into account the additional suction term related to the chemical potential of water in the pores, the osmotic suction (Fredlund *et al.*, 2012). However, the osmotic component of suction will be neglected, since the chemical problem is out of the scope of this Thesis.

3.3.1. STRESS INVARIANTS

Within the framework of the Continuum Mechanics, it is common to describe the mechanical constitutive laws in terms of the stress and strain invariants rather than writing them in terms of stress and strain tensor components (Prat and Gens, 2003). The more relevant equations in the mathematical formulation of constitutive models for unsaturated porous media, such as the elastoplastic Barcelona Basic Model (BBM) and the Double-Porosity Model (DPM) described in this Thesis, are expressed in terms of the following stress invariants

$$p = \frac{1}{3} tr(\tilde{\boldsymbol{\sigma}}) = \frac{1}{3}(\tilde{\sigma}_1 + \tilde{\sigma}_2 + \tilde{\sigma}_3) \tag{3-32}$$

$$J = \sqrt{\frac{1}{2} tr(\boldsymbol{s}:\boldsymbol{s})} \tag{3-33}$$

$$\theta = \frac{1}{3} arcsin\left(-\frac{3}{2} \cdot \frac{\sqrt{3} \cdot det(\boldsymbol{s})}{J^3}\right) \tag{3-34}$$

where p is the mean stress related to the isotropic stress states, J is a stress invariant related to the deviatoric stress tensor ($\boldsymbol{s}$) and θ is known as the Lode angle. $\tilde{\sigma}_1$, $\tilde{\sigma}_2$, $\tilde{\sigma}_3$ are the principal stress components of the stress tensor $\tilde{\boldsymbol{\sigma}}$. The deviatoric stress tensor is defined as the difference between the stress tensor ($\tilde{\boldsymbol{\sigma}}$) and its hydrostatic component, that is,

$$\boldsymbol{s} = \tilde{\boldsymbol{\sigma}} - p\mathbf{I} \tag{3-35}$$

and serves to indicate how far the current stress point is from the isotropic state. A schematic representation of these three stress invariants in the principal stress space is shown in Figure 3-4**.**

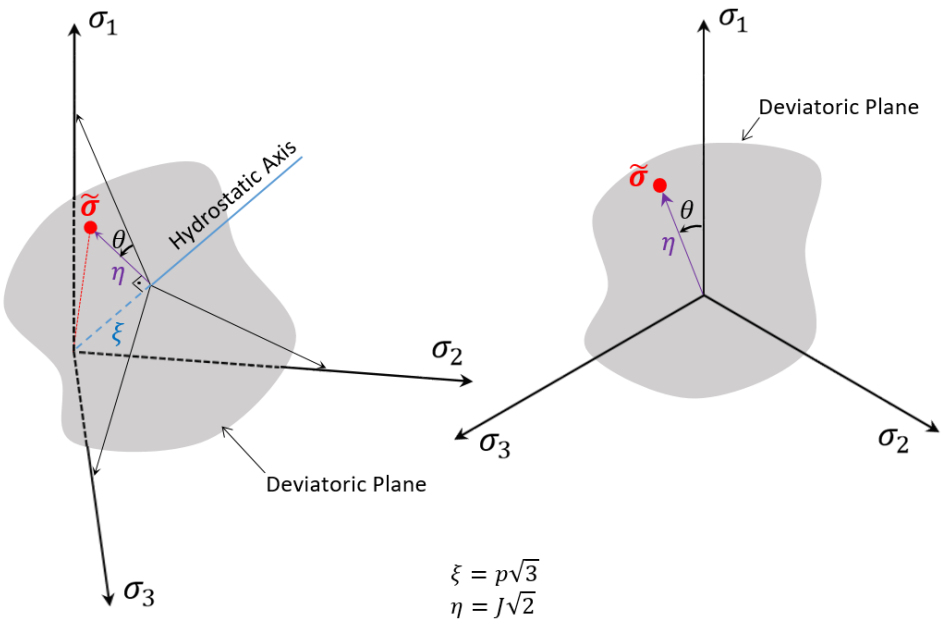

Figure 3-4: Schematic representation of a generic stress state ($\tilde{\boldsymbol{\sigma}}$), in the principal stress space, by means of its invariants (p, J, θ).

3.3.2. THE EFFECTIVE STRESS COEFFICIENT

The effective stress parameter (χ or χ_β) is usually assumed as a function of the degree of saturation of a soil (Bishop, 1959). The present double-porosity approach allows the definition of a χ factor for each structural level. As a consequence, $\chi_m = \chi(S_{lm})$ only takes into account the fraction of water filling micro-pores while $\chi_M = \chi(S_{lM})$ is a function of the degree of saturation of macrostructure.

Different proposals for the Bishop coefficient are given in the literature (Khalili and Khabbaz, 1998; Khalili *et al.*, 2004; Nikooee *et al.*, 2011; Mašin, 2011; Pereira *et al.*, 2011) but the most common expression for this parameter is given by a linear dependency on the degree of saturation, that is, $\chi(S_l) = S_l$. This linear function of the degree of saturation defines the classical Bishop's stress concept. Another common relationship between the Bishop coefficient and the saturation state of a porous medium is given by a step function defined as

$$\chi(S_l) = \begin{cases} 0 \;\; if \;\; 0 < S_l < 1 \\ 1 \;\; if \;\;\;\; S_l = 1 \end{cases} \tag{3-36}$$

According to this step function, the net stress tensor (given by Equation (3-27)) is the constitutive stress for non-saturated conditions while Terzaghi's effective stress concept (Terzaghi, 1936) denotes the constitutive stress tensor for fully saturated conditions. The smooth transition between these two effective stress concepts can be achieved by means of the definition of a family of functions $\chi(S_l)$ as the ones depicted in Figure 3-5.

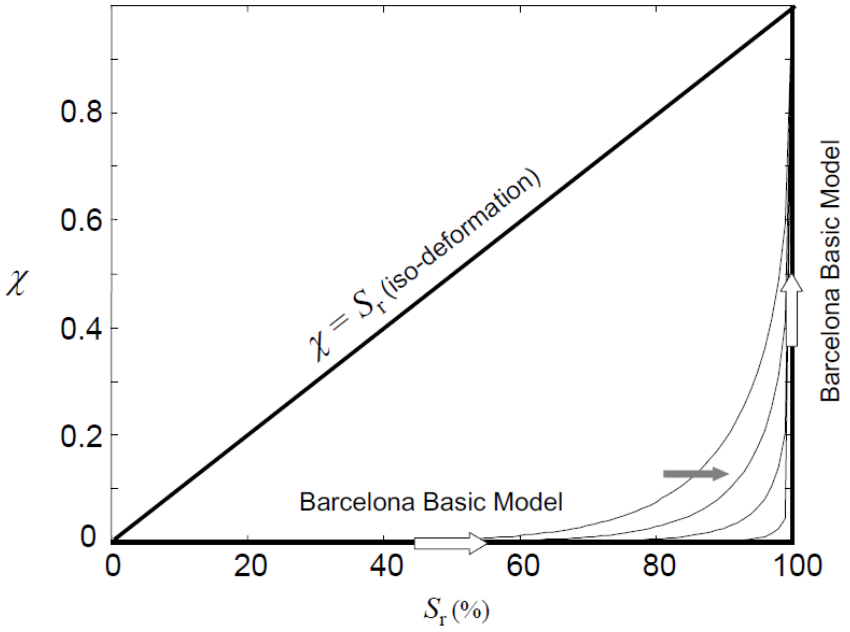

Figure 3-5: Family of functions for the Bishop coefficient suitable for defining the extended Bishop's effective stress (Pereira *et al.*, 2011).

Gesto (2014) proposed an exponential smoothing function on the degree of saturation for the χ_β coefficient, expressed as follows

$$\chi_\beta = \frac{1}{ln2 - q_\chi} \cdot ln\left(e^{-q_\chi \cdot (S_{l\beta})^{p_\chi}} + e^{-q_\chi \cdot (2 - S_{l\beta})^{p_\chi}}\right) \tag{3-37}$$

where p_χ and q_χ are shape parameters. Two families of smoothed χ-functions for different values of these shape parameters are shown in Figure 3-6. Note that, for a fixed value of p_χ ($p_\chi = 1.0$, in Figure 3-6(a)), the commonly used choice for χ_β, that is, $\chi_\beta = S_{l\beta}$, is achieved for higher values of q_χ. On the other hand, as p_χ increases (Figure 3-6(b)), the expression in Equation (3-37) tends to the step function given in Equation (3-36).

Experimental evidences have shown that the "total" degree of saturation may not describe satisfactorily the suction contribution to the effective stress for relatively high plasticity soils (Pereira *et al.*, 2011). On the contrary, the suction contribution to the constitutive stress is better described through a function of an effective degree of saturation that only accounts for the water filling macro-pores. Therefore, the definition of a Bishop parameter function for each structural medium (each one depending on the saturation state of each pore level) allows to obtain more realistic constitutive modelling responses in comparison to those formulations with a single function for χ that only depends on the overall degree of saturation of a soil.

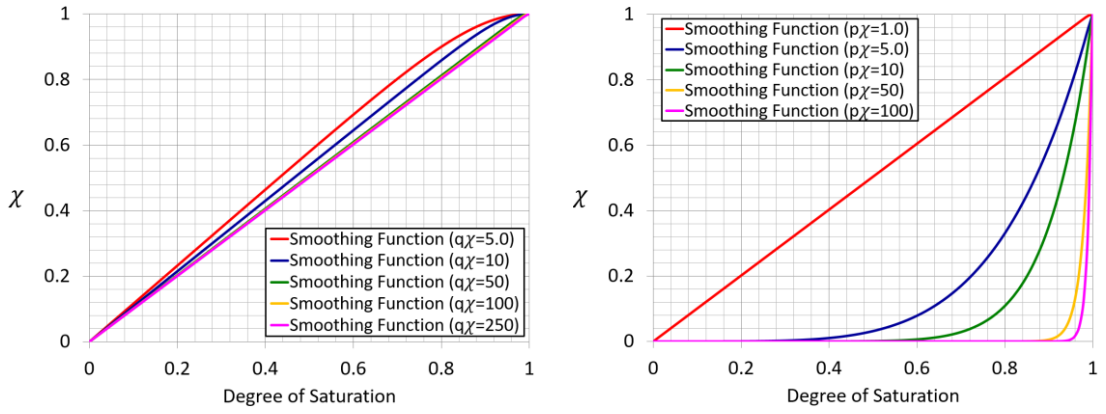

Figure 3-6: Family of curves obtained from the smoothed function $\chi(S_l)$ in Equation (3-37) for **(a)** $p_\chi = 1$ and **(b)** $q_\chi = 100$.

The Bishop parameter function in Equation (3-36) is the one used in the classical BBM formulation (Pereira *et al.*, 2011). For this particular case, the general macrostructural effective stress tensor $\boldsymbol{\sigma}_M$, given in Equation (3-28) – see Table 3-1– becomes

$$\boldsymbol{\sigma}_M = \boldsymbol{\sigma} = \begin{cases} \boldsymbol{\sigma}_t - P_{gM}\mathbf{I} & if \;\; 0 < S_{lM} < 1 \\ \boldsymbol{\sigma}_t - P_{lM}\mathbf{I} & if \;\; S_{lM} = 1 \end{cases} = \boldsymbol{\sigma}_t - max\left(P_{gM}, P_{lM}\right)\mathbf{I} \tag{3-38}$$

and the general microstructural effective stress, given in Equation (3-31), is simplified to the following expression:

$$\boldsymbol{\sigma}_m = \boldsymbol{\sigma} + \left(\chi_m \cdot \left(P_{gm} - P_{lm}\right) - P_{gm} + max\left(P_{gM}, P_{lM}\right)\right)\mathbf{I} \tag{3-39}$$

The pair of stress tensors in Equation (3-38) represents the effective stress tensors acting on the porous medium.

3.4. TOTAL, MICRO AND MACRO VOLUMETRIC STRAIN RATES

The movement of each point in a continuum is described by the displacement field, $\boldsymbol{u}$. This vectorial entity is the primary variable (unknown) in mechanical problems. When finite element techniques are used to solve the global stiffness equations and, consequently, to find the increments of nodal displacements, the strain increment at each integration point is calculated through the strain-displacement relationship. If the infinitesimal strain theory (that is, under the assumption of small strains and small strain rates) is always satisfied, the strain rate tensor, $\dot{\boldsymbol{\varepsilon}}$, is evaluated as follows

$$\dot{\boldsymbol{\varepsilon}} = \frac{1}{2}(\boldsymbol{\nabla}\dot{\boldsymbol{u}} + (\boldsymbol{\nabla}\dot{\boldsymbol{u}})^T) \tag{3-40}$$

where $\dot{\boldsymbol{u}}$ is the velocity field vector. It is very usual to express the strain rate tensor as an additive decomposition in terms of two components: the volumetric strain rate tensor ($\dot{\boldsymbol{\varepsilon}}^{vol}$) defined as

the relative volume change due to dilation or compression of the material and the deviatoric strain rate component ($\dot{\boldsymbol{\varepsilon}}^{dev}$) defined as the deformation associated to distortion with no volume changes. These two components are defined as

$$\dot{\boldsymbol{\varepsilon}}^{vol} = (\boldsymbol{\nabla} \cdot \dot{\boldsymbol{u}})\mathbf{I} = tr(\dot{\boldsymbol{\varepsilon}})\mathbf{I} \equiv \dot{\varepsilon}^{vol}\mathbf{I} \tag{3-41}$$

$$\dot{\boldsymbol{\varepsilon}}^{dev} = \dot{\boldsymbol{\varepsilon}} - \dot{\varepsilon}^{vol}\mathbf{I} \tag{3-42}$$

where

$$\dot{\varepsilon}^{vol} = \frac{\dot{V}}{V} = \frac{\dot{V}_s + \dot{V}_p}{V} \tag{3-43}$$

is the classical definition of the volumetric strain (rate) for porous media. In the context of a double-porosity approach it is assumed that $\dot{V}_p = \dot{V}_{pm} + \dot{V}_{pM}$ and Equation (3-43) can be rewritten as

$$\dot{\varepsilon}^{vol} = \frac{\dot{V}}{V} = \frac{\dot{V}_s + \dot{V}_{p,m} + \dot{V}_{p,M}}{V} = \frac{\dot{V}_s + \dot{V}_{p,m}}{V} + \frac{\dot{V}_{p,M}}{V} \tag{3-44}$$

which leads to an additive decomposition of the infinitesimal volumetric strain into two strain components and, consequently, the definition of a micro ($\dot{\varepsilon}_m^{vol}$) and a macro ($\dot{\varepsilon}_M^{vol}$) volumetric strain rate according to

$$\dot{\varepsilon}^{vol} = \dot{\varepsilon}_m^{vol} + \dot{\varepsilon}_M^{vol} \tag{3-45}$$

with

$$\dot{\varepsilon}_m^{vol} \equiv \frac{\dot{V}_s + \dot{V}_{p,m}}{V} \tag{3-46}$$

$$\dot{\varepsilon}_M^{vol} \equiv \frac{\dot{V}_{p,M}}{V} \tag{3-47}$$

If the clay aggregates are considered incompressible ($\dot{\varepsilon}_m^{vol} = 0$), the volumetric strain for the macrostructural medium defined by Equation (3-47) coincides with the volumetric strain for the whole soil. However, when the microstructural medium is compressible, $\dot{\varepsilon}_M^{vol}$ is only a component of the total volumetric strain that accounts for the volumetric changes of the inter-aggregate voids and then, it cannot be considered as the "true" volumetric strain. Not even the micro strain component defined according to Equation (3-46) can be considered as the "true" volumetric strain because it is defined in terms of the total volume (V) instead of the aggregate volume (V_m). Nevertheless, the two strain components in Equation (3-45) are necessary to distinguish and to take into account the volumetric strain contributions of all the deformation mechanisms in each structural level. A relationship between the "true" microstructural strain ($\dot{\varepsilon}_m^{vol}$), that is, the actual deformation of the clay aggregate, and the micro strain component defined by Equation (3-46) can be established as follows

$$\dot{\varepsilon}_m^{vol} = \frac{\dot{V}_m}{V_m} = \frac{\dot{V}_s + \dot{V}_{p,m}}{V_m} = \frac{V}{V_m} \cdot \frac{\dot{V}_s + \dot{V}_{p,m}}{V} = \frac{V}{V_m} \cdot \dot{\varepsilon}_m^{vol} = \frac{1+e}{1+e_m} \cdot \dot{\varepsilon}_m^{vol} \tag{3-48}$$

where e_m and e are the void ratios for the micro medium and for the soil, respectively, defined by Equation (3-4) and Equation (3-3).

It is important to mention that inside the subroutines for the constitutive models (compression positive), the volumetric components of strain in Equation (3-43) to Equation (3-48) take negative values.

3.5. CHANGES IN TOTAL POROSITY AND IN PORE VOLUME FRACTIONS

The volumetric strain in a porous medium is directly related to changes in its porosity. Taking into account Equation (3-5) in which the pore volume fractions for microstructure and macrostructure are defined, it is possible to express the variation of porosities, for the double structure formulation, by the following relationship

$$\dot{\phi}_\beta = \frac{\partial}{\partial t}\left(\frac{V_{p\beta}}{V}\right) = \frac{\dot{V}_{p\beta}.V - V_{p\beta}\cdot\dot{V}}{V^2} = \frac{\dot{V}_{p\beta}}{V} - \frac{V_{p\beta}}{V}\cdot\frac{\dot{V}}{V} \tag{3-49}$$

This general expression together with Equation (3-43), Equation (3-46) and Equation (3-47) allows the determination of the changes in the micro- and macro-pore fractions, respectively, by

$$\dot{\phi}_M = \frac{\partial}{\partial t}\left(\frac{V_{pM}}{V}\right) = \frac{\dot{V}_{pM}}{V} - \frac{V_{pM}}{V}\cdot\frac{\dot{V}}{V} = \dot{\bar{\varepsilon}}_M^{vol} - \bar{\phi}_M\cdot\dot{\varepsilon}^{vol} \tag{3-50}$$

$$\begin{aligned}\dot{\phi}_m = \frac{\partial}{\partial t}\left(\frac{V_{pm}}{V}\right) = \frac{\dot{V}_{pm}}{V} - \frac{V_{pm}}{V}\cdot\frac{\dot{V}}{V} &= \left(\frac{\dot{V}_s + \dot{V}_{pm}}{V} - \frac{\dot{V}_s}{V}\right) - \frac{V_{pm}}{V}\cdot\frac{\dot{V}}{V} \\ &= \dot{\bar{\varepsilon}}_m^{vol} - \frac{\dot{V}_s}{V} - \bar{\phi}_m\cdot\dot{\varepsilon}^{vol}\end{aligned} \tag{3-51}$$

in which the volumetric strain rates are positive when the material swells. Assuming the principle of mass conservation for the solid species ($\dot{m}_s = 0$), the variation of the volume occupied by the solid phase over the whole soil volume is calculated as follows:

$$\begin{aligned}\frac{\dot{V}_s}{V} = \frac{\dot{V}_s}{V_s}\cdot\frac{V_s}{V} = \frac{\dot{V}_s}{V_s}\cdot(1-\phi) &= \frac{(1-\phi)}{V_s}\cdot\frac{\partial}{\partial t}\left(\frac{m_s}{\rho_s}\right) \\ &= -\frac{(1-\phi)}{V_s}\cdot\frac{m_s\dot{\rho}_s}{\rho_s^2} = -(1-\phi)\cdot\frac{\dot{\rho}_s}{\rho_s}\end{aligned} \tag{3-52}$$

Replacing Equation (3-52) into Equation (3-51), the variation in the micro-pore volume fraction is given by:

$$\dot{\phi}_m = \dot{\bar{\varepsilon}}_m^{vol} + (1-\phi)\cdot\frac{\dot{\rho}_s}{\rho_s} - \bar{\phi}_m\dot{\varepsilon}^{vol} \tag{3-53}$$

Taking into account the decomposition of the volumetric strain in Equation (3-45) and the expressions for the porosity changes given by Equation (3-50) and Equation (3-53), the rate of the total porosity ($\dot{\phi}$) in a double porosity model is obtained through

$$\dot{\phi} = \dot{\phi}_m + \dot{\phi}_M = (1-\phi)\cdot\left(\frac{\dot{\rho}_s}{\rho_s} + \dot{\varepsilon}^{vol}\right) \tag{3-54}$$

3.6. THE MICRO-MACRO WATER EXCHANGE: A MATHEMATICAL APPROACH

As discussed in **Section 2.4.3**, the presence of two classes of pores containing fluid species in them suggests the existence of a gradient in the soil water potential between microstructural and macrostructural water (Alonso and Navarro, 2005). Consequently, a local mass transfer of water between both media is induced so that the equilibrium of the water potential can be eventually reached (Gens *et al.*, 2011). The micro-macro water exchange can be considered as a phase change between two states of the same fluid (Alonso and Navarro, 2005), since the mass of water found in micro-pores is commonly counted as part of the solid phase in analysis of fluid flows in porous media. For the sake of convenience and taking into account the assumption that the osmotic forces are not considered during the development of the mathematical formulation for the double-porosity approach discussed in this document, the matric suction in each porous level is chosen as the thermodynamic force that controls the mass transfer between media. The amount of water transferred between micro-pores and macro-pores (Γ^w) is assumed to be proportional to the differences in micro and macro suctions (Wilson and Aifantis, 1982), as shown in Figure 3-7. Thereby,

$$\Gamma^w = \gamma^w \cdot (s_m - s_M) \tag{3-55}$$

where γ^w is a leakage parameter related to geometric characteristics of the porous media (Sánchez, 2004; Alonso and Navarro, 2005); s_m and s_M are the microstructural and the macrostructural suctions, respectively. According to Equation (3-55), the water mass exchange is considered positive if water is transferred from macro-pores to micro-pores, that is, if the suction in microstructure is greater than the macrostructural suction; otherwise, when the water mass transfer occurs from micro- to macro-pores, Γ^w assumes a negative value. If the gas mobility between the two continua is considered high enough to assume the equilibrium between the gas pressure in both media and recalling the expression for the suction ($s_\beta = P_{g\beta} - P_{l\beta}$), Equation (3-55) reduces to

$$\Gamma^w = \gamma^w \cdot (P_{lM} - P_{lm}) \tag{3-56}$$

and the water mass transfer process is driven by the difference between the pore liquid pressures in each structural pore level.

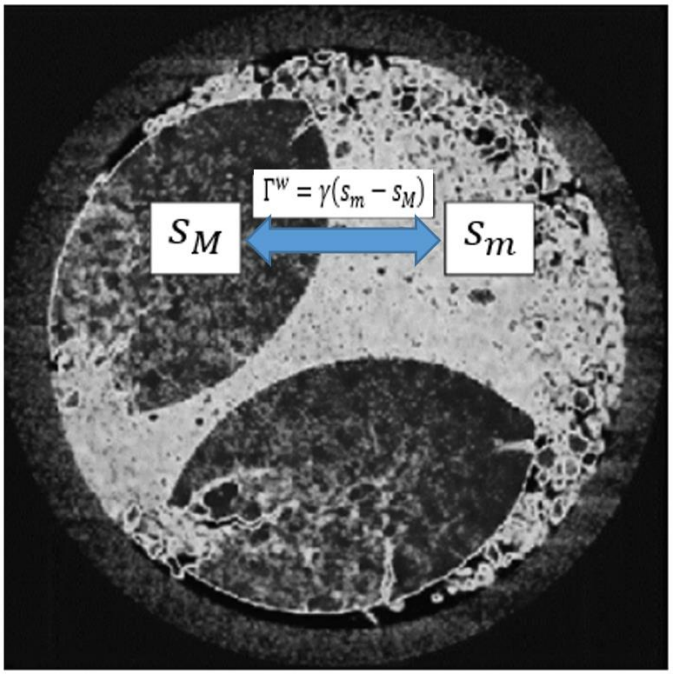

Figure 3-7: Schematic representation of a double porosity medium with a micro-macro water exchange term (Gens *et al.*, 2011).

3.7. BALANCE EQUATIONS

One of the main aspects considered in the mathematical formulation is the solution of the balance equations (mass, energy and momentum balance) for non-isothermal phenomena that take place in deformable porous media. Balance equations, together with the constitutive THM constitutive laws, state the set of governing equations that must be solved to model (numerically) the response of a large range of geotechnical materials and of boundary conditions commonly found in practical engineering problems.

Mass balance equations are solved for the species (mineral, water and air) rather than the phases (solid, liquid and gas) while the equation for balance of energy is solved for the porous medium as a whole (CODE_BRIGHT User's Guide, 2014). This compositional approach is very useful because phase change is already included implicitly in the governing equations (Olivella *et al.*, 1994). The general expression of balance equations for any thermodynamic property, π, is given by

$$\frac{\partial(\pi \cdot \tilde{\rho})}{\partial t} + \boldsymbol{\nabla} \cdot \boldsymbol{j}_\pi = f_\pi \tag{3-57}$$

where the first term on the left-hand side of Equation (3-57) represents the variation of the property π per unit mass of continuum; the second term denotes the variation of π due to the total flux of this property (which includes advective and non-advective fluxes) with respect to a fixed reference system. f_π is the internal source/sink term of π.

A useful tool for dealing with balance equations is the material derivative concept, expressed through

$$\frac{D_s(*)}{Dt} = \frac{\partial(*)}{\partial t} + \dot{\boldsymbol{u}} \cdot \boldsymbol{\nabla}(*) \tag{3-58}$$

in which $D_s(*)/Dt$ denotes the material derivative, $\partial(*)/\partial t$ is the local derivative and the second term on the right side of Equation (3-58) is the convective derivative related to the mass transport inside the medium. Another important mathematical concept is the divergence operator defined as

$$\boldsymbol{\nabla} \cdot (f\boldsymbol{v}) \equiv \boldsymbol{\nabla} f \cdot \boldsymbol{v} + f \cdot (\boldsymbol{\nabla} \cdot \boldsymbol{v}) \tag{3-59}$$

where f and $\boldsymbol{v}$ are a generic scalar and vector, respectively. The general expressions for the mass balance of solid and fluid species in each structural level, the balance of energy for the soil and the momentum balance for the porous medium are obtained in the following sections. These balance equations are formulated in terms of the main state variables (unknowns): displacements (for equilibrium of stresses), liquid pressure (for the balance of pore-water mass), gas pressure (for the balance of pore-air mass) and temperature (for the balance of internal energy). A detailed mathematical development of the general balance equations for deformable porous media can be found in Olivella (1995).

3.7.1. THE MASS BALANCE OF SOLID

The mass balance of solid grains in the porous medium is expressed, according to the general expression presented in Equation (3-57), as follows

$$\frac{\partial \tilde{\rho}^s}{\partial t} + \boldsymbol{\nabla} \cdot \boldsymbol{j}^s = f^s \tag{3-60}$$

The total mass flux of solid in the medium, $\boldsymbol{j}^s$, is defined as

$$\boldsymbol{j}^s = \boldsymbol{j}'^s + \tilde{\rho}^s \dot{\boldsymbol{u}} = \tilde{\rho}^s \dot{\boldsymbol{u}} \tag{3-61}$$

where $\boldsymbol{j}'^s$ is the mass flux of solid respect to the solid skeleton and $\dot{\boldsymbol{u}}$ is the solid velocity vector. The vector $\boldsymbol{j}'^s$ is assumed null as a consequence of its own definition. It is also assumed that there is no source or sink of solid species in the medium, which leads to $f^s = 0$ in Equation (3-60). Recalling the definition of the bulk solid density given in Equation (3-24), Equation (3-60) can be written as

$$\frac{\partial\big(\rho_s \cdot (1-\phi)\big)}{\partial t} + \boldsymbol{\nabla} \cdot (\rho_s \cdot (1-\phi)\dot{\boldsymbol{u}}) = 0 \tag{3-62}$$

Using the concept of material derivative with respect to the solid in Equation (3-62), the balance mass equation for the solid phase is given by

$$\frac{D_s\left(\rho_s \cdot (1-\phi)\right)}{Dt} + \rho_s \cdot (1-\phi)\boldsymbol{\nabla} \cdot \dot{\boldsymbol{u}} = 0 \tag{3-63}$$

which leads, after some algebraic manipulation, to

$$\frac{D_s\phi}{Dt} = \frac{(1-\phi)}{\rho_s} \cdot \frac{D_s\rho_s}{Dt} + (1-\phi) \cdot \dot{\varepsilon}^{vol} \tag{3-64}$$

This latter equation expresses the contribution of the changes in the solid density and the volumetric strain evolution of the solid skeleton ($\dot{\varepsilon}^{vol}$) to the variations of the total porosity. The sign convention for the strains in Equation (3-64) and in all strain terms that appear in the following balance equations assumes a positive value for tensile strain components. For a double-porosity model, Equation (3-64) is extended to (Sánchez, 2004)

$$\begin{aligned}\frac{D_s\phi}{Dt} &= \frac{D_s\bar{\phi}_m}{Dt} + \frac{D_s\bar{\phi}_M}{Dt} \\ &= \frac{(1-\phi)}{\rho_s} \cdot \frac{D_s\rho_s}{Dt} + (1-\bar{\phi}_m-\bar{\phi}_M) \cdot \left(\dot{\bar{\varepsilon}}_m^{vol} + \dot{\bar{\varepsilon}}_M^{vol}\right) \\ &= \left(\frac{(1-\phi)}{\rho_s} \cdot \frac{D_s\rho_s}{Dt} + \dot{\bar{\varepsilon}}_m^{vol} - \bar{\phi}_m \cdot \dot{\varepsilon}^{vol}\right) + \left(\dot{\bar{\varepsilon}}_M^{vol} - \bar{\phi}_M\dot{\varepsilon}^{vol}\right)\end{aligned} \tag{3-65}$$

where the additive decompositions of the total porosity (see Equation (3-5)) and the volumetric deformation (see Equation (3-45)) have been used.

3.7.2. THE MASS BALANCE OF WATER

Water in pores can be found in liquid and gas phases. The mass balance of water in porous media is mainly related to the pore-water pressure and the liquid degree of saturation. In a double-porosity framework, the general form of the water mass balance equation is

$$\frac{\partial\tilde{\rho}_\beta^w}{\partial t} + \boldsymbol{\nabla} \cdot \boldsymbol{j}_\beta^w \pm \Gamma^w = f_\beta^w \tag{3-66}$$

where $\boldsymbol{j}_\beta^w = \boldsymbol{j}_{l\beta}^w + \boldsymbol{j}_{g\beta}^w$ is the total mass flux of water (as liquid water, $\boldsymbol{j}_{l\beta}^w$, or in vapour form, $\boldsymbol{j}_{g\beta}^w$) and f_β^w is the external mass supply of water per unit volume for the β-medium. Γ^w is the micro-macro water exchange term that represents the hydraulic coupling between the two continua, as mentioned in **Section 3.6**. This micro-macro interaction term acts as an "internal" supply of water (taking the whole porous medium as reference) for both structural media. The total water flux term in a phase, $\boldsymbol{j}_{\alpha\beta}^w$, includes non-advective fluxes ($\boldsymbol{i}_{\alpha\beta}^w$), fluid motion advective fluxes ($\theta_{\alpha\beta}^w\boldsymbol{q}_{\alpha\beta}$) and advective fluxes caused by solid phase motion ($\tilde{\rho}_{\alpha\beta}^w\dot{\boldsymbol{u}}$) according to

$$\begin{aligned}\boldsymbol{j}_{\alpha\beta}^w = \boldsymbol{j'}_{\alpha\beta}^w + \tilde{\rho}_{\alpha\beta}^w\dot{\boldsymbol{u}} &= \boldsymbol{j'}_{\alpha\beta}^w + \theta_{\alpha\beta}^w \cdot S_{\alpha\beta} \cdot \bar{\phi}_\beta\dot{\boldsymbol{u}} \\ &= \boldsymbol{i}_{\alpha\beta}^w + \theta_{\alpha\beta}^w\boldsymbol{q}_{\alpha\beta} + \theta_{\alpha\beta}^w \cdot S_{\alpha\beta} \cdot \bar{\phi}_\beta\dot{\boldsymbol{u}}\end{aligned} \tag{3-67}$$

in which the mass flux of water respect to the solid skeleton, $\boldsymbol{j'}_{\alpha\beta}^w$, is defined as

$$\boldsymbol{j}'^{w}_{\alpha\beta} = \boldsymbol{i}^{w}_{\alpha\beta} + \theta^{w}_{\alpha\beta}\boldsymbol{q}_{\alpha\beta} \tag{3-68}$$

In these equations, the non-advective flux of water is associated with the water vapour diffusion through the porous medium, that is, $\boldsymbol{i}^{w}_{\alpha\beta} = \boldsymbol{i}^{w}_{g\beta}$. The advective flux caused by water motion is also known as Darcy's flux of water (a brief explanation about this type of flux is given in **Section 3.8.2**). When the deformation of solid skeleton is negligible, $\boldsymbol{j}^{w}_{\alpha\beta} \approx \boldsymbol{j}'^{w}_{\alpha\beta}$.

Taking into account the previous flux vector expressions and Equation (3-16), the mass balance of water in each structural level is given by

$$\begin{aligned}&\frac{\partial\left(\left(\theta^{w}_{l\beta}\cdot S_{l\beta} + \theta^{w}_{g\beta}\cdot S_{g\beta}\right)\cdot\bar{\phi}_{\beta}\right)}{\partial t}\\ &+\boldsymbol{\nabla}\cdot\left(\boldsymbol{j}'^{w}_{l\beta} + \boldsymbol{j}'^{w}_{g\beta} + \left(\theta^{w}_{l\beta}\cdot S_{l\beta} + \theta^{w}_{g\beta}\cdot S_{g\beta}\right)\cdot\bar{\phi}_{\beta}\dot{\boldsymbol{u}}\right) \pm \Gamma^{w} = f^{w}_{\beta}\end{aligned} \tag{3-69}$$

In this equation, it is assumed that the water exchange term, Γ^{w}, is positive when water "flows" from macro-pores to the microstructural medium while a negative value is assigned to such a term when the water mass transfer is established in the opposite direction. The explicit form of the water mass balance equations for macrostructure and microstructure will be given in the two following sub-sections.

3.7.2.1. THE MASS BALANCE OF WATER IN MACROSTRUCTURE

Taking into account the general expression in Equation (3-69), the mass balance of water in macro-pores is given by

$$\begin{aligned}&\frac{\partial\left(\left(\theta^{w}_{lM}\cdot S_{lM} + \theta^{w}_{gM}\cdot S_{gM}\right)\cdot\bar{\phi}_{M}\right)}{\partial t}\\ &+\boldsymbol{\nabla}\cdot\left(\boldsymbol{j}'^{w}_{lM} + \boldsymbol{j}'^{w}_{gM} + \left(\theta^{w}_{lM}\cdot S_{lM} + \theta^{w}_{gM}\cdot S_{gM}\right)\cdot\bar{\phi}_{M}\dot{\boldsymbol{u}}\right) + \Gamma^{w} = f^{w}_{M}\end{aligned} \tag{3-70}$$

According to the sign convention established previously, the micro-macro water exchange term as expressed in Equation (3-70) represents a sink when its value is positive. It is important to highlight the difference between the term related to the mass of water interchanged between the two structural levels, Γ^{w}, and the one corresponding to the external mass supply of water per unit volume of macro medium, f^{w}_{M}. For those problems in which the external sink/source of water is negligible, it is assumed that $f^{w}_{M} \approx 0$. Applying the material derivative to the first term on the left-hand side of Equation (3-70), and after some algebraic operations, the following expression is obtained

$$\begin{aligned}&\bar{\phi}_{M}\cdot\frac{D_{s}\left(\theta^{w}_{lM}\cdot S_{lM} + \theta^{w}_{gM}\cdot S_{gM}\right)}{Dt} + \left(\theta^{w}_{lM}\cdot S_{lM} + \theta^{w}_{gM}\cdot S_{gM}\right)\cdot\frac{D_{s}\bar{\phi}_{M}}{Dt}\\ &+\left(\theta^{w}_{lM}\cdot S_{lM} + \theta^{w}_{gM}\cdot S_{gM}\right)\cdot\bar{\phi}_{M}\boldsymbol{\nabla}\cdot\dot{\boldsymbol{u}} + \boldsymbol{\nabla}\cdot\left(\boldsymbol{j}'^{w}_{lM} + \boldsymbol{j}'^{w}_{gM}\right) + \Gamma^{w} = f^{w}_{M}\end{aligned} \tag{3-71}$$

Considering that the hypothesis of small-strain rates is valid and recalling Equation (3-41) and Equation (3-65), the final form of the mass balance equation of water in macrostructure is written as

$$\bar{\phi}_M \cdot \frac{D_s\left(\theta_{lM}^w \cdot S_{lM} + \theta_{gM}^w \cdot S_{gM}\right)}{Dt} + \left(\theta_{lM}^w \cdot S_{lM} + \theta_{gM}^w \cdot S_{gM}\right) \cdot \dot{\varepsilon}_M^{vol} + \boldsymbol{\nabla} \cdot \left(\boldsymbol{j}'^w_{lM} + \boldsymbol{j}'^w_{gM}\right) + \Gamma^w = f_M^w \tag{3-72}$$

A more detailed mathematical development of the balance equation of macrostructural water content in a double-porosity approach can be found in Gesto (2014).

3.7.2.2. THE MASS BALANCE OF WATER IN MICROSTRUCTURE

The general form of the mass balance equation of microstructural water, according to Equation (3-69), is given by

$$\frac{\partial\left(\left(\theta_{lm}^w \cdot S_{lm} + \theta_{gm}^w \cdot S_{gm}\right) \cdot \bar{\phi}_m\right)}{\partial t} + \boldsymbol{\nabla} \cdot \left(\boldsymbol{j}'^w_{lm} + \boldsymbol{j}'^w_{gm} + \left(\theta_{lm}^w \cdot S_{lm} + \theta_{gm}^w \cdot S_{gm}\right) \cdot \bar{\phi}_m \dot{\boldsymbol{u}}\right) - \Gamma^w = f_m^w \tag{3-73}$$

where f_m^w represents an external supply of water for microstructure. If it is assumed that all "external" water supply to micro-pores corresponds to the water mass transferred from or to the macro-pores by the water exchange mechanism discussed in **Section 3.6**, then $f_m^w \approx 0$. In such a scenario, the mass of water interchanged between both pore levels is already accounted for the term Γ^w. Applying the concept of the material derivative to Equation (3-73), an expression similar to that one obtained for the water mass in macrostructure is achieved, that is,

$$\bar{\phi}_m \cdot \frac{D_s\left(\theta_{lm}^w \cdot S_{lm} + \theta_{gm}^w \cdot S_{gm}\right)}{Dt} + \left(\theta_{lm}^w \cdot S_{lm} + \theta_{gm}^w \cdot S_{gm}\right) \cdot \frac{D_s \bar{\phi}_m}{Dt} + \left(\theta_{lm}^w \cdot S_{lm} + \theta_{gm}^w \cdot S_{gm}\right) \cdot \bar{\phi}_m \boldsymbol{\nabla} \cdot \dot{\boldsymbol{u}} + \boldsymbol{\nabla} \cdot \left(\boldsymbol{j}'^w_{lm} + \boldsymbol{j}'^w_{gm}\right) - \Gamma^w = 0 \tag{3-74}$$

Combining the relationships in Equation (3-41) and Equation (3-65) together with the latter one, and after some algebraic operations on the resulting expression, the following equation is obtained for the conservation of mass of pore-water in microstructure

$$\bar{\phi}_m \cdot \frac{D_s\left(\theta_{lm}^w \cdot S_{lm} + \theta_{gm}^w \cdot S_{gm}\right)}{Dt} + \left(\theta_{lm}^w \cdot S_{lm} + \theta_{gm}^w \cdot S_{gm}\right) \cdot \left(\dot{\varepsilon}_m^{vol} + (1-\phi) \cdot \frac{\dot{\rho}_s}{\rho_s}\right) + \boldsymbol{\nabla} \cdot \left(\boldsymbol{j}'^w_{lm} + \boldsymbol{j}'^w_{gm}\right) - \Gamma^w = 0 \tag{3-75}$$

Experimental evidences have shown that the water in micro-pores in low permeability media does not participate to the Darcien advective transport of water (Romero, 1999). Consequently, the flux of water inside the microstructural level, expressed into the divergence term of Equation (3-75), can be neglected. This assumption leads to

$$\bar{\phi}_m \cdot \frac{D_s\left(\theta^w_{lm} \cdot S_{lm} + \theta^w_{gm} \cdot S_{gm}\right)}{Dt} + \left(\theta^w_{lm} \cdot S_{lm} + \theta^w_{gm} \cdot S_{gm}\right) \cdot \left(\dot{\varepsilon}^{vol}_m + (1-\phi) \cdot \frac{\dot{\rho}_s}{\rho_s}\right) - \Gamma^w = 0 \tag{3-76}$$

This simplified form of mass balance equation of water in micro-pores is considered in the double-porosity formulation developed in this Thesis. Furthermore, the assumption ($\boldsymbol{j'}^{w}_{lm} + \boldsymbol{j'}^{w}_{gm} \approx \mathbf{0}$) allows to treat the microstructural pore-water pressure (the unknown in the balance equation for the water mass in micro-pores) as a history variable to be integrated/updated at Gauss point level during the constitutive integration of stresses – see **Chapter 5** for more details.

3.7.3. THE MASS BALANCE OF AIR IN MACRO AND MICRO MEDIA

Once the balance equations for the pore-water in micro and macro media are established, it is quite simple to write equivalent mass conservation equations for the species air. Dry air is the main component of gas phase and it can also be found dissolved in the liquid phase. Consequently, the general balance equation for the mass of air moving through the porous medium is given by

$$\frac{\partial\left(\left(\theta^a_{l\beta} \cdot S_{l\beta} + \theta^a_{g\beta} \cdot S_{g\beta}\right) \cdot \bar{\phi}_\beta\right)}{\partial t} + \boldsymbol{\nabla} \cdot \left(\boldsymbol{j'}^{a}_{l\beta} + \boldsymbol{j'}^{a}_{g\beta} + \left(\theta^a_{l\beta} \cdot S_{l\beta} + \theta^a_{g\beta} \cdot S_{g\beta}\right) \cdot \bar{\phi}_\beta \dot{\boldsymbol{u}}\right) \pm \Gamma^a = f^a_\beta \tag{3-77}$$

In this expression, $\boldsymbol{j'}^{a}_{l\beta}$ and $\boldsymbol{j'}^{a}_{g\beta}$ denote the mass fluxes of air in liquid and gas phases with respect to the solid skeleton in the medium β. These flux vectors are defined as their analogous flux vectors for the species water (see Equation (3-68)). Γ^a is the term related to the air mass exchange between the two structural media and f^a_β represents the sink/source air term. Equation (3-77) derives into two equations, each of them corresponding to a structural level. Then, the balance equation of mass of air in macro-pores is expressed through

$$\bar{\phi}_M \cdot \frac{D_s\left(\theta^a_{lM} \cdot S_{lM} + \theta^a_{gM} \cdot S_{gM}\right)}{Dt} + \left(\theta^a_{lM} \cdot S_{lM} + \theta^a_{gM} \cdot S_{gM}\right) \cdot \dot{\varepsilon}^{vol}_M + \boldsymbol{\nabla} \cdot \left(\boldsymbol{j'}^{a}_{lM} + \boldsymbol{j'}^{a}_{gM}\right) + \Gamma^a = f^a_M \tag{3-78}$$

while the balance of mass of air of microstructure is

$$\bar{\phi}_m \cdot \frac{D_s\left(\theta_{lm}^a \cdot S_{lm} + \theta_{gm}^a \cdot S_{gm}\right)}{Dt} + \left(\theta_{lm}^a \cdot S_{lm} + \theta_{gm}^a \cdot S_{gm}\right) \cdot \left(\dot{\varepsilon}_m^{vol} + (1-\phi) \cdot \frac{\dot{\rho}_s}{\rho_s}\right) + \boldsymbol{\nabla} \cdot \left(\boldsymbol{j}'^a_{lm} + \boldsymbol{j}'^a_{gm}\right) - \Gamma^a = 0 \quad (3\text{-}79)$$

If it is assumed that the gas mobility through micro-pores is low enough to neglect the advective flux of air in this structural level, then the divergence term in Equation (3-79) disappears and the balance equation of air in microstructure reduces to

$$\bar{\phi}_m \cdot \frac{D_s\left(\theta_{lm}^a \cdot S_{lm} + \theta_{gm}^a \cdot S_{gm}\right)}{Dt} + \left(\theta_{lm}^a \cdot S_{lm} + \theta_{gm}^a \cdot S_{gm}\right) \cdot \left(\dot{\varepsilon}_m^{vol} + (1-\phi) \cdot \frac{\dot{\rho}_s}{\rho_s}\right) - \Gamma^a = 0 \quad (3\text{-}80)$$

It is important to mention that the assumption of a local equilibrium between the pore-air pressures in micro-pores and macro-pores (see **Section 3.6**) implies that $\Gamma^a \approx 0$ in Equation (3-79) and Equation (3-80).

3.7.4. THE BALANCE OF INTERNAL ENERGY FOR THE POROUS MEDIUM

The internal energy balance equation is established for the porous medium as a whole through the accounting of the energy stored in each phase. This balance equation considers the most important processes related to the energy transfer in porous media, that is, heat conduction, advection and phase changes. The main hypothesis assumed when solving the internal energy balance in low permeability media is the thermal equilibrium among the phases. Hence, only one equation is required. Its general form is expressed by

$$\frac{\partial\left(E_s \cdot \tilde{\rho}_s + E_l \cdot \tilde{\rho}_l + E_g \cdot \tilde{\rho}_g\right)}{\partial t} + \boldsymbol{\nabla} \cdot \boldsymbol{j}_E = f^Q \quad (3\text{-}81)$$

where E_s is the solid specific internal energy and E_l, E_g are the specific internal energies corresponding to the liquid and gas phases respectively. $\tilde{\rho}_s$, $\tilde{\rho}_l$, $\tilde{\rho}_g$ are the bulk densities for the solid, liquid and gas phases which, in the double-porosity context, are expressed by Equation (3-22) to Equation (3-24). $\boldsymbol{j}_E$ is the total heat flux through the porous medium with respect to a fixed reference system and f^Q is an internal/external energy supply per unit volume of soil. The total energy flux is defined as

$$\boldsymbol{j}_E = \boldsymbol{i}_c + \boldsymbol{j}_{E,s} + \boldsymbol{j}_{E,l} + \boldsymbol{j}_{E,g} \quad (3\text{-}82)$$

which includes a term related to the transport of energy in the porous medium by conduction ($\boldsymbol{i}_c$) and the terms corresponding to advective fluxes of energy caused by the motion of each phase in the medium ($\boldsymbol{j}_{E,s}$, $\boldsymbol{j}_{E,l}$, $\boldsymbol{j}_{E,g}$). Fourier's law governs the heat flux by conduction and this

thermal constitutive law is discussed briefly in **Section 3.8.1**. Another way to express the total heat flux through the soil is

$$\boldsymbol{j}_E = \boldsymbol{j'}_E + \left(E_s \cdot \tilde{\rho}_s + E_l \cdot \tilde{\rho}_l + E_g \cdot \tilde{\rho}_g\right)\dot{\boldsymbol{u}} \tag{3-83}$$

where $\boldsymbol{j'}_E$ represents the heat flux with respect to the solid skeleton. For a double-porosity formulation, this energy flux vector is defined through the following expression

$$\boldsymbol{j'}_E = \boldsymbol{i}_c + E_l \cdot (\rho_{lm}\boldsymbol{q}_{lm} + \rho_{lM}\boldsymbol{q}_{lM}) + E_g \cdot \left(\rho_{gm}\boldsymbol{q}_{gm} + \rho_{gM}\boldsymbol{q}_{gM}\right) \tag{3-84}$$

where $\boldsymbol{q}_{lm}$, $\boldsymbol{q}_{gm}$ and $\boldsymbol{q}_{lM}$, $\boldsymbol{q}_{gM}$ are the advective fluxes of the liquid and gas phases with respect to the solid skeleton in micro and macro media, respectively. Due to low mobility of fluid species through micro-pores, it is assumed that the advective fluxes at microstructural level are negligible, that is, $\boldsymbol{q}_{lm} = \boldsymbol{q}_{gm} \approx \boldsymbol{0}$. Combining Equation (3-83) and Equation (3-84) and comparing the resulting expression with Equation (3-82), the energy fluxes due to the motion of each phase in the soil are obtained as follows

$$\boldsymbol{j}_{Es} = E_s\tilde{\rho}_s\dot{\boldsymbol{u}} \tag{3-85}$$

$$\boldsymbol{j}_{El} = E_l \cdot (\rho_{lm}\boldsymbol{q}_{lm} + \rho_{lM}\boldsymbol{q}_{lM}) + E_l \cdot \tilde{\rho}_l\dot{\boldsymbol{u}} \approx E_l \cdot \rho_{lM}\boldsymbol{q}_{lM} + E_l \cdot \tilde{\rho}_l\dot{\boldsymbol{u}} \tag{3-86}$$

$$\boldsymbol{j}_{Eg} = E_g \cdot \left(\rho_{gm}\boldsymbol{q}_{gm} + \rho_{gM}\boldsymbol{q}_{gM}\right) + E_g \cdot \tilde{\rho}_g\dot{\boldsymbol{u}} \approx E_g \cdot \rho_{gM}\boldsymbol{q}_{gM} + E_g \cdot \tilde{\rho}_g\dot{\boldsymbol{u}} \tag{3-87}$$

It is important to remark that the energy transported by advection in each fluid phase is given by the sum of a component due to fluid motion through the pore spaces ($E_\alpha \cdot \rho_{\alpha\beta}\boldsymbol{q}_{\alpha\beta}$) and another one due to the motion of the solid skeleton ($E_\alpha \cdot \tilde{\rho}_\alpha\dot{\boldsymbol{u}}$).

Replacing these previous expressions together with Equation (3-22) to Equation (3-24) into Equation (3-81) and applying the material derivative with respect to the solid to the resulting expression, the energy balance equation for the porous medium, in the context of a double-porosity approach, can be written as

$$\begin{aligned}(1-\phi)\cdot\frac{D_s(E_s\cdot\rho_s)}{Dt} &+ \bar{\phi}_m\cdot\frac{D_s\left(E_l\cdot\rho_{lm}\cdot S_{lm} + E_g\cdot\rho_{gm}\cdot S_{gm}\right)}{Dt}\\ &+\bar{\phi}_M\cdot\frac{D_s\left(E_l\cdot\rho_{lM}\cdot S_{lM} + E_g\cdot\rho_{gM}\cdot S_{gM}\right)}{Dt}\\ &+\left(E_l\cdot\rho_{lm}\cdot S_{lm} + E_g\cdot\rho_{gm}\cdot S_{gm} - E_s\cdot\rho_s\right)\cdot(1-\phi)\cdot\frac{\dot{\rho}_s}{\rho_s}\\ &+\left(E_l\cdot\rho_{lm}\cdot S_{lm} + E_g\cdot\rho_{gm}\cdot S_{gm}\right)\cdot\dot{\varepsilon}_m^{vol}\\ &+\left(E_l\cdot\rho_{lM}\cdot S_{lM} + E_g\cdot\rho_{gM}\cdot S_{gM}\right)\cdot\dot{\varepsilon}_M^{vol}\\ &+\boldsymbol{\nabla}\cdot\left(\boldsymbol{i}_c + E_l\cdot\rho_{lM}\boldsymbol{q}_{lM} + E_g\cdot\rho_{gM}\boldsymbol{q}_{gM}\right) = f^Q\end{aligned} \tag{3-88}$$

3.7.5. THE MOMENTUM BALANCE FOR THE POROUS MEDIUM

The balance of momentum reduces to the equilibrium of stresses in the soil and it is given by Cauchy's expression

$$\boldsymbol{\nabla} \cdot \boldsymbol{\sigma}_t + \boldsymbol{b} = \mathbf{0} \tag{3-89}$$

in which inertial terms are neglected and $\boldsymbol{b}$ is the vector of body forces. This vector is expressed, in the context of a double-porosity formulation, as it follows

$$\begin{aligned} \boldsymbol{b} = \tilde{\rho}\boldsymbol{g} = \left(\rho_s \cdot (1-\phi) + \left(\rho_{lm} \cdot S_{lm} + \rho_{gm} \cdot S_{gm}\right) \cdot \bar{\phi}_m \right. \\ \left. + \left(\rho_{lM} \cdot S_{lM} + \rho_{gM} \cdot S_{gM}\right) \cdot \bar{\phi}_M\right)\boldsymbol{g} \end{aligned} \tag{3-90}$$

where $\boldsymbol{g}$ is the gravity vector. The momentum equilibrium equation is related to the displacement field throughout the porous medium. When the mechanical constitutive law is substituted in Equation (3-89), this balance equation is transformed into an expression in terms of displacements, fluid pressures and temperatures (the unknowns of the coupled THM problem).

3.8. CONSTITUTIVE EQUATIONS

In addition to the balance equations described in the previous sections, the THM formulation also requires a set of constitutive equations that completes the mathematical problem and, in addition, provides the coupling among the main thermal, hydraulic and mechanical phenomena taking place in the porous medium (Sánchez and Gens, 2006). This set of equations relates the independent variables (the unknowns of the coupled THM problems) with the dependent ones. The advective fluxes of liquid and gas, the water vapour and air non-advective fluxes, the conductive heat flux, the liquid degree of saturation, the liquid and gas densities and the stress tensor are some of the dependent variables considered when thermal, hydraulic and mechanical analyses are performed.

The basic main equations of the coupled problem are written in terms of the unknowns when the constitutive equations are incorporated into the balance equations (Olivella *et al.*, 1994; Sánchez and Gens, 2006; CODE_BRIGHT User's Guide, 2014). The general expressions of the constitutive laws used in the proposed double-porosity approach are presented below. A key aspect is the definition of specific constitutive laws for each structural level taking into account the behaviour characteristics of each medium.

3.8.1. THERMAL CONSTITUTIVE EQUATIONS

Heat conduction through the soil is driven by temperature gradients (∇T) and it is described by Fourier's law as follows

$$\boldsymbol{i}_c = -\lambda \cdot \nabla T \tag{3-91}$$

where λ is the global thermal conductivity of the porous medium, generally dependent on temperature (T), degree of saturation (S_l) and porosity (ϕ). This dependence is computed as a function of the thermal conductivities of each phase in the soil in order to consider its heterogeneous nature. One of such expressions, based on the weighted geometric mean of thermal conductivities of solid (λ_s), liquid (λ_l) and gas (λ_g) phases, is

$$\lambda = \lambda_s^{(1-\phi)} \cdot \lambda_l^{\phi \cdot S_l} \cdot \lambda_g^{\phi \cdot (1-S_l)} \tag{3-92}$$

The thermal conductivity in Equation (3-92) can be also expressed as a function of the water content in the soil through the thermal conductivity of the dry soil (λ_{dry}) and the thermal conductivity of the water saturated soil (λ_{sat}). Thus, the global thermal conductivity is written as

$$\lambda = \lambda_{sat}^{S_l} \cdot \lambda_{dry}^{(1-S_l)} \tag{3-93}$$

where the dry and the saturated thermal conductivities can be determined experimentally or calculated through the following relationships

$$\lambda_{dry} = \lambda_s^{(1-\phi)} \cdot \lambda_g^{\phi} \tag{3-94}$$

$$\lambda_{sat} = \lambda_s^{(1-\phi)} \cdot \lambda_l^{\phi} \tag{3-95}$$

Other porosity and water saturation-dependent empirical functions for the global and for the dry and saturated thermal conductivities can be found in the literature (Olivella *et al.*, 1994; Chen and Ledesma, 2009; Gran *et al.*, 2011). Some of such empirical thermal conductivity functions are also implemented in the finite element code (CODE_BRIGHT) to be used in the modelling tasks (see CODE_BRIGHT User's Guide, 2014). The dependence of the solid phase thermal conductivity on temperature is also taken into account in the mathematical formulation. Some experimental measurements of thermal conductivities on bentonites that evidence the dependency of this thermal property on water content are shown in Figure 3-8. Some thermal conductivity functions implemented in CODE_BRIGHT, like the relationship in Equation (3-93), are also depicted.

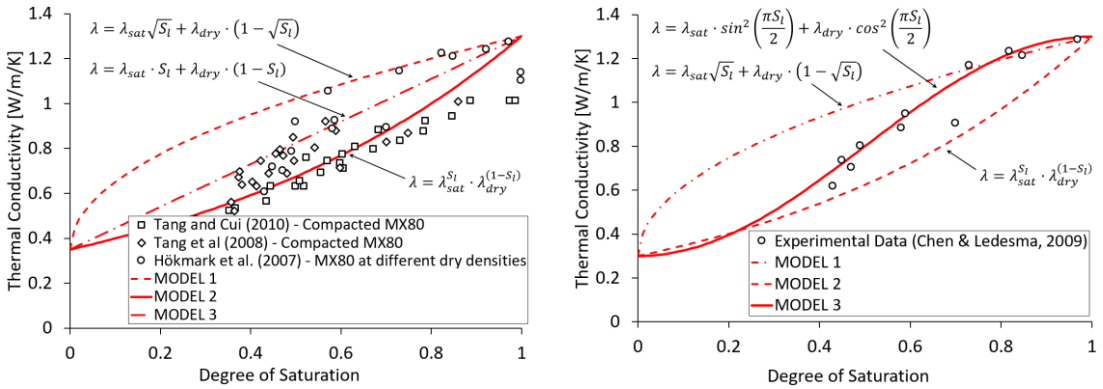

Figure 3-8: Dependence of the thermal conductivity on the water content for compacted bentonites: data and several thermal constitutive functions proposed in the literature to fit them.

Concerning the dependence of the thermal conductivity on the degree of saturation, it is also important to emphasize that, in a double-porosity model, the micro and the macro media may be under different water saturation conditions due to the assumption of the non-local hydraulic equilibrium between these both structural pore levels, as mentioned in **Section 3.6**. Furthermore, even if the hydraulic equilibrium between both media is reached, the degree of saturation may be different once the double-structure model described in this Thesis assigns a different water retention curve for each structural level, as will be addressed in **Section 3.8.2.2**. As a consequence, the use of Equation (3-92) or Equation (3-93) to estimate the soil thermal conductivity parameter requires the evaluation of an "average" degree of saturation for the porous medium as a whole, S_l, so that that the water content in each class of pores (micro- and macro-pores) can be properly considered. Hence, this "average" degree of saturation is calculated as

$$S_l = \frac{S_{lm} \cdot \bar{\phi}_m + S_{lM} \cdot \bar{\phi}_M}{\bar{\phi}_m + \bar{\phi}_M} = \frac{S_{lm} \cdot \bar{\phi}_m + S_{lM} \cdot \bar{\phi}_M}{\phi} \tag{3-96}$$

in which the additive decomposition of total porosity is recalled, according to Equation (3-5). The porosity variable that must be introduced in Equation (3-92) or in Equation (3-94) and Equation (3-95), even for THM analyses performed with the double-porosity model, corresponds to the total porosity.

3.8.2. HYDRAULIC CONSTITUTIVE EQUATIONS

3.8.2.1. THE GENERALIZED DARCY'S LAW

Water and gas advective fluxes are driven by fluid potential gradients and are defined by means of the generalized Darcy's law (Bear, 1972). In a double-porosity formulation, this volumetric flux ($\boldsymbol{q}_{\alpha\beta}$) is evaluated for each fluid phase, α, in each structural medium, β, as (see Sánchez, 2004)

$$\boldsymbol{q}_{\alpha\beta} = -\boldsymbol{K}_{\alpha\beta} \cdot \left(\nabla P_{\alpha\beta} - \rho_{\alpha\beta}\boldsymbol{g}\right) \tag{3-97}$$

where $\boldsymbol{K}_{\alpha\beta}$ is the hydraulic conductivity tensor, which depends on temperature, degree of saturation and porosity. This hydraulic parameter is given by

$$\boldsymbol{K}_{\alpha\beta} = \boldsymbol{k}_{\beta} \cdot \frac{k_{r_{\alpha\beta}}}{\mu_{\alpha\beta}} \tag{3-98}$$

in which $\boldsymbol{k}_{\beta}$, $k_{r_{\alpha\beta}}$ and $\mu_{\alpha\beta}$ represent the intrinsic permeability tensor, the phase relative permeability and the fluid dynamic viscosity, respectively. In order to apply Equation (3-97), it is necessary to evaluate the intrinsic and relative permeabilities, the viscosity and the density for each fluid phase in each pore structure. In the following sub-sections, the most relevant laws and expressions used for this purpose are described.

INTRINSIC AND RELATIVE PERMEABILITIES

The intrinsic permeability is a porous medium property that depends primarily on the pore structure (Olivella *et al.*, 1996; Sánchez, 2004). Two widely employed laws to express this dependence on porosity are: the empirical model based on the Kozeny-Carman equation (Gens *et al.*, 1998), called as Kozeny's model from now on, and the exponential law proposed by Sánchez (2004) to model mass fluxes in highly expansive clays. Figure 3-9 presents experimental measurements of saturated permeability at different densities for a compacted bentonite material (FEBEX bentonite) and the curves fitted by these two models.

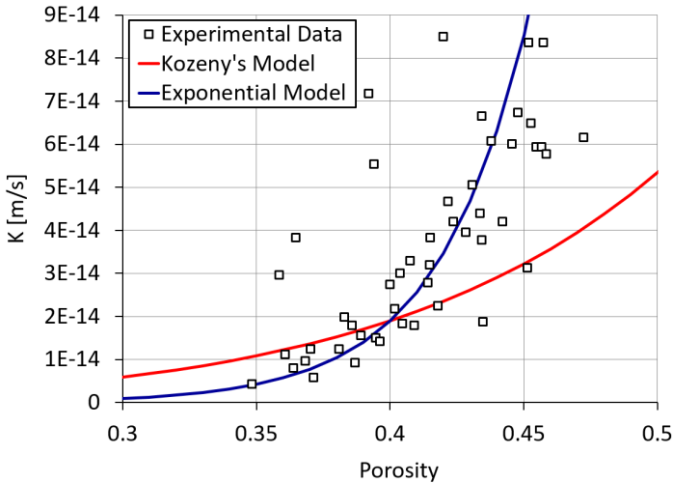

Figure 3-9: Fitted curves by Kozeny and exponential models together with experimental data for the saturated conductivity of FEBEX bentontie at different porosities (from Sánchez, 2004).

In the context of a double-porosity formulation, the expression for Kozeny's model is re-defined as follows:

$$\boldsymbol{k}_{\beta} = \boldsymbol{k}_{0,\beta} \cdot \frac{\bar{\phi}_{\beta}^{3}}{\left(1-\bar{\phi}_{\beta}\right)^{2}} \cdot \frac{\left(1-\phi_{0,\beta}\right)^{2}}{\phi_{0,\beta}^{3}} \tag{3-99}$$

The other empirical law to determine the dependence of intrinsic permeability on porous medium structure is the exponential equation, expressed as:

$$\boldsymbol{k}_{\beta} = \boldsymbol{k}_{0,\beta} \cdot e^{b_{\beta} \cdot (\bar{\phi}_{\beta} - \phi_{0,\beta})} \tag{3-100}$$

In such expressions, $\phi_{0,\beta}$ is the porosity for which the intrinsic permeability tensor $\boldsymbol{k}_{0,\beta}$ is estimated, $\bar{\phi}_{\beta}$ is the current porosity related to the β-structural level and b_{β} is a shape parameter. These intrinsic permeability functions are suitable to relate pronounced changes in hydraulic permeability with the variations of porosity observed in some clay barriers. The latter expression has been introduced in the numerical code in order to fit better many experimental data of water permeability obtained from infiltration tests performed on bentonite-based materials (Sánchez, 2004; Sánchez and Gens, 2006), as illustrated in Figure 3-9. It is assumed that the contribution of the mass flux of fluid species through micro-pores (micro-micro flux) to the total flux in an expansive soil (a porous medium with a very low fluid mobility) can be neglected in comparison with the transport of fluid species through macro-pores. As a consequence, the generalized Darcy's law in Equation (3-97) is only required for describing water and gas fluxes through the macrostructural porous medium.

The relative permeability of liquid phase, $k_{r_{l\beta}}$, expresses the dependence of the hydraulic permeability on the degree of saturation in the β-medium. In this way, the well-known decrease in water permeability with the reduction of water saturation can be considered in the mathematical formulation by means of a non-linear scalar function, defined as

$$k_{r_{l\beta}} = \frac{\boldsymbol{K}_{l\beta}(S_{l\beta})}{\boldsymbol{K}_{\beta,sat}} \tag{3-101}$$

where $\boldsymbol{K}_{l\beta}(S_{l\beta})$ is the water conductivity at a specific partial saturation $S_{l\beta} < 1$ and $\boldsymbol{K}_{\beta,sat}$ is the water permeability at fully saturated conditions. Several liquid relative permeability functions are given in the literature as the ones based on the soil suction (Campbell, 1974), on the effective degree of saturation (Brooks and Corey, 1964; Mualem and Dagan, 1978), on the water retention capacity (van Genuchten, 1978, 1980; Fredlund and Xing, 1994) among others.

The relative permeability function derived from the water retention curve and proposed by van Genuchten (1980) is expressed as follows

$$k_{r_{l\beta}} = \sqrt{S_{e_{l\beta}}} \cdot \left(1 - \left(1 - S_{e_{l\beta}}^{1/\lambda_{kr}}\right)^{\lambda_{kr}}\right)^2 \tag{3-102}$$

in which the effective degree of saturation, $S_{e_{l\beta}}$, is computed as

$$S_{e_{l\beta}} = \frac{S_{l\beta} - S_{lr,\beta}}{S_{ls,\beta} - S_{lr,\beta}} \tag{3-103}$$

where $S_{lr,\beta}$ is the residual saturation and $S_{ls,\beta}$ is the maximum degree of saturation. In models based on a macroscopic approach, a generalized power function is used to evaluate the dependence of the relative liquid permeability on the effective degree of saturation

$$k_{r_{l\beta}} = A_{rl} \cdot S_{e_{l\beta}}^{\lambda_{rl}} \tag{3-104}$$

where A_{rl} and λ_{rl} are model parameters. The power function is suitable for modelling fine-grained soils when experimental data are available. A smoothing dependence of the liquid relative permeability on the macrostructural water saturation has also been proposed (Gesto, 2014), whose expression is given as follows

$$k_{r_{lM}} = \frac{1}{ln2 - q_{kr}} \cdot ln\left(e^{-q_{kr} \cdot S_{lM}^{p_{kr}}} + e^{-q_{kr} \cdot (2 - S_{lM})^{p_{kr}}}\right) \tag{3-105}$$

for which two fitting parameters are required: p_{kr} and q_{kr}. Figure 3-10 shows some experimental data for the relative permeability to water at different water saturation conditions for different porous materials: unconsolidated sands (Piquemal, 1994) and silica sands (Sánchez and Schechter, 1990), sandstones (Satik, 1998; Mahiya, 1999; O'Connor, 2001) and unsaturated clays (Olchitzky, 2002). Furthermore, several relative permeability curves are also depicted, including the ones obtained through the expression in Equation (3-105) – see the curves plotted on the right-hand side in Figure 3-10– for different values of p_{kr} ($q_{kr} = 100$ for all those curves). It is clear that a convenient choice for the shape parameters can give reliable estimates for the hydraulic behaviour of partially saturated porous media.

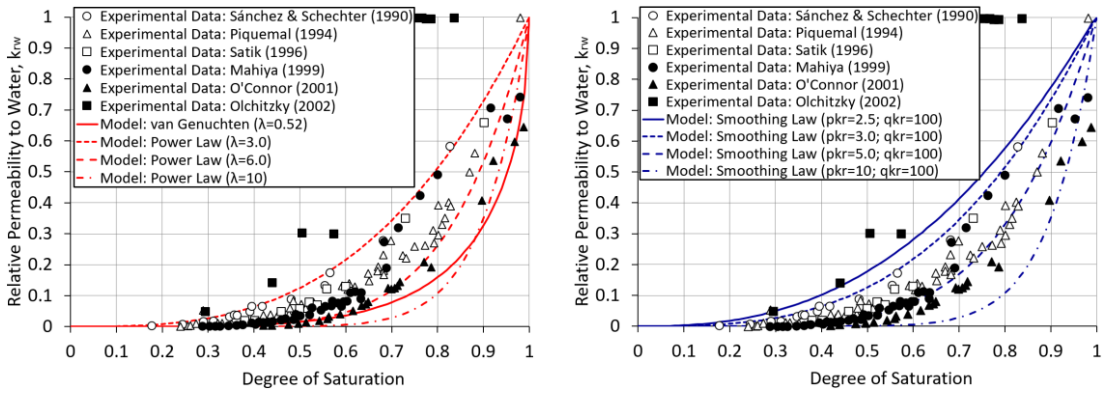

Figure 3-10: Experimental data and adjusted empirical curves (van Genuchten model and power law, on the left; smoothed function, on the right) for relative permeability as a function of water saturation.

The relative permeability of the gas phase in the β-structural level, $k_{r_{g\beta}}$, can be evaluated from the relative permeability to water according to the following expression

$$k_{r_{g\beta}} = A_{rg} \cdot \left(1 - k_{r_{l\beta}}\right) \tag{3-106}$$

or through a generalized power law as

$$k_{r_{g\beta}} = A_{rg} \cdot S_{e_{g\beta}}^{\lambda_{rg}} \tag{3-107}$$

wherein the gas effective saturation, $S_{e_{g\beta}}$, is defined similarly to the liquid effective saturation in Equation (3-103). The shape parameters in Equation (3-107), A_{rg} and λ_{rg}, can be assigned so that the differences in the magnitude of the measured water and gas permeabilities of compacted bentonites can be properly modelled (Villar and Lloret, 2001; Sánchez, 2004). In such materials and conditions, the water-saturated permeability is several orders of magnitude smaller than the gas permeability at non-saturated conditions. In order to ensure a modelled gas permeability close to the values measured in laboratory tests (Sánchez, 2004) and to maintain the concept of intrinsic permeability not dependent on the fluid species flowing through the pores, it is advisable to set a high enough value to A_{rg} in Equation (3-106) or in Equation (3-107), that is, $A_{rg} \gg A_{rl}$.

FLUID VISCOSITIES

Fluid viscosities are considered as functions of temperature. In **Section 3.7.4** it has been assumed that temperature is the same for each phase in each porous level in low permeability media. Consequently, it can be assumed that the liquid viscosity is the same for water in micro and macro voids. The same assumption is also made for the viscosity of gas phase in both media. Therefore, the viscosity of the liquid phase (in microstructure and macrostructure) is given by

$$\mu_l = \mu_{lm} = \mu_{lM} = A_{\mu l} \cdot e^{\left(\frac{B_{\mu l}}{273.15+T}\right)} \tag{3-108}$$

while the thermal effects on gas viscosity can be expressed as

$$\mu_g = \mu_{gm} = \mu_{gM} = A_{\mu g} \cdot e^{\left(\frac{B_{\mu g}}{273.15+T}\right)} \tag{3-109}$$

or calculated through

$$\mu_g = \mu_{gm} = \mu_{gM} = A_{\mu g} \cdot \left(\frac{\sqrt{273.15+T}}{1+\frac{B_{\mu g}}{273.15+T}} \right) f_{\mu g} \tag{3-110}$$

where $f_{\mu g}$ is a reduction coefficient that takes into account the possibility of Knudsen diffusion (Welty *et al.*, 2008), i.e., the Klinkenberg effect. Reference values for the fluid viscosity parameters from Equation (3-108) to Equation (3-110) are: $A_{\mu l} =$ 2.10e-12 MPa·s, $B_{\mu l} =$ 1,808.5 K^{-1}, $A_{\mu g} =$ 1.48e-12 MPa·s and $B_{\mu g} =$ 119.4 K^{-1}. In these equations temperature, T, is expressed in °C.

LIQUID AND GAS DENSITIES

The dependence of liquid phase density on water pressure and temperature in coupled THM analyses can be established through an exponential expression as follows

$$\rho_{l\beta} = \rho_{l0,\beta} \cdot e^{(\beta_{\rho l,\beta}\cdot(P_{l\beta}-P_{l0,\beta})+\alpha_{\rho l,\beta}\cdot T)} \tag{3-111}$$

in which the water compressibility ($\beta_{\rho l,\beta}$) and the volumetric thermal expansion coefficient ($\alpha_{\rho l,\beta}$) are defined for each each structural level. $\rho_{l0,\beta}$ is the reference water density and $P_{l0,\beta}$ is a reference pressure (usually taken as the atmospheric pressure). The density of the liquid phase can also be given by a linear function of liquid pressure and temperature according to

$$\rho_{l\beta} = \rho_{l0,\beta} \cdot \left(1 + \beta_{\rho l,\beta} \cdot \left(P_{l\beta} - P_{l0,\beta}\right) + \alpha_{\rho l,\beta} \cdot T\right) \tag{3-112}$$

The thermal expansion of water, $\alpha_{\rho l,\beta}$, in these expressions is a function of temperature, as discussed in **Section 2.5.1.3**. A typical value for the water compressibility in most geotechnical analysis is $\beta_{\rho l,\beta} = 4.5\text{e-}04$ MPa^{-1}.

Gesto (2014) implemented an additional law for the water density in order to give a smooth transition from a linear law (according to Equation (3-112)) to a constant water density. The main purpose of this additional function is to introduce a cut-off for large negative liquid pressures in order to prevent non-realistic low liquid densities. This new function is defined as

$$\rho_{l\beta} = \frac{1}{p_{\rho l,\beta}} \cdot ln\left(e^{p_{\rho l,\beta}\cdot\rho_{l0,\beta}\cdot\beta_{\rho l,\beta}\cdot P_{l\beta}} + e^{p_{\rho l,\beta}\cdot\rho_{l0,\beta}\cdot\beta_{\rho l,\beta}\cdot P_{l\beta}^{cutoff}}\right) + \rho_{l0,\beta} \cdot \left(1 - \beta_{\rho l,\beta} \cdot P_{l0,\beta} + \alpha_{\rho l,\beta} \cdot T\right) \tag{3-113}$$

in which $\rho_{l0,\beta}$ corresponds to the water density value at high suctions, $p_{\rho l,\beta}$ is a shape parameter that controls the curvature of the smoothed function around a cut-off point defined by the liquid pressure parameter $P_{l\beta}^{cutoff}$. The shape of water density curves described above for a temperature of 20°C are illustrated in Figure 3-11. For the smoothing liquid density model (see Figure 3-11(b)), the value used for the cut-off in liquid pressure is $P_l^{cutoff} = $ -10 MPa.

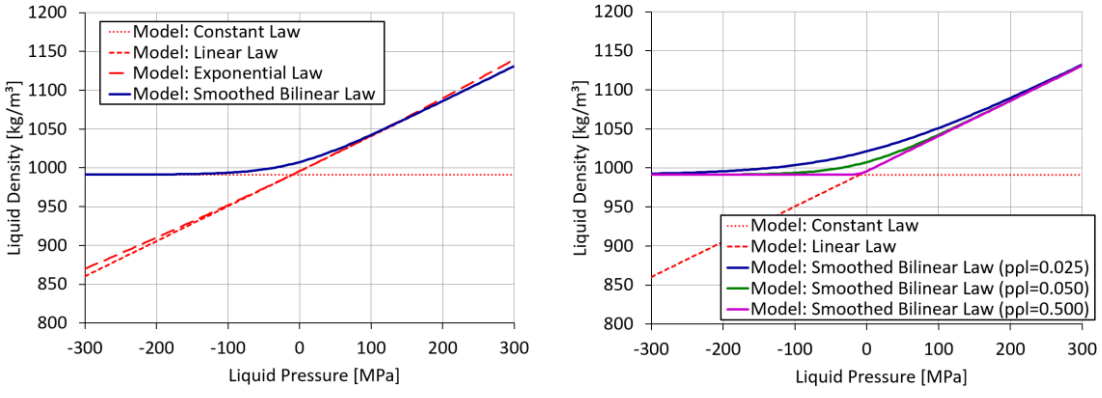

Figure 3-11: **(a)** Comparison of different liquid density functions available in the numerical code CODE_BRIGHT; **(b)** a family of smoothed bilinear liquid density laws for isothermal conditions (T = 20°C).

It is important to remark that the high-density state of water in micro-pores discussed in **Section 2.4.2** can be modelled by any of the previous water density functions with a convenient choice for the model parameters required in each of them.

The density of the gas phase is calculated adding the partial densities of water vapour (θ_g^w) and dry air (θ_g^a). Using the law of ideal gases and defining a gas density expression for each structural level, the gas density is given by

$$\rho_{g\beta} = \theta_{g\beta}^w + \theta_{g\beta}^a = \frac{P_{v,\beta} \cdot M_v}{R \cdot (273.15 + T)} + \frac{P_{a,\beta} \cdot M_a}{R \cdot (273.15 + T)} \tag{3-114}$$

where P_v and P_a are the partial pressures of vapour and dry air, respectively; $M_v = 0.018$ kg/mol and $M_a = 0.028$ kg/mol are the molecular masses of vapour and air and R is the ideal gas constant (R =8.314 J/(mol·K)). Vapour partial pressure is calculated according to the following expression

$$P_v(\psi, T) = P_v(T) \cdot F(\psi, T) \tag{3-115}$$

in which $P_v(T)$ is the saturated water vapour pressure at a given temperature. This function defines the boundary between liquid-water region and the water-vapour region in the water phase change diagram displayed in Figure 3-12. For pure water the saturated vapour pressure dependence on temperature is approximated by

$$P_v(T) = 136{,}075 \cdot e^{\left(-\frac{5{,}239.7}{273.15+T}\right)} \tag{3-116}$$

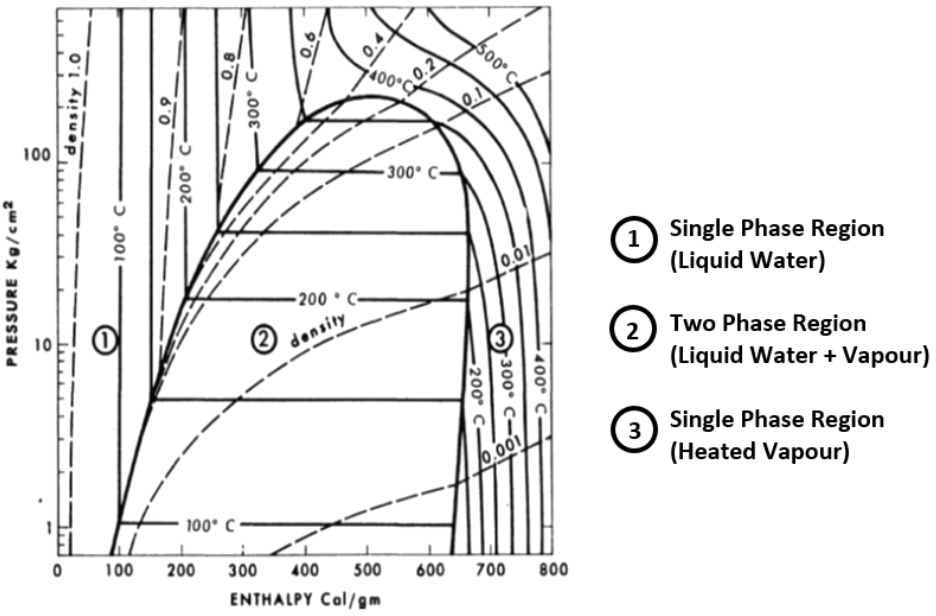

Figure 3-12: Pressure-enthalpy diagram for pure water and water vapour showing isotherm lines for several temperatures (from 100℃ to 500℃) (after Faust and Mercer, 1977).

In Equation (3-115), the scalar function $F(\psi, T)$ is related to the capillary effects in partially saturated porous media and it is described by the psychrometric law (see **Section 3.9**). The total water potential, ψ, is related to the degree of saturation through the water retention capacity curve.

3.8.2.2. THE WATER RETENTION CURVE: A MATHEMATICAL APPROACH

The retention curve plays a crucial role in the determination of unsaturated soil property functions (Fredlund *et al.*, 2012) and in the subsequent development and implementation of unsaturated soil mechanics. The water retention curve of a porous medium establishes a link between its water content (or degree of saturation) and the pore-water potential (suction) – see **Section 2.4.1**. The water retention capacity of a soil can be readily measured through laboratory tests and may be fitted by means of several different empirical models found in the literature (Brooks and Corey, 1964; van Genuchten, 1980; Fredlund and Xing, 1994; Fredlund and Pham, 2006). Some of these expressions includes behaviour aspects observed experimentally in soils as the dependence of the water retention curve on dry density (Lloret and Villar, 2007; Wayllace, 2008) and on temperature changes (Philip and de Vries, 1957; Hopmans and Dane, 1985; Olivella and Gens, 2000; Arifin, 2008; Gao and Shao, 2015) besides the hysteretic behaviour observed during drying/wetting paths (Philip, 1964; Mualem and Miller, 1979; Nimmo, 1992; Feng and Fredlund, 1999; Pham *et al.*, 2005; Seiphoori *et al.*, 2014). One of the commonly used models for many coupled THM analyses is the van Genuchten law (van Genuchten, 1980), expressed as

$$S_{el} = \frac{S_l - S_{lr}}{S_{ls} - S_{lr}} = \left(1 + \left(\frac{P_g - P_l}{P}\right)^{\frac{1}{1-\lambda_{rc}}}\right)^{-\lambda_{rc}} \tag{3-117}$$

in which the thermal effect on the retention water capacity can be considered according to the following relationship suggested by Olivella and Gens (2000)

$$P = P_0 \cdot \frac{\sigma}{\sigma_0(T_0)} \tag{3-118}$$

where λ_{rc} and P are model parameters. λ_{rc} is the same parameter used in the relative permeability expression given by van Genuchten model (parameter λ_{kr} in Equation (3-102)). This model parameter defines the shape of the water retention curve. The parameter P controls the height of the retention curve and can be interpreted as a measure of the capillary pressure required to start the desaturation of the porous medium and P_0 is its corresponding value at a reference temperature T_0. Surface tension, σ (in N/m), is a function of temperature (see **Section 2.5.2** and **Section 2.5.5**) and σ_0 corresponds to the surface tension at the same temperature at which P_0 is measured.

A modified form of the van Genuchten model includes a function f_d in order to determine properly the water retention capacity at high suction values. The modified van Genuchten law is then expressed according to

$$S_{el} = \left(1 + \left(\frac{P_g - P_l}{P}\right)^{\frac{1}{1-\lambda_{rc}}}\right)^{-\lambda_{rc}} \cdot f_d \tag{3-119}$$

where the scalar factor f_d is given by

$$f_d = \left(1 - \frac{P_g - P_l}{P_d}\right)^{\lambda_d} \tag{3-120}$$

in which P_d corresponds to the suction value at fully dry conditions while λ_d is a shape parameter. This modified retention curve has been used successfully in many numerical analyses in the context of the THM behavior of bentonite-based materials (Sánchez and Gens, 2006; Hoffmann *et al.*, 2007; Gens *et al.*, 2011; Gaus *et al.*, 2014a; Gens and Vasconcelos, 2019). Furthermore, it is important to mention that the current mathematical formulation for a double-porosity model allows to define a different retention curve for each structural level. In the absence of experimental data, water retention curves of expansive clays compacted at high dry densities can be used for fitting the shape of the microstructural retention curve at the aggregate level. Typical shapes for pore-water retention curves given by the van Genuchten law are shown in Figure 3-13.

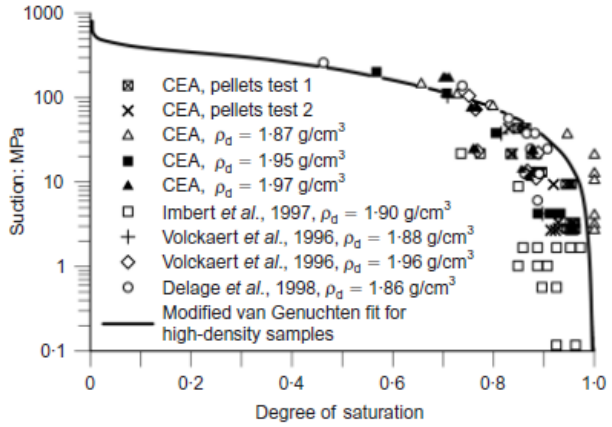

(a)

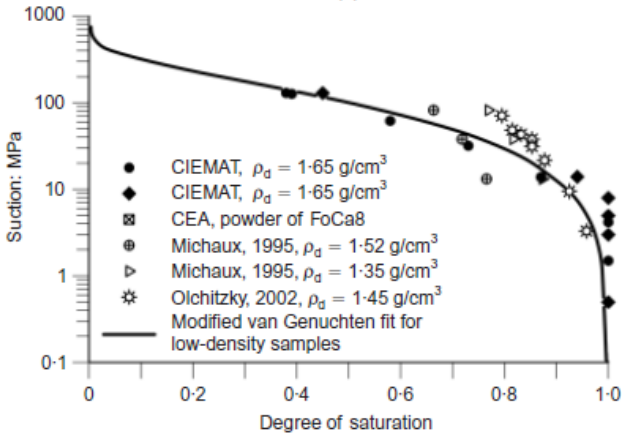

(b)

Figure 3-13: Experimental data and the modified van Genuchten law for the water retention curves of a compacted bentonite at **(a)** higher and **(b)** lower dry densities (Gens *et al.*, 2011).

3.8.2.3. WATER VAPOUR AND DISSOLVED AIR FLUXES

Non-advective fluxes of vapour inside the gas phase ($\boldsymbol{i}_g^w$) and of dissolved air in the liquid phase ($\boldsymbol{i}_l^a$) are driven by the mass fraction gradients and described by Fick's law. For vapour diffusion in the gas phase, the following expression is adopted

$$\boldsymbol{i}_{g\beta}^{w} = -\boldsymbol{D}_{g\beta}^{w} \cdot \boldsymbol{\nabla}\omega_{g\beta}^{w} = -\left(\rho_{g\beta} \cdot \bar{\phi}_{\beta} \cdot S_{g\beta} \cdot \tau_{\beta} \cdot D_{\beta}^{w}\mathbf{I} + \rho_{g\beta} \cdot \boldsymbol{D}_{g\beta}'\right) \cdot \boldsymbol{\nabla}\omega_{g\beta}^{w} \quad (3\text{-}121)$$

where $\boldsymbol{D}_{g\beta}^{w}$ is the dispersion tensor of the β-medium, D_{β}^{w} is the dispersion coefficient related to molecular diffusion of vapour in air, $\boldsymbol{D}_{g\beta}'$ is the mechanical dispersion tensor and τ_{β} is the tortuosity, a reduction factor that takes in account the fact that the vapour diffusion takes place through the pores of a medium. Molecular diffusion is usually a dominant process in comparison to the mechanical dispersion of vapour and, consequently, the mechanical dispersion term can be neglected in many geotechnical problems. The molecular diffusion coefficient of vapour, D_{β}^{w}, is calculated as

$$D_{\beta}^{w} = D \cdot \left(\frac{(273.15 + T)^{n}}{P_{g\beta}}\right) \quad (3\text{-}122)$$

where D and n are model parameters usually taken as D = 5.9e-06 m^2 s^{-1} K^{-n} Pa and n = 2.3 . Similar considerations are made regarding the diffusion of air in the liquid phase. The non-advective flux of dissolved air is defined by

$$\boldsymbol{i}_{l\beta}^{a} = -\boldsymbol{D}_{l\beta}^{a} \cdot \boldsymbol{\nabla}\omega_{l\beta}^{a} = -\left(\rho_{l\beta} \cdot \bar{\phi}_{\beta} \cdot S_{l\beta} \cdot \tau_{\beta} \cdot D_{\beta}^{a}\mathbf{I} + \rho_{l\beta} \cdot \boldsymbol{D}_{l\beta}'\right) \cdot \boldsymbol{\nabla}\omega_{l\beta}^{a} \quad (3\text{-}123)$$

where the dispersion coefficient for the molecular diffusivity of air in water, D_{β}^{a}, is given by

$$D_{\beta}^{a} = D \cdot e^{\left(\frac{-Q}{R \cdot (273.15+T)}\right)} \quad (3\text{-}124)$$

in which the default values D = 1.1e-04 m^2/s and Q = 24,530 J/mol are assumed for these model parameters.

3.8.3. MECHANICAL CONSTITUTIVE EQUATION

Due to the strong influence of the mechanical problem on the swelling clay behavior, the mechanical constitutive law is a key element in the modelling of these materials (Sánchez and Gens, 2006). A generalized expression for the mechanical constitutive equation, in which the changes in strain, temperature and fluid pressures are explicitly considered in the context of a double-porosity formulation, can be established as

$$\dot{\boldsymbol{\sigma}}_{\beta} = \left[\boldsymbol{D}_{\beta}\right]\dot{\boldsymbol{\varepsilon}}_{\beta} + \boldsymbol{h}_{l\beta}\dot{P}_{l\beta} + \boldsymbol{h}_{g\beta}\dot{P}_{g\beta} + \boldsymbol{h}_{\beta}\dot{T}_{\beta} \quad (3\text{-}125)$$

where $\dot{\boldsymbol{\sigma}}_{\beta}$ is the constitutive stress rate vector, $\dot{\boldsymbol{\varepsilon}}_{\beta}$ is the strain rate vector, $\left[\boldsymbol{D}_{\beta}\right]$ is the constitutive stiffness matrix, $\boldsymbol{h}_{l\beta}$, $\boldsymbol{h}_{g\beta}$ are the generic constitutive vectors relating changes in liquid and gas pressures, respectively, to stress increments while $\boldsymbol{h}_{\beta}$ is a constitutive vector relating stress to temperature changes. Equation (3-125) can be written in a more compacted form as

$$\dot{\boldsymbol{\sigma}}_{\beta} = \left[\boldsymbol{D}_{\beta}^{*}\right]\dot{\boldsymbol{\varepsilon}}_{\beta}^{g} \quad (3\text{-}126)$$

where $\left[\boldsymbol{D}_{\beta}^{*}\right]$ is the generalized constitutive tensor defined in the framework of a generalized plasticity theory. The generalized strain rate vector, $\dot{\boldsymbol{\varepsilon}}_{\beta}^{g}$, is then expressed by

$$\dot{\boldsymbol{\varepsilon}}_{\beta}^{g} = \begin{Bmatrix} \dot{\boldsymbol{\varepsilon}}_{\beta} \\ \dot{P}_{l\beta} \\ \dot{P}_{g\beta} \\ \dot{T}_{\beta} \end{Bmatrix} \tag{3-127}$$

The next chapter is devoted to describing the main features of the stress-strain behavior in each structural level and the mathematical formulation developed to treat the strong THM coupling behaviour of expansive clays in the framework of a double-porosity theory. In this Thesis, it is assumed that the macrostructural behavior can be described by models for unsaturated non-expansive soils – such as the thermo-elastoplastic BBM model (Alonso *et al.*, 1990; Gens, 1995) – while the mechanical response of microstructure to changes in the generalized stress state acting on this structural level ($\dot{\boldsymbol{\sigma}}_{m}$) will be assumed volumetric and non-linear elastic.

3.9. EQUILIBRIUM RESTRICTIONS

The equilibrium restrictions relate dependent variables with unknowns assuming a local equilibrium of the dissolved species (air and vapour) in fluid phases. These restrictions consider that phase changes and chemical processes are fast enough in comparison to other processes involving mass transport in the porous medium (Olivella, 1995). In a THM problem, the concentration of water vapour in gas phase (governed by the psychrometric law) and the concentration of dissolved air in liquid phase (described by Henry's law) are the dependent variables.

The vapour density in the gaseous phase ($\theta_{g\beta}^{w}$) depends on temperature and suction and it is expressed by Kelvin's law as follows

$$\theta_{g\beta}^{w} = \rho_{g\beta} \cdot \omega_{g\beta}^{w} = \left(\theta_{g\beta}^{w}\right)_{0} \cdot F\left(\psi_{\beta}, T\right) \tag{3-128}$$

where $\left(\theta_{g\beta}^{w}\right)_{0}$ is the vapour concentration in equilibrium with a flat water surface (at a given temperature T) and $F\left(\psi_{\beta}, T\right)$ is a function that takes into account the capillary effects in non-saturated conditions. According to Equation (3-128), $F\left(\psi_{\beta}, T\right)$ is defined as the ratio between the partial pressure of vapour and the vapour pressure in water-saturated conditions at a given temperature. This scalar function is also known as the relative humidity function, estimated through the psychrometric law as follows

$$F\left(\psi_{\beta}, T\right) = \frac{\theta_{g\beta}^{w}}{\left(\theta_{g\beta}^{w}\right)_{0}} = e^{\left(\frac{\psi_{\beta} \cdot M_{w}}{R \cdot (273.15+T) \cdot \rho_{l\beta}}\right)} \tag{3-129}$$

in which M_w is the molecular mass of water (M_w = 0.018 kg/mol). Typical curves for representing the dependence of the relative humidity on suction and temperature are shown in Figure 3-14. The total water potential in the β-medium, ψ_β, is given by the matric suction when osmotic effects are negligible.

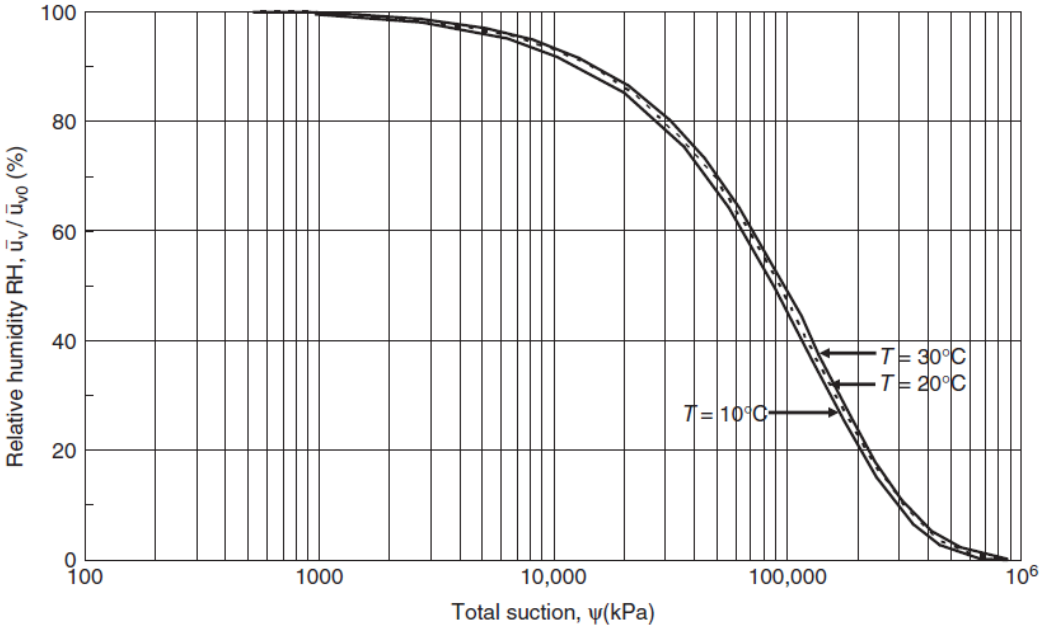

Figure 3-14: Thermodynamic equilibrium between the relative humidity (RH) and the total suction at different temperatures (Fredlund *et al.*, 2012).

The amount of air dissolved in water is given by Henry's law through a linear relationship between the concentration of air in dissolution ($\theta^a_{l\beta}$) and the partial pressure of air in the gas phase, $P_{a\beta}$. This law is expressed as

$$\theta^a_{l\beta} = \rho_{l\beta} \cdot \omega^a_{l\beta} = \frac{P_{a\beta}}{H} \cdot \frac{M_a}{M_w} \cdot \rho_{l\beta} \tag{3-130}$$

where H (H = 1,000 MPa) is Henry's constant. It is expected that the influence of air dissolved in the general problem is small so that this law is kept as an approximation (Olivella, 1995).

3.10. COMPUTER CODE

As mentioned before, the computer code CODE_BRIGHT (Olivella *et al.*, 1996; CODE_BRIGHT User's Guide, 2014) is the finite element code used to implement the double-porosity formulation (presented in this Thesis) and to handle coupled THM problems in geological media. The governing equations (balance equations) and the constitutive laws described in the previous sections are incorporated into the code in several subroutines written in FORTRAN.

A system of Partial Differential Equations (PDE's) arising from the balance equations presented in **Section 3.7** are solved numerically, in which solid displacements (for mechanical problems),

liquid and gas pressures (for hydraulic problems) and temperatures (for thermal problems) are the state variables (unknowns). Once the state variables are calculated, dependent variables are determined through the constitutive equations or the equilibrium restrictions. Thermal and fluid advective and non-advective flows, strains, stresses, concentration of water vapour and dissolved air are some of those dependent variables. The theoretical approach is formulated under the assumption of small strains and small rates for solid deformations. Prescribed forces or displacement rate in any spatial direction and at any node are the boundary conditions that can be used in mechanical problems. Mass flow rate of water and air or liquid/gas pressures (in hydraulic analyses) and heat flow or temperature (for thermal problems) can be prescribed at any node of the mesh (Olivella *et al.*, 1996).

The numerical approach is formulated by means of the use of Galerkin finite element method for the spatial discretization while finite differences are used for the discretization in time (CODE_BRIGHT User's Guide, 2014). Regarding the spatial discretization, it is important to remark that different types of elements are available (segments, triangles, quadrilaterals, tetrahedrons, triangular and quadrilateral prisms). Hence, one dimensional (uniaxial confined strain and axisymmetric), two dimensional (plane strain and axisymmetric) and three dimensional analyses can be performed. The temporal discretization is linear and the iterative Newton-Raphson method is adopted as the numerical scheme employed to solve the non-linear system of PDE's. Furthermore, an automatic discretization of time that depends on the variation of unknowns per iteration or on the number of iterations to reach convergence is included in the code. Convergence criteria are evaluated by means of the simultaneous accomplishment of predefined error tolerances for forces or flows and/or for the state variables of each problem (mechanical, hydraulic, thermal, etc.) solved during the performance of a numerical analysis (CODE_BRIGHT User's Guide, 2014).

4. DOUBLE POROSITY FORMULATION: STRESS-STRAIN CONSTITUTIVE LAWS IN A THERMO-ELASTOPLASTICITY FRAMEWORK

4.1. INTRODUCTION

The mechanical constitutive model is considered as the key element of the double-structure model described in this Thesis. Due to that, the main aspects of the mechanical part of the mathematical formulation need to be addressed properly, especially those ones related to stress-strain relationships for both media and the structural interaction between them.

The stress/strain field in a porous medium, when thermo-hydro-mechanical (THM) analyses are performed, is strongly affected by:

i. the thermal effects induced by changes in temperature. As already discussed in **Section 2.5**, the application of thermal loads essentially induces the volumetric expansion (or contraction) of minerals (Campanella and Mitchell, 1968) and the differential expansion between the solid particles and the fluid species present in a volume of the porous material (Baldi *et al.*, 1988). The thermal softening of the elastic domain (as temperature increases) and the thermally-induced hardening (structural collapse) in fine-grained soils with an open structure are some of the thermo-mechanical (TM) coupling effects observed experimentally (Hueckel and Baldi, 1990; Hueckel and Pellegrini, 1996; Delage *et al.*, 2000; Laloui and Cekerevac, 2003; Salager *et al.*, 2008). Moreover, heating tests carried out on over-consolidated clays have also shown a dependence of the magnitude and the nature of the thermal volumetric strains (thermal expansion/contraction) on the over-consolidation ratio (OCR) (Baldi *et al.*, 1988; Hueckel and Baldi, 1990; Towhata *et al.*, 1993; Delage *et al.*, 2000; Laloui and Cekerevac, 2008);

ii. the hydraulic effects related to suction changes under non-saturated conditions or to the excess of water pressure in saturated pores (effective stress concept). Suction plays an important role in partially saturated soils as its evolution alters the capillary inter-

particle forces and the proneness of open structures to collapse during wetting under high confining pressures (Karube and Kato, 1994; Wheeler and Karube, 1995; Karube and Kawai, 2001; Gallipoli *et al.*, 2003). On the other hand, the drying process in unsaturated soils usually leads to an increment in the effective stress acting on the soil skeleton and to a stiffer response of the soil when loaded (Alonso *et al.*, 1990; Bagherieh *et al.*, 2009). Furthermore, moderate and highly expansive materials subjected to wetting-drying cycles under constant confining stresses may exhibit accumulative (non-reversible) expansion or shrinkage at the end of each cycle (Pousada, 1984; Dif and Bluemel, 1991);

iii. the stress level and the stress history. Dilatant or contractant behaviour of a soil under shear loading depends on the magnitude of the confining stresses applied to the porous skeleton while strength parameters are dependent on the history of stress loadings applied to a soil (Nishimura *et al.*, 1999; Lipinski and Wdowska, 2011). In addition, it is also known that the mechanical behavior of a soil is also dependent on the solid particle arrangement and the pore size distribution (Mitchell, 1976; Leroueil and Vaughan, 1990; Vanapalli *et al.*, 1999). This fact evidences the importance of the prevailing conditions during soil formation and throughout its geological/geotechnical history on the way the porous medium experiences elastoplastic deformations when subjected to loading.

In view of the above-mentioned THM effects on the mechanical constitutive behaviour, the development of a fully coupled elastoplastic formulation is required to reproduce the main mechanical features observed from laboratory tests and in situ engineering practices. The main goal of this chapter is to find a stress-strain relationship suitable to simulate the mechanical behaviour of expansive clays subjected to thermal loadings in the framework of a multi-porosity approach. Due to the strong non-linearity of the proposed elastoplastic constitutive law, the stress-strain relationship is formulated in incremental/rate form. Consequently, all the relevant relations defined hereafter are given by means of rate equations. The general expressions for the strain and the stress vectors for each structural level (macro and micro) when subjected to temperature changes are also provided.

4.2. STRESS-STRAIN RELATIONSHIP IN A DOUBLE-POROSITY APPROACH

A direct consequence of assuming the expansive clay as two interacting continuous media coupled through leakage terms is the possibility of establishing distinct stress-strain constitutive relationships for each structural level. For that purpose, it is desirable to describe the main phenomena that governs the mechanical response in each porous medium by its own properties (porosity, permeability, degree of saturation among others) and state variables. The coupling between media is accomplished through the mass transfer processes (see **Section 3.6**) and through the interaction strain mechanisms that account for the portion of macrostructural strains arising from the deformations that occur at particle level (microstructure). Furthermore, the definition of the micro- and macro-pore volume fractions according to Equation (3-5) lays the conceptual basis for the additive decomposition of total strains into a micro and a macro strain components (see **Section 4.2.1**). Stress-small strain constitutive laws are then defined for each level (**Sections 4.2.2** and **Section 4.2.3**) but a special effort is devoted to describe the

mechanical response of the expansive clay (as a whole) from the mechanical behaviour of individual active clay particles (that is, microstructure). The reason for assuming such a constitutive approach is the fact that the observable strain irreversibility and the stress path dependency in compacted expansive soils can be explained as a consequence of the physico-chemical phenomena occurring at clay particle level (Gens and Alonso, 1992; Sánchez and Gens, 2006).

4.2.1. ADDITIVE DECOMPOSITION OF THE TOTAL STRAIN TENSOR

In order to postulate a proper relationship between strain and stress tensors in the framework of a double-porosity model, it is assumed the existence of two strain tensors: one arising from the volumetric deformation of individual particles/aggregates (the "micro" component, $\dot{\boldsymbol{\varepsilon}}_m$) and the other related to the particle arrangement in the soil skeleton (the "macro" component, $\dot{\boldsymbol{\varepsilon}}_M$). Consequently, the total strain rate of an expansive soil ($\dot{\boldsymbol{\varepsilon}}$) is given by the following "geometric" decomposition

$$\dot{\boldsymbol{\varepsilon}} = \dot{\bar{\boldsymbol{\varepsilon}}}_m + \dot{\bar{\boldsymbol{\varepsilon}}}_M \tag{4-1}$$

Note that the "micro" strain tensor in Equation (4-1) is defined as the change of microstructural volume (micro-pores + solid particles) over the total volume of the soil. This strain component is referred to as the "global" micro strain component hereafter, or simply, as the micro strain component. As discussed in the preceding chapter (**Section 3.4**, Equation (3-48)), this micro strain tensor can be related to the "local" (the "aggregate") micro strain tensor, $\dot{\boldsymbol{\varepsilon}}_m$, according to

$$\dot{\bar{\boldsymbol{\varepsilon}}}_m = \frac{1+e_m}{1+e}\,\dot{\boldsymbol{\varepsilon}}_m \tag{4-2}$$

The latter equation takes into account the volumetric ratio between the actual micro medium, expressed by its specific volume, $v_m = 1 + e_m$, and the whole soil, whose specific volume is given by $v = 1 + e$.

Microstructural strains are considered volumetric and fully reversible (Sánchez and Gens, 2006). As a consequence, the vector notation of the micro strain component at isotropic conditions is given by

$$\dot{\bar{\boldsymbol{\varepsilon}}}_m \equiv \dot{\bar{\boldsymbol{\varepsilon}}}_m^e = \frac{1}{3}\,\dot{\varepsilon}_m^{e,vol}\,\boldsymbol{m} \tag{4-3}$$

where $\dot{\varepsilon}_m^{e,vol}$ is the volumetric (elastic) micro strain rate and $\boldsymbol{m} = [1 \quad 1 \quad 1 \quad 0 \quad 0 \quad 0]^T$ is an auxiliary vector. Assuming the split of micro deformations into a component related to changes in the effective stress (see **Section 3.3**) acting on the expansive soil, $\dot{\bar{\boldsymbol{\varepsilon}}}_{m,\Delta\sigma}$, and into a micro strain component due to temperature changes, $\dot{\bar{\boldsymbol{\varepsilon}}}_{m,\Delta T}$, the following additive relationship is achieved

$$\dot{\boldsymbol{\varepsilon}}_m = \dot{\boldsymbol{\varepsilon}}_{m,\Delta\sigma_m} + \dot{\boldsymbol{\varepsilon}}_{m,\Delta T} \tag{4-4}$$

in which $\dot{\boldsymbol{\varepsilon}}_{m,\Delta T}$ measures the changes in the volumetric thermal expansion of an individual clay aggregate with respect to the total volume of the porous medium. This component is related to the "local" (true) volumetric thermal expansion of the microstructure (when this volumetric deformation is considered over the volume of the clay aggregate itself), $\dot{\boldsymbol{\varepsilon}}_{m,\Delta T}$, as follows

$$\dot{\boldsymbol{\varepsilon}}_{m,\Delta T} = \frac{1+e_m}{1+e}\,\dot{\boldsymbol{\varepsilon}}_{m,\Delta T} \tag{4-5}$$

The strain field of the macro medium ($\dot{\boldsymbol{\varepsilon}}_M$) is split into an elastic tensor ($\dot{\boldsymbol{\varepsilon}}_M^e$) which accounts for all the reversible deformations that take place at this structural level and a non-reversible component ($\dot{\boldsymbol{\varepsilon}}_M^p$) responsible for the structural changes observed in the soil fabric. This additive decomposition is expressed by

$$\dot{\boldsymbol{\varepsilon}}_M = \dot{\boldsymbol{\varepsilon}}_M^e + \dot{\boldsymbol{\varepsilon}}_M^p \tag{4-6}$$

An important feature to take into account when dealing with expansive soils is the fact that the macro-pore structure can be affected by microstructural deformations (Gens and Alonso, 1992; Alonso *et al.*, 1999; Sánchez *et al.*, 2005). In a general framework, it can be assumed that deformations of macrostructure due to microstructural strains ($\dot{\boldsymbol{\varepsilon}}_{m\to M}$) are composed by a reversible ($\dot{\boldsymbol{\varepsilon}}_{m\to M}^e$) and an irreversible ($\dot{\boldsymbol{\varepsilon}}_{m\to M}^p$) component, according to

$$\dot{\boldsymbol{\varepsilon}}_{m\to M} = \dot{\boldsymbol{\varepsilon}}_{m\to M}^e + \dot{\boldsymbol{\varepsilon}}_{m\to M}^p = \dot{\boldsymbol{\varepsilon}}_{m\to M,HM}^e + \dot{\boldsymbol{\varepsilon}}_{m\to M,\Delta T}^e + \dot{\boldsymbol{\varepsilon}}_{M,\beta}^p \tag{4-7}$$

in which the elastic component of the macro strains due to micro-macro coupling expresses, in an explicit way, the strain contributions due to hydro-mechanical ($\dot{\boldsymbol{\varepsilon}}_{m\to M,HM}^e$) and thermal ($\dot{\boldsymbol{\varepsilon}}_{m\to M,\Delta T}^e$) changes. The irreversible deformations of the macrostructure due to microstructural response ($\dot{\boldsymbol{\varepsilon}}_{M,\beta}^p$) are related to (what is defined from now on as) the "β-mechanism". A detailed explanation about this plastic mechanism is presented in **Section 4.4.2**. Despite the fact that micro strains can induce strains at macrostructural level, it is assumed that the microstructural behaviour is not affected by the deformations of macrostructure (Sánchez and Gens, 2006).

Irreversible collapse of porous structure in a partially saturated soil may occur during the performance of wetting paths, for a given confining stress, in open macrostructures. The magnitude of this structural collapse usually increases with increasing the net confining pressures (Alonso *et al.*, 1990). In fact, the wetting-induced swelling or collapse observed in many unsaturated non-expansive soils is dependent on the applied stress level. Moreover, the increase in the shear strength and the apparent pre-consolidation stress with suction is another typical mechanical response observed in non-saturated soils. The elastoplastic ***B**arcelona **B**asic **M**odel* (BBM) developed by Alonso *et al.* (1990) has demonstrated the ability to predict such mechanical behaviour features. Moreover, an extended version of the original BBM was implemented by Gens (1995) in order to enable the performance of numerical analyses under non-isothermal conditions (as mentioned in **Section 2.5.5**). The thermo-elastoplastic BBM formulation has been used to model many practical geotechnical problems in clayey materials,

reproducing satisfactorily most of the experimental observations and relevant phenomena that take place in unsaturated porous media (Sánchez and Gens, 2006; Hoffman *et al.*, 2007; Gens *et al.*, 2009b; Gaus *et al.*, 2014b; Rutqvist *et al.*, 2014; Toprak *et al.*, 2016; Gens and Vasconcelos, 2019). Due to that, this model has been selected to describe the loading-collapse (LC) mechanism of macrostructure in this Thesis. A brief description of the main features of the BBM model is given in **Section 4.4.1**.

From all those assumptions presented previously, the following general expressions for the elastic ($\dot{\boldsymbol{\varepsilon}}_M^e$) and the plastic ($\dot{\boldsymbol{\varepsilon}}_M^p$) rate components of the macrostructural strains are obtained:

$$\begin{aligned} \dot{\boldsymbol{\varepsilon}}_M^e &= \dot{\boldsymbol{\varepsilon}}_{M,\Delta\sigma_M}^e + \dot{\boldsymbol{\varepsilon}}_{M,\Delta s}^e + \dot{\boldsymbol{\varepsilon}}_{m\to M}^e = \dot{\boldsymbol{\varepsilon}}_{M,\Delta\sigma_M}^e + \dot{\boldsymbol{\varepsilon}}_{M,\Delta s}^e + \dot{\boldsymbol{\varepsilon}}_{m\to M,HM}^e + \dot{\boldsymbol{\varepsilon}}_{m\to M,\Delta T}^e \\ \dot{\boldsymbol{\varepsilon}}_M^p &= \dot{\boldsymbol{\varepsilon}}_{M,LC}^p + \dot{\boldsymbol{\varepsilon}}_{m\to M}^p = \dot{\boldsymbol{\varepsilon}}_{M,LC}^p + \dot{\boldsymbol{\varepsilon}}_{M,\beta}^p \end{aligned} \tag{4-8}$$

and then, the strain rate tensor for the macro medium is expressed by

$$\dot{\boldsymbol{\varepsilon}}_M = \dot{\boldsymbol{\varepsilon}}_{M,\Delta\sigma_M}^e + \dot{\boldsymbol{\varepsilon}}_{M,\Delta s}^e + \dot{\boldsymbol{\varepsilon}}_{m\to M,HM}^e + \dot{\boldsymbol{\varepsilon}}_{m\to M,\Delta T}^e + \dot{\boldsymbol{\varepsilon}}_{M,LC}^p + \dot{\boldsymbol{\varepsilon}}_{M,\beta}^p \tag{4-9}$$

where $\dot{\boldsymbol{\varepsilon}}_{M,\Delta\sigma_M}^e$ and $\dot{\boldsymbol{\varepsilon}}_{M,\Delta s}^e$ are the elastic macro strain rate components due changes in the (net/constitutive) mean stress and in the macrostructural suction, respectively, while $\dot{\boldsymbol{\varepsilon}}_{M,LC}^p$ is the plastic deformation rate related to the loading-collapse mechanism (plastic mechanism considered in the BBM formulation). An important hypothesis/simplification assumed in this Thesis is that temperature variations are not the direct cause of irreversible collapse of macrostructure. Consequently, the plastic strain component in Equation (4-8) does not depend on temperature, at least not explicitly. Nevertheless, structural rearrangements of the soil skeleton due to the thermally-induced changes in pore-water state and content are allowed. In such conditions, irreversible strains arise from the significant changes in suction as pores are dried or re-saturated in response to the applied thermal loading. It is important to remark that the thermo-elastoplastic BBM formulation by Gens (1995) includes the dependence of the elastic domain size on temperature.

The total strain rate in Equation (4-1) can be also written in terms of its elastic ($\dot{\boldsymbol{\varepsilon}}^e$) and plastic ($\dot{\boldsymbol{\varepsilon}}^p$) parts, according to the following general expression:

$$\dot{\boldsymbol{\varepsilon}} = \dot{\boldsymbol{\varepsilon}}^e + \dot{\boldsymbol{\varepsilon}}^p = \left(\dot{\boldsymbol{\varepsilon}}_m^e + \dot{\boldsymbol{\varepsilon}}_M^e\right) + \dot{\boldsymbol{\varepsilon}}_M^p \tag{4-10}$$

Recalling Equation (4-4) and Equation (4-9), these strain components are expressed, respectively, as

$$\begin{aligned} \dot{\boldsymbol{\varepsilon}}^e &= \underbrace{\left(\dot{\boldsymbol{\varepsilon}}_{m,\Delta\sigma_m}^e + \dot{\boldsymbol{\varepsilon}}_{m,\Delta T}^e\right)}_{\dot{\boldsymbol{\varepsilon}}_m^e} + \underbrace{\left(\dot{\boldsymbol{\varepsilon}}_{M,\Delta\sigma_M}^e + \dot{\boldsymbol{\varepsilon}}_{M,\Delta s}^e + \dot{\boldsymbol{\varepsilon}}_{m\to M,HM}^e + \dot{\boldsymbol{\varepsilon}}_{m\to M,\Delta T}^e\right)}_{\dot{\boldsymbol{\varepsilon}}_M^e} \\ \dot{\boldsymbol{\varepsilon}}^p &= \dot{\boldsymbol{\varepsilon}}_{M,LC}^p + \dot{\boldsymbol{\varepsilon}}_{M,\beta}^p \end{aligned} \tag{4-11}$$

Thus, the "expanded" rate form of the total strains, obtained from the elastic and plastic strain components developed in micro and macro media, is written as

$$\dot{\boldsymbol{\varepsilon}} = \underbrace{\left(\dot{\bar{\boldsymbol{\varepsilon}}}^{e}_{m,\Delta\sigma_m} + \dot{\bar{\boldsymbol{\varepsilon}}}^{e}_{m,\Delta T} + \dot{\bar{\boldsymbol{\varepsilon}}}^{e}_{M,\Delta\sigma_M} + \dot{\bar{\boldsymbol{\varepsilon}}}^{e}_{M,\Delta s} + \dot{\bar{\boldsymbol{\varepsilon}}}^{e}_{m\to M,HM} + \dot{\bar{\boldsymbol{\varepsilon}}}^{e}_{m\to M,\Delta T}\right)}_{\dot{\boldsymbol{\varepsilon}}^{e}} + \underbrace{\left(\dot{\bar{\boldsymbol{\varepsilon}}}^{p}_{M,LC} + \dot{\bar{\boldsymbol{\varepsilon}}}^{p}_{M,\beta}\right)}_{\dot{\boldsymbol{\varepsilon}}^{p}} \tag{4-12}$$

4.2.2. STRESS-STRAIN AT MACROSTRUCTURAL LEVEL

Based on the considerations exposed in the previous section and taking in account the macrostructural strain components in Equation (4-9), it is possible to establish a straight relationship between the changes in the constitutive (effective) stress acting on macrostructure ($\dot{\boldsymbol{\sigma}}_M$) and the corresponding elastic strain rates ($\dot{\bar{\boldsymbol{\varepsilon}}}^{e}_{M,\Delta\sigma_M}$) given by

$$\dot{\boldsymbol{\sigma}}_M = [\bar{\boldsymbol{D}}^{e}_{M}]\dot{\bar{\boldsymbol{\varepsilon}}}^{e}_{M,\Delta\sigma_M} = [\bar{\boldsymbol{D}}^{e}_{M}]\left(\dot{\bar{\boldsymbol{\varepsilon}}}_M - \dot{\bar{\boldsymbol{\varepsilon}}}^{e}_{M,\Delta s} - \dot{\bar{\boldsymbol{\varepsilon}}}^{e}_{m\to M} - \dot{\bar{\boldsymbol{\varepsilon}}}^{p}_{M,LC} - \dot{\bar{\boldsymbol{\varepsilon}}}^{p}_{M,\beta}\right) \tag{4-13}$$

where $[\bar{\boldsymbol{D}}^{e}_{M}]$ is the elastic macrostructural constitutive tensor. It is important to remark that the effective stress level (and the effective stress rates as well) on macrostructure is assumed to be the stress field that acts on the porous medium as a whole, that is, $\boldsymbol{\sigma_M} = \boldsymbol{\sigma}$ (see **Section 3.3**). Consequently, the macrostructural effective stress rate is assumed to be equal to the rate of effective stress applied to the expansive soil, $\dot{\boldsymbol{\sigma}}_{\boldsymbol{M}} = \dot{\boldsymbol{\sigma}}$. Therefore,

$$\dot{\boldsymbol{\sigma}} = [\bar{\boldsymbol{D}}^{e}_{M}]\left(\dot{\bar{\boldsymbol{\varepsilon}}}_M - \dot{\bar{\boldsymbol{\varepsilon}}}^{e}_{M,\Delta s} - \dot{\bar{\boldsymbol{\varepsilon}}}^{e}_{m\to M} - \dot{\bar{\boldsymbol{\varepsilon}}}^{p}_{M,LC} - \dot{\bar{\boldsymbol{\varepsilon}}}^{p}_{M,\beta}\right) \tag{4-14}$$

Moreover, and since the BBM model is used to describe the mechanical behaviour of macrostructure, the effective stress state in this structural level is given by Equation (3-38), taken as a particular case of the general stress state defined by Equation (3-28). This particular situation has already been taken into account when defining the macrostructural strain components in Equation (4-8) and the constitutive stress-strain relationship in Equation (4-13).

The macrostructural constitutive tensor is defined according to

$$[\bar{\boldsymbol{D}}^{e}_{M}] = \begin{bmatrix} \bar{K}_M + \frac{4}{3}\bar{G}_M & \bar{K}_M - \frac{2}{3}\bar{G}_M & \bar{K}_M - \frac{2}{3}\bar{G}_M & 0 & 0 & 0 \\ \bar{K}_M - \frac{2}{3}\bar{G}_M & \bar{K}_M + \frac{4}{3}\bar{G}_M & \bar{K}_M - \frac{2}{3}\bar{G}_M & 0 & 0 & 0 \\ \bar{K}_M - \frac{2}{3}\bar{G}_M & \bar{K}_M - \frac{2}{3}\bar{G}_M & \bar{K}_M + \frac{4}{3}\bar{G}_M & 0 & 0 & 0 \\ 0 & 0 & 0 & \bar{G}_M & 0 & 0 \\ 0 & 0 & 0 & 0 & \bar{G}_M & 0 \\ 0 & 0 & 0 & 0 & 0 & \bar{G}_M \end{bmatrix} \tag{4-15}$$

where $\bar{K}_M$ and $\bar{G}_M$ are, respectively, the macrostructural bulk and the shear moduli for changes in the stress level. These elastic moduli are defined by the following expressions:

$$\bar{K}_M = \frac{(1+\bar{e}_M)}{\bar{\kappa}_M} p \tag{4-16}$$

and

$$\bar{G}_M = \frac{3(1-2\bar{\upsilon}_M)}{2(1+\bar{\upsilon}_M)} \bar{K}_M \tag{4-17}$$

where $\bar{\kappa}_M$ is a macrostructural elastic stiffness parameter for the BBM model associated to changes in the mean effective stress (p), $\bar{\upsilon}_M$ is the macro Poisson's ratio and $\bar{e}_M$ ($\bar{e}_M = \frac{\bar{\phi}_M}{1-\bar{\phi}_M}$) is defined as the macrostructural void ratio.

Another important elastic coefficient is the bulk modulus against changes in the macro suction, $\bar{K}_s$, expressed by

$$\bar{K}_s = \frac{(1+\bar{e}_M)(s_M + p_{atm})}{\bar{\kappa}_s} \tag{4-18}$$

which defines the macro strain component $\dot{\bar{\boldsymbol{\varepsilon}}}^e_{M,\Delta s}$ as follows

$$\dot{\bar{\boldsymbol{\varepsilon}}}^e_{M,\Delta s} = \frac{1}{3\bar{K}_s} \dot{s}_M \boldsymbol{m} \tag{4-19}$$

where s_M is the macrostructural suction, $\bar{\kappa}_s$ is the (macro) compression parameter model related to the changes in the water potential in macro-pores and p_{atm} is the atmospheric pressure. It is important to highlight that the values of some mechanical parameters used in the classical formulation of the BBM (a single-porosity model) do not necessarily coincide with the values of their "analogous" macrostructural parameters in the double-porosity model here proposed. A simple comparison of the expressions in Equation (4-16) and Equation (4-18) with the corresponding bulk moduli expressions presented in Alonso *et al.* (1990) makes this clear.

The total macrostructural deformations (Equation (4-9)) can be expressed in terms of the rate of the effective stress in the expansive soil ($\dot{\boldsymbol{\sigma}}$) according to

$$\dot{\bar{\boldsymbol{\varepsilon}}}_M = [\bar{\boldsymbol{D}}^e_M]^{-1} \dot{\boldsymbol{\sigma}} + \dot{\bar{\boldsymbol{\varepsilon}}}^e_{M,\Delta s} + \dot{\bar{\boldsymbol{\varepsilon}}}^e_{m\to M} + \dot{\bar{\boldsymbol{\varepsilon}}}^p_{M,LC} + \dot{\bar{\boldsymbol{\varepsilon}}}^p_{M,\beta} \tag{4-20}$$

obtained by applying the tensor $[\bar{\boldsymbol{D}}^e_M]^{-1}$ to both sides of Equation (4-14) and rearranging the terms of the resulting expression. Explicit expressions for the plastic components ($\dot{\bar{\boldsymbol{\varepsilon}}}^p_{M,LC}$ and $\dot{\bar{\boldsymbol{\varepsilon}}}^p_{M,\beta}$) and the elastic micro-macro coupling term ($\dot{\bar{\boldsymbol{\varepsilon}}}^e_{m\to M}$) of the total macrostructural deformations ($\dot{\bar{\boldsymbol{\varepsilon}}}_M$) are given in the following sections.

4.2.3. STRESS-STRAIN AT MICROSTRUCTURAL LEVEL

It has been assumed that the mechanical behaviour of microstructure is not affected by the macrostructure state but it only depends on the physico-chemical phenomena that take place at this structural level (Gens and Alonso, 1992; Sánchez *et al.*, 2005; Sánchez and Gens, 2006). In other words, the deformation response of microstructure is related to changes in the local (microstructural) stresses and environmental variables (water content, temperature, etc.). Furthermore, these microstructural strains are purely elastic (i.e. reversible) and volumetric (Alonso *et al.*, 1999; Sánchez *et al.*, 2005; Sánchez and Gens, 2006; Gens *et al.*, 2011). Since the mechanical behaviour of the expansive clay is formulated in function of the evolution of the pore volume fractions (see **Section 3.5** and Equation (4-1)), the tensor expression for the microstructural stress-strain relationship can be expressed as

$$\dot{\boldsymbol{\sigma}}_m = [\bar{\boldsymbol{D}}_m^e]\dot{\boldsymbol{\varepsilon}}_{m,\Delta\sigma_m}^e = [\bar{\boldsymbol{D}}_m^e]\left(\dot{\boldsymbol{\varepsilon}}_m^e - \dot{\boldsymbol{\varepsilon}}_{m,\Delta T}^e\right) \tag{4-21}$$

where the elastic constitutive tensor of microstructure, $[\bar{\boldsymbol{D}}_m^e]$, written in terms of the microstructural bulk ($\bar{K}_m$) and shear ($\bar{G}_m$) moduli, is given by

$$[\bar{\boldsymbol{D}}_m^e] = \begin{bmatrix} \bar{K}_m + \frac{4}{3}\bar{G}_m & \bar{K}_m - \frac{2}{3}\bar{G}_m & \bar{K}_m - \frac{2}{3}\bar{G}_m & & & \\ \bar{K}_m - \frac{2}{3}\bar{G}_m & \bar{K}_m + \frac{4}{3}\bar{G}_m & \bar{K}_m - \frac{2}{3}\bar{G}_m & \begin{matrix}0&0&0\\0&0&0\\0&0&0\end{matrix} & & \\ \bar{K}_m - \frac{2}{3}\bar{G}_m & \bar{K}_m - \frac{2}{3}\bar{G}_m & \bar{K}_m + \frac{4}{3}\bar{G}_m & & & \\ & \begin{matrix}0&0&0\\0&0&0\\0&0&0\end{matrix} & & \begin{matrix}\bar{G}_m&0&0\\0&\bar{G}_m&0\\0&0&\bar{G}_m\end{matrix} \end{bmatrix} \tag{4-22}$$

On the other hand, the local microstructural stress-strain relationship (at the clay aggregate level) is given by

$$\dot{\boldsymbol{\sigma}}_m = [\boldsymbol{D}_m^e]\dot{\boldsymbol{\varepsilon}}_{m,\Delta\sigma_m}^e = [\boldsymbol{D}_m^e]\left(\dot{\boldsymbol{\varepsilon}}_m^e - \dot{\boldsymbol{\varepsilon}}_{m,\Delta T}^e\right) \tag{4-23}$$

where $[\boldsymbol{D}_m^e]$ is the elastic tensor that relates the changes in the microstructural effective stresses acting on a clay aggregate ($\dot{\boldsymbol{\sigma}}_m$) to the volumetric deformations experienced by the aggregate ($\dot{\boldsymbol{\varepsilon}}_{m,\Delta\sigma_m}^e$) due to changes in microstructural stresses and suctions. This elastic tensor is evaluated by means of the bulk (K_m) and shear (G_m) moduli of the clay aggregates ("actual" microstructure) as follows:

$$[\boldsymbol{D}_m^e] = \begin{bmatrix} K_m + \frac{4}{3}G_m & K_m - \frac{2}{3}G_m & K_m - \frac{2}{3}G_m & & & \\ K_m - \frac{2}{3}G_m & K_m + \frac{4}{3}G_m & K_m - \frac{2}{3}G_m & & \mathbf{0} & \\ K_m - \frac{2}{3}G_m & K_m - \frac{2}{3}G_m & K_m + \frac{4}{3}G_m & & & \\ & \mathbf{0} & & G_m & 0 & 0 \\ & & & 0 & G_m & 0 \\ & & & 0 & 0 & G_m \end{bmatrix} \tag{4-24}$$

The elastic parameters used to determine the microstructural constitutive tensors are defined by the following expressions:

$$\bar{K}_m = \frac{1+e}{1+e_m} K_m \tag{4-25}$$

$$\bar{G}_m = \frac{3(1-2\bar{\upsilon}_m)}{2(1+\bar{\upsilon}_m)} \bar{K}_m \tag{4-26}$$

with

$$K_m = \frac{1+e_m}{\kappa_m} p_m \tag{4-27}$$

where κ_m is the elastic stiffness parameter of an individual clay aggregate related to changes in the mean micro effective stress (p_m) and $\bar{\upsilon}_m$ is the "global" Poisson's ratio for the micro medium. Note that the bulk modulus $\bar{K}_m$ is an elastic parameter associated with the volumetric deformation of microstructure respect to the volume of the whole expansive soil.

Taking into account the general expression for the microstructural constitutive stress defined by Equation (3-31), the rate of the micro effective stress is expressed according to

$$\begin{aligned} \dot{\boldsymbol{\sigma}}_m = \dot{\boldsymbol{\sigma}} &+ \left(\left(P_{gm} - P_{lm}\right)\dot{\chi}_m + \chi_m\left(\dot{P}_{gm} - \dot{P}_{lm}\right) - \dot{P}_{gm} \right) \boldsymbol{m} \\ &- \left(\left(P_{gM} - P_{lM}\right)\dot{\chi}_M + \chi_M\left(\dot{P}_{gM} - \dot{P}_{lM}\right) - \dot{P}_{gM} \right) \boldsymbol{m} \end{aligned} \tag{4-28}$$

in which the dependence of the Bishop parameters (χ_m and χ_M) on the saturation state of each structural level is considered as well as the retention curve dependency on changes in the fluid pressures and temperature, that is,

$$\dot{\chi}_m = \frac{\partial \chi_m}{\partial S_{lm}} \dot{S}_{lm} = \frac{\partial \chi_m}{\partial S_{lm}} \left(\frac{\partial S_{lm}}{\partial P_{lm}} \dot{P}_{lm} + \frac{\partial S_{lm}}{\partial P_{gm}} \dot{P}_{gm} + \frac{\partial S_{lm}}{\partial T} \dot{T} \right) \tag{4-29}$$

$$\dot{\chi}_M = \frac{\partial \chi_M}{\partial S_{lM}} \dot{S}_{lM} = \frac{\partial \chi_M}{\partial S_{lM}} \left(\frac{\partial S_{lM}}{\partial P_{lM}} \dot{P}_{lM} + \frac{\partial S_{lM}}{\partial P_{gM}} \dot{P}_{gM} + \frac{\partial S_{lM}}{\partial T} \dot{T} \right) \tag{4-30}$$

Applying the tensor $[\overline{\boldsymbol{D}}_m^e]^{-1}$ to both sides of Equation (4-21) and after rearranging the terms of the resultant relationship, an explicit expression for the (total) microstructural strain rate, $\dot{\boldsymbol{\varepsilon}}_m^e$, is obtained:

$$\dot{\boldsymbol{\varepsilon}}_m^e = [\overline{\boldsymbol{D}}_m^e]^{-1}\dot{\boldsymbol{\sigma}}_m + \dot{\boldsymbol{\varepsilon}}_{m,\Delta T}^e \tag{4-31}$$

On the other hand, an expression for the microstructural deformation rate, in terms of the changes in the effective stress acting on the whole soil ($\dot{\boldsymbol{\sigma}}$), can be achieved by means of inserting Equation (4-28) into Equation (4-31), that is,

$$\begin{aligned}\dot{\boldsymbol{\varepsilon}}_m^e = {} & [\overline{\boldsymbol{D}}_m^e]^{-1}\dot{\boldsymbol{\sigma}} \\ & + \frac{1}{3\overline{K}_m}\Big(\big(\zeta_{gm}\dot{P}_{gm} + \zeta_{lm}\dot{P}_{lm}\big) - \big(\zeta_{gM}\dot{P}_{gM} + \zeta_{lM}\dot{P}_{lM}\big) + \zeta_T\dot{T}\Big)\boldsymbol{m} \\ & + \dot{\boldsymbol{\varepsilon}}_{m,\Delta T}^e\end{aligned} \tag{4-32}$$

in which the following functions of saturation (for the micro and macro media) are defined

$$\zeta_{gm} = \big(P_{gm} - P_{lm}\big)\frac{\partial \chi_m}{\partial S_{lm}}\frac{\partial S_{lm}}{\partial P_{gm}} + \chi_m - 1 \tag{4-33}$$

$$\zeta_{lm} = \big(P_{gm} - P_{lm}\big)\frac{\partial \chi_m}{\partial S_{lm}}\frac{\partial S_{lm}}{\partial P_{lm}} - \chi_m \tag{4-34}$$

$$\zeta_{gM} = \big(P_{gM} - P_{lM}\big)\frac{\partial \chi_M}{\partial S_{lM}}\frac{\partial S_{lM}}{\partial P_{gM}} + \chi_M - 1 \tag{4-35}$$

$$\zeta_{lM} = \big(P_{gM} - P_{lM}\big)\frac{\partial \chi_M}{\partial S_{lM}}\frac{\partial S_{lM}}{\partial P_{gM}} - \chi_M \tag{4-36}$$

$$\zeta_T = \big(P_{gm} - P_{lm}\big)\frac{\partial \chi_m}{\partial S_{lm}}\frac{\partial S_{lm}}{\partial T} - \big(P_{gM} - P_{lM}\big)\frac{\partial \chi_M}{\partial S_{lM}}\frac{\partial S_{lM}}{\partial T} \tag{4-37}$$

A more compacted (and useful) expression for the micro effective stress rate (Equation (4-28)) can be obtained. After some algebraic manipulation, the following expression is achieved, in which the factors defined from Equation (4-33) to Equation (4-37) have been used:

$$\dot{\boldsymbol{\sigma}}_m = \dot{\boldsymbol{\sigma}} + \big(\zeta_{gm}\dot{P}_{gm} + \zeta_{lm}\dot{P}_{lm} - \zeta_{gM}\dot{P}_{gM} - \zeta_{lM}\dot{P}_{lM} + \zeta_T\dot{T}\big)\boldsymbol{m} \tag{4-38}$$

However, for the particular case in which χ_M is defined by a step-shape function (see Equation (3-36)) with $\chi_M = 1$ when macro-pores are fully saturated with water ($S_{lM} = 1$) and $\chi_M = 0$ otherwise, the microstructural effective stress is expressed by Equation (3-39) and its rate form reduces to

$$\dot{\boldsymbol{\sigma}}_m = \dot{\boldsymbol{\sigma}} + \left(\left(P_{gm} - P_{lm}\right)\dot{\chi}_m + \chi_m\left(\dot{P}_{gm} - \dot{P}_{lm}\right) - \dot{P}_{gm} + \dot{P}_{fM}\right)\boldsymbol{m} \tag{4-39}$$

or, in its compacted form,

$$\dot{\boldsymbol{\sigma}}_m = \dot{\boldsymbol{\sigma}} + \left(\zeta_{gm}\dot{P}_{gm} + \zeta_{lm}\dot{P}_{lm} + \zeta_T\dot{T} + \dot{P}_{fM}\right)\boldsymbol{m} \tag{4-40}$$

with

$$\dot{P}_{fM} = \begin{cases} \dot{P}_{gM} \;\; if \;\; 0 < S_{lM} < 1 \\ \dot{P}_{lM} \;\; if \;\; S_{lM} = 1 \end{cases} \tag{4-41}$$

and

$$\zeta_T = \left(P_{gm} - P_{lm}\right)\frac{\partial \chi_m}{\partial S_{lm}}\frac{\partial S_{lm}}{\partial T} \tag{4-42}$$

In such conditions, Equation (4-32) is simplified to

$$\dot{\boldsymbol{\varepsilon}}^e_m = [\overline{\boldsymbol{D}}^e_m]^{-1}\dot{\boldsymbol{\sigma}} + \frac{1}{3\overline{K}_m}\left(\zeta_{gm}\dot{P}_{gm} + \zeta_{lm}\dot{P}_{lm} + \zeta_T\dot{T} + \dot{P}_{fM}\right)\boldsymbol{m} + \dot{\boldsymbol{\varepsilon}}^e_{m,\Delta T} \tag{4-43}$$

For the sake of simplicity, and taking into account that the mechanical response of macrostructure is described in terms of net stresses, Equation (4-40) and Equation (4-43) are used to establish the microstructural stress-strain relationship in the formulation of the double-porosity model, instead of Equation (4-38) and Equation (4-32). It is important to note that the previous expressions evidence the strong THM coupling of the mathematical formulation. In fact, the effects of the thermal variable on the retention curves of both structural levels are explicitly expressed in Equation (4-37) and Equation (4-42). As a consequence, it can be concluded that temperature changes affect the microstructure deformation behaviour by means of the dependence of hydraulic variables on temperature and through the thermal expansion of the microstructure itself. The thermal strain components (macro and micro) are defined in **Section 4.2.5**.

4.2.4. GLOBAL STRESS-STRAIN RELATIONSHIP (FOR THE EXPANSIVE SOIL)

The stress-strain constitutive equation for the expansive porous medium (that is, the soil as whole) can be found when the stress-strain relationships for macrostructure (Equation (4-20)) and microstructure (Equation (4-43)) are combined according to the assumption of the strain rate partition (Equation (4-1)). Then, the resulting constitutive relationship for the expansive clay is expressed by

$$\begin{aligned} \dot{\boldsymbol{\varepsilon}} = [\boldsymbol{D}^e]^{-1}\dot{\boldsymbol{\sigma}} + \frac{1}{3\overline{K}_m}\left(\zeta_{gm}\dot{P}_{gm} + \zeta_{lm}\dot{P}_{lm} + \zeta_T\dot{T} + \dot{P}_{fM}\right)\boldsymbol{m} + \dot{\boldsymbol{\varepsilon}}^e_{m,\Delta T} \\ + \dot{\boldsymbol{\varepsilon}}^e_{M,\Delta s} + \dot{\boldsymbol{\varepsilon}}^e_{m\to M} + \dot{\boldsymbol{\varepsilon}}^p_{M,LC} + \dot{\boldsymbol{\varepsilon}}^p_{M,\beta} \end{aligned} \tag{4-44}$$

where $[\boldsymbol{D}^e]$ is the global elastic matrix, expressed in terms of the macro and micro constitutive matrices as follows

$$[\boldsymbol{D}^e]^{-1} = [\overline{\boldsymbol{D}}_m^e]^{-1} + [\overline{\boldsymbol{D}}_M^e]^{-1} \tag{4-45}$$

and defined by the bulk (K) and the shear (G) moduli for the whole soil according to

$$[\boldsymbol{D}^e] = \begin{bmatrix} K+\frac{4}{3}G & K-\frac{2}{3}G & K-\frac{2}{3}G & & & \\ K-\frac{2}{3}G & K+\frac{4}{3}G & K-\frac{2}{3}G & \begin{matrix}0&0&0\\0&0&0\\0&0&0\end{matrix} & & \\ K-\frac{2}{3}G & K-\frac{2}{3}G & K+\frac{4}{3}G & & & \\ & \begin{matrix}0&0&0\\0&0&0\\0&0&0\end{matrix} & & \begin{matrix}G&0&0\\0&G&0\\0&0&G\end{matrix} \end{bmatrix} \tag{4-46}$$

The mechanical behaviour of an expansive clay to external loadings and to changes in environmental conditions is mainly controlled by the response of its active clay minerals (microstructure) to such changes (see **Section 2.7.1**). Consider a THM loading for which the expansive soil only undergoes reversible deformations, that is, $\dot{\bar{\boldsymbol{\varepsilon}}}^p_{M,LC} = \dot{\bar{\boldsymbol{\varepsilon}}}^p_{M,\beta} = \mathbf{0}$. Thus, no changes in the fabric of the porous medium due to structural collapse, particle slippage or reorientation, particle breakage, etc. are expected to occur during the loading process. In fact, particle slippage between adjacent clay aggregates is considered as the main factor related to structural changes at macrostructural level (Ruiz, 2020). Consequently, such an assumption implies the existence of stable aggregate-to-aggregate contact points (see Figure 4-1). Furthermore, and since the changes in the soil suction in active clays are usually accompanied by a certain degree of structural rearrangement of the clay particles and aggregates, it can be assumed that the suction-induced macrostructural reversible deformations can be neglected (Alonso *et al.*, 2005), that is, $\dot{\bar{\boldsymbol{\varepsilon}}}^e_{M,\Delta s} \approx \mathbf{0}$. Under such circumstances, it is quite reasonable to assume that the elastic strains experienced by the porous medium ($\dot{\boldsymbol{\varepsilon}}^e$) are essentially volumetric and equivalent to the deformations that take place in the clay aggregate ($\dot{\boldsymbol{\varepsilon}}^e_m$). Therefore, in such conditions,

$$\dot{\varepsilon}^e = \dot{\bar{\boldsymbol{\varepsilon}}}^e_m + \dot{\bar{\boldsymbol{\varepsilon}}}^e_M = \dot{\boldsymbol{\varepsilon}}^e_m \tag{4-47}$$

where the deformations of the clay aggregate (actual microstructure) are expressed by

$$\begin{aligned} \dot{\boldsymbol{\varepsilon}}^e_m &= \dot{\boldsymbol{\varepsilon}}^e_{m,\Delta\sigma_m} + \dot{\boldsymbol{\varepsilon}}^e_{m,\Delta T} = [\boldsymbol{D}^e_m]^{-1}\dot{\boldsymbol{\sigma}}_m + \dot{\boldsymbol{\varepsilon}}^e_{m,\Delta T} \\ &= [\boldsymbol{D}^e_m]^{-1}\dot{\boldsymbol{\sigma}} + \frac{1}{3K_m}\left(\zeta_{gm}\dot{P}_{gm} + \zeta_{lm}\dot{P}_{lm} + \zeta_T\dot{T} + \dot{P}_{fM}\right)\boldsymbol{m} + \dot{\boldsymbol{\varepsilon}}^e_{m,\Delta T} \end{aligned} \tag{4-48}$$

and the purely elastic (and volumetric) strains taking place in the expansive clay are given by

$$\begin{aligned} \dot{\varepsilon}^e = [\boldsymbol{D}^e]^{-1}\dot{\boldsymbol{\sigma}} &+ \frac{1}{3\overline{K}_m}\left(\zeta_{gm}\dot{P}_{gm} + \zeta_{lm}\dot{P}_{lm} + \zeta_T\dot{T} + \dot{P}_{fM}\right)\boldsymbol{m} + \dot{\bar{\boldsymbol{\varepsilon}}}^e_{m,\Delta T} \\ &+ \dot{\bar{\boldsymbol{\varepsilon}}}^e_{m\to M} \end{aligned} \tag{4-49}$$

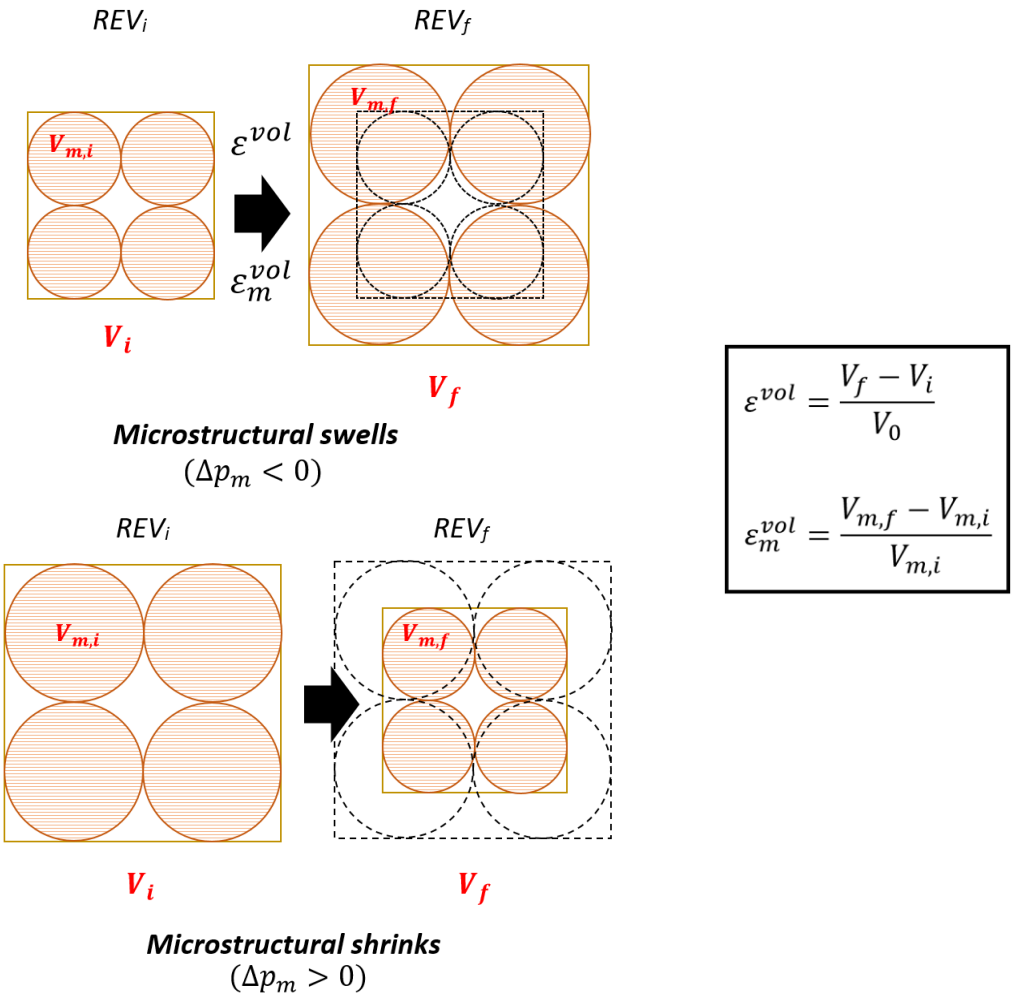

Figure 4-1: Schematic representation of the purely elastic swelling and shrinkage of individual clay aggregates and of the porous skeleton within a representative elementary volume (REV).

These two latter expressions have been obtained from the combination of Equation (4-23) and Equation (4-40) and from Equation (4-44), respectively.

Equating these last two strain tensors, as stated by Equation (4-47), a general expression for the reversible strain component of the micro-macro mechanical coupling ($\dot{\boldsymbol{\varepsilon}}^e_{m\to M}$) is achieved

$$\dot{\boldsymbol{\varepsilon}}^e_{m\to M} = \underbrace{([\boldsymbol{D}^e_m]^{-1} - [\boldsymbol{D}^e]^{-1})\dot{\boldsymbol{\sigma}} + \frac{1}{3}\left(\frac{1}{K_m} - \frac{1}{\overline{K}_m}\right)\left(\zeta_{gm}\dot{P}_{gm} + \zeta_{lm}\dot{P}_{lm} + \zeta_T\dot{T} + \dot{P}_{fM}\right)\boldsymbol{m}}_{\dot{\boldsymbol{\varepsilon}}^e_{m\to M,\Delta\sigma}} + \underbrace{\left(\dot{\boldsymbol{\varepsilon}}^e_{m,\Delta T} - \dot{\overline{\boldsymbol{\varepsilon}}}^e_{m,\Delta T}\right)}_{\dot{\boldsymbol{\varepsilon}}^e_{m\to M,\Delta T}} \quad (4\text{-}50)$$

Inserting Equation (4-50) into the mechanical constitutive law in Equation (4-44), the following stress-strain relationship for the soil response in terms of the mechanical behaviour of the clay aggregates/particles arises:

$$\dot{\boldsymbol{\varepsilon}} = [\boldsymbol{D}_m^e]^{-1}\dot{\boldsymbol{\sigma}} + \frac{1}{3K_m}\left(\zeta_{gm}\dot{P}_{gm} + \zeta_{lm}\dot{P}_{lm} + \zeta_T\dot{T} + \dot{P}_{fM}\right)\boldsymbol{m} + \dot{\boldsymbol{\varepsilon}}_{m,\Delta T}^e + \dot{\bar{\boldsymbol{\varepsilon}}}_{M,\Delta s}^e + \dot{\bar{\boldsymbol{\varepsilon}}}_{M,LC}^p + \dot{\bar{\boldsymbol{\varepsilon}}}_{M,\beta}^p \tag{4-51}$$

The elastic micro-macro coupling strain term in Equation (4-50), $\dot{\boldsymbol{\varepsilon}}_{m\to M}^e$, is volumetric because of the assumption of a constant porous skeleton arrangement for an elastic deformation response of the expansive soil. Due to that, the following relationship is assumed

$$[\boldsymbol{D}^e]^{-1} = [\boldsymbol{D}_m^e]^{-1} \tag{4-52}$$

which means that the elastic behaviour of the expansive clay is controlled by the deformation response of the clay aggregates (microstructure), in accordance with Equation (4-47) and explicitly evidenced by the expression in Equation (4-51). Moreover, the elastic structural coupling allows obtaining an explicit relationship between micro and macro elastic parameters. Combining the latter equation with Equation (4-45), it may be stated that

$$[\boldsymbol{D}_m^e]^{-1} = [\bar{\boldsymbol{D}}_m^e]^{-1} + [\bar{\boldsymbol{D}}_M^e]^{-1} \tag{4-53}$$

and, hence, the following expressions relating the macro, the micro and the soil bulk and shear moduli are obtained

$$\frac{1}{K_m} = \frac{1}{\bar{K}_m} + \frac{1}{\bar{K}_M} \equiv \frac{1}{K} \tag{4-54}$$

$$\frac{1}{G_m} = \frac{1}{\bar{G}_m} + \frac{1}{\bar{G}_M} \equiv \frac{1}{G} \tag{4-55}$$

in which the same value of Poisson's coefficient (υ) has been adopted for all the porous media considered in the double-porosity formulation, that is, $\upsilon_m = \bar{\upsilon}_m = \bar{\upsilon}_M \equiv \upsilon$. It is important to mention that there is no experimental evidence, beyond the simplification of the mathematical formulation, which justifies the assumption of the latter hypothesis. Recalling Equation (4-17), Equation (4-25) and Equation (4-26) and after some algebra, some useful relationships among the global, the macro and the micro bulk and shear elastic moduli can be easily obtained from Equation (4-54) and Equation (4-55), as given in the Table 4-1.

Table 4-1: Relationships among "local" and "global" micro/macro elastic moduli.

	Bulk Modulus (micro): K_m	Bulk Modulus (micro): $\overline{K}_m$	Bulk Modulus (macro): $\overline{K}_M$
$K \equiv K_m$	K_m	$\left(\frac{1+e_m}{1+e}\right)\overline{K}_m$	$\bar{\phi}_M\overline{K}_M = \left(\frac{e-e_m}{1+e}\right)\overline{K}_M$
$\overline{K}_m$	$\left(\frac{1+e}{1+e_m}\right)K_m$	$\overline{K}_m$	$\bar{e}_M\overline{K}_M = \left(\frac{e-e_m}{1+e_m}\right)\overline{K}_M$
$\overline{K}_M$	$\left(\frac{1+e}{e-e_m}\right)K_m$	$\left(\frac{1+e_m}{e-e_m}\right)\overline{K}_m$	$\overline{K}_M$
$G \equiv G_m$	$\frac{3(1-2\upsilon)}{2(1+\upsilon)}K_m$	$\frac{3(1-2\upsilon)}{2(1+\upsilon)}\left(\frac{1+e_m}{1+e}\right)\overline{K}_m$	$\frac{3(1-2\upsilon)}{2(1+\upsilon)}\left(\frac{e-e_m}{1+e}\right)\overline{K}_M$
$\bar{G}_m$	$\frac{3(1-2\upsilon)}{2(1+\upsilon)}\left(\frac{1+e}{1+e_m}\right)K_m$	$\frac{3(1-2\upsilon)}{2(1+\upsilon)}\overline{K}_m$	$\frac{3(1-2\upsilon)}{2(1+\upsilon)}\left(\frac{e-e_m}{1+e_m}\right)\overline{K}_M$
$\bar{G}_M$	$\frac{3(1-2\upsilon)}{2(1+\upsilon)}\left(\frac{1+e}{e-e_m}\right)K_m$	$\frac{3(1-2\upsilon)}{2(1+\upsilon)}\left(\frac{1+e_m}{e-e_m}\right)\overline{K}_m$	$\frac{3(1-2\upsilon)}{2(1+\upsilon)}\overline{K}_M$

From Equation (4-51) and Equation (4-52), and taking into account the relationships in Table 4-1, the rate of total strains for the expansive porous medium, in terms of the soil (global) elastic parameters, is given as follows:

$$\dot{\boldsymbol{\varepsilon}} = [\boldsymbol{D}^e]^{-1}\dot{\boldsymbol{\sigma}} + \frac{1}{3K}\left(\zeta_{gm}\dot{P}_{gm} + \zeta_{lm}\dot{P}_{lm} + \zeta_T\dot{T} + \dot{P}_{fM}\right)\boldsymbol{m} + \dot{\boldsymbol{\varepsilon}}^e_{m,\Delta T} + \dot{\bar{\boldsymbol{\varepsilon}}}^e_{M,\Delta s} + \dot{\bar{\boldsymbol{\varepsilon}}}^p_{M,LC} + \dot{\bar{\boldsymbol{\varepsilon}}}^p_{M,\beta} \tag{4-56}$$

4.2.5. THERMAL STRAIN COMPONENTS

One of the main goals of this Thesis is to incorporate the thermal variable to the double-porosity formulation implemented by Gesto (2014) and, consequently, to check its numerical performance on non-isothermal problems. It is assumed that the thermal strain components are volumetric and purely elastic at constant confining stress and liquid pressure conditions. In such a situation, where only thermal effects are relevant but without inducing water phase changes, the material is free for shrinking or swelling under the applied thermal loadings (see Figure 4-2). In practice, it is expected the occurrence of some thermally-induced plastic strains due to the strong coupling between the thermal and the hydro-mechanical variables. Despite that and for the sake of simplicity, the hypothesis that only volumetric thermo-elastic strains are generated during a thermal loading is kept during the mathematical development of the double-porosity model presented here.

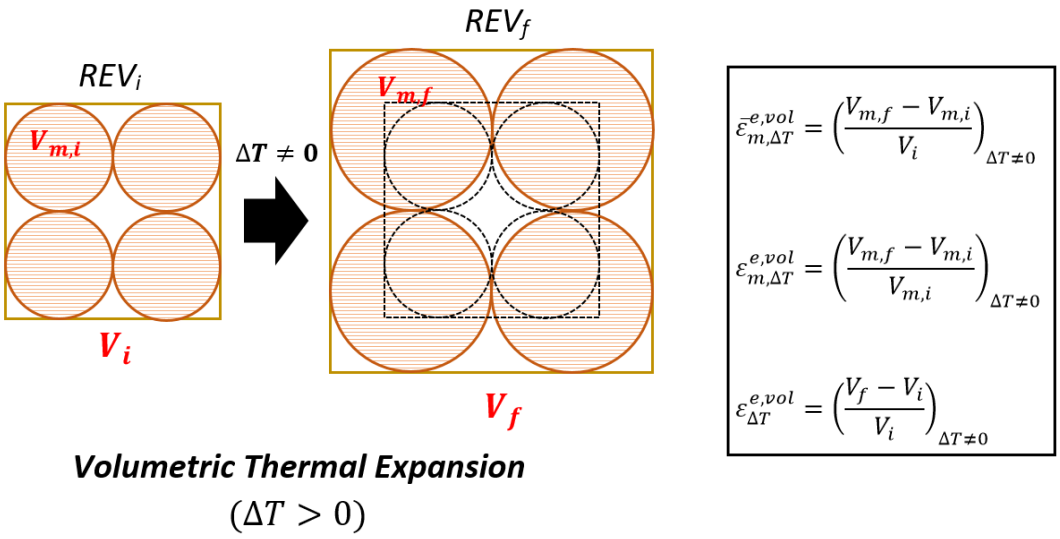

Figure 4-2: Schematic representation of the purely elastic thermal expansion of individual clay aggregates and of a representative elementary volume (REV) at constant mean stress and macro suction.

Thermal effects at microstructural level are taken into account in Equation (4-4) through the (elastic) micro strain component $\dot{\bar{\boldsymbol{\varepsilon}}}^{e}_{m,\Delta T}$, defined as follows

$$\dot{\bar{\boldsymbol{\varepsilon}}}^{e}_{m,\Delta T} = \frac{1}{3\bar{K}_{T,m}} \dot{T}\boldsymbol{m} \tag{4-57}$$

where $\bar{K}_{T,m}$ is the microstructural bulk modulus related to temperature changes. The thermal expansion of the clay particles and aggregates ($\dot{\boldsymbol{\varepsilon}}^{e}_{m,\Delta T}$) is defined by

$$\dot{\boldsymbol{\varepsilon}}^{e}_{m,\Delta T} = \frac{1}{3K_{T,m}} \dot{T}\boldsymbol{m} \tag{4-58}$$

where $K_{T,m}$ represents the thermal bulk modulus of the clay aggregates. These two thermal strain tensors are related according to Equation (4-5). Consequently,

$$\bar{K}_{T,m} = \frac{1+e}{1+e_m} K_{T,m} \tag{4-59}$$

On the other hand, the thermal expansion of the expansive soil ($\dot{\boldsymbol{\varepsilon}}^{e}_{\Delta T}$) is evaluated through the expression

$$\dot{\boldsymbol{\varepsilon}}^{e}_{\Delta T} = \frac{1}{3K_T} \dot{T}\boldsymbol{m} \tag{4-60}$$

where the soil bulk modulus due to changes in temperature (K_T) can be computed as (Gens, 1995)

$$K_T = \frac{1}{\alpha_0 + 2\alpha_2 \Delta T} \tag{4-61}$$

in which α_0 and α_2 are model parameters. A simple and clear definition of these three elastic thermal strain components is also shown in Figure 4-2.

Palciauskas and Domenico (1982) stated that the thermal expansion coefficient for the solid skeleton (α_{sk}) is related to the thermal expansivities of solid particles (α_s) and pores (α_p) according to

$$\alpha_{sk} = (1-\phi)\cdot\alpha_s + \phi\cdot\alpha_p = \alpha_s + \phi\cdot(\alpha_p - \alpha_s) \tag{4-62}$$

On the other hand (and as discussed in **Section 2.5.1.3**), a purely thermo-elastic volumetric expansion of a porous medium requires that all the soil particles to be in contact, forming a stable porous skeleton under the applied stress state (Campanella and Mitchell, 1968). In such conditions, the thermal expansion coefficient of the soil skeleton can be assumed as equivalent to the thermal expansion coefficient of the solid grains (Walsh, 1973; Palciauskas and Domenico, 1982; Khalili *et al.*, 2010), that is, $\alpha_{sk} \approx \alpha_s$. Furthermore, under stress-free thermo-elastic expansion conditions, the thermal deformations of a porous medium is not dependent on the size of pores or on its porosity but only on the thermal expansion of the solid constituent (Khalili *et al.*, 2010). If the same assumption is extended to the thermal expansion of porous aggregates (as in expansive clays), the hypothesis of reversible thermal strains (in micro and macro media) also implies that the thermal expansion of pores are equivalent to the thermal expansion of solid grains ($\alpha_s = \alpha_p$). Consequently, Equation (4-62) leads to

$$\alpha_{sk} = \alpha_s = \alpha_p \tag{4-63}$$

Taking into account the thermal strain components defined in Equation (4-57), Equation (4-58) and Equation (4-60) and the above-mentioned hypotheses related to the thermal expansivity coefficients under the assumption of null changes in the soil fabric during the thermal loading, the thermo-elastic micro-macro coupling leads to

$$\dot{\boldsymbol{\varepsilon}}^e_{\Delta T} = \dot{\boldsymbol{\varepsilon}}^e_{m,\Delta T} \tag{4-64}$$

which implies that the volumetric expansion of the expansive soil due to temperature changes is equal to the volumetric thermal expansion experienced by individual clay aggregates. Consequently, the following relationship between the bulk thermal moduli may be established

$$K_T = K_{T,m} \tag{4-65}$$

In the mathematical formulation of the double-porosity model described in this document. Temperature changes also generate a thermal strain component arising from the interaction between the two structural levels ($\dot{\bar{\boldsymbol{\varepsilon}}}^e_{m\to M,\Delta T}$). According to Equation (4-50) this strain component is given by

$$\dot{\bar{\boldsymbol{\varepsilon}}}^e_{m\to M,\Delta T} = \dot{\boldsymbol{\varepsilon}}^e_{m,\Delta T} - \dot{\bar{\boldsymbol{\varepsilon}}}^e_{m,\Delta T} \tag{4-66}$$

Substituting the strain components defined by Equation (4-57) and Equation (4-58) into Equation (4-66), the (volumetric) thermal micro-macro interaction strain is expressed by

$$\dot{\varepsilon}^{e,vol}_{m\to M,\Delta T} = \varepsilon^{e,vol}_{m,\Delta T} - \dot{\varepsilon}^{e,vol}_{m,\Delta T} = \left(\frac{1}{K_{T,m}} - \frac{1}{\overline{K}_{T,m}}\right)\dot{T} \tag{4-67}$$

or, when the relationship given by Equation (4-59) is inserted in the latter expression and after some algebraic manipulations,

$$\dot{\varepsilon}^{e,vol}_{m\to M,\Delta T} = \left(\frac{e - e_m}{1+e}\right)\cdot \dot{\varepsilon}^{e,vol}_{m,\Delta T} = \bar{\phi}_M \cdot \dot{\varepsilon}^{e,vol}_{m,\Delta T} = \bar{\phi}_M \cdot \dot{\varepsilon}^{e,vol}_{\Delta T} \tag{4-68}$$

The expression for the thermal strain arising from the micro-macro coupling in Equation (4-68) suggests that this strain component computes the thermal expansion of macro-pores when temperature is raised, since it represents the thermal effects on the macro pore in non-isothermal conditions. If the thermal expansion of the soil constituents do not generate any irreversible strains (one of the hypotheses assumed in this Thesis), the macrostructure configuration is maintained when thermal loadings at constant confining pressures take place. Consequently, the "macro" void ratio remains constant during thermal loading (Palciauskas and Domenico, 1982; Khalili *et al.*, 2010). From the definition of the macro void ratio ($\bar{e}_M = \frac{\bar{\phi}_M}{1-\bar{\phi}_M}$), this assertion corresponds to $\dot{\bar{\phi}}_M = 0$. Equation (4-68) is in accordance with the macrostructural volumetric strain obtained through the relationship in Equation (3-50) when $\dot{\bar{\phi}}_M = 0$ for thermal problems. The strain component defined in Equation (4-68) inspires an alternative way to express the "global" thermal expansion of microstructure, $\dot{\varepsilon}^{e,vol}_{m,\Delta T}$, as it follows

$$\dot{\varepsilon}^{e,vol}_{m,\Delta T} = (1-\bar{\phi}_M)\cdot \dot{\varepsilon}^{e,vol}_{m,\Delta T} \tag{4-69}$$

in such a way that the thermal expansion of the soil skeleton ($\dot{\varepsilon}^{e,vol}_{\Delta T}$) is expressed, in terms of the thermal strain components in both structural levels, by

$$\dot{\varepsilon}^{e,vol}_{\Delta T} = \dot{\varepsilon}^{e,vol}_{m,\Delta T} = \dot{\varepsilon}^{e,vol}_{m,\Delta T} + \dot{\varepsilon}^{e,vol}_{m\to M,\Delta T} = (1-\bar{\phi}_M)\cdot \dot{\varepsilon}^{e,vol}_{m,\Delta T} + \bar{\phi}_M \cdot \dot{\varepsilon}^{e,vol}_{m,\Delta T} \tag{4-70}$$

Note that the thermal expansion at the microstructural level, in Equation (4-69), does not depend on the micro-pore volume fraction, $\bar{\phi}_m$. In other words, that thermal expansion component depends exclusively on the volume occupied by the solid grains (clay aggregates) and not on its internal pore geometry/distribution. This observation is in agreement with the conclusions presented in Khalili *et al.* (2010) about the thermal expansion of homogeneous porous media.

4.3. ELASTIC CONSTITUTIVE LAW FOR A DOUBLE-POROSITY MODEL

All the assumptions and definitions presented in the preceding sections allows writing the rate of the elastic deformation in the expansive soil, $\dot{\boldsymbol{\varepsilon}}^e$, in a double-porosity approach, as

$$\dot{\boldsymbol{\varepsilon}}^e = \dot{\bar{\boldsymbol{\varepsilon}}}_m^e + \dot{\bar{\boldsymbol{\varepsilon}}}_M^e = [\boldsymbol{D}^e]^{-1}\dot{\boldsymbol{\sigma}} + \frac{1}{3K}\left(\zeta_{gm}\dot{P}_{gm} + \zeta_{lm}\dot{P}_{lm} + \zeta_T\dot{T} + \dot{P}_{fM}\right)\boldsymbol{m} + \dot{\bar{\boldsymbol{\varepsilon}}}_{M,\Delta s}^e + \dot{\boldsymbol{\varepsilon}}_{\Delta T}^e \tag{4-71}$$

where the expressions given in Equation (4-56) and Equation (4-64) have been used. For an isotropic stress state, this elastic constitutive law can be expressed by

$$\dot{\varepsilon}^{e,vol} = \dot{\bar{\varepsilon}}_m^{e,vol} + \dot{\bar{\varepsilon}}_M^{e,vol} = \boldsymbol{m}^T\dot{\boldsymbol{\varepsilon}}^e = \frac{\dot{p}_m}{K} + \frac{\dot{s}_M}{\bar{K}_s} + \frac{\dot{T}}{K_T} = \frac{\bar{\kappa}_M}{\bar{e}_M p}\dot{p}_m + \frac{\bar{\kappa}_s}{(1+\bar{e}_M)(s_M + p_{atm})}\dot{s}_M + \dot{\varepsilon}_{\Delta T}^{e,vol} \tag{4-72}$$

where $\dot{\varepsilon}^{e,vol}$ is the volumetric component of the elastic strain in the porous medium and $\dot{p}_m$ is the mean effective stress rate at microstructural level, defined as (see Equation (4-40))

$$\dot{p}_m = \dot{p} + \zeta_{gm}\dot{P}_{gm} + \zeta_{lm}\dot{P}_{lm} + \zeta_T\dot{T} + \dot{P}_{fM} \tag{4-73}$$

The rate of the volumetric microstructural strains is given by

$$\dot{\bar{\varepsilon}}_m^{e,vol} = \frac{\dot{p}_m}{\bar{K}_m} + \dot{\bar{\varepsilon}}_{m,\Delta T}^{e,vol} = \frac{\bar{\kappa}_M}{\bar{e}_M(1+\bar{e}_M)p}\dot{p}_m + (1-\bar{\phi}_M)\dot{\varepsilon}_{\Delta T}^{e,vol} \tag{4-74}$$

while the volumetric elastic law at macrostructural level can be written as

$$\begin{aligned}\dot{\bar{\varepsilon}}_M^{e,vol} &= \dot{\varepsilon}^{e,vol} - \dot{\bar{\varepsilon}}_m^{e,vol} = \left(\frac{1}{K} - \frac{1}{\bar{K}_m}\right)\dot{p}_m + \frac{\dot{s}_M}{\bar{K}_s} + \left(\dot{\varepsilon}_{\Delta T}^{e,vol} - \dot{\bar{\varepsilon}}_{m,\Delta T}^{e,vol}\right) \\ &= \frac{\dot{p}_m}{\bar{K}_M} + \frac{\bar{\kappa}_s}{(1+\bar{e}_M)(s_M + p_{atm})}\dot{s}_M + \bar{\phi}_M\dot{\varepsilon}_{\Delta T}^{e,vol} \\ &= \frac{\bar{\kappa}_M}{(1+\bar{e}_M)p}\dot{p} + \frac{\bar{\kappa}_s}{(1+\bar{e}_M)(s_M + p_{atm})}\dot{s}_M \\ &\quad + \underbrace{\left(\bar{\phi}_M\dot{\varepsilon}_{\Delta T}^{e,vol} + \frac{\bar{\kappa}_M}{(1+\bar{e}_M)p}(\dot{p}_m - \dot{p})\right)}_{\dot{\bar{\varepsilon}}_{m\to M}^{e,vol}}\end{aligned} \tag{4-75}$$

For a general tridimensional stress state (as illustrated in Figure 4-3(a)), the elastic shear law is given by the following expression (Sánchez and Gens, 2006)

$$\dot{\varepsilon}^{e,dev} = \frac{\dot{J}}{G} = \bar{\phi}_M\frac{\dot{J}}{\bar{G}_M} \tag{4-76}$$

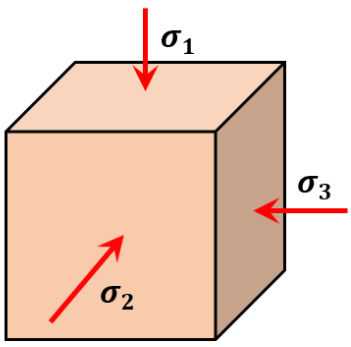

$$p = \frac{1}{3}(\sigma_1 + \sigma_2 + \sigma_3)$$
$$q = \frac{1}{\sqrt{2}}\sqrt{(\sigma_1 - \sigma_2)^2 + (\sigma_2 - \sigma_3)^2 + (\sigma_3 - \sigma_1)^2}$$

(a)

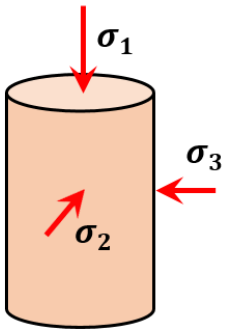

$(\sigma_1 > \sigma_2 = \sigma_3)$

$$p = \frac{1}{3}(\sigma_1 + 2\sigma_3)$$
$$q = \sigma_1 - \sigma_3$$

(b)

Figure 4-3: Schematic representation (in the principal stress axes) of **(a)** a generalized 3D stress state; **(b)** a triaxial stress state.

where $\dot{\varepsilon}^{e,dev}$ is the shear deformation rate of the expansive soil due to changes in the deviatoric stresses, expressed by means of the stress invariant J (see Equation (3-33)). In the case of triaxial states (see Figure 4-3(b)), the elastic shear model is expressed as (Atkinson and Bransby, 1978)

$$\dot{\varepsilon}^{e,dev} = \frac{\dot{q}}{3G} = \bar{\phi}_M \frac{\dot{q}}{3\bar{G}_M} \tag{4-77}$$

where the rate of the deviatoric component of stress, $\dot{q}$, is evaluated in terms of the principal stresses ($\sigma_1 > \sigma_2 \equiv \sigma_3$) and related to the stress invariant J according to

$$q = \sigma_1 - \sigma_3 = \sqrt{3}J \tag{4-78}$$

The expressions for the macrostructural bulk moduli given in **Section 4.2.2** as well as the relationships relating the elastic moduli at different structural levels (as shown in Table 4-1) have been used to obtain the explicit volumetric and shear stress-strain laws defined in Equation (4-72) and in Equation (4-74) to Equation (4-77).

4.4. PLASTIC MECHANISMS IN A DOUBLE-POROSITY APPROACH

As discussed in the previous sections, the main features related to the deformation response of expansive clays are intrinsically related to the (non-linear) elastic behaviour of microstructure and can be described from the micro-macro interaction mechanisms between both media. However, the explicit description of the mechanical constitutive law for macrostructure in Equation (4-20) evidences the importance of also including this structural level in the double-structure formulation in order to consider the phenomena that generate irreversible changes in

the clay fabric (Ruiz, 2020). Irreversible changes in the soil structure are related to the occurrence of plastic strains. If cracking of the soil particles is neglected, these irreversible structural changes are mainly characterized by the permanent macro-porosity (or macro-pore volume fraction) evolution due to:

- the collapse of macro-pores when suction decreases at high confining stress. This class of plastic response can be easily reproduced by classical elastoplastic models for unsaturated non-expansive soils such as the BBM model (Alonso *et al.*, 1990), for example;
- shrinkage or swelling of highly expansive minerals due to changes in some environmental variables (like the soil water content, the concentration or chemical composition of species transported by fluids through the pores or the temperature distribution/evolution in the porous medium) generating a non-recoverable rearrangement of soil particles. The amount of these permanent changes depends on the mineralogy of the clay fraction in the soil, on the degree of openness of the soil structure (related to the magnitude of the confining stresses and the OCR) and on the stress paths followed during the loading process. This portion of the plastic strains can be properly modelled by those elastoplastic approaches based on the consideration of two (or more) levels of structure such as the BExM model developed by Alonso *et al.* (1999) and Sánchez (2004) (see **Section 2.7.2**) or the double-porosity approach, described in this Thesis as well as in Ruiz (2020).

The first of these two plastic mechanisms is associated with the so-called loading-collapse (**LC**) yield curve, the yield locus that delimits the elastic region of the BBM model. This plastic mechanism will be referred to as the "BBM (or the LC) mechanism" from now on. The second plastic mechanism (called the "β-mechanism" hereafter) represents the coupling between microstructure and macrostructure that accounts for the macrostructural elastoplastic strains induced by the elastic microstructural strains. The main mathematical ingredients for each of these plastic mechanisms is briefly discussed in the following sections. A more in-depth and detailed description regarding the theoretical and mathematical aspects of the BBM model and the micro-macro coupling mechanisms can be found in Alonso *et al.* (1990; 1994; 1999), Gens and Alonso (1992), Gens (1995), Yang *et al.* (1998), Sánchez (2004), Sánchez *et al.* (2005) among others.

4.4.1. THE LC PLASTIC MECHANISM

The BBM model (Alonso *et al.*, 1990; Gens, 1995) has been selected to describe the macrostructural behaviour due to its ability to reproduce many of the features observed in unsaturated non-expansive soils (Sánchez *et al.*, 2005). In a double-porosity framework, this elastoplastic model is formulated in terms of two independent stress variables: the macro net stress ($\widehat{\boldsymbol{\sigma}}_M$), defined as the excess of the total stresses over the (macro) gas pressure according to Equation (3-27), and the matric suction at macrostructural level (s_M). As discussed in **Section 3.3**, the macro net stress is taken as the soil net stress ($\widehat{\boldsymbol{\sigma}}_M \equiv \widehat{\boldsymbol{\sigma}}$). The BBM yield surface (F_{LC}) depends not only on stresses and history variables but also on the matric suction and

temperature. The yield function, the plastic potential and the plastic flow rule for the BBM are described in the following sections.

4.4.1.1. THE YIELD FUNCTION

The BBM yield surface for a general stress state, expressed in terms of the stress invariants (p, J and θ), is given as follows

$$F_{LC} = F(p, J, \theta, s_M, T) = 3J^2 - \left(\frac{g_F(\theta, \alpha_F)}{g_F\left(-\frac{\pi}{6}, \alpha_F\right)}\right)^2 \cdot M_F^2 \cdot (p + p_s) \cdot (p_0 - p) = 0 \quad (4\text{-}79)$$

where M_F is the slope of the critical state line, p_0 is the apparent non-saturated pre-consolidation pressure, g_F is a function of Lode's angle (θ) , α_F is a model parameter and p_s considers the dependence of shear strength on suction and temperature (Gens, 1995). The stress invariants are defined according to Equation (3-32) through Equation (3-34) in the previous chapter (see **Section 3.3.1**). A three dimensional representation of the BBM yield surface in p: J: s_M space is given in Figure 4-4.

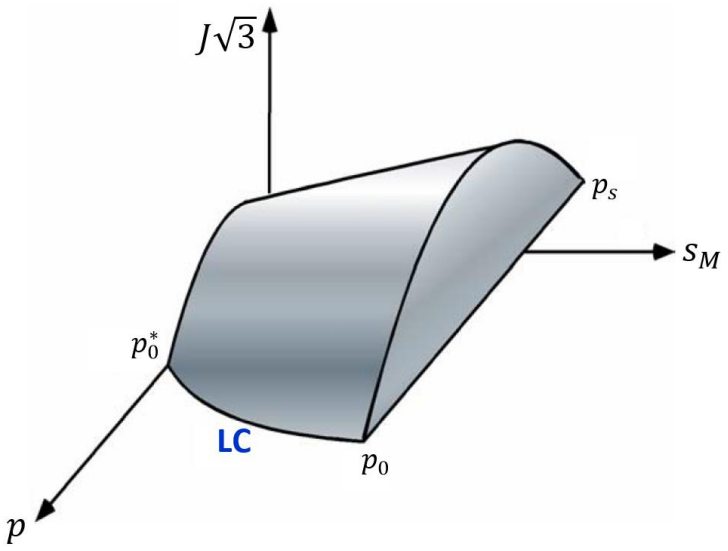

Figure 4-4: Schematic representation of the BBM yield surface in p: J: s_M plane.

The slope of the critical state line (M_F) can be computed from the internal friction angle of the porous medium, φ'. Its expression for compression states in the triaxial stress space is given as follows

$$M_F = \frac{6 \cdot sin\varphi'}{3 - sin\varphi'} \quad (4\text{-}80)$$

while the over-consolidation pressure dependency on the macrostructural suction is given by

$$p_0 = p_c \cdot \left(\frac{p_{0,T}^*}{p_c}\right)^{\frac{\lambda_{(0)} - \bar{\kappa}_M}{\lambda_{(s_M)} - \bar{\kappa}_M}} \tag{4-81}$$

where p_c is a reference stress and $p_{0,T}^*$ is the pre-consolidation net mean stress for saturated conditions and at the current temperature. The pre-consolidation pressure is considered the hardening parameter of the BBM model. A thermal dependence of $p_{0,T}^*$ is also included in the BBM formulation according to the following expression (Gens, 1995)

$$p_{0,T}^* = p_0^* + 2(\alpha_1 \cdot \Delta T + \alpha_3 \cdot \Delta T \cdot |\Delta T|) \tag{4-82}$$

in which α_1 and α_3 are material parameters, ΔT is the temperature difference with respect to an arbitrary temperature T_0 and p_0^* is the net mean yield stress for saturated conditions at the reference temperature. If the dependence of the BBM surface size on temperature is modelled, the coefficients α_1 and α_3 are usually negative so that $p_{0,T}^*$ can decrease with temperature (Hueckel and Baldi, 1990). In Equation (4-81), $\lambda_{(s_M)}$ is the slope of the virgin macrostructural compression line for isotropic conditions, the dependence of which on the macro suction is expressed through

$$\lambda_{(s_M)} = \lambda_{(0)} \cdot \left(r + (1 - r) \cdot e^{-\beta \cdot s_M}\right) \tag{4-83}$$

where $\lambda_{(0)}$ is the macrostructural compressibility parameter at saturated conditions, r is the model parameter defining the minimum macrostructural soil compressibility (at infinity suction) and β is a constitutive parameter that controls the rate of increase of soil stiffness with macrostructural suction.

On the other hand, the dependence of tensile strength (p_s) on suction and temperature is given by

$$p_s = p_{s0} + k_s \cdot s_M \cdot e^{-\rho_T \cdot \Delta T} \tag{4-84}$$

where p_{s0} is the tensile strength in saturated conditions, k_s is a parameter that computes the increase in apparent cohesion with macrostructural suction and ρ_T is a model parameter that takes into account the decreasing of p_s when temperature increases. Equation (4-81) and Equation (4-84) give the trace of the yield locus on $p: s_M$ plane (as sketched in Figure 4-5(a)) and define the elastic domain of the BBM model under isotropic conditions. The curve determined by Equation (4-81) is called the **LC** (**L**oading-**C**ollapse) yield curve because it represents the locus of activation of irreversible collapse due to loading or wetting at high confining pressures. For triaxial stress states, the elastic domain is bounded by a family of ellipses (see Figure 4-5(b)) obtained from the intersection of the yield surface with vertical planes parallel to $p: q$ plane, where $q = J\sqrt{3}$ is the deviatoric stress.

The shape of the yield surface in the principal stress space is defined by the g_F function (see Equation (4.079)). Several expressions for this stress function can be found in the literature, such as the Von Mises expression for numerical analyses in perfect plastic materials or the Mohr-Coulomb criterion for cohesive and stress dependent porous media. Despite the fact that the Mohr-Coulomb yield criterion is widely used in most of the geotechnical analyses, the gradient discontinuities at the edges and the tip of the hexagonal yield surface introduce numerical singularities into the stress integration schemes (Abbo and Sloan, 1995). Moreover, multi-mechanism elastoplastic models are described by means of multiple yield surfaces, which can lead to the occurrence of "corners" in the intersection of two or more of these surfaces. Due to that, several surface "regularization" techniques have been proposed in order to eliminate these surface edges by rounding the yield surface in the vicinity of these singularities (van Eekelen, 1980; Sloan and Booker, 1986; Abbo and Sloan, 1995). Gesto et al. (2011) proposed a smooth approximation to describe the Mohr-Coulomb function on the deviatoric plane, whose expression is given by

$$g_F(\theta,\alpha_F)=\frac{1}{\alpha_F}ln\left(e^{\alpha_F\cdot g(\theta)}+e^{\alpha_F\cdot g\left(\frac{\pi}{3}-\theta\right)}+e^{\alpha_F\cdot g\left(-\frac{\pi}{3}-\theta\right)}+e^{\alpha_F\cdot g(\pi-\theta)}+e^{\alpha_F\cdot g\left(\frac{2\pi}{3}+\theta\right)}+e^{\alpha_F\cdot g\left(\frac{4\pi}{3}+\theta\right)}\right) \tag{4-85}$$

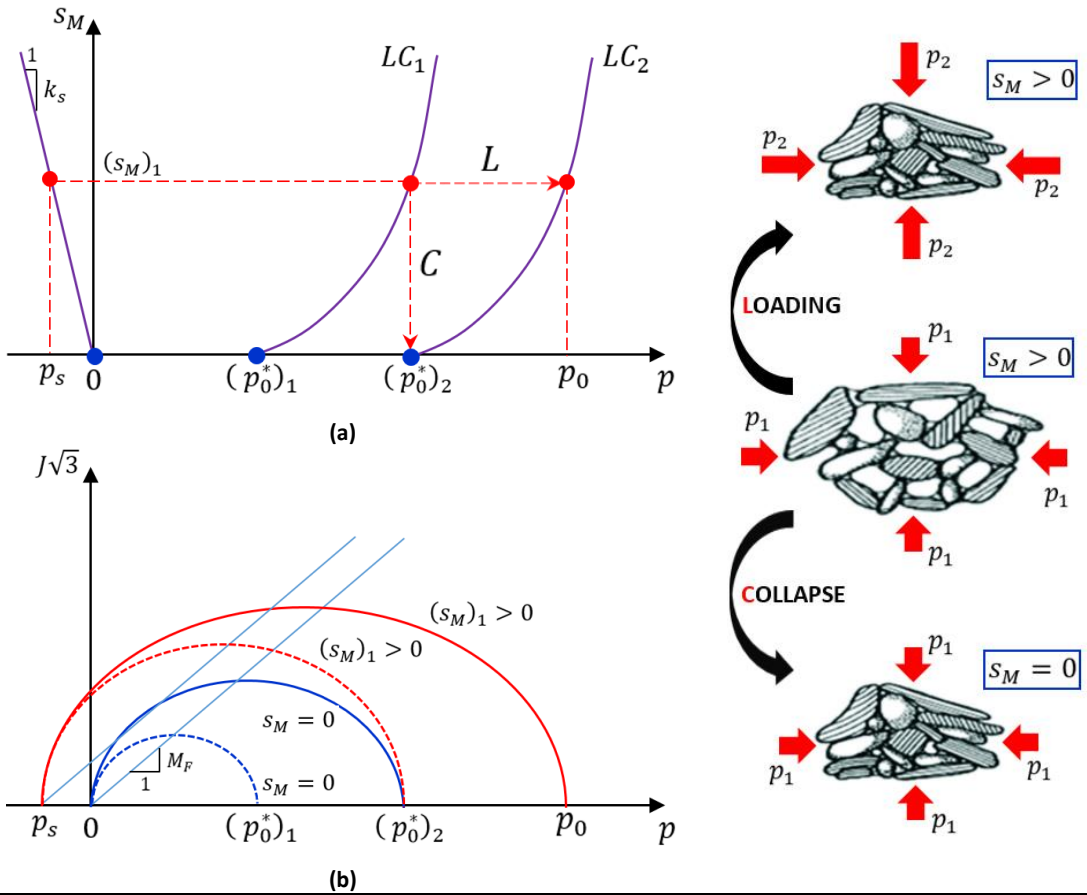

Figure 4-5: The BBM yield surface and schematic representation of a typical movement of the loading-collapse curve on **(a)** the p: s_M plane; **(b)** the p: J plane (after Alonso and Gens, 1994).

where α_F accounts for the "degree of roundness" in the vicinity of the yield surface vertices and $g(\theta)$ is a Lode's angle function expressed by

$$g(\theta) = cos\theta + \frac{1}{\sqrt{3}} sin\theta \cdot sin\hat{\varphi} \tag{4-86}$$

where $\hat{\varphi}$ is dependent on the internal friction angle as follows

$$\hat{\varphi} = \left(1 + \frac{0.8}{\alpha_F - p_{\varphi'}}\right)\varphi' \tag{4-87}$$

and $p_{\varphi'}$ is a quadratic function defined as

$$p_{\varphi'} = 0.024(\varphi')^2 - 0.0321\varphi' + 0.38 \tag{4-88}$$

Figure 4-6 shows this smoothed approximation to the Mohr-Coulomb yield surface by adjusting the shape parameter (α_F) for two different internal friction angles.

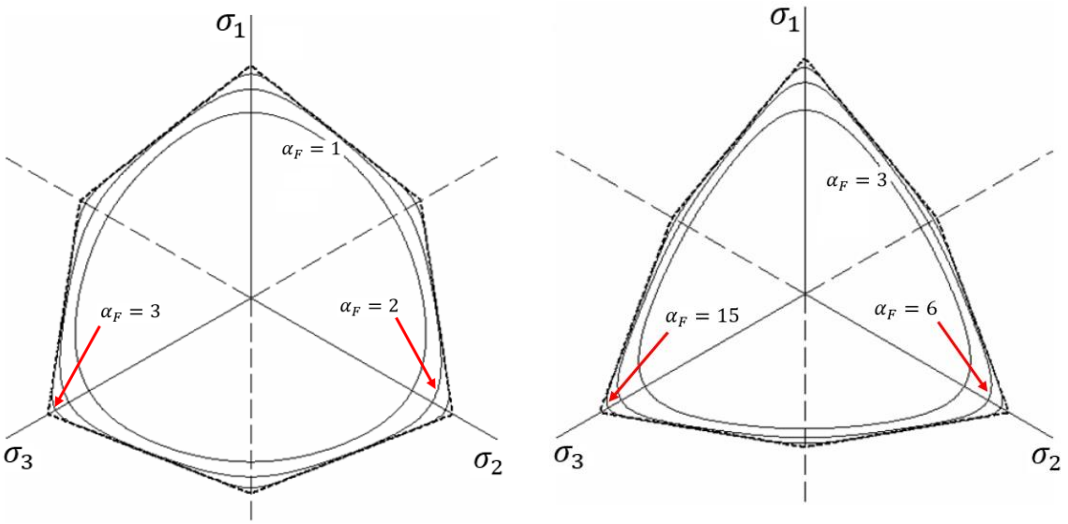

Figure 4-6: Smoothed surfaces for the Mohr-Coulomb criterion in the deviatoric plane for **(a)** $\varphi' = 15°$; **(b)** $\varphi' = 40°$ (Gesto *et al.*, 2011).

4.4.1.2. THE PLASTIC POTENTIAL FUNCTION

The plastic potential function for the BBM mechanism (G_{LC}) uses the smoothed approximation technique proposed by Gesto *et al.* (2011) through the function $g_G(\theta, \alpha_G)$. The expression for such a plastic function is given by

$$G_{LC} = 3\omega J^2 - \left(\frac{g_G(\theta, \alpha_G)}{g_G\left(-\frac{\pi}{6}, \alpha_G\right)}\right)^2 M_F^2 (p + p_s)(p_0 - p) = 0 \tag{4-89}$$

where ω is the non-associativy parameter and α_G is the smoothed shape parameter for the plastic potential function. Two options for $g_G(\theta, \alpha_G)$ are considered:

$$g_G(\theta, \alpha_G) = \left(cos^{\alpha_G}(\theta) + cos^{\alpha_G}\left(\frac{\pi}{3} + \theta\right) + cos^{\alpha_G}\left(\frac{\pi}{3} - \theta\right) \right)^{\frac{1}{\alpha_G}} \quad (4\text{-}90)$$

$$g_G(\theta, \alpha_G) \equiv g_F(\theta, \alpha_F) \quad (4\text{-}91)$$

where the expression in Equation (4-90) corresponds to a (smoothed) plastic potential for the Tresca criterion while Equation (4-91) expresses the condition of associated plasticity in octahedral planes.

4.4.1.3. THE PLASTIC FLOW RULE (BBM MECHANISM)

Once the plastic potential function (G_{LC}) is established, the macro plastic strains due to the BBM mechanism are obtained as

$$\dot{\boldsymbol{\varepsilon}}^p_{M,LC} = \dot{\lambda}_{LC} \boldsymbol{m}_{LC} \quad (4\text{-}92)$$

where $\dot{\lambda}_{LC}$ is the scalar plastic multiplier in its rate form ($\dot{\lambda}_{LC} \geq 0$), which estimates the magnitude of the plastic deformation rate. $\boldsymbol{m}_{LC}$ is the gradient of the plastic potential ($\boldsymbol{m}_{LC} = \frac{\partial G_{LC}}{\partial \boldsymbol{\sigma}}$) and gives the direction of the plastic strain increment in the strain space, which is perpendicular to the surface (in the stress space) defined by Equation (4-89). The plastic stress-strain law expressed in Equation (4-92) is known as the flow rule for the loading-collapse mechanism. In the case of associated plasticity, it is assumed that $G_{LC} \equiv F_{LC}$ (i.e., $\omega = 1$ in Equation (4-89)) and the second option for the function $g_G(\theta, \alpha_G)$, given by Equation (4-91), is taken. In such a situation, the gradient of the plastic potential and the normal vector to the yield surface ($\boldsymbol{n}_{LC} = \frac{\partial F_{LC}}{\partial \boldsymbol{\sigma}}$) are parallel. A schematic representation of a smoothed Mohr-Coulomb yield surface with some plastic strain rate vectors in the octahedral plane, for an associated plasticity situation, is depicted in Figure 4-7**.**

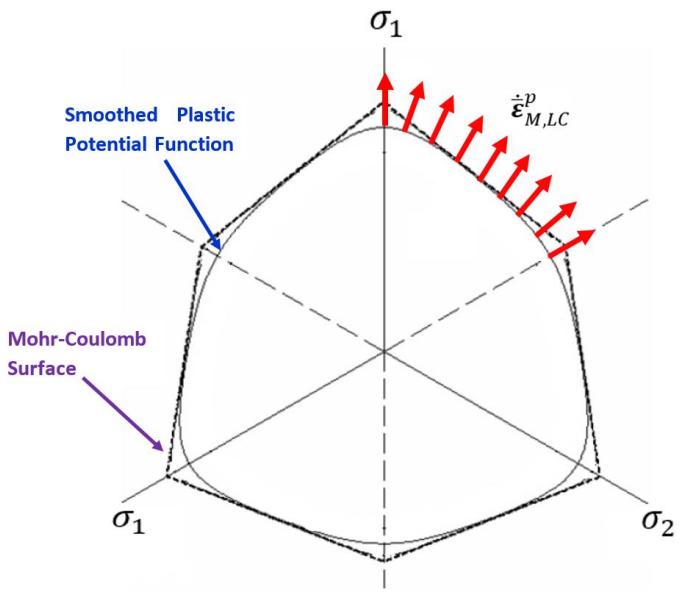

Figure 4-7: Smoothed Mohr-Coulomb yield surface in the deviatoric plane and the plastic strain rate directions in an associated plasticity.

4.4.2. INTERACTION BETWEEN STRUCTURAL LEVELS: THE β-MECHANISM

The other plastic mechanism considered in a double-porosity formulation is the one related to the interaction between the macro and the micro structural levels (the "β-mechanism"). It has been assumed that the microstructural behaviour is not affected by the macrostructural state. In contrast, the volumetric deformations of microstructure may induce plastic strains at the macrostructural level (Gens and Alonso, 1992). Furthermore, these plastic macrostructural strains due to the β-mechanism are taken as proportional to the microstructural elastic strains (Gens and Alonso, 1992; Yang *et al.*, 1998; Alonso *et al.*, 1999; Sánchez *et al.*, 2005). Thus, the magnitude of the plastic deformations induced by the β-mechanism, $\dot{\boldsymbol{\varepsilon}}^p_{M,\beta}$, is expressed as

$$\dot{\boldsymbol{\varepsilon}}^p_{M,\beta} = f_\beta \dot{\boldsymbol{\varepsilon}}_m \tag{4-93}$$

where f_β represents two micro-macro coupling functions in order to distinguish **M**icrostructural **C**ontraction (MC) paths from **M**icrostructural **S**welling (MS) paths. In this way, an index parameter (ω_β) is introduced into the mathematical formulation in order to identify the two main microstructural stress paths from the sign of the microstructural effective stress rate ($\dot{p}_m$). as follows:

i. $\dot{p}_m > 0 \Longrightarrow$ microstructural contraction path and $\omega_\beta = 1$

ii. $\dot{p}_m < 0 \Longrightarrow$ microstructural swelling path and $\omega_\beta = -1$

Note that the Soil Mechanics sign convention (where a compression state is expressed as a positive quantity) has been employed here.

The coupling functions, f_β, are dependent on the degree of openness of macrostructure which, in isotropic stress paths, is expressed by the (macro) stress ratio $\mu_\beta = \frac{p}{p_0}$, where p and p_0 are the current and the yield mean net stress, respectively, at the same macrostructural suction level and $0 \leq \mu_\beta \leq 1$. This ratio is a measure of the distance from the current macro stress state to the loading-collapse yield surface. Dense packing configurations of the porous medium occur for low values of μ_β while values close to 1 ($\mu_\beta \to 1$) suggest an open macrostructure relative to the applied stress state. Under microstructural swelling paths (MS paths) the irreversible changes in the global arrangements of clay aggregates due to the microstructure expansion are more relevant for initially denser configurations (Gens and Alonso, 1992; Alonso *et al.*, 1999). Therefore, the higher values of the micro-macro interaction function f_β, in MS paths, are found for low values of μ_β. In such conditions, the macrostructural medium tends to exhibit a softening behaviour due to the development of a more open macrostructure induced by the microstructural swelling. On the other hand, in MC paths (when microstructure contracts under the applied hydro-mechanical loading), it is expected that the magnitude of the global structural changes is higher for looser macrostructural configurations, i.e., when $\mu_\beta \to 1$. In such scenarios, the stress state of the expansive clay approaches the BBM yield surface and the material tends to collapse, which reflects on the hardening of macrostructure. The individual or mutual contributions of both plastic mechanisms (the BBM and the β-mechanisms) are considered in the mathematical expression for the macrostructural hardening law (see **Section 4.4.3**) so that the onset and the evolution of the permanent structure changes in expansive materials can be properly modelled.

From experimental suction-controlled paths performed on samples of compacted expansive clays at several stress levels (Pousada, 1984; Alonso *et al.*, 2005), it has been stated that f_β should decrease as μ_β increases in MS paths while in MC paths, it should be an increasing function of μ_β (Alonso *et al.*, 1999). Moreover, the hydration of highly expansive clays with open macrostructure suggested that the swelling of microstructure generated an invasion of macro-pores (Komine and Ogata, 1994). In contrast, some behaviour features observed during strong drying in plastic clays (MC paths), as the increase in their hydraulic conductivity (Shear *et al.*, 1992) or the reduction in their swelling pressure (Al-Homoud *et al.*, 1995), was related to the development of macro-porosity, which induced a more open structure under low confining stresses. Both of these micro-macro interaction mechanisms (macro-pore invasion in MS paths and macro-pore generation in MC paths) can be accounted for the model by taking negative values for the interaction functions at μ_β values for which these phenomena are expected to occur (Alonso *et al.*, 1999). A general representation of the micro-macro coupling functions, including the main behaviour features expected during wetting and drying paths, is shown in Figure 4-8.

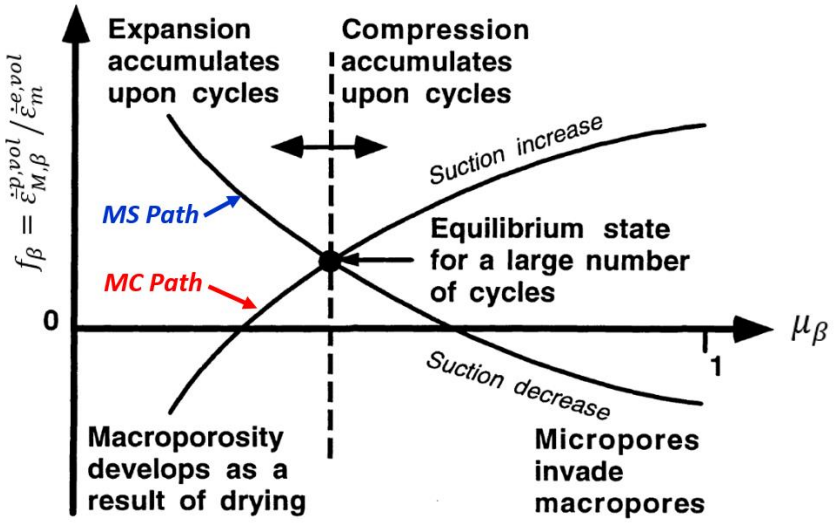

Figure 4-8: Distinct micro-macro pore interaction mechanisms and the structural coupling functions (after Alonso *et al.*, 1999).

Regarding the shape of the coupling functions, several expressions have been suggested in the literature in order to model the micro-macrostructure interaction mechanisms (Alonso *et al.*, 1994, 1999, 2005; Yang *et al.*, 1998; Sánchez *et al.*, 2005). Nevertheless, the general expression proposed in Gesto (2014) and given as follows

$$f_\beta = \begin{cases} f_{MC}^{(1)} + \left(f_{MC}^{(0)} - f_{MC}^{(1)}\right)\left(1-\mu_\beta\right)^{n_{MC}} & if \quad \omega_\beta = 1 \\ f_{MS}^{(1)} + \left(f_{MS}^{(0)} - f_{MS}^{(1)}\right)\left(1-\mu_\beta\right)^{n_{MS}} & if \;\; \omega_\beta = -1 \end{cases} \tag{4-94}$$

is used in the double-porosity formulation described in this document. In Equation (4-94), $f_{MC}^{(0)}$, $f_{MC}^{(1)}$, n_{MC} and $f_{MS}^{(0)}$, $f_{MS}^{(1)}$, n_{MS} are shape parameters for describing the coupling functions at *MC paths* and *MS paths*, respectively. Note that $f_{MC}^{(0)}$, $f_{MS}^{(0)}$ give the values of the interaction functions when $\mu_\beta = 0$ while $f_{MC}^{(1)}$, $f_{MS}^{(1)}$ represent the corresponding values at $\mu_\beta = 1$.

For generic stress states, the distance from the current stress state to the LC surface is determined from a homothetic center (C_p) in the $p{:}J$ plane (Gesto, 2014) with the macro stress ratio, μ_β, redefined as

$$\mu_\beta = \frac{p - C_p}{p^* - C_p} \tag{4-95}$$

where p is the current mean stress and p^* corresponds to its the image point, that is, the projection of that stress state on the BBM yield surface (Sánchez *et al.*, 2005) at a given matric suction s_M. For triaxial stress states ($J \neq 0$), Equation (4-95) is expressed as

$$\mu_\beta = \frac{J}{J^*} \tag{4-96}$$

so that the coordinates of the current state stress and of its image point, in the $p{:}J$ plane, are $\left(p, J\sqrt{3}\right)$ and $\left(p^*, J^*\sqrt{3}\right)$, respectively (see Figure 4-9). In isotropic stress conditions ($J = 0$), $p^* \equiv p_0$ in Equation (4-95). The position of the homothetic center (C_p) on the isotropic axis is set by a model parameter c, $0 \leq c \leq 1$, according to the following expression

$$C_p = -p_s + c(p_0 + p_s) \tag{4-97}$$

where p_s is the stress variable given in Equation (4-84). If the macro suction, the Lode angle and temperature are kept constant, the coordinates of the image stress point for a given current non-isotropic stress state are evaluated, from Equation (4-95) and Equation (4-96), as

$$\begin{aligned} p^* &= C_p + k \cdot \left(p - C_p\right) \\ J^* &= k \cdot J \end{aligned} \tag{4-98}$$

with

$$k = \frac{1}{\mu_\beta} \tag{4-99}$$

Since the image point belongs to the yield surface, it must satisfy the yield function condition given by Equation (4-79), that is,

$$\begin{aligned} F_{LC}(p^*, J^*, \theta, s_M, T) &= 3(J^*)^2 - \left(\frac{g_F(\theta, \alpha_F)}{g_F\left(-\frac{\pi}{6}, \alpha_F\right)}\right)^2 M_F^2 (p^* + p_s)(p_0 - p^*) \\ &= 0 \end{aligned} \tag{4-100}$$

The stress ratio μ_β for the current stress state can be evaluated by solving the latter equation for the scalar k, when the expressions in Equation (4-98) are inserted into Equation (4-100). As a consequence of the definition of μ_β, only the positive solution for k is selected. Note that the classical definition of the stress ratio for isotropic stress conditions ($\mu_\beta = \frac{p}{p_0}$), at a specific suction, can be obtained assuming $c = \frac{p_s}{p_0 + p_s}$ in Equation (4-97). In the same way, the general expression of μ_β in Sánchez *et al.* (2005) for non-isotropic stress states ($J \neq 0$) is also achieved for $c = \frac{p_s}{p_0 + p_s}$. Figure 4-9 shows a schematic representation of the geometric procedure used for estimating the distance from the current deviatoric stress state to the LC yield locus for two different values of the parameter c ($c = 0$ and $c = 0.25$).

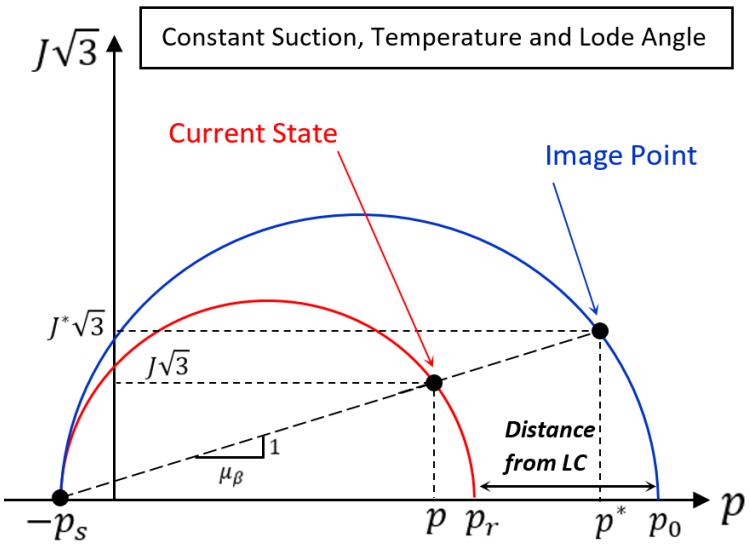

(a)

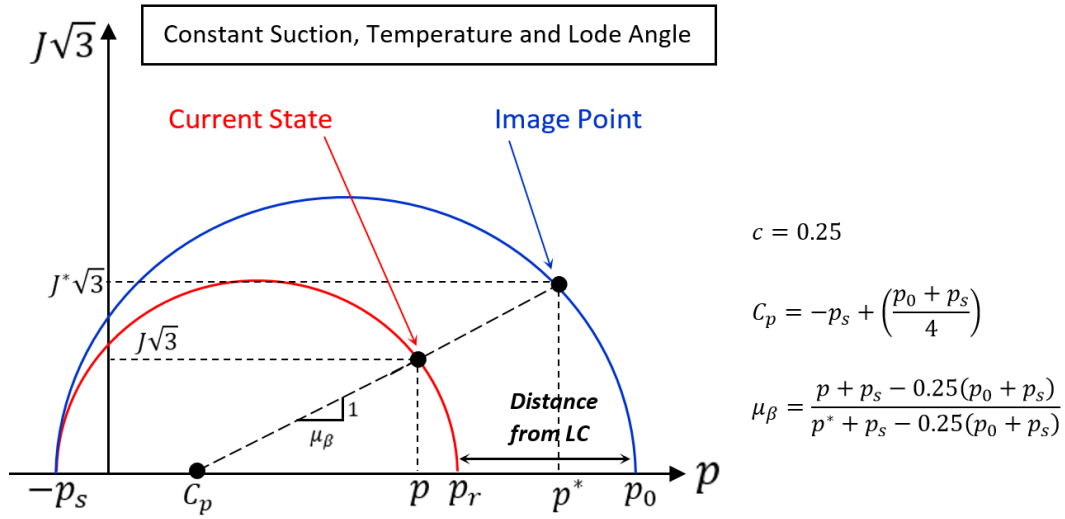

(b)

Figure 4-9: Evaluation of the macrostructural openness degree (μ_β) in non-isotropic loading conditions for **(a)** $c = 0$ and **(b)** $c = 0.25$.

The assumption of elastic thermal deformations at both structural levels requires the modification of Equation (4-93) to discount the microstructural deformations related to the thermal expansion of microstructure ($\dot{\boldsymbol{\varepsilon}}_{m,\Delta T}$) from the total microstructural strains ($\dot{\boldsymbol{\varepsilon}}_m$), that is,

$$\dot{\boldsymbol{\varepsilon}}^p_{M,\beta} = f_\beta\left(\dot{\boldsymbol{\varepsilon}}_m - \dot{\boldsymbol{\varepsilon}}_{m,\Delta T}\right) \tag{4-101}$$

which ensures that the plastic structural coupling mechanism does not account for the soil structure changes (as thermal collapse) due to the thermal expansion of microstructure, as discussed in **Section 4.2.5**. The fact that only the elastic part of the thermal micro-macro coupling is considered in the double-porosity model developed in this Thesis is merely a strategy to simplify the mathematical formulation. Despite the fact the BBM formulation considers the dependence of the yield surface on temperature through Equation (4-82) and Equation (4-84), it is not a simple task to estimate the irreversible changes on the soil structure arising from the micro-macro thermal interactions.

An important aspect to mention is that the *β-mechanism* is modelled here without the requirement of defining additional yield functions (at least, not explicitly) to the BBM yield function. This is a direct consequence of using a generalized plasticity theory to describe the micro-macro plastic coupling mechanism. The main advantage of this general approach lies in the fact that, in expansive soils, it is quite difficult to determine the shape of the internal yield surfaces and the initiation of the irreversible behaviour due to the micro-macro coupling mechanisms (Sánchez *et al.*, 2005).

4.4.3. HARDENING RULE

The hardening law in its rate form is defined as the relation between the total plastic volumetric strain ($\dot{\bar{\varepsilon}}_M^{p,vol}$) and the saturated isotropic pre-consolidation pressure (the hardening parameter, p_0^*), according to

$$\dot{p}_0^* = \frac{\partial p_0^*}{\partial \bar{\varepsilon}_M^{p,vol}} \dot{\bar{\varepsilon}}_M^{p,vol} = \frac{(1+\bar{e}_M)p_0^*}{\lambda_{(0)} - \bar{\kappa}_M} \dot{\bar{\varepsilon}}_M^{p,vol} \tag{4-102}$$

in which the contribution of both plastic mechanisms described previously are considered in the evolution of the region for admissible stress states in $p{:}J{:}s_M$ space , assuming that

$$\dot{\bar{\varepsilon}}_M^{p,vol} = \dot{\bar{\varepsilon}}_{M,LC}^{p,vol} + \dot{\bar{\varepsilon}}_{M,\beta}^{p,vol} = \boldsymbol{m}^T \left(\dot{\bar{\boldsymbol{\varepsilon}}}_{M,LC}^{p} + \dot{\bar{\boldsymbol{\varepsilon}}}_{M,\beta}^{p} \right) \tag{4-103}$$

where $\dot{\bar{\varepsilon}}_{M,LC}^{p,vol}$ is the irreversible volumetric strain rate induced by the yielding of macrostructure due to the loading-collapse mechanism and $\dot{\bar{\varepsilon}}_{M,\beta}^{p,vol}$ is the plastic volumetric deformation rate that quantifies the rearrangement of macrostructure in response to the microstructural deformations, as discussed in **Section 4.4.2**. Substituting the expressions in Equation (4-92) and Equation (4-101) into Equation (4-103) and recalling the definition of the thermal expansion at the microstructural medium as given in Equation (4-57) together with the relationships in Equation (4-59) and Equation (4-65), the rate of the total plastic volumetric deformation is given by

$$\dot{\bar{\varepsilon}}_M^{p,vol} = \boldsymbol{m}^T \left(\dot{\lambda}_{LC} \boldsymbol{m}_{LC} + f_\beta \left(\dot{\bar{\boldsymbol{\varepsilon}}}_m - \frac{1}{3K_T} \left(\frac{1+e_m}{1+e} \right) \dot{T} \boldsymbol{m} \right) \right) \tag{4-104}$$

Note that the hardening rule for the standard BBM model (in single-porosity approaches) is recovered when the micro-macro coupling plastic mechanism is neglected, that is, when $f_\beta = 0$. The dependence of the hardening parameter (p_0^*) on temperature may also be introduced in the mathematical description of the double-porosity model through the model parameters α_1 and α_3 in Equation (4-82) and, consequently, the hardening law would be determined as follows

$$\dot{p}_{0,T}^{*} = \frac{(1+\bar{e}_M)p_{0,T}^{*}}{\lambda_{(0)} - \bar{\kappa}_M}\boldsymbol{m}^T\left(\dot{\lambda}_{LC}\boldsymbol{m}_{LC} + f_\beta\left(\dot{\bar{\boldsymbol{\varepsilon}}}_m - \frac{1}{3K_T}\left(\frac{1+e_m}{1+e}\right)\dot{T}\boldsymbol{m}\right)\right) + 2(\alpha_1 \pm 2\alpha_3\Delta T)\dot{T} \tag{4-105}$$

where $\Delta T = T - T_0$. Nevertheless, and as mentioned above, thermoplastic mechanisms are out of the scope of this Thesis, which leads to the assumption of $\alpha_1 = \alpha_3 = 0$ in Equation (4-82) and Equation (4-105).

4.5. LOCAL STRESS EQUILIBRIUM AND FUNDAMENTAL COMPATIBILITY CONDITION

The total strain in its rate form for the expansive soil as given in Equation (4-56) is now recalled. If the global elastic matrix $[\boldsymbol{D}^e]$ is applied to both sides of that expression, the following relationship is obtained

$$[\boldsymbol{D}^e]\dot{\boldsymbol{\varepsilon}} = \dot{\boldsymbol{\sigma}} + \left(\zeta_{gm}\dot{P}_{gm} + \zeta_{lm}\dot{P}_{lm} + \zeta_T\dot{T} + \dot{P}_{fM}\right)\boldsymbol{m} + [\boldsymbol{D}^e]\left(\dot{\boldsymbol{\varepsilon}}_{m,\Delta T}^{e} + \dot{\bar{\boldsymbol{\varepsilon}}}_{M,\Delta s}^{e} + \dot{\bar{\boldsymbol{\varepsilon}}}_{M,LC}^{p} + \dot{\bar{\boldsymbol{\varepsilon}}}_{M,\beta}^{p}\right) \tag{4-106}$$

According to the thermo-elastic approach adopted in this Thesis and as discussed in **Section 4.2.5**, $\dot{\boldsymbol{\varepsilon}}_{m,\Delta T}^{e} = \dot{\boldsymbol{\varepsilon}}_{\Delta T}^{e}$. The rate of effective stress acting on the soil ($\dot{\boldsymbol{\sigma}}$) can be expressed, from Equation (4-106), as

$$\dot{\boldsymbol{\sigma}} = [\boldsymbol{D}^e]\left(\dot{\boldsymbol{\varepsilon}} - \dot{\bar{\boldsymbol{\varepsilon}}}_{M,\Delta s}^{e} - \dot{\boldsymbol{\varepsilon}}_{\Delta T}^{e} - \dot{\bar{\boldsymbol{\varepsilon}}}_{M,LC}^{p} - \dot{\bar{\boldsymbol{\varepsilon}}}_{M,\beta}^{p}\right) - \left(\zeta_{gm}\dot{P}_{gm} + \zeta_{lm}\dot{P}_{lm} + \zeta_T\dot{T} + \dot{P}_{fM}\right)\boldsymbol{m} \tag{4-107}$$

Inserting into this latter equation the expressions for the macro plastic strain components related to the BBM mechanism and to the micro-macro coupling ($\dot{\bar{\boldsymbol{\varepsilon}}}_{M,\beta}^{p}$) as defined in Equation (4-92) and Equation (4-101), respectively, it leads to

$$\dot{\boldsymbol{\sigma}} = [\boldsymbol{D}^e]\left(\dot{\boldsymbol{\varepsilon}} - \dot{\bar{\boldsymbol{\varepsilon}}}_{M,\Delta s}^{e} - \dot{\boldsymbol{\varepsilon}}_{\Delta T}^{e} - \dot{\lambda}_{LC}\boldsymbol{m}_{LC}\right) - f_\beta[\boldsymbol{D}^e]\left(\dot{\bar{\boldsymbol{\varepsilon}}}_{m}^{e} - \dot{\bar{\boldsymbol{\varepsilon}}}_{m,\Delta T}^{e}\right) - \left(\zeta_{gm}\dot{P}_{gm} + \zeta_{lm}\dot{P}_{lm} + \zeta_T\dot{T} + \dot{P}_{fM}\right)\boldsymbol{m} \tag{4-108}$$

Combining the thermal strain components in Equation (4-108) and recalling the relation between the "local" ($\dot{\boldsymbol{\varepsilon}}_{m,\Delta T}^{e}$) and the "global" ($\dot{\bar{\boldsymbol{\varepsilon}}}_{m,\Delta T}^{e}$) microstructural thermal strains as given in Equation (4-5), Equation (4-108) can be re-written as

$$\dot{\boldsymbol{\sigma}} = [\boldsymbol{D}^e]\left(\dot{\boldsymbol{\varepsilon}} - \dot{\bar{\boldsymbol{\varepsilon}}}_{s_M}^{e} - \left(1 - f_\beta\left(\frac{1+e_m}{1+e}\right)\right)\dot{\boldsymbol{\varepsilon}}_{\Delta T}^{e} - \dot{\lambda}_{LC}\boldsymbol{m}_{LC} - f_\beta\dot{\bar{\boldsymbol{\varepsilon}}}_{m}^{e}\right) - \left(\zeta_{gm}\dot{P}_{gm} + \zeta_{lm}\dot{P}_{lm} + \zeta_T\dot{T} + \dot{P}_{fM}\right)\boldsymbol{m} \tag{4-109}$$

It has been established that the local (at particle level) mechanical behaviour of expansive clays is governed by the microstructural effective stress, which can be expressed by Equation (4-40). Combining such an expression with the "global" microstructural stress-strain law in Equation (4-21) and solving for $\dot{\boldsymbol{\sigma}}$, the stress-strain relationship for the expansive material, written in terms of the "local" mechanical behaviour, is given by

$$\dot{\boldsymbol{\sigma}} = \underbrace{[\overline{\boldsymbol{D}}_m^e]\left(\dot{\boldsymbol{\varepsilon}}_m^e - \dot{\bar{\boldsymbol{\varepsilon}}}_{m,\Delta T}^e\right)}_{\dot{\boldsymbol{\sigma}}_m} - \left(\zeta_{gm}\dot{P}_{gm} + \zeta_{lm}\dot{P}_{lm} + \zeta_T\dot{T} + \dot{P}_{fM}\right)\boldsymbol{m} \tag{4-110}$$

Taking into account the relationships among the elastic moduli shown in Table 4-1, it can be stated that $[\overline{\boldsymbol{D}}_m^e] = \frac{1+e}{1+e_m}[\boldsymbol{D}^e]$ and, consequently,

$$\dot{\boldsymbol{\sigma}} = \left(\frac{1+e}{1+e_m}\right)[\boldsymbol{D}^e]\left(\dot{\boldsymbol{\varepsilon}}_m^e - \dot{\bar{\boldsymbol{\varepsilon}}}_{m,\Delta T}^e\right) - \left(\zeta_{gm}\dot{P}_{gm} + \zeta_{lm}\dot{P}_{lm} + \zeta_T\dot{T} + \dot{P}_{fM}\right)\boldsymbol{m} \tag{4-111}$$

The requirement of local stress equilibrium at each point in the porous medium allows equating the relations in Equation (4-108) and Equation (4-111). Therefore, the following compatibility condition is obtained

$$\left(\frac{1+e}{1+e_m} + f_\beta\right)[\boldsymbol{D}^e]\left(\dot{\boldsymbol{\varepsilon}}_m^e - \dot{\bar{\boldsymbol{\varepsilon}}}_{m,\Delta T}^e\right) = [\boldsymbol{D}^e]\left(\dot{\boldsymbol{\varepsilon}} - \dot{\boldsymbol{\varepsilon}}_{\Delta T}^e - \dot{\bar{\boldsymbol{\varepsilon}}}_{M,\Delta s}^e - \dot{\lambda}_{LC}\boldsymbol{m}_{LC}\right) \tag{4-112}$$

from which, it is possible to determine an explicit expression for the "global" microstructural strain rate ($\dot{\bar{\boldsymbol{\varepsilon}}}_m^e$) as follows

$$\dot{\bar{\boldsymbol{\varepsilon}}}_m^e = \left(\frac{1+e}{1+e_m} + f_\beta\right)^{-1} \cdot \left(\dot{\boldsymbol{\varepsilon}} - \dot{\boldsymbol{\varepsilon}}_{\Delta T}^e - \dot{\bar{\boldsymbol{\varepsilon}}}_{M,\Delta s}^e - \dot{\lambda}_{LC}\boldsymbol{m}_{LC}\right) + \dot{\bar{\boldsymbol{\varepsilon}}}_{m,\Delta T}^e \tag{4-113}$$

Recalling the relationship between $\dot{\boldsymbol{\varepsilon}}_{\Delta T}^e = \dot{\boldsymbol{\varepsilon}}_{m,\Delta T}^e$ and $\dot{\bar{\boldsymbol{\varepsilon}}}_{m,\Delta T}^e$ (see Equation (4-5)) and making explicit the dependence of the strain rate components in Equation (4-113) on temperature and macro suction changes, then

$$\begin{aligned}\dot{\bar{\boldsymbol{\varepsilon}}}_m^e = \left(\frac{1+e}{1+e_m} + f_\beta\right)^{-1} \cdot \left(\dot{\boldsymbol{\varepsilon}} - \frac{1}{3K_T}\dot{T}\boldsymbol{m} - \frac{1}{3\overline{K}_s}\dot{s}_M\boldsymbol{m} - \dot{\lambda}_{LC}\boldsymbol{m}_{LC}\right) \\ + \frac{1}{3K_T}\left(\frac{1+e_m}{1+e}\right)\dot{T}\boldsymbol{m}\end{aligned} \tag{4-114}$$

Equation (4-114) expresses the changes in the "global" microstructural deformation in terms of macro and global state variables as well. This relationship plays an important role in the mathematical development of the stress integration algorithm for the double-porosity model. The stress point algorithm is described in the next chapter.

Under isothermal conditions ($\dot{T} = 0$), the microstructural strain rate, given in Equation (4-114), reduces to

$$\dot{\boldsymbol{\varepsilon}}_m^e = \left(\frac{1+e}{1+e_m} + f_\beta\right)^{-1} \cdot \left(\dot{\boldsymbol{\varepsilon}} - \frac{1}{3\overline{K}_s}\dot{s}_M \boldsymbol{m} - \dot{\lambda}_{LC}\boldsymbol{m}_{LC}\right) \tag{4-115}$$

If the micro-macro coupling mechanism is neglected, $f_\beta = 0$, and the loading-collapse mechanism is the only plastic mechanism considered in the numerical analysis, the "standard BBM model formulation" is recovered. In such case, the following relationship is obtained from Equation (4-114),

$$\begin{aligned}
\dot{\boldsymbol{\varepsilon}}_m^e &= \overbrace{\left(\frac{1+e_m}{1+e}\right)\left(\dot{\boldsymbol{\varepsilon}} - \dot{\boldsymbol{\varepsilon}}_{\Delta T}^e - \frac{1}{3\overline{K}_s}\dot{s}_M \boldsymbol{m} - \dot{\lambda}_{LC}\boldsymbol{m}_{LC}\right)}^{\dot{\boldsymbol{\varepsilon}}_{m,HM}^e} + \dot{\boldsymbol{\varepsilon}}_{m,\Delta T}^e \\
&= \left(\frac{1+e_m}{1+e}\right)\left(\dot{\boldsymbol{\varepsilon}} - \frac{1}{3\overline{K}_s}\dot{s}_M \boldsymbol{m} - \dot{\lambda}_{LC}\boldsymbol{m}_{LC}\right) + \underbrace{\left(\dot{\boldsymbol{\varepsilon}}_{m,\Delta T}^e - \left(\frac{1+e_m}{1+e}\right)\dot{\boldsymbol{\varepsilon}}_{\Delta T}^e\right)}_{=0} \\
&= \left(\frac{1+e_m}{1+e}\right)\left(\dot{\boldsymbol{\varepsilon}} - \frac{1}{3\overline{K}_s}\dot{s}_M \boldsymbol{m} - \dot{\lambda}_{LC}\boldsymbol{m}_{LC}\right)
\end{aligned} \tag{4-116}$$

Despite the fact that no thermal terms appear explicitly in the final expression shown in Equation (4-116), it is still consistent with the assumption that only elastic thermal strains are allowed. As a consequence, the microstructural thermal expansion term ($\dot{\boldsymbol{\varepsilon}}_{m,\Delta T}^e$) is balanced by the term related to the thermal expansion of the expansive soil ($\dot{\boldsymbol{\varepsilon}}_{\Delta T}^e$). However, the thermal effects are included implicitly in Equation (4-116) and it is quite simple to demonstrate, from the insertion of the expression for the total strain rate tensor ($\dot{\boldsymbol{\varepsilon}}$) in Equation (4-56) into the latter expression. Therefore,

$$\begin{aligned}
\dot{\boldsymbol{\varepsilon}}_m^e &= \left(\frac{1+e_m}{1+e}\right)\left(\dot{\boldsymbol{\varepsilon}} - \frac{1}{3\overline{K}_s}\dot{s}_M \boldsymbol{m} - \dot{\lambda}_{LC}\boldsymbol{m}_{LC}\right) \\
&= \left(\frac{1+e_m}{1+e}\right)\left([\boldsymbol{D}^e]^{-1}\dot{\boldsymbol{\sigma}} + \frac{1}{3K}\left(\zeta_{gm}\dot{P}_{gm} + \zeta_{lm}\dot{P}_{lm} + \zeta_T\dot{T} + \dot{P}_{fM}\right)\boldsymbol{m} + \dot{\boldsymbol{\varepsilon}}_{\Delta T}^e\right) \\
&= \left(\frac{1+e_m}{1+e}\right)\left(\dot{\boldsymbol{\varepsilon}}_{m,\Delta\sigma_m}^e + \dot{\boldsymbol{\varepsilon}}_{\Delta T}^e\right) = \dot{\boldsymbol{\varepsilon}}_{m,\Delta\sigma_m}^e + \dot{\boldsymbol{\varepsilon}}_{m,\Delta T}^e
\end{aligned} \tag{4-117}$$

Finally, if Equation (4-109) and Equation (4-114) are combined, and after some algebraic manipulation of the resulting expression, the following useful stress-strain relationship is achieved

$$\begin{aligned}
\dot{\boldsymbol{\sigma}} = (1-A)[\boldsymbol{D}^e]\left(\dot{\boldsymbol{\varepsilon}} - \frac{1}{3\overline{K}_s}\dot{s}_M \boldsymbol{m} - \frac{1}{3K_T}\dot{T}\boldsymbol{m} - \dot{\lambda}_{LC}\boldsymbol{m}_{LC}\right) \\
- \left(\zeta_{gm}\dot{P}_{gm} + \zeta_{lm}\dot{P}_{lm} + \zeta_T\dot{T} + \dot{P}_{fM}\right)\boldsymbol{m}
\end{aligned} \tag{4-118}$$

where the coefficient A is defined as

$$A = f_\beta \left(\frac{1+e}{1+e_m} + f_\beta \right)^{-1} \tag{4-119}$$

For a more detailed insight on the mathematical procedure followed in order to reach all the previous expressions, see Gesto (2014). It is important to highlight that the stress-strain constitutive law in Equation (4-118) is one of the main ingredients used to implement the double-porosity model discussed in this document into the finite element code CODE_BRIGHT (as presented in the following chapter).

5. DOUBLE POROSITY FORMULATION: EXPLICIT INTEGRATION OF THE STRESS TENSOR IN THE CONTEXT OF A FINITE ELEMENT APPROACH

5.1. INTRODUCTION

The intrinsic complexity of geotechnical materials due to their non-linear constitutive behavior leads to the use of advanced numerical strategies to assess the evolution of strains, stresses, pore fluid pressures and temperature in the porous medium when subjected to a generic loading path. In the case of a double-porosity model, in which the material mechanical behavior is better described through a generalized plasticity formulation due to the plastic mechanism arising from the micro-macro coupling (Sánchez, 2004), this assertion is much more relevant. One of the most powerful tools used to deal with this kind of constitutive model is the Finite Element Method (FEM). The FEM provides a spatial discretization that, in addition to the temporal discretization through finite differences, underlies the numerical structure found in many computational codes for solving the system of partial differential equations governing the behavior of the porous medium. The numerical code used in this Thesis (CODE_BRIGHT) can be counted among them.

Any acceptable solution for a geotechnical boundary value problem must satisfy equilibrium, compatibility, material constitutive behaviour and boundary conditions (Potts and Zdravković, 1999). Due to that, all the solution strategies should ensure that the numerical solution to the system of algebraic equations (resulting from the space and time discretizations) accomplishes these four basic requirements. The non-linearities in soil behaviour requires that a solution should be achieved when the change in boundary conditions is applied incrementally so that the governing finite element equations have to be solved for each one of those increments. The final solution is given by the sum of each incremental solution.

The iterative Newton-Raphson method (and its variants like the Modified Newton-Raphson and the Quasi Newton schemes) is reported to produce accurate solutions that are essentially independent of the increment size (Potts and Zdravković, 1999). Nevertheless, it is expected that such a numerical prediction at the end of a given iterative step may not fulfill the convergence criteria and then, the resulting residual load vector must be accounted for. In that sense, the current incremental vector of nodal unknowns (the solution to the global system of governing equations at the end of a given iteration) serves to estimate the incremental generalized strain vector at each integration point. Consequently, the constitutive stress-strain relationship is integrated locally (at each Gauss integration point), the stress increments and the stress state at each integration point are obtained and the equivalent nodal forces are then estimated. The residual load vector is calculated as the difference between these nodal forces and the externally applied loads (due to the boundary conditions), which is added to the current applied loads for the next iteration step. This iterative process is repeated until the convergence criteria are satisfied. The finite element code CODE_BRIGHT adopts the Newton-Raphson approach to find the numerical solution of the non-linear system of (global) governing equations for non-isothermal analyses in unsaturated porous media (Olivella *et al.*, 1996).

Since the success of the Newton-Raphson procedure depends strongly on the accuracy of the numerical strategies for integrating the constitutive equations (Potts and Zdravković, 1999) and considering that the material constitutive behaviour may change during an incremental loading, several stress point algorithms have been proposed in the literature. These stress integration algorithms are commonly classified as implicit (backward) or explicit (forward) schemes, depending on the time-position at which the gradients are determined. In explicit approaches, the yield function, the hardening parameters and all derivatives are estimated at the beginning of the time increment, that is, at known stress states, and iterative algorithms to predict the final stresses are not strictly necessary (Ding *et al.*, 2005). In an implicit integration scheme these variables and derivatives are evaluated at the end of the increment, that is, at unknown stress states, requiring then an iterative scheme (like the Newton-Raphson method) to solve the system of equations at the Gauss point level (Ding *et al.*, 2005; Pedroso and Farias, 2005).

Implicit schemes, like the well-known *Backward Euler* algorithm, are known for their excellent convergent performance, especially in non-linear analysis. Another advantage of these algorithms is that there is no need to restore the consistency condition when plastic mechanisms are activated during a loading path, since the resulting stress states automatically satisfy the yield criterion (Sloan *et al.*, 2001; Ding *et al.*, 2005, 2007; Pedroso and Farias, 2005). Consequently, the determination of the intersection point of a stress path with the yield surface is not required. However, implicit algorithms may lose their generality when dealing with some complex constitutive models when their stress integration process may require specific implementation that contemplates their own peculiarities (Sloan *et al.*, 2001; Pedroso and Farias, 2005). The use of implicit algorithms for integrating complex yield functions and hardening laws can lead to formulations that are very difficult to implement numerically (Potts and Zdravković, 1999). Furthermore, the convergence is not always guaranteed for some strain paths and the CPU time demanded to obtain an accurate solution may increase drastically when the number of loading steps for its convergence is not controlled (Abbo and Sloan, 1996; Pedroso and Farias, 2005). A more detailed explanation about the advantages, disadvantages and applications of implicit schemes to geotechnical problems can be found, for instance, in

Ortiz and Simo (1986), Runesson (1987), Borja and Lee (1990), Borja (1991), Alawaji *et al.* (1992), Potts and Ganendra (1994), Macari *et al.* (1997), Potts and Zdravković (1999), Rouainia and Wood (2001) and Pedroso and Farias (2005).

On the other hand, explicit schemes are easier to implement in comparison with implicit ones and when they are used with error control by adjusting automatically the size of loading sub-step, accurate solutions can be found with short computational times (Pedroso and Farias, 2005). Moreover, explicit integration schemes are more suitable for including, in a direct, robust and structured manner, new phenomena or more complex models to already existent mathematical formulations (Potts and Zdravković, 1999; Sloan *et al.*, 2001). The *Forward Euler* algorithms, the explicit sub-stepping schemes proposed by Sloan (1987) (the so-called *Modified Euler*) enhanced by Sloan and Booker (1992) and Sloan *et al.* (2001) or the higher order Runge-Kutta algorithms are some explicit stress integration schemes widely used throughout the last decades. A disadvantage of the explicit schemes lies in the fact that the integration procedure can lead to stress states that do not satisfy the yield criterion, that is, the computed stress state may lie outside the yield locus (Ding *et al.*, 2005, 2007). Consequently, the consistency condition needs to be checked at the end of the integration process. If the calculated stresses violate the consistency condition, an additional correction of these stresses becomes necessary to restore them to the yield surface. More useful information related to explicit integration schemes, their capabilities/drawbacks and their accuracy and efficiency to solve boundary value problems are reported in Sloan (1987), Sloan and Booker (1992), Abbo and Sloan (1996), Potts and Zdravković (1999), Sloan *et al.* (2001), Zhao *et al.* (2005), Pedroso and Farias (2005), Sołowski and Gallipoli (2006, 2010), Ding *et al.* (2005, 2007), Hiley and Rouainia (2008), among others.

5.2. EXPLICIT STRESS INTEGRATION IN THE CONTEXT OF A DOUBLE-POROSITY APPROACH

The numerical strategy employed in this Thesis to integrate the elastoplastic stress-strain relationship is a refined Euler scheme with automatic sub-step size and local error control based on Sloan's algorithm (Sloan, 1987; Sloan *et al.*, 2001). The incremental algorithm chosen for that purpose is the explicit Modified Euler scheme. Some important aspects of this choice are:

- The fact that the DPM model has an inherent complexity arising from the coupling between the micro and macro structural levels. In fact, it is quite difficult to determine the onset of plastic deformations associated with this plastic mechanism or even to postulate a yield function defining the transition from elasticity to plasticity. Due to that, the plastic mechanism related to the interaction between both structural levels is described by a generalized plasticity theory (Sánchez, 2004; Sánchez *et al.*, 2005, 2008).
- As a direct consequence of the point stated above, the implementation of a model based on the generalized plasticity theory into a numerical code may become a cumbersome task if an implicit scheme is employed to integrate the elastoplastic constitutive laws. This is because the backward Euler return method requires second order derivatives of the yield function and of the plastic potential (Sloan *et al.*, 2001) which can lead to extremely complicated expressions. Numerical explicit schemes, as mentioned

previously, are simpler to implement (they only require first derivatives) and can easily accommodate such complex constitutive models in their mathematical formulation.

- Explicit algorithms, when combined with an automatic time step and error control, can produce very accurate solutions at low computational cost (Wissmann and Hauck, 1983; Sloan, 1987; Potts and Ganendra, 1994; Pedroso and Farias, 2005). The Modified Euler scheme is a good representative of this category of explicit methods.
- New extended versions of the numerical code due to the incorporation of other elastoplastic or time-dependent mechanisms, as a result of a better understanding of the main phenomena governing the mechanical behavior, are easier to implement when an explicit integration scheme is employed (Sánchez, 2004).

The main aspects of the Modified Euler with automatic error control to update the stresses in the double-porosity formulation considered here are briefly discussed in **Section 5.2.10**. Afterwards, a general and robust description of the mathematical expressions and the numerical issues related to the plastic behaviour inside the yield surface (**Section 5.2.4**), the algorithm for the crossing of the yield surface (**Section 5.2.5**) and the stress correction algorithm (**Section 5.2.8**) when the yield criterion at the end of the elastoplastic integration is not satisfied are addressed in this chapter.

5.2.1. EVOLUTION EQUATIONS

The stress-strain relationships in elastoplastic models are usually formulated as rate or infinitesimal incremental equations, generating a system of differential equations. The stress integration algorithm aims to solve this boundary value problem expressed (in rate form) as

$$\begin{aligned} \dot{\boldsymbol{\sigma}} &= [\boldsymbol{D}^{ep}]\dot{\boldsymbol{\varepsilon}} + \sum \boldsymbol{h}_\theta \dot{\theta} \\ \dot{\boldsymbol{\alpha}}_i &= \dot{\lambda}_i \mathbf{H}_i + \dot{\theta}\boldsymbol{\eta}_i \end{aligned} \tag{5-1}$$

or, when the additive decomposition of total strain (into its elastic and plastic components) is explicitly employed in order to describe the mechanical behaviour, as

$$\begin{aligned} \dot{\boldsymbol{\sigma}} &= [\boldsymbol{D}^{e}](\dot{\boldsymbol{\varepsilon}} - \dot{\boldsymbol{\varepsilon}}^{p}) + \sum \boldsymbol{h}_\theta \dot{\theta} \\ \dot{\boldsymbol{\varepsilon}}^{p} &= \sum \dot{\lambda}_i \frac{\partial g_i}{\partial \boldsymbol{\sigma}} \\ \dot{\boldsymbol{\alpha}}_i &= \dot{\lambda}_i \mathbf{H}_i + \dot{\theta}\boldsymbol{\eta}_i \end{aligned} \tag{5-2}$$

The Kuhn-Tucker restrictions precribe that

$$\dot{\lambda}_i \geq 0$$
$$f_i(\boldsymbol{\sigma}, \boldsymbol{\alpha}_i) \leq 0 \tag{5-3}$$
$$\dot{\lambda}_i f_i(\boldsymbol{\sigma}, \boldsymbol{\alpha}_i) = 0$$

and the consistency condition, which must be satisfied for all permissible stress states and loading paths, is given by

$$\sum \dot{\lambda}_i \dot{f}_i(\boldsymbol{\sigma}, \boldsymbol{\alpha}_i) = 0 \tag{5-4}$$

In the previous expressions, $[\boldsymbol{D^e}]$, $[\boldsymbol{D^{ep}}]$ are, respectively, the elastic and the elastoplastic constitutive tensor; $\dot{\theta}$ represents the rate of any non-mechanical strain variable (that is, fluid pressures and/or temperature), whose effects on stress state are computed through the constitutive vector $\boldsymbol{h}_\theta$. $\dot{\boldsymbol{\alpha}}_i$ is the rate-form of the vector of internal variables, $\dot{\lambda}_i$ is the rate of the plastic multiplier and $\boldsymbol{H}_i$, $\boldsymbol{\eta}_i$ are vectors containing the prescribed hardening functions. The first term on the right-hand side of the second equation in (5-1) (also the third equation in (5-2)) provides the changes in hardening parameters due to the changes in plastic strains while the second term in the same expression quantifies all non-mechanical plastic processes induced by changes in environmental conditions (Tamagnini *et al.*, 2004). The second equation in (5-2) is a general flow rule that accounts for the contribution of each plastic mechanism (in a multi-plasticity framework) on the evolution of irreversible strains.

From the expressions in Equation (5-3), it is straightforward to conclude that a null value for the plastic multiplier rate ($\dot{\lambda}_i = 0$) is obtained when the loading process leads to stress states within the yield surface, that is, when $f_i(\boldsymbol{\sigma}, \boldsymbol{\alpha}_i) < 0$. When plastic loading takes place, the stress state remains on the yield surface ($f_i(\boldsymbol{\sigma}, \boldsymbol{\alpha}_i) = 0$) and the plasticity theory establishes a non-negative value for $\dot{\lambda}_i$. This value is determined by ensuring the consistency condition (Equation (5-4)) for each activated plastic mechanism, that is, $\dot{f}_i(\boldsymbol{\sigma}, \boldsymbol{\alpha}_i) = 0$.

For the double-porosity model discussed in this Thesis, the evolution equations analogous to those described in Equation (5-1) are expressed as follows

$$\dot{\boldsymbol{\sigma}} = [\boldsymbol{D^{ep}}]\dot{\boldsymbol{\varepsilon}} + \boldsymbol{h}_s \dot{s}_M + \boldsymbol{h}_g \dot{P}_{gM} + \boldsymbol{h}_l \dot{P}_{lM} + \boldsymbol{h}_T \dot{T} + \boldsymbol{h}_t \dot{t}$$
$$\frac{\dot{p}_o^*}{p_0^*} = \frac{(1+\bar{e}_M)}{\lambda_{sat} - \bar{\kappa}_M}\left(\dot{\lambda}_{LC}\boldsymbol{m}^T\boldsymbol{m}_{LC} + f_\beta \boldsymbol{m}^T \dot{\bar{\boldsymbol{\varepsilon}}}_m^e - \frac{f_\beta}{K_T}\left(\frac{1+e_m}{1+e}\right)\dot{T}\right) \tag{5-5}$$

where the constitutive vectors $\boldsymbol{h}_s$, $\boldsymbol{h}_f$, $\boldsymbol{h}_T$, $\boldsymbol{h}_t$ compute the changes in the stress state in response to the changes in the macrostructural suction ($\dot{s}_M$), in fluid pressures (water, $\dot{P}_{lM}$, or air, $\dot{P}_{gM}$, depending on the saturation state of macrostructure), in temperature ($\dot{T}$) and in time ($\dot{t}$), respectively. The second relationship in Equation (5-5) gives the evolution for the hardening parameter (p_0^*), which is obtained from Equation (4-105), assuming that the dependence of the elastic domain size on temperature is neglected. In other words, thermoplastic mechanisms are not considered in the current mathematical formulation of the double-porosity approach.

Recalling the generalized stress-strain constitutive law expressed in Equation (3-126), the definition for the generalized strain rate, $\dot{\boldsymbol{\varepsilon}}^g$, in accordance with the stress-strain relationship in Equation (5-5), is given by

$$\dot{\boldsymbol{\varepsilon}}^g = \begin{Bmatrix} \dot{\boldsymbol{\varepsilon}} \\ \dot{P}_{lM} \\ \dot{P}_{gM} \\ \dot{T} \\ \dot{t} \end{Bmatrix} \tag{5-6}$$

in which the changes in the macrostructural fluid pressures, in temperature and in time are taken as additional components of this enlarged strain vector (see the first relationship in Equation (5-1)).

The time dependency in Equation (5-5) is associated with the transient mass transfer process that arises from the differences in the water potential of each structural medium. Due to the high hydraulic conductivity of gas phase through connected pores and for the sake of simplicity, it is assumed that the difference in gas pressures at both pore levels is negligible, that is, $P_{lm} \equiv P_{lM}$ at each point of the porous medium. It implies that the micro-macro water exchange term defined in Equation (3-55) is reduced to the difference between the pore water pressures at each structural level, as expressed by Equation (3-56). This simplifying hypothesis leads to the expressions and relations presented in the next sections.

Another important simplification to take into account is the role of the microstructural pore-water pressure (P_{lm}) in the numerical implementation of the double-porosity model in a finite element context. As mentioned in **Section 3.7.2.2**, the rate of the microstructural liquid pressure ($\dot{P}_{lm}$) is the state variable (unknown) of the balance equation of water in micro-pores. Consequently, and according to the compositional approach used in the numerical code CODE_BRIGHT, this equation should be solved together with the other balance equations (in a non-linear system of algebraic equations) through a Newton-Raphson iteration scheme (see CODE_BRIGHT User's Guide (2014) and **Section 5.3** in this document for more information). Nevertheless, this variable is considered here as a history variable (Gesto, 2014) and it is updated when the stress point algorithm is performed. Moreover, updated microstructural liquid pressures are stored at the Gauss points of each element while macrostructural liquid pressures (unknowns of the hydraulic problem) are nodal variables.

5.2.2. EXPLICIT STRESS POINT ALGORITHMS: THE STANDARD PROCEDURE

The numerical procedure to perform the stress point algorithm in many elastoplastic models starts with the assumption that the material behaves elastically (Potts and Zdravković, 1999; Tamagnini *et al.*, 2004). Thus, the mechanical constitutive relationship is integrated along the incremental loading at each integration point and the estimates for the stress increments ($\Delta\boldsymbol{\sigma}^{trial}$) are obtained without considering the evolution of the hardening parameters, that is, $\dot{\boldsymbol{\alpha}} = \mathbf{0}$ in Equation (5-1). The accumulated stress state (also called *trial elastic state*), $\boldsymbol{\sigma}_n^{trial}$, is

updated adding these trial stress increments to the previous accumulated stresses ($\boldsymbol{\sigma}_{n-1}$). Then, the trial state is checked for consistency with the yield function. If $f\left(\boldsymbol{\sigma}_n^{trial}, \boldsymbol{\alpha}_{n-1}\right) \leq 0$, the loading process is declared elastic and the trial state represents the actual final state of the material (see Figure 5-1(a)). If the yield surface criterion is violated, that is $f\left(\boldsymbol{\sigma}_n^{trial}, \boldsymbol{\alpha}_{n-1}\right) > 0$, the stress increments found during the trial step are not correct (see Figure 5-1(b)). In this situation, plastic strains are generated and the yield surface evolves during the loading process. In such a case, it is necessary to determine the portion of the stress increments ($\Delta\boldsymbol{\sigma}^e$) for which the material behavior changes from elastic to elastoplastic. In other words, the crossing of the yield surface point in the stress space is sought (as for instance, point B in Figure 5-1(b)). Furthermore, the amount of plastic strains generated during the loading path must also be evaluated so that the resulting stresses, $\boldsymbol{\sigma}_n^f = \boldsymbol{\sigma}_{n-1} + \Delta\boldsymbol{\sigma}^e + \Delta\boldsymbol{\sigma}^{ep}$ ($\Delta\boldsymbol{\sigma}^{ep}$ is integrated through the elastoplastic constitutive matrix) and the hardening/softening parameters, $\boldsymbol{\alpha}_n$, satisfy the yield condition, i.e., $f\left(\boldsymbol{\sigma}_n^f, \boldsymbol{\alpha}_n\right) \leq 0$.

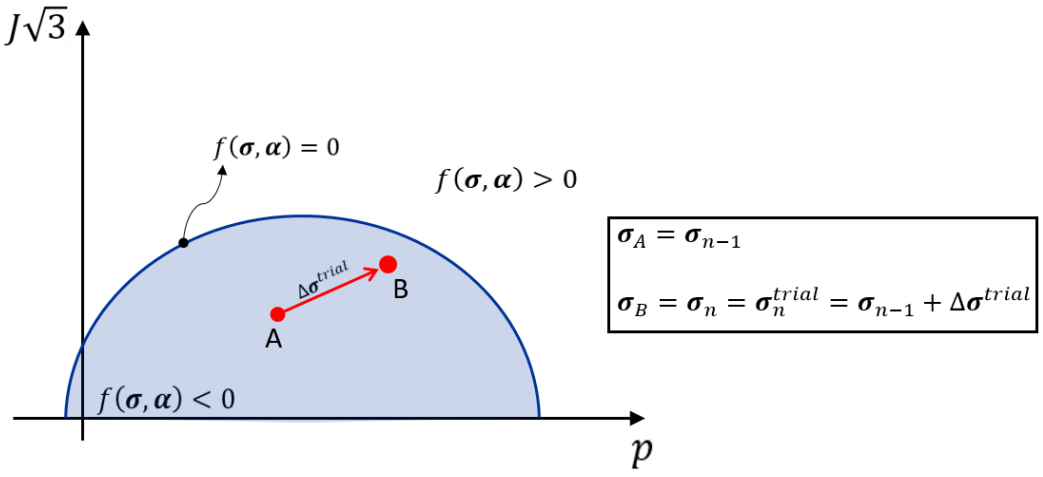

(a)

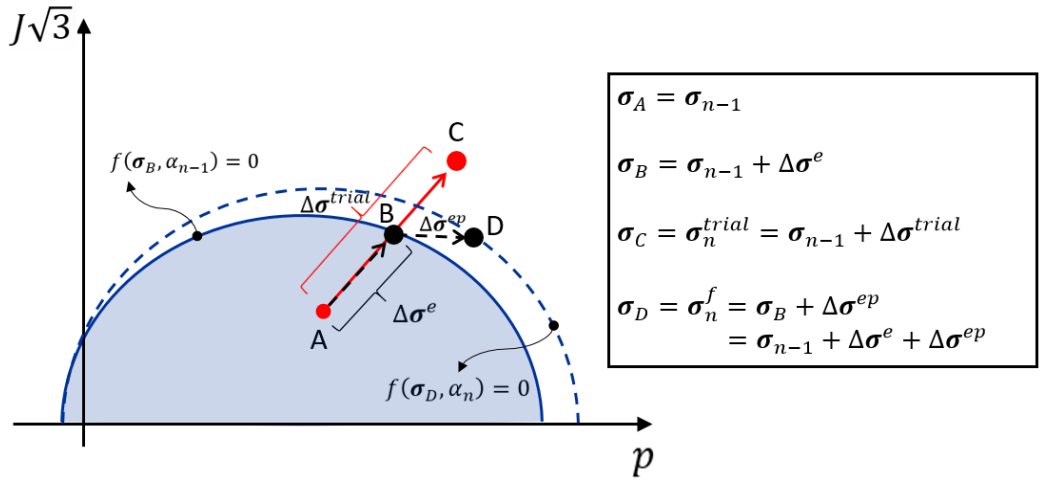

(b)

Figure 5-1: Stress integration procedure for classical elastoplastic models in which the stress state at the end of the elastic predictor is **(a)** inside the yield surface (point B) and; **(b)** outside the yield surface (point C), which leads to the generation of plastic strains and a final stress state lying on the updated yield locus (point D).

For the double-porosity model, this standard procedure to integrate the stresses needs to be modified to account for the generation of plastic straining in loading paths inside the yield

surface. This is a consequence of the hypothesis that the plastic mechanism due to the mechanical coupling between both structural levels is active for any loading path. The only way to *freeze* the plastic flow inside the yield surface is imposing $f_\beta = 0$ in the expression given in Equation (5-5).

5.2.3. THE SUB-STEPPING ALGORITHM

The numerical strategy for integrating the incremental stress-strain relationship over a given incremental generalized strain path, $\Delta\boldsymbol{\varepsilon}^g$, consists in a partition of the time interval of interest into several time sub-steps. Then, the incremental sub-step loading is applied and the corresponding incremental stress (and other variables) is calculated at the integration points over each sub-step. The applied sub-step loading is assumed to be a fraction of $\Delta\boldsymbol{\varepsilon}^g$. In order to perform the integration process, it is convenient to first define a dimensionless pseudo-time τ, $\tau \in (0,1)$, according to

$$\tau = \frac{t - t_0}{\Delta t} \tag{5-7}$$

where t_0 is the time at the beginning of the (global) load increment and $t_0 + \Delta t$ represents the time at the end of this loading. The derivation of Equation (5-7) with respect to time gives $d\tau/dt = 1/\Delta t$. Using this result when applying the chain rule to the pair of expressions in Equation (5-5), the following initial value problem to be integrated over the pseudo-time interval $\tau = 0$ to $\tau = 1$ is obtained

$$\begin{aligned}
\Delta\boldsymbol{\sigma} &= \frac{d\boldsymbol{\sigma}}{d\tau} = [\boldsymbol{D}^*]\Delta\boldsymbol{\varepsilon}^g \\
&= [\boldsymbol{D^{ep}}]\Delta\boldsymbol{\varepsilon} + \boldsymbol{h}_s \underbrace{\left(\Delta P_{gM} - \Delta P_{lM}\right)}_{\Delta s_M} + \boldsymbol{h}_g \Delta P_{gM} + \boldsymbol{h}_l \Delta P_{lM} + \boldsymbol{h}_T \Delta T \\
&\quad + \boldsymbol{h}_t \Delta t \\
\Delta p_0^* &= \frac{dp_o^*}{d\tau} \\
&= \frac{(1+\bar{e}_M)p_0^*}{\lambda_{sat} - \bar{\kappa}_M}\left(\Delta\lambda_{LC}\boldsymbol{m}^T\boldsymbol{m}_{LC} + f_\beta \boldsymbol{m}^T \Delta\bar{\boldsymbol{\varepsilon}}_m^e - \frac{f_\beta}{K_T}\left(\frac{1+e_m}{1+e}\right)\Delta T\right)
\end{aligned} \tag{5-8}$$

where the already known values in those expressions are the applied generalized strain increments (control variables) and the applied stresses, the hardening parameter and the history variables at $\tau = 0$. The increment in microstructural deformation, $\Delta\bar{\boldsymbol{\varepsilon}}_m^e$, on the right-hand side of the second equation in (5-8), is related to the components of the generalized strain ($\Delta\boldsymbol{\varepsilon}$) according to Equation (4-114).

Due to the non-linearity of the constitutive relations in most elastoplastic formulations (including the double-porosity model), it is not possible to apply the entire loading increment in

one single step and then, a subdivision of the pseudo-time interval becomes necessary. Let $0 \leq \Delta\tau_{(i)} \leq 1$ a given pseudo-time sub-increment so that

$$\tau_{(i)} = \tau_{(i-1)} + \Delta\tau_{(i)} \text{ , with } \tau_{(0)} = 0$$
$$\sum_{i=1}^{n} \Delta\tau_{(i)} = 1 \tag{5-9}$$

If all the main quantities at the pseudo-time $\tau_{(i-1)}$ are known ("old" values), the increments of these control variables for the new sub-incremental loading are computed as follows

$$\delta\boldsymbol{\varepsilon}_{(i)} = \Delta\tau_{(i)}\Delta\boldsymbol{\varepsilon}$$
$$\delta P_{lM,(i)} = \Delta\tau_{(i)}\Delta P_{lM}$$
$$\delta P_{gM,(i)} = \Delta\tau_{(i)}\Delta P_{g,M} \tag{5-10}$$
$$\delta T_{(i)} = \Delta\tau_{(i)}\Delta T$$
$$\delta t_{(i)} = \Delta\tau_{(i)}\Delta t$$

and then,

$$\Delta\boldsymbol{\varepsilon}_{(i)} = \Delta\boldsymbol{\varepsilon}_{(i-1)} + \delta\boldsymbol{\varepsilon}_{(i)}$$
$$\Delta P_{lM,(i)} = \Delta P_{lM,(i-1)} + \delta P_{lM,(i)}$$
$$\Delta P_{gM,(i)} = \Delta P_{gM,(i-1)} + \delta P_{gM,(i)} \tag{5-11}$$
$$\Delta T_{(i)} = \Delta T_{(i-1)} + \delta T_{(i)}$$
$$\Delta t_{(i)} = \Delta t_{(i-1)} + \delta t_{(i)}$$

The size of each sub-step ($\Delta\tau$) may vary during the integration process and this variation is estimated by fixing an error tolerance for the sub-stepping stress point algorithm so that the errors resulting from the numerical integration procedure are negligible (Potts and Zdravković, 1999; Sloan *et al.*, 2001). Due to the highly non-linear stress-strain relationship of the double-porosity model, a value of 0.5 is adopted as the initial pseudo-time step, that is, $\Delta\tau_{(1)}$ =0.5 . It means that, at least, two loading steps are required in each incremental loading.

5.2.4. THE TRIAL STEP

As mentioned in **Section 5.2.2**, in a classical elastoplastic formulation, the numerical stress integration process for stress states initially inside the yield locus imposes a purely elastic behaviour at each integration point by "freezing" any plastic mechanism during the trial step. However, the assumption of a purely elastic step for the double-porosity formulation described in this Thesis is no longer valid because it is assumed that plastic strains can develop inside the yield locus due to the micro-macro coupling mechanism. Instead, it is supposed that only the

plastic mechanism related to the macrostructural loading-collapse (the BBM mechanism) remains inactive during the trial step, that is, $\dot{\lambda}_{LC}^{trial} = 0$. Consequently, and from the second equation in (5-5), the hardening parameter evolution at this stage is evaluated as

$$\dot{p}_0^{*,trial} = f_\beta \frac{(1+\bar{e}_M)p_0^*}{\lambda_{sat} - \bar{\kappa}_M}\left(\boldsymbol{m}^T \dot{\boldsymbol{\varepsilon}}_m^{e,trial} - \frac{1}{K_T}\left(\frac{1+e_m}{1+e}\right)\dot{T}\right) \tag{5-12}$$

which implies that the size of the yield surface may change during the trial step. Two possible scenarios for the evolution of the region of admissible stresses, when the trial stress state is accepted, are schematically shown in Figure 5-2. In the first case, the trial loading increment induces a hardening (related to a collapse of macro-pores) which implies that $\dot{p}_0^{*,trial} > 0$ and, consequently, the yield surface increases during this loading process. The second case represents a typical situation of softening, which leads to a size decrease of the yield locus due to $\dot{p}_0^{*,trial} < 0$.

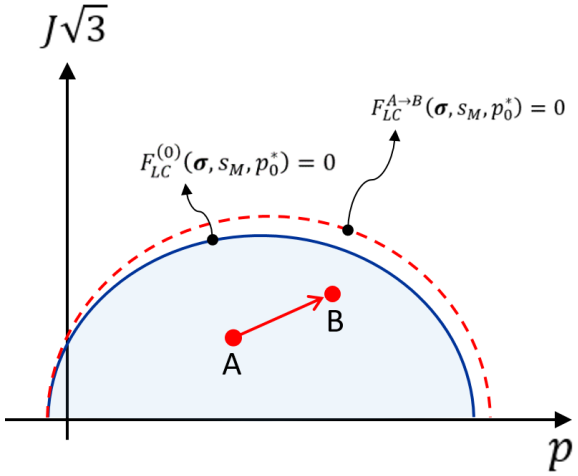

(a)

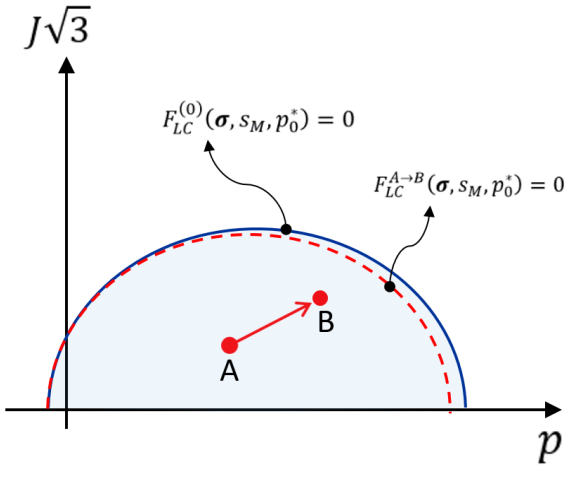

(b)

Figure 5-2: Two possible scenarios at the end of a trial sub-step loading inside the current yield surface: **(a)** hardening and **(b)** softening.

The microstructural volumetric strain rate generated during the trial step, $\dot{\varepsilon}_m^{vol,trial} = \boldsymbol{m}^T \dot{\boldsymbol{\varepsilon}}_m^{e,trial}$, in Equation (5-12), is evaluated as follows

$$\dot{\varepsilon}_m^{vol,trial} = \dot{\varepsilon}_m^{e,vol} = \frac{\bar{\phi}_m}{\rho_{lm}S_{lm}}\frac{\partial(\rho_{lm}S_{lm})}{\partial P_{lm}}\dot{P}_{lm} + \left(\frac{1-\phi}{\rho_s}\frac{\partial\rho_s}{\partial T} + \frac{\bar{\phi}_m}{\rho_{lm}S_{lm}}\frac{\partial(\rho_{lm}S_{lm})}{\partial T}\right)\dot{T} - \frac{\Gamma^w}{\rho_{lm}S_{lm}}\dot{t} \tag{5-13}$$

where this expression has been obtained from the mass balance equation of water in the microstructure, according to Equation (3-76), assuming that $\theta_{lm}^w S_{lm} + \theta_{gm}^w S_{gm} \approx \rho_{lm}S_{lm}$ and $f_m^w = 0$ and solving the resulting expression for $\dot{\varepsilon}_m^{vol}$. Moreover, for the sake of simplicity, the expression in Equation (5-13) has been obtained by assuming that $\dot{P}_{gm} = \dot{P}_{gM} = 0$. Such a mathematical simplification is adopted in the development of the expressions to be implemented for the double-porosity approach presented from now on. Note that the thermal dependence of the liquid density and of the retention curve for the water in micro-pores are also taken into account in Equation (5-13).

The rate of microstructural liquid pressure ($\dot{P}_{lm}$) that appears in Equation (5-13) must be calculated at each Gauss point during the trial step of the stress integration algorithm since the pore-water pressure in micro-pores is assumed as a history variable of the double-porosity approach (Gesto, 2014). In order to determine an explicit dependence of this history variable on the main variables (total strains, macrostructural fluid pressures and temperature), it is necessary to recall the expression for the microstructural strain given in Equation (4-114). Using this relationship, the volumetric component of the microstructural strain vector (in rate form) is given by

$$\begin{aligned}\dot{\varepsilon}_m^{e,vol} &= \boldsymbol{m}^T\dot{\boldsymbol{\varepsilon}}_m^e \\ &= \left(\frac{1+e}{1+e_m} + f_\beta\right)^{-1}\boldsymbol{m}^T\left(\dot{\boldsymbol{\varepsilon}} - \frac{1}{3\overline{K}_s}\dot{s}_M\boldsymbol{m} - \frac{1}{3K_T}\dot{T}\boldsymbol{m} - \dot{\lambda}_{LC}\boldsymbol{m}_{LC}\right) \\ &\quad + \frac{1}{K_T}\left(\frac{1+e_m}{1+e}\right)\dot{T}\end{aligned} \tag{5-14}$$

Grouping the thermal terms in the latter equation, then

$$\begin{aligned}\dot{\varepsilon}_m^{e,vol} &= \left(\frac{1+e}{1+e_m} + f_\beta\right)^{-1}\left(\boldsymbol{m}^T\dot{\boldsymbol{\varepsilon}} - \frac{1}{\overline{K}_s}\dot{s}_M - \dot{\lambda}_{LC}\boldsymbol{m}^T\boldsymbol{m}_{LC}\right) \\ &\quad + \frac{A}{K_T}\left(\frac{1+e_m}{1+e}\right)\dot{T}\end{aligned} \tag{5-15}$$

where the scalar A is defined according to the expression in Equation (4-119). Both expressions given by Equation (5-13) or Equation (5-15) provide an estimate for the same microstructural amount and, consequently, they must always coincide. Equating them (and after some algebraic operations) the following general expression is found

$$\dot{\lambda}_{LC}\boldsymbol{m}^T\boldsymbol{m}_{LC} + \frac{\bar{\phi}_m}{\rho_{lm}S_{lm}}\left(\frac{1+e}{1+e_m}+f_\beta\right)\frac{\partial(\rho_{lm}S_{lm})}{\partial P_{lm}}\dot{P}_{lm} = \underbrace{\boldsymbol{m}^T\dot{\boldsymbol{\varepsilon}}}_{\dot{\varepsilon}^{vol}} - \frac{1}{\bar{K}_s}\dot{s}_M - \frac{\eta_T}{K_T}\dot{T} + \frac{\Gamma^w}{\rho_{lm}S_{lm}}\left(\frac{1+e}{1+e_m}+f_\beta\right)\dot{t} \tag{5-16}$$

where the coefficient η_T, in the temperature-dependent term, is given by

$$\eta_T = K_T\left(\frac{1+e}{1+e_m}+f_\beta\right)\left(\frac{\bar{\phi}_m}{\rho_{lm}S_{lm}}\frac{\partial(\rho_{lm}S_{lm})}{\partial T}+\frac{1-\phi}{\rho_s}\frac{\partial\rho_s}{\partial T}\right) - f_\beta\left(\frac{1+e_m}{1+e}\right) \tag{5-17}$$

The first term on the left-side hand in Equation (5-16) has a null value during the trial step since, as stated before, $\dot{\lambda}_{LC}^{trial}=0$. In such conditions, that equation becomes

$$\bar{\phi}_m\frac{\left(\frac{1+e}{1+e_m}+f_\beta\right)}{\rho_{lm}S_{lm}}\frac{\partial(\rho_{lm}S_{lm})}{\partial P_{lm}}\dot{P}_{lm} = \dot{\varepsilon}^{vol} - \frac{1}{\bar{K}_s}\dot{s}_M - \frac{\eta_T}{K_T}\dot{T} + \frac{\left(\frac{1+e}{1+e_m}+f_\beta\right)}{\rho_{lm}S_{lm}}\Gamma^w\dot{t} \tag{5-18}$$

which can be rearranged to give an estimate for $\dot{P}_{lm}^{trial}$, according to

$$\boldsymbol{\dot{P}_{lm}^{trial}} = \frac{\mathbf{1}}{\bar{\boldsymbol{\phi}}_{\boldsymbol{m}}\frac{\left(\frac{\mathbf{1+e}}{\mathbf{1+e_m}}+\boldsymbol{f_\beta}\right)}{\boldsymbol{\rho_{lm}S_{lm}}}\frac{\boldsymbol{\partial(\rho_{lm}S_{lm})}}{\boldsymbol{\partial P_{lm}}}}\left(\dot{\boldsymbol{\varepsilon}}^{\boldsymbol{vol}} - \frac{\mathbf{1}}{\bar{\boldsymbol{K}}_{\boldsymbol{s}}}\dot{\boldsymbol{s}}_{\boldsymbol{M}} - \frac{\boldsymbol{\eta_T}}{\boldsymbol{K_T}}\dot{\boldsymbol{T}} + \frac{\left(\frac{\mathbf{1+e}}{\mathbf{1+e_m}}+\boldsymbol{f_\beta}\right)}{\boldsymbol{\rho_{lm}S_{lm}}}\boldsymbol{\Gamma^w}\dot{\boldsymbol{t}}\right) \tag{5-19}$$

A closer inspection of Equation (5-19) shows that, even for special isothermal conditions ($\dot{T}=0$) in which $\dot{\varepsilon}^{vol}=0$ and $\dot{s}_M=0$ – and, consequently, $\dot{\varepsilon}_m^{vol,trial}=0$, in accordance with Equation (5-15) –, the trial value for the micro water pressure rate can be still estimated. In such special conditions, Equation (5-19) reduces to

$$\dot{P}_{lm} = \frac{\Gamma^w}{\bar{\phi}_m\frac{\partial(\rho_{lm}S_{lm})}{\partial P_{lm}}}\dot{t} = \frac{\gamma^w(s_m-s_M)}{\bar{\phi}_m\left(S_{lm}\frac{\partial\rho_{lm}}{\partial P_{lm}}+\rho_{lm}\frac{\partial S_{lm}}{\partial P_{lm}}\right)}\dot{t} \tag{5-20}$$

indicating that the changes of pore pressures in micro-voids are mainly related to the exchange of water mass between both family of pores when $s_m \neq s_M$, which is equivalent to $P_{lm}\neq P_{lM}$ under the assumption of $P_{gm}\equiv P_{gM}$ (see Equation (3-56)). The existence of this hydraulic potential driving the mass transfer of water between the micro and the macro media introduces a time-dependent term into the mathematical formulation. This fact can be easily observed in Equation (5-13) and in all equations arising from it (for example, Equation (5-19)). This time-dependent term may be neglected if it is assumed the hydraulic potential equilibrium between both structural media at each point in the soil. In laboratory practice, this equilibrium condition is accomplished when the suction (macro) is applied (during a wetting or a drying path) in a very

slow rate so that $s_m \approx s_M$ at any time (Hoffmann, 2005). If a high enough value for the leakage parameter (γ^w) is adopted (when modelling tasks are performed), the numerical results may become strongly dependent on the magnitude of the time sub-step (δt). On the other hand, for very low values of that parameter, this dependency on time step size tends to vanish.

Once the rate of microstructural water pressure during the trial step is calculated through Equation (5-19), the increments in the trial stresses ($\dot{\boldsymbol{\sigma}}^{trial}$) can be computed from Equation (4-109), that is,

$$\dot{\boldsymbol{\sigma}}^{trial} = [\boldsymbol{D}^e]\left(\dot{\boldsymbol{\varepsilon}} - \frac{1}{3\overline{K}_s}\dot{s}_M\boldsymbol{m} - \frac{1}{3K_T}\left(1 - f_\beta\left(\frac{1+e_m}{1+e}\right)\right)\dot{T}\boldsymbol{m} - f_\beta\dot{\bar{\boldsymbol{\varepsilon}}}_m^{e,trial}\right) - \left(\zeta_{lm}\dot{P}_{lm}^{trial} + \zeta_T\dot{T} + \dot{P}_{fM}\right)\boldsymbol{m} \tag{5-21}$$

The latter expression contains another trial variable that needs to be estimated: the trial microstructural deformation rate ($\dot{\bar{\boldsymbol{\varepsilon}}}_m^{e,trial}$). In order to remove this vector from the previous equation, the fundamental relationship in Equation (4-114) is inserted into Equation (5-21), resulting in the following alternative expression for $\dot{\boldsymbol{\sigma}}^{trial}$:

$$\begin{aligned}\dot{\boldsymbol{\sigma}}^{trial} = {} & \left((1-A)[\boldsymbol{D}^e] - A^*\boldsymbol{m}\boldsymbol{m}^T\right)\dot{\boldsymbol{\varepsilon}} - \frac{1}{\overline{K}_s}\left((1-A)K - A^*\right)\boldsymbol{m}\dot{s}_M \\ & - \dot{P}_{fM}\boldsymbol{m} - \frac{1}{K_T}\left((1-A)K + K_T\zeta_T - A^*\eta_T\right)\boldsymbol{m}\dot{T} \\ & - A^*\frac{\left(\frac{1+e}{1+e_m} + f_\beta\right)}{\rho_{lm}S_{lm}}\Gamma^w\dot{t}\boldsymbol{m}\end{aligned} \tag{5-22}$$

where the coefficient A^* is given by

$$A^* = \frac{\zeta_{lm}\rho_{lm}S_{lm}}{\bar{\phi}_m\left(\frac{1+e}{1+e_m} + f_\beta\right)\left(S_{lm}\frac{\partial\rho_{lm}}{\partial P_{lm}} + \rho_{lm}\frac{\partial S_{lm}}{\partial P_{lm}}\right)} \tag{5-23}$$

Comparing the expression for the trial stress in Equation (5-22) with the general form of the constitutive stress in Equation (5-5), the elastoplastic constitutive tensor and the constitutive vectors for the trial step are defined as

$$[\boldsymbol{D}^{ep}] = (1-A)[\boldsymbol{D}^e] - A^*\boldsymbol{m}\boldsymbol{m}^{\boldsymbol{T}} \tag{5-24}$$

$$\boldsymbol{h}_s = -\frac{1}{\overline{K}_s}\left((1-A)K - A^*\right)\boldsymbol{m} \tag{5-25}$$

$$\boldsymbol{h}_g = \begin{cases} -\boldsymbol{m} & if\ \ 0 \le S_{lM} < 1 \\ \boldsymbol{0} & if\ \ S_{lM} = 1 \end{cases} \tag{5-26}$$

$$\boldsymbol{h}_l = \begin{cases} \boldsymbol{0} & if \;\; 0 \leq S_{lM} < 1 \\ -\boldsymbol{m} & if \;\; S_{lM} = 1 \end{cases} \tag{5-27}$$

$$\boldsymbol{h}_T = -\frac{1}{K_T}\left((1-A)K + K_T\zeta_T - A^*\eta_T\right)\boldsymbol{m} \tag{5-28}$$

$$\boldsymbol{h}_t = -\frac{\zeta_{lm}}{\bar{\phi}_m\left(S_{lm}\dfrac{\partial \rho_{lm}}{\partial P_{lm}} + \rho_{lm}\dfrac{\partial S_{lm}}{\partial P_{lm}}\right)}\Gamma^w\boldsymbol{m} \tag{5-29}$$

These tensor/vector entities are required to evaluate the residual of stresses arising from the application of the finite element method to the solution of the mechanical equilibrium equations (see **Section 5.3.3**).

The numerical solution obtained during the trial step is not necessarily the actual solution for the elastoplastic boundary value problem expressed by the system of equations in Equation (5-8). To be considered the actual solution, the trial solution ($\boldsymbol{\sigma}_n^{trial}$; $p_{0,n}^{*,trial}$) must satisfy the constraint

$$F_{LC}^{trial}\left(\boldsymbol{\sigma}_n^{trial}, p_{0,n}^{*,trial}\right) \leq 0 \tag{5-30}$$

where

$$\begin{aligned} \boldsymbol{\sigma}_n^{trial} &= \boldsymbol{\sigma}_{n-1} + \dot{\boldsymbol{\sigma}}^{trial} \\ p_{0,n}^{*,trial} &= p_{0,n-1}^{*} + \dot{p}_0^{*,trial} \end{aligned} \tag{5-31}$$

In other words, the final stress state must lie within or on the yield surface at the end of the trial step. If this condition is fulfilled (see Figure 5-3(a)), the trial variables are accepted and updated as follows

$$\begin{aligned} P_{lm,n} &= P_{lm,n-1} + \dot{P}_{lm}^{trial} \\ \bar{\boldsymbol{\varepsilon}}_{m,n}^{e} &= \bar{\boldsymbol{\varepsilon}}_{m,n-1}^{e} + \dot{\bar{\boldsymbol{\varepsilon}}}_{m}^{e,trial} \\ \boldsymbol{\sigma}_n &= \boldsymbol{\sigma}_n^{trial} = \boldsymbol{\sigma}_{n-1} + \dot{\boldsymbol{\sigma}}^{trial} \\ p_{0,n}^{*} &= p_{0,n}^{*,trial} = p_{0,n-1}^{*} + \dot{p}_0^{*,trial} \end{aligned} \tag{5-32}$$

and the next integration point can be considered. Otherwise, the stress state found by the trial algorithm belongs to a plastically inadmissible region (outside the updated yield surface) and the plastic surface is crossed during the trial loading process (see Figure 5-3(b)). In this case, the trial state is rejected and an iterative algorithm is performed in order to find the intersection with the yield surface and, consequently, to determine which portion of the applied generalized strains activates the BBM mechanism. A suitable iterative algorithm to obtain the crossing with the yield surface is described in **Section 5.2.5**.

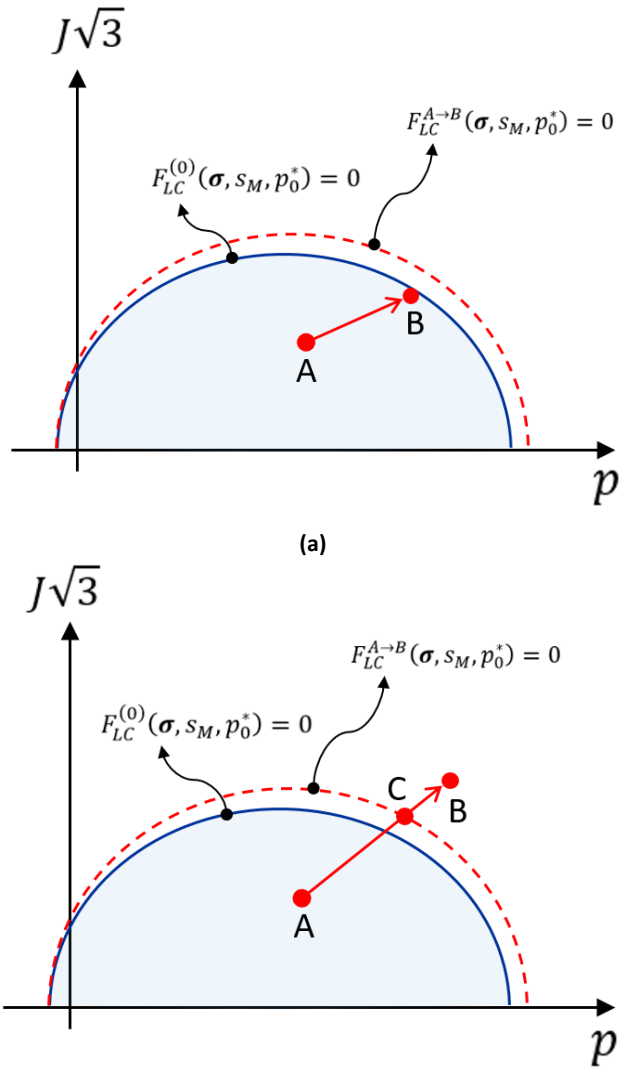

Figure 5-3: Illustration of a trial stress increment in which **(a)** the loading path develops completely inside the "updated" yield surface (point B represents the actual stress state after trial) and **(b)** the "updated" yield surface is crossed during the trial step (point C). Plastic strains due to the BBM mechanism must be accounted for.

It is important to remark that Equation (5-19) may become mathematically indeterminate. Due to that, a pair of mathematical restrictions must be satisfied in order to prevent numerical problems during the performance of the trial step (Gesto, 2014). The first of these mathematical constraints is given by

$$\frac{\partial(\rho_{lm}S_{lm})}{\partial P_{lm}} = S_{lm}\frac{\partial \rho_{lm}}{\partial P_{lm}} + \rho_{lm}\frac{\partial S_{lm}}{\partial P_{lm}} \neq 0 \tag{5-33}$$

This restraint is always accomplished while the microstructural medium remains unsaturated, once $\frac{\partial \rho_{lm}}{\partial P_{lm}} \geq 0$ and $\frac{\partial S_{lm}}{\partial P_{lm}} > 0$ (see **Section 3.8.2.1** and **Section 3.8.2.2**). Nevertheless, when the microstructure becomes saturated ($\frac{\partial S_{lm}}{\partial P_{lm}} = 0$) and the micro liquid density is constant ($\frac{\partial \rho_{lm}}{\partial P_{lm}} = 0$), problems with consistency appear. In order to avoid this limitation in the mathematical formulation, it is assumed that the following additional constraint must be fulfilled

$$\frac{\partial \rho_{lm}}{\partial P_{lm}} > 0 \tag{5-34}$$

at any integration point in all time steps. The other important mathematical requirement is

$$\left(\frac{1+e}{1+e_m} + f_\beta\right) \neq 0 \tag{5-35}$$

Since the inequality $\frac{1+e}{1+e_m} \geq 1$ is always obeyed, the following two set of values for the micro-macro interaction functions are possible: $f_\beta > -\frac{1+e}{1+e_m} \geq -1$ or $f_\beta < -\frac{1+e}{1+e_m} \leq -1$. Based on available data of plastic strain evolution in cyclic controlled-suction tests on compacted expansive clays (Pousada, 1984; Subba Rao and Styadas, 1987; Dif and Bluemel, 1991; Day, 1994; Al-Homoud *et al.*, 1995; Alonso *et al.*, 1995; Alonso *et al.*, 2005) and on the dependence of the magnitude and nature of these irreversible deformations with the degree of macrostructure openness relative to the applied stresses (Gens and Alonso, 1992; Komine and Ogata, 1994; Alonso *et al.*, 1999; Sánchez *et al.*, 2005), it seems reasonable to select $f_\beta > -1$ as the admissible region in f_β: μ plane that contains the pair of micro-macro coupling functions (see Figure 5-4).

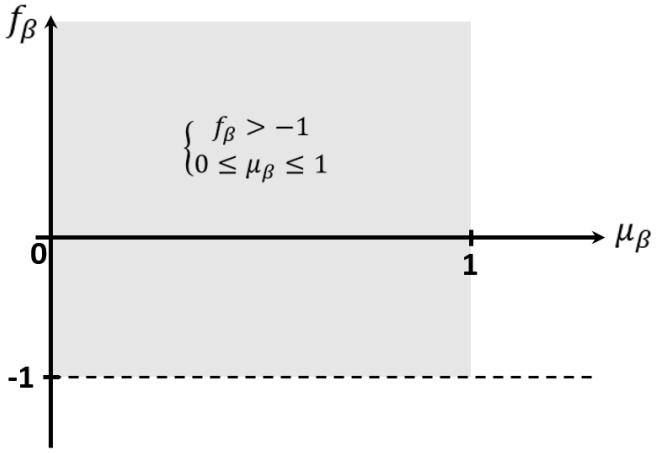

Figure 5-4: Representation of the admissible region for f_β.

5.2.5. INTERSECTION WITH THE LC YIELD SURFACE

If $F_{LC}\left(\boldsymbol{\sigma}_{n-1}, p^*_{0,n-1}\right) < 0$ and $F_{LC}\left(\boldsymbol{\sigma}^{trial}_n, p^{*,trial}_{0,n}\right) > 0$, the *LC* yield surface is crossed and the plastic mechanism related to the macrostructural *LC* curve is activated. Consequently, the basic assumption considered during the trial step ($\Delta\lambda_{LC} = 0$) does not hold for the current generalized strain sub-increment ($\delta\boldsymbol{\varepsilon}^g$). It becomes necessary to determine the portion of the trial stress increment ($\delta\boldsymbol{\sigma}^{trial}_{int}$) that lies inside the yield surface (as sketched in Figure 5-5). This is achieved by finding a scalar, α, so that

$$F_{LC}\left(\boldsymbol{\sigma}_{int}, p^*_{0,int}\right) = 0 \tag{5-36}$$

where

$$\boldsymbol{\sigma}_{int} = \boldsymbol{\sigma}_{n-1} + \delta\boldsymbol{\sigma}_{int}^{trial} = \boldsymbol{\sigma}_{n-1} + h_1(\alpha \cdot \delta\boldsymbol{\varepsilon}^g)$$
$$p_{0,int}^* = p_{0,n-1}^* + h_2\left(\alpha \cdot \delta\varepsilon^{p,vol}, \alpha \cdot \delta\boldsymbol{\varepsilon}^g\right) \quad (5\text{-}37)$$

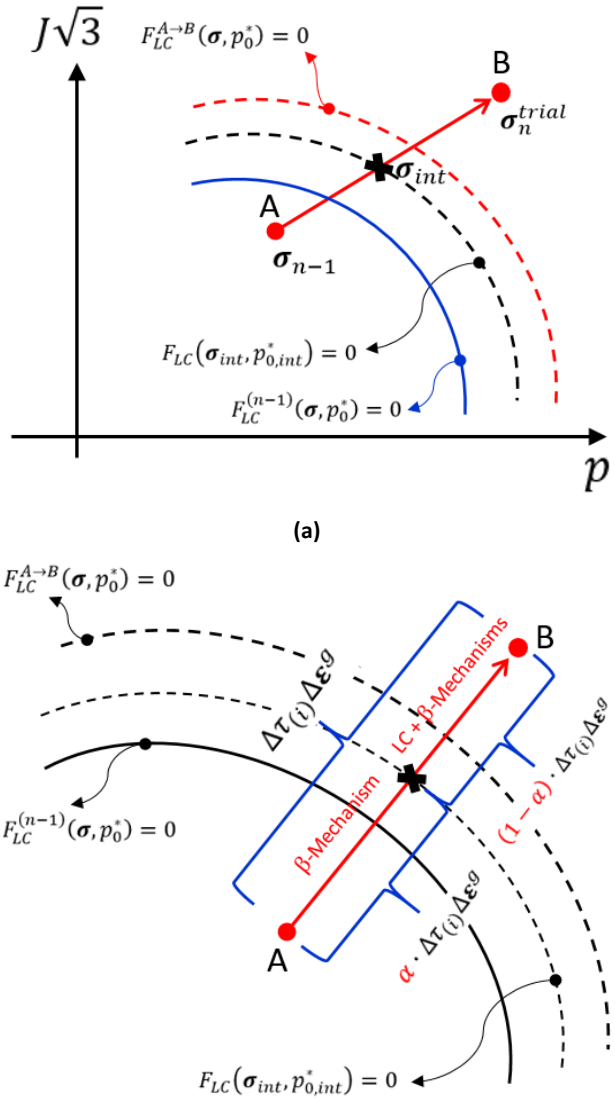

Figure 5-5: **(a)** Schematic representation of a (trial) loading path that intersects the yield surface; **(b)** Plastic mechanisms activated inside the yield locus (due to the micro-macro mechanical coupling) and beyond the intersection point with the yield surface (LC + micro-macro coupling).

In those expressions, $\boldsymbol{\sigma}_{int}$ and $p_{0,int}^*$ are the stress state and the hardening parameter at the intersection point with the yield surface. h_1 is a vectorial function of the generalized strain sub-increments and h_2 is a scalar function of the increments in the volumetric component of the macrostructural plastic deformations ($\Delta\varepsilon^{p,vol}$) due to the interaction between the two pore structures (the only plastic mechanism activated inside the yield surface). The exact yield condition in Equation (5-36) is replaced by $\left|F_{LC}(\boldsymbol{\sigma}_{int}, p_{0,int}^*)\right| \leq FTOL$, where $FTOL$ is a small positive tolerance (Sloan *et al.*, 2001). The scalar α varies in the range $0 < \alpha < 1$ and gives the portion of the generalized strains (during the sub-incremental loading) that moves the stresses

from $\boldsymbol{\sigma}_{n-1}$ to $\boldsymbol{\sigma}_{int}$ (Sánchez *et al.*, 2008). Having determined α, the portion of the generalized strain increment for which the two irreversible mechanisms are simultaneously active, i.e., the *LC* macrostructural yielding ($\delta\lambda_{LC} > 0$) and the mechanical coupling between both structural media, is equal to $(1-\alpha)\cdot\delta\boldsymbol{\varepsilon}^{g}$. The integration process over this part of the generalized strain increment is discussed in **Section 5.2.7**.

Several numerical schemes for determining the scalar α are available. The simplest method is the linear interpolation (Owen and Hinton, 1980), which gives theoretically correct estimates for α only if the yield function is linearly dependent on stresses (Potts and Zdravković, 1999). The Newton-Raphson and the secant techniques are some iterative zero-finding algorithms used to solve the intersection point problem for most of the (non-linear) elastoplastic models. These schemes usually have a high rate of convergence to a solution satisfying the condition expressed in Equation (5-36) but they may diverge in some circumstances because the value for α is not constrained to any specified bounds (Sloan *et al.*, 2001). The numerical procedure for finding the intersection point with the yield function adopted in this Thesis is the one employed in Sloan *et al.* (2001). This iterative scheme, known as the *Pegasus algorithm*, is a bracketing-type method that requires, for each iteration, two different start values that determine an interval where the approximated solution is located. A brief description of the implementation of this algorithm (in CODE_BRIGHT), performed when the trial stress prediction is outside of the current yield surface, is given in **Appendix A**.

5.2.6. ELASTOPLASTIC UNLOADING

When the stress state at the beginning of the incremental sub-loading lies on the yield surface, $F_{LC}\left(\boldsymbol{\sigma}_A, p^*_{0,A}\right) = 0$, the application of an elastoplastic stress increment may move the stress state to a final position that violates the consistency condition, $F_{LC}\left(\boldsymbol{\sigma}_B, p^*_{0,B}\right) > 0$. In such conditions, two different scenarios are possible for the final stress state, as shown in Figure 5-6. In the first case (Figure 5-6(a)), the two plastic mechanisms are simultaneously activated over the entire stress increment, which means that $\alpha = 0$ in Figure 5-5(b). In the second situation (Figure 5-6(b)), a portion of the stress increment occurs inside the yield surface and only the micro-macro coupling mechanism is activated during this stress path. The remaining portion of the stress increment (beyond the intersection point with the yield surface) is integrated numerically considering $\dot{\lambda}_{LC}^{C\rightarrow B} > 0$. A correct value of α ($\alpha \neq 0$) must be estimated in order to determine the stress point on the yield surface (point C). Then, it is necessary to find a stress point inside the yield surface and, together with the stress state at the end of the incremental sub-loading, use them as the initial conditions for the Pegasus algorithm (or another iterative root-finding method) so that the crossing with the yield surface may be achieved, as depicted in Figure 5-7. A detailed description about the implementation of the Pegasus scheme for elastoplastic unloading conditions is given in Sloan *et al.* (2001).

The case shown in Figure 5-6(b*)* represents an elastoplastic unloading from the yield surface and arises when the angle between the yield surface gradient and the stress increment is larger than

90° (Sloan *et al.*, 2001). To distinguish between these two situations, it is necessary to evaluate the following scalar product:

$$\frac{\partial F_{LC}\left(\boldsymbol{\sigma}_A, p^*_{0,A}\right)}{\partial \boldsymbol{\sigma}} \cdot \Delta\boldsymbol{\sigma}_{A\to B} = \boldsymbol{n}_{LC,A} \cdot \Delta\boldsymbol{\sigma}_{A\to B} \tag{5-38}$$

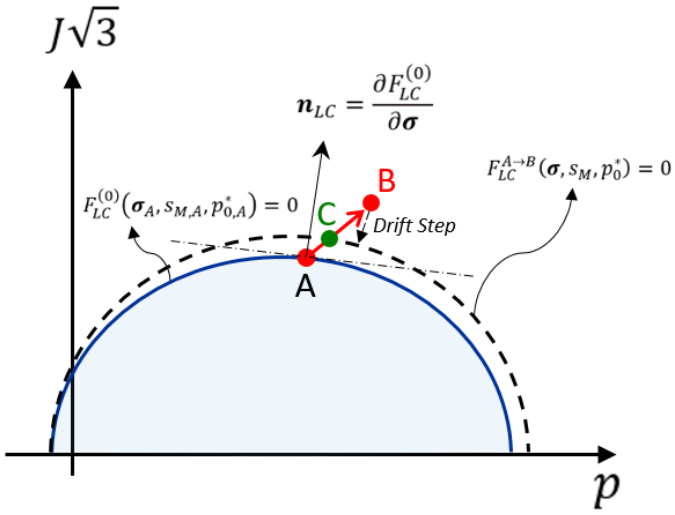

(a)

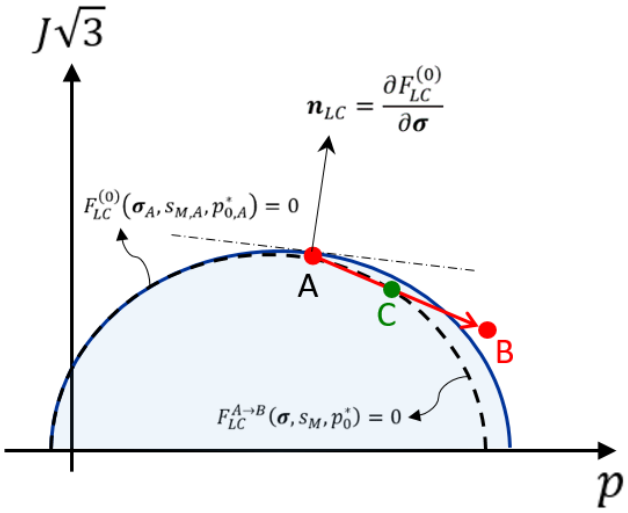

(b)

Figure 5-6: **(a)** Elastoplastic loading in which the two plastic mechanisms are activated; **(b)** elastoplastic unloading starting on the yield surface (point A) and for which the final stress state (point B) is outside the updated yield surface.

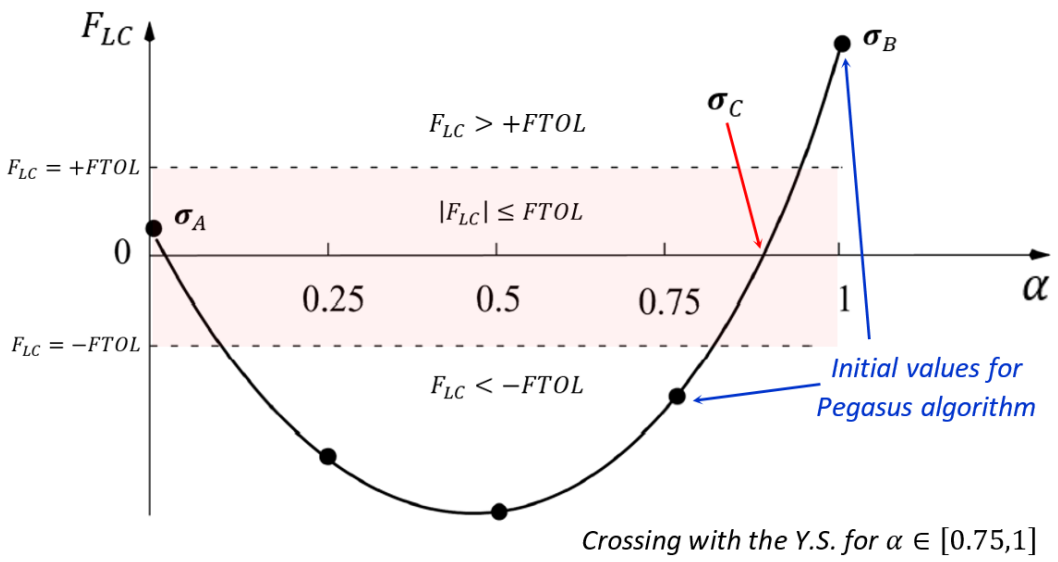

Figure 5-7: Starting values for the yield-crossing algorithm in an elastoplastic unloading path starting on the yield surface (after Sloan *et al.*, 2001).

If the quantity in Equation (5-38) is non-negative, the scenario displayed in Figure 5-6(a) is considered. The stress integration algorithm for this situation is described in the next section. If the dot product in Equation (5-38) is a negative quantity, an elastoplastic unloading takes place. In practice, the elastoplastic unloading occurs when

$$\frac{\partial F_{LC}\left(\boldsymbol{\sigma}_A, p_{0,A}^*\right)}{\partial \boldsymbol{\sigma}} \cdot \Delta\boldsymbol{\sigma}_{A\to B} < -LTOL \tag{5-39}$$

where $LTOL$ is a suitable tolerance (Sloan *et al.*, 2001).

Figure 5-8 illustrates another stress path that satisfies the condition expressed in Equation (5-39). In the classical plasticity approach, it would represent an elastic unloading path since the final stress point is still inside the yield surface ($F_{LC}^{(n)}\left(\boldsymbol{\sigma}_B, p_{0,B}^*\right) < 0$). However, in the double-porosity framework, it represents an elastoplastic unloading in which irreversible strains can occur due to micro-macro interaction mechanism. In such a case, $\dot{\lambda}_{LC}^{A\to B} = 0$, but the size of the yield locus may evolve. In this case, the numerical procedure to integrate the stresses is the one described in **Section 5.2.4**.

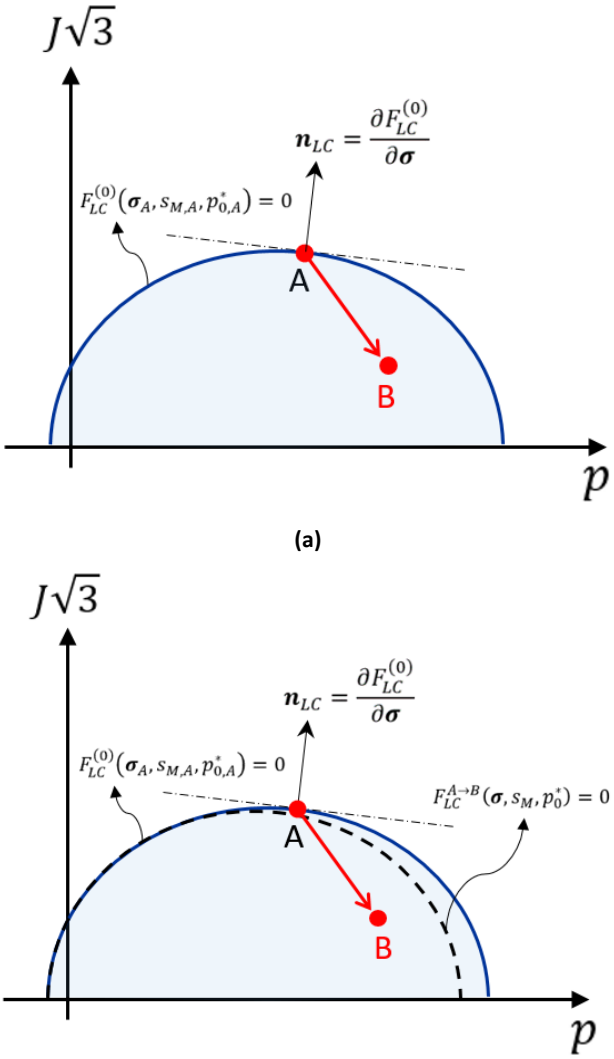

Figure 5-8: Representation of an unloading path from the yield surface for **(a)** a classical elastoplastic model (left), in which only purely elastic deformations are allowed, and **(b)** the DPM approach (right), in which the yield surface may evolve due to the micro-macro coupling mechanism.

5.2.7. ELASTOPLASTIC INTEGRATION WITH BOTH PLASTIC MECHANISMS ACTIVATED

In this section, the case of the yielding of macrostructure due to the activation of both plastic mechanisms considered in the double-porosity framework is described. In such a case, the stress state is initially on the current yield surface and the additional applied straining, given by $(1-\alpha)\cdot\delta\boldsymbol{\varepsilon}^g$ (see Figure 5-5(b)), generates plastic deformations also related to the macrostructural loading-collapse mechanism (the LC mechanism). Therefore, an estimation for the rate of the plastic multiplier associated to this plastic mechanism ($\dot{\lambda}_{LC}$) is required to integrate the stresses since $\dot{\lambda}_{LC} > 0$. In that case, the consistency condition expressed by Equation (5-4) is used. As discussed previously, this condition guarantees that the stress state satisfies the yield function condition when a plastic straining takes place during any sub-loading path. Thus, the following equation is obtained

$$\dot{F}_{LC} = \left(\frac{\partial F_{LC}}{\partial \boldsymbol{\sigma}}\right)^T \dot{\boldsymbol{\sigma}} + \frac{\partial F_{LC}}{\partial s_M}\dot{s}_M + \frac{\partial F_{LC}}{\partial p_0^*}\dot{p}_0^* = 0 \tag{5-40}$$

in which the hardening parameter of the constitutive model (p_0^*) is now dependent on the accumulated volumetric plastic strain rate ($\dot{\bar{\varepsilon}}_M^{p,vol}$) - see Equation (4-102) and Equation (4-104). Hence, the consistency equation can be written as

$$\begin{aligned}\dot{F}_{LC} = &\left(\frac{\partial F_{LC}}{\partial \boldsymbol{\sigma}}\right)^T \dot{\boldsymbol{\sigma}} + \frac{\partial F_{LC}}{\partial s_M}\dot{s}_M \\ &+ \frac{\partial F_{LC}}{\partial \bar{\varepsilon}_M^{p,vol}}\boldsymbol{m}^T\left(\dot{\lambda}_{LC}\boldsymbol{m}_{LC} + f_\beta\left(\dot{\bar{\boldsymbol{\varepsilon}}}_m - \frac{1}{3K_T}\left(\frac{1+e_m}{1+e}\right)\dot{T}\boldsymbol{m}\right)\right) \\ = &\ 0\end{aligned} \tag{5-41}$$

where

$$\frac{\partial F_{LC}}{\partial \bar{\varepsilon}_M^{p,vol}} = \frac{\partial F_{LC}}{\partial p_0}\frac{\partial p_0}{\partial p_0^*}\frac{\partial p_0^*}{\partial \bar{\varepsilon}_M^{p,vol}} \tag{5-42}$$

If the expression for the rate of the effective stress tensor ($\dot{\boldsymbol{\sigma}}$), as defined in (4-118), is inserted into (5-41) and taken into account that $\dot{P}_{gm} = \dot{P}_{gM} = 0$, then

$$\begin{aligned}\dot{F}_{LC} = &(1-A)\left(\frac{\partial F_{LC}}{\partial \boldsymbol{\sigma}}\right)^T [\boldsymbol{D}^e]\left(\dot{\boldsymbol{\varepsilon}} - \frac{1}{3\bar{K}_s}\dot{s}_M\boldsymbol{m} - \frac{1}{3K_T}\dot{T}\boldsymbol{m} - \dot{\lambda}_{LC}\boldsymbol{m}_{LC}\right) \\ &-\left(\zeta_{lm}\dot{P}_{lm} + \zeta_T\dot{T} + \dot{P}_{fM}\right)\left(\frac{\partial F_{LC}}{\partial \boldsymbol{\sigma}}\right)^T \boldsymbol{m} + \frac{\partial F_{LC}}{\partial s_M}\dot{s}_M \\ &+\frac{\partial F_{LC}}{\partial \bar{\boldsymbol{\varepsilon}}_M^{p,vol}}\boldsymbol{m}^T\left(\dot{\lambda}_{LC}\boldsymbol{m}_{LC} + f_\beta\left(\dot{\bar{\boldsymbol{\varepsilon}}}_m - \frac{1}{3K_T}\left(\frac{1+e_m}{1+e}\right)\dot{T}\boldsymbol{m}\right)\right) = 0\end{aligned} \tag{5-43}$$

Recalling the mathematical expression for the deformation rate at micro level, ($\dot{\bar{\boldsymbol{\varepsilon}}}_m \equiv \dot{\bar{\boldsymbol{\varepsilon}}}_m^e$), expressed by Equation (4-114), and after some algebraic operations and grouping of common terms, Equation (5-43) becomes

$$\begin{aligned}&(\boldsymbol{n}_{LC}^T[\boldsymbol{D}^e] + A\boldsymbol{v}^T)\dot{\boldsymbol{\varepsilon}} - \left(\frac{1}{3\bar{K}_s}(\boldsymbol{n}_{LC}^T[\boldsymbol{D}^e] + A\boldsymbol{v}^T)\boldsymbol{m} - \frac{\partial F_{LC}}{\partial s_M}\right)\dot{s}_M \\ &\quad - \frac{1}{3K_T}(\boldsymbol{n}_{LC}^T[\boldsymbol{D}^e] + A\boldsymbol{v}^T)\boldsymbol{m}\dot{T} + \dot{\lambda}_{LC}(1-A)\boldsymbol{v}^T\boldsymbol{m}_{LC} \\ &\quad - \left(\zeta_{lm}\dot{P}_{lm} + \zeta_T\dot{T} + \dot{P}_{fM}\right)\boldsymbol{n}_{LC}^T\boldsymbol{m} = 0\end{aligned} \tag{5-44}$$

where $\boldsymbol{n}_{LC} = \frac{\partial F_{LC}}{\partial \boldsymbol{\sigma}}$ and $\boldsymbol{m}_{LC} = \frac{\partial G_{LC}}{\partial \boldsymbol{\sigma}}$ gives the plastic flow direction for the BBM mechanism. The auxiliary vector v is defined as

$$v = \frac{\partial F_{LC}}{\partial \bar{\varepsilon}_M^{p,vol}}\boldsymbol{m} - [\boldsymbol{D}^e]\boldsymbol{n}_{LC} = \frac{\partial F_{LC}}{\partial p_0}\frac{\partial p_0}{\partial p_0^*}\frac{\partial p_0^*}{\partial \bar{\varepsilon}_M^{p,vol}}\boldsymbol{m} - [\boldsymbol{D}^e]\boldsymbol{n}_{LC} \tag{5-45}$$

A detailed description of the algebraic steps that lead to Equation (5-44) is given in Gesto (2014). Equation (5-44) together with Equation (5-16) form a system of algebraic equations whose unknowns are the rate of the plastic multiplier ($\dot{\lambda}_{LC}$) and the microstructural water pressure rate ($\dot{P}_{lm}$). The terms of these equations can be rearranged in order to isolate these unknowns from the terms related to the rates of the main (primary) variables. Therefore,

$$-\dot{\lambda}_{LC}(1-A)\boldsymbol{v}^T\boldsymbol{m}_{LC} + \dot{P}_{lm}\zeta_{lm}\boldsymbol{n}_{LC}^T\boldsymbol{m} = (\boldsymbol{n}_{LC}^T[\boldsymbol{D}^e] + A\boldsymbol{v}^T)\dot{\boldsymbol{\varepsilon}} - \left(\frac{1}{3\bar{K}_s}(\boldsymbol{n}_{LC}^T[\boldsymbol{D}^e] + A\boldsymbol{v}^T)\boldsymbol{m} - \frac{\partial F_{LC}}{\partial s_M}\right)\dot{s}_M - \left(\frac{1}{3K_T}(\boldsymbol{n}_{LC}^T[\boldsymbol{D}^e] + A\boldsymbol{v}^T) + \zeta_T\boldsymbol{n}_{LC}^T\right)\boldsymbol{m}\dot{T} - \boldsymbol{n}_{LC}^T\boldsymbol{m}\dot{P}_{fM} = 0 \quad (5\text{-}46)$$

$$\dot{\lambda}_{LC}\boldsymbol{m}^T\boldsymbol{m}_{LC} + \frac{\bar{\phi}_m}{\rho_{lm}S_{lm}}\left(\frac{1+e}{1+e_m} + f_\beta\right)\frac{\partial(\rho_{lm}S_{lm})}{\partial P_{lm}}\dot{P}_{l,m} = \boldsymbol{m}^T\dot{\boldsymbol{\varepsilon}} - \frac{1}{\bar{K}_s}\dot{s}_M - \frac{\eta_T}{K_T}\dot{T} + \frac{\Gamma^w}{\rho_{lm}S_{lm}}\left(\frac{1+e}{1+e_m} + f_\beta\right)\dot{t}$$

This resulting system of equations (that must be solved to integrate the stress-strain law) can be written in its matrix form as

$$[\boldsymbol{H}]\begin{bmatrix}\dot{\lambda}_{LC}\\ \dot{P}_{lm}\end{bmatrix} + \begin{bmatrix}h_1\\ h_2\end{bmatrix}\dot{T} = \begin{bmatrix}C_1\\ C_2\end{bmatrix} \quad (5\text{-}47)$$

in which the matrix of coefficients $[\boldsymbol{H}]$ is defined by

$$[\boldsymbol{H}] = \begin{bmatrix}H_{11} & H_{12}\\ H_{21} & H_{22}\end{bmatrix} \quad (5\text{-}48)$$

and its scalar components are described as follows

$$H_{11} = -(1-A)\boldsymbol{v}^T\boldsymbol{m}_{LC} = \boldsymbol{n}_{LC}^T[\boldsymbol{D}^e]\boldsymbol{m}_{LC} + A\boldsymbol{v}^T\boldsymbol{m}_{LC} - \frac{\partial F_{LC}}{\partial \bar{\varepsilon}_M^{p,vol}}\boldsymbol{m}^T\boldsymbol{m}_{LC} \quad (5\text{-}49)$$

$$H_{12} = \zeta_{lm}\boldsymbol{n}_{LC}^T\boldsymbol{m} \quad (5\text{-}50)$$

$$H_{21} = \boldsymbol{m}^T\boldsymbol{m}_{LC} \quad (5\text{-}51)$$

$$H_{22} = \frac{\bar{\phi}_m}{\rho_{lm}S_{lm}}\left(\frac{1+e}{1+e_m} + f_\beta\right)\frac{\partial(\rho_{lm}S_{lm})}{\partial P_{lm}} \quad (5\text{-}52)$$

The coefficients that define the thermal vector are expressed by

$$h_1 = \left(\frac{1}{3K_T}(\boldsymbol{n}_{LC}^T[\boldsymbol{D}^e] + A\boldsymbol{v}^T) + \zeta_T \boldsymbol{n}_{LC}^T\right)\boldsymbol{m}$$
$$= \frac{A}{K_T}\frac{\partial F_{LC}}{\partial \bar{\varepsilon}_M^{p,vol}} + \left((1-A)\frac{K}{K_T} + \zeta_T\right)\boldsymbol{n}_{LC}^T\,\boldsymbol{m} \tag{5-53}$$

$$h_2 = \frac{\eta_T}{K_T}$$
$$= \left(\frac{1+e}{1+e_m} + f_\beta\right)\left(\frac{\bar{\phi}_m}{\rho_{lm}S_{lm}}\frac{\partial(\rho_{lm}S_{lm})}{\partial T} + \frac{1-\phi}{\rho_s}\frac{\partial \rho_s}{\partial T}\right) - \frac{f_\beta}{K_T}\left(\frac{1+e_m}{1+e}\right) \tag{5-54}$$

while the components of the vector on the right-hand side of the matrix equation in Equation (5-47) are

$$C_1 = (\boldsymbol{n}_{LC}^T[\boldsymbol{D}^e] + A\boldsymbol{v}^T)\dot{\boldsymbol{\varepsilon}} - \left(\frac{1}{3\overline{K}_s}(\boldsymbol{n}_{LC}^T[\boldsymbol{D}^e] + A\boldsymbol{v}^T)\boldsymbol{m} - \frac{\partial F_{LC}}{\partial s_M}\right)\dot{s}_M$$
$$-\boldsymbol{n}_{LC}^T\boldsymbol{m}\dot{P}_{fM}$$
$$= (\boldsymbol{n}_{LC}^T[\boldsymbol{D}^e] + A\boldsymbol{v}^T)\dot{\boldsymbol{\varepsilon}}$$
$$+\frac{1}{\overline{K}_s}\left(\overline{K}_s\frac{\partial F_{LC}}{\partial s_M} - A\frac{\partial F_{LC}}{\partial \bar{\varepsilon}_M^{p,vol}} - (1-A)K\boldsymbol{n}_{LC}^T\boldsymbol{m}\right)\dot{s}_M - \boldsymbol{n}_{LC}^T\boldsymbol{m}\dot{P}_{fM} \tag{5-55}$$

$$C_2 = \boldsymbol{m}^T\dot{\boldsymbol{\varepsilon}} - \frac{1}{\overline{K}_s}\dot{s}_M + \frac{\Gamma^w}{\rho_{lm}S_{lm}}\left(\frac{1+e}{1+e_m} + f_\beta\right)\dot{t} \tag{5-56}$$

Hence, the solution for the matrix system expressed in Equation (5-47) is given by

$$\begin{bmatrix}\dot{\lambda}_{LC}\\ \dot{P}_{lm}\end{bmatrix} = [\boldsymbol{H}]^{-1}\left(\begin{bmatrix}C_1\\ C_2\end{bmatrix} - \begin{bmatrix}h_1\\ h_2\end{bmatrix}\dot{T}\right) \tag{5-57}$$

in which the inverse of the matrix of coefficients, $[\boldsymbol{H}]^{-1}$, is

$$[\boldsymbol{H}]^{-1} = \frac{1}{det[\boldsymbol{H}]}\begin{bmatrix}H_{22} & -H_{12}\\ -H_{21} & H_{11}\end{bmatrix} \tag{5-58}$$

with $det[\boldsymbol{H}] = H_{11}\cdot H_{22} - H_{12}\cdot H_{21} \neq 0$. Consequently, the explicit expressions for the rates of the plastic multiplier and the liquid pressure at the microstructural medium are, respectively,

$$\dot{\lambda}_{LC} = \frac{1}{det[\boldsymbol{H}]}\left(\left(C_1 - h_1\dot{T}\right)\cdot H_{22} - \left(C_2 - h_2\dot{T}\right)\cdot H_{12}\right) \tag{5-59}$$

$$\dot{P}_{lm} = \frac{1}{det[\boldsymbol{H}]}\left(-\left(C_1 - h_1\dot{T}\right)\cdot H_{21} + \left(C_2 - h_2\dot{T}\right)\cdot H_{11}\right) \tag{5-60}$$

Inserting the expressions from Equation (5-53) to Equation (5-56) into these two latter equations and after some algebraic operations, the following relationships (in rate form) in terms of the components of the generalized strain vector (the main variables) are obtained

$$\dot{\lambda}_{LC} = \boldsymbol{w}_1^T \dot{\boldsymbol{\varepsilon}} + B_1 \dot{s}_M + B_2 \dot{P}_{fM} + B_3 \dot{T} + B_4 \Gamma^w \dot{t} \tag{5-61}$$

$$\dot{P}_{lm} = \boldsymbol{w}_2^T \dot{\boldsymbol{\varepsilon}} + B_5 \dot{s}_M + B_6 \dot{P}_{fM} + B_7 \dot{T} + B_8 \Gamma^w \dot{t} \tag{5-62}$$

where the vectors, $\boldsymbol{w}_1^T$ and $\boldsymbol{w}_2^T$, and the scalars, B_1 to B_8, that appear in these equations are defined as follows

$$\boldsymbol{w}_1^T = \frac{1}{det[\boldsymbol{H}]}\left(H_{22}\left((1-A)\boldsymbol{n}_{LC}^T[\boldsymbol{D^e}] + A\frac{\partial F_{LC}}{\partial \bar{\varepsilon}_M^{p,vol}}\boldsymbol{m}^T \right) - H_{12}\boldsymbol{m}^T \right) \tag{5-63}$$

$$\boldsymbol{w}_2^T = \frac{1}{det[\boldsymbol{H}]}\left(H_{11}\boldsymbol{m}^T - H_{21}\left((1-A)\boldsymbol{n}_{LC}^T[\boldsymbol{D^e}] + A\frac{\partial F_{LC}}{\partial \bar{\varepsilon}_M^{p,vol}}\boldsymbol{m}^T \right) \right) \tag{5-64}$$

$$B_1 = \frac{1}{det[\boldsymbol{H}]}\cdot\frac{1}{\overline{K}_s}\left(H_{22}\left(\overline{K}_s\frac{\partial F_{LC}}{\partial s_M} - A\frac{\partial F_{LC}}{\partial \bar{\varepsilon}_M^{p,vol}} - K\cdot(1-A)\boldsymbol{n}_{LC}^T\boldsymbol{m} \right) + H_{12} \right) \tag{5-65}$$

$$B_2 = -\frac{1}{det[\boldsymbol{H}]}\cdot H_{22}\boldsymbol{n}_{LC}^T\boldsymbol{m} \tag{5-66}$$

$$B_3 = -\frac{1}{det[\boldsymbol{H}]}\cdot\frac{1}{K_T}\left(H_{12}\eta_T - H_{22}\left((K(1-A)+K_T\zeta_T)\boldsymbol{n}_{LC}^T\boldsymbol{m} + A\frac{\partial F_{LC}}{\partial \bar{\varepsilon}_M^{p,vol}} \right) \right) \tag{5-67}$$

$$B_4 = -\frac{1}{det[\boldsymbol{H}]}\cdot\frac{H_{12}}{\rho_{lm}S_{lm}}\left(\frac{1+e}{1+e_m} + f_\beta \right) \tag{5-68}$$

$$B_5 = \frac{1}{det[\boldsymbol{H}]}\cdot\frac{1}{\overline{K}_s}\left(H_{21}\left(A\frac{\partial F_{LC}}{\partial \bar{\varepsilon}_M^{p,vol}} - \overline{K}_s\frac{\partial F_{LC}}{\partial s_M} + K\cdot(1-A)\boldsymbol{n}_{LC}^T\boldsymbol{m} \right) - H_{11} \right) \tag{5-69}$$

$$B_6 = \frac{1}{det[\boldsymbol{H}]}\cdot H_{21}\boldsymbol{n}_{LC}^T\boldsymbol{m} \tag{5-70}$$

$$B_7 = \frac{1}{det[\boldsymbol{H}]}\cdot\frac{1}{K_T}\left(H_{21}\left((K(1-A)+K_T\zeta_T)\boldsymbol{n}_{LC}^T\boldsymbol{m} + A\frac{\partial F_{LC}}{\partial \bar{\varepsilon}_M^{p,vol}} \right) - H_{11}\eta_T \right) \tag{5-71}$$

$$B_8 = \frac{1}{det[\boldsymbol{H}]} \cdot \frac{H_{11}}{\rho_{lm} S_{lm}} \left(\frac{1+e}{1+e_m} + f_\beta \right) \tag{5-72}$$

The evolution of the stress state for loading paths in which the two plastic mechanisms are activated can be evaluated now. The following expression is obtained when Equation (4-118) is used:

$$\begin{aligned} \dot{\boldsymbol{\sigma}} = (1-A)[\boldsymbol{D^e}]\dot{\boldsymbol{\varepsilon}} - (1-A)\frac{K}{\overline{K}_s}\dot{s}_M \boldsymbol{m} - \zeta_{lm}\dot{P}_{lm}\boldsymbol{m} - \dot{P}_{fM}\boldsymbol{m} \\ - \frac{1}{K_T}(K(1-A) + K_T\zeta_T)\dot{T}\boldsymbol{m} - \dot{\lambda}_{LC}(1-A)[\boldsymbol{D^e}]\boldsymbol{m}_{LC} \end{aligned} \tag{5-73}$$

Inserting the expressions in Equation (5-61) and Equation (5-62) – the solution for the system of equations given in Equation (5-46) – into Equation (5-73), the effective stress rate, expressed in terms of the main global variables, is computed as

$$\begin{aligned} \dot{\boldsymbol{\sigma}} = & \left((1-A)[\boldsymbol{D^e}] - (1-A)[\boldsymbol{D^e}]\boldsymbol{m}_{LC}\boldsymbol{w}_1^T - \zeta_{lm}\boldsymbol{m}\boldsymbol{w}_2^T \right)\dot{\boldsymbol{\varepsilon}} \\ & - \frac{1}{\overline{K}_s}\left((K(1-A) - \overline{K}_s\zeta_{lm}B_5)\boldsymbol{m} + \overline{K}_s(1-A)B_1[\boldsymbol{D^e}]\boldsymbol{m}_{LC} \right)\dot{s}_M \\ & - \left((\zeta_{lm}B_6 + 1)\boldsymbol{m} + (1-A)B_2[\boldsymbol{D^e}]\boldsymbol{m}_{LC} \right)\dot{P}_{fM} \\ & - \frac{1}{K_T}\left((K(1-A) + K_T\zeta_{lm}B_7 + K_T\zeta_T)\boldsymbol{m} - K_T(1-A)B_3[\boldsymbol{D^e}]\boldsymbol{m}_{LC} \right)\dot{T} \\ & - \left((1-A)B_4[\boldsymbol{D^e}]\boldsymbol{m}_{LC} + \zeta_{lm}B_8\boldsymbol{m} \right)\Gamma^w\dot{t} \end{aligned} \tag{5-74}$$

and the following tensor/vector entities are then defined (see the first equation in (5-5))

$$[\boldsymbol{D^{ep}}] = (1-A)[\boldsymbol{D^e}]([\mathbf{I}] - \boldsymbol{m}_{LC}\boldsymbol{w}_1^T) - \zeta_{lm}\boldsymbol{m}\boldsymbol{w}_2^T \tag{5-75}$$

$$\boldsymbol{h}_s = -\frac{1}{\overline{K}_s}\left(\left(\zeta_{lm}\overline{K}_s B_5 + K(1-A) \right)\boldsymbol{m} + (1-A)B_1[\boldsymbol{D^e}]\boldsymbol{m}_{LC} \right) \tag{5-76}$$

$$\boldsymbol{h}_{P_{fM}} = -(\zeta_{lm}B_6 + 1)\boldsymbol{m} - (1-A)B_2[\boldsymbol{D^e}]\boldsymbol{m}_{LC} \tag{5-77}$$

$$\boldsymbol{h}_T = -\frac{1}{K_T}\left((K(1-A) + \zeta_{lm}K_T B_7 + \zeta_T K_T)\boldsymbol{m} + K_T(1-A)B_3[\boldsymbol{D^e}]\boldsymbol{m}_{LC} \right) \tag{5-78}$$

$$\boldsymbol{h}_t = -(\zeta_{lm}B_8\boldsymbol{m} + (1-A)B_4[\boldsymbol{D^e}]\boldsymbol{m}_{LC})\Gamma^w \tag{5-79}$$

Although the constitutive vector $\boldsymbol{h}_{P_{fM}}$ given in Equation (5-77) does not appear in Equation (5-5), it arises from the adoption of the BBM effective stress concept for macrostructure (see Equation (3-36)). This vector relates the changes in the effective stresses due to changes in the

pore pressures of the fluid (air or water) that drives the mechanical behaviour of the soil. In other words, the contribution of the third and the fourth terms on the right-hand side of the first equation in (5-5) are replaced by the term $\boldsymbol{h}_{P_{fM}}\dot{P}_{fM}$, where $\dot{P}_{fM}$ is defined as in Equation (4-41).

Having updated the stress state and all the internal variables, the yield criterion is checked again (as it has been done at the end of the trial sub-incrementation), so that

$$\left|F_{LC}\left(\boldsymbol{\sigma}_n, p_{0,n}^*\right)\right| \leq FTOL \tag{5-80}$$

where

$$\begin{aligned} \boldsymbol{\sigma}_n &= \boldsymbol{\sigma}_{n-1} + \dot{\boldsymbol{\sigma}} \\ p_{0,n}^* &= p_{0,n-1}^* + \dot{p}_0^* \end{aligned} \tag{5-81}$$

The expression shown in Equation (5-74) and the second expression in Equation (5-5) give the increments in the stress field ($\dot{\boldsymbol{\sigma}}$) and in the hardening/softening parameter ($\dot{p}_0^*$), respectively. If the stress state at the end of the elastoplastic integration does not fulfill the updated yield function, the stresses, the plastic strains and hardening/softening parameter must be corrected back to the yield surface. This yield surface drift occurs due to the cumulative errors arising from the numerical integration procedure. The magnitude of these errors depends on the degree of constitutive non-linearities, on the geometry of the problem under consideration and on the size of the loading increments (Potts and Zdravković, 1999). A suitable and accurate method for correcting the stress state so that the yield function is still satisfied at the end of the sub-incrementation process is described in the following section.

5.2.8. THE YIELD SURFACE DRIFT CORRECTION

In explicit integration processes, the stress state at the end of an incremental loading that starts at the yield locus can drift away from the updated yield surface. The amount of this drift depends on the nature of the constitutive model and on the combination of the user-defined tolerance parameters, $FTOL$ and $STOL$ (Potts and Zdravković, 1999; Sloan *et al.*, 2001). $FTOL$, as discussed in previous sections, is the yield function tolerance while $STOL$ is an error-controlling tolerance related to the numerical integration scheme used (in this Thesis, it corresponds to the Modified explicit Euler scheme, that is addressed in **Section 5.2.10**). The yield surface drift problem dealt in this section is illustrated in Figure 5-9. Consider an initial stress state (represented by the point A) located on the yield surface, i.e., $F_{LC}^{(n-1)} \equiv F_{LC}\left(\boldsymbol{\sigma}_A, p_{0,A}^*\right) = 0$, and subjected to a loading path that generates additional plastic deformation. Consequently, the yield locus moves during the loading process to a final (updated) yield surface position defined by $F_{LC}^{(n)} \equiv F_{LC}\left(\boldsymbol{\sigma}_A + \Delta\boldsymbol{\sigma}, p_{0,A}^* + \Delta p_0^*\right) = 0$. Nevertheless, the stress state at the end of this sub-step (represented by the point B, for the case in which the incremental loading is applied in one step) may lie outside this new yield surface, $\left|F_{LC}^{(n)}\left(\boldsymbol{\sigma}_B, p_{0,B}^*\right)\right| > FTOL$, as shown in Figure 5-9. The drift correction problem consists, then, in returning the stresses, plastic strains and

hardening parameters that violate the yield condition to a corrected set of variables lying on the updated yield surface (the point C in Figure 5-9).

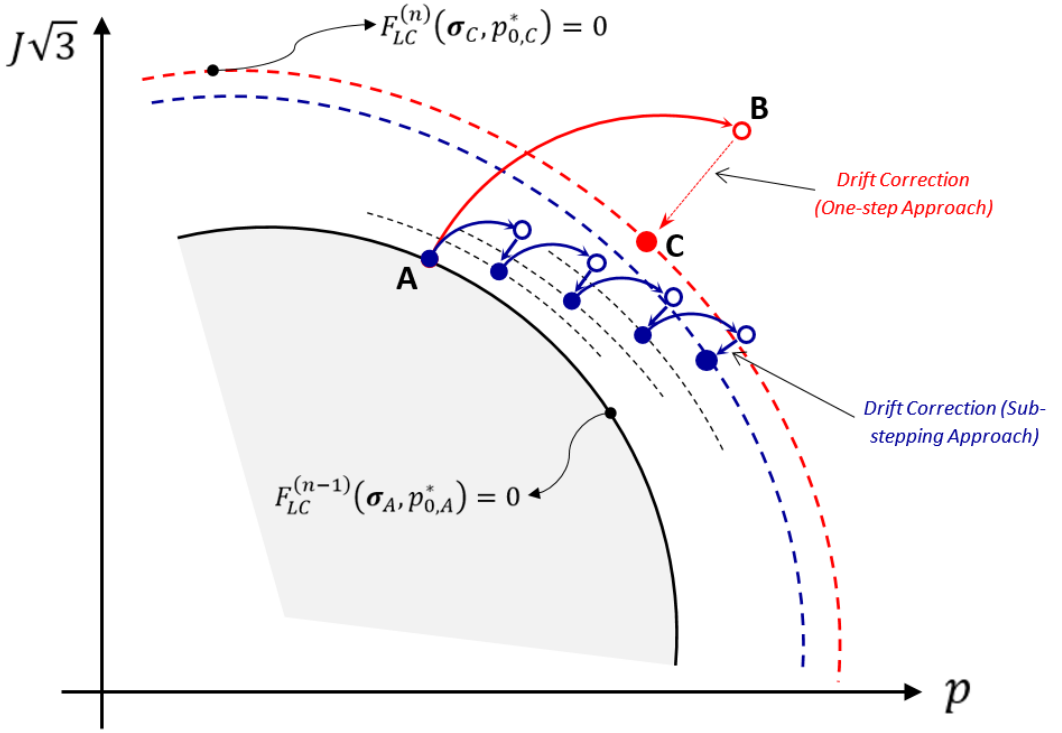

Figure 5-9: Schematic representation of the yield surface drift correction when the stress-strain relationship is integrated in a single step (one-step approach) or into a series of smaller sub-steps (sub-stepping approach).

Several projecting back methods have been proposed in the literature (Nayak and Zienkiewicz, 1972; Vermeer, 1980; Owen and Hinton, 1980; Sloan and Randolph, 1982) whose advantages and drawbacks for modelling the elastoplastic response of geomaterials in finite element analyses are discussed and compared in Potts and Gens (1985). The alternative method proposed by Potts and Gens (1985) is the stress correction method used in this Thesis. The main distinguishing aspect of this method (in comparison to the other ones) is to account for the changes in the elastic strains during the drift correction (Potts and Gens, 1985; Potts and Zdravković, 1999). Taking as reference the schematic situation shown in Figure 5-9, the change in the (generalized) elastic strains due to the stress correction from point B to point C, $\delta\boldsymbol{\varepsilon}_{B\to C}^{e,drift}$,is given by

$$\delta\boldsymbol{\varepsilon}_{B\to C}^{e,drift} = [\boldsymbol{D}^{*,e}]^{-1}(\boldsymbol{\sigma}_C - \boldsymbol{\sigma}_B) \tag{5-82}$$

where $[\boldsymbol{D}^{*,e}]$ is the generalized elastic constitutive tensor.

It is established that the correction process occurs under the assumption of no change in the total strain increment, that is, $\delta\boldsymbol{\varepsilon}_{B\to C}^{drift} = \delta\boldsymbol{\varepsilon}_{B\to C}^{e,drift} + \delta\boldsymbol{\varepsilon}_{B\to C}^{p,drift} = \mathbf{0}$. Recalling the general expression for the infinitesimal total deformations (Equation (4-56)) and considering all the hypotheses adopted so far, the latter assumption leads to

$$\begin{aligned}\delta\boldsymbol{\varepsilon}^{drift} &= \delta\boldsymbol{\varepsilon}^{e,drift} + \delta\boldsymbol{\varepsilon}^{p,drift} = \left(\delta\bar{\boldsymbol{\varepsilon}}_m^{e,drift} + \delta\bar{\boldsymbol{\varepsilon}}_M^{e,drift}\right) + \delta\bar{\boldsymbol{\varepsilon}}_M^{p,drift} \\ &= [\boldsymbol{D}^e]^{-1}\delta\boldsymbol{\sigma}^{drift} + \frac{1}{3K}\left(\zeta_{lm}\delta P_{lm}^{drift} + \zeta_T\delta T^{drift} + \delta P_{fM}^{drift}\right)\boldsymbol{m} \\ &\quad + \frac{1}{3\bar{K}_s}\delta s_M^{drift}\boldsymbol{m} + \frac{1}{3K_T}\delta T^{drift}\boldsymbol{m} + \delta\bar{\boldsymbol{\varepsilon}}_{M,LC}^{p,drift} \\ &\quad + \delta\bar{\boldsymbol{\varepsilon}}_{M,\beta}^{p,drift} = \boldsymbol{0}\end{aligned} \tag{5-83}$$

where $\delta(*)^{drift}$ represents the incremental correction (of any variable subjected to correction) imposed during the drift step. Equation (5-83) shows that any elastic strain change during the drift correction must be balanced by an equal and opposite change in the plastic deformations (Potts and Gens, 1985). Therefore,

$$\begin{aligned}\delta\bar{\boldsymbol{\varepsilon}}_M^{p,drift} &= -\delta\boldsymbol{\varepsilon}^{e,drift} \\ &= -[\boldsymbol{D}^e]^{-1}\delta\boldsymbol{\sigma}^{drift} \\ &\quad - \frac{1}{3K}\left(\zeta_{lm}\delta P_{lm}^{drift} + \zeta_T\delta T^{drift} + \delta P_{fM}^{drift}\right)\boldsymbol{m} \\ &\quad - \frac{1}{3\bar{K}_s}\delta s_M^{drift}\boldsymbol{m} - \frac{1}{3K_T}\delta T^{drift}\boldsymbol{m}\end{aligned} \tag{5-84}$$

It is also assumed that temperature, the fluid pressures in macro-pores (and consequently, the macro suction as well) and all time-dependent terms remain unchanged during the drift correction step, that is, $\delta T^{drift} = \delta P_{lM}^{drift} = \delta P_{gM}^{drift} = \delta s_M^{drift} = \delta t^{drift} = 0$. Nevertheless, the microstructural pore-water pressure is allowed to change during the correction process(Gesto, 2014), i.e. $\delta P_{lm}^{drift} \neq 0$, which implies that the previous equation reduces to

$$\delta\bar{\boldsymbol{\varepsilon}}_M^{p,drift} = -[\boldsymbol{D}^e]^{-1}\delta\boldsymbol{\sigma}^{drift} - \frac{1}{3K}\zeta_{lm}\delta P_{lm}^{drift}\boldsymbol{m} \tag{5-85}$$

On the other hand, the total plastic strain increments during the drift correction step ($\delta\bar{\boldsymbol{\varepsilon}}_M^{p,drift}$) can be obtained by adding the two vectorial expressions given in Equation (4-92) and in Equation (4-101). Thus,

$$\begin{aligned}\delta\bar{\boldsymbol{\varepsilon}}_M^{p,drift} = \delta\bar{\boldsymbol{\varepsilon}}_{M,LC}^{p,drift} + \delta\bar{\boldsymbol{\varepsilon}}_{M,\beta}^{p,drift} &= \delta\lambda_{LC}^{drift}\boldsymbol{m}_{LC} + f_\beta\left(\delta\bar{\boldsymbol{\varepsilon}}_m^{drift} - \delta\bar{\boldsymbol{\varepsilon}}_{m,\Delta T}^{drift}\right) \\ &= \delta\lambda_{LC}^{drift}\boldsymbol{m}_{LC} + f_\beta\delta\bar{\boldsymbol{\varepsilon}}_m^{drift}\end{aligned} \tag{5-86}$$

where $\delta\lambda_{LC}^{drift}$ is an unknown factor that must be determined during the stress correction process. The microstructural strain increments during the drift step, $\delta\bar{\boldsymbol{\varepsilon}}_m^{drift}$, is calculated from the expression in Equation (4-114),

$$\delta\bar{\boldsymbol{\varepsilon}}_m^{drift} = \left(\frac{1+e}{1+e_m}+f_\beta\right)^{-1}\left(\delta\boldsymbol{\varepsilon}^{drift} - \frac{1}{3K_T}\delta T^{drift}\boldsymbol{m} - \frac{1}{3\bar{K}_s}\delta s_M^{drift}\boldsymbol{m} - \delta\lambda_{LC}^{drift}\boldsymbol{m}_{LC}\right) + \frac{1}{3K_T}\left(\frac{1+e_m}{1+e}\right)\delta T^{drift}\boldsymbol{m} \quad (5\text{-}87)$$

$$= -\left(\frac{1+e}{1+e_m}+f_\beta\right)^{-1}\delta\lambda_{LC}^{drift}\boldsymbol{m}_{LC}$$

Replacing the latter expression into Equation (5-86), and after some algebra, it results that

$$\delta\bar{\boldsymbol{\varepsilon}}_M^{p,drift} = \delta\lambda_{LC}^{drift}(1-A)\boldsymbol{m}_{LC} \quad (5\text{-}88)$$

where the variable A is defined in Equation (4-119). Equating the expressions in Equation (5-85) and Equation (5-88) and solving for $\delta\boldsymbol{\sigma}^{drift}$, the correction in the stress state during the drift step obeys the following relation

$$\delta\boldsymbol{\sigma}^{drift} = -\delta\lambda_{LC}^{drift}(1-A)[\boldsymbol{D}^e]\boldsymbol{m}_{LC} - \zeta_{lm}\delta P_{lm}^{drift}\boldsymbol{m} \quad (5\text{-}89)$$

As δP_{lm}^{drift} is not necessarily null during the drift correction, it must be also determined before correcting the stresses given in Equation (5-89). In order to estimate the correction in the microstructural liquid pressure, Equation (5-16) is recalled, that is,

$$\lambda_{LC}^{drift}\boldsymbol{m}^T\boldsymbol{m}_{LC} + \frac{\bar{\phi}_m}{\rho_{lm}S_{lm}}\left(\frac{1+e}{1+e_m}+f_\beta\right)\left(S_{lm}\frac{\partial\rho_{lm}}{\partial P_{lm}} + \rho_{lm}\frac{\partial S_{lm}}{\partial P_{lm}}\right)\delta P_{lm}^{drift} = \boldsymbol{m}^T\delta\boldsymbol{\varepsilon}^{drift} - \frac{1}{\bar{K}_s}\delta s_M^{drift} - \frac{\eta_T}{K_T}\delta T^{drift} + \frac{\Gamma^w}{\rho_{lm}S_{lm}}\left(\frac{1+e}{1+e_m}+f_\beta\right)\delta t^{drift} \quad (5\text{-}90)$$

Note that, because of the assumptions considered previously, the terms on the right-hand side of Equation (5-90) are equal to zero. Taking this into account and solving the resulting expression for δP_{lm}^{drift}, then

$$\delta P_{lm}^{drift} = -\frac{A^*}{\zeta_{lm}}\delta\lambda_{LC}^{drift}\boldsymbol{m}^T\boldsymbol{m}_{LC} \quad (5\text{-}91)$$

where A^* is the coefficient defined by the expression in Equation (5-23).

Changes in the hardening/softening parameter, p_0^*, are also expected during the drift correction due to the changes in plastic strains (see Equation (5-85)). The expression for the hardening parameter correction, $\delta p_0^{*,drift}$, is obtained from the second equation in (5-5) and reads as

$$\delta p_0^{*,drift} = \frac{(1+\bar{e}_M)p_0^*}{\lambda_{sat}-\bar{\kappa}_M}\left(\delta\lambda_{LC}^{drift}\boldsymbol{m}^T\boldsymbol{m}_{LC} + f_\beta \boldsymbol{m}^T\delta\bar{\boldsymbol{\varepsilon}}_m^{drift}\right) \tag{5-92}$$

Combining Equation (5-87) and Equation (5-92), the following expression is obtained

$$\delta p_0^{*,drift} = \delta\lambda_{LC}^{drift}(1-A)\frac{(1+\bar{e}_M)p_0^*}{\lambda_{sat}-\bar{\kappa}_M}\boldsymbol{m}^T\boldsymbol{m}_{LC} \tag{5-93}$$

Thus, the stresses, $\boldsymbol{\sigma}_C$, the macrostructural plastic strains, $\bar{\boldsymbol{\varepsilon}}_{M,C}^p$, and the hardening/softening parameter, $p_{0,C}^*$, at the end of the correction process, are given as follows

$$\boldsymbol{\sigma}_C = \boldsymbol{\sigma}_B + \delta\boldsymbol{\sigma}^{drift} = \boldsymbol{\sigma}_B - \delta\lambda_{LC}^{drift}\left((1-A)[\boldsymbol{D^e}] - A^*\boldsymbol{m}\boldsymbol{m}^T\right)\boldsymbol{m}_{LC} \tag{5-94}$$

$$\bar{\boldsymbol{\varepsilon}}_{M,C}^p = \bar{\boldsymbol{\varepsilon}}_{M,B}^p + \delta\bar{\boldsymbol{\varepsilon}}_M^{p,drift} = \bar{\boldsymbol{\varepsilon}}_{M,B}^p + \delta\lambda_{LC}^{drift}(1-A)\boldsymbol{m}_{LC} \tag{5-95}$$

$$p_{0,C}^* = p_{0,B}^* + \delta p_0^{*,drift} = p_{0,B}^* + \delta\lambda_{LC}^{drift}(1-A)\frac{(1+\bar{e}_M)p_0^*}{\lambda_{sat}-\bar{\kappa}_M}\boldsymbol{m}^T\boldsymbol{m}_{LC} \tag{5-96}$$

The corrected stress state and the hardening parameter must satisfy the yield condition, $F_{LC}(\boldsymbol{\sigma}_C, p_{0,C}^*) = F_{LC}(\boldsymbol{\sigma}_B + \delta\boldsymbol{\sigma}^{drift}, p_{0,B}^* + \delta p_0^{*,drift}) = 0$, whose expansion as a Taylor's series gives

$$F_{LC}(\boldsymbol{\sigma}_C, p_{0,C}^*) \approx F_{LC}(\boldsymbol{\sigma}_B, p_{0,B}^*) + \left(\frac{\partial F_{LC}}{\partial\boldsymbol{\sigma}}\right)^T\delta\boldsymbol{\sigma}^{drift} + \left(\frac{\partial F_{LC}}{\partial p_0^*}\right)\delta p_0^{*,drift} = 0 \tag{5-97}$$

in which the second-order (and higher) terms are neglected. Recalling Equation (5-89) and Equation (5.091) and using the following relationship,

$$\begin{aligned}\left(\frac{\partial F_{LC}}{\partial p_0^*}\right)\delta p_0^{*,drift} &= \left(\frac{\partial F_{LC}}{\partial p_0^*}\right)\left(\frac{\partial p_0^*}{\partial\bar{\varepsilon}_M^{p,vol}}\right)\boldsymbol{m}^T\delta\bar{\boldsymbol{\varepsilon}}_M^{p,drift} \\ &= \left(\frac{\partial F_{LC}}{\partial\bar{\varepsilon}_M^{p,vol}}\right)\delta\lambda_{LC}^{drift}(1-A)\boldsymbol{m}^T\boldsymbol{m}_{LC}\end{aligned} \tag{5-98}$$

after some rearrangement, an estimate for $\delta\lambda_{LC}^{drift}$ is obtained as follows

$$\delta\lambda_{LC}^{drift} = \frac{F_{LC}(\boldsymbol{\sigma}_B, p_{0,B}^*)}{(A-1)\left(\left(\frac{\partial F_{LC}}{\partial\bar{\varepsilon}_M^{p,vol}}\right)\boldsymbol{m}^T - \boldsymbol{n}_{LC}^T[\boldsymbol{D^e}]\right)\boldsymbol{m}_{LC} - A^*(\boldsymbol{n}_{LC}^T\boldsymbol{m})(\boldsymbol{m}^T\boldsymbol{m}_{LC})} \tag{5-99}$$

A comprehensive description of the algebraic steps followed to determine the expression in Equation (5-99) can be found in Gesto (2014). Note that the values for the partial derivatives in

Equation (5-99), $\boldsymbol{n}_{LC} = \frac{\partial F_{LC}}{\partial \boldsymbol{\sigma}}$, $\boldsymbol{m}_{LC} = \frac{\partial G_{LC}}{\partial \boldsymbol{\sigma}}$ and $\frac{\partial F_{LC}}{\partial \bar{\varepsilon}_M^{p,vol}}$ are required. In the present formulation, these quantities are evaluated at the end of the elastoplastic sub-step (the point B, in Figure 5-9). However, they may be also evaluated at the beginning (the point A) or even at an intermediate point between them without compromising the accuracy of the model predictions if the sub-stepping tolerance ($STOL$) is sufficiently small (Potts and Gens, 1985). If an inadequate tolerance is set, the yield surface drift at the end of the sub-step could be large and, consequently, substantial errors could occur if the partial derivatives in Equation (5-99) are computed at the end of that sub-step (Potts and Zdravković, 1999). If this option is used to assess the quantities in Equation (5-99), it is advisable to check that the combination of the corrected stress state and the hardening parameter keeps fulfilling the yield condition. If this is not the case, an iterative correction procedure is performed in which an improved estimate for $\delta\lambda_{LC}^{drift}$ is searched so that the yield condition, at the $(l+1)th$ iteration, is satisfied for a small tolerance, i.e. $\left|F_{LC}^{(n),l+1}\left(\boldsymbol{\sigma}_C^{(l+1)}, p_{0,C}^{*,(l+1)}\right)\right| \leq FTOL$ (Potts and Gens, 1985; Potts and Zdravković, 1999).

Having calculated $\delta\lambda_{LC}^{drift}$, the corrected stresses, macrostructural irreversible strains and hardening variable are computed according to the expressions from Equation (5-94) to Equation (5-96) while the liquid pressure in micro-pores at the end of the drift process is corrected as follows

$$P_{lm,C} = P_{lm,B} + \delta P_{lm}^{drift} = P_{lm,B} - \delta\lambda_{LC}^{drift} \frac{A^*}{\zeta_{lm}} \boldsymbol{m}^T \boldsymbol{m}_{LC} \tag{5-100}$$

Since the drift step is performed at constant total strain conditions, then the total porosity during the correction process also remains unchanged, that is, $\phi_C = \phi_B$. Nevertheless, the micro ($\bar{\phi}_m$) and macro ($\bar{\phi}_M$) volume fractions may change during the drift correction so that the total porosity is kept constant. From Equation (3-53), the correction in the microstructural porosity during the drift step, $\delta\bar{\phi}_m^{drift}$, is given by (for a positive compression)

$$\begin{aligned} \delta\bar{\phi}_m^{drift} &= -\delta\bar{\varepsilon}_m^{vol,drift} + \frac{(1-\phi)}{\rho_s}\frac{\partial\rho_s}{\partial T}\delta T^{drift} + \bar{\phi}_m \delta\varepsilon^{vol,drift} \\ &= -\boldsymbol{m}^T \delta\bar{\boldsymbol{\varepsilon}}_m^{drift} == \frac{\delta\lambda_{LC}^{drift}}{\left(\frac{1+e}{1+e_m} + f_\beta\right)} \boldsymbol{m}^T \boldsymbol{m}_{LC} \end{aligned} \tag{5-101}$$

Therefore, the values for the pore volume fractions (micro and macro) at the end of the correction process are:

$$\bar{\phi}_{m,C} = \bar{\phi}_{m,B} + \delta\bar{\phi}_m^{drift} = \bar{\phi}_{m,B} + \frac{\delta\lambda_{LC}^{drift}}{\left(\frac{1+e}{1+e_m} + f_\beta\right)}\boldsymbol{m}^T\boldsymbol{m}_{LC}$$
$$\bar{\phi}_{M,C} = \phi_B - \bar{\phi}_{m,C} = \bar{\phi}_{M,B} - \frac{\delta\lambda_{LC}^{drift}}{\left(\frac{1+e}{1+e_m} + f_\beta\right)}\boldsymbol{m}^T\boldsymbol{m}_{LC} \quad (5\text{-}102)$$

5.2.9. THE SIGN OF THE MICROSTRUCTURAL EFFECTIVE MEAN STRESS

A final issue related to the stress integration procedure that must be addressed refers to the sign of the microstructural effective mean stress. As discussed in **Section 4.4.2**, the sign of the effective mean stress increment acting on microstructure determines the mechanical behavior at this structural pore level (expansion or contraction) and, due to micro-macro coupling, also affects the deformation response of macro-voids. As discussed in **Section 4.2.3**, the microstructural mechanical behavior is essentially volumetric, which means that the main stress variable governing this structural level is the effective mean stress, $\dot{p}_m$, whose expression, for a THM analysis, is given as follows

$$\dot{p}_m = \frac{1}{3}\boldsymbol{m}^T\dot{\boldsymbol{\sigma}}_m = \dot{p} + \left(\zeta_{gm}\dot{P}_{gm} + \zeta_{lm}\dot{P}_{lm} + \zeta_T\dot{T} + \dot{P}_{fM}\right) \quad (5\text{-}103)$$

in which the micro constitutive stress tensor, $\dot{\boldsymbol{\sigma}}_m$, in Equation (4-40) has been evoked. The evolution of the effective mean stress acting on the soil, $\dot{p}$, is obtained from the global constitutive stress tensor in Equation (4-118), which leads to

$$\dot{p} = \frac{1}{3}\boldsymbol{m}^T\dot{\boldsymbol{\sigma}} = \frac{q}{q+f_\beta}K\left(\dot{\varepsilon}^{vol} - \frac{1}{\overline{K}_s}\dot{s}_M - \frac{1}{K_T}\dot{T} - \dot{\lambda}_{LC}\frac{\partial G_{LC}}{\partial p}\right) - \left(\zeta_{gm}\dot{P}_{gm} + \zeta_{lm}\dot{P}_{lm} + \zeta_T\dot{T} + \dot{P}_{fM}\right) \quad (5\text{-}104)$$

where

$$q = \frac{1+e}{1+e_m} \quad (5\text{-}105)$$

and

$$\frac{\partial G_{LC}}{\partial p} = \boldsymbol{m}^T\boldsymbol{m}_{LC} = \boldsymbol{m}^T\left(\frac{\partial G_{LC}}{\partial \boldsymbol{\sigma}}\right) \quad (5\text{-}106)$$

The combination of Equation (5-103) and Equation (5-104) leads to the following expression of the effective mean stress evolution for microstructure in terms of the global THM variables, that is,

$$\dot{p}_m = \frac{q}{q+f_\beta}K\left(\dot{\varepsilon}^{vol} - \frac{1}{\overline{K}_s}\dot{s}_M - \frac{1}{K_T}\dot{T} - \dot{\lambda}_{LC}\frac{\partial G_{LC}}{\partial p}\right) \quad (5\text{-}107)$$

In loading paths inside the yield surface, for which $\dot{\lambda}_{LC} = 0$, the latter expression becomes

$$\dot{p}_m = \frac{q}{q + f_\beta} K \left(\dot{\varepsilon}^{vol} - \frac{1}{\overline{K}_s} \dot{s}_M - \frac{1}{K_T} \dot{T} \right) \tag{5-108}$$

A couple of comments comes from the scrutiny of the relationships shown in Equation (5-107) and in Equation (5-108):

i. for admissible values for the micro-macro interaction function f_β, the sign of $\dot{p}_m$ does not depend on the values assumed by this function since, as explained in **Section 5.2.4**, $f_\beta > -1$ which implies that $\frac{q}{q+f_\beta} > 0$;

ii. consequently, the sign of $\dot{p}_m$, for each incremental sub-loading, is the same as $\left(\dot{\varepsilon}^{vol} - \frac{1}{\overline{K}_s} \dot{s}_M - \frac{1}{K_T} \dot{T} - \dot{\lambda}_{LC} \frac{\partial G_{LC}}{\partial p} \right)$ or $\left(\dot{\varepsilon}^{vol} - \frac{1}{\overline{K}_s} \dot{s}_M - \frac{1}{K_T} \dot{T} \right)$, depending on whether the BBM plastic mechanism is active or not, respectively. The manner in which these generalized strain components evolve during the sub-loading responds for the microstructural volumetric behavior: a positive value arising from the combination of these quantities implies that $\dot{p}_m > 0$. It means that the microstructural medium tends to shrink during the loading path (using the Soil Mechanics sign convention). In contrast, a negative value leads to $\dot{p}_m < 0$ and, consequently, the microstructure is prone to swell.

If the sign of $\dot{p}_m$ changes for a given incremental loading, it is advisable to reduce the size of the sub-step in order to prevent a change in microstructural behavior over the course of the incrementation process.

5.2.10. THE MODIFIED EULER SCHEME WITH ERROR CONTROL

The explicit schemes known as the Modified Euler schemes with automatic error control are based on the approach proposed by Sloan (1987). The key point in the Modified Euler scheme is to provide two estimates for the stress state and the hardening parameter, whose order of accuracy differs by one, in order to predict the solution at the end of each sub-step. Instead of using a constant time step, this explicit scheme evaluates the sub-step size by taking as a guide the local truncation error obtained as the difference between these two solutions of different accuracy (Sloan *et al.*, 2001). As a consequence, the yield surface drift and the computational costs may be reduced substantially (Pedroso and Farias, 2005). This procedure aims to control the global relative error in the stresses and the stress-like internal variables (arising from the approximated solution of the system of equations in (5-5)) by means of the local relative error control for each sub-step. In Sloan and Booker (1992) and Sloan *et al.* (2001) some enhancements were included to the original algorithm by Sloan (1987) in order to improve the accuracy, efficiency and robustness of this family of stress integration schemes. In this Thesis, this type of explicit scheme has been selected to formulate a stress integration algorithm taking into consideration the particularities of a double-structure model. Moreover, it is important to remark that, in classical elastoplastic formulations, stress integration algorithms like the

Modified Euler scheme are employed to integrate the elastoplastic constitutive matrix over the portion of the generalized strain increment expressed by $(1-\alpha)\cdot\Delta\boldsymbol{\varepsilon}^{g}$ (as illustrated in Figure 5-5(b)) . For the double-porosity formulation, the explicit Modified Euler is also used to integrate the stresses for loading paths inside the yield surface (when the trial step is performed and the yield surface is not crossed yet).

Consider a given incremental pseudo-time, $0<\Delta\tau_n\leq 1$ (see **Section 5.2.3**), and let the subscripts $n-1$ and n denote the quantities estimated at the pseudo-times τ_{n-1} and $\tau_n=\tau_{n-1}+\Delta\tau_n$, respectively. If the generalized strain increment, $\delta\boldsymbol{\varepsilon}_n^{g}$, for the time step $\Delta\tau_n$ is given by

$$\delta\boldsymbol{\varepsilon}_n^{g}=\Delta\tau_n\cdot\Delta\boldsymbol{\varepsilon}^{g}=\Delta\tau_n\cdot\begin{Bmatrix}\Delta\boldsymbol{\varepsilon}\\ \Delta P_{lM}\\ \Delta P_{gM}\\ \Delta T\\ \Delta t\end{Bmatrix}=\begin{Bmatrix}\delta\boldsymbol{\varepsilon}\\ \delta P_{lM}\\ \delta P_{gM}\\ \delta T\\ \delta t\end{Bmatrix} \tag{5-109}$$

then, the first evaluation of the updated stress and hardening parameter at the end of the sub-step, using the explicit Euler method, is computed as

$$\begin{aligned}\boldsymbol{\sigma}_{n,1}&=\boldsymbol{\sigma}_{n-1}+\delta\boldsymbol{\sigma}_1\\ \left(p_{0,n}^{*}\right)_1&=p_{0,n-1}^{*}+\delta p_{0,1}^{*}\end{aligned} \tag{5-110}$$

where

$$\begin{aligned}\delta\boldsymbol{\sigma}_1&=\left[\boldsymbol{D}^{*}\left(\boldsymbol{\sigma}_{n-1},p_{0,n-1}^{*}\right)\right]\delta\boldsymbol{\varepsilon}_n^{g}\\ &=\left[\boldsymbol{D}_{n-1}^{\boldsymbol{ep}}\right]\delta\boldsymbol{\varepsilon}_n+\boldsymbol{h}_{s,n-1}\cdot\delta s_{M,n}+\boldsymbol{h}_{P_{fM},n-1}\cdot\delta P_{fM,n}+\boldsymbol{h}_{T,n-1}\cdot\delta T_n\\ &\quad+\boldsymbol{h}_{t,n-1}\cdot\delta t_n\\ \delta p_{0,1}^{*}&=p_{0,n-1}^{*}\cdot\frac{\left(1+\bar{e}_{M,n-1}\right)}{\lambda_{sat}-\bar{\kappa}_M}\\ &\quad\cdot\left(\delta\lambda_{LC,1}\boldsymbol{m}^{T}\boldsymbol{m}_{LC,n-1}+f_\beta\cdot\delta\bar{\varepsilon}_{m,1}^{vol}-\frac{f_\beta}{K_T}\left(\frac{1+e_{m,n-1}}{1+e_{n-1}}\right)\delta T_n\right)\end{aligned} \tag{5-111}$$

in which the constitutive tensor, $\left[\boldsymbol{D}_{n-1}^{\boldsymbol{ep}}\right]$, the constituve vectors, $\boldsymbol{h}_{s,n-1}$, $\boldsymbol{h}_{P_{fM},n-1}$, $\boldsymbol{h}_{T,n-1}$, $\boldsymbol{h}_{t,n-1}$, all derivatives and other geotechnical variables are computed at the initial stress state, that is, at τ_{n-1} . The *subscript "1"* indicates the first order Euler approximation for any variable at the end of the pseudo-time step $\Delta\tau_n$. The plastic multiplier increment ($\delta\lambda_{LC,1}$), the liquid pressure increment at microtructural level ($\delta P_{lm,1}$) and the volumetric micro deformation increment ($\delta\bar{\varepsilon}_{m,1}^{vol}$) are obtained from the general expressions in Equation (5-61), Equation (5-62) and the relation expressed in Equation (5-13), respectively, that is,

$$\begin{aligned}\delta\lambda_{LC,1}=\boldsymbol{w}_{1,n-1}^{T}\delta\boldsymbol{\varepsilon}_n+B_{1,n-1}\cdot\delta s_{M,n}+B_{2,n-1}\cdot\delta P_{fM,n}\\ +B_{3,n-1}\cdot\delta T_n+B_{4,n-1}\Gamma^{w}\cdot\delta t_n\end{aligned} \tag{5-112}$$

$$\delta P_{lm,1} = \boldsymbol{w}_{2,n-1}^{T}\delta\boldsymbol{\varepsilon}_n + B_{5,n-1}\cdot\delta s_{M,n} + B_{6,n-1}\cdot\delta P_{fM,n} + B_{7,n-1}\cdot\delta T_n + B_{8,n-1}\Gamma^{w}\cdot\delta t_n \tag{5-113}$$

$$\delta\bar{\varepsilon}_{m,1}^{vol} = \frac{\bar{\phi}_{m,n-1}}{\rho_{lm,n-1}S_{lm,n-1}}\cdot\frac{\partial\left(\rho_{lm,n-1}S_{lm,n-1}\right)}{\partial P_{lm}}\delta P_{lm,1} + \left(\frac{1-\phi_{n-1}}{\rho_{s,n-1}}\cdot\frac{\partial\rho_{s,n-1}}{\partial T} + \frac{\bar{\phi}_{m,n-1}}{\rho_{lm,n-1}S_{lm,n-1}}\frac{\partial\left(\rho_{lm,n-1}S_{lm,n-1}\right)}{\partial T}\right)\delta T_n - \frac{\Gamma^{w}}{\rho_{lm,n-1}S_{lm,n-1}}\delta t_n \tag{5-114}$$

When the trial algorithm is performed, $\delta\lambda_{LC,1} = 0$ and the expression in Equation (5-19) is used for evaluating the changes in the microstructural pore-water pressure.

Other useful quantities updated with the Euler scheme are the total porosity and the pore fraction volumes (micro and macro), according to

$$\begin{aligned}
\phi_{n,1} &= \phi_{n-1} + \delta\phi_1 \\
&= \phi_{n-1} - (1-\phi_{n-1})\left(\delta\varepsilon_n^{vol} - \frac{1}{\rho_{s,n-1}}\cdot\frac{\partial\rho_{s,n-1}}{\partial T}\delta T_n\right) \\
\left(\bar{\phi}_{m,n}\right)_1 &= \bar{\phi}_{m,n-1} + \delta\bar{\phi}_{m,1} \\
&= \bar{\phi}_{m,n-1} - \left(\delta\bar{\varepsilon}_{m,1}^{vol} - \frac{1-\phi_{n-1}}{\rho_{s,n-1}}\cdot\frac{\partial\rho_{s,n-1}}{\partial T}\delta T_n - \bar{\phi}_{m,n-1}\cdot\delta\varepsilon_n^{vol}\right) \\
\left(\bar{\phi}_{M,n}\right)_1 &= \phi_{n,1} - \left(\bar{\phi}_{m,n}\right)_1
\end{aligned} \tag{5-115}$$

where

$$\delta\varepsilon_n^{vol} = \boldsymbol{m}^{T}\delta\boldsymbol{\varepsilon}_n \tag{5-116}$$

from which the void ratios of the expansive soil and of both structural levels for the next Euler estimate are calculated.

The updated variables at the end of the simple Euler algorithm are then used to calculate a more accurate modified Euler estimate of stresses and hardening parameter,

$$\begin{aligned}
\boldsymbol{\sigma}_{n,2} &= \boldsymbol{\sigma}_{n-1} + \frac{1}{2}(\delta\boldsymbol{\sigma}_1 + \delta\boldsymbol{\sigma}_2) \\
\left(p_{0,n}^{*}\right)_2 &= p_{0,n-1}^{*} + \frac{1}{2}\left(\delta p_{0,1}^{*} + \delta p_{0,2}^{*}\right)
\end{aligned} \tag{5-117}$$

where $\delta\boldsymbol{\sigma}_1$ and $\delta p_{0,1}^{*}$ are computed from the Euler scheme (Equation (5-111)) and

$$\begin{aligned}\delta\boldsymbol{\sigma}_2 &= \left[\boldsymbol{D}^*\left(\boldsymbol{\sigma}_{n-1}+\delta\boldsymbol{\sigma}_1, p^*_{0,n-1}+\delta p^*_{0,1}\right)\right]\delta\boldsymbol{\varepsilon}^g_n \\ &= \left[\boldsymbol{D}^{\boldsymbol{ep}}_{\boldsymbol{1}}\right]\delta\boldsymbol{\varepsilon}_n + \boldsymbol{h}_{s,1}\cdot\delta s_{M,n} + \boldsymbol{h}_{P_{fM},1}\cdot\delta P_{fM,n} + \boldsymbol{h}_{T,1}\cdot\delta T_n + \boldsymbol{h}_{t,1}\cdot\delta t_n \\ \delta p^*_{0,2} &= \left(p^*_{0,n}\right)_1\cdot\frac{\left(1+\left(\bar{e}_{M,n}\right)_1\right)}{\lambda_{sat}-\bar{\kappa}_M} \\ &\quad\cdot\left(\delta\lambda_{LC,2}\boldsymbol{m}^T\left(\boldsymbol{m}_{LC,n}\right)_1 + f_\beta\cdot\delta\bar{\varepsilon}^{vol}_{m,2} - \frac{f_\beta}{K_T}\left(\frac{1+\left(e_{m,n}\right)_1}{1+e_{n,1}}\right)\delta T_n\right)\end{aligned} \tag{5-118}$$

The *subscript "2"* refers to the quantities evaluated at the end of the interval $\Delta\tau_n$ through the Modified Euler procedure. The changes in the plastic multiplier ($\delta\lambda_{LC,2}$) and in the microstructural pore-water pressure ($\delta P_{lm,2}$), in this case, are expressed as

$$\begin{aligned}\delta\lambda_{LC,2} = \left(\boldsymbol{w}^T_{1,n}\right)_1\delta\boldsymbol{\varepsilon}_n + \left(B_{1,n}\right)_1\cdot\delta s_{M,n} + \left(B_{2,n}\right)_1\cdot\delta P_{fM,n} \\ +\left(B_{3,n}\right)_1\cdot\delta T_n + \left(B_{4,n}\right)_1\Gamma^w\cdot\delta t_n\end{aligned} \tag{5-119}$$

$$\begin{aligned}\delta P_{lm,2} = \left(\boldsymbol{w}^T_{2,n}\right)_1\delta\boldsymbol{\varepsilon}_n + \left(B_{5,n}\right)_1\cdot\delta s_{M,n} + \left(B_{6,n}\right)_1\cdot\delta P_{fM,n} \\ +\left(B_{7,n}\right)_1\cdot\delta T_n + \left(B_{8,n}\right)_1\Gamma^w\cdot\delta t_n\end{aligned} \tag{5-120}$$

while the increments of the volumetric microstructural strain, $\delta\bar{\varepsilon}^{vol}_{m,2}$, are computed as

$$\begin{aligned}\delta\bar{\varepsilon}^{vol}_{m,2} = \frac{\bar{\phi}_{m,1}}{\rho_{lm,1}S_{lm,1}}\cdot\frac{\partial\left(\rho_{lm,1}S_{lm,1}\right)}{\partial P_{lm}}\delta P_{lm,2} \\ +\left(\frac{1-\phi_1}{\rho_{s,1}}\cdot\frac{\partial\rho_{s,1}}{\partial T}+\frac{\bar{\phi}_{m,1}}{\rho_{lm,1}S_{lm,1}}\frac{\partial\left(\rho_{lm,1}S_{lm,1}\right)}{\partial T}\right)\delta T_n \\ -\frac{\Gamma^w}{\rho_{lm,1}S_{lm,1}}\delta t_n\end{aligned} \tag{5-121}$$

The micro pore-water pressure and the pore fraction volumes are then evaluated, at the end of the second-order Euler integration, according to the following expressions

$$\begin{aligned}\left(P_{lm,n}\right)_2 &= P_{lm,n-1}+\frac{1}{2}\left(\delta P_{lm,1}+\delta P_{lm,2}\right) \\ \phi_{n,2} &= \phi_{n-1}+\frac{1}{2}\left(\delta\phi_1+\delta\phi_2\right) \\ \left(\bar{\phi}_{m,n}\right)_2 &= \bar{\phi}_{m,n-1}+\frac{1}{2}\left(\delta\bar{\phi}_{m,1}+\delta\bar{\phi}_{m,2}\right) \\ \left(\bar{\phi}_{M,n}\right)_2 &= \phi_{n,2}-\left(\bar{\phi}_{m,n}\right)_2\end{aligned} \tag{5-122}$$

where the changes in the total porosity ($\delta\phi_2$) and in the micro-pore volume fraction ($\delta\bar{\phi}_{m,2}$) are given by

$$\delta\phi_2 = -(1-\phi_{n,1})\left(\delta\varepsilon_n^{vol} - \frac{1}{(\rho_{s,n})_1}\cdot\frac{\partial(\rho_{s,n})_1}{\partial T}\delta T_n\right)$$
$$\delta\bar{\phi}_{m,2} = -\left(\delta\bar{\varepsilon}_{m,2}^{vol} - \frac{1-\phi_{n,1}}{(\rho_{s,n})_1}\cdot\frac{\partial(\rho_{s,n})_1}{\partial T}\delta T_n - (\bar{\phi}_{m,n})_1\delta\varepsilon_n^{vol}\right) \quad (5\text{-}123)$$

Based on the two sets of solutions available, estimates of the local relative errors are obtained by the difference between the updated variables by the Modified Euler scheme (Equation (5-117) and Equation (5-122)) and those given by the explicit Euler scheme (Equation (5-110) and Equation (5-115)) as follows

$$Re_{\sigma,n} = \frac{\sqrt{(\boldsymbol{\sigma}_{n,2}-\boldsymbol{\sigma}_{n,1})^T(\boldsymbol{\sigma}_{n,2}-\boldsymbol{\sigma}_{n,1})}}{\|\boldsymbol{\sigma}_{n,2}\|}$$
$$Re_{p_{0,n}^*} = \frac{\left|(p_{0,n}^*)_2 - (p_{0,n}^*)_1\right|}{(p_{0,n}^*)_2}$$
$$Re_{P_{lm,n}} = \frac{\left|(P_{lm,n})_2 - (P_{lm,n})_1\right|}{(P_{lm,n})_2} \quad (5\text{-}124)$$
$$Re_{\phi,n} = \frac{|\phi_{n,2}-\phi_{n,1}|}{\phi_{n,2}}$$
$$Re_{\bar{\phi}_{m,n}} = \frac{\left|(\bar{\phi}_{M,n})_2 - (\bar{\phi}_{M,n})_1\right|}{(\bar{\phi}_{M,n})_2}$$

where

$$\boldsymbol{\sigma}_{n,2}-\boldsymbol{\sigma}_{n,1} = \frac{1}{2}(\delta\boldsymbol{\sigma}_2 - \delta\boldsymbol{\sigma}_1)$$
$$(p_{0,n}^*)_2 - (p_{0,n}^*)_1 = \frac{1}{2}(\delta p_{0,2}^* - \delta p_{0,1}^*)$$
$$(P_{lm,n})_2 - (P_{lm,n})_1 = \frac{1}{2}(\delta P_{lm,2} - \delta P_{lm,1}) \quad (5\text{-}125)$$
$$\phi_{n,2}-\phi_{n,1} = \frac{1}{2}(\delta\phi_2 - \delta\phi_1)$$
$$(\bar{\phi}_{M,n})_2 - (\bar{\phi}_{M,n})_1 = \frac{1}{2}(\delta\bar{\phi}_{m,2} - \delta\bar{\phi}_{m,1})$$

The relative error measure, Re_n, for a given sub-step is dependent on the dominant error term and it is calculated as

$$Re_n = max\left(Re_{\sigma,n}; Re_{p_{0,n}^*}; Re_{P_{lm,n}}; Re_{\phi,n}; Re_{\bar{\phi}_{m,n}}\right) \quad (5\text{-}126)$$

whose value serves as a guide for evaluating the size of the next time sub-step, $\Delta\tau_{n+1}$. The current generalized strain increment, $\delta\boldsymbol{\varepsilon}_n^g$, is accepted if $Re_n \leq STOL$, where $STOL$ is a prescribed defined tolerance, typically in the range of 10^{-2} to 10^{-5} (Potts and Zdravković, 1999). Otherwise, the generalized strain increment is rejected and the sub-step size given by $\Delta\tau_n$ must be reduced. Whether the sub-increment is accepted or not, the next sub-step size ($\Delta\tau_{n+1}$) is determined from the following relation

$$\Delta\tau_{n+1} = q \cdot \Delta\tau_n \tag{5-127}$$

A suitable and conservative choice for the reduction factor, q, in order to minimize the number of rejected sub-increments during the course of the integration process (Sloan *et al.*, 2001) is

$$q = min\left\{1.1;\ max\left\{0.1;\ 0.9 \cdot \sqrt{\frac{STOL}{Re_n}}\right\}\right\} \tag{5-128}$$

The constants 1.1 and 0.1 in this expression prevent an abrupt change in the sub-step size and the safety factor of 0.9 reduces the probability that the next sub-step is rejected (Sloan *et al.*, 2001).

If $Re_n > STOL$, as mentioned above, the sub-incremental integration is repeated with $\Delta\tau_n \equiv \Delta\tau_{n+1}$ (instead of the current value of $\Delta\tau_n$), where $\Delta\tau_{n+1}$ is evaluated by expressions in Equation (5-127) and Equation (5-128). If necessary, the sub-step size is reduced further until an acceptable sub-increment size is found. If $Re_n \leq STOL$, the current sub-step size is accepted and the accumulated stresses, the plastic strains, the hardening parameter and the other geotechnical variables are updated using Equation (5-117) and Equation (5-122), for instance. Once the yield condition is checked and satisfied for the accumulated stresses and hardening/softening parameter, i.e. $F_{LC}\left(\boldsymbol{\sigma}_{n,2}, \left(p_{0,n}^*\right)_2\right) \leq +FTOL$, a new pseudo-time increment ($\Delta\tau_{n+1}$) is calculated through the relation given in Equation (5-127) and the next sub-incremental loading ($\delta\boldsymbol{\varepsilon}_{n+1}^g$) can be applied in order to evaluate the stress state at the end of the next pseudo-time $\tau_{n+1} = \tau_n + \Delta\tau_{n+1}$. This integration procedure continues until the entire increment of the generalized strains is applied, which occurs when the condition $\sum \Delta\tau = \tau = 1$ is achieved.

5.3. THE FINITE ELEMENT APPROACH AND THE NUMERICAL SOLUTION VIA NEWTON-RAPHSON METHOD

As mentioned in **Chapter 3**, the governing equations to be solved in a coupled THM boundary value problem are the stress equilibrium equations (see **Section 3.7.5**), the mass balance equations (as given in **Sections 3.7.1** and **Section 3.7.2**) and the internal energy balance equations for the porous medium as a whole (as described in **Section 3.7.4**). The mass and energy balance equations are composed of storage terms (related to the variation of mass or

energy content), advective and non-advective flux terms, volumetric strain terms (also a storage term associated with the volumetric strain rate) and sink/source terms. As discussed in Olivella *et al.* (1996), each of these terms requires specific treatment when the finite element technique is applied to those partial differential equations. Furthermore, for the present double-porosity formulation, the pore-water pressure at microstructural medium is updated inside the stress-point algorithm, according to Equation (5-19) or Equation (5-62), and not by solving the mass balance of water in micro-pores as given by Equation (3-76). As a consequence, the unknowns of the system of global equations are: the displacement field (with as many components as dimensions of the problem), the macro liquid and gas pressure and temperature.

The numerical modelling procedure consists in replacing the geometry under investigation by an equivalent finite element mesh (spatial discretization) in such a way that the governing balance equations must be solved at all the nodes of that mesh. The discretization in time uses finite differences and an implicit scheme is employed for time integration. Due to that, two intermediate points are defined between the initial t^k and final t^{k+1} times: one related to the point where the non-linear functions are computed ($t^{k+\varepsilon}$) and the other one representing the point where the global equations will be satisfied ($t^{k+\theta}$). After the spatial and time discretizations are performed, the compacted form of the residual vector, $\boldsymbol{r}(\boldsymbol{X}^{k+1})$, representing the system of balance equations that must be solved numerically, is written as

$$\boldsymbol{r}(\boldsymbol{X}^{k+1}) = \frac{\boldsymbol{d}^{k+1} - \boldsymbol{d}^{k}}{\Delta t^{k}} + \boldsymbol{A}(\boldsymbol{X}^{k+\varepsilon})\boldsymbol{X}^{k+\theta} + \boldsymbol{b}(\boldsymbol{X}^{k+\theta}) = \boldsymbol{0} \tag{5-129}$$

where k is the time step index, $\boldsymbol{X}$ is the vector of nodal unknowns, $\boldsymbol{d}$ represents the mass or energy contents (storage terms), $\boldsymbol{A}$ is the conductance matrix (related to the flux terms), and $\boldsymbol{b}$ are the sink/source and the boundary condition terms. The numerical code CODE_BRIGHT uses the standard Galerkin method (also known as the weighted residual method) to discretize the governing partial differential equations, including some numerical modifications (Olivella *et al.*, 1996) that guarantee successful computations when dealing with the different terms in Equation (5-129). The general aspects related to the Galerkin finite element method applied to geotechnical problems can be found in Abbo (1997), Potts and Zdravković (1999), Zienkiewicz and Taylor (2000a, 2000b).

When the weighted residual method is applied to the balance equations, the general expression for the residuals at node i, $\boldsymbol{r}_i(\boldsymbol{X}^{k+1})$, is given as follows

$$\boldsymbol{r}_i(\boldsymbol{X}^{k+1}) = \int_V \xi_i \left(\frac{\boldsymbol{d}^{k+1} - \boldsymbol{d}^{k}}{\Delta t^{k}} \right) dV + \int_V \xi_i \boldsymbol{A}(\boldsymbol{X}^{k+\varepsilon})\boldsymbol{X}^{k+\theta} dV + \int_V \xi_i \boldsymbol{b}(\boldsymbol{X}^{k+\theta}) dV = \boldsymbol{0} \tag{5-130}$$

where ξ_i is the shape function for node i. Consequently, the integral operators in Equation (5-130) assume non-null values only for those elements that contain node i. For instance, the storage term in Equation (5-130) is computed as

$$\int_V \xi_i \left(\frac{\boldsymbol{d}^{k+1} - \boldsymbol{d}^k}{\Delta t^k} \right) dV = \int_{e_1} \xi_i \left(\frac{\boldsymbol{d}^{k+1} - \boldsymbol{d}^k}{\Delta t^k} \right) dV_e + \cdots + \int_{e_j} \xi_i \left(\frac{\boldsymbol{d}^{k+1} - \boldsymbol{d}^k}{\Delta t^k} \right) dV_e \tag{5-131}$$

where e_1,…, e_j denote the elements connected by node i, which defines a cell centered in that node (as shown in Figure 5-10). The number of elements that share a common node varies from node to node and it is not related to the number of nodes per element (Olivella *et al.*, 1996).

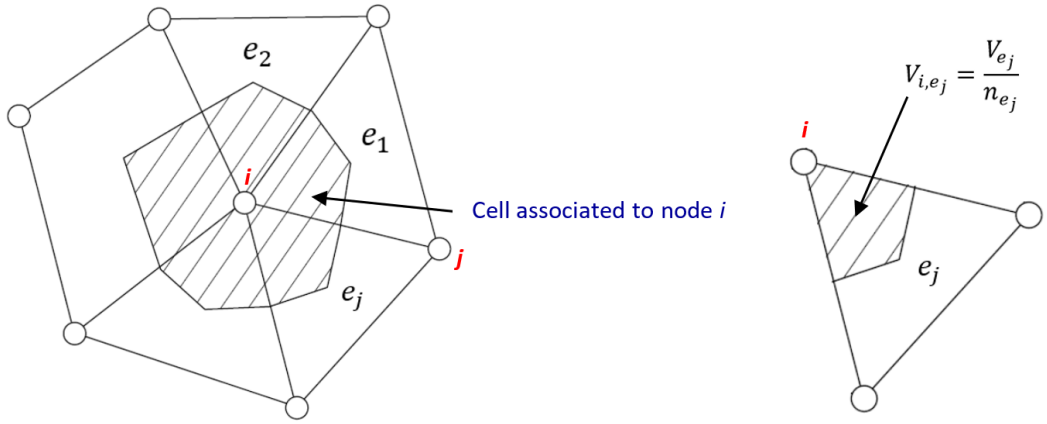

Figure 5-10: Representation of a cell centered in node i in a finite element mesh (left) and the concept of volume of influence (V_{i,e_j}) of the element e_j around node i (right) (after Olivella, 1995); n_{e_j} represents the number of nodes of the element e_j and V_{e_j} its volume.

The mass or energy contents and the volumetric strain terms (included into the storage terms), the advective and non-advective fluxes (considered in the conductance matrix) and the sink/source terms in Equation (5-130) require a specific numerical treatment. In Olivella (1995) and Olivella *et al.* (1996) a detailed explanation is given about the assumptions and the mathematical/numerical simplifications adopted in order to compute the contribution of each one of these terms into the matrices and vectors that constitute the system of global equations to be solved numerically. In **Section 5.3.2**, only the numerical treatment of the additional terms in the mass and energy balance equations arising from the double-porosity formulation is described. These additional terms are essentially storage terms. Their mathematical expressions are presented in the next section.

The numerical scheme used in CODE_BRIGHT to solve the system of algebraic equations given in Equation (5-129) is the Newton-Raphson method, expressed by the general equation

$$\boldsymbol{r}\left(\boldsymbol{X}^{k+1,l+1}\right) = \boldsymbol{r}\left(\boldsymbol{X}^{k+1,l}\right) + \frac{\partial \boldsymbol{r}\left(\boldsymbol{X}^{k+1}\right)}{\partial \boldsymbol{X}^{k+1}} \left(\boldsymbol{X}^{k+1,l+1} - \boldsymbol{X}^{k+1,l}\right) = \boldsymbol{0} \tag{5-132}$$

and whose estimate for the numerical solution at the end of the next iteration ($\boldsymbol{X}^{k+1,l+1}$) is given by

$$\boldsymbol{X}^{k+1,l+1} = \boldsymbol{X}^{k+1,l} - \left(\boldsymbol{J}^{k+1,l}\right)^{-1}\boldsymbol{r}\left(\boldsymbol{X}^{k+1,l}\right) \tag{5-133}$$

where l denotes the iteration index and $\boldsymbol{J} = \frac{\partial \boldsymbol{r}(\boldsymbol{X})}{\partial \boldsymbol{X}}$ is the Jacobian matrix, containing the derivatives of the residual vector with respect to the unknowns of the problem. When the full Newton-Raphson method is employed, the matrix $\boldsymbol{J}$ is recalculated and inverted for each iteration. An alternative version of this method is the so-called modified Newton-Raphson, for which the Jacobian matrix is only updated and inverted at the beginning of each increment, keeping unchanged for all iterations within the increment. An extensive description of the potentialities and limitations of the family of algorithms arising from the Newton-Raphson method and their applications to single and multi-field static or time dependent problems can be found in Dennis and More (1977), Geradin *et al.* (1980), Crisfield (1991), Halama and Poruba (2009) among others.

5.3.1. THE ADDITIONAL TERMS IN BALANCE EQUATIONS DUE TO THE DOUBLE-POROSITY APPROACH

As the micro pore-water pressure (in the present formulation) is not taken as one of the nodal unknowns to be evaluated by solving the system of global algebraic equations then, the mass balance of water at microstructural level is not solved together with other mass balance equations. Due to that, the mass balance of pore-water in macrostructure (one of the equations solved numerically) must account for the changes in the amount of water in micro-pores through any relationship between micro and macrostructural properties/variables. This can be achieved by re-writing the mass balance of water at macrostructural level (Equation (3-72)) as follows

$$\begin{aligned}\bar{\phi}_M \frac{D_s\left(\theta_{lM}^w S_{lM} + \theta_{gM}^w S_{gM}\right)}{Dt} + \left(\theta_{lM}^w S_{lM} + \theta_{gM}^w S_{gM}\right)\left(\dot{\varepsilon}^{vol} - \dot{\varepsilon}_m^{vol}\right) \\ + \boldsymbol{\nabla}\cdot\left(\boldsymbol{j}'^w_{lM} + \boldsymbol{j}'^w_{gM}\right) + \Gamma^w - f_M^w = 0\end{aligned} \tag{5-134}$$

in which the relationship in Equation (3-45) has been used to express the macrostructural volumetric strain variation, $\dot{\varepsilon}_M^{vol}$, in terms of the total and the micro volumetric strain components. In Equation (5-134), the sign convention used in Continuum Solid Mechanics is employed (that is, extensions are taken as positive quantities).

If the water mobility through in micro-pores is neglected, Equation (3-76) for the mass balance of water at the microstructural medium can be solved for $\dot{\varepsilon}_m^{vol}$, resulting in

$$\begin{aligned}\dot{\varepsilon}_m^{vol} = \frac{1}{\theta_{lm}^w S_{lm} + \theta_{gm}^w S_{gm}}\left(\Gamma^w - \bar{\phi}_m \frac{D_s\left(\theta_{lm}^w S_{lm} + \theta_{gm}^w S_{gm}\right)}{Dt} - f_m^w\right) \\ -(1-\phi)\frac{\dot{\rho}_s}{\rho_s}\end{aligned} \tag{5-135}$$

Combining the two latter equations, then

$$\begin{aligned}\bar{\phi}_M \frac{D_s\left(\theta_{lM}^w S_{lM} + \theta_{gM}^w S_{gM}\right)}{Dt} + \left(\theta_{lM}^w S_{lM} + \theta_{gM}^w S_{gM}\right)\dot{\varepsilon}^{vol} \\ + \left(1 - \frac{\theta_{lM}^w S_{lM} + \theta_{gM}^w S_{gM}}{\theta_{lm}^w S_{lm} + \theta_{gm}^w S_{gm}}\right)\Gamma^w \\ + \bar{\phi}_m \left(\frac{\theta_{lM}^w S_{lM} + \theta_{gM}^w S_{gM}}{\theta_{lm}^w S_{lm} + \theta_{gm}^w S_{gm}}\right)\frac{D_s\left(\theta_{lm}^w S_{lm} + \theta_{gm}^w S_{gm}\right)}{Dt} \\ + (1-\phi)\left(\theta_{lM}^w S_{lM} + \theta_{gM}^w S_{gM}\right)\frac{\dot{\rho}_s}{\rho_s} + \boldsymbol{\nabla}\cdot\left(\boldsymbol{j}'^w_{lM} + \boldsymbol{j}'^w_{gM}\right) \\ - f^w = 0\end{aligned} \tag{5-136}$$

where

$$f^w = f_m^w + f_M^w \tag{5-137}$$

Comparing Equation (5-136) with the equivalent mass balance equation for single-porosity approaches,

$$\begin{aligned}\phi \frac{D_s\left(\theta_l^w S_l + \theta_g^w S_g\right)}{Dt} + \left(\theta_l^w S_l + \theta_g^w S_g\right)\dot{\varepsilon}^{vol} + (1-\phi)\left(\theta_l^w S_l + \theta_g^w S_g\right)\frac{\dot{\rho}_s}{\rho_s} \\ +\boldsymbol{\nabla}\cdot\left(\boldsymbol{j}'^w_l + \boldsymbol{j}'^w_g\right) - f^w = 0\end{aligned} \tag{5-138}$$

it is quite simple to note that:

i. macrostructural properties in Equation (5-136) – i.e., macro pore volume fraction, degree of saturation of water and air species, mass fraction of fluid species, etc. – assume the same role played by the overall properties in those water mass balance equations for single-porosity models;

ii. some additional terms appear in Equation (5-136), more specifically, the third and the fourth ones on the left-hand side of this equation. The first of these terms is associated with the water exchanged between both structural levels while the other one is a storage term related to the variation of water in micro-pores.

If it is assumed that

$$\theta_{lm}^w S_{lm} + \theta_{gm}^w S_{gm} \approx \rho_{lm} S_{lm} \tag{5-139}$$

$$\theta_{lM}^w S_{lM} + \theta_{gM}^w S_{gM} \approx \rho_{lM} S_{lM} \tag{5-140}$$

the balance of water at macrostructural medium given in Equation (5-136) is expressed by

$$\begin{aligned}\bar{\phi}_M \frac{D_s(\rho_{lM} S_{lM})}{Dt} + (\rho_{lM} S_{lM})\left(\dot{\varepsilon}^{vol} + (1-\phi)\frac{\dot{\rho}_s}{\rho_s}\right) + \left(1 - \frac{\rho_{lM} S_{lM}}{\rho_{lm} S_{lm}}\right)\Gamma^w \\ + \bar{\phi}_m \left(\frac{\rho_{lM} S_{lM}}{\rho_{lm} S_{lm}}\right)\frac{D_s(\rho_{lm} S_{lm})}{Dt} + \boldsymbol{\nabla}\cdot\left(\boldsymbol{j}'^w_{lM} + \boldsymbol{j}'^w_{gM}\right) - f^w = 0\end{aligned} \tag{5-141}$$

Additional terms also appear in the internal energy balance equation for the soil when a double-structure approach is considered. This assertion becomes evident when Equation (3-88) is recalled, i.e.,

$$\begin{aligned}(1-\phi)\frac{D_s(E_s\rho_s)}{Dt}+\bar{\phi}_m\frac{D_s\left(E_l\rho_{lm}S_{lm}+E_g\rho_{gm}S_{gm}\right)}{Dt}\\+\bar{\phi}_M\frac{D_s\left(E_l\rho_{lM}S_{lM}+E_g\rho_{gM}S_{gM}\right)}{Dt}\\+\left(E_l\rho_{lm}S_{lm}+E_g\rho_{gm}S_{gm}-E_s\rho_s\right)(1-\phi)\frac{\dot{\rho}_s}{\rho_s}\\+\left(E_l\rho_{lm}S_{lm}+E_g\rho_{gm}S_{gm}\right)\dot{\bar{\varepsilon}}_m^{vol}\\+\left(E_l\rho_{lM}S_{lM}+E_g\rho_{gM}S_{gM}\right)\left(\dot{\varepsilon}^{vol}-\dot{\bar{\varepsilon}}_m^{vol}\right)\\+\boldsymbol{\nabla}\cdot\left(\boldsymbol{i}_c+E_l\rho_{lM}\boldsymbol{q}_{lM}+E_g\rho_{gM}\boldsymbol{q}_{gM}\right)=f^Q\end{aligned}\tag{5-142}$$

Again, the additive decomposition of the volumetric total strain in Equation (3-45) has been evoked and used in the previous expression. Inserting Equation (5-135) into Equation (5-142) and assuming that $f_m^w \approx 0$ (see **Section 3.7.2.2**), after few algebraic operations, the balance equation of internal energy for non-isothermal analysis in double-porosity models is expressed as

$$\begin{aligned}(1-\phi)\left(\frac{D_s(E_s\rho_s)}{Dt}-E_s\dot{\rho}_s\right)+\bar{\phi}_M\frac{D_s\left(E_l\rho_{lM}S_{lM}+E_g\rho_{gM}S_{gM}\right)}{Dt}\\+\left(E_l\rho_{lM}S_{lM}+E_g\rho_{gM}S_{gM}\right)\left(\dot{\varepsilon}^{vol}+(1-\phi)\frac{\dot{\rho}_s}{\rho_s}\right)\\+\bar{\phi}_m\frac{D_s\left(E_l\rho_{lm}S_{lm}+E_g\rho_{gm}S_{gm}\right)}{Dt}\\-\frac{\bar{\phi}_m}{\rho_{lm}S_{lm}}\left(E_l(\rho_{lm}S_{lm}-\rho_{lM}S_{lM})+E_g\left(\rho_{gm}S_{gm}-\rho_{gM}S_{gM}\right)\right)\frac{D_s(\rho_{lm}S_{lm})}{Dt}\\+\frac{1}{\rho_{lm}S_{lm}}\left(E_l(\rho_{lm}S_{lm}-\rho_{lM}S_{lM})+E_g\left(\rho_{gm}S_{gm}-\rho_{gM}S_{gM}\right)\right)\Gamma^w\\+\boldsymbol{\nabla}\cdot\left(\boldsymbol{i}_c+E_l\rho_{lM}\boldsymbol{q}_{lM}+E_g\rho_{gM}\boldsymbol{q}_{gM}\right)-f^Q=0\end{aligned}\tag{5-143}$$

On the other hand, the equivalent expression for single-porosity models is given by

$$\begin{aligned}(1-\phi)\left(\frac{D_s(E_s\rho_s)}{Dt}-E_s\dot{\rho}_s\right)+\phi\frac{D_s\left(E_l\rho_lS_l+E_g\rho_gS_g\right)}{Dt}\\+\left(E_l\rho_lS_l+E_g\rho_gS_g\right)\left(\dot{\varepsilon}^{vol}+(1-\phi)\frac{\dot{\rho}_s}{\rho_s}\right)\\+\boldsymbol{\nabla}\cdot\left(\boldsymbol{i}_c+E_l\rho_l\boldsymbol{q}_l+E_g\rho_g\boldsymbol{q}_g\right)-f^Q=0\end{aligned}\tag{5-144}$$

The comparison between the energy balance in Equation (5-143) and Equation (5-144) shows that the additional terms are basically related to the energy stored in fluid species, which ones are divided into micro and macro terms due to the total porosity partition into the pore fraction

volumes ($\bar{\phi}_m$ and $\bar{\phi}_M$). A term associated with the water mass transfer mechanism between both structural media is also present in Equation (5-143) – the sixth term on the left-hand side of that equation. Moreover, the quantity of energy transported through the double structural medium only takes into account the portion related to the fluid motion in macro-pores (the terms in Equation (5-143) expressed by Darcy's flux vectors, $\boldsymbol{q}_{lM}$ and $\boldsymbol{q}_{gM}$). This is a direct consequence of the assumption of negligible microstructural mass fluxes in comparison to the mass fluxes through the macro-voids (see **Section 3.7.4** for more details).

5.3.2. NUMERICAL TREATMENT OF THE ADDITIONAL STORAGE TERMS

In CODE_BRIGHT, the storage terms in the balance equations are computed in a mass conservative approach (Olivella *et al.*, 1996). It means that the discretization in time is applied directly to each accumulation term and approximated by a finite difference in time. Under the assumption of small strain rate (which allows to use the eulerian derivative as an approximation to the material derivative with respect to the solid), the mass conservative approach, when applied to a typical storage property, $(*)$, leads to

$$\phi \frac{D_s(*)}{Dt} \approx \phi \frac{\partial(*)}{\partial t} = \phi \frac{(*)^{k+1} - (*)^k}{t^{k+1} - t^k} \tag{5-145}$$

On the other hand, the spatial discretization via finite element approach guarantees the mass conservation (Milly, 1984).

Concerning the computation of the total porosity (the unknown of the solid mass balance equation), it is assumed that its variation over the time increment occurs at very slow rates (Olivella, 1995; Olivella *et al.*, 1996). Consequently, this element-wise variable is integrated explicitly (that is, the values at t^k are used) at the centroid of elements in all the single-porosity formulations implemented in CODE_BRIGHT. An element-wise variable is defined as space-constant over every element (Voss and Provost, 2010), but can change from element to element. Nevertheless, for the double-porosity formulation, the total porosity and the micro pore fraction volume are updated at the Gauss integration points, since they are defined as history variables of that model. An average value for total porosity and pore fraction volumes (micro and macro), obtained from the values at all integration points within an element, is defined then as the porosity "variable" for each element (according to the structure of CODE_BRIGHT). However, these average porosity variables are still evaluated at time t^k when the system of governing equations is solved.

Another important feature to take into account is the existence of different classes of numerical entities in the balance equations, like the element-wise, node-wise, cell-wise variables in addition to those ones computed at integration points. Node-wise quantities are evaluated by their nodal values and can be interpolated on the elements through the shape functions (Olivella *et al.*, 1996) while a cell-wise variable is space-constant over the cell centered in the node under consideration (Voss and Provost, 2010), as illustrated in Figure 5-10. For this reason, the

following notation becomes helpful when dealing with the different terms arising from the governing equations:

- $(*)_{ej}$: the quantity is computed at the center (that is, through the average of nodal values) of element e_j.
- $(\hat{*})_{ej}$: the quantity is computed using the average of Gauss point values in element e_j.
- $(*)_i$: the quantity is computed in node i as a function of the unknowns at the same node.
- $(*)_{i,ej}$: the quantity is computed in node i with the material properties of element e_j.

5.3.2.1. THE ADDITIONAL STORAGE TERM IN THE MASS BALANCE OF WATER

The weighted residual method is applied to each term of the balance equation in Equation (5-141). For node i, the additional storage term (the fourth one on the left-hand side) becomes

$$\int_V \xi_i \bar{\phi}_m \left(\frac{\rho_{lM} S_{lM}}{\rho_{lm} S_{lm}}\right) \frac{\partial(\rho_{lm} S_{lm})}{\partial t} dV = \int_{e_1} \xi_i \bar{\phi}_m \left(\frac{\rho_{lM} S_{lM}}{\rho_{lm} S_{lm}}\right) \frac{\partial(\rho_{lm} S_{lm})}{\partial t} dV_e + \cdots + \int_{e_j} \xi_i \bar{\phi}_m \left(\frac{\rho_{lM} S_{lM}}{\rho_{lm} S_{lm}}\right) \frac{\partial(\rho_{lm} S_{lm})}{\partial t} dV_e \quad (5\text{-}146)$$

in which, the numerical approximation defined in Equation (5-145) has been used. The summation of the j-terms in Equation (5-146) to estimate the integral of the residual in node i is due to the nature of the macrostructural degree of saturation (S_{lM}), since this parameter depends not only on the nodal unknowns but also on the material properties (Olivella *et al.*, 1996). The macro liquid density (ρ_{lM}) is computed in the node, since it is only dependent on temperature and liquid/gas pressures (nodal variables). Nevertheless, all micro properties in Equation (5-146) – pore fraction volume ($\bar{\phi}_m$), density (ρ_{lm}) and degree of saturation (S_{lm}) – are considered element-wise variables, since they are evaluated from the average of the micro variables (porosity and liquid pressure) computed at each integration point of the element. Therefore, any integral term in Equation (5-146) can be calculated by the following approximation

$$\int_{e_j} \xi_i \bar{\phi}_m \left(\frac{\rho_{lM} S_{lM}}{\rho_{lm} S_{lm}}\right) \frac{\partial(\rho_{lm} S_{lm})}{\partial t} dV_e$$

$$\approx \left(\hat{\bar{\phi}}_m\right)_{e_j}^{k} \frac{(\rho_{lM} S_{lM})_{i,e_j}^{k+1}}{\left(\hat{\rho}_{lm} \hat{S}_{lm}\right)_{e_j}^{k+1}} \left(\frac{\left(\hat{\rho}_{lm} \hat{S}_{lm}\right)_{e_j}^{k+1} - \left(\hat{\rho}_{lm} \hat{S}_{lm}\right)_{e_j}^{k}}{t^{k+1} - t^{k}}\right) \int_{e_j} \xi_i dV_e \qquad (5\text{-}147)$$

$$= \frac{1}{\Delta t^k} \left(1 - \frac{\left(\hat{\rho}_{lm} \hat{S}_{lm}\right)_{e_j}^{k}}{\left(\hat{\rho}_{lm} \hat{S}_{lm}\right)_{e_j}^{k+1}}\right) \left(\hat{\bar{\phi}}_m\right)_{e_j}^{k} (\rho_{lM} S_{lM})_{i,e_j}^{k+1} \int_{e_j} \xi_i dV_e$$

where $\Delta t^k = t^{k+1} - t^k$. The integral of the shape function (ξ_i) over an element only needs to be computed once for each finite element in the mesh. For the case of linear shape functions, it corresponds to

$$\int_{e_j} \xi_i dV = \frac{V_{ej}}{n_{ej}} \qquad (5\text{-}148)$$

where n_{e_j} is the number of nodes in element e_j and V_{e_j} represents its volume. These integrals can be determined analytically or numerically and are known as the influence (or geometrical) coefficients.

The numerical treatment of the other storage terms in Equation (5-141) is similar to that described in Olivella *et al.* (1996) for this type of terms, except for the nature of some of the physical and material properties in them (overall/macro) and the place where the element-wise parameters are computed or averaged (nodes or integration points).

5.3.2.2. THE ADDITIONAL STORAGE TERMS IN THE INTERNAL ENERGY BALANCE

Applying the weighted residual method to the internal energy balance equation in (5-143), one of the additional terms obtained for a double-structure framework can be expressed, at node i, as follows

$$\int_V \xi_i \bar{\phi}_m \frac{\partial\left(E_l \rho_{lm} S_{lm} + E_g \rho_{gm} S_{gm}\right)}{\partial t} dV_e$$

$$= \int_{e_1} \xi_i \bar{\phi}_m \frac{\partial\left(E_l \rho_{lm} S_{lm} + E_g \rho_{gm} S_{gm}\right)}{\partial t} dV_e + \cdots \qquad (5\text{-}149)$$

$$+ \int_{e_j} \xi_i \bar{\phi}_m \frac{\partial\left(E_l \rho_{lm} S_{lm} + E_g \rho_{gm} S_{gm}\right)}{\partial t} dV_e$$

Using similar arguments to the ones presented in the previous section, the numerical treatment of any integral in the latter equation leads to

$$\int_{e_j} \xi_i \bar{\phi}_m \frac{\partial\left(E_l \rho_{lm} S_{lm} + E_g \rho_{gm} S_{gm}\right)}{\partial t} dV_e$$
$$\approx \left(\hat{\bar{\phi}}_m\right)_{e_j}^{k} \left(\frac{\left(E_l \hat{\rho}_{lm} \hat{S}_{lm} + E_g \hat{\rho}_{gm} \hat{S}_{gm}\right)_{e_j}^{k+1} - \left(E_l \hat{\rho}_{lm} \hat{S}_{lm} + E_g \hat{\rho}_{gm} \hat{S}_{gm}\right)_{e_j}^{k}}{t^{k+1} - t^{k}} \right) \int_{e_j} \xi_i dV \quad (5\text{-}150)$$

Another additional accumulation term (corresponding to the fifth one on the left-hand side in Equation (5-143)) that arises from the residual of the internal energy associated with node i is given by

$$\int_V \xi_i \bar{\phi}_m \alpha \frac{\partial(\rho_{lm} S_{lm})}{\partial t} dV_e = \int_{e_1} \xi_i \bar{\phi}_m \alpha \frac{\partial(\rho_{lm} S_{lm})}{\partial t} dV_e + \cdots + \int_{e_j} \xi_i \bar{\phi}_m \alpha \frac{\partial(\rho_{lm} S_{lm})}{\partial t} dV_e \quad (5\text{-}151)$$

where the scalar coefficient α is defined as

$$\alpha = -\frac{1}{\rho_{lm} S_{lm}} \left(E_l (\rho_{lm} S_{lm} - \rho_{lM} S_{lM}) + E_g \left(\rho_{gm} S_{gm} - \rho_{gM} S_{gM}\right) \right) \quad (5\text{-}152)$$

Thus, any integral term in Equation (5-151), for node i, is approximated as

$$\int_{e_j} \xi_i \bar{\phi}_m \alpha \frac{\partial(\rho_{lm} S_{lm})}{\partial t} dV_e$$
$$\approx \left(\hat{\bar{\phi}}_m\right)_{e_j}^{k} (\hat{\alpha})_{e_j}^{k+1} \left(\frac{\left(\hat{\rho}_{lm} \hat{S}_{lm}\right)_{e_j}^{k+1} - \left(\hat{\rho}_{lm} \hat{S}_{lm}\right)_{e_j}^{k}}{t^{k+1} - t^{k}} \right) \int_{e_j} \xi_i dV_e$$
$$= \frac{1}{\Delta t^k} \left(\hat{\bar{\phi}}_m\right)_{e_j}^{k} \left(\left(E_l \hat{\rho}_{lm} \hat{S}_{lm}\right)_{e_j}^{k+1} - \left(E_l \rho_{lM} S_{lM}\right)_{i,e_j}^{k+1} \right) \left(1 - \frac{\left(\hat{\rho}_{lm} \hat{S}_{lm}\right)_{e_j}^{k}}{\left(\hat{\rho}_{lm} \hat{S}_{lm}\right)_{e_j}^{k+1}} \right) \int_{e_j} \xi_i dV_e \quad (5\text{-}153)$$
$$= \frac{1}{\Delta t^k} \left(\hat{\bar{\phi}}_m\right)_{e_j}^{k} \left(\left(E_g \hat{\rho}_{gm} \hat{S}_{gm}\right)_{e_j}^{k+1} - \left(E_g \rho_{gM} S_{gM}\right)_{i,e_j}^{k+1} \right) \left(1 - \frac{\left(\hat{\rho}_{lm} \hat{S}_{lm}\right)_{e_j}^{k}}{\left(\hat{\rho}_{lm} \hat{S}_{lm}\right)_{e_j}^{k+1}} \right) \int_{e_j} \xi_i dV_e$$

5.3.2.3. THE MICRO-MACRO WATER TRANSFER TERM IN THE MASS BALANCE OF WATER

The weighted residual method applied to the water exchange term that appears in the water balance equation generates the following integrals associated with node i

$$\int_V \xi_i \left(1-\frac{\rho_{lM}S_{lM}}{\rho_{lm}S_{lm}}\right)\Gamma^w dV_e = \int_{e_1} \xi_i \left(1-\frac{\rho_{lM}S_{lM}}{\rho_{lm}S_{lm}}\right)\Gamma^w dV_e + \cdots + \int_{e_j} \xi_i \left(1-\frac{\rho_{lM}S_{lM}}{\rho_{lm}S_{lm}}\right)\Gamma^w dV_e \tag{5-154}$$

If equilibrium between the gas pressures at both structural media is assumed, the mass transfer process is given by the expression in Equation (3-56) and then, any integral in Equation (5-154) is approximated by

$$\begin{aligned}\int_{e_j} \xi_i \left(1-\frac{\rho_{lM}S_{lM}}{\rho_{lm}S_{lm}}\right)\Gamma^w dV_e &\approx \left(1-\frac{(\rho_{lM}S_{lM})_{i,e_j}^{k+\varepsilon}}{\left(\hat{\rho}_{lm}\hat{S}_{lm}\right)_{e_j}^{k+\varepsilon}}\right)\left(\hat{\Gamma}^w\right)_{i,e_j}^{k+\theta}\int_{e_j}\xi_i dV_e \\ &= \gamma^w\left(1-\frac{(\rho_{lM}S_{lM})_{i,e_j}^{k+\varepsilon}}{\left(\hat{\rho}_{lm}\hat{S}_{lm}\right)_{e_j}^{k+\varepsilon}}\right)\left((P_{lM})_i^{k+\theta}-\left(\hat{P}_{lm}\right)_{e_j}^{k+\theta}\right)\int_{e_j}\xi_i dV_e\end{aligned} \tag{5-155}$$

Note that the macrostructural pore-water pressure is computed at node i (because it is a nodal unknown) while the microstructural liquid pressure (an element-wise variable) is approximated by the average of the values calculated at the integration points of every element that shares that node.

5.3.2.4. THE EXCHANGE MICRO-MACRO TERM IN THE INTERNAL ENERGY BALANCE

The term related to the mass transfer process in the energy balance equation, when the weighted residual method is applied to that equation, gives, for node i, the following expression

$$\int_V \xi_i \alpha \Gamma^w dV_e = \int_{e_1} \xi_i \alpha \Gamma^w dV_e + \cdots + \int_{e_j} \xi_i \alpha \Gamma^w dV_e \tag{5-156}$$

where the coefficient α is given in Equation (5-152). Therefore, the contribution of element e_j to the internal energy transferred between both media, due to the water mass exchange between them, is approximated as

$$\int_{e_j} \xi_i \alpha \Gamma^w dV_e \approx \gamma^w (\hat{\alpha})_{i,e_j}^{k+\varepsilon} \left((P_{lM})_i^{k+\theta} - \left(\hat{P}_{lm}\right)_{e_j}^{k+\theta} \right) \int_{e_j} \xi_i dV_e$$

$$= \gamma^w \left(E_l + E_g \frac{\hat{\rho}_{gm} \hat{S}_{gm}}{\hat{\rho}_{lm} \hat{S}_{lm}} \right)_{e_j}^{k+\varepsilon} \left((P_{lM})_i^{k+\theta} - \left(\hat{P}_{lm}\right)_{e_j}^{k+\theta} \right) \int_{e_j} \xi_i dV_e \tag{5-157}$$

$$-\gamma^w \frac{\left(E_l \rho_{lM} S_{lM} + E_g \rho_{gM} S_{gM}\right)_{i,e_j}^{k+\varepsilon}}{\left(\hat{\rho}_{lm} \hat{S}_{lm}\right)_{e_j}^{k+\varepsilon}} \cdot \left((P_{lM})_i^{k+\theta} - \left(\hat{P}_{lm}\right)_{e_j}^{k+\theta} \right) \int_{e_j} \xi_i dV_e$$

5.3.3. TREATMENT OF THE MECHANICAL EQUILIBRIUM EQUATION

The residual of the mechanical problem is obtained by the application of the method of weighted residuals followed by the Green-Gauss theorem (that serves to reduce the order of the derivatives) to the stress equilibrium equation (Equation (3-89)). That residual vector, $\boldsymbol{r}\left(\boldsymbol{\sigma}_{\boldsymbol{t}}^{k+1}\right)$, is evaluated in terms of the total stress vector as

$$\boldsymbol{r}\left(\boldsymbol{\sigma}_{\boldsymbol{t}}^{k+1}\right) = \int_{V_e} \boldsymbol{B}^T \boldsymbol{\sigma}_{\boldsymbol{t}}^{k+1} dV_e - \boldsymbol{b}^{k+1} = \boldsymbol{0} \tag{5-158}$$

where the matrix $\boldsymbol{B}$, composed by the gradients of nodal shape functions, relates the nodal displacement field ($\boldsymbol{u}$) to the internal strain vector ($\boldsymbol{\varepsilon}$) according to

$$\boldsymbol{\varepsilon} = \boldsymbol{B}\boldsymbol{u} \tag{5-159}$$

The body forces and the boundary tractions are accounted for in the vector of external forces, $\boldsymbol{b}^{k+1}$. The integral term in Equation (5-158) defines a vector of internal forces that represents the nodal forces supported by the internal stresses in the element (Abbo, 1997). The general expression for the total stress vector at each point of the porous medium, $\boldsymbol{\sigma}_t$, can be obtained from the expressions for the stress tensors defined in Table 3-1. In terms of macrostructural fluid pressures, it is expressed by

$$\boldsymbol{\sigma}_t = \boldsymbol{\sigma} + P_{gM}\boldsymbol{m} - \chi_M\left(P_{gM} - P_{lM}\right)\boldsymbol{m} \quad \text{(compression positive)} \tag{5-160}$$

For the particular cases in which $\chi_M = 1$ (when macro-pores are fully saturated by water) or $\chi_M = 0$ the expression in Equation (5-160) respectively reduces to

$$\begin{aligned} &\boldsymbol{\sigma}_t = \boldsymbol{\sigma} + P_{lM}\boldsymbol{m} && \text{(full water-saturation conditions)} \\ &\boldsymbol{\sigma}_t = \boldsymbol{\sigma} + P_{gM}\boldsymbol{m} && \text{(partial water-saturation conditions)} \end{aligned} \tag{5-161}$$

The equilibrium equation in (5-158) usually defines a non-linear problem and, consequently, an iterative procedure (in this case, the Newton-Raphson method) is required to solve it. Expressing

that residual vector as a Taylor series, and precribing that it must vanish at the $(l+1)th$ iteration, then

$$\begin{aligned}\left(\boldsymbol{\sigma}_{\boldsymbol{t}}^{k+1,l+1}\right) = \boldsymbol{r}\left(\boldsymbol{\sigma}_{\boldsymbol{t}}^{k+1,l}\right) &+ \int_{V_e} \boldsymbol{B}^T \left(\frac{\partial \boldsymbol{\sigma}_{\boldsymbol{t}}^{k+1,l}}{\partial \boldsymbol{\varepsilon}}\right)\left(\frac{\partial \boldsymbol{\varepsilon}}{\partial \boldsymbol{u}}\right)\left(\boldsymbol{u}^{k+1,l+1} - \boldsymbol{u}^{k+1,l}\right) dV_e \\ &+ \int_{V_e} \boldsymbol{B}^T \left(\frac{\partial \boldsymbol{\sigma}_{\boldsymbol{t}}^{k+1,l}}{\partial P_{gM}}\right)\left(P_{gM}^{k+1,l+1} - P_{gM}^{k+1,l}\right) dV_e \\ &+ \int_{V_e} \boldsymbol{B}^T \left(\frac{\partial \boldsymbol{\sigma}_{\boldsymbol{t}}^{k+1,l}}{\partial P_{lM}}\right)\left(P_{lM}^{k+1,l+1} - P_{lM}^{k+1,l}\right) dV_e \\ &+ \int_{V_e} \boldsymbol{B}^T \left(\frac{\partial \boldsymbol{\sigma}_{\boldsymbol{t}}^{k+1,l}}{\partial T}\right)\left(T^{k+1,l+1} - T^{k+1,l}\right) dV_e = \boldsymbol{0}\end{aligned} \tag{5-162}$$

where

$$\boldsymbol{r}\left(\boldsymbol{\sigma}_{\boldsymbol{t}}^{k+1,l}\right) = \int_{V_e} \boldsymbol{B}^T \boldsymbol{\sigma}_{\boldsymbol{t}}^{k+1,l} dV_e - \boldsymbol{b}^{k+1} = \boldsymbol{0} \tag{5-163}$$

The terms involving second derivatives in the Taylor expansion have been neglected and the dependence of the total stresses on the state variables of the THM problem (that is, nodal displacements, liquid and gas pressures and temperature) are considered explicitly in Equation (5-162). The derivative of strains with respect to nodal displacements is obtained by differentiating the strain-displacement relation given in Equation (5-159), that is,

$$\frac{\partial \boldsymbol{\varepsilon}}{\partial \boldsymbol{u}} = \boldsymbol{B} \tag{5-164}$$

while the derivative of $\boldsymbol{\sigma_t}$ with respect to $\boldsymbol{\varepsilon}$ defines the elastoplastic consistent tangent tensor, $[\boldsymbol{D}^{ep}]$,

$$\frac{\partial \boldsymbol{\sigma}_t}{\partial \boldsymbol{\varepsilon}} = \frac{\partial \boldsymbol{\sigma}}{\partial \boldsymbol{\varepsilon}} = [\boldsymbol{D}^{ep}] \tag{5-165}$$

In the double-porosity approach discussed here, this constitutive tensor is determined through Equation (5-24) or Equation (5-75). Note that the difference in the main state variables in Equation (5-162) represents the difference between two consecutive iterations and, consequently, these terms are computed at a fixed time (t^{k+1}). Due to that, the partial derivative of total stresses with respect time does not appear in that equation.

The derivatives of the total stress vector with respect to water and gas pressures and temperature are obtained from the set of constitutive vectors given by Equation (5-25) to Equation (5-28) or from Equation (5-76) to Equation (5-78). For the general expression of total stress (Equation (5-160)), these vector quantities are computed as (for compression positive)

$$\frac{\partial \boldsymbol{\sigma}_t}{\partial P_{gM}} = \boldsymbol{h}_g + \boldsymbol{h}_s + (1 - \chi_M)\boldsymbol{m} \tag{5-166}$$

$$\frac{\partial \boldsymbol{\sigma}_t}{\partial P_{lM}} = \boldsymbol{h}_l - \boldsymbol{h}_s + \chi_M \boldsymbol{m} \tag{5-167}$$

$$\frac{\partial \boldsymbol{\sigma}_t}{\partial T} = \frac{\partial \boldsymbol{\sigma}}{\partial T} = \boldsymbol{h}_T \tag{5-168}$$

On the other, if the total stress vector is defined according to Equation (5-161), these derivatives are expressed by

$$\frac{\partial \boldsymbol{\sigma}_t}{\partial P_{gM}} = \begin{cases} \dfrac{\partial \boldsymbol{\sigma}}{\partial P_{gM}} + \boldsymbol{m} = \boldsymbol{h}_s + \boldsymbol{h}_{P_{fM}} + \boldsymbol{m} & if\ S_{lM} < 1 \\ \dfrac{\partial \boldsymbol{\sigma}}{\partial P_{gM}} = \boldsymbol{0} & if\ S_{lM} = 1 \end{cases} \tag{5-169}$$

$$\frac{\partial \boldsymbol{\sigma}_t}{\partial P_{lM}} = \begin{cases} \dfrac{\partial \boldsymbol{\sigma}}{\partial P_{lM}} = -\boldsymbol{h}_s & if\ S_{lM} < 1 \\ \dfrac{\partial \boldsymbol{\sigma}}{\partial P_{lM}} + \boldsymbol{m} = \boldsymbol{h}_{P_{fM}} + \boldsymbol{m} & if\ S_{lM} = 1 \end{cases} \tag{5-170}$$

$$\frac{\partial \boldsymbol{\sigma}_t}{\partial T} = \frac{\partial \boldsymbol{\sigma}}{\partial T} = \boldsymbol{h}_T \tag{5-171}$$

Finally, the global elastoplastic tangent stiffness, $[\boldsymbol{K^{ep}}]$, can be computed by the assembly of the elastoplastic tangent matrices of individual elements, $[\boldsymbol{k^{ep}}]$, as follows

$$\begin{aligned} [\boldsymbol{K^{ep}}] = \sum_{elements} [\boldsymbol{k^{ep}}] &= \sum_{elements} \int_{V_e} \boldsymbol{B}^T \left(\frac{\partial \boldsymbol{\sigma}_t}{\partial \boldsymbol{\varepsilon}}\right)\left(\frac{\partial \boldsymbol{\varepsilon}}{\partial \boldsymbol{u}}\right) dV_e \\ &= \sum_{elements} \int_{V_e} \boldsymbol{B}^T [\boldsymbol{D}^{ep}] \boldsymbol{B} dV_e \end{aligned} \tag{5-172}$$

whereas the global constitutive vectors are evaluated as

$$\boldsymbol{H}_g = \sum_{elements} \int_{V_e} \boldsymbol{B}^T \left(\frac{\partial \boldsymbol{\sigma}_t}{\partial P_{gM}}\right) dV_e \tag{5-173}$$

$$\boldsymbol{H}_l = \sum_{elements} \int_{V_e} \boldsymbol{B}^T \left(\frac{\partial \boldsymbol{\sigma}_t}{\partial P_{lM}}\right) dV_e \tag{5-174}$$

$$\boldsymbol{H}_T = \sum_{elements} \int_{V_e} \boldsymbol{B}^T \left(\frac{\partial \boldsymbol{\sigma}_t}{\partial T}\right) dV_e \tag{5-175}$$

and then, the global residual of stresses that arises from Equation (5-162) can be solved at each point in the porous medium.

It is important to remark that the sign convention used in all the stress expressions found in this chapter is the one adopted in Soil Mechanics, for which the compressive stresses are taken as positive quantities. That is also the sign convention used in CODE_BRIGHT for performing the stress integration algorithm and for computing the tangent matrices (constitutive subroutines). Nevertheless, in the rest of the numerical code, the sign convention for stresses is the same employed in the Continuum Solid Mechanics, in which compressions are assumed to be negative. Consequently, special care must be taken when computing the residual of stresses (Equation (5-158)) and the terms of the matrix equation given in Equation (5-162), since compressive stresses are considered as negative quantities in those expressions.

6. APPLICATION OF THE DOUBLE-POROSITY MODEL (DPM) TO STRESS PATHS UNDER ISOTHERMAL CONDITIONS: CONSTITUTIVE AND SENSITIVITY ANALYSES

6.1. INTRODUCTION

In order to review the modelling capabilities of the double-porosity formulation presented in previous chapters, a series of constitutive analyses following wetting or drying paths under isothermal conditions and some sensitivity studies involving several model parameters were performed. Unlike the boundary value problems, the constitutive analysis in a finite element (FE) context applies, at each time step, the unknown values (the solution for the differential constitutive equations) at each node of the generated mesh. In addition, the sensitivity analysis aims to establish a correlation between uncertainties in modelling outcomes to uncertainties in input parameters by means of numerical recalculations under alternative assumptions (Saltelli *et al.*, 1993; Hamby, 1994; Smith *et al.*, 2008). Furthermore, model sensitivity and uncertainty analyses are useful for assessing and increasing the robustness of a mathematical formulation by the identification and the numerical adjustment of those critical parameters and by the validation (or not) of some model assumptions and simplifications (Smith *et al.*, 2008).

These numerical tasks represent a key point for the development of the double-porosity model because they can provide a good understanding of the main phenomena occurring at each structural level. Any constitutive model that attempts to reproduce the behaviour of expansive soils must deal with the intrinsic complexity of these materials and with the large number of parameters required in their modelling, many of them difficult to estimate in laboratory (Alonso *et al.*, 2005; Wang and Wei, 2015) or even without an evident physical meaning. Such model uncertainties arise mainly from the highly complex hydro-mechanical micro-macro coupling mechanisms. One of these sources of uncertainties is associated with the magnitude and nature of the plastic deformations at macrostructural level due to the volumetric expansion or

contraction of microstructure. In that sense, the shape of the micro-macro interaction functions plays an essential role in predicting the observed mechanical behaviour of such materials, as discussed in **Section 4.4.2**. Another structural coupling in the double-porosity model developed in this Thesis is the water transfer mechanism between both structural media due to local differences in their water potentials. Again, this complex micro-macro interaction process is approached by a linear dependence on the difference of the matric suction in each porous level, as established in **Section 3.6**. In such a mass transfer mechanism, the only required input parameter is the phenomenological transfer coefficient (also termed as the leakage coefficient), γ^w, that controls the rate in which micro-pores are saturated or dried in response to the saturation state of macro-pores.

In the following sections, the most relevant information for the sensitivity analyses performed with the current double-porosity approach is briefly described together with the simplifications and hypotheses assumed during the numerical modelling. The main representative results and conclusions taken from such numerical simulations are also presented and discussed. In the present chapter, the sensitivity calculations were carried out under isothermal conditions. Sensitivity analyses for non-isothermal situations are addressed in **Chapter 7**. The mathematical tool used in all simulations is the finite element code CODE_BRIGHT (Olivella, 1995; Olivella *et al.*, 1996), a fully coupled numerical program developed by the UPC Geotechnical Group. The major characteristics of such a numerical code were already described briefly in **Section 3.10** and in **Section 5.3**. Interested readers are referred to Olivella *et al.* (2020) for further details.

6.2. MODELLING FEATURES

The performance of any numerical analysis in a FE code demands a geometry on which a FE mesh is generated together with the assignment of initial and boundary conditions and some physical restrictions. The modelling tasks also require the definition of the main constitutive laws with their input and fitting parameters. These three model features (geometry, initial and boundary conditions and model parameters) are addressed in the next sections. Two major classes of hydro-mechanical (HM) constitutive analyses were considered: wetting (or drying) at constant external load and wetting at constant volume. Moreover, and for each type of analysis, the effects of the hydraulic and the mechanical coupling mechanisms between micro and macro media were also studied.

Since the modelling of those stress paths is merely constitutive, the hydraulic problem (wetting/drying) is not solved, but the “exact” value of the macrostructural liquid pressure is prescribed at all nodes of the FE mesh. The mechanical problem is dealt as a boundary value problem in wetting/drying paths at unconfined conditions. In contrast, a prescription of null-displacements was imposed at all nodes of the mesh in those paths carried out under isochoric conditions.

6.2.1. MODELLED DOMAIN, INITIAL AND BOUNDARY CONDITIONS

A cubic sample of expansive soil, with a volume of 1.0 cm^3, was selected to represent the geometry to be modelled. The generated mesh is composed of 125 identical hexahedral elements. In the wetting or drying paths at constant load conditions ("free" volume conditions), the confining pressures are applied on the upper surface and on the four lateral surfaces. In such a condition, vertical displacements (in the z-axis orientation) are prevented at the lower surface. The FE mesh and three orthogonal views with the applied mechanical boundary conditions for wetting/drying paths under unconfined (free volume) and confined conditions are displayed in Figure 6-1.

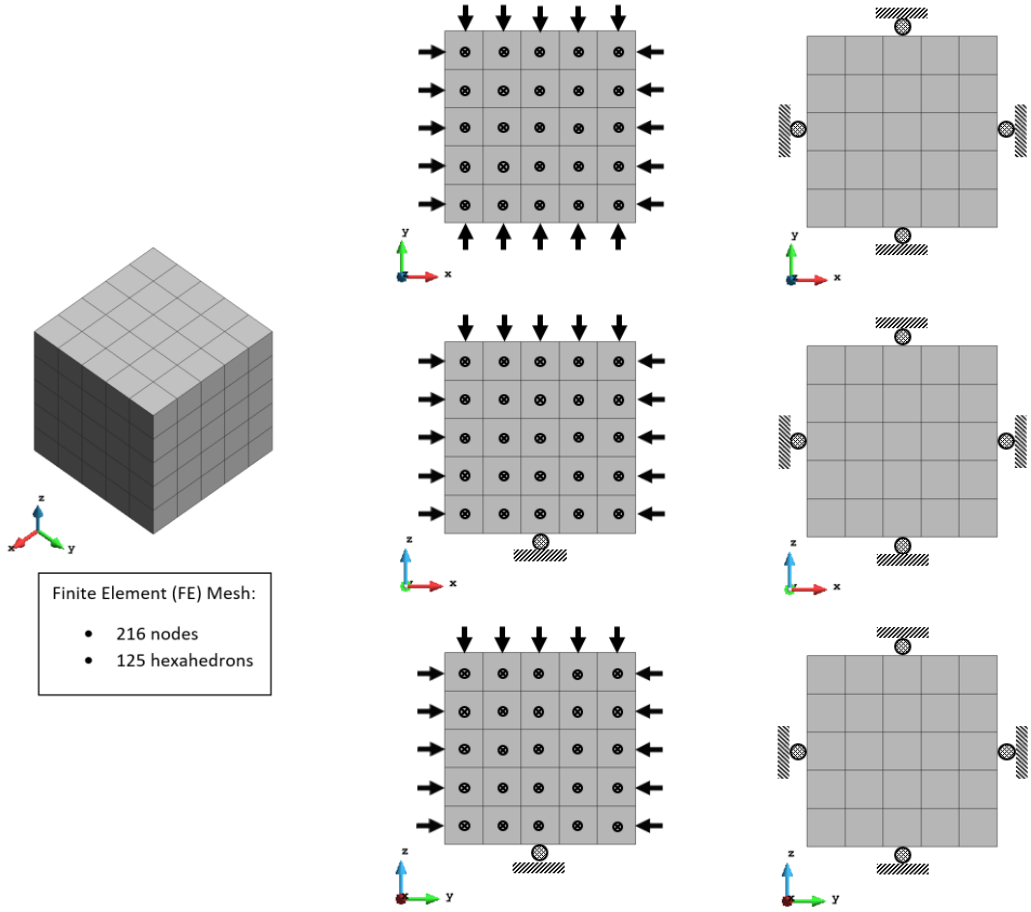

Figure 6-1: **(a)** Schematic representation of the modelled geometry (FE mesh) of a cubic element of expansive soil together with the mechanical boundary conditions under **(b)** unconfined and **(c)** confined swelling/shrinkage evolution.

The wetting (or drying) at constant external load (CSP) was performed following two different strategies: ***i.*** the material was wetted (or dried) at a low confining pressure until the target suction and then, it was loaded until reaching a final mean pressure of 1.0 MPa; or, ***ii.*** the sample was firstly loaded to a mean confining pressure of 1.0 MPa and then, it was soaked (or dried) until its target final suction. In both procedures, the increment in mean stresses was applied in a short period of time (in one day's time) while the hydration (or dehydration) process was modelled at different rates. In that sense, the effects of a rapid and a slow wetting (or drying) process on the evolution of micro and macro variables could be also examined. The stress paths

considered in the numerical calculations are summarized in Table 6-1 and some of them are illustrated in Figure 6-2. The identification of the current stress path depends on its initial conditions. For example, the cases termed as CSP_A-123 and CSP_A-75 correspond to wetting performed at a constant loading of 0.1 MPa in which the initial matric suctions are 123 MPa and 75 MPa, respectively, followed by an increment in the confining stresses until reaching a final value of 1.0 MPa. The choice of the final confining pressure (of 1.0 MPa) is merely an attempt of performing a fully elastic analysis of the double-porosity model following a wetting path when the mechanical micro-macro coupling is not activated (see **Section 6.3.1** and Figure 6-2).

Table 6-1: Identification of the modelled wetting (CSP_A, CSP_B, CSP_C, CSP_D) and drying (CSP_E, CSP_F, CSP_G, CSP_H) paths under constant confining pressures.

	Initial Mean Stress (MPa)	Initial Macro Suction (MPa)	Final Mean Stress (MPa)	Final Macro Suction (MPa)	Sequence of operations
CSP_A	0.1	25 / 75 / 123	1.0	0.1	wetting-loading
CSP_B	0.5	25 / 75 / 123	1.0	0.1	wetting-loading
CSP_C	1.0	25 / 75 / 123	1.0	0.1	wetting
CSP_D	0.1	123	1.0	0.1	loading-wetting
CSP_E	0.1	1 – 123	1.0	250	drying-loading
CSP_F	0.5	25 / 75 / 123	1.0	250	drying-loading
CSP_G	1.0	25 / 75 / 123	1.0	250	drying
CSP_H	0.1	123	1.0	250	loading-drying

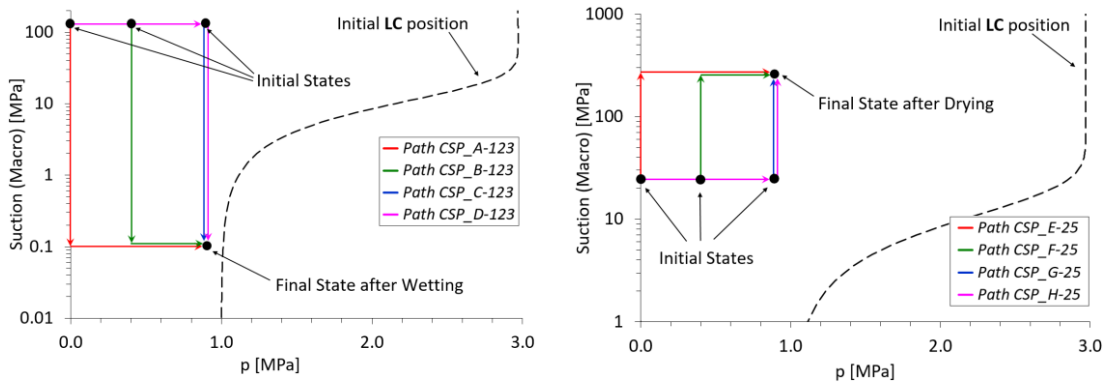

Figure 6-2: Schematic representation (in the p: s_M plane) of the wetting (left) and drying (right) paths at constant load conditions considered in the performance of the model sensitivity analyses.

The wetting at constant volume conditions (CVP) was modelled for four different initial stress states so that the effects of the initial macro suctions and confining pressures on the expansive material response could be also taken into account. Two different values for the initial matric suction are considered, that is, 123 and 75 MPa; the initial confining pressures used in calculations are 0.1, 0.5 and 1.0 MPa, as indicated in Table 6-2 and illustrated in Figure 6-3. The wetting of the swelling material was simulated by gradually reducing the macro-suction from its initial value to 0.1 MPa. Like the hydration process under constant load conditions, such a suction decrease was carried out at different rates. An additional modelling time was left, after the end of the hydration of macro-pores, in order to enable the full development of the swelling

potential of the expansive material, once a continuous increase in the saturation state of microstructure is expected to occur in response to the saturation of macrostructure.

Table 6-2: Identification of the wetting paths under constant volume conditions.

	Initial Mean Stress (MPa)	Initial Macro Suction (MPa)	Final Macro Suction (MPa)
CVP_A-123	0.1	123	0.1
CVP_B-123	0.5	123	0.1
CVP_C-123	1.0	123	0.1
CVP_A-75	0.1	75	0.1

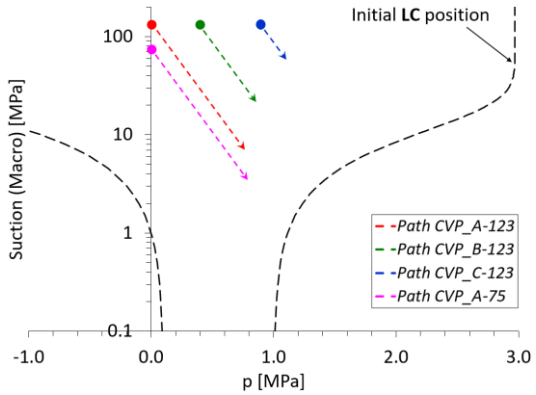

Figure 6-3: Schematic representation (in the $p{:}s_M$ plane) of the wetting paths at constant volume conditions considered in the performance of the model sensitivity analyses.

In all the cases considered in the numerical sensitivity analyses, the variations in the water content of macro-pores (wetting or drying) were simulated by applying the changes in macro-liquid pressure (the unknown of the balance equation for the mass of macrostructural pore-water) directly at all nodes of the FE mesh (i.e., in the whole volume). Gas pressure does not change during the calculations and takes a constant value of 0.1 MPa. Furthermore, local equilibrium of the initial matric suctions in both structural media is assumed. The initial stress state is isotropic, with values in the range of 0.1 MPa and 1.0 MPa, depending on the case of analysis (see Table 6-1 and Table 6-2). As the HM response of the cubic soil sample in Figure 6-1 is modelled using a double-porosity approach, a partition of the total porosity into the micro- and macro-pore volume fractions is required. Such porosity variables are the ones defined over the total volume of the soil sample, according to Equation (3-5). Values of 0.16 and 0.28 are assigned to the initial micro- and macro-pore volume fractions, respectively. Therefore, an initial (total) porosity of 0.44 is prescribed to the expansive soil sample.

6.2.2. MODEL PARAMETERS

The material parameters used in the simulations were taken from previous modelling experiences (Sánchez and Gens, 2006; Czaikowski *et al.*, 2012; Gaus *et al.*, 2014a; Garitte *et al.*,

2015; Vasconcelos and Gens, 2015; Gens and Vasconcelos, 2019*)* and also from experimental investigations (Hoffmann *et al.*, 2007; Villar *et al.*, 2012b, 2016; Rizzi *et al*., 2012; Seiphoori *et al.*, 2014) on compacted and pelletized expansive clays, such as the FEBEX and the MX-80 bentonites. Many of those key properties were adopted by the CIMNE Team for modelling an engineered barrier made of MX-80 pellets in the HE-E experiment, as reported in Gaus *et al.* (2014a) and Gens and Vasconcelos (2019). The input parameters of the constitutive laws implemented in CODE_BRIGHT and required to solve the coupled (T)HM problem in the framework of the double-porosity approach described in this document, are listed from Table 6-3 to Table 6-9. A more detailed explanation about the choice of those constitutive laws and parameters is given in **Section 2.6** and **Sections 8.2.1** and **8.3.3**, where the material characterization and the modelling of a pair of artificial hydration tests on heated columns of bentonite-based materials are presented and discussed. In the current chapter and in the next one, only a general view of the theoretical and the numerical modelling aspects is considered, since the main goal of these analyses is to assess the capabilities of the double-porosity model to reproduce the swelling and the shrinkage responses of expansive clays.

As described in **Section 3.8.2.2**, the hydraulic response of an unsaturated porous medium is driven by its water retention curve. Since the double-porosity model developed in this Thesis considers that the microstructure may be unsaturated, it is necessary to define a retention curve for such a pore level. Thus, the double-porosity model requires two sets of parameters associated with the storage capacity of water in the expansive soil, each one of them related to a different structural medium. The input parameters of the modified van Genuchten law used for modelling the water retention capacity at micro and macro levels are given in Table 6-3. The shape of both retention curves obtained from such model parameters is illustrated in Figure 6-4(a). The dependence of water permeability on the macro-porosity of the expansive soil sample was simulated through Kozeny's law (see Equation (3-99)) while its dependence on the degree of saturation was reproduced by means of a generalized power law, according to the expression given in Equation (3-104). As mentioned in **Section 2.4.3** and **Section 3.8.2**, it is assumed that the liquid and gas phases in expansive porous media only flow through macro-pores and due to that, the water permeability parameters were defined for macrostructure. The hydraulic parameters required for modelling the water mass fluxes in macrostructure are shown in Table 6-4, which ones define the curves drawn in Figure 6-4(b). The density of water in macro and micro voids and its dependence on changes in temperature and pressures was modelled, in CODE_BRIGHT, through the exponential function expressed in Equation (3-111). Water density parameters considered in calculations are given in Table 6-5.

Table 6-3: Hydraulic parameters used in the numerical simulations for modelling the water retention capacity.

		Retention Curve Parameters for Micro	**Retention Curve Parameters for Macro**
Measured *P* at 20°C, P_0	[MPa]	100	10.0
Surface tension at 20°C, σ_0	[Nm^{-1}]	0.072	0.072
Shape function for retention curve, λ_{rc}	-	0.60	0.40
Pressure related with the suction at zero degree of saturation, P_d	[MPa]	1.0e+27	1500
Model parameter, λ_d	-	0.00	1.00
Residual saturation, S_{lr}	-	0.01	0.01
Maximum saturation, S_{ls}	-	1.00	1.00

Table 6-4: Hydraulic parameters used in the numerical simulations for modelling the water mobility through macro-pores.

Water Permeability Parameters		
Intrinsic permeability, k_0	[m^2]	3.50e-20
Reference porosity, ϕ_0	-	0.28
Model parameter (for relative permeability), A_{rl}	-	1.00
Model parameter (for relative permeability), λ_{rl}	-	6.0

Table 6-5: Input parameters adopted in the numerical simulations for modelling the pore-water density.

Parameters for the exponential water density law (macro and micro)		
Reference water density, ρ_{l0}	[kg/m^3]	1002.6
Water compressibility, $\beta_{\rho l}$	[MPa^{-1}]	4.5e-04
Volumetric thermal expansion for water, $\alpha_{\rho l}$	[°C^{-1}]	3.4e-04*
Solute variation, $\gamma_{\rho l}$	-	0.0
Reference pressure, P_{l0}	[MPa]	0.10

* In CODE_BRIGHT, such a model parameter assumes a negative value because the thermal expansion of pore-water leads to a reduction of its density in non-isothermal problems.

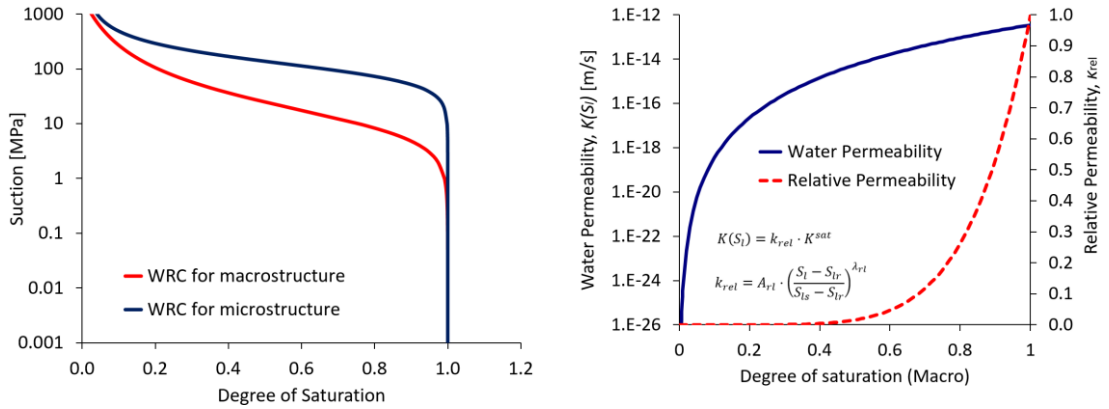

Figure 6-4: **(a)** Modelled water retention curves of macrostructure and microstructure; **(b)** liquid permeability (full line) and relative permeability (dashed line) evolution as functions of the macro-pore saturation.

The mechanical behaviour of micro and macro media was simulated through the mathematical formulation and the numerical approach presented in previous chapters. The volumetric elastic behaviour of microstructure is determined by the Bishop effective stress, as defined in **Section 3.3**, which is governed by the Bishop's coefficient function, $\chi_m(S_{lm})$. In the double-porosity formulation, such a function is completely defined by two fitting parameters, p_χ and q_χ, according to Equation (3-37). In Table 6-6 the model parameters of the Bishop function adopted in calculations are given; the function is represented by the red curve in Figure 6-5. The elastoplastic behaviour of macrostructure is described by means of the classical BBM formulation. Therefore, the effective stress acting on macrostructure is given by Equation (3-38), in which the net stress tensor (as defined in Equation (3-27)) is the stress variable controlling the deformation of macro-pores under non-saturated conditions. The mechanical parameters used to model the elastic and the plastic responses of the macrostructural porous medium are given in Table 6-6 and Table 6-7, respectively. Some of those parameters were taken from the modelling dataset by ENRESA (2000) and Gaus *et al.* (2014a*)* and from the experimental information reported in the literature (Hoffmann *et al.*, 2007; Rizzi *et al.*, 2012; Rothfuchs *et al.*, 2012; Villar *et al.*, 2012b, 2016; Seiphoori *et al.*, 2014; Toprak *et al.*, 2016).

Table 6-6: Mechanical input parameters for modelling the elastic response of microstructure and macrostructure.

Elastic Parameters for Microstructure (Bishop effective stress)		
Parameter for Bishop's coefficient, p_χ	-	1.00
Parameter for Bishop's coefficient, q_χ	-	100
Elastic Parameters for Macrostructure		
Elastic slope (macro) for specific volume-mean stress, $\overline{\kappa}_M$	-	0.006
Elastic slope (macro) for specific volume-macro suction, $\overline{\kappa}_s$	-	0.010
Minimum bulk modulus (macro), $\overline{K}_{M,min}$	[MPa]	45
Minimum bulk modulus (macro), $\overline{K}_{s,min}$	[MPa]	45
Poisson's ratio, υ	-	0.30

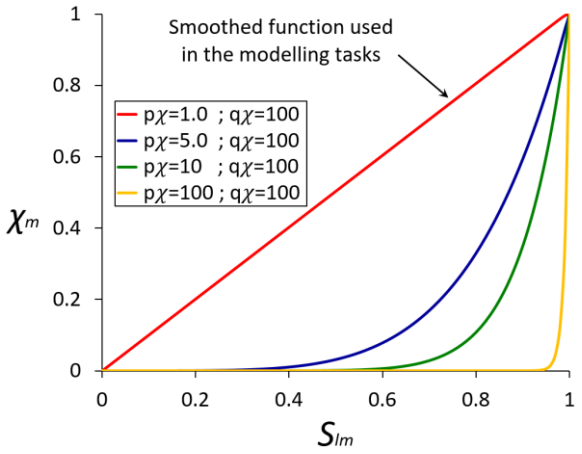

Figure 6-5: Dependence of the Bishop coefficient on the microstructural degree of saturation. A linear Bishop function (the red line) was selected for modelling the mechanical behaviour of microstructure.

Table 6-7: Mechanical input parameters for modelling the macrostructural elastoplastic behaviour (BBM model).

Elastoplastic Behaviour for Macrostructure (BBM Parameters)		
Slope of void ratio-mean stress at saturation, λ_{sat}	-	0.165
Parameter defining the maximum soil stiffness, r	-	0.70
Parameter controlling the rate of increase of stiffness with macro suction, β	[MPa^{-1}]	0.15
Reference pressure, p_c	[MPa]	0.09
Initial pre-consolidation mean stress at saturation, p_0^*	[MPa]	1.00
Tensile strength in saturated conditions, p_{s0}	[MPa]	0.10
Parameter that takes into account increase of tensile strength due to macro suction, k	-	0.10
Friction angle, φ'	[°]	27
Smoothed model parameter for the Mohr-Coulomb function in the deviatoric plane, α_F	-	8
Smoothed model parameter for the plastic potential function, α_G	-	8
Non-associativity parameter, ω	-	1.00
Model parameter that defines the position of the homotetic center (for triaxial stress states), c	-	0.20

The mechanical micro-macro coupling (β-mechanism) was simulated by defining the shape of the interaction functions (f_β), whose mathematical expression is given in Equation (4-94). The model parameters of some micro-macro coupling functions considered in the sensitivity analyses are shown in Table 6-8. Those generic interaction functions are plotted in Figure 6-6. It is interesting to remark that the pair of interaction functions termed as "Functions #1" in Table 6-8 simulates a situation in which no plastic strain is generated due to volumetric deformation of microstructure, that is, when the β-mechanism is deactivated. In such a case, the occurrence of plastic deformations would only be related to the activation of the plastic loading-collapse mechanism (the LC mechanism), when the stress path "crosses" the current LC locus.

Table 6-8: Model parameters for the mechanical micro-macro coupling mechanism (the plastic β-mechanism).

	Functions #1	Functions #2	Functions #3	Functions #4
$f_{MS}^{(0)}$	0.0	0.5	1.0	1.5
$f_{MS}^{(1)}$	0.0	-0.1	-0.1	-0.1
n_{MS}	3.0	3.0	3.0	3.0
$f_{MC}^{(0)}$	0.0	-0.1	-0.1	-0.1
$f_{MC}^{(1)}$	0.0	0.5	1.0	1.5
n_{MC}	3.0	3.0	3.0	3.0

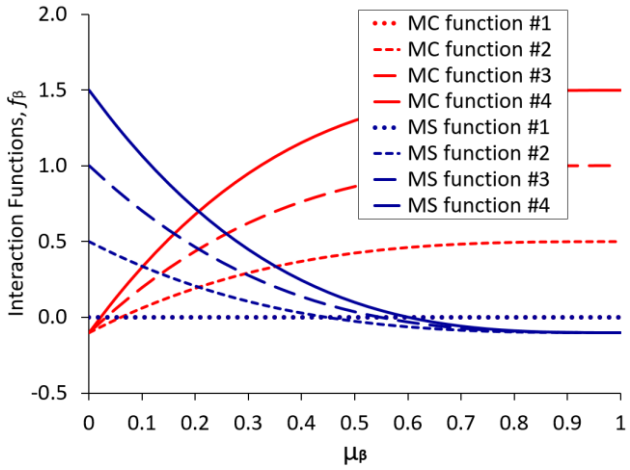

Figure 6-6: Distinct micro-macro interaction function shapes used in the numerical analyses.

The hydraulic coupling mechanism is the main phenomenological process controlling the water content at microstructural level. As discussed in **Section 2.4.3** and in **Section 3.6**, changes in the saturation state of microstructure are due to the local mass transfer of water from or to micro-pores in response to the changes in the saturation state of macro-pores. The rate of such a water transfer is determined by the leakage coefficient, γ^w, the only input parameter required for modelling the micro-macro mass exchange of water in the multi-porosity approach developed in this work. Three different scenarios were studied, as indicated in Table 6-9, in order to evaluate the "sensitivity" of the material response to this parameter.

Table 6-9: Leakage coefficient values used for modelling the micro-macro water mass transfer.

		Scenario #1	Scenario #2	Scenario #3
Leakage Coefficient, γ^w	[kg s^{-1} m^{-3} MPa^{-1}]	1.0e-09	1.0e-07	1.0e-06

6.3. WETTING AT CONSTANT CONFINING PRESSURE

The first set of stress paths to be studied corresponds to the wetting of a sample of expansive soil at a certain (and constant) confining stress level. The initial and final states and the sequence of events followed in each of such constitutive wetting paths are listed in Table 6-1. In order to

evaluate the capability, the versatility and the consistency of the double-porosity formulation in reproducing the swelling potential of expansive clays, two situations were considered. In the first one, to be addressed in **Section 6.3.1**, the volumetric expansion of microstructure due to the saturation of the soil sample does not generate any plastic deformation in the clay fabric, because the mechanical coupling mechanism is deactivated. This situation was modelled by assuming a null value for the coupling function f_{MS} (Functions #1 in Table 6-8). Plastic deformations due to the micro-macro coupling mechanism are allowed during the wetting paths analysed in **Section 6.3.2**.

6.3.1. ANALYSES WITH THE β-MECHANISM DEACTIVATED

The most notable consequence of deactivating the micro-macro coupling mechanism, in wetting paths under constant confining stresses, is the fact that the swelling process occurs under elastic conditions, unless the stress path crosses the initial LC locus, activating then the loading-collapse plastic mechanism. In order to avoid the generation of plastic deformations, the wetting paths at constant loading conditions were selected so that they could not intersect the LC curve, as displayed in Figure 6-2. Therefore, only the reversible strain component of swelling will develop during the wetting of the cubic sample of soil. It means that the soil structure remains unchanged throughout the wetting under constant loading. In other words, reorientation or cracking of aggregates, occlusion of macro-pores by smaller particles or irreversible collapse of macrostructure will not occur during the soaking of the expansive material. Nevertheless, for unsaturated highly expansive clays, wetting under unconfined conditions may induce large volumetric deformations, which could lead to significant irreversible structural changes in the clayey soil as it becomes saturated. Consequently, the deactivation of the coupling mechanism between the mechanical behaviour of the two structural levels would not be realistic in representing the swelling (or the shrinkage) response of expansive soils. This situation could be considered as a particular case of the more general double-porosity formulation related to the classical elastoplastic BBM formulation (Alonso *et al.*, 1990), which adequately predicts the elastic response of unsaturated non-expansive soils inside the yield surface.

The swelling potential of expansive soils is dependent on the factors that affect the migration process of pore-water from large pores (bulk water) to micro-pores (intra-aggregate and inter-layer water). In the double-porosity model, this water exchange process is controlled by the micro-macro water transfer coefficient, γ^w. Therefore, a model sensitivity analysis was performed in order to assess the impact of the leakage coefficient on the swelling of the cubic soil sample. The most relevant modelling results obtained from this analysis, for two stress paths (CSP_A-123 and CSP_D-123), are plotted from Figure 6-7 to Figure 6-12. As expected, the mass of water exchanged between both structural media is higher as the leakage coefficient increases. This is illustrated in Figure 6-7, where the evolutions of macro and micro suctions and degrees of saturation for the two selected stress paths are plotted. Therefore, the reduction in the microstructural suction due to the macro-pore saturation is greater for Scenario #3, for which the micro-macro water transfer rate is higher ($\gamma^w = 10^{-6}$ kg/s/m^3/MPa). Consequently, the increase in the degree of saturation of microstructure is also higher for Scenario #3. Note that for Scenario #1, in which the leakage coefficient is lower ($\gamma^w = 10^{-9}$ kg/s/m^3/MPa), microstructure is almost insensitive to the re-saturation of macro-pores, even when this

saturation process is performed at a slower rate (i.e., in 720 days). The time prescribed to re-saturate the macro-pores (Δt_{hydr}) varied between 30 days (fast hydration) and 3650 days (slow hydration). However, the model results shown in the following charts have been determined for Δt_{hydr} =720 days (Scenario #1) and Δt_{hydr} =180 days (Scenario #2 and Scenario #3). Although the macro suction at the end of this hydration process was 0.1 MPa, the degree of saturation of macro-pores at this situation is higher than 0.999. For comparison purposes, in the graphs plotted from now on, the evolution of the hydro-mechanical variables is given against a standardized time variable, in which the current time is divided by Δt_{hydr}.

The evolution of the porosity variables (pore volume fractions, aggregate and total porosities) for the CSP_A-123 and the CSP_D-123 paths is given in Figure 6-8 and Figure 6-9, respectively. From these results, it can be observed a general trend of the cubic element of soil to expand (in both structural levels) as macro-pores are re-saturated. The swelling process occurs firstly at microstructural level by the progressive increase of intra-aggregate pores (inter-particle and inter-layer voids) as they become saturated with water taken from macro voids. As mentioned previously, this water mass exchange arises from the local differences in the water potential between both classes of pores and is driven by the hydraulic coupling mechanism between both structural media. Such a swelling response becomes more prominent as the micro-macro leakage coefficient increases. The swelling of the clay aggregates leads to an increase in the volume of inter-aggregate voids (macro-pores), which produces a global expansion of the soil element (increase in total porosity). The changes in the microstructural (aggregate) porosity is intrinsically related to the magnitude and the evolution of the mean effective stresses, p_m, acting on the expansive clay aggregates. Under isothermal conditions and taking into account the concept of net stresses for representing the effective stress at macrostructure, the expression for the mean microstructural effective stresses arises from Equation (3-39) and it is given as follows

$$p_m = \frac{1}{3}\boldsymbol{m}^T\boldsymbol{\sigma}_m = p + \left[\chi_m\left(P_{gm} - P_{lm}\right) - P_{gm} + max\left(P_{gM}, P_{lM}\right)\right] \tag{6-1}$$

Under the assumption of a local equilibrium between the pore-air pressures in both pore levels, $P_{gM} = P_{gm}$, and while the macrostructural suction remains positive, the latter equation reduces to

$$p_m = p + \chi_m\left(P_{gm} - P_{lm}\right) \tag{6-2}$$

The evolution of the total and the incremental microstructural effective stresses is drawn in Figure 6-10 (for the CSP_A-123 paths) and in Figure 6-11 (for the CSP_D-123 paths) together with the evolution of the microstructural Bishop coefficient, χ_m. A graphical representation of the stress paths CSP_A-123 and CSP_D-123, in the p: s_M plane, is shown in Figure 6-12, together with the evolution of the model hardening parameter, that is, the pre-consolidation pressure (p_0^*). Since $\Delta p_0^* = 0$ throughout the wetting-loading (CSP_A-123) and the loading-wetting (CSP_D-123) paths, only reversible swelling strains are generated during the wetting process. This result is due to the deactivation of the plastic β-mechanism and the selection of a set of stress paths that do not cross the initial LC locus.

Although the hydro-mechanical (HM) CSP_A-123 and CSP_D-123 paths have the same initial and final stress states, the performance of wetting after or before an increase in the confining stresses may introduce significant differences in the expansive response of the soil sample. In that sense, the modelling results obtained from the CSP_A-123 and CSP_D-123 paths are plotted and analysed together, in Figure 6-13 to Figure 6-15. The initial increase in the confining stresses before wetting (CSP_D-123) induces a slight reduction in micro-porosity variables (aggregate porosity and micro-pore volume fraction), since the aggregate volume also tends to decrease due to the compressive action caused by such a loading increment, as displayed in Figure 6-14 (for Scenario #1) and in Figure 6-15 (for Scenario #3). Nevertheless, macro-pore volume fraction seems not to be affected by that initial loading (at least, not for the level of stresses reached at the end of the loading process). It could be a consequence of the purely elastic and volumetric response of the porous medium to the increment in confining pressures, as the volume of the cubic sample and the volume occupied by aggregates are reduced proportionally. Thus, the initial reduction of total porosity for the path CSP_D-123 is due to the initial decrease of micro-porosity variables. Moreover, such an initial (and fast) compression at microstructural level also leads to a marked increase of micro-saturation (and to a decrease in micro suction), as illustrated by the graphs plotted in Figure 6-13.

The differences in the HM response between the paths CSP_A-123 and CSP_D-123 reveal the impact of performing (or not) a previous loading step to wetting on the final saturation state in each structural medium and on the amount of swelling, especially for Scenario #3. In fact, the swelling expansion of the clay aggregates due to the development of micro-porosity is lower when the re-saturation of macro-pores occurs at higher confining pressures, as in the CSP_D-123 path. As a consequence, the degree of saturation of microstructure also tends to be higher for higher values of confining pressures, since the volume of the intra-aggregate voids to be filled with water transferred from macro- to micro-pores tends to be somewhat lower in such conditions. This leads to lower values of micro suction at the end of the hydration of macrostructure, as observed in the modelling results for Scenario #3 in Figure 6-13. However, for Scenario #1, in which the hydraulic micro-macro coupling process has less relevance in the hydration of micro-pores, such behaviour differences and that dependence on the sequence of operations (load-wetting or wetting-load) are almost imperceptible (see Figure 6-13 and Figure 6-14).

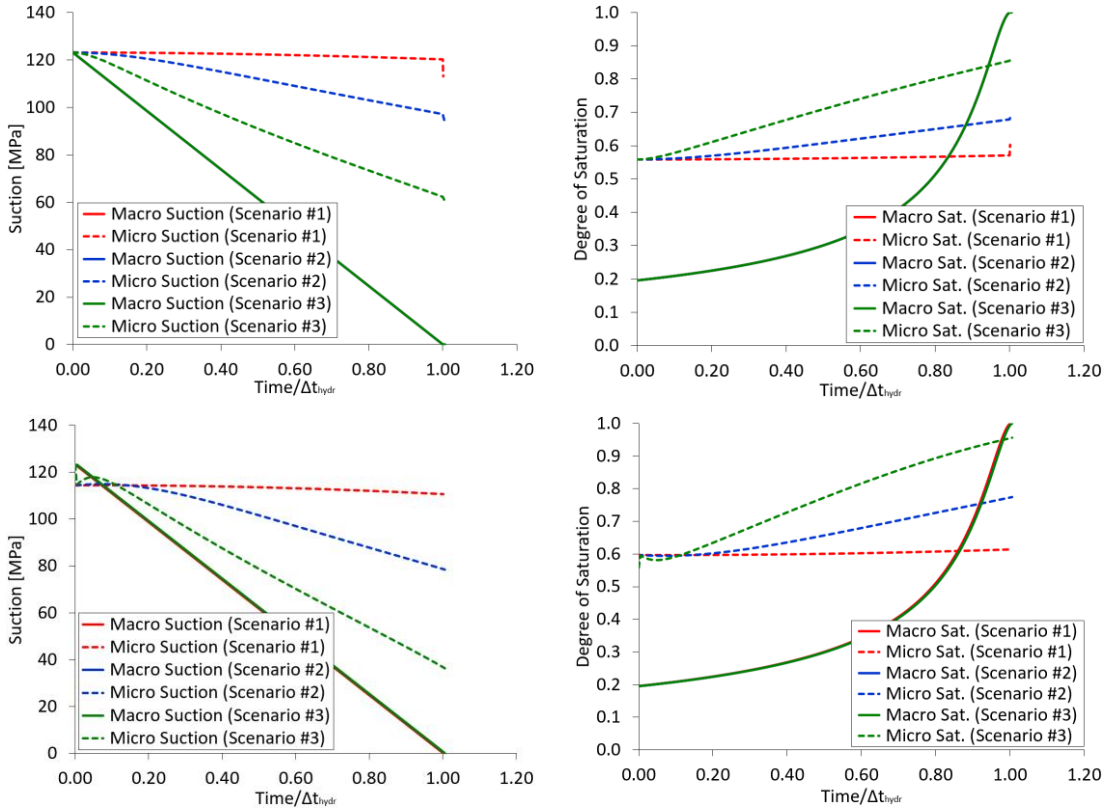

Figure 6-7: Suction (left) and degree of saturation (right) for the CSP_A-123 (up) and CSP_D-123 (down) paths.

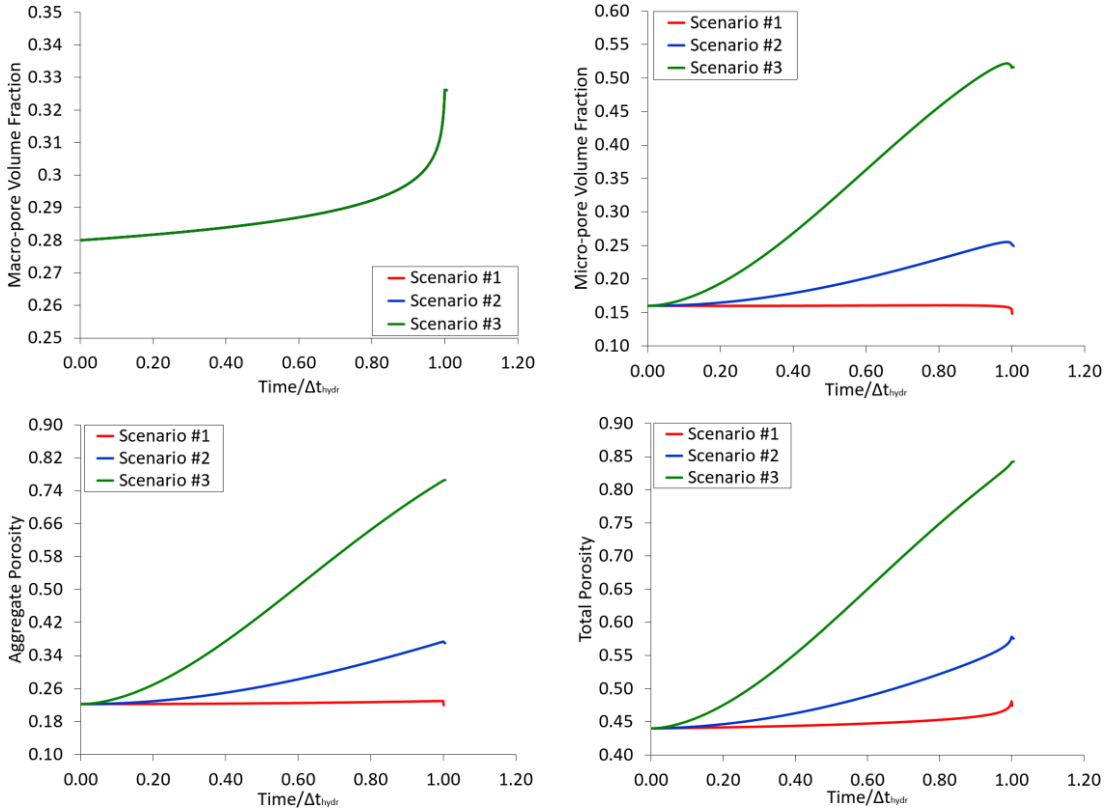

Figure 6-8: Pore volume fractions (up) and porosities (down) for the wetting-loading path CSP_A-123.

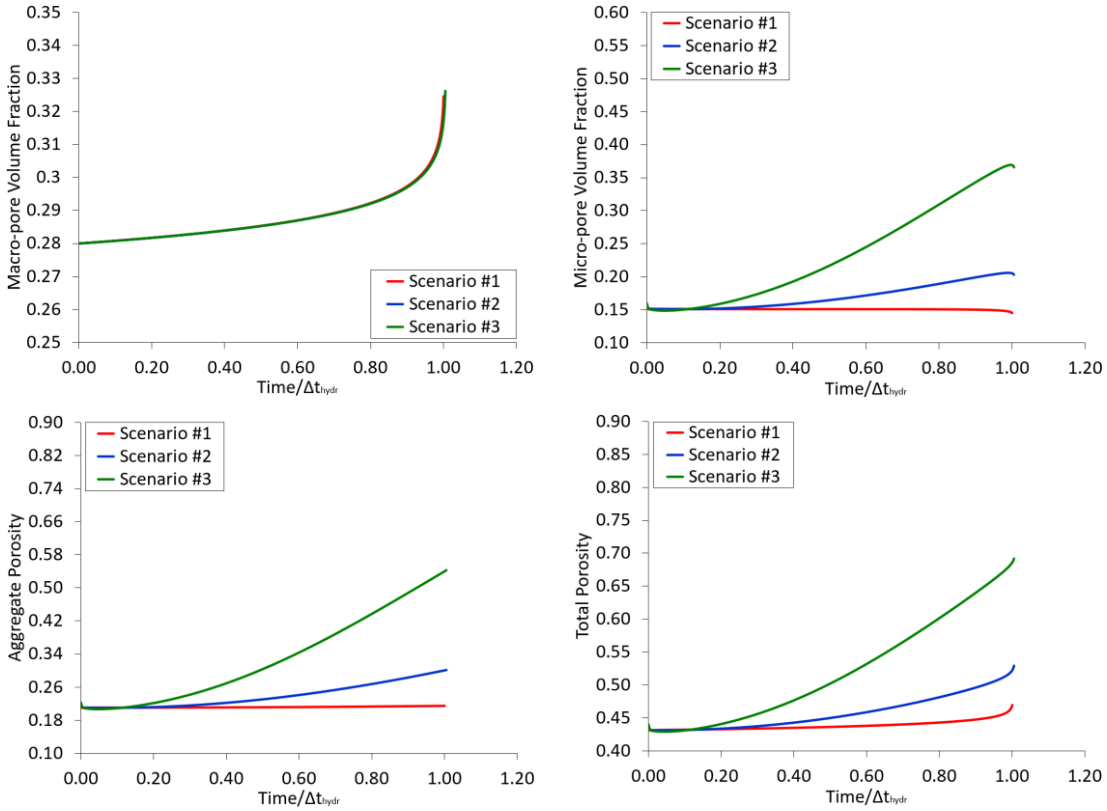

Figure 6-9: Pore volume fractions (up) and porosities (down) for the loading-wetting path CSP_D-123.

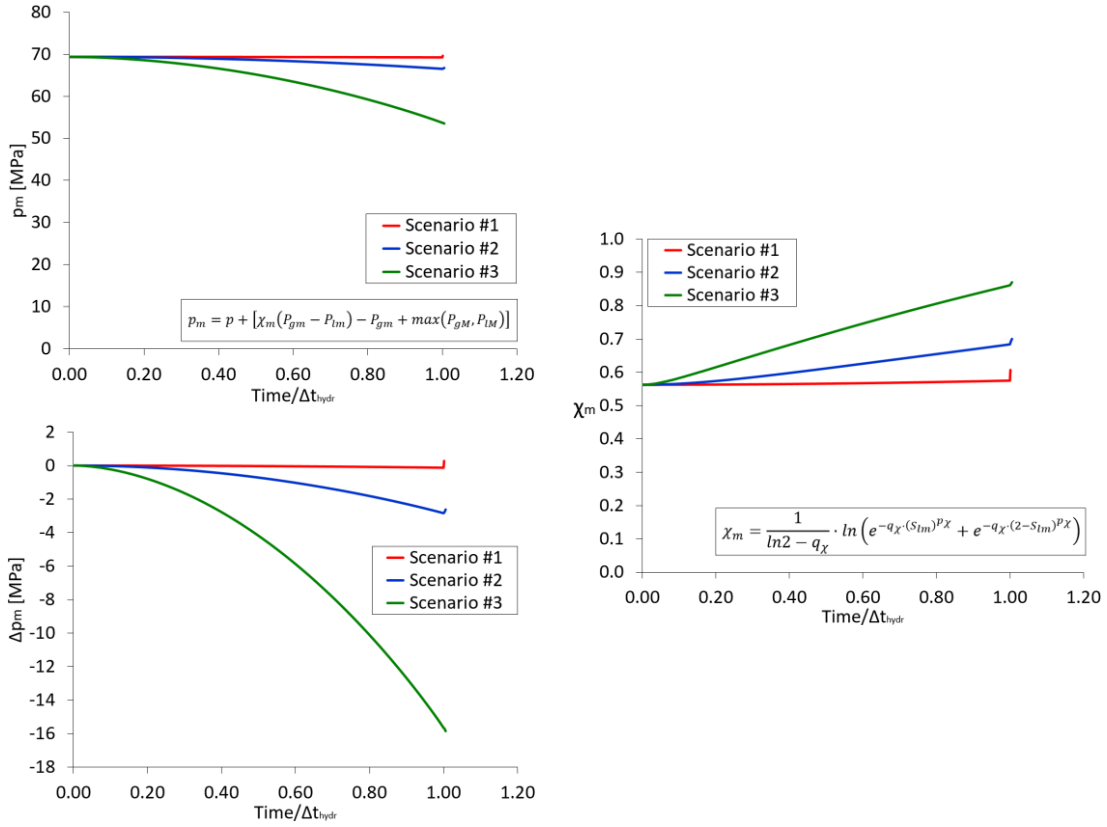

Figure 6-10: Total values and the increments of microstructural mean effective stress (left) and the Bishop function parameter (right) for the wetting-loading path CSP_A-123.

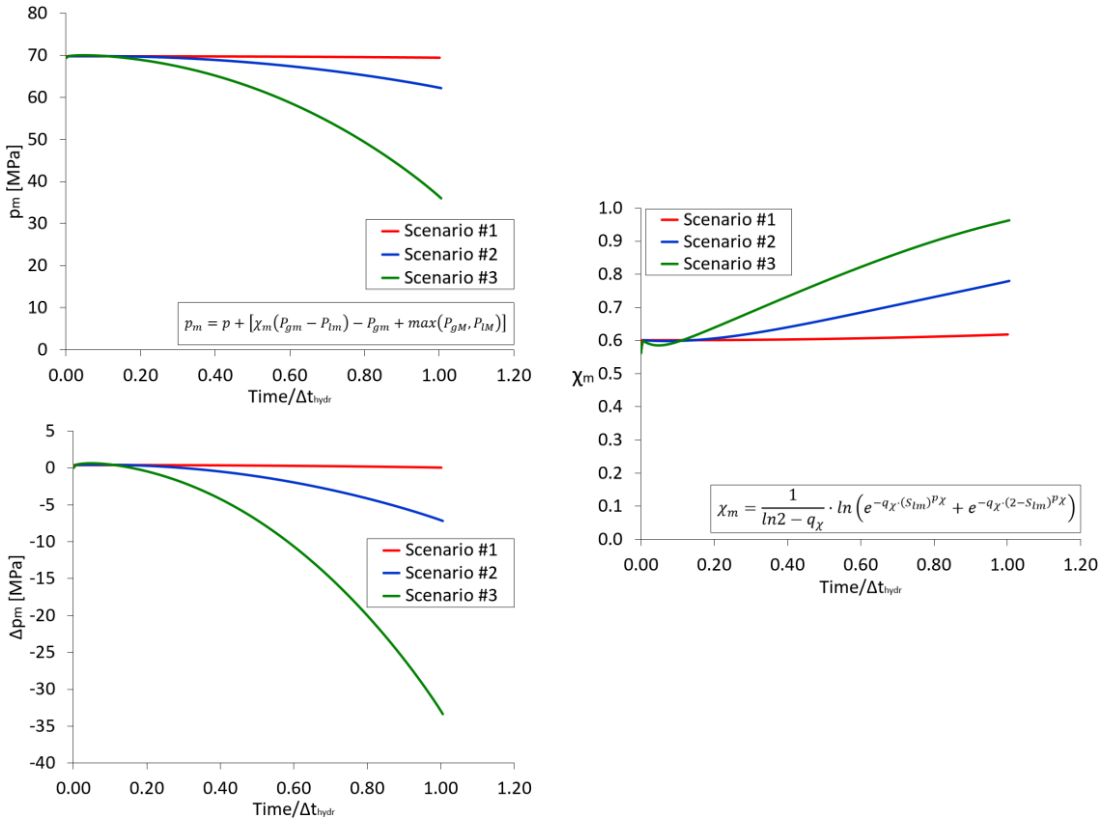

Figure 6-11: Total values and the increments of microstructural mean effective stress (left) and the Bishop parameter function (right) for the loading-wetting path CSP_D-123.

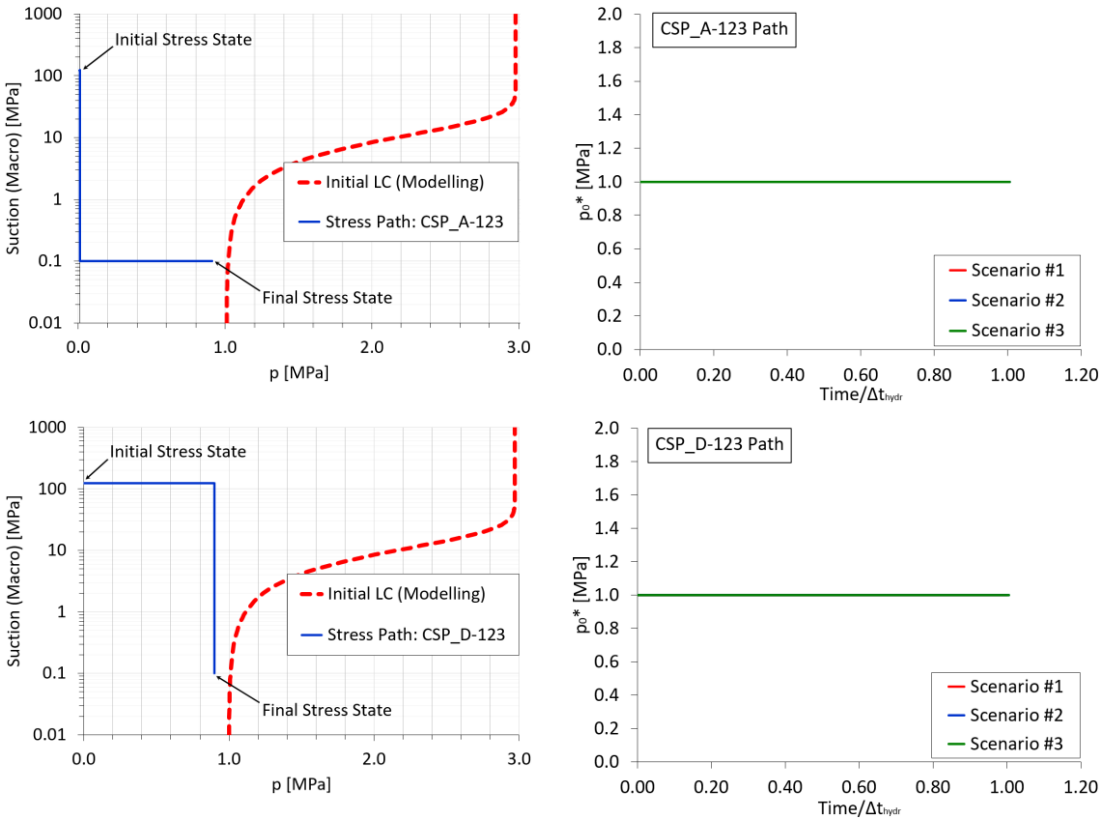

Figure 6-12: CSP_A-123 (up) and CSP_D-123 (down) paths plotted in the p: s_M plane (left) and the evolution of the saturated pre-consolidation pressure (right) in each stress path under distinct local water mass transfer conditions.

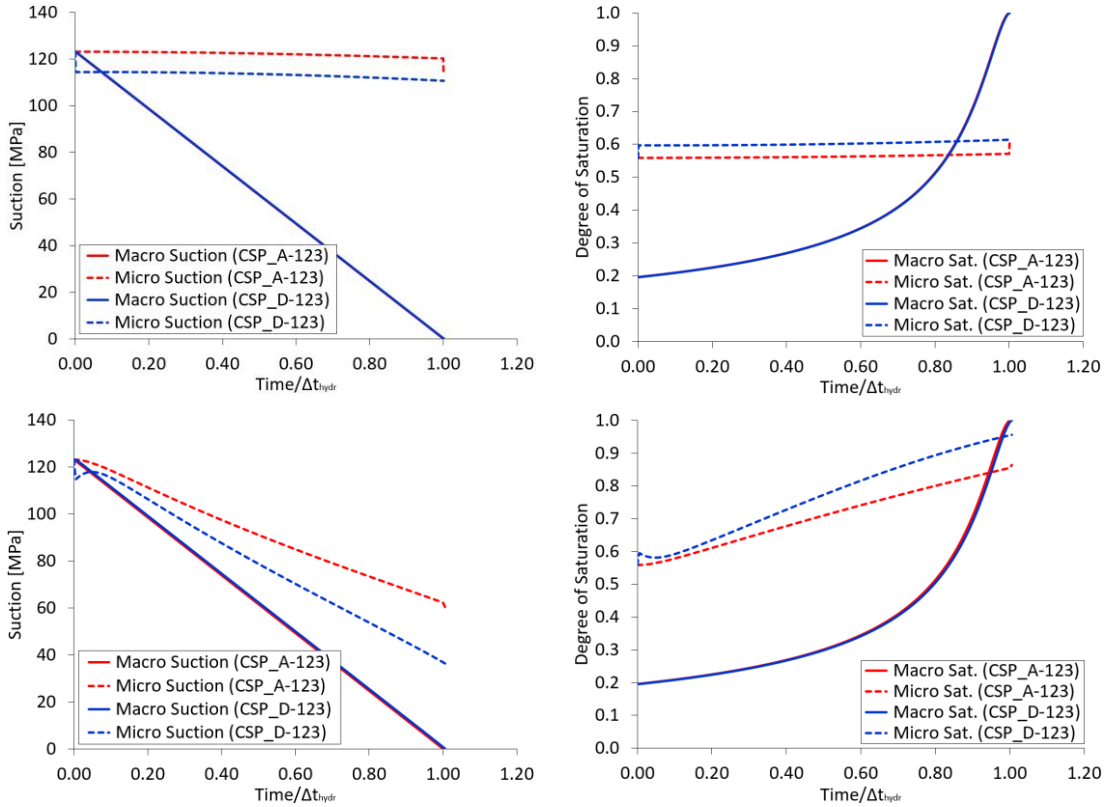

Figure 6-13: Comparison between the suction and degree of saturation for the HM CSP_A-123 and CSP_D-123 paths when $\gamma^w = 10^{-9}$ kg/s/m^3/MPa (Scenario #1) (up) and $\gamma^w = 10^{-6}$ kg/s/m^3/MPa (Scenario #3) (down).

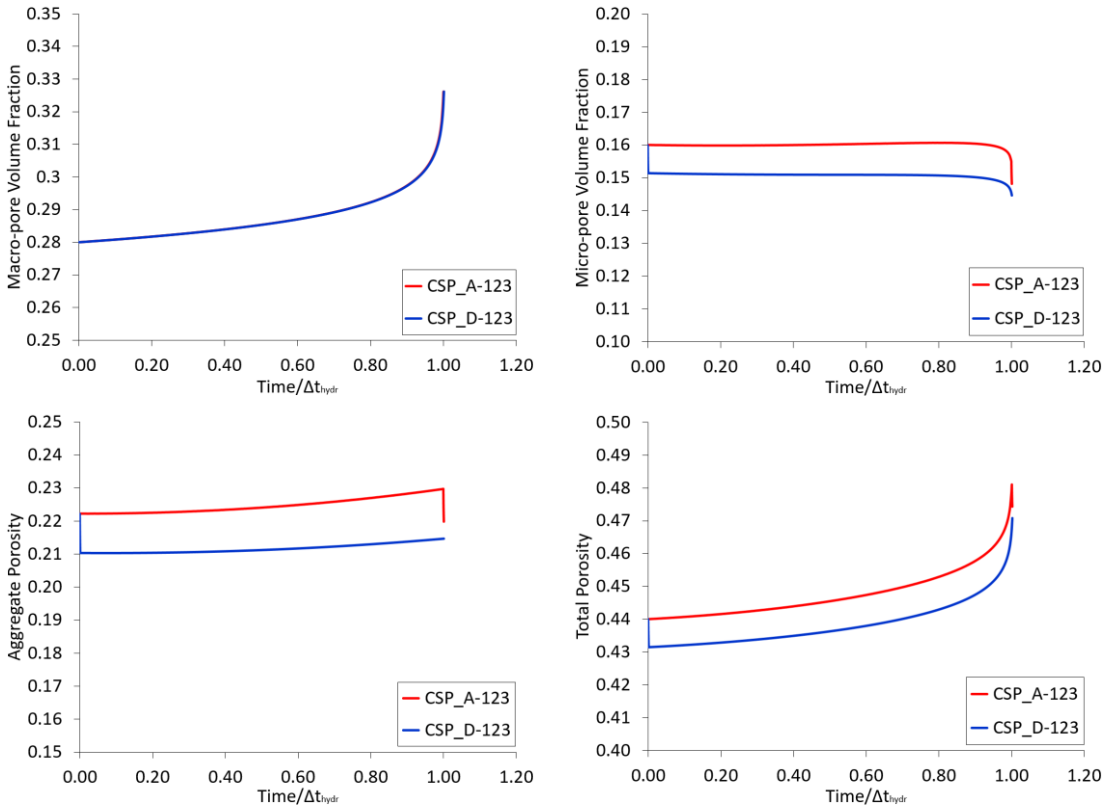

Figure 6-14: Comparison between the pore volume fractions (up) and the aggregate and total porosities (down) for the HM CSP_A-123 and CSP_D-123 paths when $\gamma^w = 10^{-9}$ kg/s/m^3/MPa.

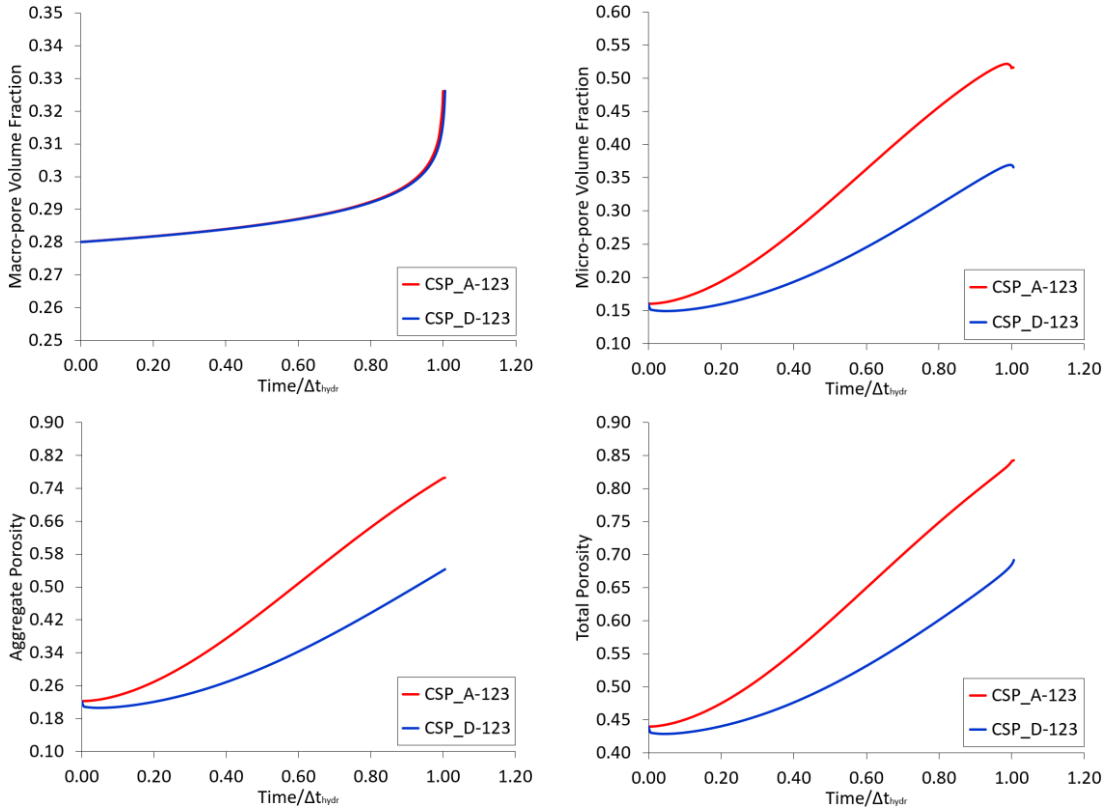

Figure 6-15: Comparison between the pore volume fractions (up) and the aggregate and total porosities (down) for the HM CSP_A-123 and CSP_D-123 paths when $\gamma^w = 10^{-6}$ kg/s/m^3/MPa.

A number of stress paths starting at different initial stress and suction values were also modelled. The role of the confining stresses on the swelling behaviour of an expansive soil during the hydration of its macrostructure is analysed through the modelling of wetting paths at three distinct levels of stresses (paths termed as CSP_A, CSP_B and CSP_C in Table 6-1). The evolution of macro and micro suctions, degree of saturations and porosities, the total mean and the saturated pre-consolidation pressures obtained from such calculations are plotted from Figure 6-16 to Figure 6-19. These numerical results correspond to Scenario #1 and Scenario #3, for an initial (macro and micro) suction of 123 MPa. As expected, a higher confining pressure (the CSP_C-123 path in the following graphs) leads to a lower development of the swelling potential of the cubic element of soil, which implies in a reduction of the hydration-induced swelling of microstructure (see Figure 6-17 and Figure 6-18). As mentioned previously, for a given amount of water exchanged between both pore levels, which is controlled by the value of γ^w the saturation state of micro-pores at the end of the macrostructural hydration is also determined by the magnitude of the changes in micro-porosity variables occurred during the macrostructural wetting process. Therefore, a more saturated microstructure is found for the CSP_C-123 path in Scenario #3, in which the saturation of macrostructure is performed at a higher mean stress value and the migration process of water from macro- to micro-pores is enhanced (see Figure 6-16). This apparently contradictory finding may be attributed to the higher density state of the microstructural water (ρ_{lm}) at the end of the macrostructural wetting in the CSP_C-123 path (see Figure 6-20). The evolution of the hardening parameter for the stress paths in Scenario #3, as plotted in Figure 6-19, indicate that all these wetting-loading paths occur at purely elastic conditions.

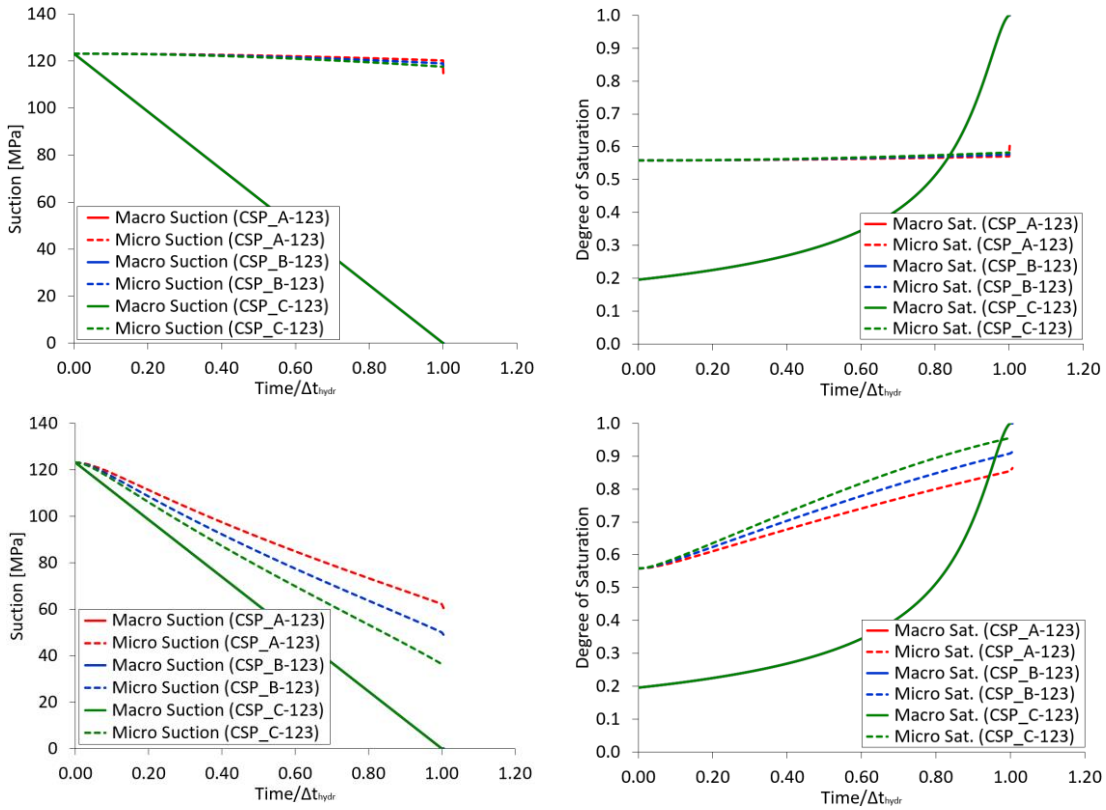

Figure 6-16: Evolution of suction (left) and degree of saturation (right) during the wetting at three confining stress levels when $\gamma^w = 10^{-9}$ kg/s/m^3/MPa (Scenario #1) (up) and $\gamma^w = 10^{-6}$ kg/s/m^3/MPa (Scenario #3) (down).

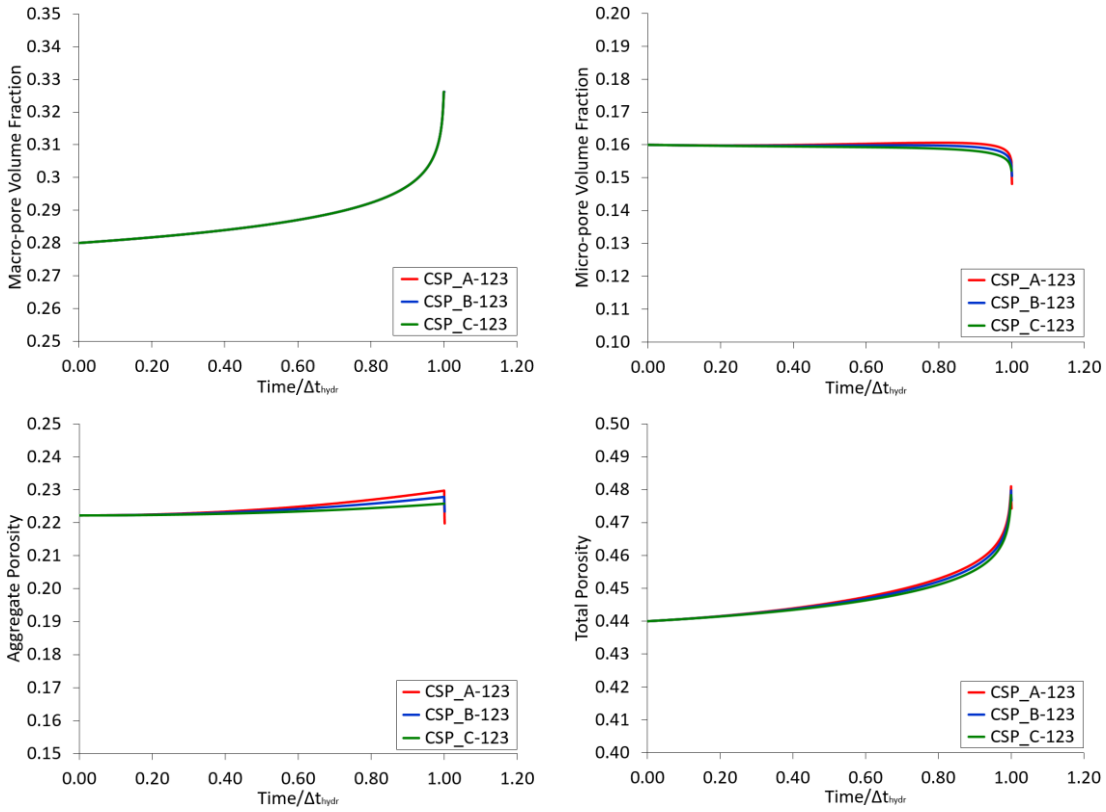

Figure 6-17: Evolution of the pore volume fractions (up) and the aggregate and total porosities (down) during the wetting at three distinct confining stress levels for Scenario #1.

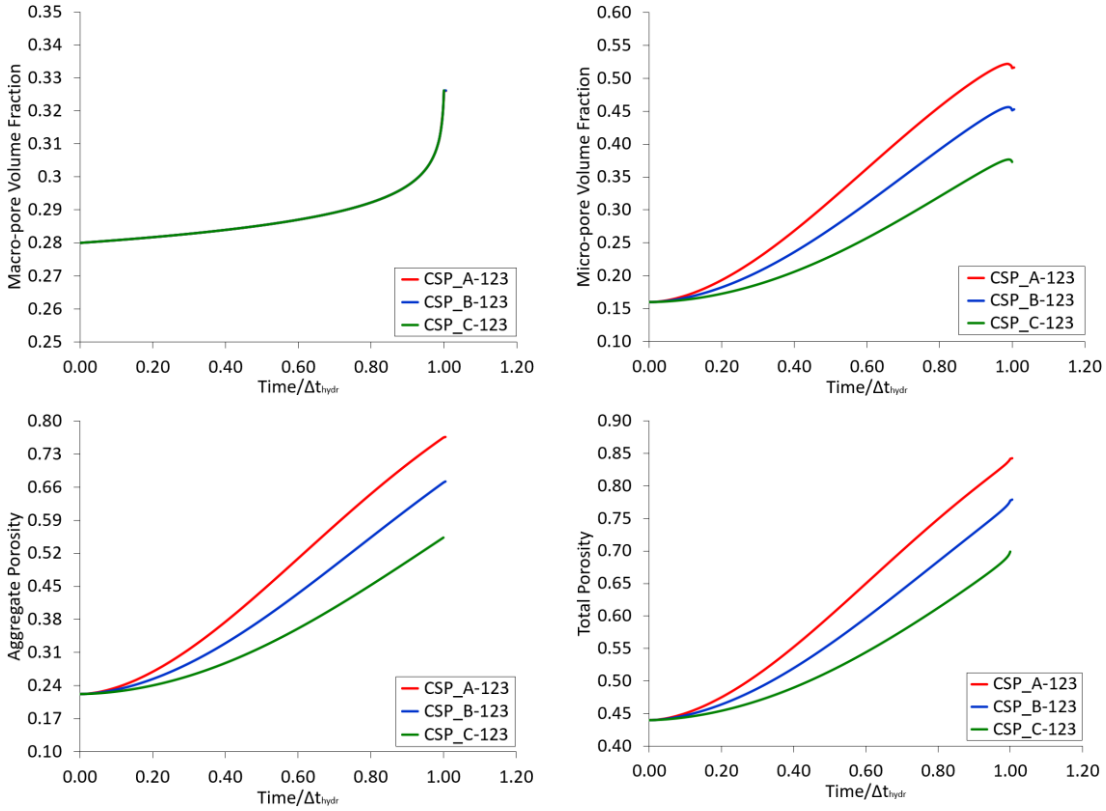

Figure 6-18: Evolution of the pore volume fractions (up) and the aggregate and total porosities (down) during the wetting at three distinct confining stress levels for Scenario #3.

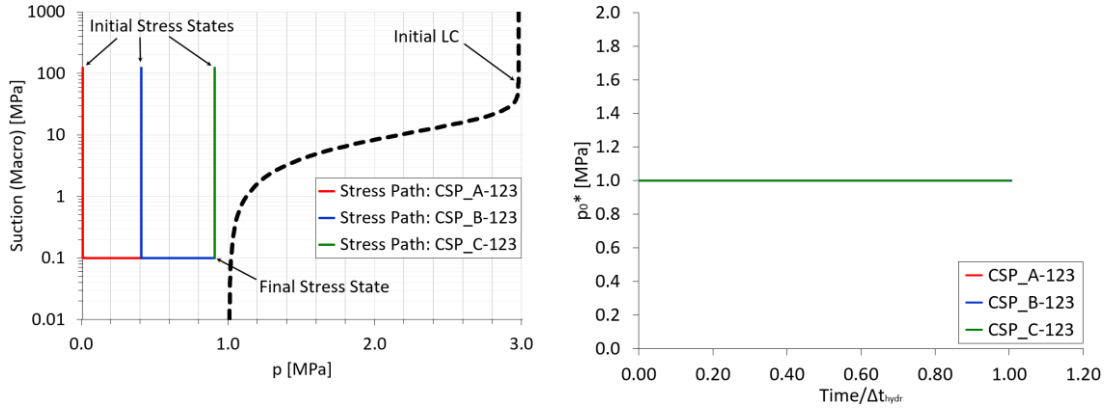

Figure 6-19: Wetting paths at distinct confining pressures in the p: s_M plane (left) and the evolution of the saturated pre-consolidation pressures (right) when $\gamma^w = 10^{-6}$ kg/s/m^3/MPa.

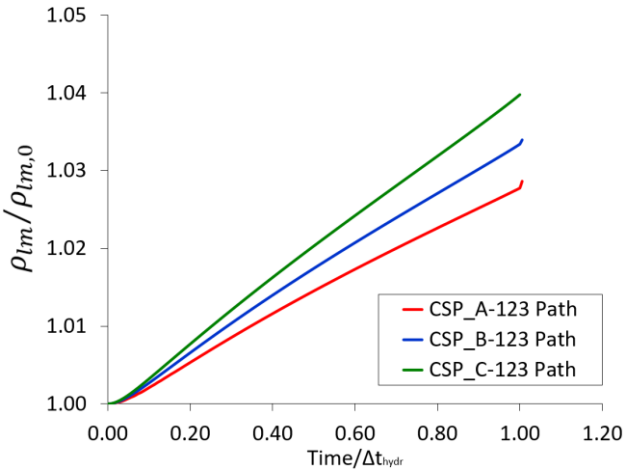

Figure 6-20: Evolution of the microstructural water density (ρ_{lm}) during the wetting at three distinct confining stress levels for Scenario #3.

For a same confining pressure level, three wetting paths were considered, each of them starting at a different suction value (123 MPa, 75 MPa and 25 MPa) and reaching a target macro suction value of 0.1 MPa at the end of the hydration phase (see Table 6-1). The modelling results taken from three of such HM paths (CSP_A-123, CSP_A-75 and CSP_A-25) are shown from Figure 6-21 to Figure 6-23. In each of them, the wetting was performed at a low and constant confining pressure of 0.1 MPa. The hydration-induced swelling of the cubic element of soil is reduced as the magnitude of the initial macro suction also reduces. In other words, the swelling deformation increases as the initial water content decreases. In that sense, all the porosity variables (micro, macro and total) in both structural media are larger for the CSP_A-123 path and lower for the HM CSP_A-25 path (see Figure 6-21 and Figure 6-22), in which the macro suction suffers a decrease of 123 MPa and 25 MPa, respectively (see Figure 6-23). Such a result is in agreement with the experimental conclusions on the swelling behaviour of bentonite-based materials compacted at the same density conditions, as reported in Villar and Lloret (2008). Moreover, the decrease in micro suction seems to be "proportional" to the variations in macro suction (at least, for Scenario #3). Nevertheless, the magnitude of these changes in microstructural suction could be also affected by the initial saturation state of micro-pores. In a more saturated microstructure (as in the CSP_A-25 path), the imbibition of water molecules into micro-pores is lesser than in a drier microstructure (as in the CSP_A-123 path), since the differences between the water potential in macro and micro media are lower in a wetting path that starts with an almost saturated microstructure. However, such a behaviour is strongly dependent on the shape of the water retention curves (for the macro and the micro media) used in calculations.

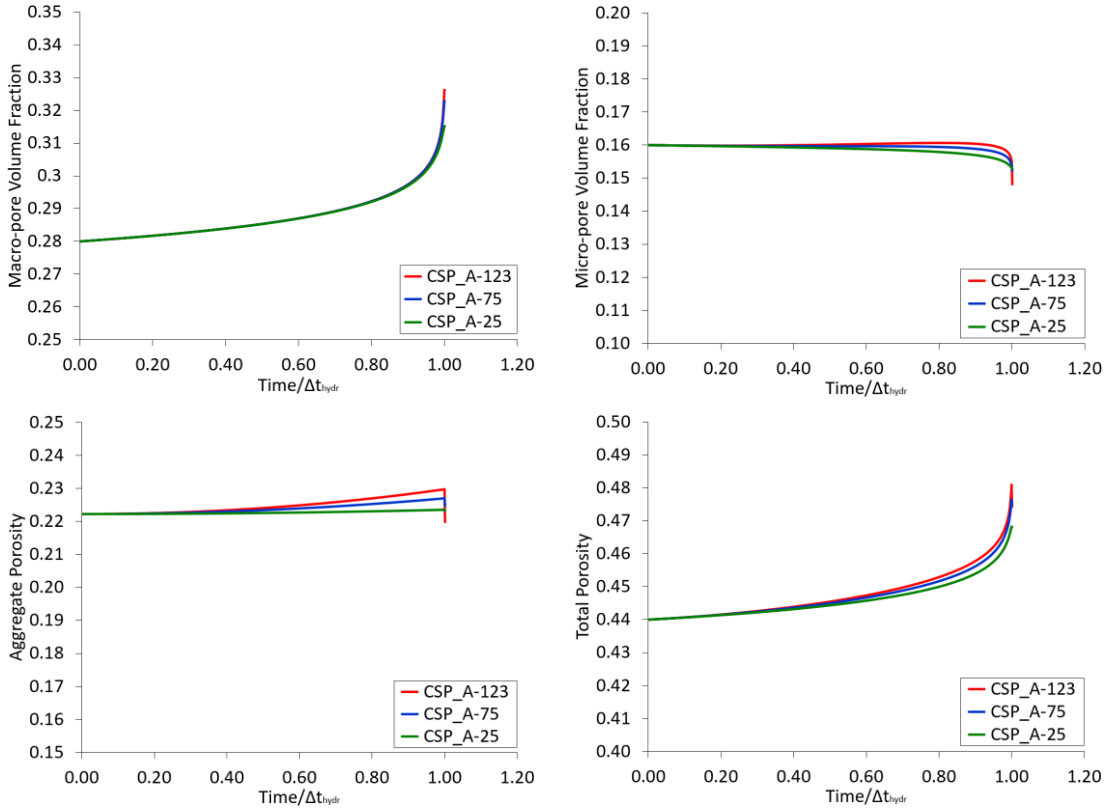

Figure 6-21: Evolution of the pore volume fractions (up) and the aggregate and total porosities (down) during the wetting under constant loading (0.1 MPa) starting at three distinct suction values when $\gamma^w = 10^{-9}$ kg/s/m³/MPa.

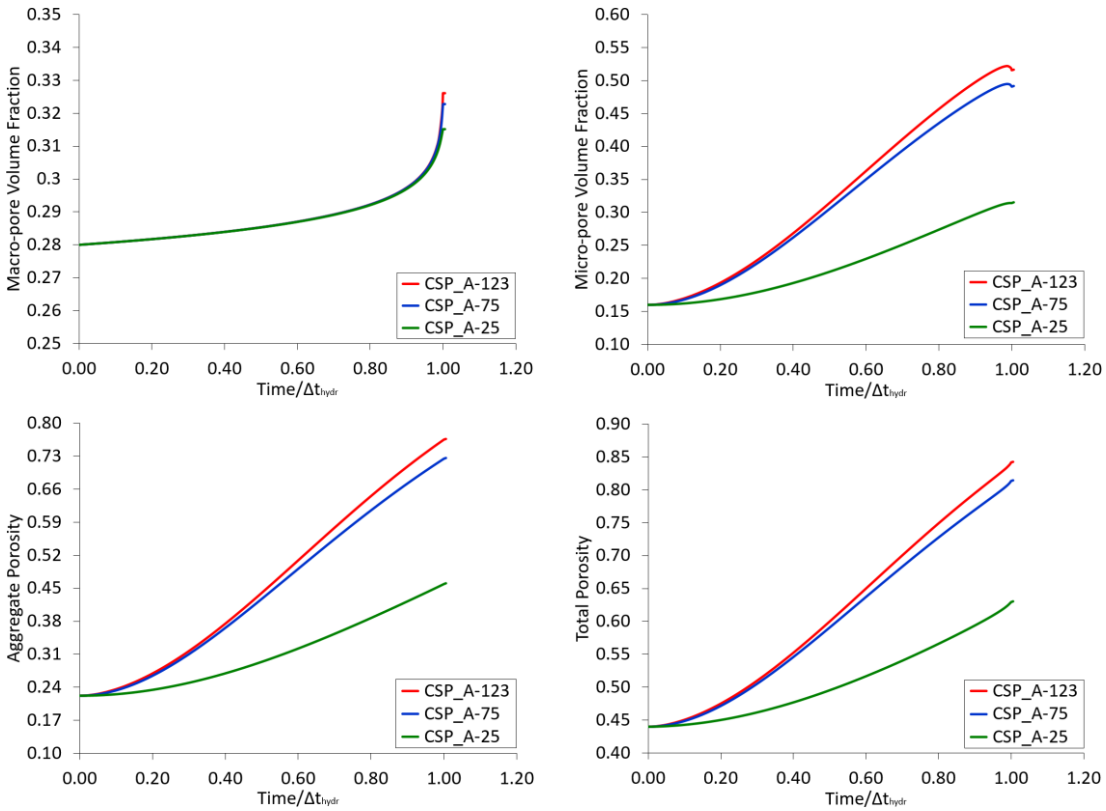

Figure 6-22: Evolution of the pore volume fractions (up) and the aggregate and total porosities (down) during the wetting under constant loading (0.1 MPa) starting at three distinct suction values when $\gamma^w = 10^{-6}$ kg/s/m³/MPa.

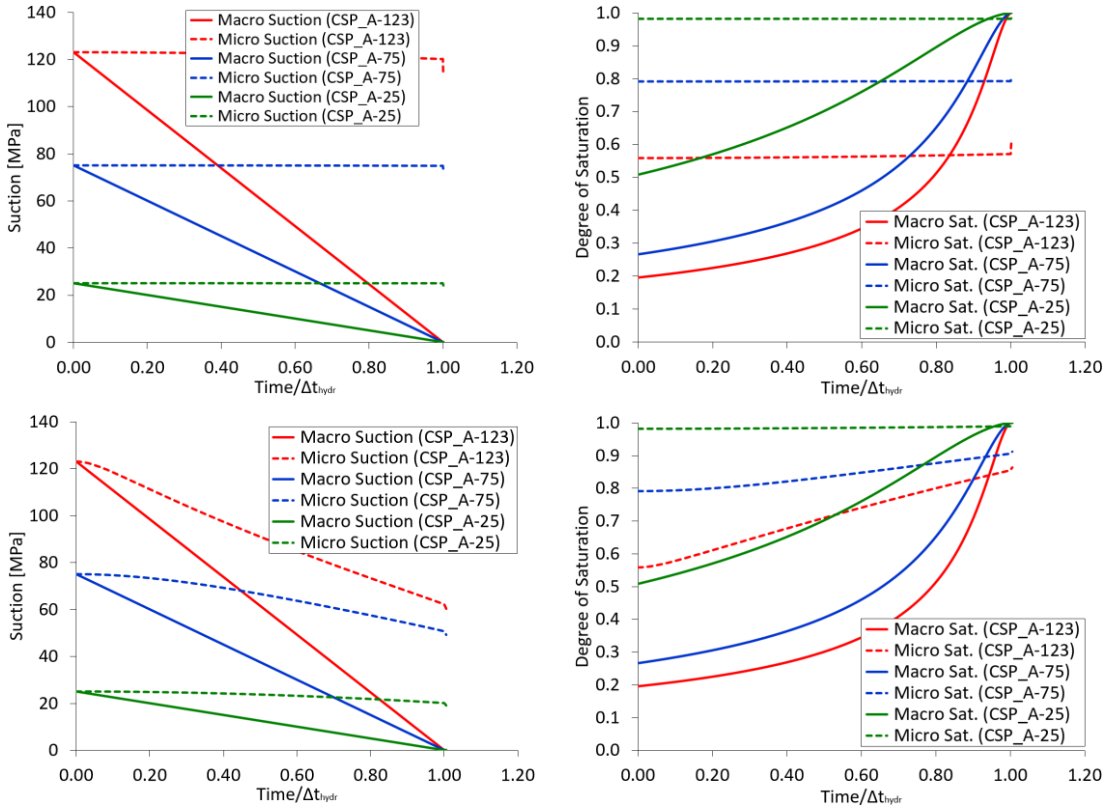

Figure 6-23: Evolution of suction and degree of saturation during the wetting under constant loading (0.1 MPa) starting at three distinct suction values, when $\gamma^w = 10^{-9}$ kg/s/m^3/MPa (up) and $\gamma^w = 10^{-6}$ kg/s/m^3/MPa (down).

Another important feature to keep in mind is the rate in which the re-saturation of macro-pores is performed. For a certain soil type and fabric, the time required to re-saturate a soil sample is also dependent on the type of fluid used and on the pressure at which such a fluid is injected into the porous medium. As discussed in **Section 2.4.3**, the flooding of a sample with liquid water injected at high-pressure characterizes a rapid wetting that only saturates the larger pores (Hoffmann, 2005). In contrast, the re-saturation of a bentonite material by the injection of water vapour is a much slower hydration procedure. However, in this situation, not only macro- but also micro-pores can be saturated (Hoffmann, 2005). Although the state of water (liquid water or vapour) used to re-saturate the soil affects the final saturation state of micro-pores, however, the micro-macro leakage parameter, γ^w, is only dependent on microstructural geometrical features (Alonso and Navarro, 2005), such as the distribution and degree of connectivity of micro-pores. The differences in the amount of microstructural water at the end of a hydration procedure with liquid water or vapour can be explained by the differences in the time required to reach the saturation of the larger pores and not necessarily by a dependence of the leakage coefficient on the type of fluid used to saturate both families of pores. Therefore, and besides the magnitude of the micro-macro water exchange coefficient, it is expected that the response of microstructure to the hydration of macrostructure is more noticeable for a slow hydration rate due to the longer period of interaction between both types of pore water (free and intra-aggregate water). A longer re-saturation process (a slower hydration rate) allows a greater amount of molecules of water to be transferred from macro- to micro-pores, which in turn, leads to a more saturated microstructure and to a significant reduction of suction at this pore level at the end of the wetting procedure. Consequently, the hydration-induced expansive deformations in such a structural medium tends to increase with hydration time and the total swelling of the soil tends to be higher for long-term wetting processes. However, if enough time is left after the

saturation of macrostructure, the water mass exchange mechanism keeps providing water to microstructure and, consequently, the swelling potential of the expansive material will develop as a result of the progressive re-saturaion of micro-pores. Such assertions can be easily checked by analyzing the graphs plotted from Figure 6-24 to Figure 6-27. It is important to re-emphasize that the hydro-mechanical behaviour described in the present section is elastic, purely volumetric and without any mechanical micro-macro coupling. Consequently, the development of the macro-pore volume fraction is not affected by the hydration process of micro-pores or by the degree of expansion of the microstructure. It only depends on the changes in the HM loading applied to the cubic sample of expansive soil (see Figure 6-25).

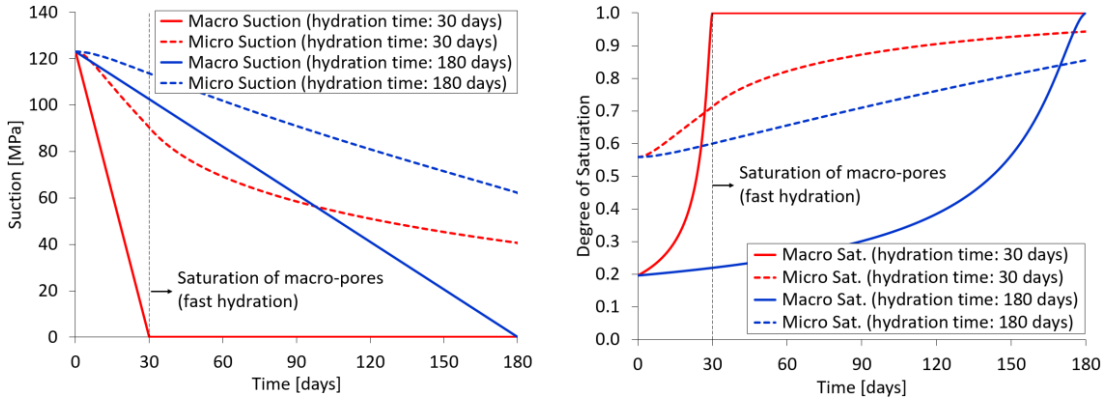

Figure 6-24: Evolution of suction and degree of saturation during the wetting-loading path (CSP_A-123) at distinct hydration rates when $\gamma^w = 10^{-6}$ kg/s/m^3/MPa.

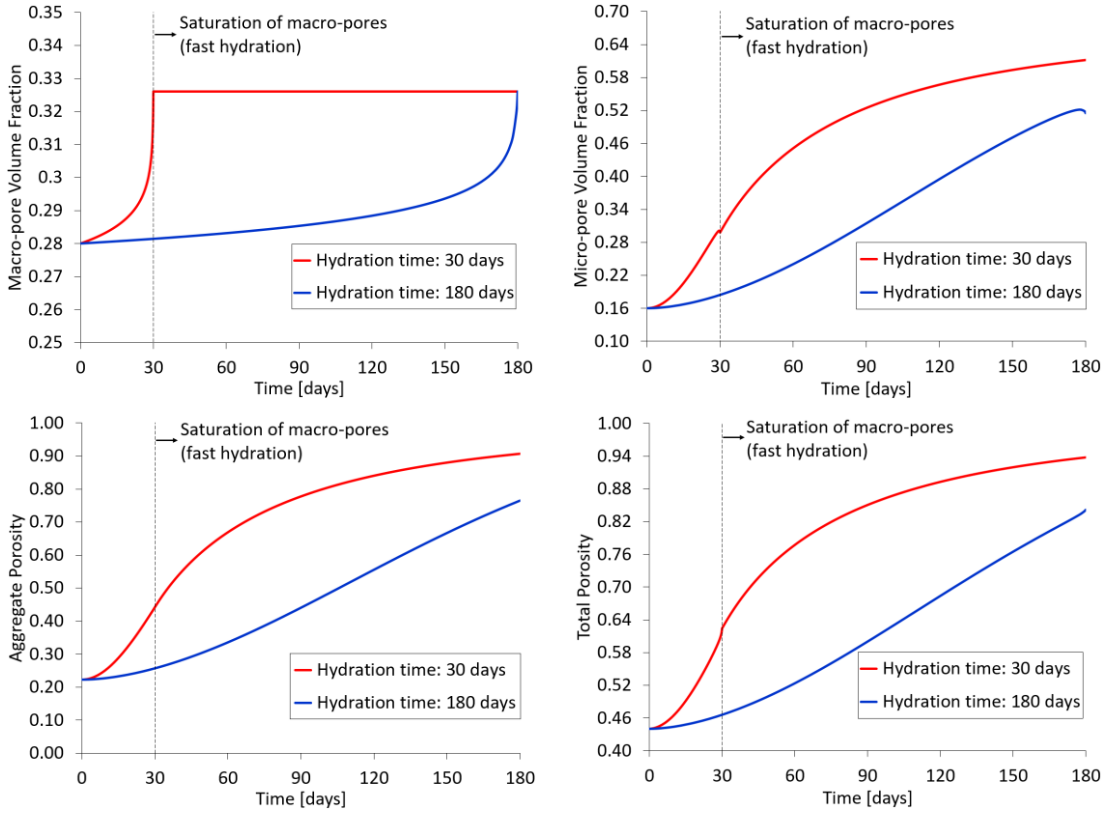

Figure 6-25: Evolution of pore-volume fractions (up) and porosities (down) during the wetting-loading path (CSP_A-123) at distinct hydration rates when $\gamma^w = 10^{-6}$ kg/s/m^3/MPa (Scenario #3).

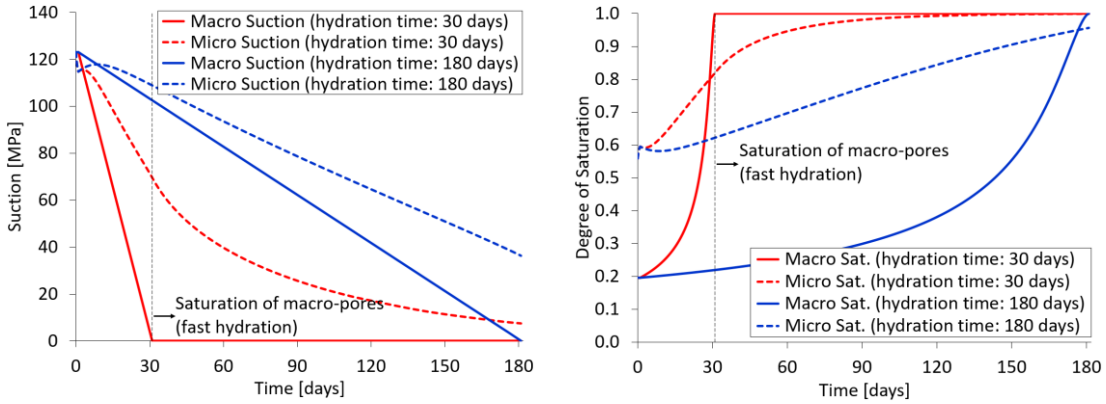

Figure 6-26: Evolution of suction and degree of saturation during the loading-wetting path (CSP_D-123) at distinct hydration rates when $\gamma^w = 10^{-6}$ kg/s/m^3/MPa (Scenario #3).

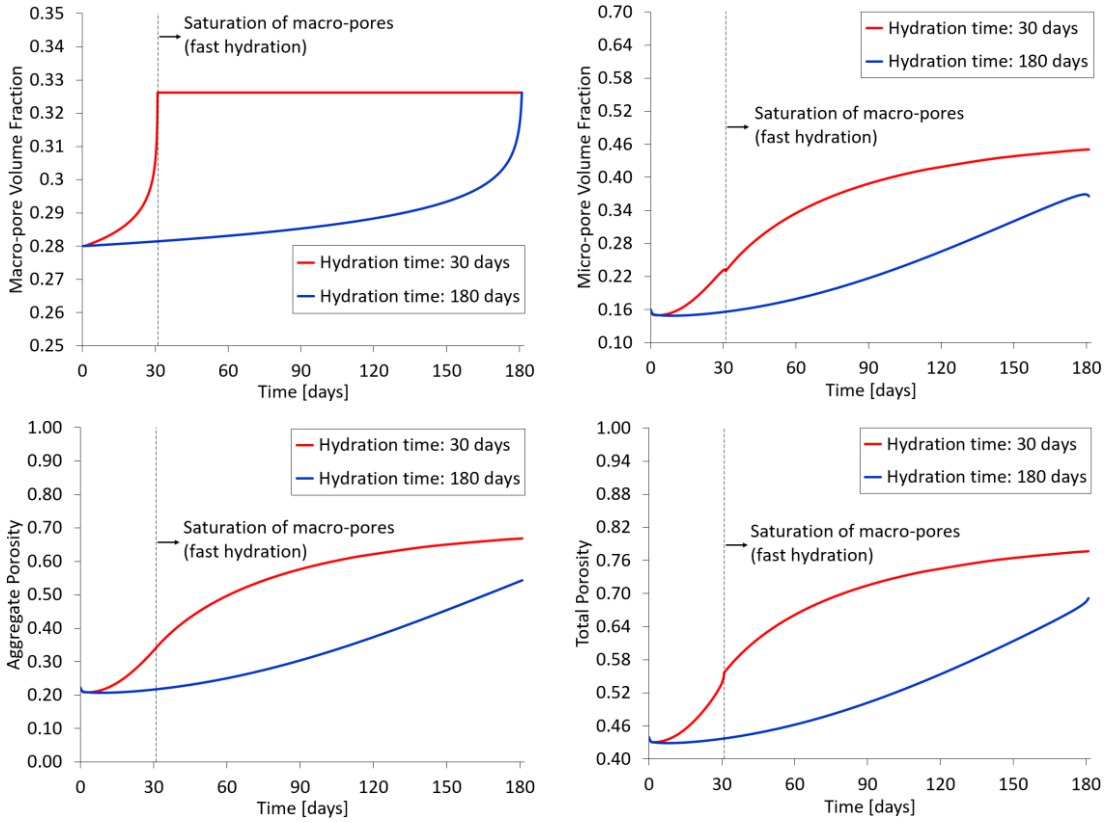

Figure 6-27: Evolution of pore-volume fractions (up) and porosities (down) during the loading-wetting path (CSP_D-123) at distinct hydration rates when $\gamma^w = 10^{-6}$ kg/s/m^3/MPa (Scenario #3).

6.3.2. ANALYSES WITH THE β-MECHANISM ACTIVATED

The most noticeable consequence of the activation of the mechanical micro-macro coupling mechanism (by means of a convenient choice of a non-zero interaction function, f_β) is the occurrence and evolution of macrostructural plastic deformations, even when the stress path is inside the yield surface delimited by the loading-collapse mechanism (BBM plastic mechanism). As explained previously, such plastic strains arise from the inter-aggregate rearrangements due to microstructural deformations. Moreover, it has been assumed that the mechanical

microstructural behaviour is not affected by macrostructural deformations, at least not in an explicit way. Therefore, it is expected that the activation of the plastic β-mechanism only exerts influence on the mechanical behaviour of macrostructure. In other words, in a wetting path under constant loading, the mechanical coupling between both structural levels affects mainly the evolution of "macro-porosity" and other mechanical variables related to the elastoplastic response of the expansive soil, such as the saturated pre-consolidation pressure. In such a situation, the hydraulic behaviour is not expected to differ considerably from the situation in which the mechanical micro-macro coupling is not considered. The modelling results plotted from Figure 6-28 to Figure 6-31 corroborate such expectations. These outcomes are taken from the numerical simulation for two stress paths (CSP_A-123 and CSP_D-123), with the hydraulic micro-macro coupling represented by Scenario #3 ($\gamma^w = 10^{-6}$ kg/s/m^3/MPa) and for distinct interaction function shapes (see Table 6-8 and Figure 6-6). In order to evaluate the impact of the activation of the plastic micro-macro coupling process on the elastoplastic response of the soil skeleton, an auxiliary macro-porosity variable ($\Delta\bar{\phi}_{M,\beta}$) is defined as the difference between the macro-pore volume fractions in wetting paths with the β-mechanism activated ($\bar{\phi}_{M,\beta}$) and when such a plastic mechanism is deactivated ($\bar{\phi}_M^e$), that is, $\Delta\bar{\phi}_{M,\beta} = \bar{\phi}_{M,\beta} - \bar{\phi}_M^e$. The evolution of this macro-porosity variable for the stress paths CSP_A-123 and CSP_D-123 is given by the curves plotted in Figure 6-32. These curves are obtained directly from the graphs of macro-pore volume fraction in Figure 6-29 and Figure 6-30, with $\bar{\phi}_M^e$ taken as the macro-porosity variable arising from the numerical calculations performed with the strictly null coupling functions (Functions #1 in Table 6-8).

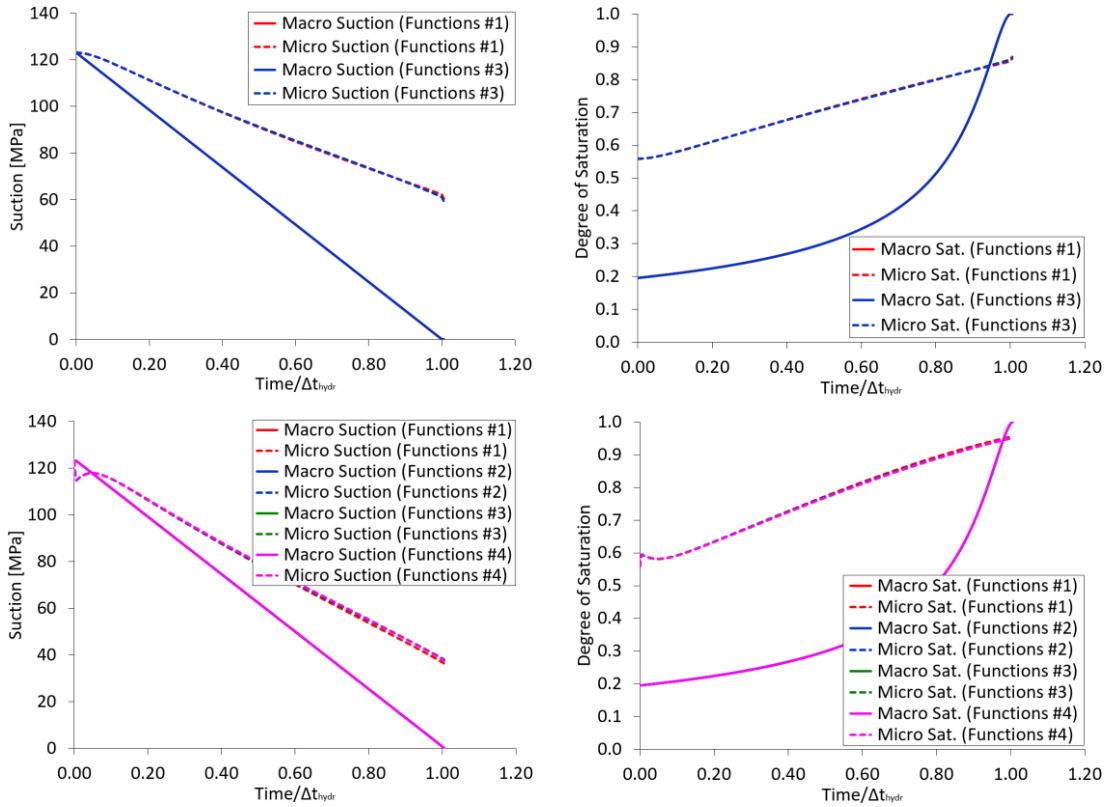

Figure 6-28: Evolution of suction and degree of saturation in the CSP_A-123 (up) and CSP_D-123 (down) paths for distinct micro-macro interaction functions and when $\gamma^w = 10^{-6}$ kg/s/m^3/MPa (Scenario #3).

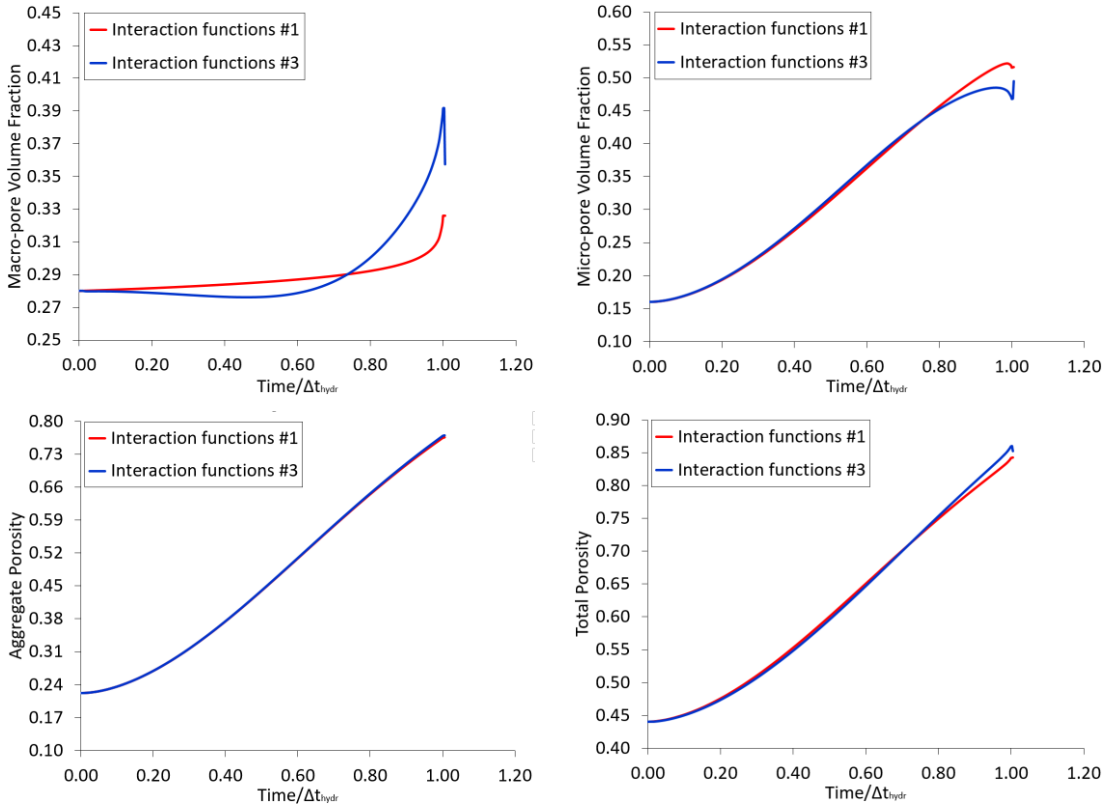

Figure 6-29: Evolution of suction and degree of saturation in the wetting path CSP_A-123 (confining pressure of 0.1 MPa) for distinct micro-macro interaction functions and when $\gamma^w = 10^{-6}$ kg/s/m^3/MPa (Scenario #3).

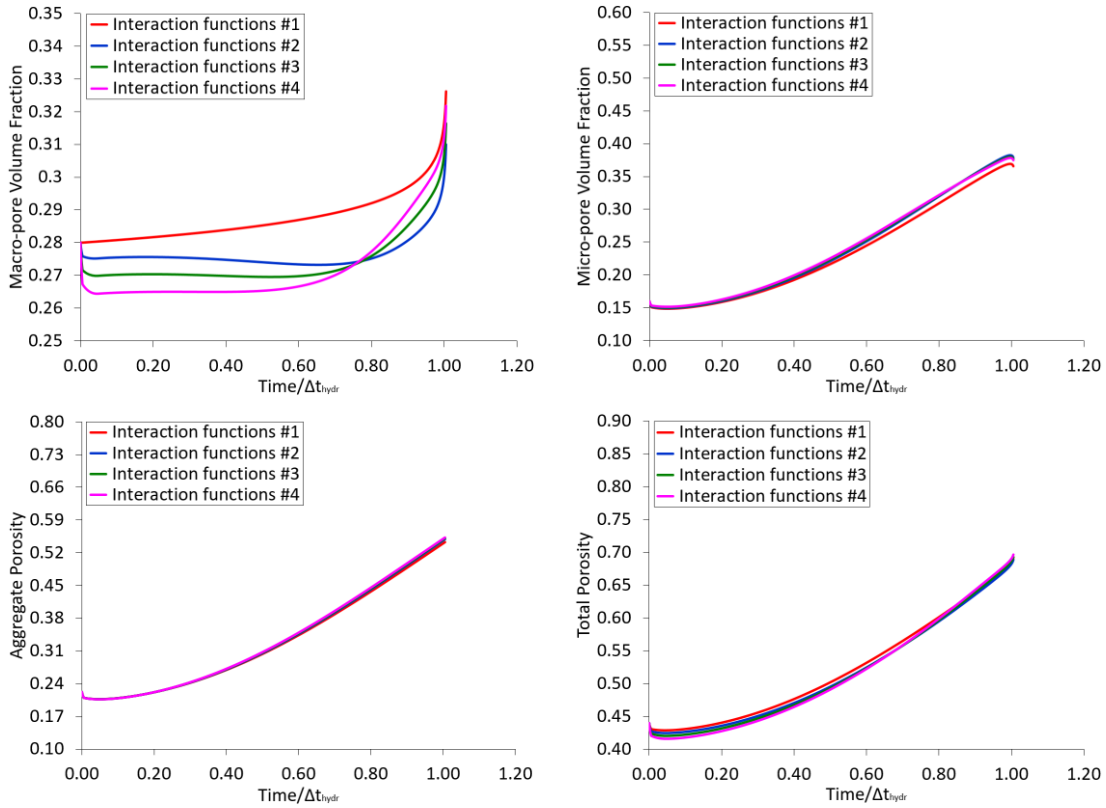

Figure 6-30: Evolution of suction and degree of saturation in the wetting path CSP_D-123 (confining pressure of 1.0 MPa) for distinct micro-macro interaction functions and when $\gamma^w = 10^{-6}$ kg/s/m^3/MPa (Scenario #3).

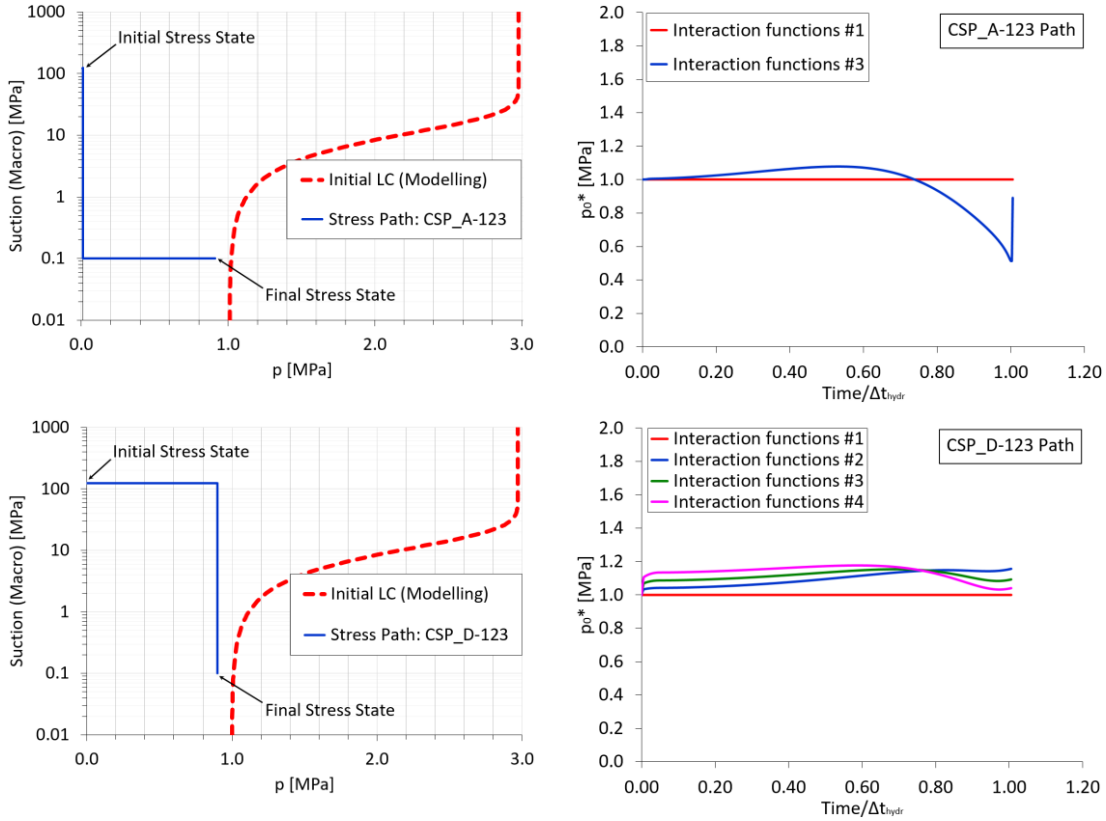

Figure 6-31: CSP_A-123 (up) and CSP_D-123 (down) paths plotted in the p: s_M plane (left) and the evolution of the saturated pre-consolidation pressures (right) for distinct micro-macro interaction functions and when $\gamma^w = 10^{-6}$ kg/s/m^3/MPa (Scenario #3).

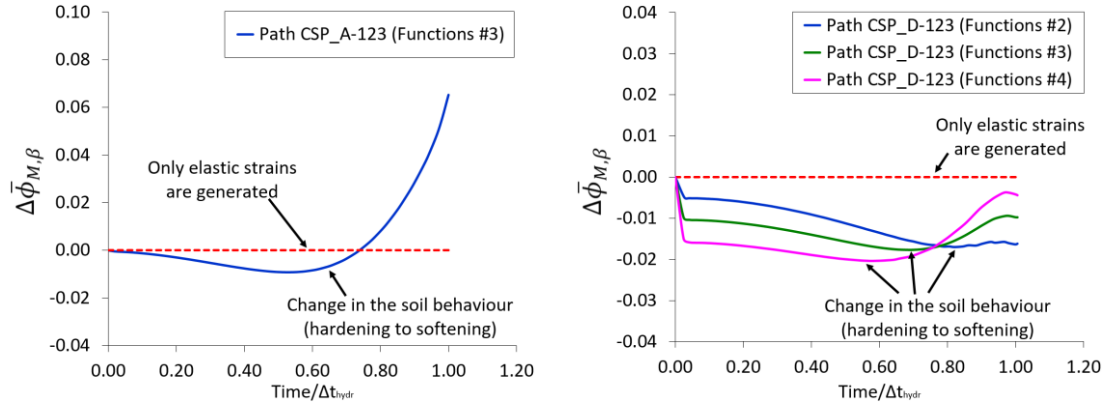

Figure 6-32: Hardening and softening response of the soil skeleton in the wetting paths CSP_A-123 (left) and CSP_D-123 (right) for distinct micro-macro interaction functions and when $\gamma^w = 10^{-6}$ kg/s/m^3/MPa. The curves for the evolution of $\Delta\bar{\phi}_{M,\beta}$ when the β-mechanism is not activated (Functions #1 in Table 6-8) are also drawn (dashed lines).

As expected, the wetting of the cubic element of expansive soil presents significant differences in the development of the inter-aggregate "porosity" ($\bar{\phi}_M$), which reflect the impact of the mechanical structural coupling on the deformation response of macrostructure (as shown in Figure 6-29 and Figure 6-30). Discrepancies in the macro-pore volume fractions are due to the magnitude of the plastic deformations generated during wetting, which depends on the shape of the interaction functions adopted in calculations. Such a macrostructural rearrangement is accompanied by the evolution of the hardening parameter, as illustrated in Figure 6-31. Furthermore, the magnitude of the confining stress level applied on the soil sample during the

wetting phase plays an important role on its (plastic) swelling behaviour. It can be noted that the wetting process in the CSP_A-123 path, performed at a confining pressure of 0.1 MPa, induces a material softening, evidenced by the pronounced (global) swelling as macro-pores become more and more saturated. Such a softening response starts when the macro suction is reduced, at least, to half of its initial value (see Figure 6-32 and the graph plotted in the upper-right corner in Figure 6-31). For the CSP_D-123 path, wetting is performed at a higher value of confining pressure and no considerable softening is observed, as shown by the curves plotted on the right-hand side of Figure 6-32. Moreover, the volumetric compression of the cubic volume of expansive soil seems to be more sensitive to the increase in the confining pressure when that load increment is carried out for a saturated macrostructure (CSP_A-123 path) and less sensitive to such changes in the mechanical loading when it is applied before hydrating macro-pores (CSP_D-123 path). In both stress paths, increments in the total mean pressure causes a reduction of macro-porosity. The differences in the deformation response of the expansive soil to changes in the external applied stresses could be a consequence of a more open structure of the saturated macrostructure in the CSP_A-123 path during the mechanical loading step, which would make this porous structure more susceptible to suffer a reduction in the volume of macro voids. Furthermore, the performance of hydration under the larger applied mechanical loading in the CSP_D-123 path diminishes substantially the swelling potential of the soil sample, which can be easily confirmed by comparing the evolution of the pore volume fractions and porosities in Figure 6-29 and in Figure 6-30.

In contrast, the evolution of the intra-aggregate porosity (the aggregate porosity, ϕ_m) is not affected by the activation of the plastic coupling mechanism because it only depends on the changes in the microstructural mean effective stresses, p_m, as discussed in **Section 5.2.9**. This effective stress is strongly dependent on the changes in the microstructural fluid pressures (see Equation (5-103)), which in turn, are driven by the water mass transfer mechanism between both structural media and not (necessarily) by the activation of the mechanical coupling mechanism (see Figure 6-28). However, the micro-pore volume fraction, $\overline{\phi}_m$, is affected by the shape and magnitude of the interaction functions (see its evolution in the corresponding graphs plotted in Figure 6-29 and Figure 6-30). The global tendency of the soil sample is to swell during wetting and to contract during the increase in the external confining stresses. Since $\overline{\phi}_m$ is related to the total volume of the soil sample, such dependence explains the differences in the evolution of this porosity variable with the micro-macro coupling functions chosen in the numerical simulations.

Despite the theoretical assumption that macrostructural deformations do not affect the strain state at microstructure, however, indirect effects due to the fully coupled thermo-hydro-mechanical (THM) approach and the micro-macro coupling mechanisms are considered in the present double-porosity formulation. In other words, the macrostructural rearrangement of the expansive particles and aggregates could lead to a “mechanical” wetting of macro-pores and consequently, to significant changes in macrostructural suction. The micro-macro water mass exchange would generate a change (although reduced) in micro suction, which could induce an increment of the microstructural swelling. It could be the case of a structural collapse in an open and unstable macrostructure subjected to wetting at high confining pressures.

6.4. DRYING AT CONSTANT CONFINING PRESSURE

The model capabilities in reproducing the response of expansive materials submitted to episodes of moderate and intense drying were also considered. In that sense, and following a similar strategy adopted during the modelling of the wetting paths addressed in the previous section, several drying paths starting at different water contents and performed under distinct confining pressures were analysed, as the ones described in Table 6-1 by the set of paths termed as CSP_E, CSP_F, CSP_G and CSP_H. Again, the impact of the mechanical coupling between microstructure and macrostructure is evaluated by means of the deactivation/activation of such a plastic mechanism in the numerical simulations. All the drying paths were chosen so that the plastic loading-collapse (LC) mechanism could not be activated during the drying step or during the increase in the confining mean stresses. Moreover, the drying process of macro-pores was simulated by the prescription (at all nodes) of a decrease in the pore-water pressure, from its initial (negative) value until a target value of -250 MPa. This macro-suction increment was performed at different dehydration rates by assuming that the drying of macro-pores lasted between 30 days and 720 days. The more important results from these model sensitivity analyses are presented and discussed in the following sections.

6.4.1. ANALYSES WITH THE β-MECHANISM DEACTIVATED

The deactivation of the mechanical micro-macro coupling mechanism together with the development of a stress path inside the region defined by the initial LC curve inhibit the generation of plastic deformations during the dehydration of the expansive material. In such conditions, it is expected that the drying process only causes reversible volumetric shrinkage in the soil mass, since the hardening parameter of the model is kept unchanged during the hydraulic/mechanical loading. The main outcomes from the numerical modelling of two drying paths under constant mechanical loading (CSP_E-75 and CSP_H-75) and for two distinct pore-water mass exchange conditions have confirmed such a conclusion, as illustrated in Figure 6-33. The evolution of micro and macro suctions, degrees of saturation, porosities and pre-consolidation pressures for such stress paths are also displayed in Figure 6-34 and Figure 6-35. These model predictions are plotted using a standardized time variable, given by the ratio between the current time and the time chosen to dry the macro-pores (Δt_{dehydr}). The two hydraulic micro-macro coupling scenarios considered in simulations are characterized by leakage coefficients equal to 10^{-9} kg/s/m^3/MPa and 10^{-7} kg/s/m^3/MPa, which correspond to Scenario #1 and Scenario #2 (see Table 6-9), respectively. In the following model results, the dehydration period (Δt_{dehydr}) is equal to 720 days for Scenario #1 and 90 days for Scenario #2.

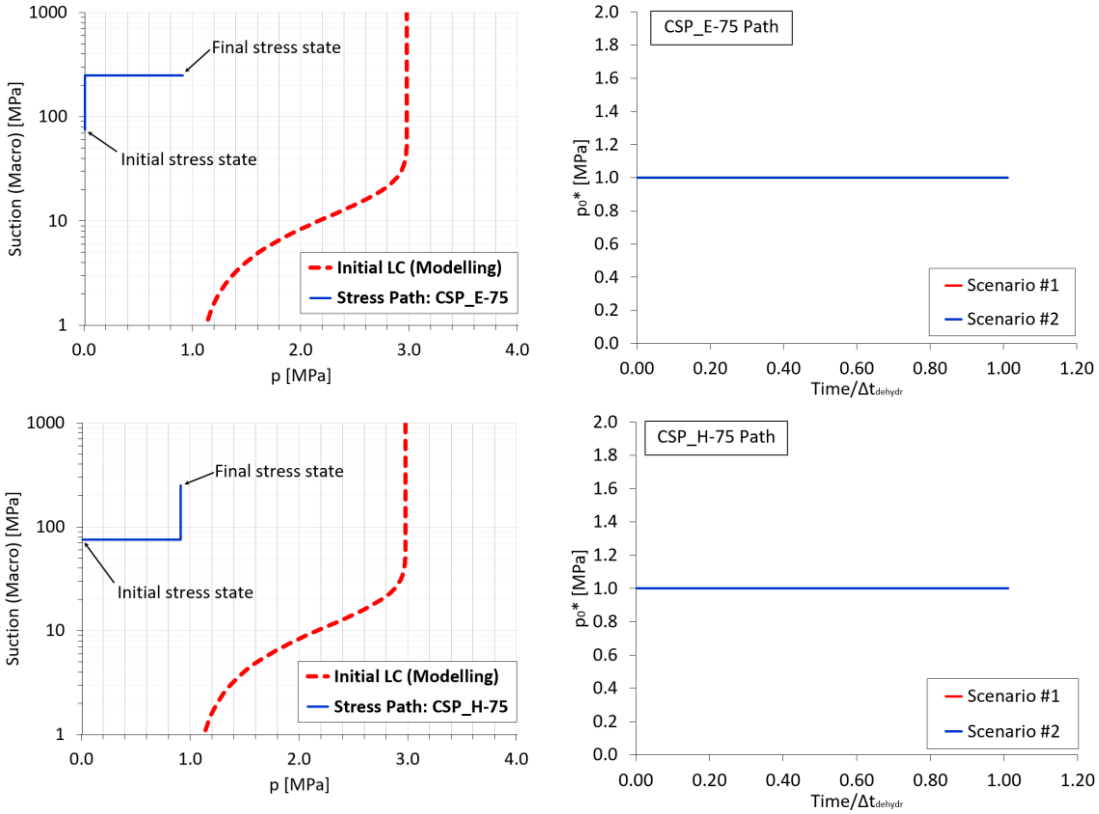

Figure 6-33: CSP_E-75 (up) and CSP_H-75 (down) paths plotted in the p: s_M plane (left) with the the evolution of the saturated pre-consolidation pressures (right) when $\gamma^w = 10^{-9}$ kg/s/m^3/MPa (Scenario #1) and $\gamma^w = 10^{-7}$ kg/s/m^3/MPa (Scenario #2).

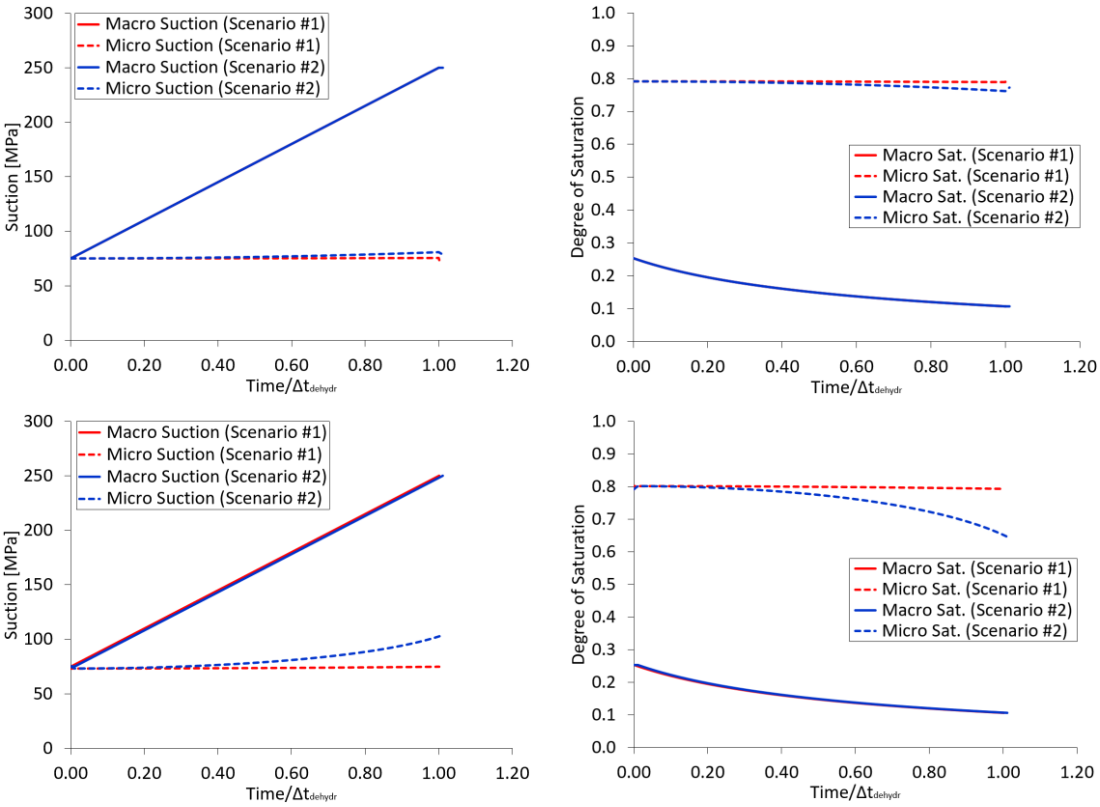

Figure 6-34: Evolution of suction and degree of saturation for the drying CSP_E-75 (up) and CSP_H-75 (down) paths when $\gamma^w = 10^{-9}$ kg/s/m^3/MPa (Scenario #1) and $\gamma^w = 10^{-7}$ kg/s/m^3/MPa (Scenario #2).

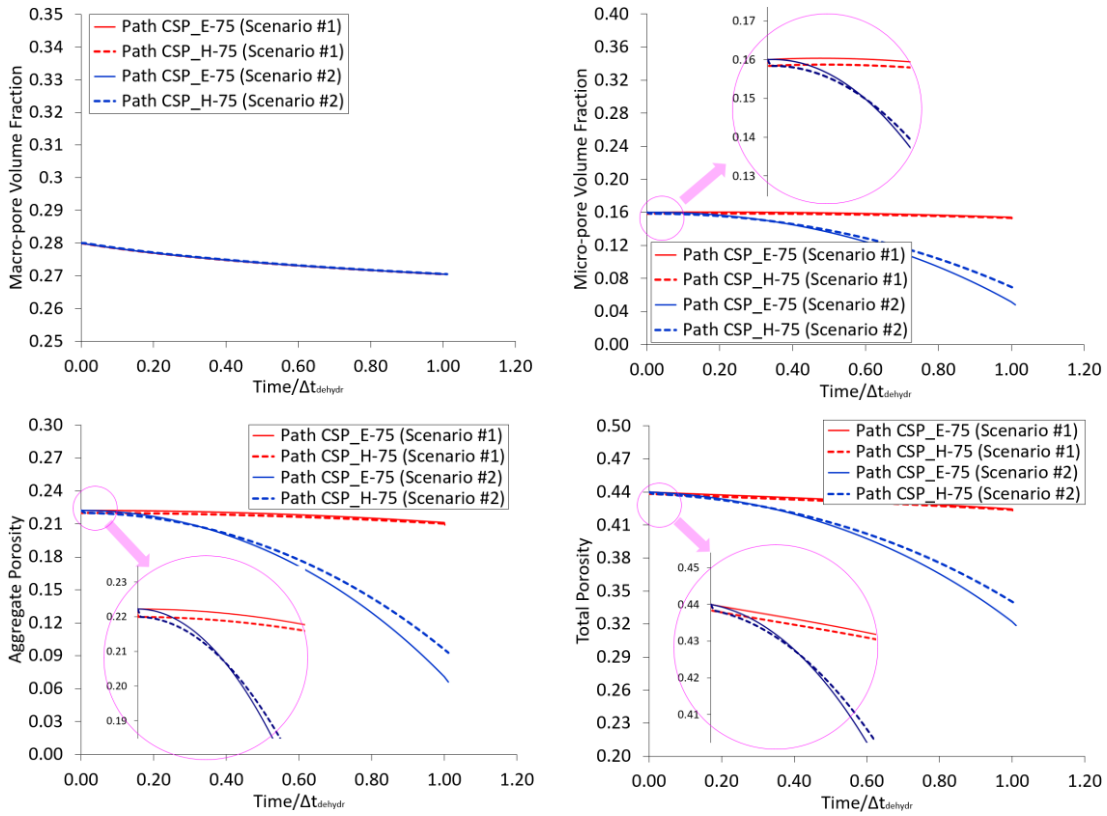

Figure 6-35: Comparison between the pore volume fractions (up) and the aggregate and total porosities (down) obtained from the drying CSP_E-75 and CSP_H-75 paths when $\gamma^w = 10^{-9}$ kg/s/m^3/MPa & $\gamma^w = 10^{-7}$ kg/s/m^3/MPa.

According to such results, the desiccation of microstructural pores is more noticeable for Scenario #2 (as expected) and when the drying process is conducted at a high confining pressure (CSP_H-75 path), as illustrated by the development of suctions and degrees of saturation in Figure 6-34. The drying process under "free" volume conditions tends to cause a global shrinking of the soil element. The desaturation of macro voids induces an increase in the capillary forces between adjacent soil particles, which leads to a resultant attractive force between them. If the relative distances between the soil particles and aggregates are reduced, the soil volume will shrink locally, resulting in a reduction of the macro-pore volume fraction. When the drying process develops in the context of purely volumetric elastic conditions – as assumed in the present section – such a decrease in porosity occurs without reorientation of soil particles nor irreversible collapse in open soil structures. In addition, the hydraulic coupling between micro and macro porous media generates an exchange of water from micro- to macro-pores, which conducts to the dehydration of microstructure. As a result, the clay aggregate also tends to shrink due to the decrease in the intra-aggregate porosity caused by the "removal" of the inter-particle and the inter-layer water. The combined effect of these two drying-induced decreasing in porosity produces a global contraction of the expansive soil. The evolution of the pore-volume fractions and porosities for the paths CSP_E-75 and CSP_H-75 shown in Figure 6-35 demonstrates the ability of the current double-porosity formulation in reproducing the contractive soil response during drying. Nevertheless, the accumulated decrease in the micro-pore volume fraction and in the aggregate and total porosities is somewhat higher for the CSP_E-75 path, where the element of soil was firstly dried at a constant load of 0.1 MPa and then, it was loaded isotropically until reaching a final confining pressure of 1.0 MPa. In the CSP_H-75 path, the cubic element of soil was dried under a confining pressure of 1.0 MPa, after being submitted to a previous mechanical loading (see the stress paths in Figure 6-33). Such

differences in the deformation response may be a consequence of the distinct compression state of microstructure under drying at constant loading conditions. In fact, the desaturation process starts at a lower microstructural porosity in the CSP_H-75 path due to the initial compression imposed to the clay aggregates in the beginning of this drying path. The higher stress level applied during the drying CSP_H-75 path affects the evolution of the local microstructural suction (see Figure 6-34)and, consequently, the exchange of water molecules from micro- to macro-pores. The microstructural desaturation process induced by the water mass transfer mechanism is more significant in the CSP_E-75 path due to the larger difference in the local water potential. Consequently, the microstructural volumetric contraction predicted at the end of the drying process is lower for the CSP_H-75 path and higher for the CSP_E-75 path (see Figure 6-35). Therefore, the changes in the degree of saturation of microstructure (and, consequently, in the microstructural suctions) are lower for the CSP_E-75 path (see Figure 6-34) although the micro-macro water exchange process promotes the transfer of a considerable amount of water from micro- to macro-pores (as suggested by the evolution of $\bar{\phi}_m$, for instance). In general terms, the expected reduction in the saturation state of microstructure induced by the dehydration of macro-pores is hidden by the volumetric shrinkage of micro-pores (and of the porous medium as a whole). In fact, the changes in the microstructural saturation in the drying paths considered in this section seem to be much more affected by the deformation response of microstructure than by the water mass exchanged between both structural media.

The dependence of the HM behaviour of the expansive soil element during the dehydration of macro-pores on the initial confining pressures was investigated by following three drying paths performed at constant isotropic loadings of 0.1 MPa (CSP_E-75), 0.5 MPa (CSP_F-75) and 1.0 MPa (CSP_G-75). After reaching the final macro suction (250 MPa), the confining pressures were increased in the HM CSP_E-75 and CSP_F-75 paths from their initial values until 1.0 MPa. The modelling results obtained from such numerical analyses and shown in Figure 6-36 and Figure 6-37 confirm the tendency of reduction of the contractive response (with a subsequent increase in the desaturation state of microstructure) with the increase of the confining pressures for which the drying process is performed.

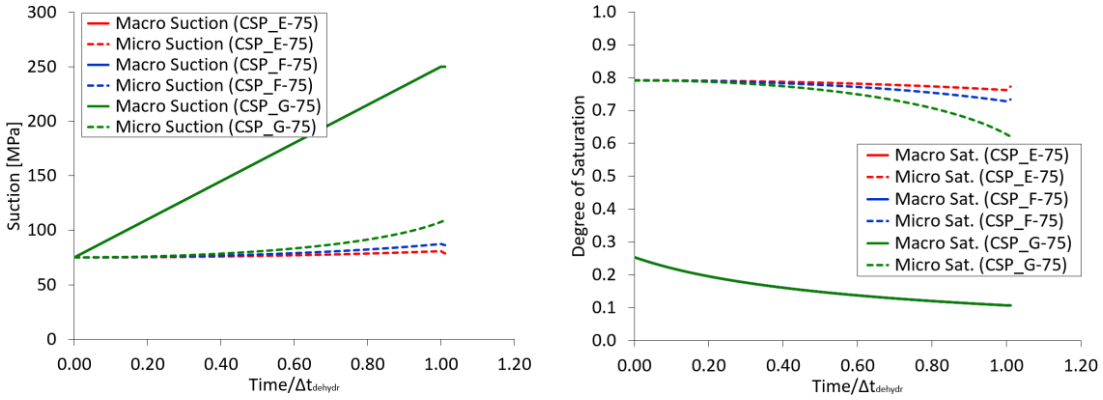

Figure 6-36: Evolution of suction and degree of saturation in drying-loading paths starting at distinct confining pressures when $\gamma^w = 10^{-7}$ kg/s/m^3/MPa.

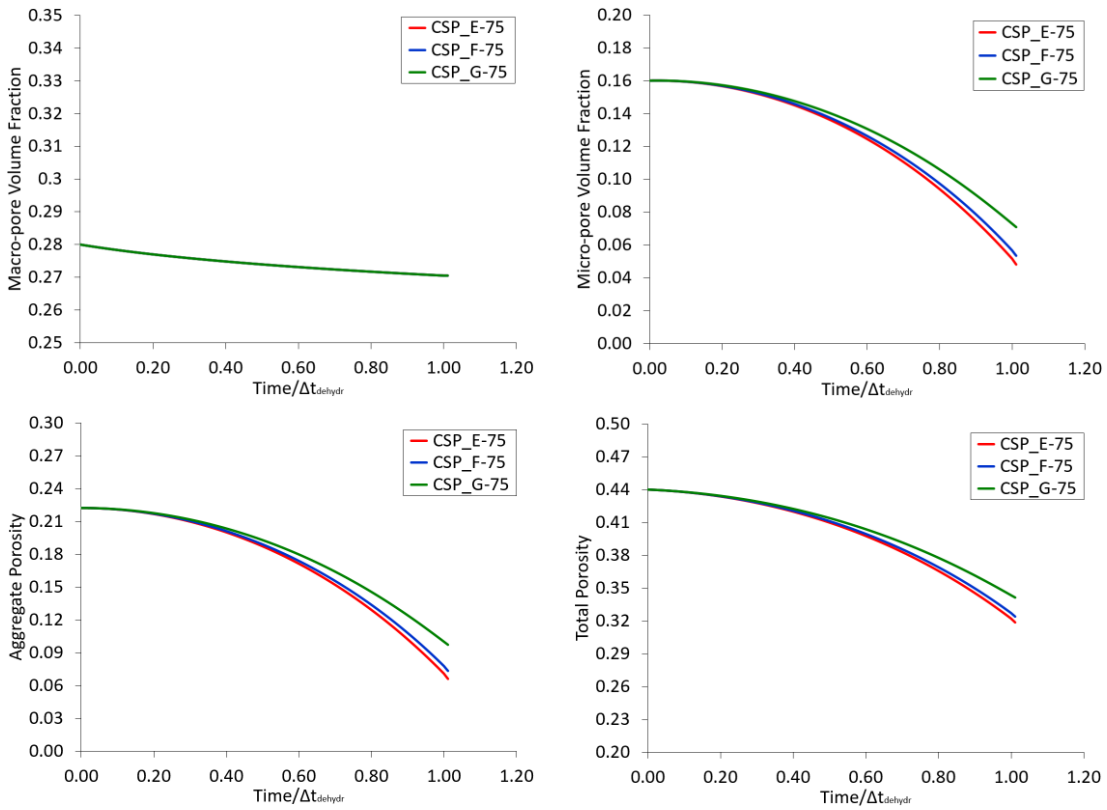

Figure 6-37: Comparison between the pore volume fractions (up) and and the aggregate and total porosities (down) obtained from drying paths starting at distinct confining pressures when $\gamma^w = 10^{-7}$ kg/s/m^3/MPa.

It is also expected that the shrinkage response of expansive soils is affected by their initial water content. Therefore, several drying paths starting at different suction values were modelled. In such stress paths, the drying step was performed under a confining pressure of 0.1 MPa until reaching the macro suction value of about 250 MPa. Then, the confining pressure was increased to its final value of 1.0 MPa. The evolution of suctions, degrees of saturation and porosity variables from four drying-loading paths (CSP_E-100, CSP_E-75, CSP_E-25 and CSP_E-01) are given in Figure 6-38 and Figure 6-39. The overall drying-induced shrinkage of the expansive soil is mainly affected by the magnitude of the applied increments in macro suction. Thus, and according to the results shown in Figure 6-39, the reduction in the macro-pore volume fraction is larger for the CSP_E-01 path and lower for the CSP_E-100 path, in which the macro suction increments are equal to 249 MPa and 150 MPa, respectively (see Figure 6-38).

The reduction of the macrostructural degree of saturation in the early stages of drying (in Figure 6-38) shows that the desaturation of initially saturated macro-pores (as in the CSP_E-01 path) is faster than drying partially saturated voids. Furthermore, it seems that the amount of shrinkage is also dependent on the initial water content in micro-pores, once a more saturated microstructure, as in the CSP_E-01 path, presents a slightly higher decrease in the intra-aggregate porosity at the end of the drying process in comparison to initially drier microstructural configurations (see Figure 6-39). Such a reduction in the micro-porosity variables can be related to the different hydration (or dehydration) stages of the tightly bound water found in the intra-aggregate pores (see **Section 2.2.1.4**). These modelling predictions reflect the increase in the energy required to remove a pore-water molecule from the water-air interface

(in macro-pores) or from the inter-layer space (micro-pores) as the porous medium becomes increasingly dry (Wayllace, 2008; Kuligiewicz and Derkowski, 2017).

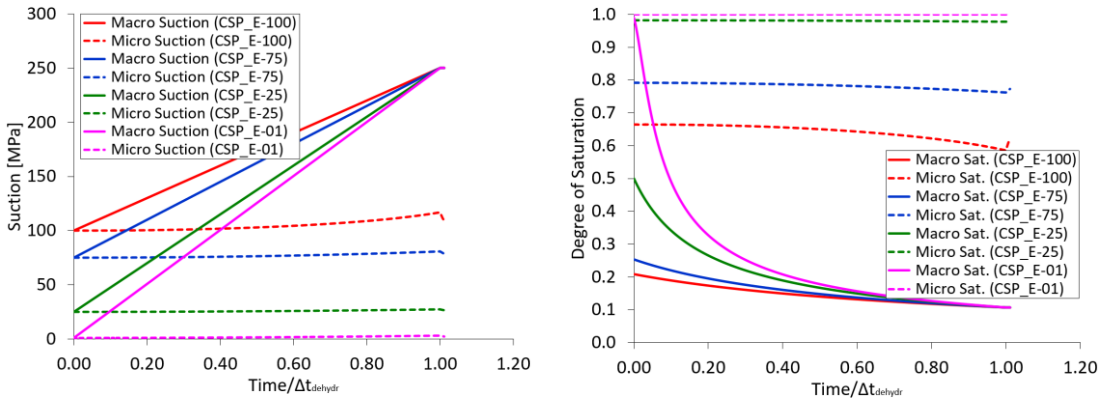

Figure 6-38: Evolution of suction and degree of saturation in drying paths starting at distinct suctions when $\gamma^w = 10^{-7}$ kg/s/m^3/MPa.

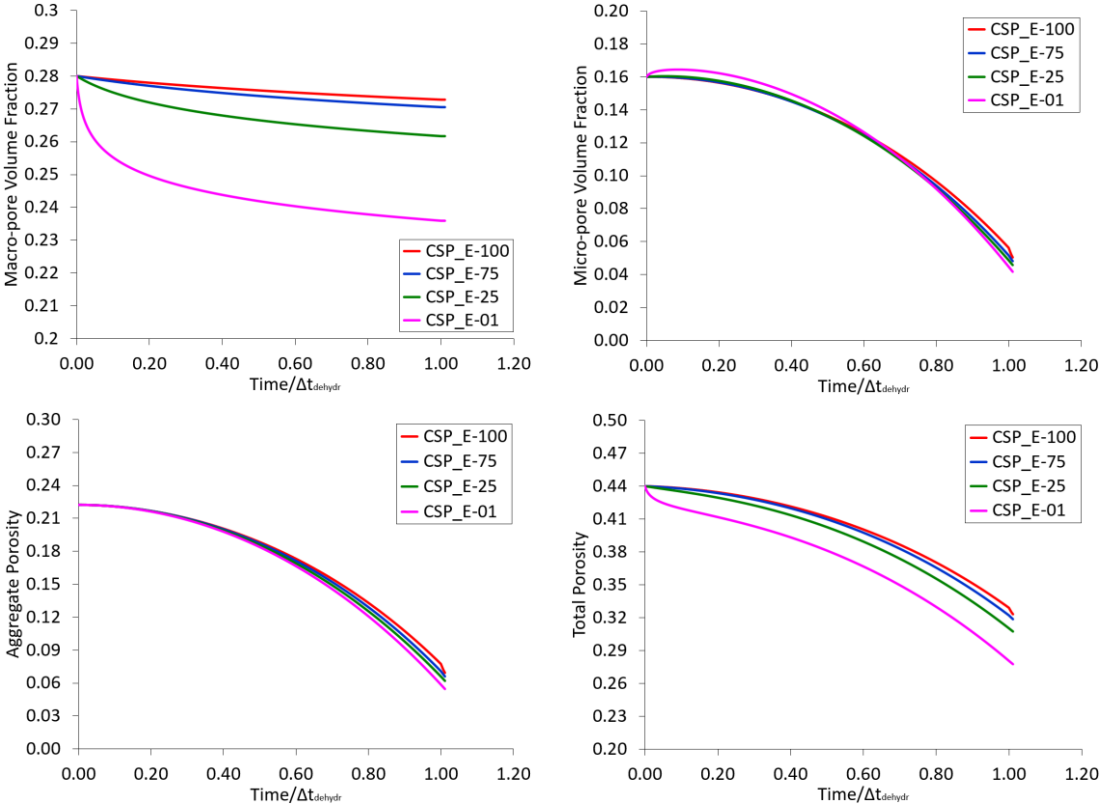

Figure 6-39: Comparison between the pore volume fractions (up) and the aggregate and total porosities (down) obtained from drying paths starting at distinct suctions when $\gamma^w = 10^{-7}$ kg/s/m^3/MPa.

The rate at which the drying process is performed was also investigated. Two situations were simulated: one of them corresponding to a rapid drying of macro-pores, with macro suction increasing from 75 to 250 MPa in a 30 days' time and the other one representing a "slow" desiccation of macro voids, in which the same hydraulic loading was applied over a period of 90 days. The most significant outcomes of such modelling analyses are plotted in Figure 6-40 and Figure 6-41. Slower macrostructural desaturation is expected to allow the removal of a slightly larger amount of microstructural water from the inter-aggregate space at the end of the drying process (i.e, when the macro suction reaches its final value). Consequently, the global shrinkage

of the expansive sample of soil is larger for a longer drying process once the numerical modelling predicts a larger decrease in the micro-porosity variables (the pore volume fraction and the aggregate porosity) at the end of the dehydration of macro-pores. However, if additional time is left after the de-saturation of macrostructure (see the model results for rapid drying), microstructural drying continues and the soil element may exhibit large shrinkage deformations due to the further dehydration of micro-pores (see Figure 6-41). As mentioned in **Section 6.3.1** (for the wetting paths carried out at different rates of hydration), the hydraulic structural coupling is behind such behaviour differences once the micro-macro water mass exchange is a time-dependent process.

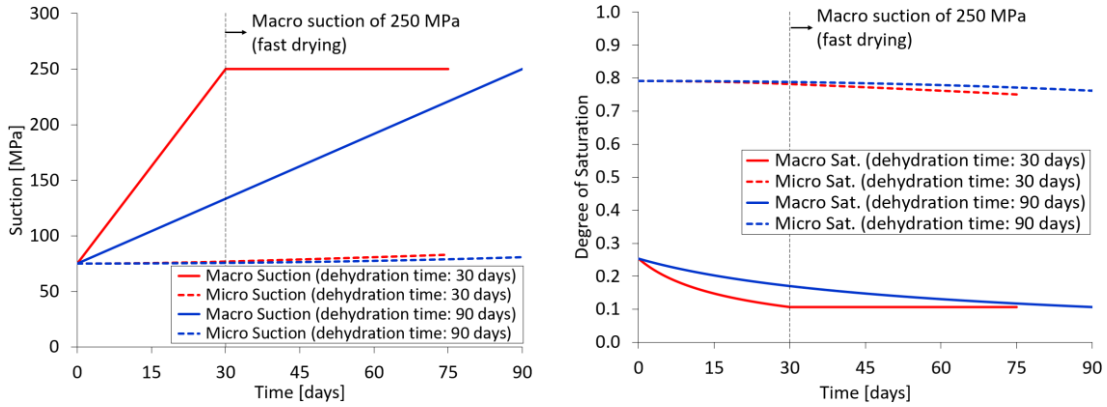

Figure 6-40: Evolution of suction and degree of saturation when the drying of macro-pores (in the CSP_E-75 path) is performed rapidly (30 days) or slowly (90 days). The leakage coefficient is $\gamma^w = 10^{-7}$ kg/s/m^3/MPa.

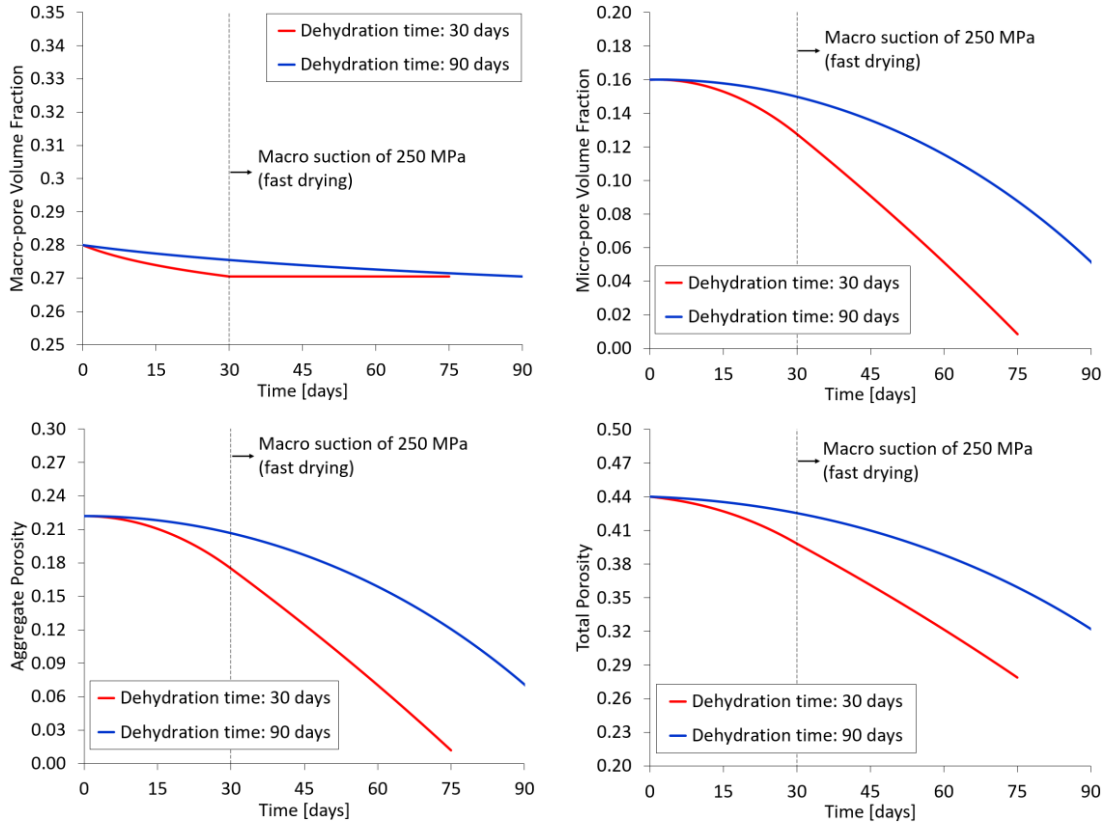

Figure 6-41: Evolution of the porosity variables when the drying of macro-pores (in the CSP_E-75 path) is performed rapidly (30 days) or slowly (90 days). The leakage coefficient is $\gamma^w = 10^{-7}$ kg/s/m^3/MPa.

6.4.2. ANALYSES WITH THE β-MECHANISM ACTIVATED

As discussed in **Section 6.3.2**, the activation of the plastic β-mechanism influences primarily the mechanical response of macrostructure, with a minor impact on the microstructural behaviour in drying paths under constant load that do not intersect the LC locus. In such conditions, the development of irreversible strains is uniquely due to the micro-macro coupling mechanism. In order to activate this energy dissipation mechanism, some numerical analyses were conducted using the pair of interaction functions termed as Functions #3 (see Table 6-8). Two distinct drying paths (CSP_E-75 and CSP_H-75) were considered, as plotted (in the p: s_M plane) in Figure 6-42.

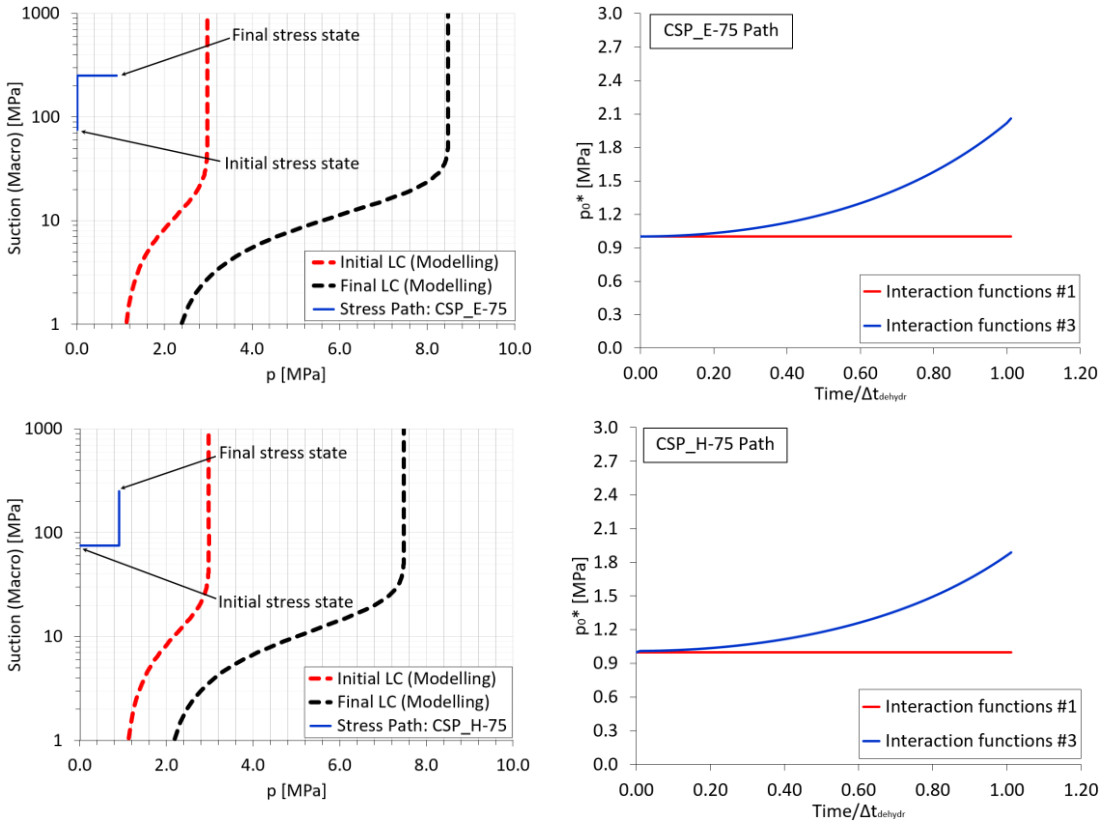

Figure 6-42: CSP_E-75 (up) and CSP_H-75 (down) paths plotted in the p: s_M plane (left) and the evolution of the saturated pre-consolidation pressures (right) when $\gamma^w = 10^{-7}$ kg/s/m^3/MPa and with the micro-macro interaction mechanism activated.

It can be noted that the activation of the mechanical coupling between both structural levels moves the initial LC curve to the left, changing the size of the elastoplastic region. This strain-hardening behaviour due to the drying of macro-pores is evidenced by the increment in the hardening parameter (p_0^*) as macro suction increases, as illustrated in Figure 6-42. The occurrence of such a suction hardening (Bagherieh *et al.*, 2009) as the soil element is dried generates an irreversible reduction of macrostructural voids, as shown in Figure 6-43 and Figure 6-44. The development of these permanent structural changes in the soil skeleton due to the macrostructural collapse induced by the intense drying can also be evaluated by means of the auxiliary macro-porosity variable ($\Delta\bar{\phi}_{M,\beta}$) – see **Section 6.3.2** – whose evolution for the drying paths CSP_E-75 and CSP_H-75 is displayed in Figure 6-45.

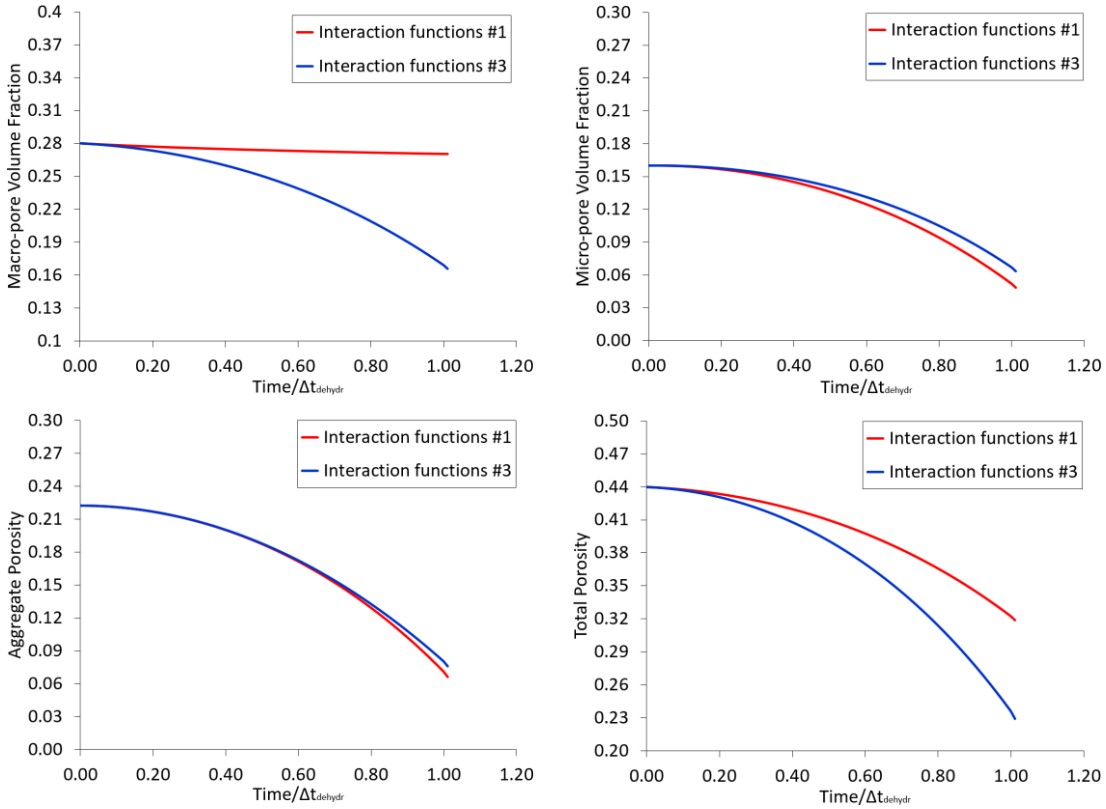

Figure 6-43: Evolution of the porosity variables for the CSP_E-75 path when $\gamma^w = 10^{-7}$ kg/s/m³/MPa and with the micro-macro coupling mechanism activated.

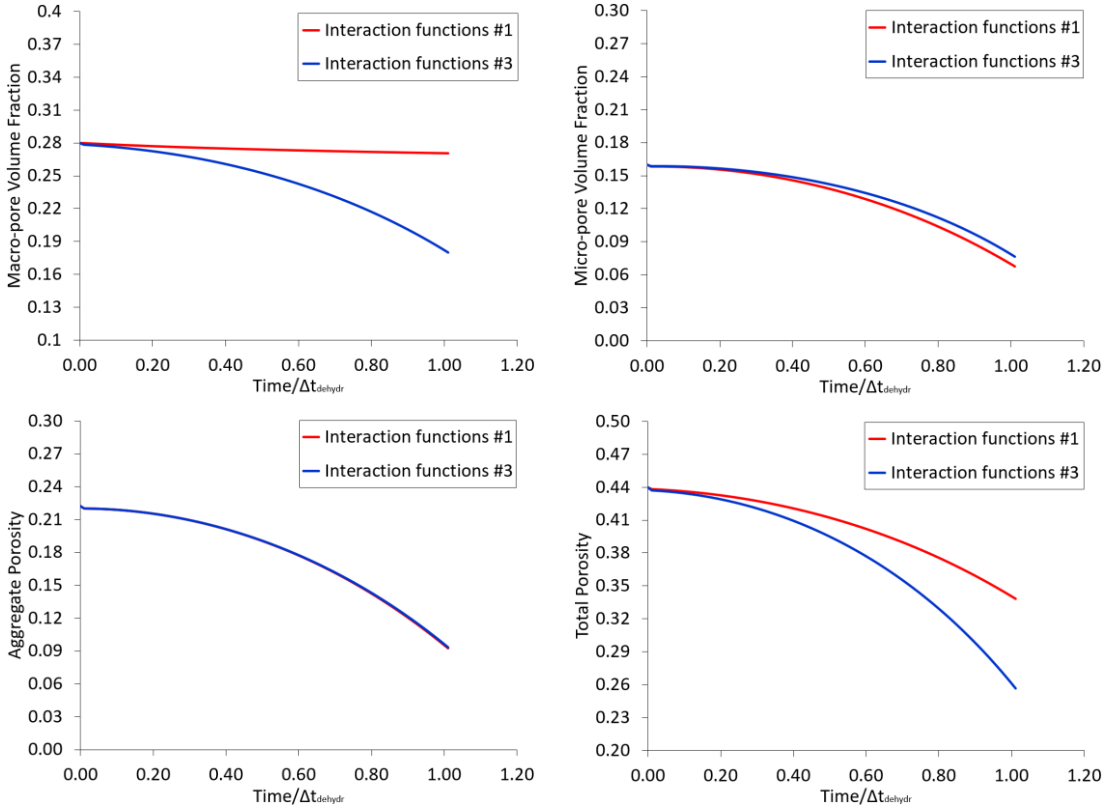

Figure 6-44: Evolution of the porosity variables for the CSP_H-75 path when $\gamma^w = 10^{-7}$ kg/s/m³/MPa and with the micro-macro coupling mechanism activated.

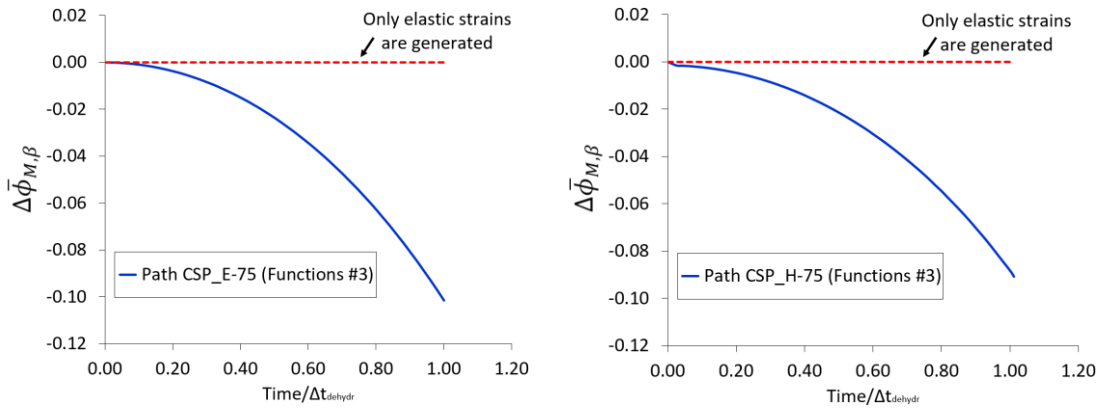

Figure 6-45: Hardening response of the soil skeleton during the drying paths CSP_E-75 (left) and CSP_H-75 (right) obtained when Functions #3 (see Table 6-8) are used. The curves for the evolution of $\Delta\bar{\phi}_{M,\beta}$ when the β-mechanism is not activated (Functions #1 in Table 6-8) are also drawn (dashed lines).

The volumetric compressive response of individual aggregates and expansive particles (actual microstructure) seems not to be affected or, at least not significantly, by the activation of the plastic β-mechanism. Therefore, the larger global shrinkage predicted by the model for the elastoplastic drying path with the mechanical structural coupling activated is mainly related to the non-reversible structural rearrangements occurring at macrostructural level.

6.5. WETTING AT CONSTANT VOLUME CONDITIONS

The components of a bentonite-engineered barrier for radioactive waste disposals are commonly designed to operate under global volume restrictions imposed by the surrounding environment in which they are emplaced. One of those processes expected to occur during the operational phase is the re-saturation of the bentonite barrier once the gap between the host rock and the expansive buffer is closed due to its initial swelling expansion. Although it is a slow process, the natural (or artificial) hydration of a bentonite barrier could generate high swelling pressures that would compromise the structural stability of the barrier system and, consequently, the requirements of isolation and safety for which it has been built. It is well-known that the magnitude of the swelling pressure depends on the initial water content and the dry density of such expansive porous materials (Villar, 2002; Nagaraj *et al.*, 2009; Wang *et al.*, 2012; Jayalath *et al.*, 2016), as already discussed in **Section 2.2.2.4**. Furthermore, the swelling potential of compacted and pelletized bentonite materials would keep increasing over time, since the re-saturation of micro-pores is an extremely slow process. Therefore, the numerical simulation of wetting paths under isochoric conditions becomes a crucial task to be performed in order to evaluate the reliability and the robustness of the implemented model in reproducing the swelling response of expansive geomaterials.

In the next sections, the main results from the numerical modelling of four wetting paths under volumetric constraint conditions, as specified in Table 6-2, are given and interpreted in the context of multi-porosity media. The fact that the hydration of macro-pores occurs without changes in the volume of the expansive soil specimen implies that the expected increase in the

micro-pore volume fraction ($\overline{\phi}_m$) during the re-saturation of the expansive soil is counteracted by a similar decrease in the macro-pore volume fraction ($\overline{\phi}_M$) so that the total porosity ($\phi = \overline{\phi}_m + \overline{\phi}_M$) remains unchanged. In **Section 6.5.1**, the model predictions represent a scenario in which non-reversible strains only occur when the stress path intersects the LC yield surface. In this situation, the mechanical coupling between both structural media is not considered in the development of plastic deformations. The occurrence of irreversible changes in macrostructure due to the elastic swelling of microstructure (through the activation of the plastic structural coupling mechanism) is discussed in **Section 6.5.2**. In both scenarios, calculations were performed using different rates of water mass transfer between micro- and macro-pores as well as distinct hydration rates to re-saturate the larger voids.

6.5.1. ANALYSES WITH THE β-MECHANISM DEACTIVATED

Initially, wetting at constant volume was carried out without considering the mechanical micro-macro coupling. It means that any irreversible change in the soil structure comes from the activation of the BBM plastic process when the stress path crosses the current LC curve. The influence of the initial conditions (stresses and fluid pressures) on the confined swelling response of the expansive soil sample was analysed by performing four distinct stress paths, as indicated in Table 6-2. The paths CVP_A-123, CVP_B-123 and CVP_C-123 start at the same macrostructural suction level, i.e., 123 MPa, but at different total mean pressures (at 0.1, 0.5 and 1.0 MPa, respectively). The paths CVP_A-123 and CVP_A-75 have the same initial confining pressure but in the latter, the wetting process starts at a suction of 75 MPa. The numerical results shown from Figure 6-46 to Figure 6-50 correspond to such stress paths, in which two different values were used for the leakage coefficient of the hydraulic coupling between both structural media (Scenario #1 and Scenario #3 in Table 6-9). In the constitutive analyses discussed in the following sections, the (imposed) time for hydrating macro-pores (Δt_{hydr}) is 180 days.

Unlike the wetting at constant load, the hydration under isochoric conditions produces an increase in the total mean stresses as macro-pores re-saturate, as illustrated by the stress paths drawn in Figure 6-47. In such a context of volumetric restrictions, the development of the swelling pressure represents the main evidence of the expansive response of a clayey material. The evolution and magnitude of the swelling pressures for the four HM paths and the two hydraulic coupling scenarios considered in calculations are given in Figure 6-48.

On the one hand, the water mass transfer mechanism induces an increment in the microstructural water content during the soil hydration process, which leads to a resultant increase in the intra-aggregate voids as water is transferred from the larger pores to the micro ones. On the other hand, such an increase in the microstructural porosity induces an irreversible reduction of macro-pores once the volume of the soil element is forced to keep unchanged during the wetting process. Consequently, and according to the stress paths shown in Figure 6-47, the elastic domain widens with hydration of macro-pores because the plastic hardening parameter also increases with the re-saturation of the expansive soil. It means that the soaking

of the soil sample leads to a denser macrostructure, characterized by a reduction of the volume occupied by the larger pores when the wetting path reaches the LC and forces it to move beyond its initial position. The hydration-induced development of the micro- and macro-pore volume fractions and the aggregate porosity for a lower and a larger micro-macro water transfer coefficient are plotted in Figure 6-49 and Figure 6-50, respectively. The volumetric behaviour at both structural media described in this paragraph is clearly observed in those wetting paths in which a larger leakage coefficient was employed, while in the other scenario considered in the numerical simulations (Scenario #1 in Table 6-9) such a behaviour is less noticeable. The mutual saturation of micro- and macro-pores for the stress paths in which $\gamma^w = 10^{-6}$ kg/s/m^3/MPa explains such behaviour differences (see Figure 6-46 and compare the differences in the saturation state of both structural media).

Regarding the evolution of the pore volume fractions, it is important to highlight a slight tendency of the macro-porosity variable ($\bar{\phi}_M$) to increase (accompanied by an equivalent decrease in the micro-pore volume fraction, $\bar{\phi}_m$) in the first stages of hydration, when the stress path is still inside the initial elastic zone. This deformation behaviour can be seen more clearly in the evolution of porosities shown in Figure 6-49 (especially in the CVP_A-123 path), where the changes in porosities due to wetting are lower (Scenario #1), but it is also observed at the beginning of the wetting paths for Scenario #3. The initial and natural response of the soil element to a decrease in macrostructural suction is to swell elastically, both at micro and macro levels, as discussed in **Section 6.3.1**. Nevertheless, microstructure is prevented from swelling freely due to the volume restrictions imposed by the boundaries of the modelled domain. Consequently, a mechanical compressive pressure arises in response to such physical constraints. The development of the swelling pressure induces a microstructural compression, causing a slight decrease in the micro-pore volume fraction and a consequent (and equal) increase in the macro-pore volume fraction. Such a deformation trend is maintained while the soil sample expands elastically and the compression stress level is not high enough to produce any rearrangement of the clay aggregates. Once the stress path intersects the initial LC curve, the structural rearrangement of the clay aggregates leads to a macrostructural collapse evidenced by the reduction in the macro-porosity variable and in the confining (swelling) pressure (see Figure 6-47 and Figure 6-48). From that moment on, macrostructural expansion is prevented while microstructure can develop its full swelling potential, resulting in an increase in the volume of the intra-aggregate pores at the expense of macro-porosity (Lloret *et al.*, 2004).

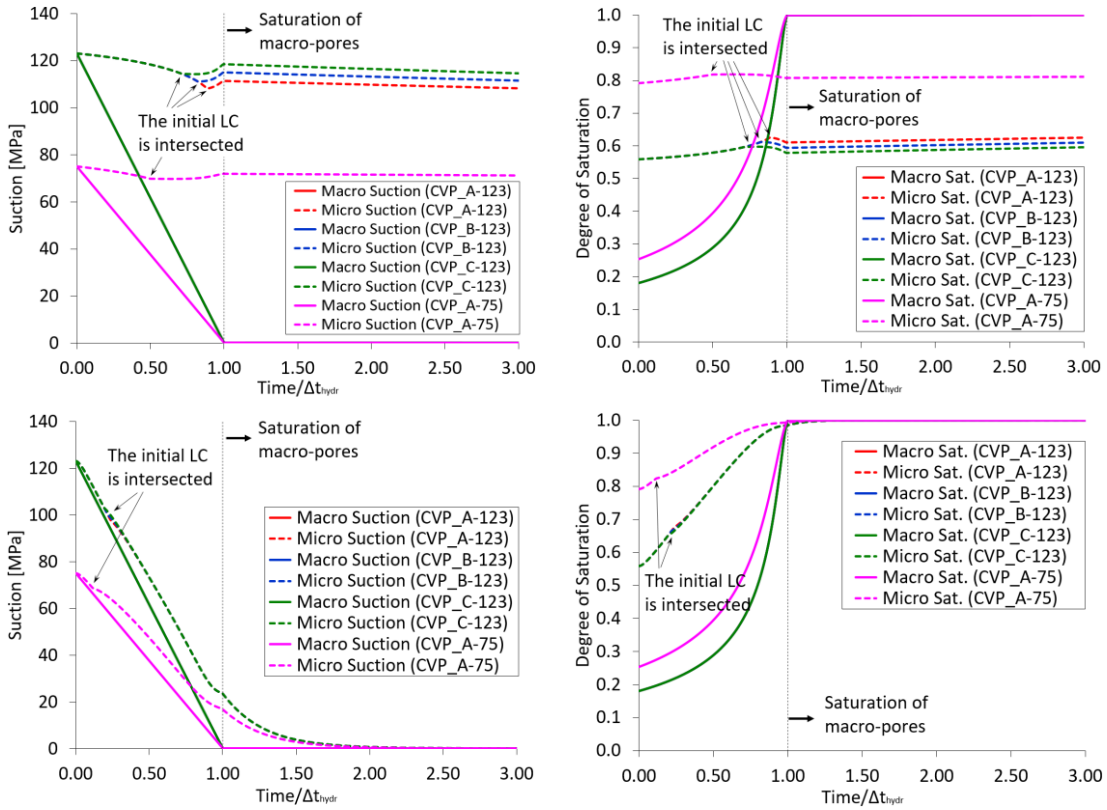

Figure 6-46: Evolution of suction and degree of saturation in wetting paths under constant volume and for distinct initial conditions, when $\gamma^w = 10^{-9}$ kg/s/m^3/MPa (up) and $\gamma^w = 10^{-6}$ kg/s/m^3/MPa (down).

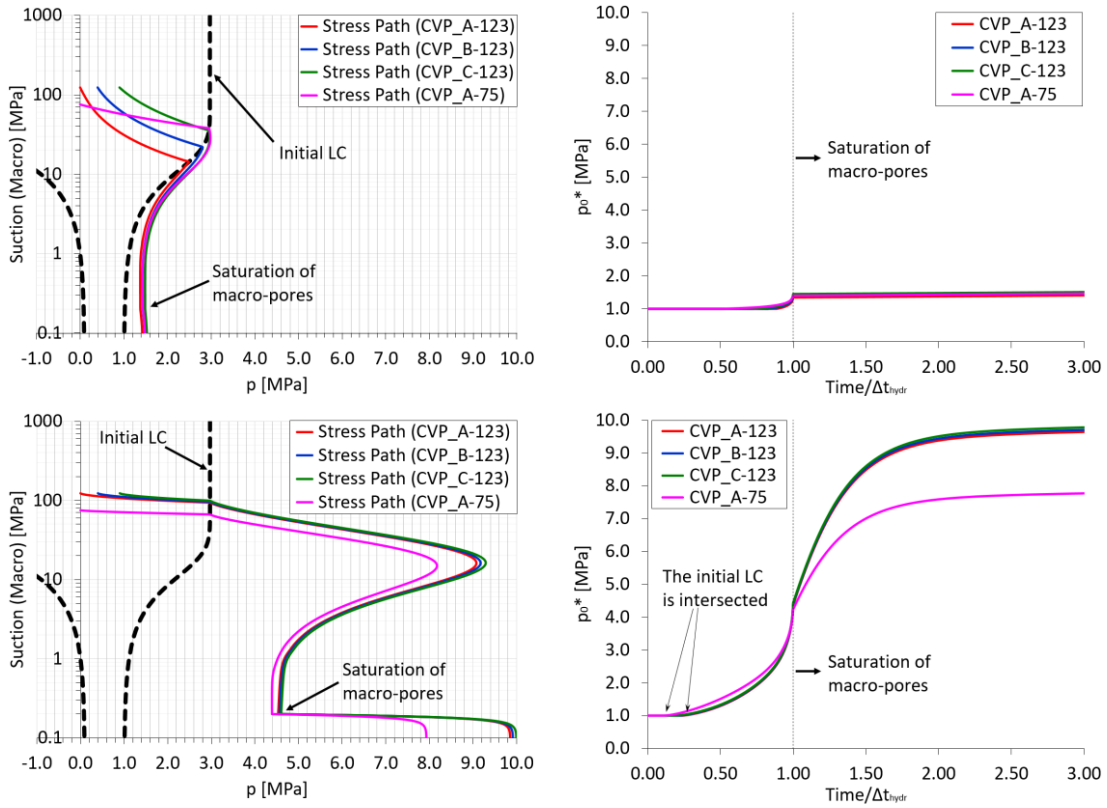

Figure 6-47: Wetting paths at isochoric conditions plotted in the p: s_M plane (left) and the evolution of the saturated pre-consolidation pressures (right) for distinct initial conditions, when $\gamma^w = 10^{-9}$ kg/s/m^3/MPa (up) and $\gamma^w = 10^{-6}$ kg/s/m^3/MPa (down).

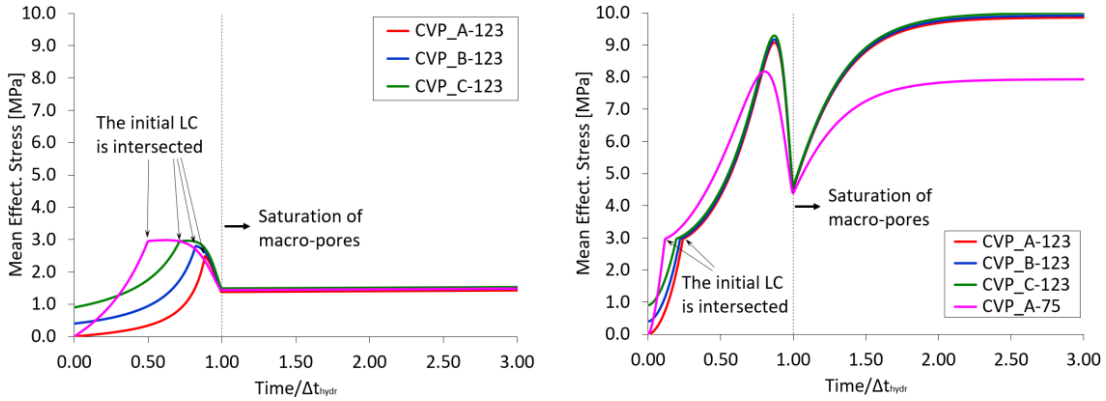

Figure 6-48: Development of swelling pressures in wetting paths under constant volume and for distinct initial conditions, when $\gamma^w = 10^{-9}$ kg/s/m^3/MPa (left) and $\gamma^w = 10^{-6}$ kg/s/m^3/MPa (right).

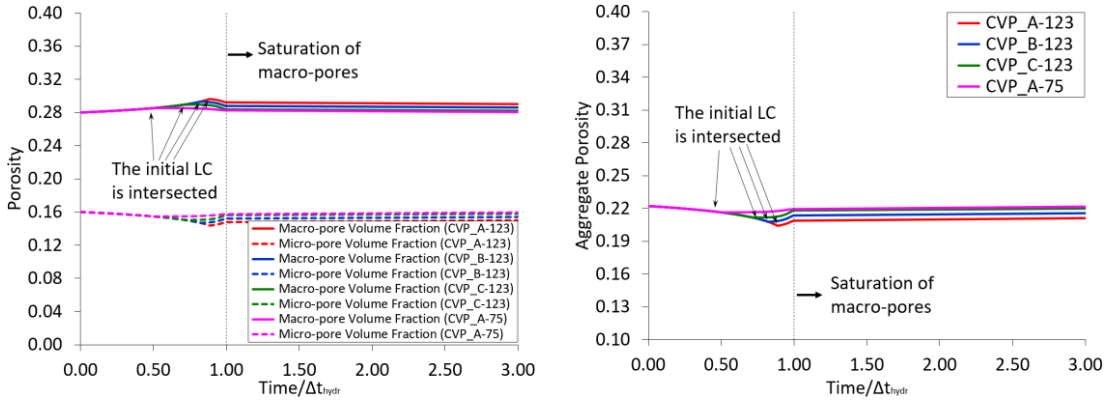

Figure 6-49: Evolution of pore volume fractions and the aggregate porosity (actual micro-porosity) in wetting paths under constant volume and for distinct initial conditions, when $\gamma^w = 10^{-9}$ kg/s/m^3/MPa.

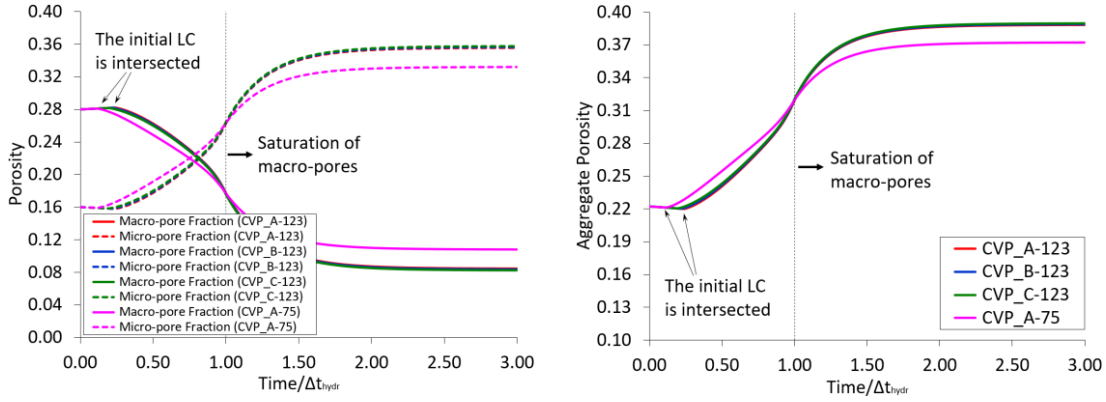

Figure 6-50: Evolution of pore volume fractions and the aggregate porosity (actual micro-porosity) in wetting paths under constant volume and for distinct initial conditions, when $\gamma^w = 10^{-6}$ kg/s/m^3/MPa.

Another important feature observed in the modelling results is related to the evolution of the swelling pressure when macro-pores are re-saturatured (see Figure 6-47 and Figure 6-48). In the wetting paths with a large micro-macro water transfer coefficient (Scenario #3 in Table 6-9), a significant increase in the swelling pressure is predicted. In such a scenario, the swelling-induced stresses reaches values close to the ones predicted in the peak of stresses registered before the saturation of macro-pores. The wetting paths characterized by a lower leakage coefficient (Scenario #1) do not show any noticeable increment of the swelling pressure in this "post-peak"

zone (see the chart on the right-hand side in Figure 6-48), even when micro-pores are still far from their saturated state. Again, such differences are intrinsically related to the rate of hydration of microstructure, which is controlled by the hydraulic micro-macro coupling mechanism. This behaviour reflects the insignificant contribution of the re-saturation of microstructure to the development of the total swelling pressure for those situations characterized by a slower water transfer rate between both pore levels. In contrast, for the wetting paths of Scenario #3 (see the chart on the left-hand side in Figure 6-48), a new increment of the swelling pressure is predicted after the saturation of macro-pores, once the higher transfer coefficient for the hydraulic micro-macro coupling allows the mutual re-saturation of both families of pores. Under such conditions, the hydration of microstructure actively contributes to the development of higher swelling pressures, even before the full saturation of macro-pores is achieved. Moreover, the post-peak increase in swelling pressures is mainly related to the saturation of the microstructure.

The different initial stress conditions for the wetting paths considered in calculations seem not to introduce meaningful differences in the development of the porosity variables, the swelling pressure and the pre-consolidation stress, at least not for the wetting paths of Scenario #1. However, for the wetting paths of Scenario #3, the magnitude of the swelling pressure peak appears to depend more on the initial suction than on the initial confining pressure (compare the evolution of stresses in the HM CVP_A-75 path with any of the other three paths in Figure 6-47 and Figure 6-48). As discussed previously, this model outcome shows that higher swelling pressures and larger aggregate expansions are expected to occur for those hydration paths in which the initial water content in macro- and micro-pores is lower (as in CVP_A-123, CVP_B-123 and CVP_C-123). Nevertheless, the analysis of the evolution of porosities in Figure 6-50 shows that the model predicts a higher intra-aggregate porosity for the CVP_A-75 path before the saturation of the macrostructure. Such an apparently contradictory result, in fact, indicates that the elastoplastic deformations, expressed through an irreversible “collapse” of macro-pores, occur earlier in this path than in the other three hydration paths. However, once the macrostructural suction approaches its final target value (of 0.1 MPa) and the expansive response is controlled predominantly by the saturation of microstructure, the accumulated micro-porosity becomes smaller for the path CVP_A-75, as expected.

In all the modelling results discussed so far, the role of the micro-macro water transfer mechanism in the development of the swelling potential of the double-porosity medium is one of the most important factors to be highlighted. In fact, a higher leakage coefficient conducts to a more saturated microstructure at the end of a re-saturation process. Under constant volume conditions, a more saturated microstructure leads to higher values of swelling pressure (including a higher and more marked peak of the confining stresses) and to larger microstructural expansion (higher intra-aggregate porosity) and macrostructural irreversible collapse (lower inter-aggregate porosity). Consequently, the evolution of the hardening parameter is more significant when the coefficient of the local water mass exchange between micro and macro voids is also increased. All these behaviour aspects can be appreciated in the following graphs (from Figure 6-51 to Figure 6-54), in which the numerical findings from the modelling of the hydration path CVP_A-123 for three different rates of water mass transfer (Scenario #1, Scenario #2 and Scenario #3 in Table 6-9) are plotted together for comparison purposes. It is important to remark that the re-saturation of micro-pores in wetting paths for

Scenario #1 and Scenario #2 can be achieved if a longer period of time is left after the saturation of the macrostructure. This additional time has been equal to 360 days (Δt_{hydr} = 180 days) in the calculations whose results are shown from Figure 6-51 to Figure 6-54.

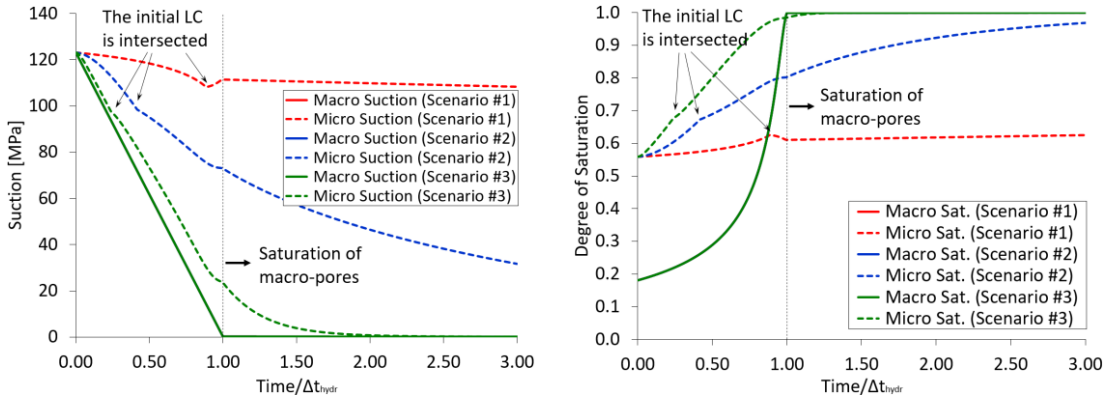

Figure 6-51: Evolution of suction and degree of saturation in the wetting path CVP_A-123 for distinct pore-water mass transfer coefficients.

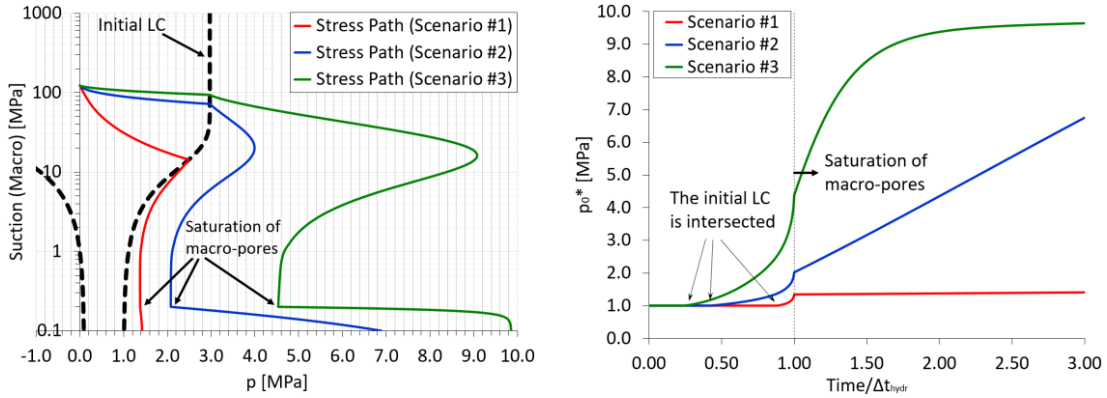

Figure 6-52: Wetting paths at isochoric conditions (CVP_A-123) plotted in the $p{:}s_M$ plane (left) and the evolution of the saturated pre-consolidation pressures (right) for distinct pore-water mass transfer coefficients.

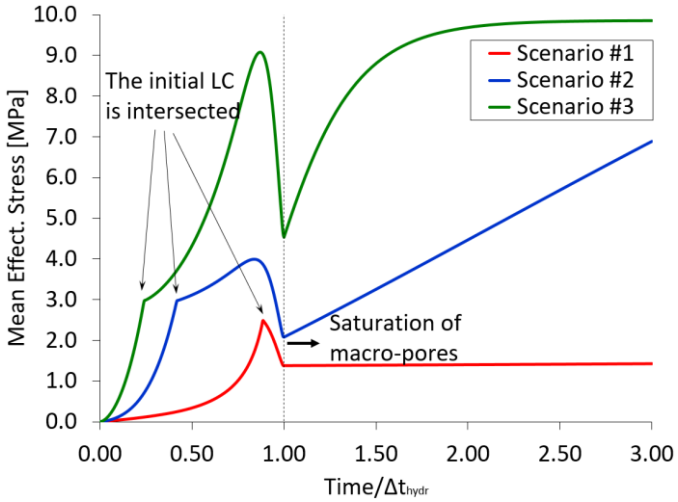

Figure 6-53: Evolution of the swelling pressure in the HM CVP_A-123 path for distinct pore-water mass transfer coefficients.

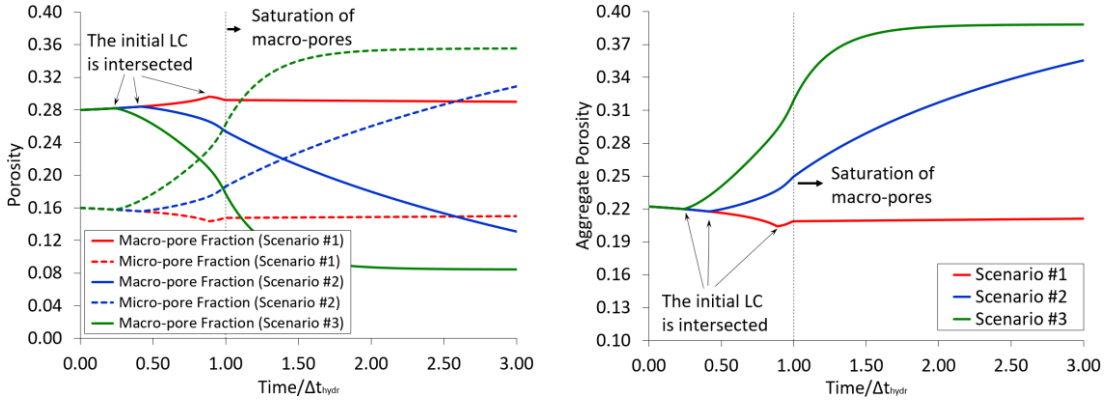

Figure 6-54: Evolution of the pore-volume fractions and the aggregate porosity in the wetting path CVP_A-123 for distinct pore-water mass transfer coefficients.

The influence of the rate of re-saturation of large voids was also evaluated through the numerical simulations of the HM CVP_A-123 path for two different macrostructural hydration times (Δt_{hydr}): 30 and 180 days. For comparison purposes, a period of time equals to 180 days was left after the re-saturation of macro-pores in both situations in order to promote the increase in the saturation state of the microstructure. A same leakage parameter was used in both cases ($\gamma^w = 10^{-6}$ kg/s/m^3/MPa). The most relevant model outcomes of this sensitivity analysis are plotted in Figure 6-55 and Figure 6-56. From these results, it can be seen that the microstructure is almost saturated at the end of the period following the fast saturation of macro-pores (see Figure 6-55). The large difference between the macrostructural and the microstructural water potentials after the rapid hydration of macrostructure intensifies the water transfer from macro- to micro-pores and, consequently, a higher swelling pressure is predicted at the end of calculation (in comparison to the value obtained from the slow hydration situation) – see Figure 6-56. Although the water mass exchange between the structural media can enhance the development of the swelling potential of a soil, it is important to remark that the magnitude of the swelling pressures (and deformations) does not depend on such a transfer mass process. Consequently, the mechanical parameters used for modelling the swelling response of an expansive clay submitted to a slow wetting procedure may lead to misleading predictions of the swelling potential obtained from rapid hydration tests. In other words, a calibration task of the model parameters is always recommended in order to properly reproduce the experimental swelling response in each case.

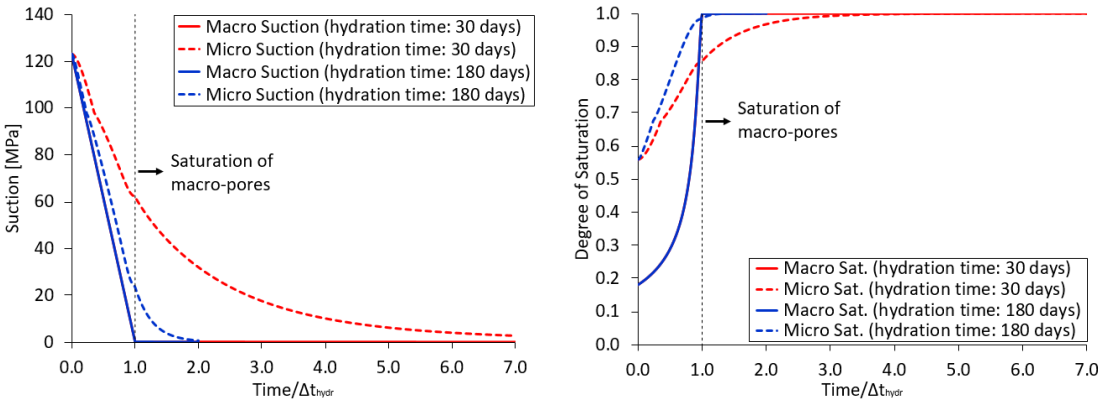

Figure 6-55: Evolution of suction and degree of saturation in the wetting path CVP_A-123 for distinct re-saturation rates of macro-pores when $\gamma^w = 10^{-6}$ kg/s/m^3/MPa (Scenario #3).

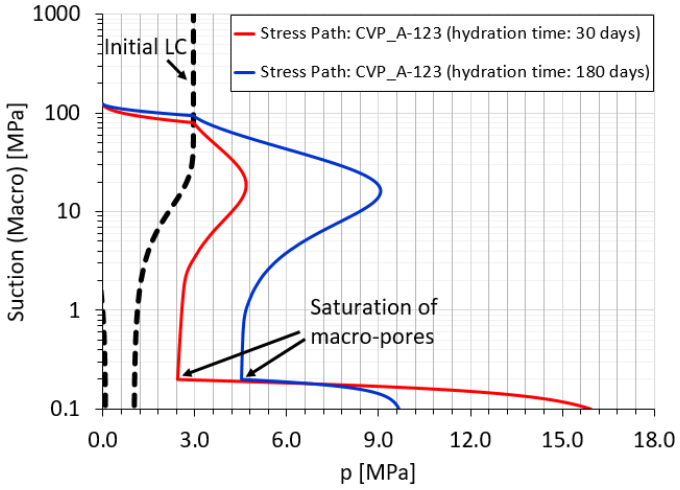

Figure 6-56: Wetting paths at isochoric conditions (CVP_A-123) plotted in the p: s_M plane for distinct re-saturation rates of macro-pores when $\gamma^w = 10^{-6}$ kg/s/m^3/MPa (Scenario #3).

6.5.2. ANALYSES WITH THE β-MECHANISM ACTIVATED

The same wetting paths studied in the preceding section were also modelled using non-zero structural coupling functions (f_β). Most of the comments and conclusions made in the previous section about the evolution of saturation, swelling pressure and porosities in both structural levels also explains the expansive soil response when both plastic mechanisms are taken into account in the numerical simulations, at least from a phenomenological standpoint. Nevertheless, since the plastic micro-macro coupling affects the mechanical part of the constitutive formulation, its activation would only induce changes in those mechanical variables closely associated with such a plastic mechanism, that is, the development of the volumetric deformations (mainly their plastic component), the hardening parameter, the tensor of stresses and the porosity variables (especially the macrostructural one).

It is expected that the dimensions of the cubic element of soil (of 1 cm^3) and the volumetric constraints imposed on it would limit or even inhibit the contribution of the plastic β-mechanism to the magnitude of the irreversible strains generated during the hydration process. Nevertheless, the prescription of a null-displacement at all nodes of the FE mesh also inhibits the expansion of the clay matrix in such a way that the microstructural volumetric strains can be neglected. Consequently, the development of the plastic deformations related to the volumetric expansion of microstructure can be also disregarded as well as its effects on the material response to the re-saturation of macro- and micro-pores. This fact is corroborated by the modelling results plotted from Figure 6-57 to Figure 6-59, which are obtained from the confined wetting path CVP_A-123 for distinct mechanical coupling functions (see Table 6-8).

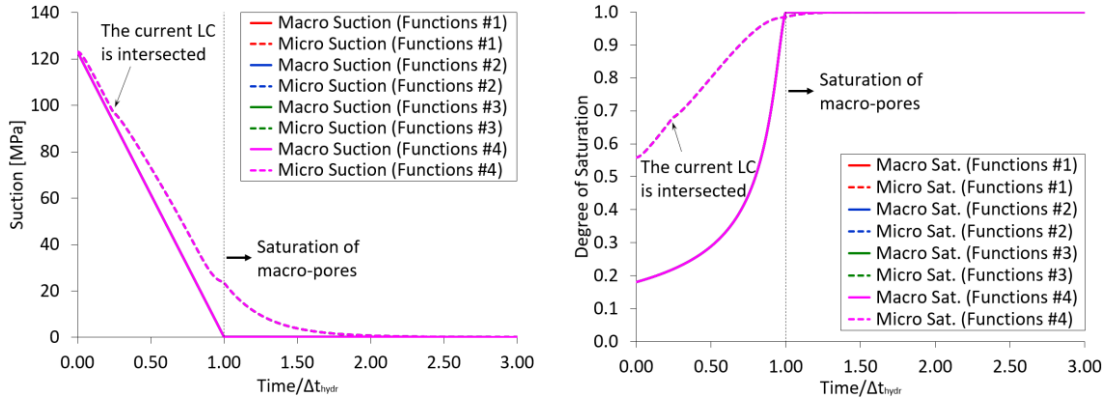

Figure 6-57: Evolution of suction and degree of saturation in the wetting path CVP_A-123 for distinct micro-macro coupling functions (see Table 6-8), when $\gamma^w = 10^{-6}$ kg/s/m^3/MPa (Scenario #3).

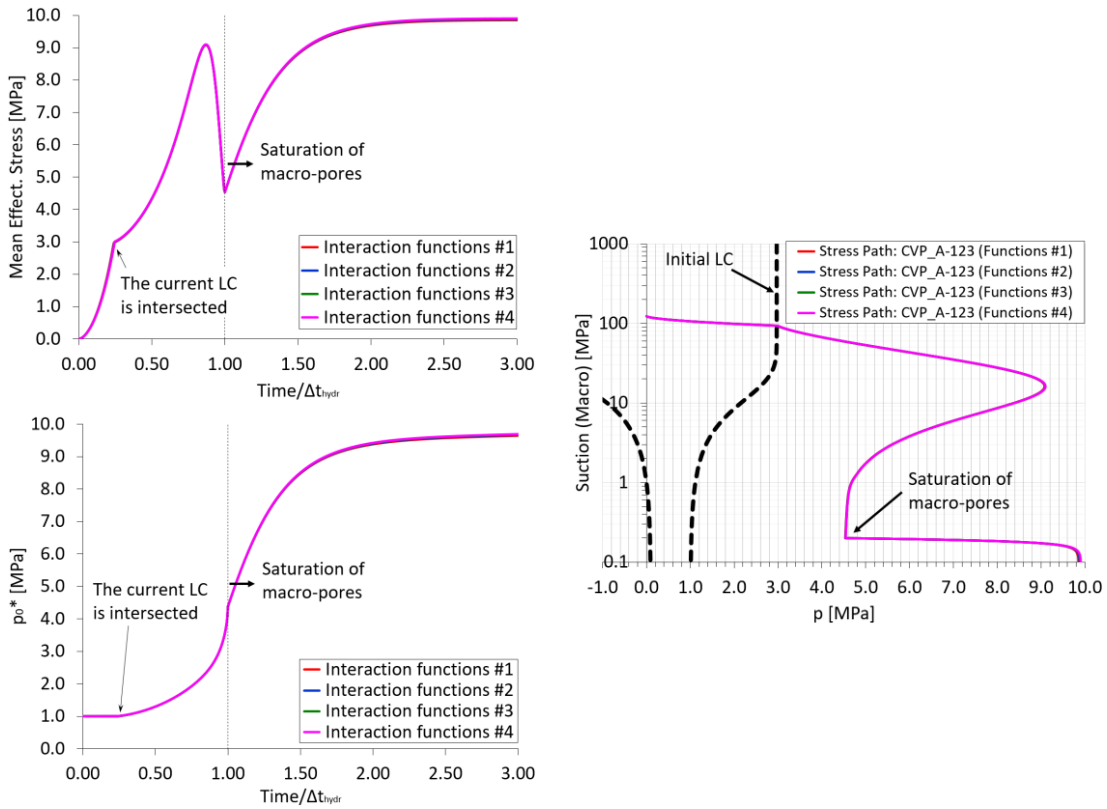

Figure 6-58: Evolution of swelling pressures (up, at left) and the saturated pre-consolidation pressures (down, at left) together with the stress paths under isochoric conditions plotted in the $p{:}s_M$ plane (right) during the simulation of the CVP_A-123 path for distinct micro-macro coupling functions (see Table 6-8), when $\gamma^w = 10^{-6}$ kg/s/m^3/MPa.

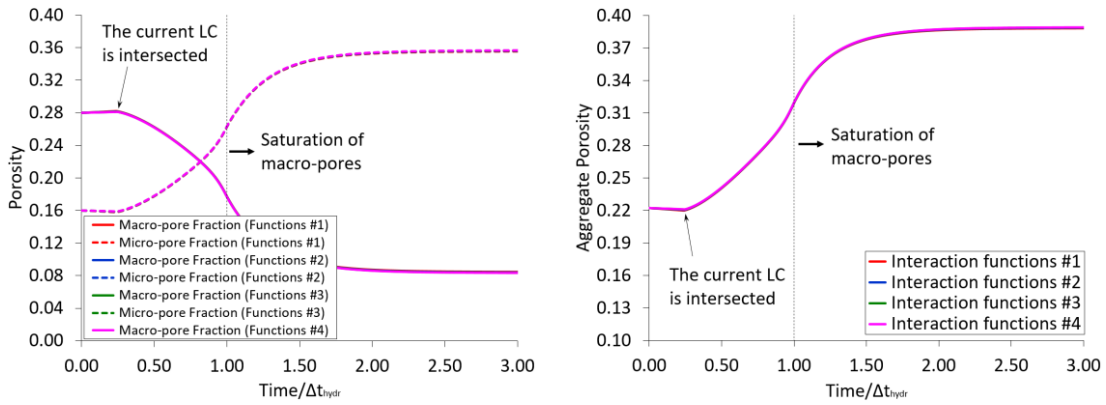

Figure 6-59: Evolution of the pore-volume fractions and the aggregate porosity in the wetting path CVP_A-123 for distinct micro-macro coupling functions (see Table 6-8), when $\gamma^w = 10^{-6}$ kg/s/m^3/MPa.

6.6. CONCLUDING REMARKS

The numerical modelling of several wetting or drying paths at constant loading or constant volume conditions using the double-porosity formulation developed in the previous chapters and implemented in the FE code CODE_BRIGHT has provided an in-depth insight into the local hydro-mechanical response to changes in the water content of macro-pores under isothermal conditions. Some sensitivity analyses were carried out in order to evaluate the dependence of the swelling potential on the initial and boundary conditions, on the stress paths, on the hydraulic and mechanical micro-macro coupling mechanisms and on the time required for hydrating or dehydrating the larger pores.

The numerical modelling predicts an increase in the swelling potential of the expansive soil specimen with increasing initial macrostructural suction and the coefficient (the rate) of the water mass exchange between micro- and macro-pores in wetting paths conducted under both "free" swell and constant volume conditions. On the one hand, the swelling strains obtained from the modelling of wetting paths at constant load conditions increase with a reduction of the magnitude of the confining pressures at which the re-saturation of macrostructure takes place. In addition, no relevant impact of the initial confining stresses is observed on the development of swelling pressures during hydration under isochoric conditions. The expansive behaviour seems to be more sensitive to the initial conditions in stress paths performed at unconfined conditions. It has also been observed a dependence of the model results on the sequence of operations (stress history) carried out between the same initial and final stress states. Such a stress path dependency is more evident for the saturation response and for the deformation behaviour of the microstructure.

The modelling of the desaturation of macro-pores at constant loading shows that the (elastic) volumetric contraction suffered by the element of expansive soil is affected by the initial suction and by the confining stresses at which the macrostructural dehydration occurs. The modelling results suggest that the magnitude of the hydraulic loading (the increase in macrostructural suction) exerts a substantial impact on the development of macro-porosity while the confining

pressure acting on the soil prior to the de-saturation of macro-pores has a major effect on the deformation response of microstructure during the subsequent drying process.

The hydraulic and the mechanical coupling processes between both structural media play a central role in the double-porosity model. Since the HM behaviour of an expansive clay can be explained in terms of the changes in the microstructural pore-water content, the leakage coefficient for the micro-macro water mass exchange is, undoubtedly, one of the most crucial model parameters to take into account when performing wetting or drying paths in swelling materials. In the numerical analyses carried out throughout this chapter, this parameter not only controls the saturation of micro-pores, but also increases the swelling (or shrinkage) potential in wetting (or drying) paths under unconfined and confined conditions. In fact, the coefficient of water mass exchange acts as a constitutive parameter that delays (or accelerates) the development of the swelling response of active clays as pore-water migrates from macro-pores to micro-pores. The mechanical structural coupling (the plastic β-mechanism), on the other hand, describes the evolution of the soil fabric due to the deformation of the microstructure in wetting/drying paths at constant load conditions and requires a total of six input parameters (three per interaction function) to be adopted. This plastic mechanism induces a hardening or a softening behaviour of the soil skeleton when the volumetric deformations of the microstructure generate a structural collapse or an irreversible dilation of macro-pores, respectively. For the wetting paths at unconfined conditions analysed in **Section 6.3.2**, the initial hardening response to the decrease in the macrostructural suction is followed by a softening of the yield surface as the expansive material approaches its saturation. However, this softening behaviour tends to reduce by increasing the confining pressures applied on the soil element during its hydration. In contrast, the activation of the plastic micro-macro interaction mechanism for modelling the dehydration paths at constant load conditions in **Section 6.4.2** generates a shrinkage in both structural media, which in turn, leads to a hardening of the yield surface as the soil element dries. However, this drying-induced hardening behaviour does not seem to depend so much on the confining pressures, at least for the level of stresses considered in the numerical simulations. The displacement restrictions imposed at all nodes for modelling the constitutive response of the cubic element of soil in wetting paths under constant volume conditions have hindered the development of plastic strains associated with the structural coupling mechanism.

7. APPLICATION OF THE DOUBLE-POROSITY MODEL (DPM) TO STRESS PATHS UNDER NON-ISOTHERMAL CONDITIONS: CONSTITUTIVE AND SENSITIVITY ANALYSES

7.1. INTRODUCTION

In the previous chapter, the capability of the double-porosity model (DPM) in reproducing the swelling and the shrinkage responses of expansive soils under isothermal conditions was investigated. Moreover, such hydro-mechanical analyses contributed to understand, from a microstructural standpoint, the essential role played by the hydraulic and the mechanical structural coupling mechanisms in the development of the swelling capacity of active clays when changes in the macro pore-water content take place. In the present chapter, the constitutive and sensitivity analyses are performed taking into account the thermal variable and its effects on the volumetric response of macro and microstructural media. In fact, the increase in temperature induces a thermal expansion of the solid and liquid phases in the porous medium. However, if such temperature increments are high enough, they could lead to a local shrinkage due to the dehydration induced by the generation of water vapour and its subsequent flux towards colder zones (Czaikowski *et al.*, 2012; Gaus *et al.*, 2014a; Vasconcelos and Gens, 2015; Gens and Vasconcelos, 2019). These two opposing behaviour trends show the additional complexity introduced by the thermal variable into the modelling of expansive soils. Therefore, the correct interpretation of the model predictions for non-isothermal problems in swelling clays must not only consider the hydro-mechanical aspects already discussed in the previous chapter, but it must also include the main thermal effects on the soil response. Furthermore, due to the coupled character of the thermo-hydro-mechanical (THM) processes that take place in a porous medium, the fully coupled mathematical formulation of the DPM must also reproduce satisfactorily the temperature-induced changes in stresses and in the saturation or de-saturation processes occurring at both pore levels.

In order to evaluate the model capabilities in predicting the expansive soil behaviour when temperature changes, some numerical analyses were carried out, adopting a strategy similar to the one followed in the sensitivity studies performed in **Chapter 6**. The impact of some key model parameters on the swelling response is also checked but, in the present case, under the performance of a local heating episode. The main modelling ingredients as the initial and boundary conditions, the model parameters and the cases and stress paths considered in the numerical analyses, together with the most relevant modelling outcomes, are described and discussed in the following sections.

7.2. MODELLING FEATURES

An important feature of the double-porosity formulation used in calculations is the hypothesis that any changes in temperature only generates thermal volumetric and elastic strains in both structural pore levels. In other words, the thermal loading has no direct effect on the evolution of the pre-consolidation pressure (p_0^*), which means that the terms associated with temperature changes in Equation (4-82) are neglected. Moreover, it is also assumed that microstructural thermal deformations do not cause (irreversible) structural changes in the macrostructure. However, the coupled THM formulation of the double-porosity model allows the occurrence of irreversible strains of macrostructure due to secondary effects of the thermal loadings. It means that temperature changes can generate important changes in the hydro-mechanical variables, whose development can lead to irreversible changes in the soil structure.

It is important to remark that the numerical analyses carried out in this chapter are merely constitutive. Therefore, the changes in temperature and macrostructural liquid pressure, when the heating episode is followed by a forced hydration of macro-pores, are prescribed at all nodes of the finite element (FE) mesh. These constitutive analyses aimed to evaluate the impact of the differential thermal expansion of pore-water on the saturation state of each structural medium. Since the swelling response of an expansive material is controlled by the changes in the saturation state of microstructure, the main purpose of performing these calculations was to understand the local impact of a thermal loading on the evolution of the swelling pressure and the role played by the micro-macro leakage coefficient in such non-isothermal scenarios. All the numerical analyses were performed under constant volume conditions with a maximum temperature not exceeding 100°C.

7.2.1. MODELLED DOMAIN, INITIAL AND BOUNDARY CONDITIONS

The thermal response of the constitutive double-porosity formulation was evaluated by means of the inclusion of a heating episode in the numerical analyses carried out in **Chapter 6**. In other words, the same geometry modelled in those studies, that is, the cubic element of expansive soil with 1 cm^3 volume, was employed in the thermal analyses as well as the FE mesh and the initial hydro-mechanical properties. The initial temperature in the soil element is set at 22°C. The heating event is reproduced as a linear increment of temperature, from its initial value until

reaching target values ranging between 50°C and 100°C. This thermal loading is performed over a period of 30 days and it is modelled by applying the temperature variations directly to all nodes (for the whole volume). The final nodal temperature remains unchanged until the end of the numerical calculations.

Different thermal and hydraulic load sequences were considered. Nevertheless, two of them are analysed here due to their practical importance in the study of the THM processes that are expected to take place during the lifetime of a clay barrier surrounding radioactive waste. The first non-isothermal scenario is characterized by a heating without any subsequent hydration of the expansive soil. This situation would represent the status of an engineered barrier in the first years after the closure of the nuclear waste deposit, when high temperatures could be registered in the vicinity of the waste container with the clay barrier still in very dry conditions. The second thermal scenario corresponds to a heating episode followed by the hydration of the soil element at a constant temperature. Such a scenario would reproduce the long-term conditions found in a clay barrier, the saturation of which could occur under a high temperature regime.

The heating without any forced re-saturation of macro-pores (CVP_He) are analysed for five stress paths. Three distinct values for the initial macro suction are considered: 123 MPa, 75 MPa and 50 MPa. Furthermore, three different thermal loadings are applied to the case with an initial suction of 123 MPa, prescribing an increment in temperature from its initial value up to 50°C, 75°C and 100°C. The final temperature for the other stress paths (CVP_He-50 and CVP_He-75) is fixed at 100°C. An initial isotropic stress state of 0.1 MPa is assumed in the cases modelled, except for the stress path identified as CVP_He-123/T-100, for which the heating of the cubic element of expansive soil is also carried out at higher initial confining stresses. The identification of these thermal stress paths (in the $p: s_M$ plane) depends on the values of the initial suction and the final temperature. Thus, the stress paths termed as CVP_He-50 and CVP_He-123/T-50 refer to the heating (without any artificial hydration) of the cubic sample of expansive material with initial matric suctions of 50 MPa and 123 MPa submitted to thermal loadings that increase the nodal temperature up to 100°C and 50°C, respectively. The non-explicit reference of temperature in the path nomenclature means that the final target temperature is 100˚C. The identification of the stress paths studied in this chapter together with the information about their initial and final conditions are summarized in Table 7-1. Once the final temperature has been reached at all nodes of the FE mesh, the non-isothermal analyses are prolonged for 150 more days, totaling a time period (Δt_{model}) of 180 days for the duration of the constitutive test.

The heating followed by a hydration step (CVP_HeW) is taken as a “natural” extension of the first (previous) heating scenario, and for which the macrostructural suction is decreased linearly from its value at the end of the previous thermal situation (heating without any artificial hydration) to 0.1 MPa. The hydration process is carried out by imposing the hydraulic loading to all nodes of the mesh (for the whole volume) and keeping the nodal temperature unchanged. The re-saturation of macro-pores occurs 90 days after the start of the hydration phase. The four stress paths considered in this heating scenario are also described in Table 7-1.

Table 7-1: Identification of the modelled thermal stress paths at constant volume conditions corresponding to a heating without artificial hydration (CVP_He) and to a forced hydration at higher temperatures (CVP_HeW).

	Initial / Final Temperature (°C)	Initial / Final Macro Suction (MPa)	Initial / Final Mean Stress (MPa)	Sequence of operations
CVP_He-50	22 / 100	50 / NC*	0.1 / NC*	heating
CvP_He-75	22 / 100	75 / NC	0.1 / NC	heating
CVP_He-123/T-50	22 / 50	123 / NC	0.1 / NC	heating
CVP_He-123/T-75	22 / 75	123 / NC	0.1 / NC	heating
CVP_He-123/T-100	22 / 100	123 / NC	0.1 - 2.0 / NC	heating
CVP_HeW-50	22 / 100	50 / 0.1	0.1 / NC	heating-wetting
CVP_HeW-75	22 / 100	75 / 0.1	0.1 / NC	heating-wetting
CVP_HeW-123/T-50	22 / 50	123 / 0.1	0.1 / NC	heating-wetting
CVP_HeW-123/T-75	22 / 75	123 / 0.1	0.1 / NC	heating-wetting
CVP_HeW-123/T-100	22 / 100	123 / 0.1	0.1 / NC	heating-wetting

* NC: not controlled

Despite the fact that the pore-air pressure tends to increase with temperature, such a thermal feature has not been considered in the numerical calculations. Furthermore, it is assumed that there is always local equilibrium between the pore-air pressure in micro and macro voids. For all the stress paths examined here, the values of the initial macrostructural suction indicated in Table 7-1 also represent the initial suction state of microstructure.

7.2.2. MODEL PARAMETERS

The hydro-mechanical parameters required for modelling the THM response of the cubic element of soil are the ones adopted in the isothermal analyses discussed in the previous chapter, whose values are given from Table 6-3 to Table 6-9. The model parameters for the thermal problem were calibrated and used in previous modelling tasks (Czaikowski *et al.*, 2012; Gaus *et al.*, 2014a; Garitte *et al.*, 2015; Gens and Vasconcelos, 2019), in which the short and the long-term responses of an MX-80 pelletized barrier subject to a heating/natural hydration (the *in-situ* HE-E experiment, in Mont Terri, Switzerland) were simulated. All the relevant thermal parameters necessary for the numerical calculations carried out in this chapter are given in Table 7-2. One of the hypotheses assumed during the development of the mathematical formulation of the double-porosity model was that the thermal loading would not generate any thermal irreversible deformation (see **Section 4.2.5**). As a consequence of this assumption, the thermal expansion coefficient for the solid phase and for the porous skeleton must have the same values (Booker and Savvidou, 1985; Khalili *et al.*, 2010). The thermal expansion coefficient of the free water is a physical parameter depending on temperature. Nevertheless, a constant value for this thermal parameter corresponding to a temperature of 40°C is employed in the numerical modelling.

Table 7-2: Model parameters used in the numerical simulations for predicting the thermal effects on the soil behaviour under non-isothermal loadings.

Thermal Expansion		
Linear thermal expansion for grains	[°C^{-1}]	2.5e-05
Volumetric thermal expansion for water (at 40°C)	[°C^{-1}]	3.4e-04*
Volumetric thermal expansion for the porous medium	[°C^{-1}]	7.5e-05
Thermo-elastoplastic parameters: Equation (4-61); Equation (4-82); Equation (4-84)		
Parameter for elastic thermal strain, α_0	[°C^{-1}]	7.5e-05
Parameter for plastic thermal strain, α_1	[MPa °C^{-1}]	0.0
Parameter for elastic thermal strain, α_2	[°C^{-2}]	0.0
Parameter for plastic thermal strain, α_3	[MPa °C^{-2}]	0.0
Param. related to decrease of tensile strength due to ΔT, ρ_T	-	0.0
Solid phase specific heat	[J/kg/K]	893

* In CODE_BRIGHT, such an input parameter assumes a negative value because the thermal expansion of pore-water leads to a reduction of its density.

7.3. HEATING AT CONSTANT VOLUME (WITHOUT ARTIFICIAL HYDRATION)

The immediate consequence of prescribing a thermal loading on a certain volume of expansive material is the generation of deformations caused by the thermal expansion of the species contained in that portion of soil. Consequently, an increase in temperature under restricted volume conditions tends to cause the development of thermally-induced stresses within the element of soil. The thermal loading could also induce a considerable shrinkage of the porous medium due to drying. Therefore, the analysis of the soil response at isochoric conditions is limited by the magnitude of the temperature increment in order to prevent the development of excessive thermal contractions. In other words, $\Delta\phi = \Delta\overline{\phi}_M + \Delta\overline{\phi}_m \approx 0$ should be satisfied for all time steps. In that sense, the heating at constant volume conditions without the inclusion of a subsequent forced hydration step is performed by prescribing the boundary conditions for the thermo-mechanical problem directly at all nodes of the FE mesh (the whole volume of soil). Therefore, the nodal temperature and the (null) nodal displacement vector are given (prescribed, known) at each time step and only the nodal fluid pressures are the primary unknowns to be determined numerically. The thermal loadings imposed to all nodes of the FE mesh of the modelled geometry are indicated in Figure 7-1.

Following the modelling strategy adopted in **Chapter 6**, the heating of the expansive soil sample is modelled with the plastic coupling mechanism between microstructure and macrostructure deactivated (**Section 7.3.1**) or activated (**Section 7.3.2**). Consequently, the impact of each plastic mechanism on the material response during a thermal loading can be evaluated separately.

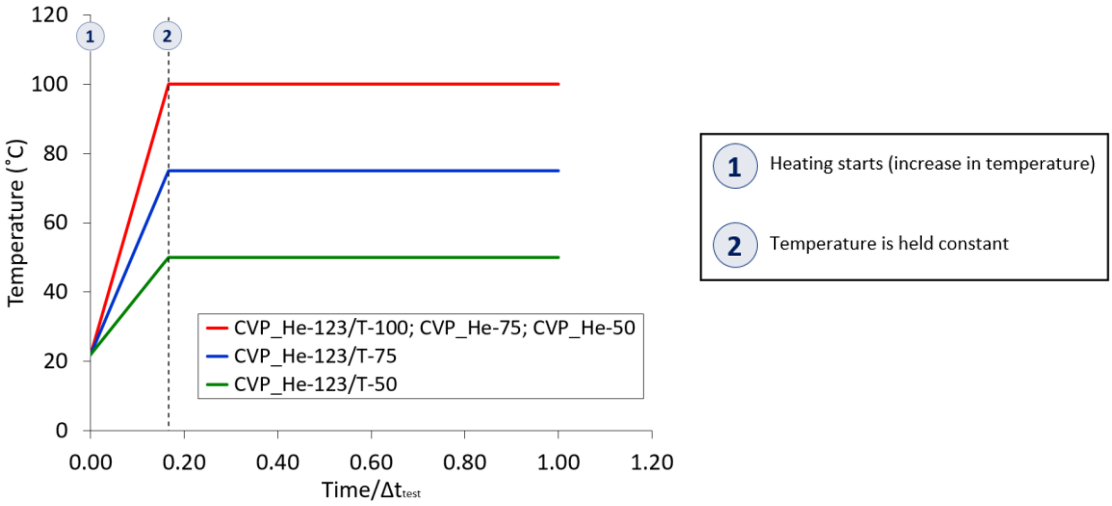

Figure 7-1: Temperature evolution prescribed at all nodes during the heating of a cubic volume of expansive soil in THM paths at constant volume conditions. Temperature is increased during the first 30 days. The "total" duration of the heating test (Δt_{model}) is equal to 180 days.

7.3.1. ANALYSES WITH THE β-MECHANISM DEACTIVATED

The impact of the magnitude of the thermal loading on the expansive soil response was analysed by following the paths CVP_He-123/T-100, CVP_He-123/T-75 and CVP_He-123/T-50 (see Table 7-1). Each one of such THM paths is simulated under two different micro-macro interaction scenarios: one corresponding to a lower rate of water mass transfer between micro- and macro-pores (Scenario #1 in Table 6-9) and the other one representing a faster micro-macro water exchange condition (Scenario #3 in Table 6-9). The most relevant model outcomes from the simulation of the distinct heating events (without any subsequent artificial re-saturation of macro-pores) are plotted from Figure 7-2 to Figure 7-6. The first and most notable aspect to be point out from such results is that the magnitude of the changes in the hydro-mechanical variables is "proportional" to the temperature changes imposed during the heating phase (see Figure 7-2), as expected. In that sense, the hardening parameter (Figure 7-3), the thermally-induced stresses (Figure 7-4), the volumetric expansion of microstructure and the irreversible collapse of macro-pores (Figure 7-5 and Figure 7-6) are higher for the stress path CVP_He-123/T-100 and lower for the path CVP_He-123/T-50. Moreover, the desaturation of microstructure is more significant for larger increments of temperature (see Figure 7-2). However, some crucial features regarding the thermal behaviour of double-porosity materials must be taken into account in order to interpret these results and to properly evaluate the model capabilities in reproducing the non-isothermal response of expansive clays.

Firstly, the differential thermal expansion of the pore-water, the solid grains and the soil skeleton controls the initial pore saturation evolution, when temperature is not high enough to produce the pore-water evaporation. As the thermal expansion coefficient for water is larger than the coefficient for the thermal expansion of pores, the initial increase in temperature induces a slight "thermal" hydration of both structural media (Figure 7-2). The hypothesis of purely volumetric and elastic thermal strains assumed in the development of the mathematical formulation has led to the choice of the same value for the thermal expansion coefficient of the

solid grains and the soil skeleton (see **Section 4.2.5**). Therefore, the thermal expansion coefficients of micro- and macro-pores are proportional to the thermal expansions of the clay aggregates and the soil skeleton, respectively. Consequently, micro- and macro-pore volume fractions remain practically unchanged during the first stages of heating (Figure 7-5 and Figure 7-6), at least as long as the initial LC curve is not intersected by the stress path. Secondly, the constant volume condition imposed to the soil element generates the development of confining stresses when its thermal expansion is prevented (Figure 7-4). Initially, such an increment of confining pressures does not produce any structural rearrangement of the clay aggregates. However, once the stress path touches the LC curve while the soil element is still subjected to a temperature rise, the soil structure can no longer withstand the thermally-induced stresses and a macrostructural collapse occurs. This irreversible decrease of the macro-pore volume fraction allows the development of micro-pores with the ongoing heating. The subsequent thermal response of microstructure (clay particles + micro-pores) causes a progressive reduction in macro-porosity as the soil element hardens plastically (see Figure 7-3 to Figure 7-6). The combined effect of the thermal expansion of the macrostructural pore-water and the thermally-induced collapse of macro-pores enhances the macrostructural saturation state. Such an increase in the thermo-mechanical hydration of macro-pores is evidenced by the decrease in the macro suction as temperature increases, especially for the situation when $\gamma^w = 10^{-9}$ kg/s/m^3/MPa (Scenario #1) – see Figure 7-2. However, the increase in the micro-pore volume fraction due to the thermal expansion of the clay aggregates under confined conditions (see Figure 7-5 and Figure 7-6) could be the main cause for the slight decrease in the micro degree of saturation after the activation of the BBM mechanism (see Figure 7-3) and before reaching the maximum temperature. The increase in the micro suction during this heating stage could be a result of the combined effect of the volumetric thermal expansion of microstructural water and the water mass exchanged from macro-pores to micro-pores.

When heating reaches its final stage and temperature is maintained constant (for 150 more days), the micro and macro suctions also reach a stationary regime (Figure 7-2) as well as the thermal confining stresses (Figure 7-4). Consequently, the degree of saturation, the porosity variables and the pre-consolidation pressure remain unchanged until the end of the numerical modelling. The application of distinct increments in temperature demonstrates that the thermally-induced changes in the hydro-mechanical variables decrease as the magnitude of these thermal loadings also reduces. Thus, for the cases considered in the numerical analyses performed here, the hydro-mechanical response of the expansive soil sample to the increments in temperature is more noticeable in the path CVP_He-123/T-100 (target temperature of 100˚C) and less significant for path CVP_He-123/T-50 (target temperature of 50˚C).

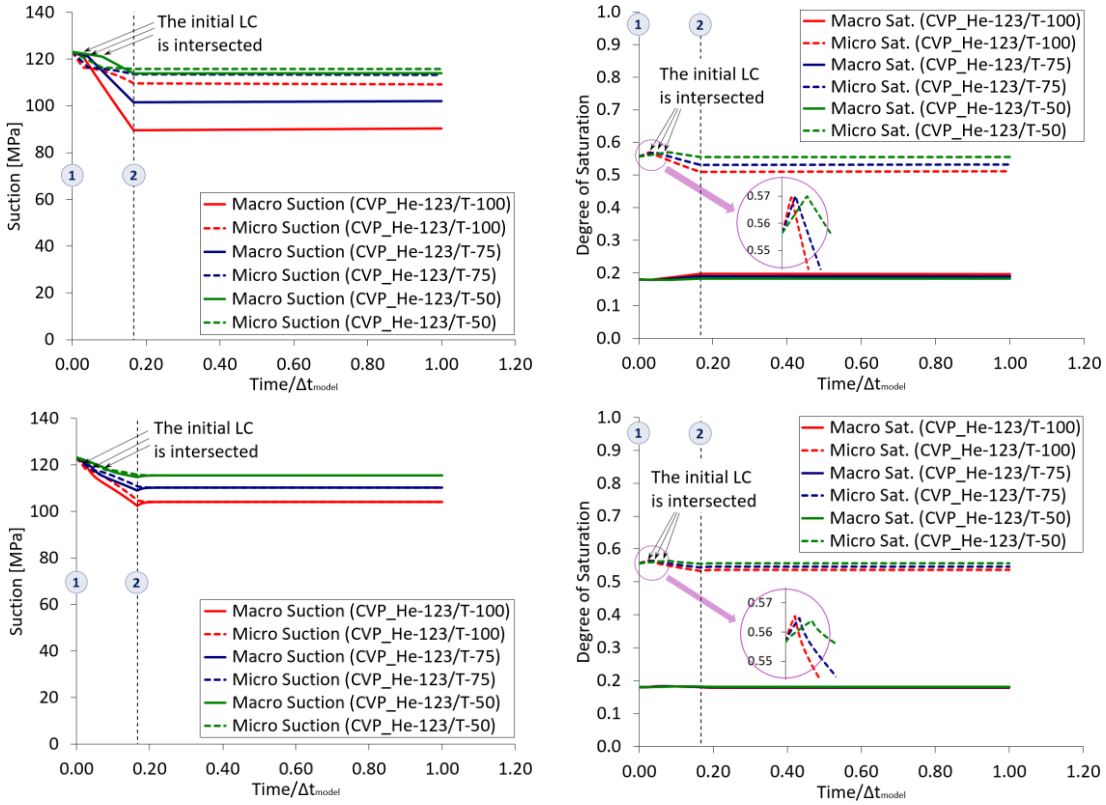

Figure 7-2: Evolution of suction and degree of saturation for distinct thermal loadings (without subsequent hydration) when $\gamma^w = 10^{-9}$ kg/s/m³/MPa (up) and $\gamma^w = 10^{-6}$ kg/s/m³/MPa (down).

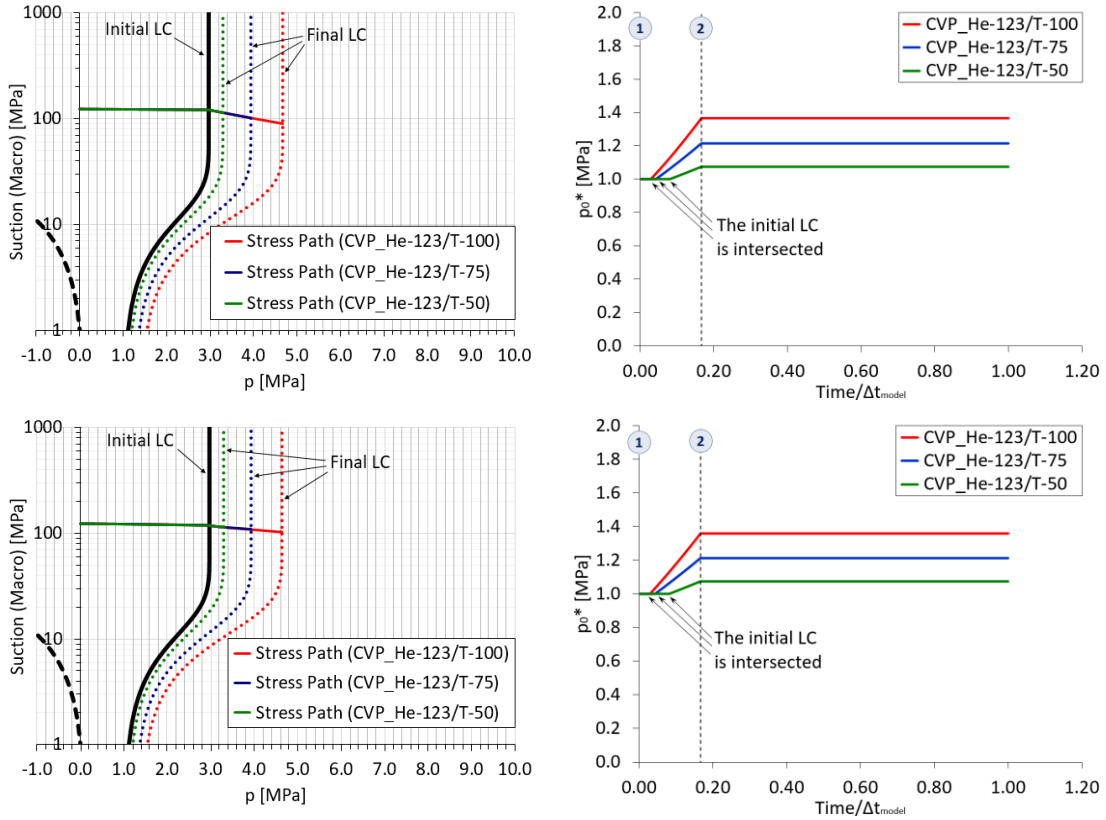

Figure 7-3: Stress paths CVP_He-123 for distinct thermal loadings plotted in the p: s_M plane (left) with the evolution of the pre-consolidation pressures (right) when $\gamma^w = 10^{-9}$ kg/s/m³/MPa (up) and $\gamma^w = 10^{-6}$ kg/s/m³/MPa (down).

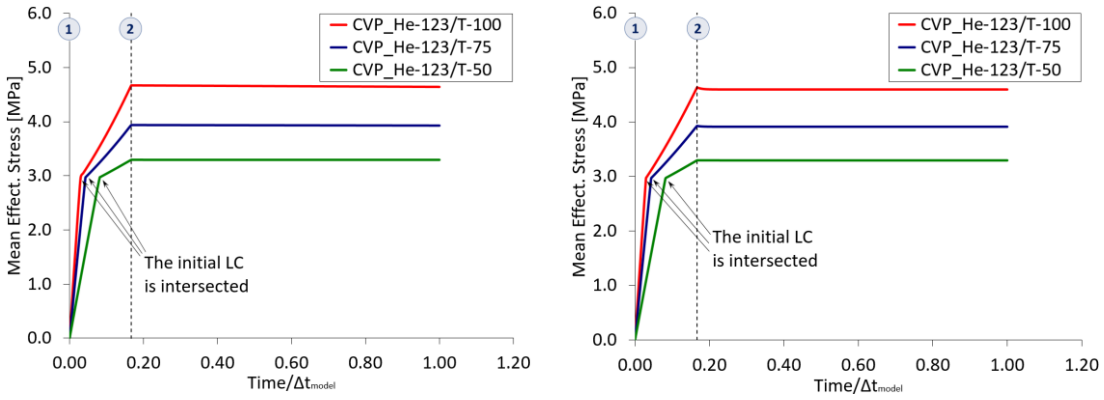

Figure 7-4: Thermally-induced stresses in the stress path CVP_He-123 for distinct thermal loadings when $\gamma^w = 10^{-9}$ kg/s/m^3/MPa (left) and $\gamma^w = 10^{-6}$ kg/s/m^3/MPa (right). Temperature is increased during the first 30 days while Δt_{model}=180 days.

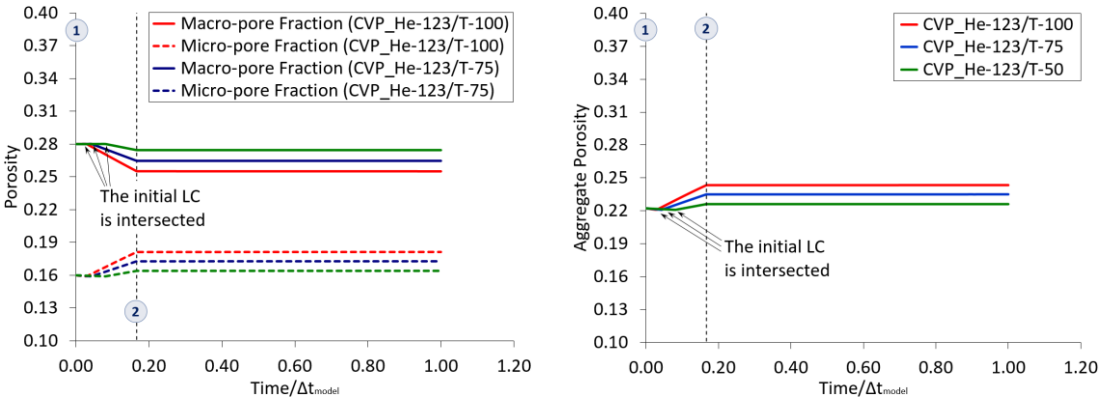

Figure 7-5: Evolution of porosity variables in the stress path CVP_He-123 for distinct thermal loadings when $\gamma^w = 10^{-9}$ kg/s/m^3/MPa (Scenario #1). Temperature is increased during the first 30 days while Δt_{model}= 180 days.

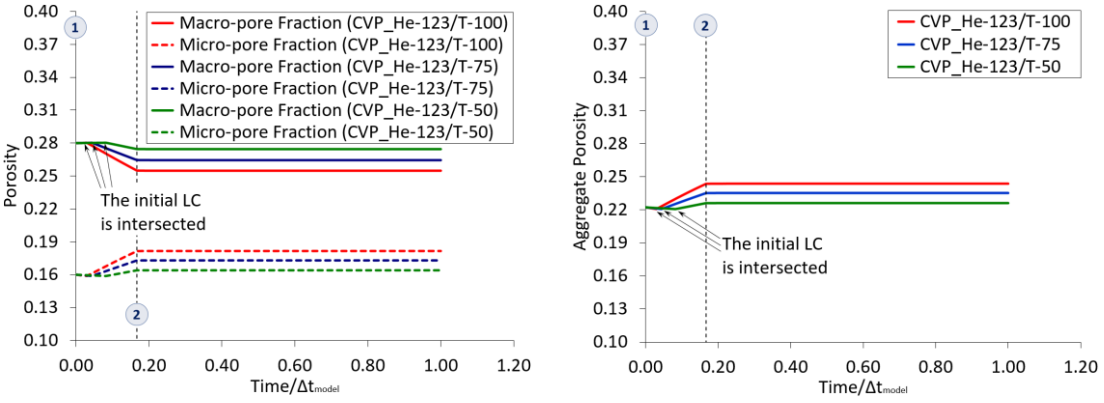

Figure 7-6: Evolution of porosity variables in the stress path CVP_He-123 for distinct thermal loadings when $\gamma^w = 10^{-6}$ kg/s/m^3/MPa (Scenario #3). Temperature is increased during the first 30 days while Δt_{model}= 180 days.

The water mass transfer mechanism plays a crucial role in the saturation process of micro- and macro-pores, as clearly observed when comparing the development of suctions and degrees of saturation in Figure 7-2. The model predictions obtained from CVP_He-123/T-100 in Scenario #1 ($\gamma^w = 10^{-9}$ kg/s/m^3/MPa) and in Scenario #3 ($\gamma^w = 10^{-6}$ kg/s/m^3/MPa) are plotted together from Figure 7-7 to Figure 7-10. For a lower value of the water exchange coefficient (Scenario #1), the very limited hydraulic interaction between both pore levels delays the occurrence of the local

balance of water potential (see Figure 7-7). In such a situation, the suction changes in each structural media during a heating episode are almost exclusively due to the differential thermal expansion of the pore-water and the solid particles in a soil and to the occurrence of the water phase change when the thermal loading and the thermal gradient are high enough to promote water vaporization. When the micro-macro leakage coefficient is high enough (as in Scenario #3), the pore-water exchange mechanism due to the unbalanced water potential induced by the changes in temperature also contributes to the re-saturation or desaturation of both families of pores (see Figure 7-7). This mass transfer process explains the differences in the evolution of the micro and the macrostructural water potentials under a same thermal loading (see Figure 7-2 and Figure 7-7). The impact of distinct coefficients for the micro-macro water mass transfer on the development of the hardening parameter (Figure 7-8), the thermal stresses (Figure 7-9) and the porosity variables (Figure 7-10) depends essentially on their impact on the evolution of the micro and macro hydraulic variables (Figure 7-7). It is important to note that in the first stage of heating (during purely thermo-elastic conditions), the volumetric thermal expansion of pore-water induces a more pronounced decrease in the micro component of suction than in the macrostructural one. In such conditions, the numerical results suggest the occurrence of a net water mass exchange from micro-pores to macro-pores, whose effects are more noticeable when $\gamma^w = 10^{-6}$ kg/s/m^3/MPa.

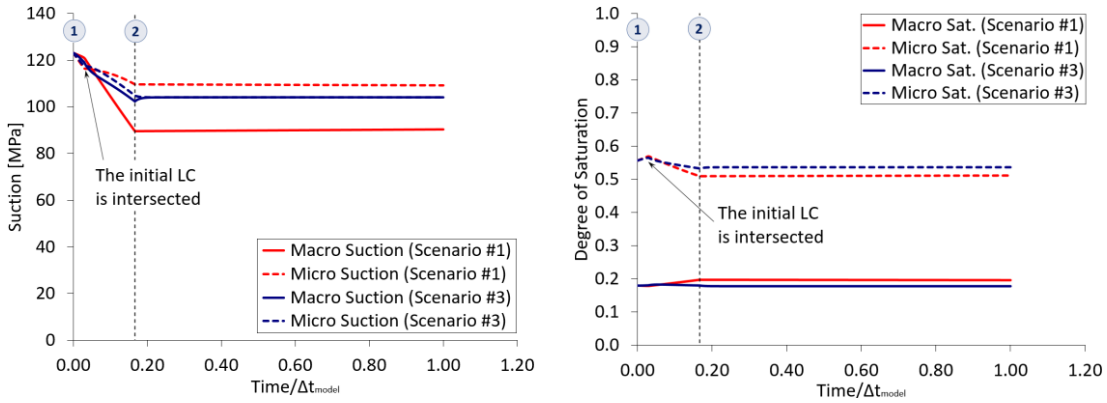

Figure 7-7: Comparison between the micro and macro suctions and degrees of saturation from the CVP_He-123/T-100 path when $\gamma^w = 10^{-9}$ kg/s/m^3/MPa (Scenario #1) and $\gamma^w = 10^{-6}$ kg/s/m^3/MPa (Scenario #3). Δt_{model}=180 days.

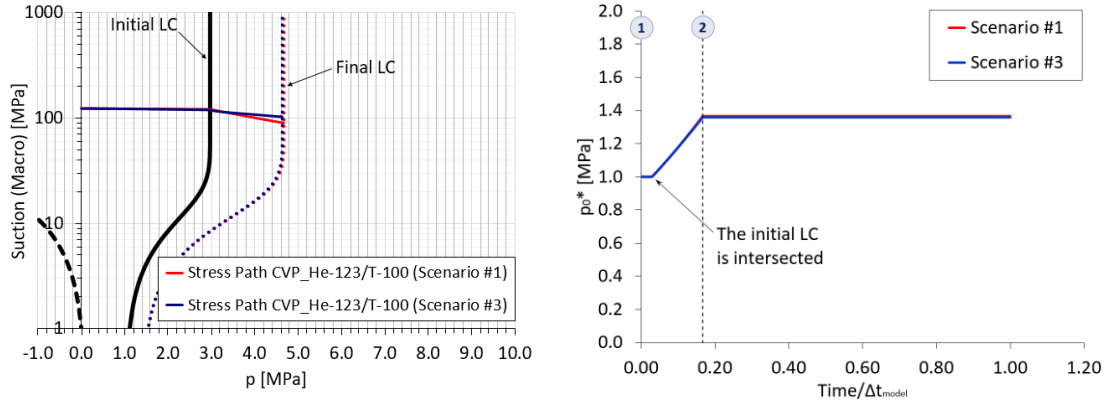

Figure 7-8: Stress paths in the p: s_M plane (left) with the evolution of the pre-consolidation pressures (right) from the CVP_He-123/T-100 path when $\gamma^w = 10^{-9}$ kg/s/m^3/MPa (Scenario #1) and $\gamma^w = 10^{-6}$ kg/s/m^3/MPa (Scenario #3). Δt_{model}= 180 days.

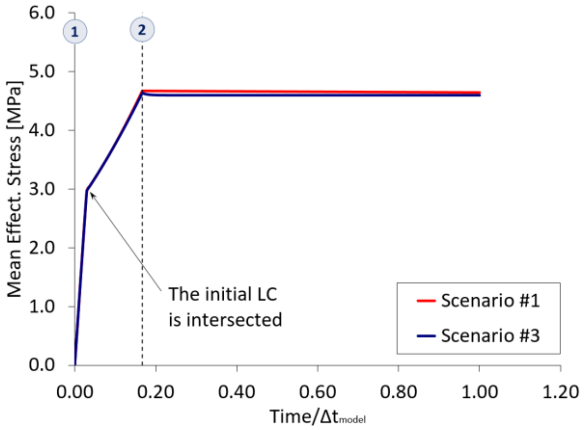

Figure 7-9: Comparison between the thermal effective stress from the CVP_He-123/T-100 path when $\gamma^w = 10^{-9}$ kg/s/m^3/MPa (Scenario #1) and $\gamma^w = 10^{-6}$ kg/s/m^3/MPa (Scenario #3). Δt_{model}=180 days.

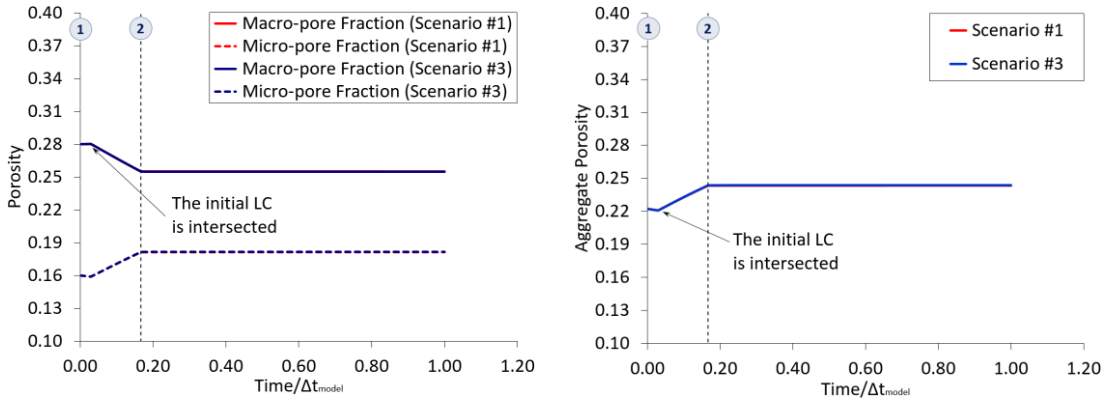

Figure 7-10: Comparison between the porosity variables from the CVP_He-123/T-100 path when $\gamma^w = 10^{-9}$ kg/s/m^3/MPa (Scenario #1) and $\gamma^w = 10^{-6}$ kg/s/m^3/MPa (Scenario #3). Δt_{model}= 180 days.

The influence of the initial suctions and confining pressures on the soil response under high and increasing temperatures was also analysed. In that sense, three THM paths starting at different suctions (CVP_He-123/T-100, CVP_He-75 and CVP_He-50) and at an initial confining pressure of 0.1 MPa have been heated from 22˚C until reaching the target temperature of 100˚C (in a 30 days' time). The numerical results comparing the evolution of suctions, degrees of saturation, pre-consolidation and thermally-induced stresses, pore volume fractions and porosities at micro and macro media for each of these cases are shown from Figure 7-11 to Figure 7-15.

The increase in the initial water content of the expansive soil specimen when submitted to the same thermal loading reduces the thermally-induced changes in the micro and macro suctions (Figure 7-11), the pre-consolidation pressures (Figure 7-12), the thermal stresses (Figure 7-13) and the porosity variables (Figure 7-14 and Figure 7-15). Such a behaviour dependence on the initial suction, especially after the activation of the plastic loading-collapse mechanism (the LC mechanism), could be a consequence of the degree of structural rearrangement of the clay aggregates under a thermal loading together with the amount of water found in macro-pores. In fact, the initial drier state in the CVP_He-123/T-100 path allows the occurrence of larger irreversible changes in the macro-pore volume fraction (by the reduction of the pore-volume occupied by the gas phase) so that a new structural configuration sustaining the increase in the thermally-induced stresses can be achieved. Moreover, the volumetric changes of non-

saturated macro-pores subjected to THM loadings are affected by the presence of low compressible fluids in them, even at high temperatures and pressures, such as pore-water (see Fine and Millero, 1973). Due to that, the volumetric decrease of the inter-aggregate pores is higher in CVP_He-123/T-100 and lower in the CVP_He-50 path (see Figure 7-14 and Figure 7-15). Consequently, the development of the hardening parameter (related to the changes in the macro-pore volume fraction) – see Figure 7-12 – and the thermo-mechanical hydration of macro-pores (in Figure 7-11) are more significant for initially drier porous skeletons. Additionally, the volumetric thermal expansion of the clay aggregates (microstructure) under isochoric conditions can develop further when macrostructural collapse is higher (as in CVP_He-123/T-100).

The modelling of the heating episode following the CVP_He-123/T-100 path was also carried out for three distinct initial stress levels (p_{t0}): 0.1 MPa (Case A), 1.0 MPa (Case B) and 2.0 MPa (Case C). The model predictions obtained from such calculations are given from Figure 7-16 to Figure 7-20. The impact of increasing the initial confining pressures on the soil response to heating is not significant (at least, not for the stress levels considered in calculations). However, and for the same initial suction, a path starting at a higher confining pressure develops non-reversible strains first, that is, such a path reaches the initial LC locus at a lower temperature (see Figure 7-17). Consequently, the magnitude of the plastic strains induced by the thermal loading is higher for Case C, which is evidenced by the slightly larger decrease in the macro-pore volume fraction along this stress path (see Figure 7-19 and Figure 7-20). Due to that, the strain hardening process associated with the plastic BBM (LC) mechanism generates a further enlargement of the elastic domain for Case C, as indicated in Figure 7-17. Although the plastic micro-macro coupling mechanism is not activated, however, it is important to remark that Case A (starting at a lower $\frac{p_{t0}}{p_0(s_M)}$) characterizes a heating performed at a denser macrostructure condition while Case C (starting at a higher $\frac{p_{t0}}{p_0(s_M)}$) simulates a heating applied to a more open soil skeleton.

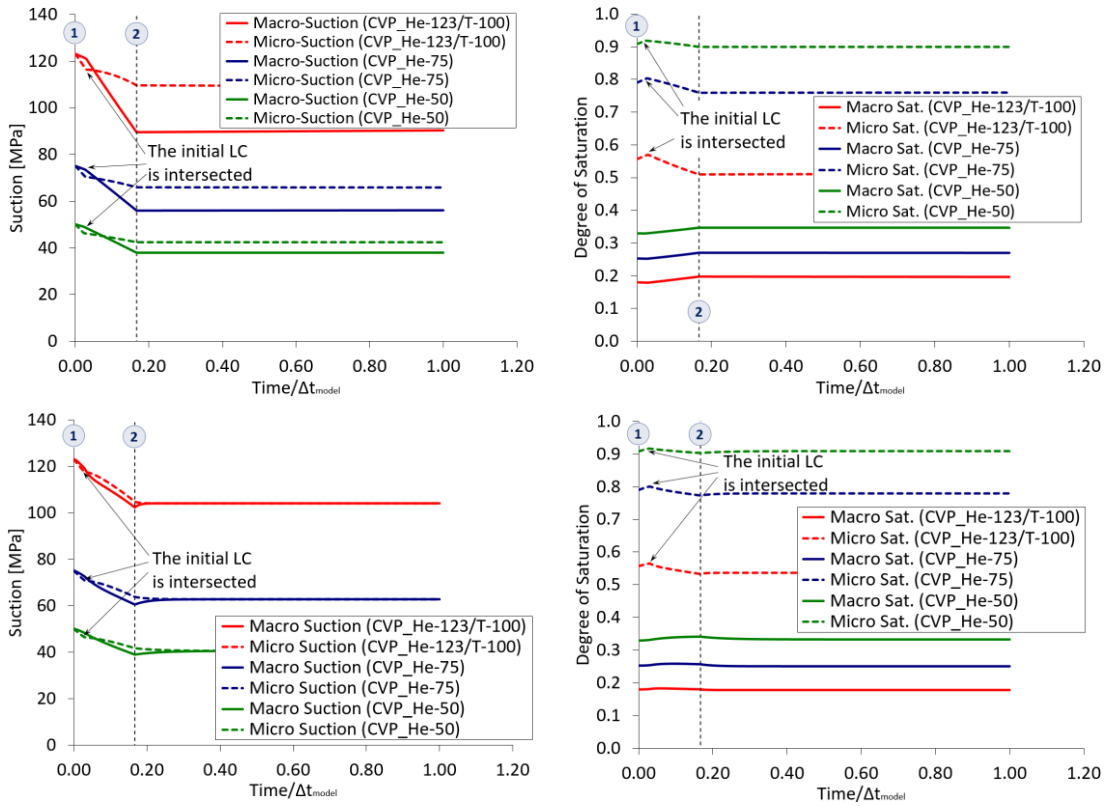

Figure 7-11: Evolution of suction and degree of saturation for a thermal loading starting at distinct suctions when $\gamma^w = 10^{-9}$ kg/s/m^3/MPa (up) and $\gamma^w = 10^{-6}$ kg/s/m^3/MPa (down). Δt_{model}=180 days..

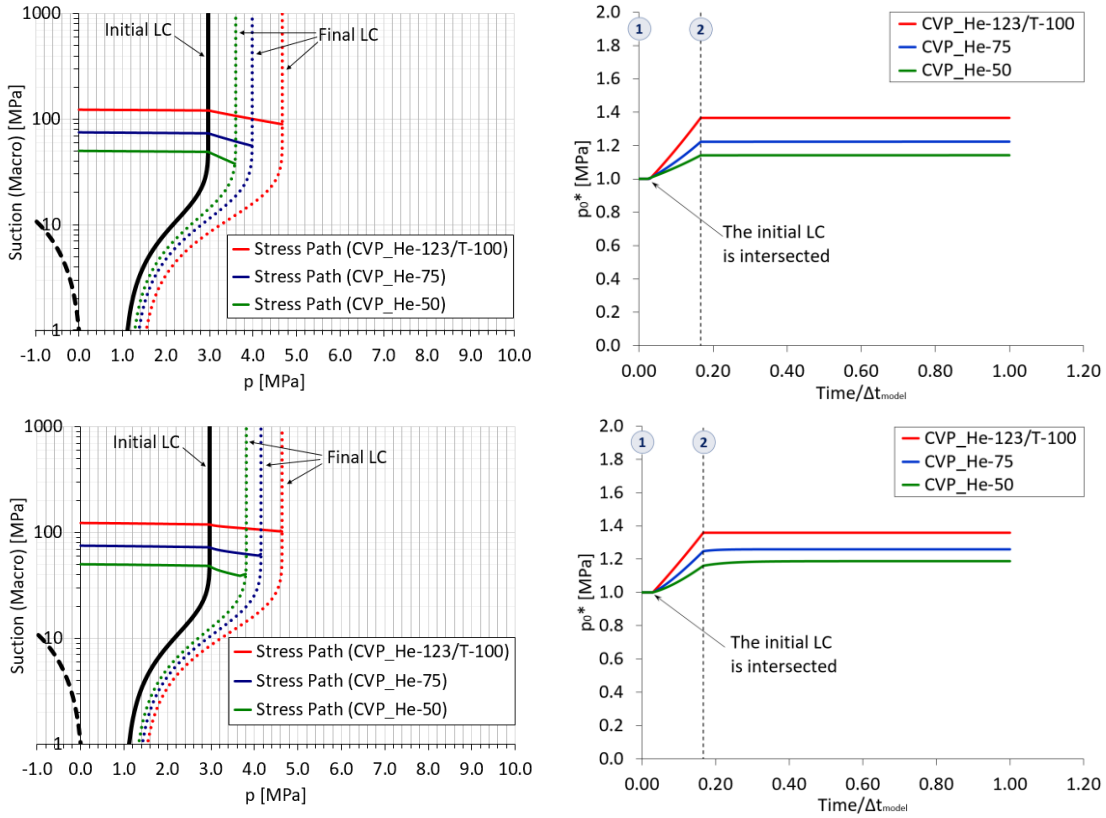

Figure 7-12: Stress paths in the p: s_M plane (left) with the evolution of the pre-consolidation pressures (right) for a thermal loading starting at distinct suctions when $\gamma^w = 10^{-9}$ kg/s/m^3/MPa (up) and $\gamma^w = 10^{-6}$ kg/s/m^3/MPa (down). Δt_{model}=180 days.

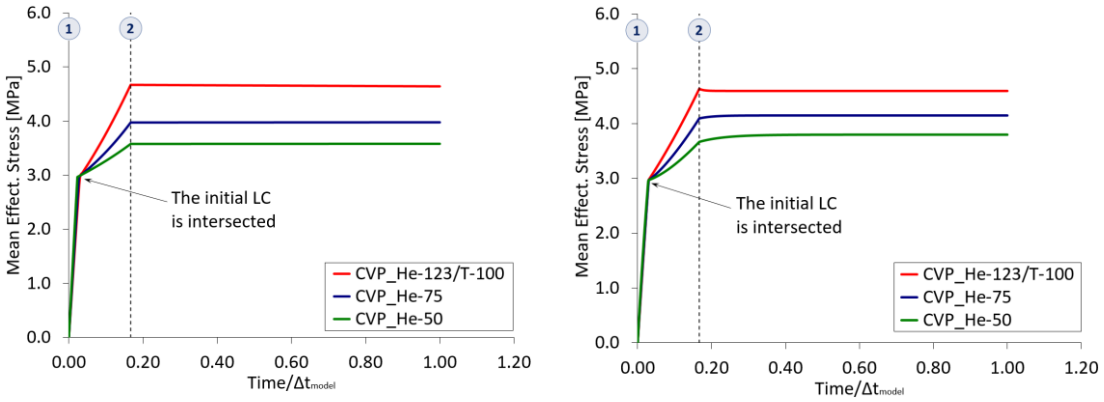

Figure 7-13: Effective stresses induced by a thermal loading starting at distinct suctions when $\gamma^w = 10^{-9}$ kg/s/m^3/MPa (left) and $\gamma^w = 10^{-6}$ kg/s/m^3/MPa (right). Δt_{model}=180 days.

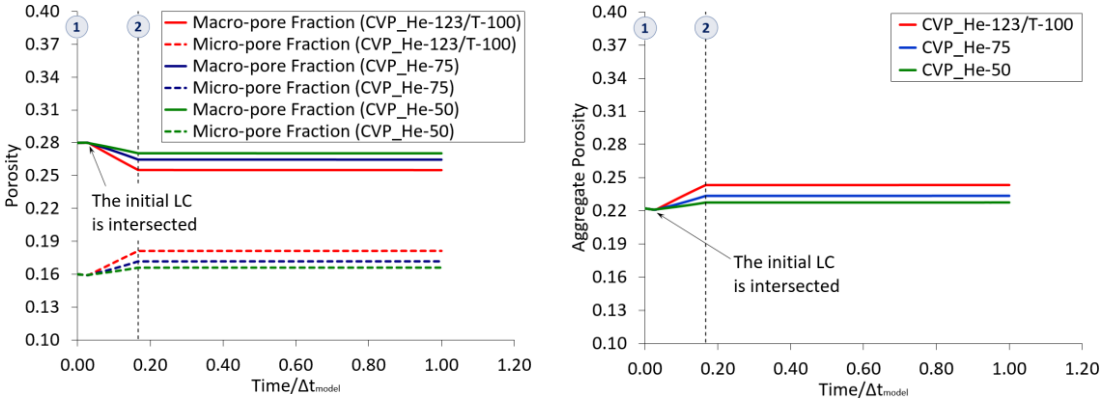

Figure 7-14: Evolution of the pore-volume fractions (left) and the aggregate porosity (right) for a thermal loading starting at distinct suctions when $\gamma^w = 10^{-9}$ kg/s/m^3/MPa (Scenario #1). Δt_{model}=180 days.

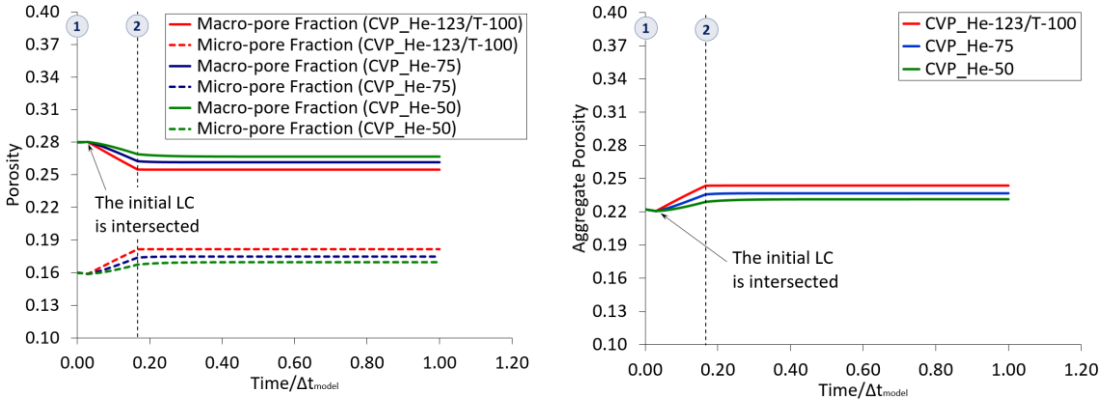

Figure 7-15: Evolution of the pore-volume fractions (left) and the aggregate porosity (right) for a thermal loading starting at distinct suctions when $\gamma^w = 10^{-6}$ kg/s/m^3/MPa (Scenario #3). Δt_{model}=180 days.

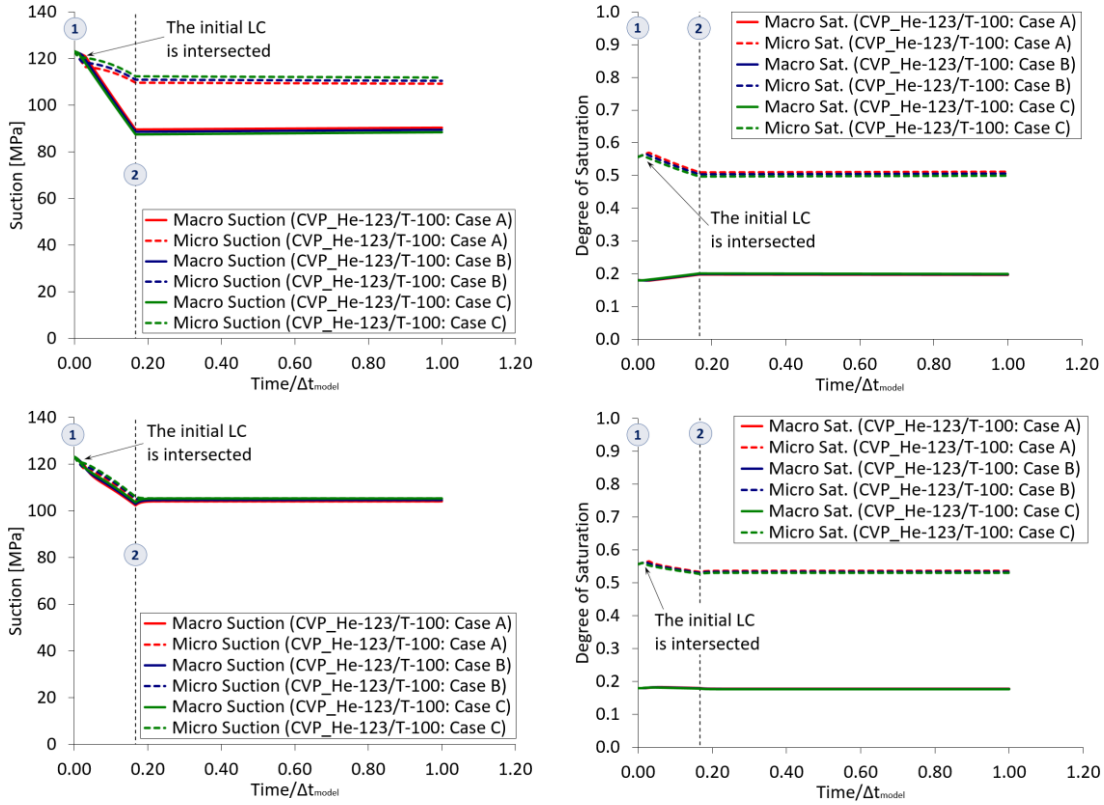

Figure 7-16: Evolution of suction and degree of saturation for a thermal loading starting at distinct initial confining pressures when $\gamma^w = 10^{-9}$ kg/s/m^3/MPa (up) and $\gamma^w = 10^{-6}$ kg/s/m^3/MPa (down). Δt_{model}=180 days.

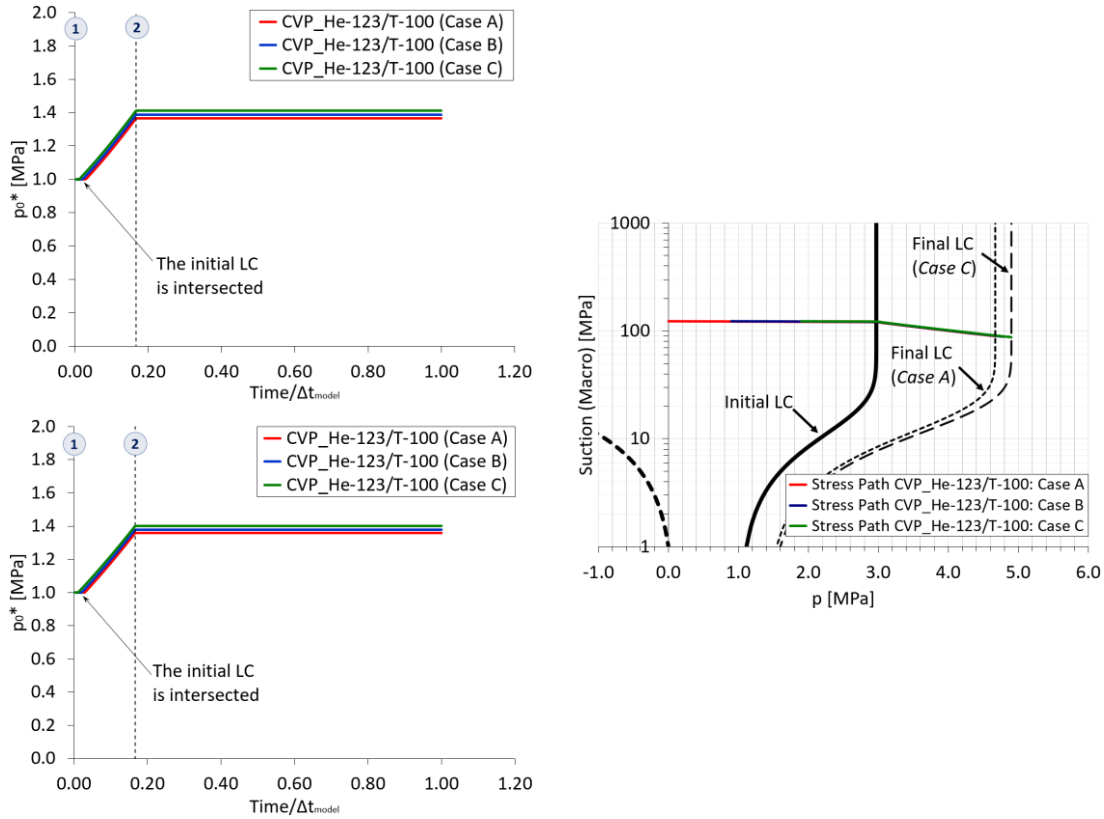

Figure 7-17: Evolution of the pre-consolidation pressures for a thermal loading starting at distinct initial confining pressures when $\gamma^w = 10^{-9}$ kg/s/m^3/MPa (up, at left) and $\gamma^w = 10^{-6}$ kg/s/m^3/MPa (down, at left) and the THM paths in the p: s_M plane (right) when $\gamma^w = 10^{-9}$ kg/s/m^3/MPa.

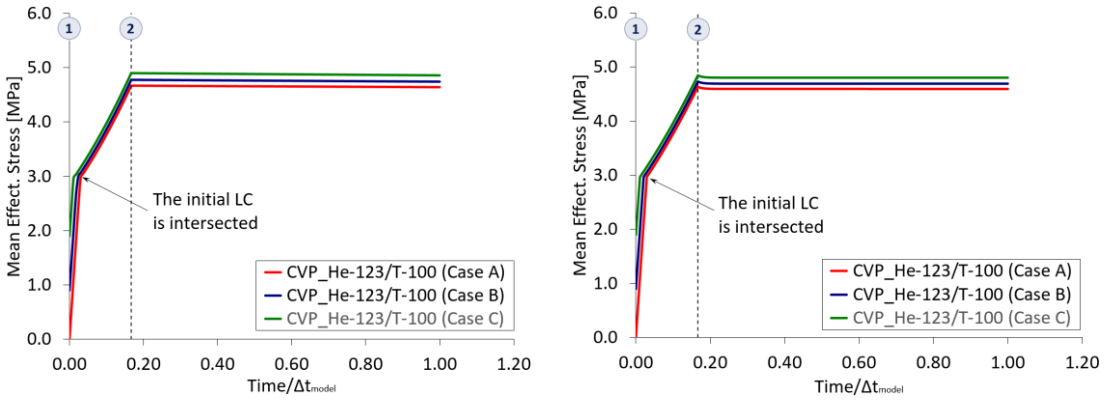

Figure 7-18: Evolution of thermally-induced effective stresses for a thermal loading starting at distinct initial confining pressures when $\gamma^w = 10^{-9}$ kg/s/m^3/MPa (left) and $\gamma^w = 10^{-6}$ kg/s/m^3/MPa (right). Δt_{model}=180 days.

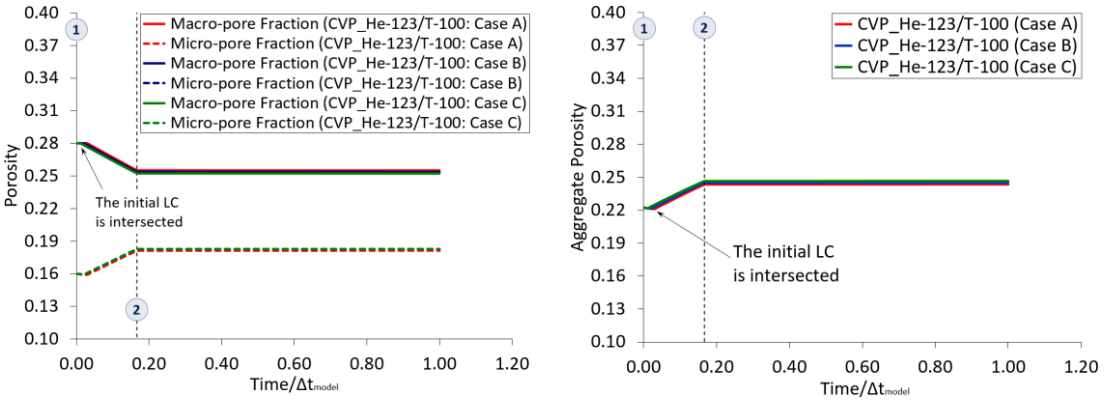

Figure 7-19: Evolution of the porosity variables for a thermal loading starting at distinct initial confining pressures when $\gamma^w = 10^{-9}$ kg/s/m^3/MPa. Δt_{model}=180 days.

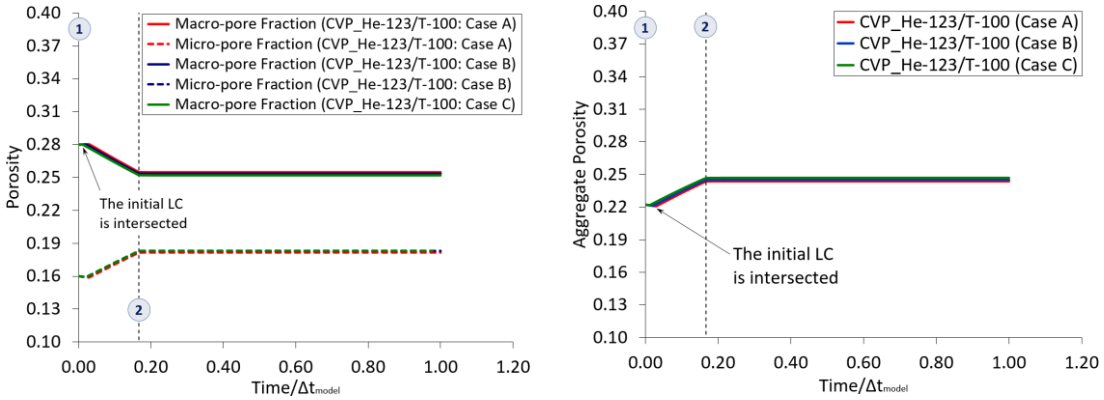

Figure 7-20: Evolution of the porosity variables for a thermal loading starting at distinct initial confining pressures when $\gamma^w = 10^{-6}$ kg/s/m^3/MPa. Δt_{model}=180 days.

7.3.2. ANALYSES WITH THE β-MECHANISM ACTIVATED

The activation of this plastic mechanism allows accounting for the irreversible structural changes arising from the mechanical interaction between both porous media. It is important to emphasize that such a plastic strain component is not dependent on the thermal volumetric strains of microstructure, but rather evolves due to the thermally-induced changes in the

microstructural hydro-mechanical variables (see Equation (4-101)). However, and due to the mechanical boundary conditions of null displacements prescribed to all nodes of the modelled domain, it is expected that the contribution of such a mechanical structural coupling to the generation of irreversible changes in the soil skeleton is less significant (or even, negligible) in comparison to the LC mechanism.

The couple of micro-macro relationships (f_β) defined by the shape parameters for the Functions #3 in Table 6-8 is used in the numerical calculations. The model predictions of suctions, degrees of saturation and porosity variables at each structural level together with the evolution of the pre-consolidation and the thermal stresses for the CVP_He-123/T-100 path when $\gamma^w = 10^{-6}$ kg/s/m^3/MPa are given from Figure 7-21 to Figure 7-23. These modelling results are plotted together with the outcomes obtained from the calculations with the mechanical micro-macro interaction mechanism deactivated (Interaction Functions #1). The results in such graphs confirm that the loading-collapse (LC) mechanism is the main – if not the only – energy dissipation process controlling the structural changes in the macrostructure (for the reasons mentioned above).

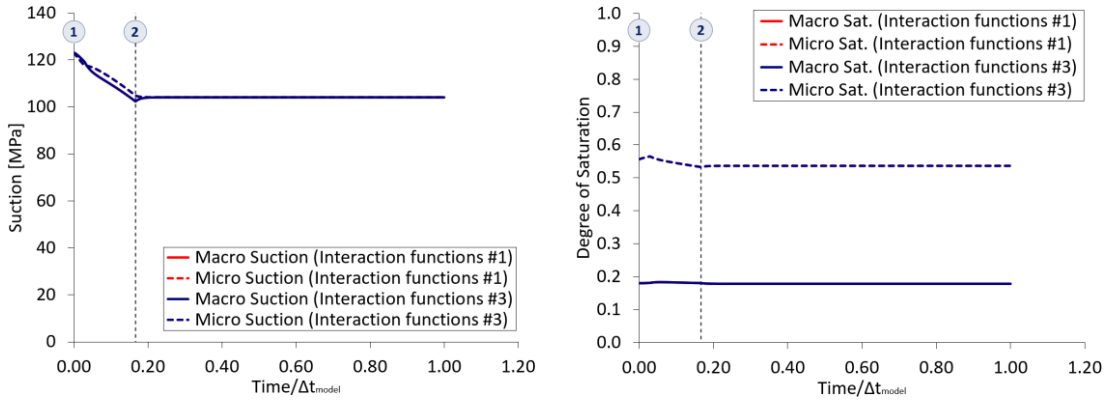

Figure 7-21: Comparing the impact of activating the plastic micro-macro coupling mechanism on the evolution of suction and degree of saturation at both structural media obtained from the THM CVP_He-123/T-100 path when $\gamma^w = 10^{-6}$ kg/s/m^3/MPa (Scenario #3).

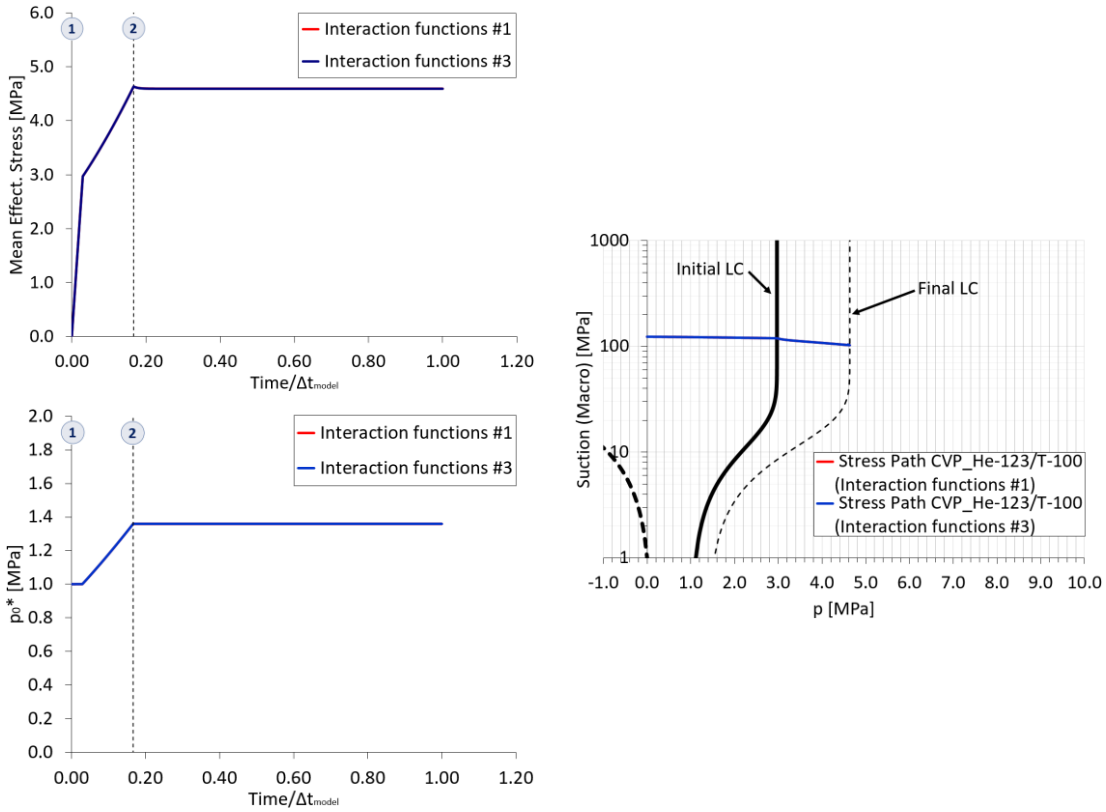

Figure 7-22: Comparing the impact of activating the plastic micro-macro coupling mechanism on the evolution of the thermal stresses (up, on the left) and the pre-consolidation pressures (down, on the left) and the THM CVP_He-123/T-100 path in the p: s_M plane (right) when $\gamma^w = 10^{-6}$ kg/s/m^3/MPa (Scenario #3).

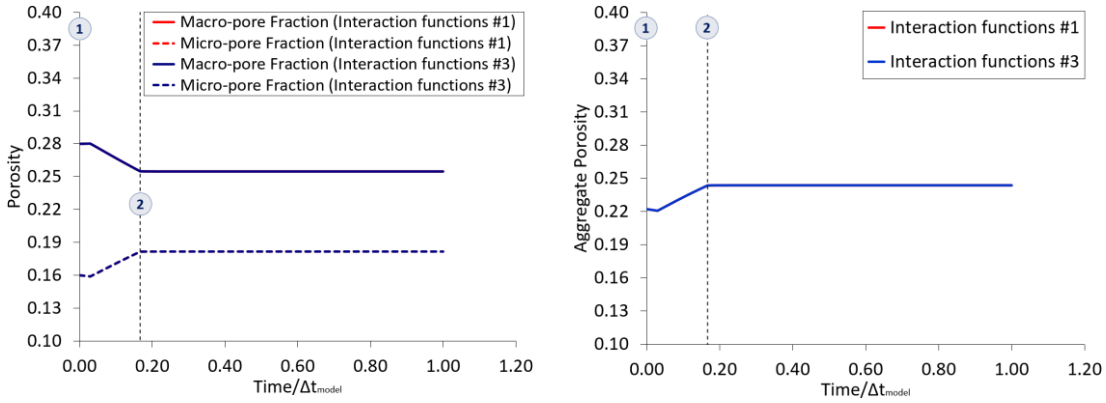

Figure 7-23: Comparing the impact of activating the plastic micro-macro coupling mechanism on the evolution of the porosity variables at both structural media obtained from the THM CVP_He-123/T-100 path when $\gamma^w = 10^{-6}$ kg/s/m^3/MPa (Scenario #3).

7.4. HEATING AT CONSTANT VOLUME (WITH ARTIFICIAL HYDRATION)

The artificial hydration of macro-pores at high (and constant) temperatures was also simulated. This re-saturation of macrostructure can be considered as an extension of the "heating test" modelled in **Section 7.3**. Thus, the hydration of macro-pores starts 180 days after the onset of heating and lasts 90 days. During this modelling step, the macrostructural liquid pressure is linearly reduced from its value at the end of the previous heating phase (without any forced

hydration) until the final value of -0.1 MPa. After that, the numerical calculations was kept running for 360 more days in order to continue the saturation of micro-pores by means of the water mass transfer between both structural media. In this heating-hydration phase, the liquid pressure in macrostructure keeps decreasing until the full saturation of macro-pores is achieved, that is, until reaching a null macrostructural pore-water pressure. The thermo-hydraulic changes prescribed in each phase of the numerical calculations are illustrated in Figure 7-24.

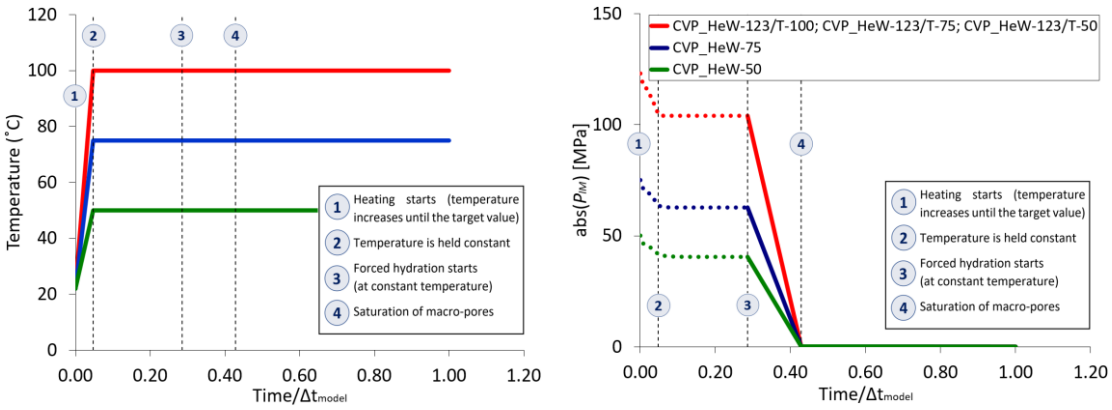

Figure 7-24: Temperature and macro liquid pressures (full lines) prescribed at all nodes during the heating-hydration under constant volume conditions. The discontinuous lines in the chart on the right-hand side represent the changes in the nodal macro liquid pressures induced by heating. Temperature is increased during the first 30 days while Δt_{model}=630 days.

The changes in the macrostructural liquid pressures during the hydration phase are applied directly to all nodes of the modelled geometry. Therefore, the nodal primary variables (the unknowns of the numerical analysis) are given at each time step during the artificial hydration at high temperatures and the governing equations of the THM problem are only solved numerically for the "secondary" variables (degree of saturation, porosities, micro liquid pressure, stresses, etc.). The impact of the energy dissipation mechanisms (the LC and the micro-macro coupling mechanisms) on the THM response of the heated cubic sample of soil during its re-saturation is analysed in the following sections. In **Section 7.4.1**, the generation of plastic strains arising from the hydration of macro-pores are exclusively due to the loading-collapse (LC) mechanism while in **Section 7.4.2**, the effects of the microstructural deformations on the structural changes of the soil skeleton (the plastic β-mechanism) are also considered in the numerical analyses.

7.4.1. ANALYSES WITH THE β-MECHANISM DEACTIVATED

The re-saturation of macro-pores in a heated element of expansive soil was studied at three different temperatures: 50˚C (CVP_HeW-123/T-50), 75˚C (CVP_HeW-123/T-75) and 100˚C (CVP_HeW-123/T-100). The most relevant model results taken from such numerical analyses, for two distinct water mass transfer conditions ($\gamma^w = 10^{-9}$ kg/s/m^3/MPa and $\gamma^w = 10^{-6}$ kg/s/m^3/MPa) are given from Figure 7-25 to Figure 7-29. It is important to mention that the THM response of the soil specimen due to the increase in temperature has already been addressed in **Section 7.3** and no further comments related to the heating phase are made in the present section. As mentioned previously, the magnitude of the thermal loading (applied during the heating phase) determines the value of the macro suction in the beginning of the forced re-

saturation of macrostructure. Consequently, it also controls the magnitude of the decrease in suction (the hydraulic loading) that must be imposed to re-saturate the macro-pores during the hydration phase. Thus, a lower hydraulic loading must be applied to the soil element when the CVP_HeW-123/T-100 path is followed, while a larger macrostructural suction decrease is required to re-saturate the expansive material in the heating-hydration CVP_HeW-123/T-50 path, as shown in Figure 7-25. In consequence, the increment in the swelling pressures due to the re-saturation of macro-pores (see Figure 7-26 and Figure 7-27) is greater for the THM CVP_HeW-123/T-50 path, as clearly indicated in Figure 7-27. Moreover, the reduction of the volume occupied by the inter-aggregate pores (macro-pore volume fraction) and, consequently, the increase in the microstructural porosity variables (micro-pore volume fraction and aggregate porosity) is more significant for hydration paths at lower temperatures (as CVP_HeW-123/T-50), as illustrated in Figure 7-28 and Figure 7-29. When both structural media are simultaneously re-saturated (for the structural leakage coefficient of $\gamma^w = 10^{-6}$ kg/s/m^3/MPa), the size of the region delimitated by the BBM plastic surface at the end of the wetting path tends to reduce with increasing temperature (see Figure 7-26). However, for the scenario in which the water mass transfer mechanism has less influence on the re-saturation of microstructure, that is, when $\gamma^w = 10^{-9}$ kg/s/m^3/MPa, the size of the zone inside the plastic surface at the end of the re-saturation of macro-pores is greater for the THM CVP_HeW-123/T-100 path (as displayed in Figure 7-26). In such a situation, microstructure is still very dry at the end of the hydration phase (see Figure 7-25) and, consequently, its full swelling potential is not developed yet. Thus, the strain hardening behaviour of the expansive soil during a heating-hydration path is related to the collapse of macrostructure induced by the thermal loading during the heating phase and to the collapse of the soil skeleton (macro-pores) caused by the re-saturation of micro-pores at high temperatures. Nevertheless, the thermally-induced collapse of macrostructure seems to be the dominant deformation process controlling the plastic response during the hydration phase in those stress paths for which the water mass exchanged between the saturated macro-pores and the unsaturated micro-pores can be neglected (see, for example, the stress path CVP_HeW-123/T-100 in Figure 7-28). For those heating-hydration paths with a higher micro-macro leakage coefficient, the generation of plastic deformations is mainly related to the macrostructural collapse arising from the saturation of microstructure.

As expected, the coefficient of the micro-macro water mass transfer is the main model parameter controlling the saturation state of micro-pores (and, consequently, the microstructural deformations) at the end of the hydration phase. For a high value of this mass transfer parameter ($\gamma^w = 10^{-6}$ kg/s/m^3/MPa), the degree of saturation of microstructure increases in response to the saturation of macro-pores (see Figure 7-25). At the end of the hydration phase, micro-pores are almost fully-saturated. Consequently, the microstructural porosity variables increase and due to the volumetric restrictions imposed to the swelling deformations, the inter-aggregate voids decrease until almost vanishing completely (as shown in Figure 7-29). Furthermore, and as already discussed in **Section 6.5**, the swelling pressures develop during hydration until reaching very high values, as indicated in Figure 7-26.

The evolution of swelling pressures for the paths in Scenario #1 (when $\gamma^w = 10^{-9}$ kg/s/m^3/MPa) is characterized by a slight increase until a peak value followed by a sharp drop close to the end of the hydration phase (see Figure 7-27). Such a sudden decrease in the swelling stresses is caused by the macrostructural collapse due to the saturation of macro-pores (Figure 7-28). The

modelling of a confined heating-hydration path imposes that the structural collapse of macrostructure (reduction of macro-pores, $\bar{\phi}_M$) is counteracted by an equal increase in the volume of micro voids ($\bar{\phi}_m$). Nevertheless, such a volumetric expansion of microstructure occurs without changing the volume of pore-water in micro-pores once the very low value of the leakage coefficient hinders the local water exchange between both structural media. Thus, the increase in the micro-pore volume fraction (and in the aggregate porosity) at the end of the hydration phase (see Figure 7-28) without changing the amount of water molecules in micro-pores induces a "desaturation" of micro-pores, as illustrated in Figure 7-25. When the saturation state of macrostructure is reached, the evolution of the confining stress practically ceases once the mechanism controlling their development at this stage is the saturation of micro-pores and such a process is delayed due to the low value assumed by the model parameter γ^w. Therefore, no significant changes in the microstructural suction and degree of saturation (Figure 7-25), in the hardening parameter (Figure 7-26) and in the porosity variables (Figure 7-28) are predicted in the period immediately after the re-saturation of macrostructure. In other words, the response of macrostructure to changes in temperature and in the water content of macro-pores governs the expansive behaviour in the short and medium term, when the saturation of micro-pores is retarded due to the negligible contribution of the structural pore-water exchange mechanism to the soil swelling (as in Scenario #1, for example).

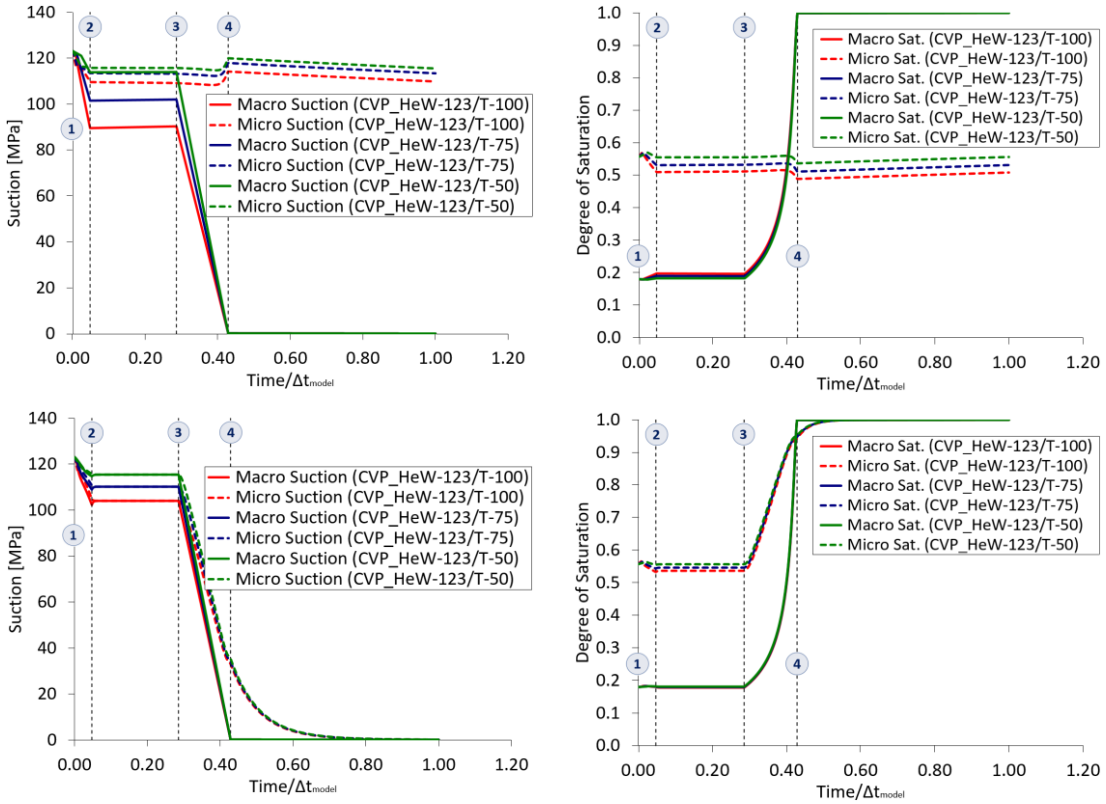

Figure 7-25: Evolution of suction and degree of saturation in the THM CVP_HeW-123 path at different final temperatures when $\gamma^w = 10^{-9}$ kg/s/m^3/MPa (up) and $\gamma^w = 10^{-6}$ kg/s/m^3/MPa (down). Hydration starts 180 days after the onset of heating and Δt_{model}= 630 days.

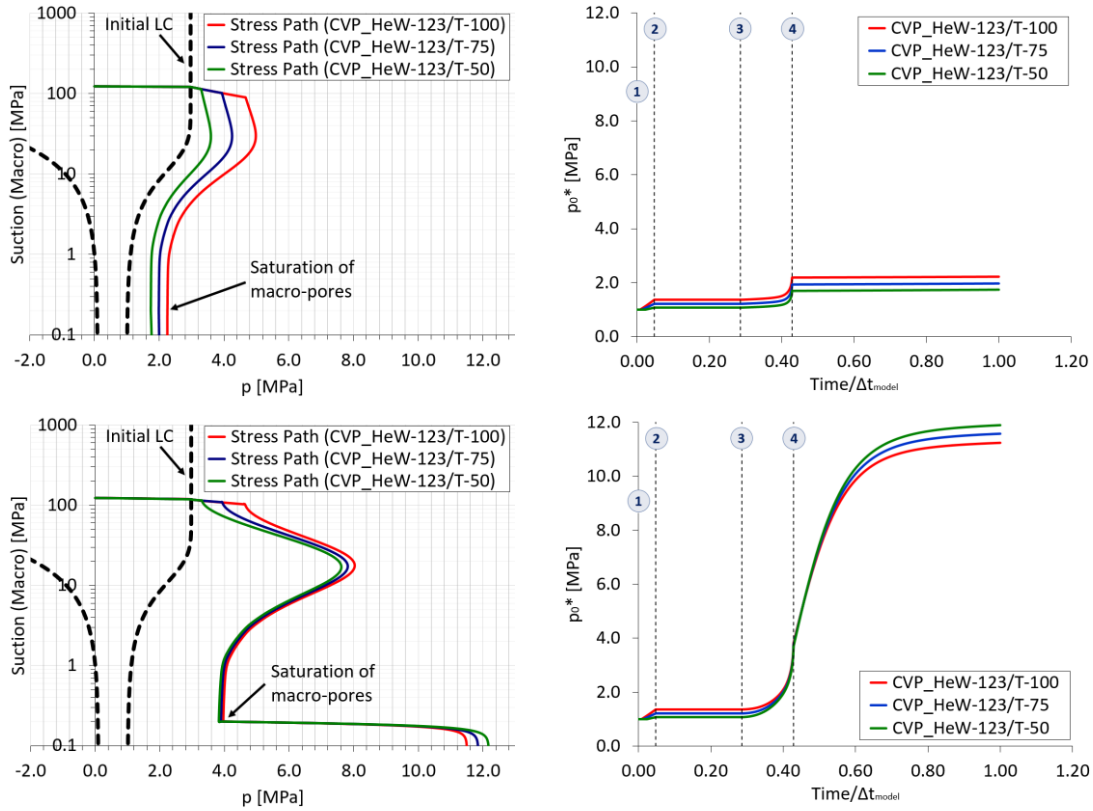

Figure 7-26: THM CVP_HeW-123 paths at distinct temperatures plotted in the p: s_M plane (left) with the evolution of the pre-consolidation pressures (right) when $\gamma^w = 10^{-9}$ kg/s/m^3/MPa (up) and $\gamma^w = 10^{-6}$ kg/s/m^3/MPa (down).

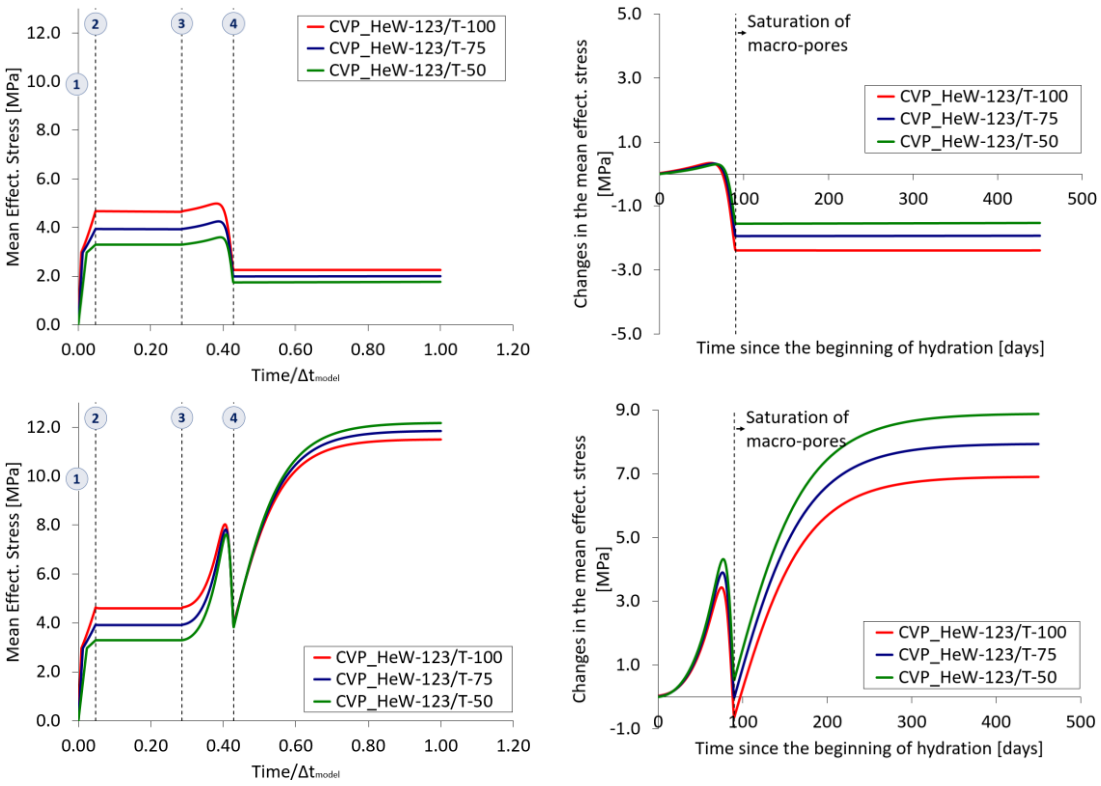

Figure 7-27: Development of thermally-induced and swelling stresses (left) and the changes in the swelling pressures (right) during the CVP_HeW-123 path at different final temperatures when $\gamma^w = 10^{-9}$ kg/s/m^3/MPa (up) and $\gamma^w = 10^{-6}$ kg/s/m^3/MPa (down).

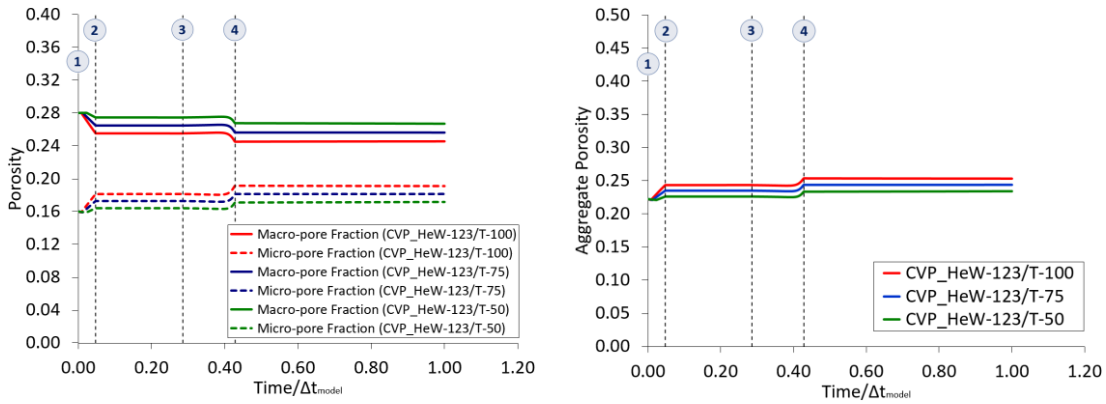

Figure 7-28: Evolution of the pore volume fractions (left) and the aggregate porosities (right) in the heating-hydration CVP_HeW-123 path at different final temperatures when $\gamma^w = 10^{-9}$ kg/s/m^3/MPa.

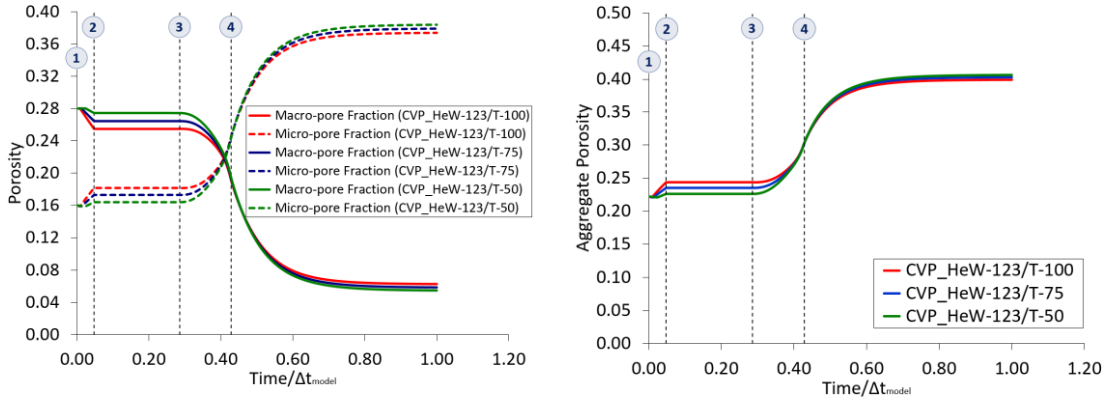

Figure 7-29: Evolution of the pore volume fractions (left) and the aggregate porosities (right) in the heating-hydration CVP_HeW-123 path at different final temperatures when $\gamma^w = 10^{-6}$ kg/s/m^3/MPa.

The role played by the micro-macro water mass transfer on the swelling behaviour at high temperatures can be clearly observed from Figure 7-30 to Figure 7-32. The numerical results obtained from the THM CVP_HeW-123/T-100 path for both water transfer scenarios analysed previously are plotted together in such graphs. Again (and as discussed before), the coefficient of the water mass exchange between micro- and macro-pores affects the evolution of micro and macro suctions during the heating phase, which in turn, affects the evolution of the swelling potential during the subsequent hydration phase. Furthermore, the expansion of a clayey soil is intrinsically related to the development of the intra-aggregate and the inter-layer pores by the imbibition of pore-water molecules coming from the larger pores (the inter-aggregate pores). Consequently, in the short and medium term, a high swelling potential (evidenced by the development of high swelling pressures under confined conditions) is directly related to a high coefficient for the water mass transfer between both pore levels .

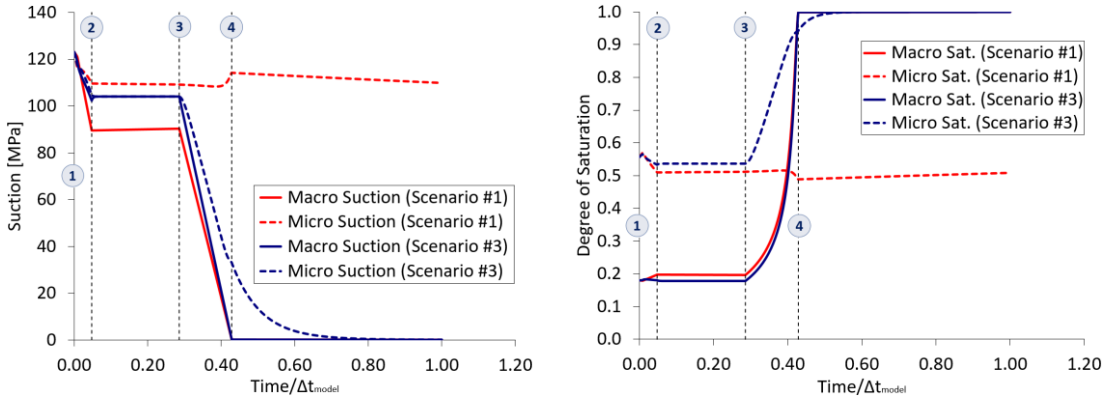

Figure 7-30: Comparison between the evolution of suction and degree of saturation in the heating-hydration CVP_HeW-123/T-100 test for distinct pore-water mass transfer conditions.

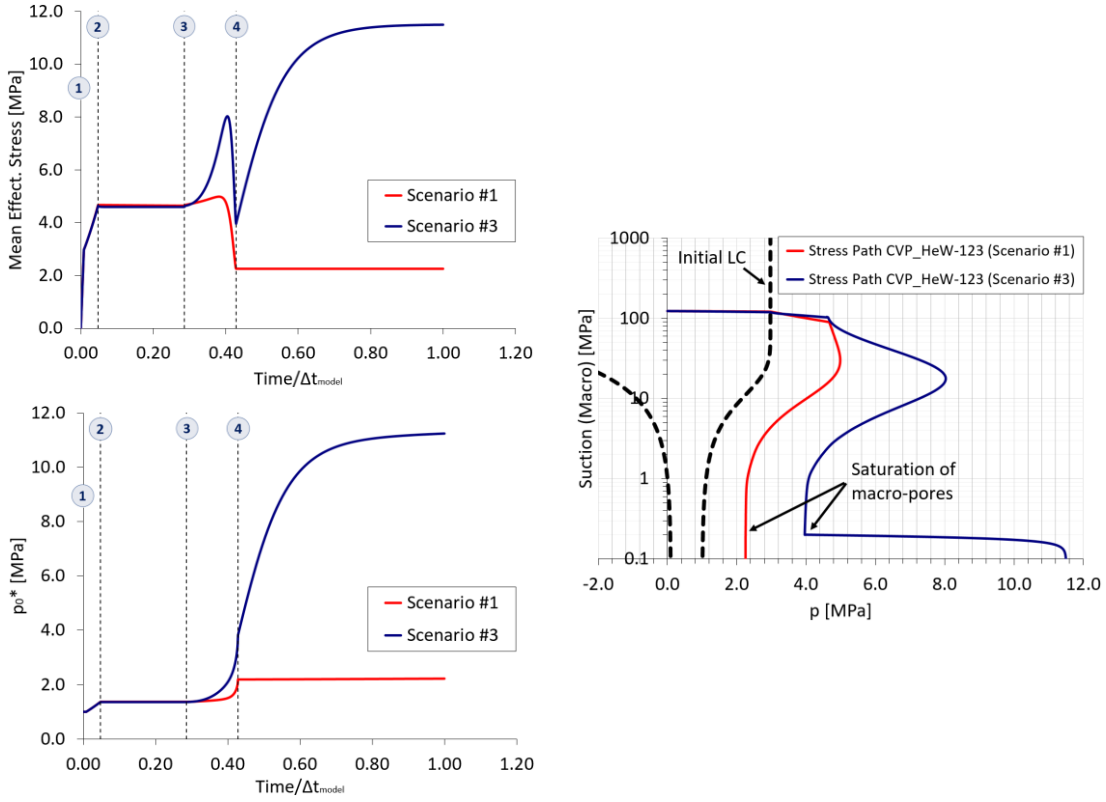

Figure 7-31: Comparison of the evolution of swelling pressures (up, on the left) and pre-consolidation pressures (down, on the left) in the heating-hydration CVP_HeW-123/T-100 test for distinct pore-water mass transfer conditions and their corresponding THM paths plotted in the p: s_M plane (right).

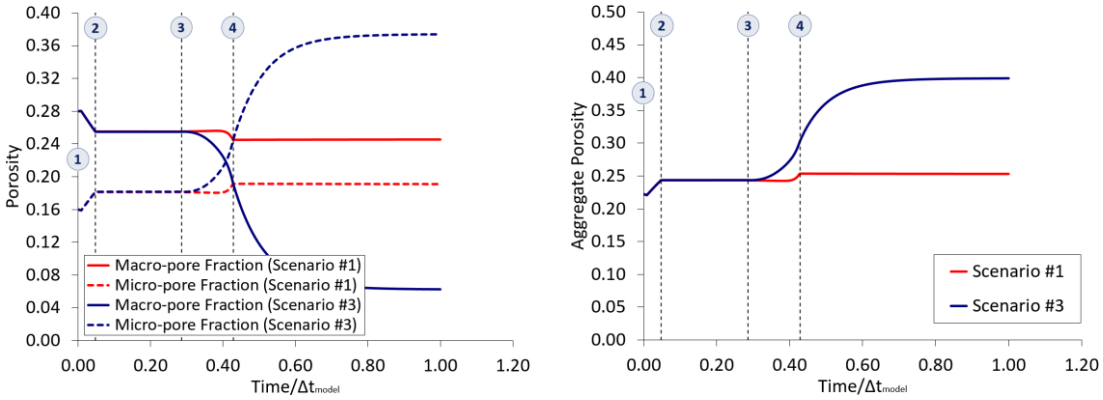

Figure 7-32: Comparison between the evolution of the pore-volume fractions and the aggregate porosities in the CVP_HeW-123/T-100 test for distinct pore-water mass transfer conditions.

The dependence of the swelling potential of an expansive clay on its initial conditions, especially on its water content (or degree of saturation) has been evidenced by several studies reported in the literature (Jayalath et al., 2016). Thus, the swelling potential increases with increasing the initial suction. Consequently, for the heating-hydration paths CVP_HeW-123/T-100, CVP_HeW-75 and CVP_HeW-50, whose modelling results for a structural leakage coefficient of $\gamma^w = 10^{-6}$ kg/s/m^3/MPa are plotted from Figure 7-33 to Figure 7-35, a higher swelling pressure is obtained for the CVP_HeW-123/T-100 path and a lower swelling potential is predicted for the CVP_HeW-50 path. As indicated in Table 7-1 and illustrated in Figure 7-24, a same temperature increment is prescribed to these three THM paths during the modelling of the heating event.

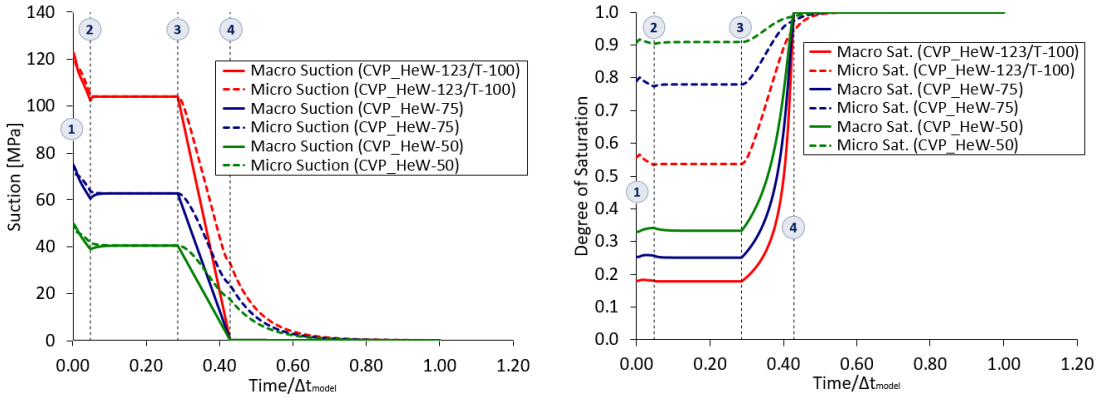

Figure 7-33: Evolution of suction and degree of saturation in heating-hydration paths starting at distinct macrostructural suctions when $\gamma^w = 10^{-6}$ kg/s/m^3/MPa. Δt_{model}=630 days.

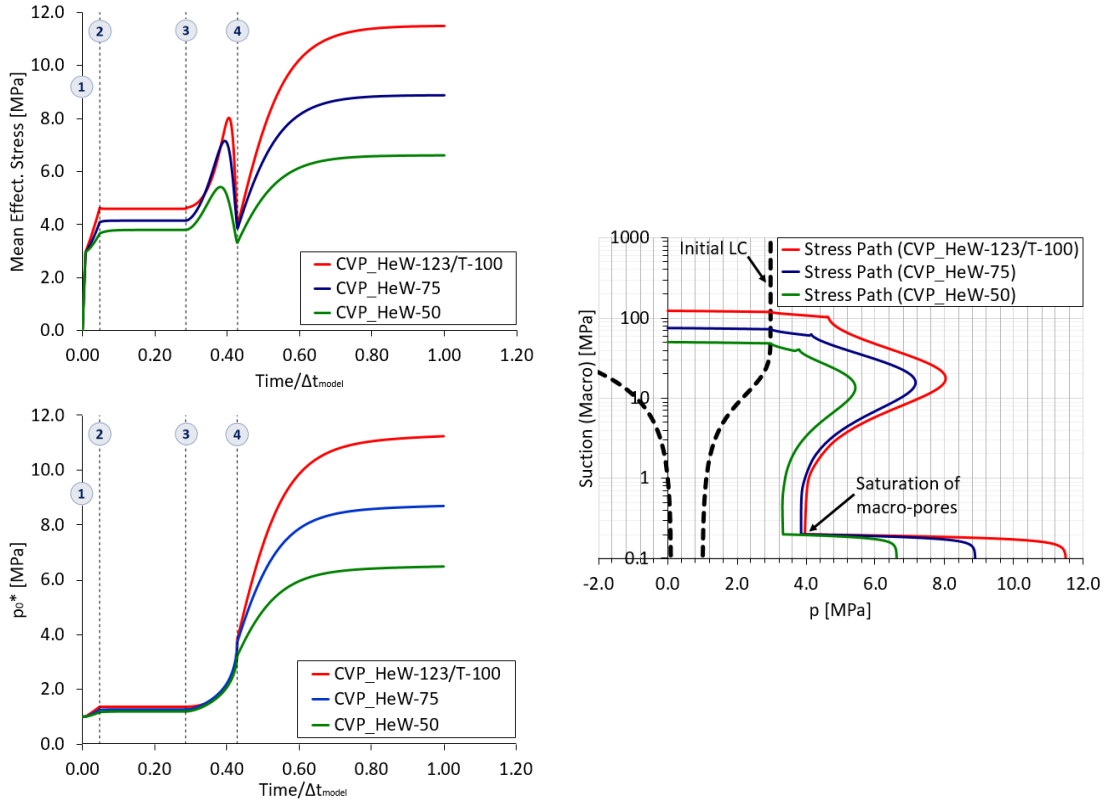

Figure 7-34: Evolution of the swelling pressures (up, on the left) and the pre-consolidation pressures (down, on the left) and the THM paths starting at distinct macro suctions plotted in the p: s_M plane (right) when $\gamma^w = 10^{-6}$ kg/s/m³/MPa. Hydration. Δt_{model}=630 days.

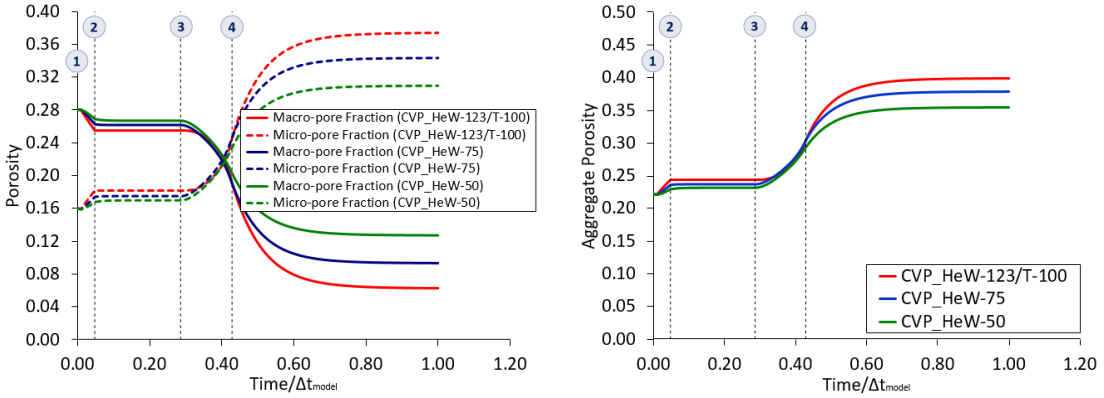

Figure 7-35: Evolution of the pore-volume fractions and the aggregate porosities in heating-hydration paths starting at distinct macrostructural suctions when $\gamma^w = 10^{-6}$ kg/s/m³/MPa. Δt_{model}=630 days.

7.4.2. ANALYSES WITH THE β-MECHANISM ACTIVATED

The modelling of the heating-wetting paths investigated in **Section 7.4.1** were repeated, but now, the development of the plastic strain component arising from the structural coupling between micro and macro media is allowed. The pair of interaction functions used in the calculations is the one identified as Functions #3 in Table 6-8.

The main conclusions on the behaviour of the expansive soil during the heating phase and before the start of hydration at high temperatures have already been discussed in **Section 7.3.2**. The material response during the hydration phase when the plastic structural coupling mechanism is also activated depends on the hydration-induced collapse of the soil skeleton (macrostructure) and on the re-saturation of the clay aggregates (microstructure). The irreversible changes in the clay fabric due to the micro-macro interaction is related to the microstructural deformation. However, the numerical restrictions applied during the modelling of the heating-hydration at constant volume conditions inhibit the development of the microstructural volumetric expansion. Consequently, the contribution of the mechanical structural coupling (the β-mechanism) to the soil behaviour is practically negligible in any THM path considered in this chapter. This assertion can be corroborated when the model results from the CVP_HeW-123/T-100 path with the plastic β-mechanism deactivated (Functions #1) and activated (Functions #3) are plotted together in Figure 7-36 through Figure 7-38. From such results and for the conditions considered during the modelling performance, it is quite evident that the permanent structural changes generated by wetting at high temperatures are essentially due to the activation of the plastic LC mechanism.

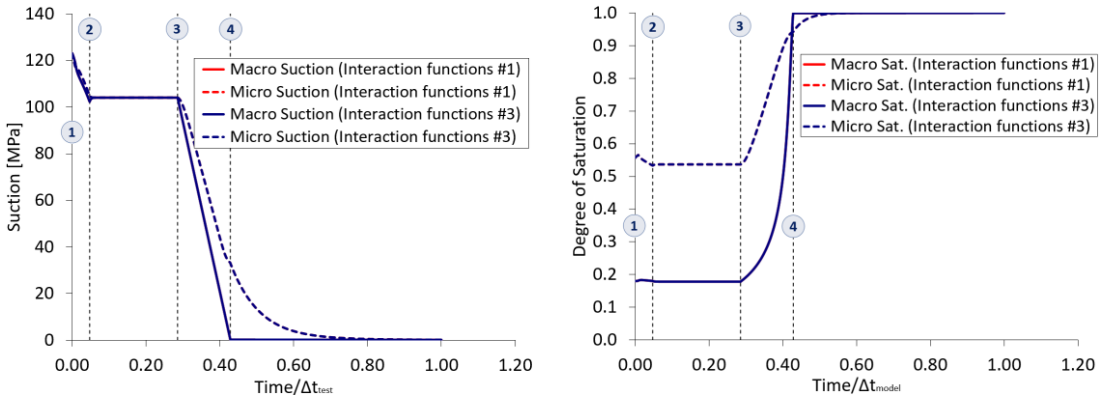

Figure 7-36: Comparing the impact of activating the plastic micro-macro coupling mechanism on the evolution of suction and degree of saturation at both structural media from the THM CVP_HeW-123/T-100 path when $\gamma^w = 10^{-6}$ kg/s/m^3/MPa.

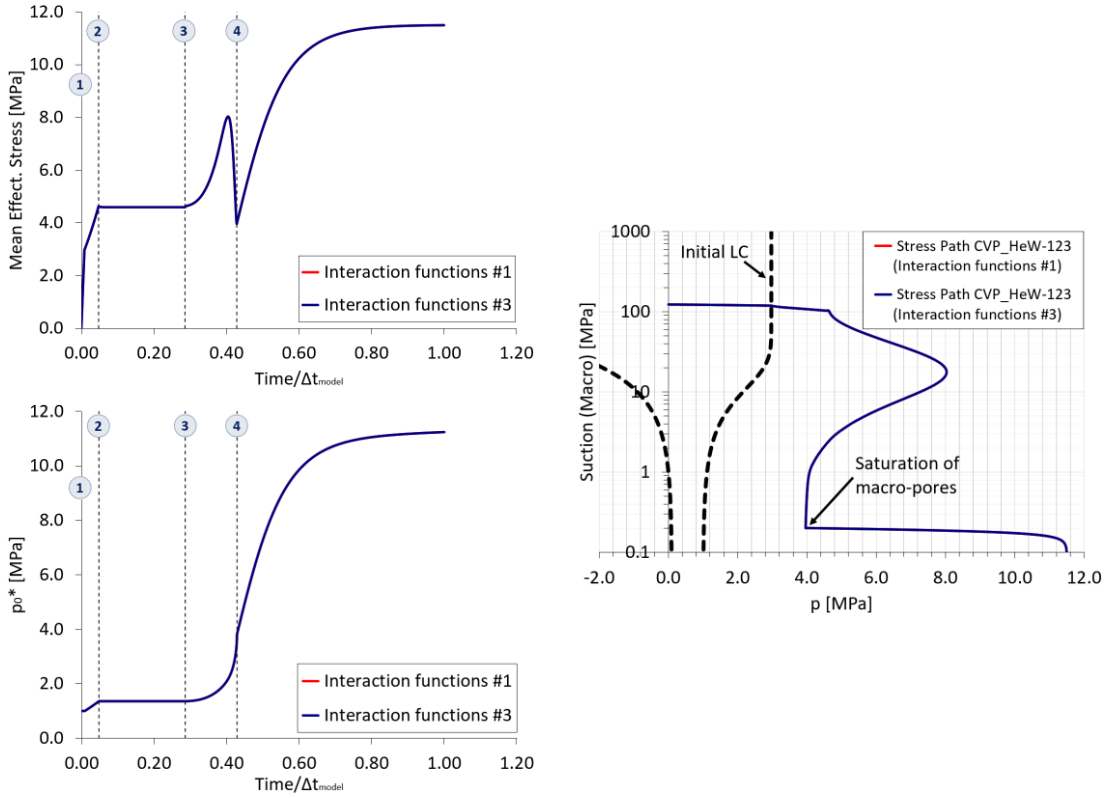

Figure 7-37: Comparing the impact of activating the β-mechanism on the evolution of the thermally-induced and the swelling stresses (up, on the left) and the pre-consolidation pressures (down, on the left) for the CVP_HeW-123/T-100 path when $\gamma^w = 10^{-6}$ kg/s/m^3/MPa. This THM path is plotted in the p: s_M plane (right).

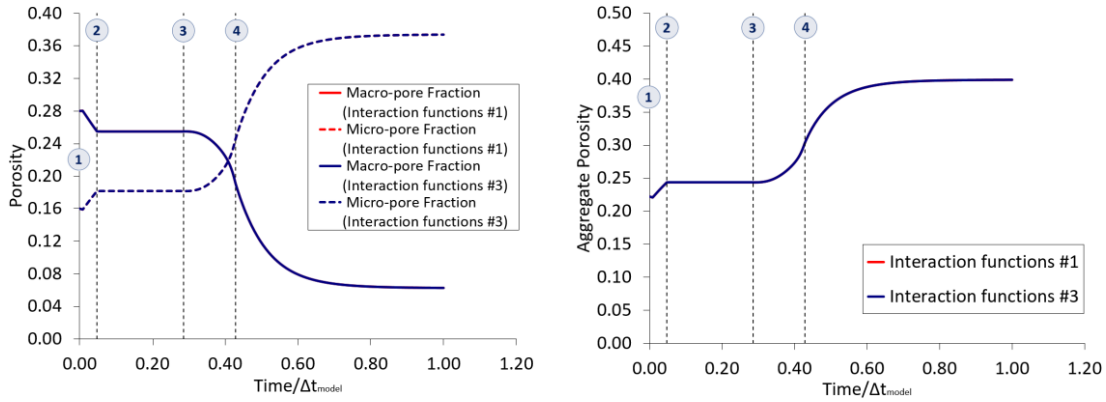

Figure 7-38: Comparing the impact of activating the β-mechanism on the evolution of the porosity variables at both structural media for the CVP_HeW-123/T-100 path when $\gamma^w = 10^{-6}$ kg/s/m^3/MPa.

7.5. CONCLUDING REMARKS

The numerical modelling of confined heating-hydration paths carried out in a cubic element of soil (with a volume of 1 cm^3) and using the constitutive model developed in this Thesis has contributed to a better understanding of the deformation response and the pore-saturation processes occurring at each structural media in non-isothermal problems in expansive media. The model capability in reproducing fully coupled THM analyses in double-porosity materials has been evaluated by the consideration of distinct heating scenarios with (or without) a

subsequent forced hydration at high temperatures. The model performance has given expected and consistent responses regarding the evolution of pore-water pressures, porosities and stresses in the soil element and at each porous medium.

The initial soil response to heating is controlled by the thermal expansion of the soil constituents and by the water-phase changes when the thermal loading is high enough to promote the generation of water vapour. However, and even for those situations in which the water-phase change is inhibited, this thermal loading affects the saturation state in micro- and macro-pores as a consequence of the differential expansion of pore-water with respect to the clay aggregates (solid particles) and to the soil skeleton. Due to that, a local thermally-induced water potential gradient can arise and the material behaviour also becomes dependent on the water mass transfer between the two families of pores. The magnitude of the leakage coefficient (γ^w) determines the impact of the micro-macro water exchange mechanism on the final state of saturation and deformation at each structural level in the heated expansive soil. In fact, and according to the modelling results shown in **Section 7.3.1** for lower values of γ^w (as in Scenario #1), the volumetric thermal expansions of the solid phase and the soil structure and the thermal differential expansion of pore-water are the processes that explain the soil response during the heating phase prior to the artificial hydration of macro-pores. However, the water exchange between the two types of pores dictates the final saturation and deformation states of the heated soil as the value for the leakage coefficient rises (as in Scenario #3). Moreover, and for the same thermal load, the macrostructural collapse induced by heating reduces with decreasing the initial suction of the element of expansive soil. This could be related to the reduction in the volumetric deformation capacity of macro-pores to contract under compressive loads as the content of incompressible fluids contained in them (as liquid pore-water) is increased. The influence of the initial confining pressure on the soil behaviour during heating has also been studied. However, the modelling results (see **Section 7.3.1**) indicate that this initial-state variable plays a minor role (in comparison to the initial suction) in the development of the thermally-induced changes of the main hydro-mechanical variables evaluated in the numerical analyses performed in this chapter.

The hydro-mechanical response of the heated expansive soil during the forced re-saturation of macro-pores is strongly dependent on the saturation state of macrostructure at the beginning of the hydration phase. In other words, the magnitude and the conditions in which the thermal loading is carried out together with the initial conditions and constitutive properties of the heated soil affect its swelling potential when wetted. Furthermore, and as already discussed in **Chapter 6**, the micro-macro water exchange is the main process related to the saturation of micro-pores. Again, the leakage coefficient plays a crucial role in the soil hardening process and in the development of swelling pressures at high temperatures. When the micro-macro water mass transfer is not sufficient to cause the saturation of micro-pores at the end of the hydration phase (due to a lower value of γ^w), the model predicts an increase in the swelling pressure with temperature (see **Section 7.4.1**). However, such a swelling pressure value is mainly related to the macrostructural response to the previous thermal loading and to the saturation of macro-pores, once micro-pores still remain very dry. In contrast, when the amount of water transferred from macro- to micro-pores during the hydration phase leads to the full saturation of microstructure (due to the higher value of γ^w), the modelling results suggest a decrease in the final swelling pressure with temperature (see **Section 7.4.1**). In this situation, the development

of the swelling potential of the expansive soil specimen arises from the pore-saturation that occurs simultaneously at both structural pore levels.

A last but not least aspect to highlight is the negligible influence of activating the plastic micro-macro coupling mechanism on the development of irreversible strains during heating and macrostructural hydration of the cubic element of expansive soil. As mentioned in **Section 7.3.2** and **Section 7.4.2** and also in **Section 6.5.2**, such a model prediction is a straight consequence of the mechanical boundary conditions imposed to the modelled domain in order to perform a heating-hydration path under constant volume conditions.

8. APPLICATION OF THE DOUBLE-POROSITY MODEL TO LABORATORY-SCALE HEATING-HYDRATION TESTS

8.1. INTRODUCTION

The potential use of bentonite-based materials as seals and engineered barriers in repositories for radioactive waste disposal and in other geotechnical problems has generated an increasing interest on the characterization and prediction of the constitutive behaviour of such materials when submitted to important changes in environmental conditions. A general view of the main geotechnical properties of compacted and granular bentonite materials and the advantages of their use as sealing and filling materials in some research programmes of relevant scientific interest have been already discussed in **Section 2.6**. Furthermore, the development of computational tools and constitutive models that take in account the multi-porosity nature of active soils has contributed to the understanding of the main physico-chemical mechanisms that govern the deformation process in expansive soils. In that sense, and as mentioned in **Section 2.7**, the conceptual double-porosity formulation by Gens and Alonso (1992) and the implementation of constitutive models in finite element (FE) codes, as the *Barcelona Expansive Model* (BExM) by Alonso *et al.* (1999) and the double-structure model by Sánchez *et al.* (2005), constitute fundamental benchmarks when modelling the THM response of bentonites. Thus, the mathematical THM formulation developed in this Thesis as well as the double-structure model for isothermal conditions described in Ruiz (2020) assume the main theoretical concepts established in Gens and Alonso (1992) and some numerical features considered in Alonso *et al.* (1999), Sánchez (2004) and Sánchez *et al.* (2008) (see **Section 2.7.3**).

In the two previous chapters, the performance of the double-porosity model implemented in the FE code CODE_BRIGHT (Olivella *et al.*, 1994) has been analysed and discussed by means of a series of numerical simulations of local hydration (or dehydration) at different temperatures under confined and unconfined conditions. Consequently, the role played by the water mass transfer between micro- and macro-pores and the magnitude of the thermal loading on the final

saturation state of pores and on the development of the swelling potential around a point in a compacted mass of expansive soil has already been discussed. Furthermore, the impact of the confinement conditions on the structural coupling processes relating the swelling/shrinkage response of microstructure to the deformation behaviour of the soil skeleton has been also addressed in **Section 6.3.2**, **Section 6.5.2** and **Section 7.4.2**, for example.

In the current chapter, however, the boundary-value problem related to the artificial hydration of two heated columns of bentonite-based materials is investigated. These heating-hydration tests (started in November, 2011) have been carried out in the CIEMAT laboratory (Madrid, Spain) as part of the characterization of the THM processes expected to take place during the re-saturation of the heated mass of granular filling materials emplaced in the *in-situ* HE-E experiment (Villar *et al.*, 2012b). A brief description of the HE-E experiment has been presented in **Section 2.6.4.5**. For more information on the selection of the bentonite materials composing the engineered barrier, the tasks carried out inside and around the experiment site before the initiation of heating and the performance of this full-scale test throughout almost ten years of uninterrupted operation, see Mayor *et al.* (2005), Gaus (2011), Teodori and Gaus (2011), Gaus *et al.* (2014a, 2014b), Wieczorek *et al.* (2017) among others. The granular bentonite-based materials used to mount the columns of the CIEMAT laboratory tests are the same ones emplaced in the two independently heated sections of the *in-situ* HE-E experiment (Villar *et al.*, 2016). The column termed as "Cell B" (Villar *et al.*, 2012b) was filled with pure MX-80 bentonite pellets compacted by their own weight. In the case of the column called "Cell S/B" (Villar *et al.*, 2012b), a granular sand/bentonite mixture in a dry mass proportion of 65/35 was poured inside the column in seven 7-cm high layers compacted at a very low energy. The evolution of temperature and relative humidity (RH) due to heating propagation and the water infiltration have been monitored by the installation of capacitive-type sensors at three different levels (10, 22 and 40 cm from the heater element) inside both bentonite columns. Additionally, the water volume intake, the heater power and the axial pressure evolution (in Cell B) have also been recorded during the laboratory heating-hydration tests. The main characteristics of the granular materials in the cells before the start of heating and the general description of the assemblage, the instrumentation and the performance of these CIEMAT laboratory tests are given in **Section 8.2**. The modelling of such heating-hydration tests by means of the double-porosity formulation implemented in this Thesis is discussed in **Section 8.3**. It is important to keep in mind that the THM properties and the model parameters of the cubic element of expansive soil in the numerical analyses conducted in **Chapter 6** and **Chapter 7** are the same input parameters employed in the modelling of the hydration of the heated column made of MX-80 bentonite pellets (see **Section 8.3.3** and **Section 8.3.4**).

8.2. GENERAL DESCRIPTION OF THE LABORATORY HEATING-HYDRATION TESTS (THE CIEMAT BENTONITE CELLS)

The design of each cylindrical cell (with an internal diameter of 7 cm and an inner length of about 50 cm) and the applied boundary conditions were defined so that the conditions found in the *in-situ* full-scale test could be reproduced properly in the laboratory. In that sense, the bentonite-based columns were initially subjected to an increase in temperature until reaching a

maximum value of 140°C followed by an artificial hydration at high temperature gradients. The heating episode has been generated by means of an electric heating system emplaced at the bottom of the cells while liquid Pearson water at laboratory temperature has been injected (at a given pressure) into the columns through their upper hydration surface. The order in which the boundary thermal and hydraulic loads were applied reflects the sequence in which the heat emission from the canister containing high-level nuclear waste and the natural re-saturation of the bentonite barrier take place. In fact, the very low water permeability of such clay barriers hinders the re-saturation process by the water-uptake from the surrounding geological formation. Therefore, the natural hydration of the bentonite buffers is expected to occur long time after the peak of temperature is reached inside the barrier (Villar *et al.*, 2012b).

Cell B was reinforced mechanically in order to support the swelling pressure developed as the mass of pellets hydrates. This steel covering was not required in Cell S/B. An external insulation system composed by several thermal isolating materials arranged in overlapped layers around the cells was also mounted in order to minimize the lateral heat dissipation. The bodies of both cells were also made of an insulation material (Teflon ®). A set of sensors for monitoring the evolution of RH and temperature was inserted into the bentonite columns at 10, 22 and 40 cm from the heater (at the bottom of the cells). Furthermore, a ring load cell was emplaced on the top of Cell B in order to register the axial pressure generated during the test. The conceptual and the final layouts of the instrumented cells are shown in Figure 8-1.

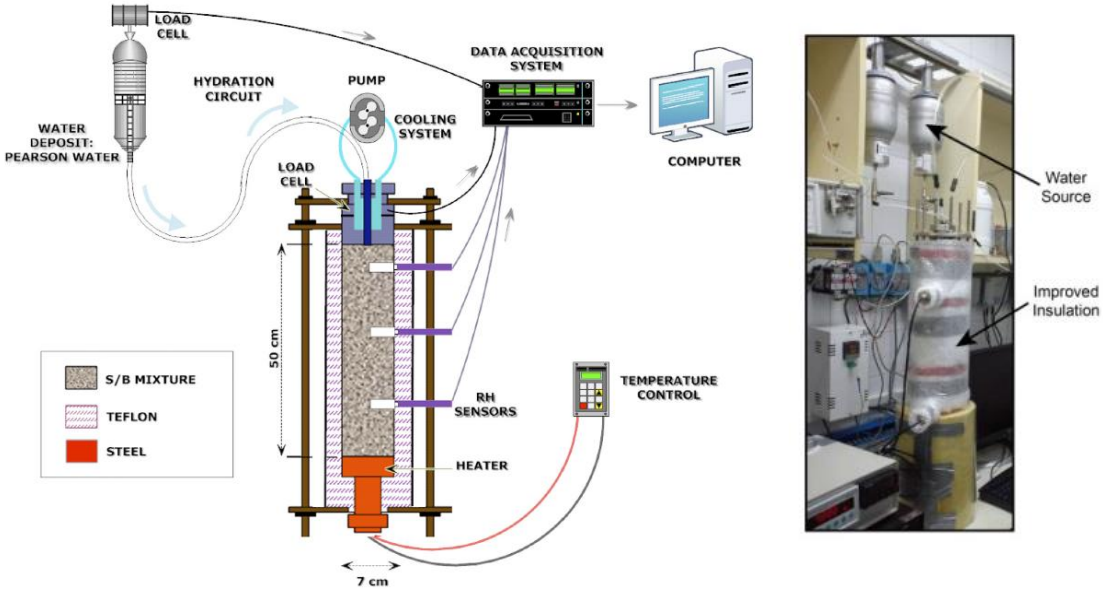

Figure 8-1: The as-conceived layout without the isolating material (left) and the actual view (right) of an instrumented bentonite column used in the heating-infiltration laboratory tests by CIEMAT (after Villar *et al.*, 2012b).

8.2.1. THE GRANULAR-BENTONITE MATERIALS

The two fill expansive materials used in the engineered multi-barrier system of the *in-situ* HE-E test and with which the laboratory bentonite columns were built are extensively characterized in the literature. For a detailed description of the chemical composition and the main thermo-

hydro-mechanical (THM) properties of such and similar granular bentonite materials, the reader is referred to Villar (2005; 2013), Imbert and Villar (2006), Plötze and Weber (2007), Fernández (2011), Wieczorek *et al.* (2011), Rizzi *et al.* (2012), Rothfuchs *et al.* (2012), Villar *et al.* (2015a, 2015b) and Molinero *et al.* (2017). In the following, only those physical and THM properties of the bentonite columns relevant to the modelling of the heating-hydration tests by means of the current double-porosity model are highlighted.

The MX-80 bentonite granulate inside Cell B corresponds to the bentonite material emplaced in the NAGRA Section of the HE-E experiment, whose granulometric curve obtained by dry sieving is shown in Figure 8-2 (down, on the right). The initial water content and the dry average density of the compacted mass of pellets in Cell B were 6.4% and 1.53 g/cm^3, respectively, while the dry density of the solid grains was found to be equal to 2.75 g/cm^3 (Villar *et al.*, 2012b). Moreover, the dry density of an MX-80 pellet usually ranges between 1.97 g/cm^3 and 2.20 g/cm^3 (Karnland *et al.*, 2008; Molinero *et al.*, 2017). Therefore, the initial degree of saturation and porosity of the bentonite column were estimated at 22% and 0.444, respectively (see Table 8-1). The thermal conductivity of the mass of MX-80 pellets at the as-emplaced state and at the *in-situ* temperature conditions (that is, at the full-scale experiment conditions prior to the beginning of heating) was obtained by means of laboratory techniques as the transient hot wire method, for instance. The measured thermal conductivity of the as-delivered material at room temperature varied between 0.12 W/m/K (Villar *et al.*, 2012b) and 0.45 W/m/K (Wieczorek *et al.*, 2011). The hydraulic conductivity of the mass of MX-80 pellets was estimated from water permeability tests performed on samples of powdered MX-80 bentonite compacted at different densities and assuming that the saturated hydro-mechanical properties of pellets are similar to those of powder mixtures (Imbert and Villar, 2006). Exponential correlations between dry density of the powder material and its saturated hydraulic conductivity and their dependence on the type of saturation fluid were obtained (Villar *et al.*, 2016), as illustrated by the chart on the left-hand side in Figure 8-3. For dry densities of the pellet mixtures between 1.40 g/cm^3 and 1.60 g/cm^3, the values of hydraulic conductivity ranged between 5.2e-13 m/s and 1.3e-13 m/s, respectively, when the granular material was percolated by deionised water. For the same range of dry densities and using saline water as permeant, these permeabilities varied between 7.5e-13 m/s and 2.5e-13 m/s, respectively. Karnland *et al.* (2008) found similar values of hydraulic conductivity for small samples of powdered and pelletized MX-80 bentonite compacted at several dry densities, as shown in the graph on the right-hand side of Figure 8-3. The swelling potential response of bentonite pellets is strongly dependent on the dry density of the compacted granular material, as already discussed in **Section 2.2.2.4**. Swelling pressures in the range of 2 – 8 MPa were measured from swelling pressure tests performed on small samples of powdered and pelletized MX-80 bentonite compacted at dry densities varying between 1.40 g/cm^3 and 1.60 g/cm^3 (Karnland *et al.*, 2008; Villar, 2013). Karnland *et al.* (2008) also determined the swelling pressures of heated samples (at 90°C) in the same range of dry densities, whose values were usually lesser than those ones obtained at room temperature conditions. Such experimental findings are plotted in Figure 8-4 together with the empirical fitting curves relating the swelling pressures to the dry densities of granular MX-80 mixtures.

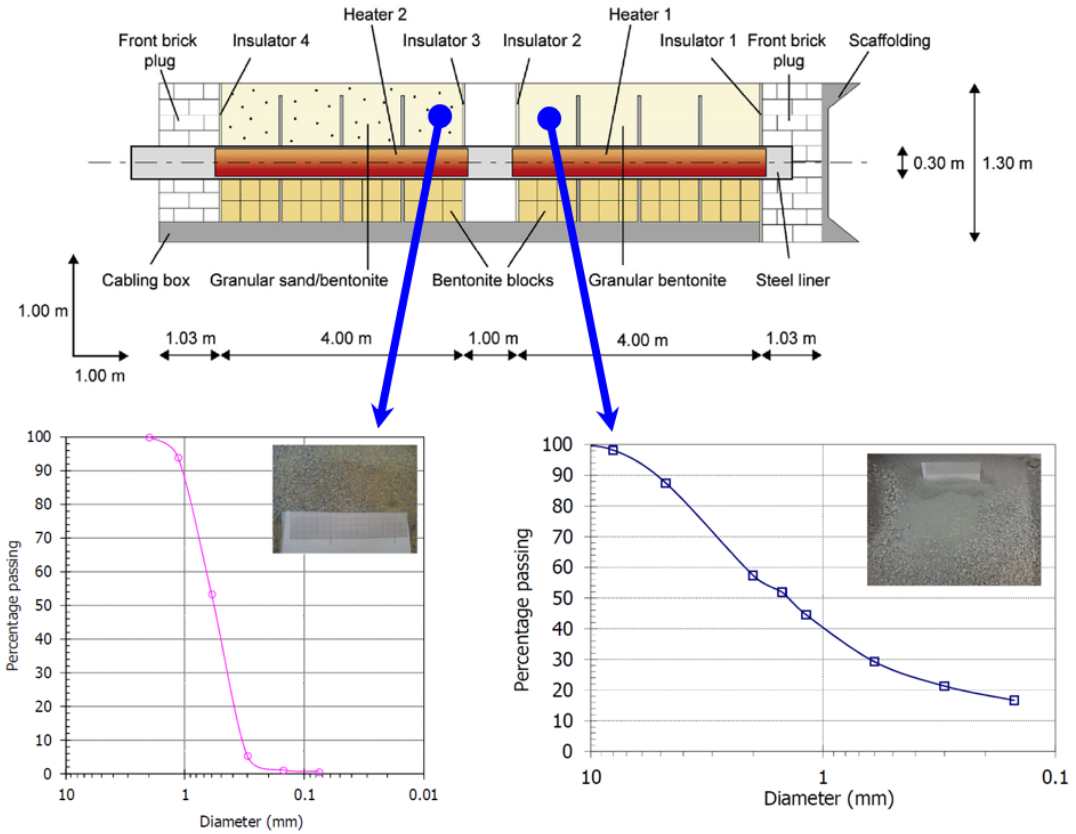

Figure 8-2: Layout of the *in-situ* HE-E experiment (up) and the grain size distribution curves of the granular bentonite-based materials emplaced in both heated sections (down) (after Gaus, 2011 and Villar *et al.*, 2012b).

Table 8-1: Initial state of the molded bentonite columns by CIEMAT (from Villar *et al.*, 2012b).

	Cell B	**Cell S/B**
Initial water content (%)	6.4	3.6
Dry density (g/cm^3)	1.53	1.45
Porosity	0.444	0.463
Void ratio	0.797	0.863
Degree of saturation (%)	22	11

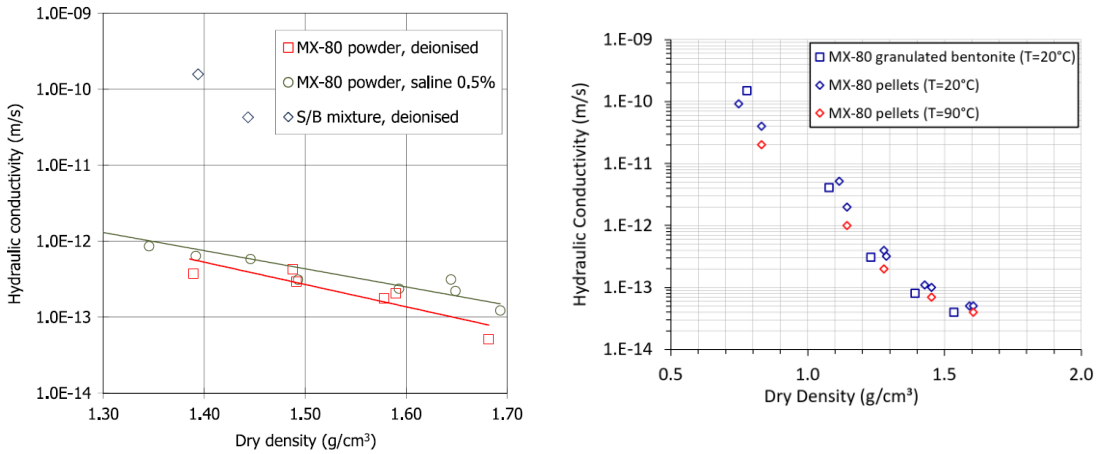

Figure 8-3: Experimental hydraulic conductivities as a function of dry density for MX-80 powder and sand/bentonite 65/35 mixtures when percolated by deionised and saline water (left, from Villar *et al.*, 2016) and for powdered and pelletized MX-80 bentonite at 20°C and 90°C when percolated by a saline solution (right, from Karnland *et al.*, 2008).

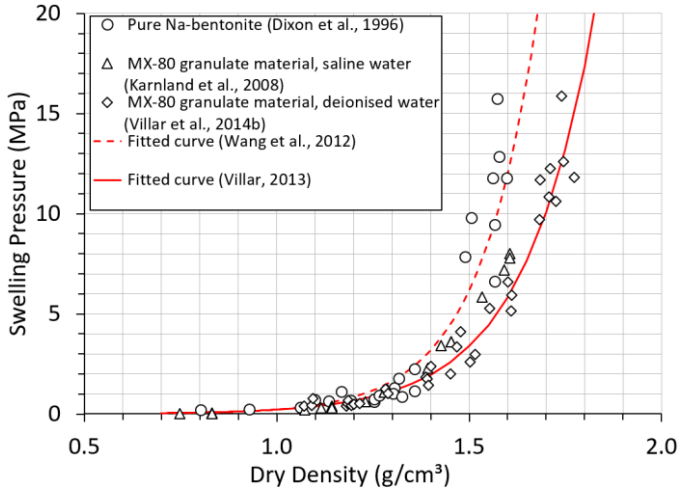

Figure 8-4: Dependence of swelling pressures on the dry density of pelletized MX-80 materials and on the chemical composition of the saturation fluid.

The granular mixture in Cell S/B was taken from the same filling material used in the GRS Section of the *in-situ* HE-E test, which was composed by 65% of quartz sand and 35% of a sodium bentonite material (GELCLAY WH2) with the same composition as MX-80. The maximum grain size of the resulting mixture was approximately 1.8 mm, as indicated in Figure 8-2 (down, on the left). The initial water content and dry density of the S/B column after compaction were around 3.6 % and 1.45 g/cm^3, respectively, with an average grain density of 2.71 g/cm^3 (Villar *et al.*, 2012b). Consequently, the average values for the initial degree of saturation and porosity for the S/B mixture were 11% and 0.463, respectively (see Table 8-1). This particle density value for the resulting S/B mixture can be obtained from the expression in Equation (2-4), assuming that the sand fraction in the mixture has a density of 2.65 g/cm^3 while the grain density of the MX-80 bentonite is taken as 2.82 g/cm^3 (Romero, 2013). A thermal conductivity value in the range of 0.30 - 0.33 W/m/K was measured for the granular S/B mixture at its as-delivered water content state and at room temperature conditions (Wieczorek *et al.*, 2011; Villar *et al.*, 2012b). The hydraulic conductivity of the S/B mixture was estimated from a pair of infiltration tests with deionised water in samples with dry densities around 1.40 g/cm^3 (see the graph plotted on the

left-hand side in Figure 8-3). A water permeability value in the order of 10^{-10} m/s can be assumed for the compacted sand/bentonite column (Villar *et al.*, 2016). Due to the proportion of sand in the mixture, the magnitude of the swelling pressure expected to develop during the artificial hydration of Cell S/B was assumed to be negligible (Villar *et al.*, 2016). In fact, some experimental data corroborate the pronounced reduction in the magnitude of the swelling pressure of a sand/bentonite mixture as the clay content in the mixture decreases (see Figure 8-5). Consequently, the lateral mechanical reinforcement around the body of Cell S/B was not required (Villar *et al.*, 2012b). Swelling pressures of 1.5 MPa and 0.7 MPa were obtained from small samples of the same granular material inside Cell S/B (compacted at a nominal dry density of 1.45 g/cm^3) when saturated with deionised and Pearson water, respectively (Villar *et al.*, 2012b). Despite that, the evolution of axial stresses on the top of the column was not recorded during the test. However, it has been assumed that the swelling pressure generated during the saturation of the heated S/B column was about 0.7 MPa (Villar, 2013), once the heating-infiltration test was performed using saline water as permeant.

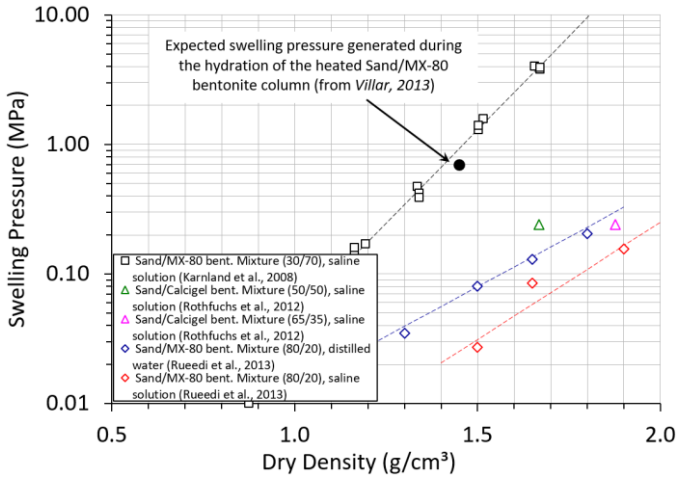

Figure 8-5: Variation of swelling pressures with dry density and with the clay content in small samples of sand/bentonite mixtures.

8.2.2. THE EXTERNAL INSULATION SYSTEM

In order to prevent any heat loss during the performance of the heating-hydration tests, a 5-mm thick dense foam was placed around both bentonite columns. Furthermore, the body of the cells (made of Teflon ®) also plays as a thermal barrier due to its low thermal conductivity. However, and despite the emplacement of this initial insulation system before the test initiation, lateral heat loss was observed in the first stages of heating, which required the installation of additional layers of materials with low thermal conductivities. In that sense, the dense foam was replaced in Cell S/B after 1566 hours of heating by a thick layer of insulation wool along the entire length of the cell. An external layer of ISOVER material was installed around the 8 cm at the bottom of the column after 1666 hours of heating. On the other hand, the entire length of Cell B was wrapped by a thick layer of wool while the 5 cm at the bottom of the cell was covered by the ISOVER material after 1518 hours of heating. The layer thickness and the thermal conductivity of the isolation materials set around the tested bentonite columns is summarized in Table 8-2.

Table 8-2: Layer thickness and thermal conductivity of the insulation materials placed around the bentonite cells (from Villar *et al.*, 2012b).

	Layer thickness [mm]	Thermal Conductivity [W/m/K]
Teflon ®	15*	0.25
Dense foam	5	0.04
Superwool 607 HT blanket	30	0.04
ISOVER BT-LV insulation	25	0.034

* Thickness of the body of both cells.

8.2.3. STAGES OF THE LABORATORY HEATING-HYDRATION TESTS

The heating of the cells was performed in two steps: an initial heating event in which the heater temperature was set at 100°C and a second heating episode (after the stabilization of the relative humidity inside the columns), in which the heater temperature was increased to the final target value of 140°C. In both heating episodes, the rise in temperature at the electric heating element was performed for a short period of time (12 – 25 min). The second heating episode (from 100°C to 140°C) occurred approximately 2497 hours and 3527 hours after the first heating episode in Cell S/B and in Cell B, respectively. This stage of the laboratory tests was carried out without any artificial hydration of the bentonite columns. The improvement of the external insulation system in both cells (see **Section 8.2.2** and **Section 8.3.2**) took place during this stage of the tests (heating without hydration).

Once temperature and relative humidity inside each bentonite column (for a heater temperature of 140°C) were stabilized, the hydration phase of the experiment started with the injection of saline water at a pressure of approximately 0.1 bar. Hydration of Cell S/B started 3696 hours after the beginning of heating and continued uninterruptedly until the dismantling of such a bentonite column (in February, 2015), after more than three years of operation (Villar *et al.*, 2015b). The forced re-saturation of Cell B started about 5015 hours after the beginning of the heating test. Since then (June 2012), this heated cell has been submitted to a continuous hydration process by the injection of water under the conditions previously mentioned. The synthetic water used to saturate the cells has a similar chemical composition of the pore-water in the geological formation (the Opalinus rock) around the *in-situ* HE-E test (Villar *et al.*, 2012b).

A comprehensive description of the sequence of laboratory activities carried out before and during the heating-hydration tests as well as the analyses of the experimental data obtained from the instrumentation of the bentonite columns can be found in Villar *et al.* (2012b; 2015b; 2016) and in Iglesias *et al.* (2018). The post-mortem analyses provided by the dismantling of Cell S/B are also reported in detail in Villar *et al.* (2015b).

8.3. THE NUMERICAL MODELLING OF THE BENTONITE COLUMNS

The capability of the double-porosity model developed in this Thesis in simulating the hydration of the heated cells has been verified by comparing the model predictions with the evolution of temperature (T), relative humidity (RH) and axial pressures (on the top of Cell B) measured during the tests. As mentioned previously, such temperature and RH data have been registered by sensors installed at 10 cm, 22 cm and 40 cm along both columns as schematized in Figure 8-6. In order to evaluate the impact of the heat propagation through the porous media and the progress of hydration inside the bentonite cells, the evolution of these variables respect to the distances to the centre of the columns (radial profiles) and to the heating element (longitudinal profiles) has also been determined. Moreover, time and spatial evolution of other HM variables – as degree of saturation and porosities – at both structural levels has also been computed. The experimental results obtained from the dismantling and the post-mortem analyses performed on samples taken from Cell S/B were also used to compare the final state of the S/B mixture with the model predictions at the end of calculations.

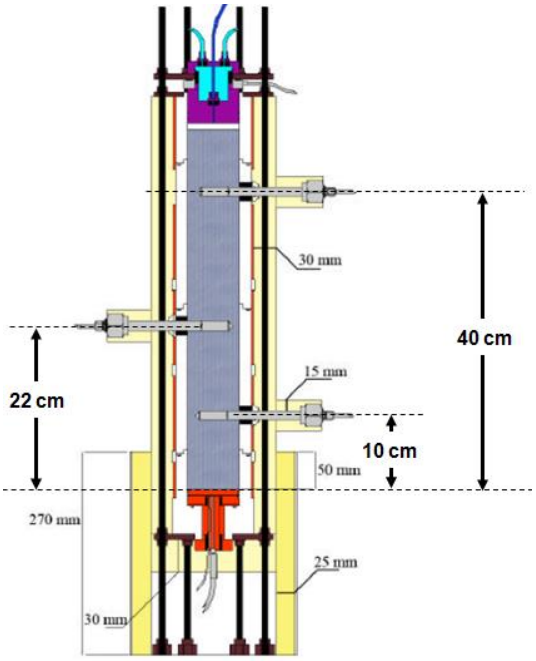

Figure 8-6: Schematic layout of each bentonite cell showing the position of the three temperature/RH sensors (from Villar *et al.*, 2012b). Heating element is located at the bottom of the cell and hydration is performed from the top to the bottom of the column.

In the numerical analyses presented in the following sections, time counting started at the onset of heating. Hence, $time = 0$ was set at 138 hours and 263 hours after the starting of the data acquisition system (RH/T sensors, load cells and heater electric power supply) in Cell B and Cell S/B, respectively. This stage of the test (prior to heating) was simulated as an initial stabilization step, in which the initial thermal, hydraulic and mechanical conditions and boundary conditions were kept unchanged in Cell B. In Cell S/B, however, an accidental water injection took place around 168 hours before the test initiation. Although such an unexpected event lasted about 5 minutes, the high permeability of the mixture led to an increase in the water content along the column. Consequently, the average initial water content in Cell S/B at the start of heating was about 4.7% instead of the as-built value of 3.6% (Villar *et al.*, 2012b).

The mechanical behavior of the external isolating materials was reproduced by means of elastic models while the mechanical response of the bentonite-based materials was governed by the thermo-elastoplastic double-porosity approach discussed from **Chapter 3** to **Chapter 5**. The body of the cells (Teflon®) was idealized as a very rigid porous medium with intrinsic permeability several orders lower than the values assigned to describe the pore structure of the bentonite-based materials inside the cells.

A brief account of the axisymmetric domain used in the calculations, the initial and boundary conditions enforced at each stage of the heating/infiltration tests and the model parameters required for the coupled THM constitutive laws is given in the following sections. The more relevant results obtained from the modelling of Cell B and Cell S/B are discussed in **Section 8.3.4** and **Section 8.3.5**, respectively.

8.3.1. MODELLED GEOMETRY

Hydration of the two heated bentonite columns was modelled by means of a finite element (FE) approach via CODE_BRIGHT (Olivella *et al.*, 1994), as already discussed in **Section 3.10** and **Section 5.3**. A 2-D axisymmetric geometry was considered. Each column of granular bentonite material is 3.5 cm wide and 50 cm high. A structured FE mesh composed of 700 linear quadrilaterals was generated for simulating such bentonite columns, as illustrated in Figure 8-7(a). The lower horizontal boundary simulates the heating element while the upper horizontal boundary represents the hydration system. The body of the cells (made of Teflon PTFE) and the thick layer of dense foam provided the external isolation of the cells during the first stage of heating. However, the improvement of the thermal isolation of the bentonite columns with the replacement of the dense foam by a thick layer of insulation wool was performed between the first and the second heating episodes (see **Section 8.2.2**). The modelled geometries before and after the enhancement of the external insulation system are shown in Figure 8-7(b). All dimensions were taken in accordance to the test dimensions specified in Villar *et al.* (2012b).

8.3.2. INITIAL AND BOUNDARY CONDITIONS

Suction values of 123 MPa and 93 MPa were adopted as the initial hydraulic state for the columns of pellets and sand/bentonite mixture, respectively. Such values correspond to an initial relative humidity around 40% (for the pellets) and 50% (for the granular mixture) and represent the average relative humidities of the as-emplaced granular filling materials in the *in-situ* test. For modelling purposes, it was considered the initial equilibrium between the pore-water potential at macrostructure and microstructure in both bentonite columns. It means that the initial macro and micro suctions were assumed to have the same values: 123 MPa for Cell B and 93 MPa for Cell S/B. A compressive stress of 0.1 MPa was taken for the initial isotropic stress

state inside the cells. The initial temperature for the cells and the insulation materials was set around 23°C.

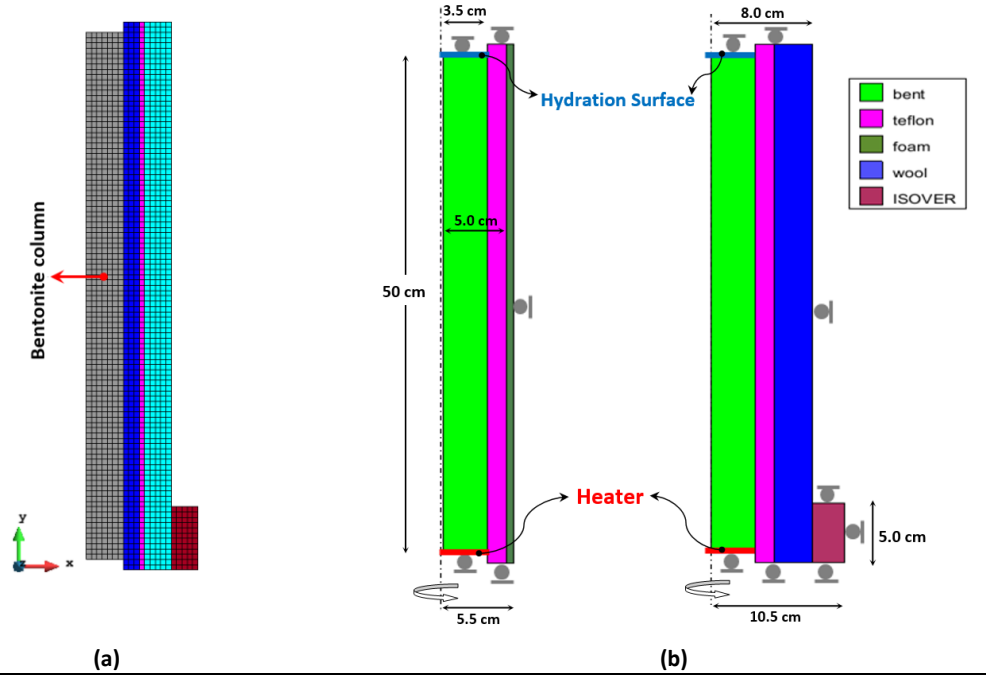

Figure 8-7: **(a)** Finite element mesh generated to simulate hydration of heated large bentonite cells; **(b)** modelled domain of the bentonite columns before (left) and after (right) the reinforcement of the external isolation system.

The initial porosity state (ϕ_0) of the modelled cells was estimated from the average dry densities of the as-built bentonite columns, as reported in Villar *et al.* (2012b) and indicated in Table 8-1. The initial soil volume fraction occupied by micro-pores ($\bar{\phi}_{m,0}$) in Cell B was determined by means of the grain density of the MX-80 bentonite and the average density of a pellet. A value of 0.159 was adopted for such a material parameter, which corresponds to a pellet density of about 2.1 g/cm^3. In the case of the granular mixture (Cell S/B), the pore-size distribution analysis by MIP performed on the original granular material indicated that about 92% of voids had a pore-size greater than 50 nm (macro-pores) while 8% of pores had a size in the range of 7 nm – 50 nm (meso-pores) (Villar, 2013; Villar *et al.*, 2015b). Assuming that both meso- and micro-pores are accounted for as the micro-pore volume fraction in the double-porosity formulation, a value of 0.04 can be considered as a suitable estimative of $\bar{\phi}_{m,0}$ for the granular mixture. However, and in order to evaluate the impact of the particle arrangements of the bentonite fraction on the hydration process of the column and on the swelling response of the resulting mixture, additional calculations were performed for different initial micro-pore volume fractions (see **Section 8.3.5**). A summary of the initial conditions adopted in the numerical simulations are given in Table 8-3.

Table 8-3: Initial conditions adopted in the numerical calculations for the bentonite granular materials in the cells.

		Cell B	Cell S/B
Temperature	[°C]	22.7	22.5
Liquid pressure at macrostructure	[MPa]	-123	-93
Liquid pressure at microstructure	[MPa]	-123	-93
Total stress (isotropic)	[MPa]	-0.1*	-0.1*
Total porosity, ϕ_0	-	0.444	0.463
Micro-pore volume fraction, $\bar{\phi}_{m,0}$	-	0.159	0.040 – 0.100

* Negative value for compressive stresses, according to the sign convention used in the pre and post processor GiD®.

Both heating episodes were simulated by prescribing the corresponding increment of temperature at the bottom of the cells. A 0-flux condition was applied on the upper boundary of the columns (the hydration line) prior to the beginning of the infiltration phase of the experiment. No vertical displacements were allowed along the upper and the lower horizontal boundaries of the bentonite columns. Furthermore, displacement restrictions were also prescribed at the external vertical boundaries so that heating and the re-saturation of the bentonite columns could be modelled under constant volume conditions. Construction, heating and hydration of the cells were simulated in steps as detailed below:

- The "instantaneous" construction of the cells and emplacement of the isolation material (the dense foam) at (constant) room temperature, with the application of the initial conditions for the bentonite columns and for the original insulation system and the prescription of the THM boundary conditions in force before the onset of heating. This modelling stage simulates the stabilization step left between the construction of the cells and the heating test initiation.

- The first heating episode, in which the heater temperature was increased linearly from its initial value (the room temperature) to 100°C. In Cell B, this target temperature was reached 33 minutes after the heater was switched on, while in Cell S/B, the final heater temperature was reached in 25 minutes. After that, temperature at the heating element was kept constant until the beginning of the second heating event. As mentioned previously, the beginning of this simulation phase also coincides with the time counter for the numerical analyses.

- The change and improvement of the insulation system at a heater temperature of 100°C. The dense foam was removed and replaced by a thick layer of insulation wool. The external thermal isolation system was replaced 1518 hours after the start of heating in Cell B. The thermal insulation was changed after 1566 hours of heating in Cell S/B, and it was reinforced again 100 hours after that, i.e., about 1666 hours since the beginning of heating.

- The second temperature increase at heater until reaching a final temperature of 140°C. This heating episode started 3527 hours after the onset of heating in Cell B and the final target temperature was reached in 17 minutes. In Cell S/B, this thermal event took place approximately 2497 hours after the startup of the heating system and lasted about 12

minutes. After that, temperature on the heater surface (heating line) remained constant until the end of the numerical calculations.

- The controlled re-saturation of the heated bentonite columns. The infiltration experiment has begun 5015 hours since the start of heating in Cell B. The start of hydration in Cell S/B occurred 3696 hours after the initiation of the heating test. A constant liquid pressure of 0.01 MPa (0.1 bar) was applied on the upper horizontal boundary of the column of pellets while a value of 0.006 MPa (0.06 bar) was imposed on the top of Cell S/B, simulating the hydration process in both cells. This flux condition remained unchanged until the end of the simulations.

The above-mentioned stages followed during the laboratory heating-hydration tests and the thermal and hydraulic loads applied on both bentonite cells are schematized in Figure 8-8 and Figure 8-9.

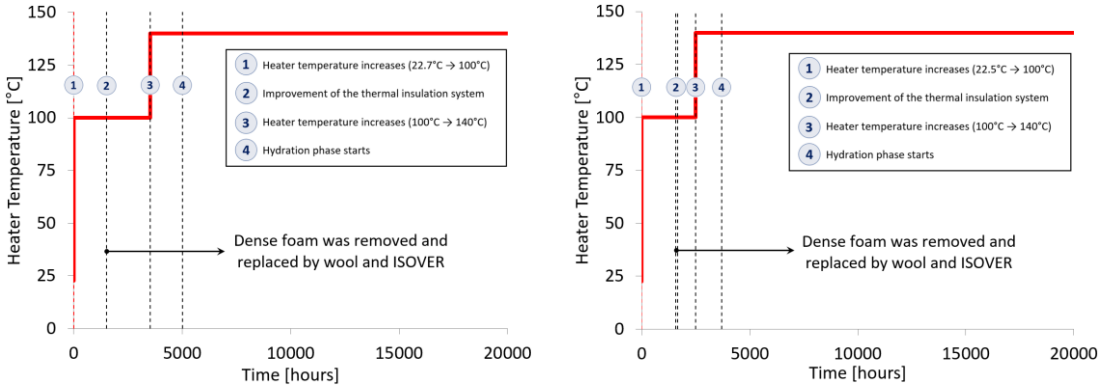

Figure 8-8: Temperature evolution at the heating element (thermal boundary conditions) and stages of heating and hydration for Cell B (left) and Cell S/B (right). Time "zero" corresponds to the beginning of heating.

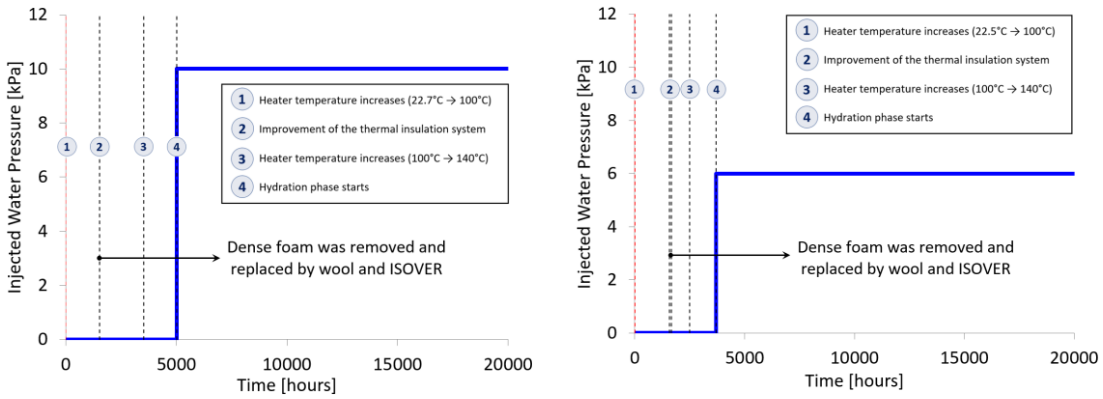

Figure 8-9: Prescribed pore-water pressure at the hydration line (on the top of the columns) and stages of heating and hydration for Cell B (left) and Cell S/B (right). Time "zero" corresponds to the beginning of heating.

It is important to mention that the accidental infiltration occurred before the heating initiation in Cell S/B was also taken into account. Such an event was simulated as a water flow prescribed at the hydration line. The estimation of the total mass of water infiltrated during this incident was based on the initial state of the compacted column and the changes in the water content due to the accidental opening of the hydration system. The actual fast infiltration (that lasted 5 minutes, as reported in Villar *et al.*, 2012b) was modelled as a very slow mass flux in which liquid

water was injected for 5 hours at an injection rate of 5 g/hour. Additionally, the expansive mixture in the 2.0 cm closest to the hydration surface was modelled as a material with higher intrinsic permeability (in comparison to the rest of the column) in order to enable the entrance of water into the column during the accidental flooding and prevent any convergence problems. The numerical modelling of Cell S/B was performed until about 28247 hours since the start of heating. This time corresponds to the end of the test and the dismantling of the column. However, none of the laboratory operations related to the shutdown of the heating element or to the dismantling of the column *S/B* was modelled.

8.3.3. MODEL PARAMETERS

Some theoretical aspects to take into account during the numerical modelling of thermal problems are: the heat propagation through the porous medium, the thermal expansion/contraction of the species present in the soil, the water phase exchange (evaporation and condensation), the water vapour diffusion and the dependence of water viscosity on temperature. Heat conductivity is described by means of Fick's law (see **Section 3.8.1**) with the global thermal conductivity (λ) defined in terms of the thermal conductivities of the saturated and the dry soil. The exponential dependence of the thermal conductivity on saturation, given by Equation (3-93), was used in calculations. The input parameters of this constitutive law (λ_{dry} and λ_{sat}) were chosen so that the thermal conductivity function could be fitted to the experimental data obtained from laboratory tests on samples of the same granular bentonite materials (Wieczorek *et al.*, 2011; Villar *et al.*, 2012b) and to the typical values reported in the literature for saturated bentonites (Knutsson, 1983; Hökmark *et al.*, 2007; Tang *et al.*, 2008; Tang and Cui, 2010). The thermal conductivity dependence on the degree of saturation of the granular bentonite materials is illustrated in Figure 8-10(a). The thermal expansions of pore-water, solid particles and soil skeleton were taken into account in calculations due to the crucial role played by the differential thermal expansion of the soil constituents and the thermal expansion of pores on the hydraulic response induced by the thermal load. As a consequence of the expected high thermal gradients generated by the combination of the intense heating and the initial dry state of the columns, water phase exchange (evaporation and condensation) was allowed as well as the subsequent water vapour diffusion from the hottest to the coolest zones inside the heated columns. The molecular diffusion of vapour through macro-pores (see **Section 3.8.2.3**) and its dependence on temperature was simulated using Equation (3-122). The thermal impact on the pore-water viscosity (see **Section 3.8.2.1.2**) was also introduced in the numerical analyses by means of the expression in Equation (3-108).

The thermal parameters required in the numerical simulations are collected in Table 8-4. As mentioned before, such input parameters were fitted in accordance to the experimental data reported in the literature (Hökmark *et al.*, 2007; Tang *et al.*, 2008; Tang and Cui, 2010; Wieczorek *et al.*, 2011; Villar *et al.*, 2012b) and by back-calculating the results of the *in-situ* HE-E test (Czaikowski *et al.*, 2012; Gaus *et al.*, 2014a; Gens and Vasconcelos, 2019). The same thermal parameters were used for both granular materials, with the exception of the specific heat of the solid particles. Furthermore, it was assumed that this physical property would remain constant in the temperature range considered in the numerical calculations (22°C – 140°C).

The macrostructural pore-water retention curves of the granular bentonite materials in both cells were calibrated from the data provided by small oedometer tests, in which compacted granular MX-80 bentonite materials (pellets and S/B mixtures) were submitted to controlled wetting or drying paths at different temperatures (Rizzi *et al.*, 2012; Wieczorek *et al.*, 2013), as shown in Figure 8-11(a). The model parameters presented in Table 8-5 adjust these experimental data to a water retention function expressed by the modified van Genuchten law according to Equation (3-119). The modified van Genuchten law was also used to model the microstructural retention curves, but due to lacking more specific information about the water retention capacity of micro-pores in MX-80 bentonites, such curves were defined by assuming a high value for the pressure parameter P_0 in Equation (3-118). This assumption is intrinsically related to the pore-water retention behaviour of denser clay fabrics, once micro-pores are the predominant pore-size fraction present in high-density specimens (Gens *et al.*, 2011). The shape of the water retention capacity of micro-pores in both bentonite columns, obtained from the model parameters listed in Table 8-5, are plotted in Figure 8-11(b) together with some experimental water retention data for granular bentonite samples compacted at high dry densities (in the range 1.69 – 2.03 g/cm^3).

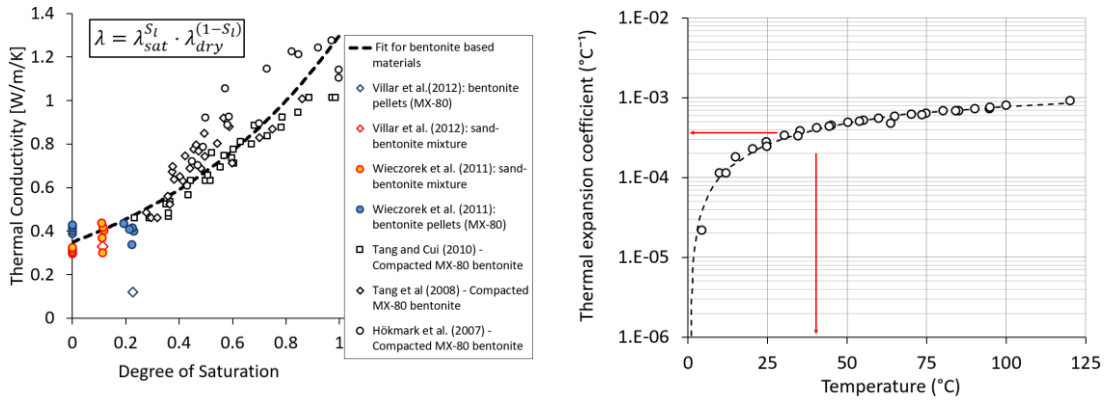

(a) **(b)**

Figure 8-10: **(a)** Thermal conductivity dependence on the degree of saturation of granular MX-80 bentonite based materials; **(b)** volumetric thermal expansion of pore-water (after Ashbaugh et al., 2002; Wang *et al.*, 2014). A constant value for this pore-water property (at 40˚C) was adopted in the numerical calculations.

Table 8-4: Input thermal parameters used in the numerical simulations of heating and hydration of both bentonite columns.

		Cell B	Cell S/B
Conductivity flux of heat			
Thermal conduct. of the dry soil, λ_{dry}	[W/m/K]	0.35	0.35
Thermal conduct. of the saturated soil, λ_{sat}	[W/m/K]	1.30	1.30
Thermal Expansion			
Linear thermal expansion for grains	[°C^{-1}]	2.5e-05	2.5e-05
Volum. thermal expansion for water (at 40°C)	[°C^{-1}]	-3.4e-04	-3.4e-04
Volum. thermal expansion for the medium	[°C^{-1}]	7.5e-05	7.5e-05
Molecular diffusion of water vapour			
Model parameter, D	[m^2 s^{-1} K^{-n} Pa]	5.9e-06	5.9e-06
Model parameter, n	-	2.3	2.3
Water Viscosity			
Model parameter, A	[MPa·s]	2.1e-12	2.1e-12
Model parameter, B	[K]	1808.5	1808.5
Thermo-elastoplastic parameters			
Parameter for elastic thermal strain, α_0	[°C^{-1}]	7.5e-05	7.5e-05
Parameter for plastic thermal strain, α_1	[MPa °C^{-1}]	0.0	0.0
Parameter for elastic thermal strain, α_2	[°C^{-2}]	0.0	0.0
Parameter for plastic thermal strain, α_3	[MPa °C^{-2}]	0.0	0.0
Param. related to decrease of tensile strength due to ΔT, ρ_T	-	0.0	0.0
Solid phase specific heat	[J/kg/K]	893	950

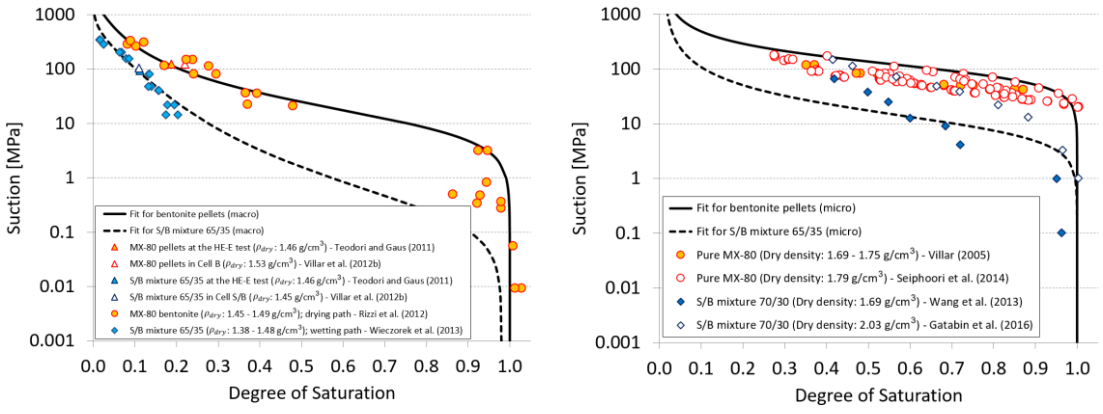

(a) **(b)**

Figure 8-11: Modelled water retention curves for **(a)** macrostructure and **(b)** microstructure of MX-80 pellets (full lines) and the sand/MX-80 bentonite mixture 65/35 (dashed lines). Symbols represent experimental results.

Table 8-5: Hydraulic parameters used for modelling the macro- and the micro-water retention capacities of the granular bentonite materials.

		Cell B	Cell S/B
Retention curve parameters for macrostructure			
Measured *P* at 20°C, P_0	[MPa]	10.0	0.20
Surface tension at 20°C, σ_0	[N/m]	0.072	0.072
Shape function for retention curve, λ_{rc}	-	0.40	0.24
Pressure related with the suction at zero degree of saturation, P_d	[MPa]	1500	5000
Model parameter, λ_d	-	1.0	15
Residual saturation, S_{lr}	-	0.01	0.01
Maximum saturation, S_{ls}	-	1.00	0.98
Retention curve parameters for microstructure			
Measured *P* at 20°C, P_0	[MPa]	100	10.0
Surface tension at 20°C, σ_0	[N/m]	0.072	0.072
Shape function for retention curve, λ_{rc}	-	0.60	0.50
Pressure related with the suction at zero degree of saturation, P_d	[MPa]	1.0e+27	1.0e+27
Model parameter, λ_d	-	0.0	0.0
Residual saturation, S_{lr}	-	0.01	0.01
Maximum saturation, S_{ls}	-	1.00	1.00

The dependence of intrinsic permeability on the pore structure of the granular expansive materials (see Figure 8-3) was modelled using Kozeny's law, which is expressed by Equation (3-99). In the double-porosity approach, such an intrinsic permeability variation is usually considered in terms of the macro-pore volume fraction ($\bar{\phi}_M$) instead of the total porosity (ϕ). Increase in the hydraulic permeability of the columns as they were re-saturated with liquid water (from the top to the bottom of the cells) was taken as a power function of the degree of saturation, as given by Equation (3-104). During the THM modelling of the HE-E test by means of a single-porosity model – see Gaus *et al.* (2014a) and Gens and Vasconcelos (2019) – the hydraulic parameters of the relative permeability law for both granular materials were estimated from back-calculating the *in-situ* measurements provided by a series of RH sensors installed inside the heated sections. The adopted parameters for the water flux through macro-pores are given in Table 8-6.

Table 8-6: Hydraulic parameters used for modelling the water mobility through macro-pores in both bentonite cells.

		Cell B	Cell S/B
Intrinsic permeability, k_0	[m^2]	3.50e-20	3.50e-18 *
Reference porosity, $\bar{\phi}_{M,0}$	-	0.28	0.40
Shape parameter (for relative permeability), A_{rl}	-	1.00	1.00
Shape parameter (for relative permeability), λ_{rl}	-	6.0	2.0 – 5.0

* A value of 1.00e-17 m^2 was used for the intrinsic permeability of the topmost 2-cm thick layer of S/B mixture.

The model parameter for the local water mass transfer between the two families of pores (γ^w) is assumed to be only related to geometric properties of the microstructural medium (size, specific surface and inter-layer permeability of the clay particles, for example), as already mentioned in **Section 3.6**. Due to the lack of relevant information on the microstructural characterization of the granular bentonite materials in the cells, the leakage coefficient used in the numerical calculations had to be obtained from back-analysis. In the case of the column made of MX-80 pellets, the evolution of the axial pressures measured on the top of the column was employed to estimate a suitable value for such an input parameter. The selected values for γ^w in calculations ranged between 10^{-12} kg/s/m^3/MPa and 10^{-8} kg/s/m^3/MPa. It is important to remark that the leakage coefficient plays a central role in the re-saturation rate of the heated columns and, consequently, in the development of their swelling potential. Consequently, the development of the axial stress at the top of the columns as well as the local changes in the micro- and the macro-porosity variables are affected by the value adopted for γ^w in calculations. However, this parameter is one of the uncertainty sources in the double-porosity formulation due to the practical difficulties in estimating its value directly from conventional laboratory procedures.

The mechanical parameters for the granular expansive materials were based on several experimental information on the mechanical characterization of pelletized and granular bentonite mixtures with analogous composition and/or with similar grain spectrum and dry density ranges. Some of such constitutive data are reported in Hoffmann *et al.* (2007), Rothfuchs *et al.* (2012), Wang *et al.* (2013), Toprak *et al.* (2016), among others. Despite that, some of the mechanical parameters used in calculations had to be calibrated during the previous modelling tasks (Gaus *et al.*, 2014a; Vasconcelos and Gens, 2015; Gens and Vasconcelos, 2019) in order to fit the model predictions to the data recorded by the sensors installed in the *in-situ* and in the laboratory heating tests. The required elastic and elastoplastic parameters to model the mechanical problem at both structural levels are summarized in Table 8-7 and Table 8-8. Note that the THM parameters adopted for the MX-80 pelletized material in Cell B are the same ones used in all the HM and THM analyses performed in **Chapter 6** and **Chapter 7**, respectively. Such input parameters were listed again in the tables presented in the current chapter to emphasize the similarities and differences between the granular bentonite materials considered in the laboratory heating tests.

Table 8-7: Mechanical parameters for modelling the elastic response of the CIEMAT bentonite columns.

		Cell B	Cell S/B
Elastic Parameters for Microstructure			
Shape parameter for Bishop's coefficient, p_χ	-	1.00	1.00
Shape parameter for Bishop's coefficient, q_χ	-	100	100
Elastic Parameters for Macrostructure			
Elastic slope (macro) for specific volume-mean stress, $\overline{\kappa}_M$	-	0.006	0.002
Elastic slope (macro) for specific volume-macro suction, $\overline{\kappa}_s$	-	0.010	0.001
Minimum bulk modulus (macro), $\overline{K}_{M,min}$	[MPa]	45	45
Minimum bulk modulus (macro), $\overline{K}_{s,min}$	[MPa]	45	45
Poisson's ratio, υ	-	0.30	0.30

Table 8-8: Mechanical parameters for modelling the macrostructural plastic response of the CIEMAT bentonite columns.

		Cell B	Cell S/B
Elastoplastic Behaviour for Macrostructure (BBM mechanism)			
Slope of void ratio-mean stress at saturation, λ_{sat}	-	0.165	0.140
Parameter defining the maximum soil stiffness, r	-	0.70	0.85
Parameter controlling the rate of increase of stiffness with macro suction, β	[MPa^{-1}]	0.15	0.05
Reference pressure, p_c	[MPa]	0.09	0.05
Initial pre-consolidation mean stress at saturation, p_0^*	[MPa]	1.00	0.50
Tensile strength in saturated conditions, p_{s0}	[MPa]	0.10	0.00
Parameter that takes into account increase of tensile strength due to macro suction, k	-	0.10	0.10
Friction angle, φ'	[°]	27	37
Smoothed shape parameter, α_F	-	8	8
Smoothed shape parameter, α_G	-	8	8
Non-associativity parameter, ω	-	1.00	1.00
Model parameter, c	-	0.20	0.20
Mechanical coupling functions (micro-macro interaction mechanism)			
$f_{MS}^{(0)}$	-	1.0	1.0
$f_{MS}^{(1)}$	-	-0.1	0.0
n_{MS}	-	3.0	3.0
$f_{MC}^{(0)}$	-	-0.1	0.0
$f_{MC}^{(1)}$	-	1.0	1.0
n_{MC}	-	3.0	3.0

8.3.4. CELL B

The first modelling task consisted in performing a numerical back-analysis based on the evolution of some THM variables measured during the laboratory test in order to estimate a suitable value for the leakage parameter (γ^w). In that sense, several calculations were carried out, each of them related to a different value of γ^w, but only three of such analyses are presented here. The evolution of temperature and relative humidity (RH) at three distances from the heater element and the development of the axial stress on the top of the column of pellets recorded by sensors are plotted together with model predictions in Figure 8-11 (temperature), Figure 8-12 (RH) and Figure 8-13 (axial pressure). In the following graphs (in this section), these experimental data (represented by symbols) were included up to 52681 hours since the beginning of hydration (*i.e.*, until June, 2018) (Iglesias *et al.*, 2018).

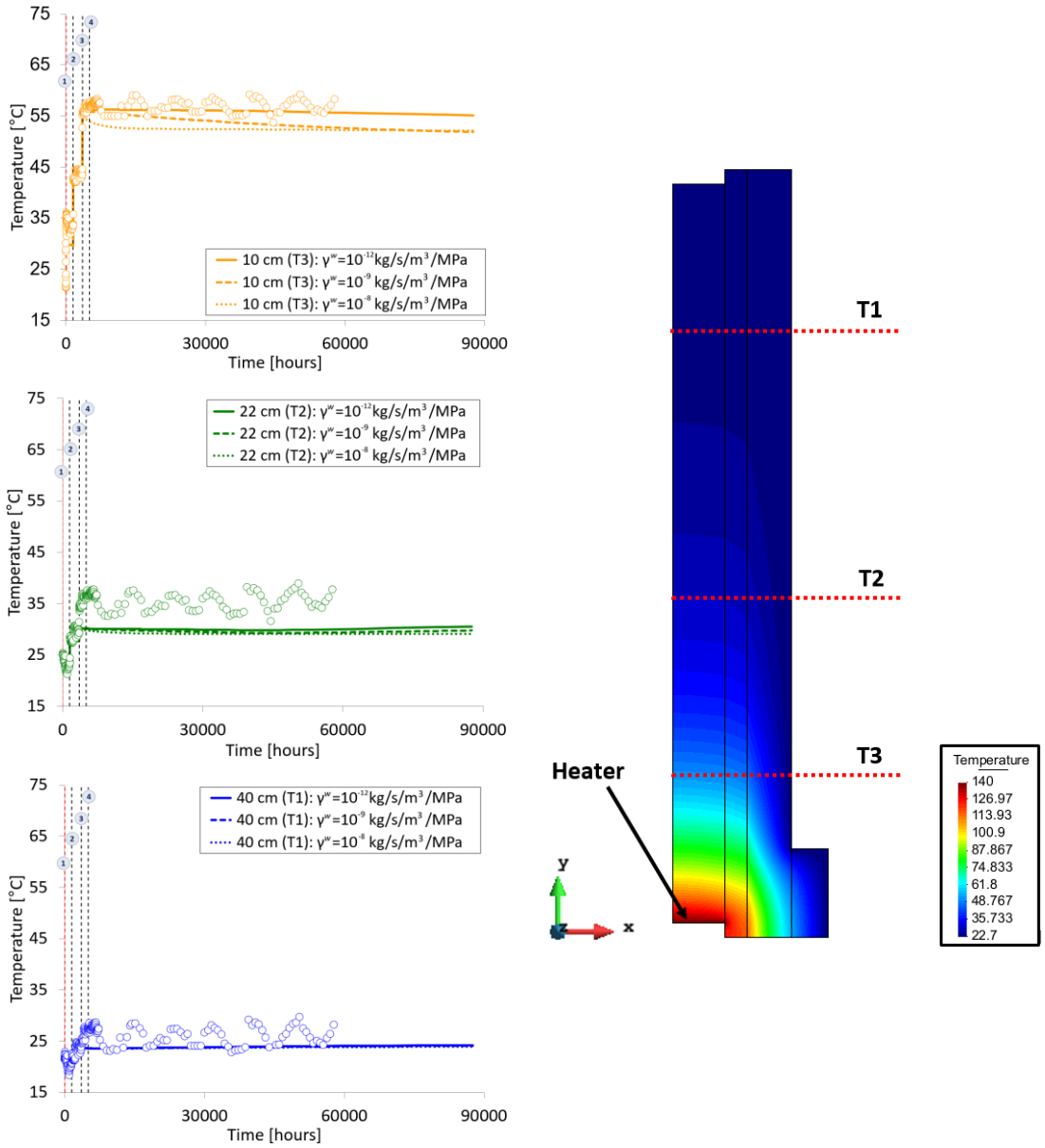

Figure 8-12: Evolution of temperature at the sensor positions for three distinct leakage coefficients (left) and spatial distribution of temperature in Cell B at the end of calculations, when $\gamma^w = 10^{-9}$ kg/s/m^3/MPa (right). Symbols represent the temperature measured by CIEMAT.

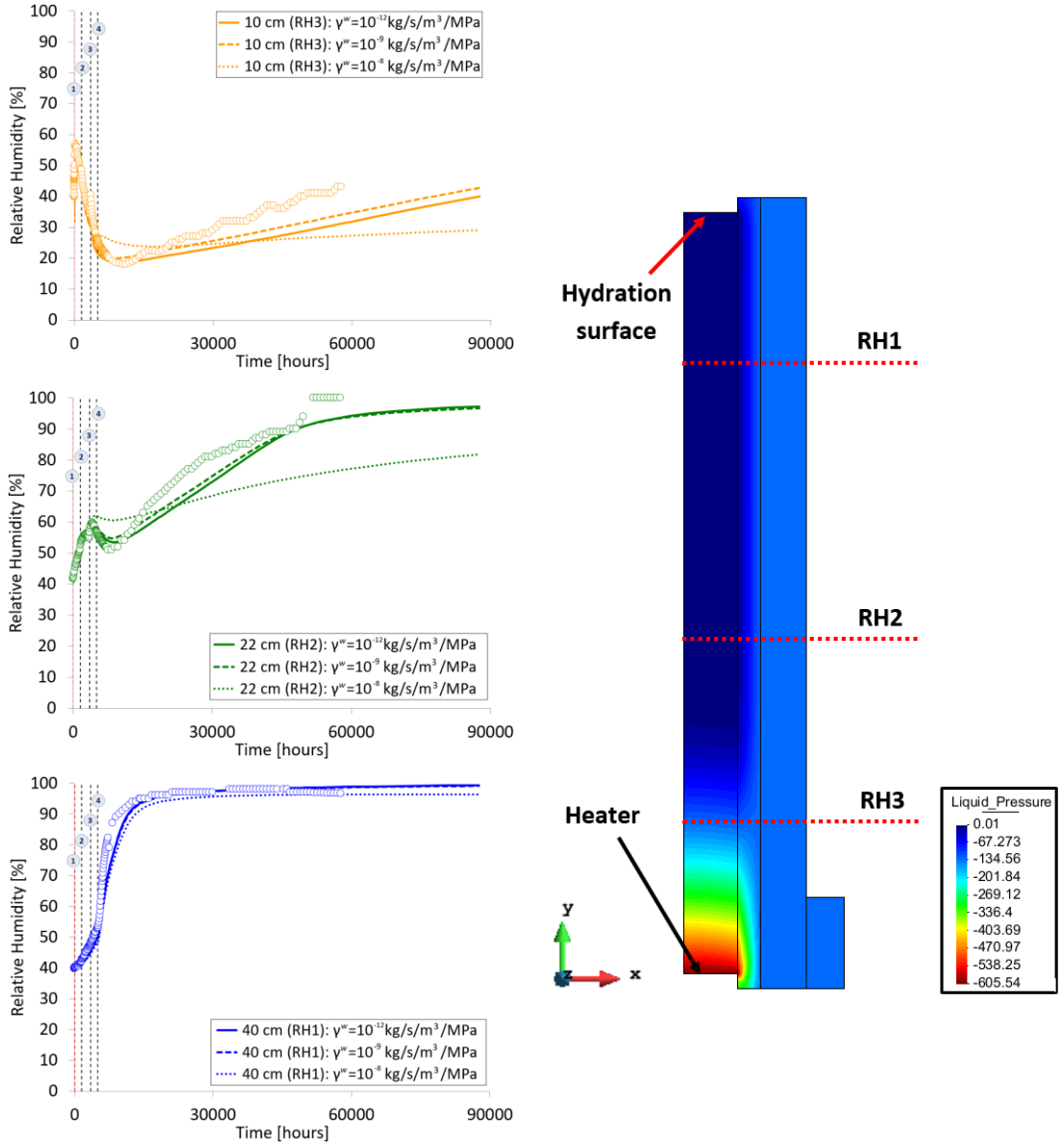

Figure 8-13: Evolution of relative humidity at the sensor positions for three distinct leakage coefficients (left) and spatial distribution of macrostructural water pressure in Cell B at the end of calculations, when $\gamma^w = 10^{-9}$ kg/s/m^3/MPa (right). Symbols represent the RH measured by CIEMAT.

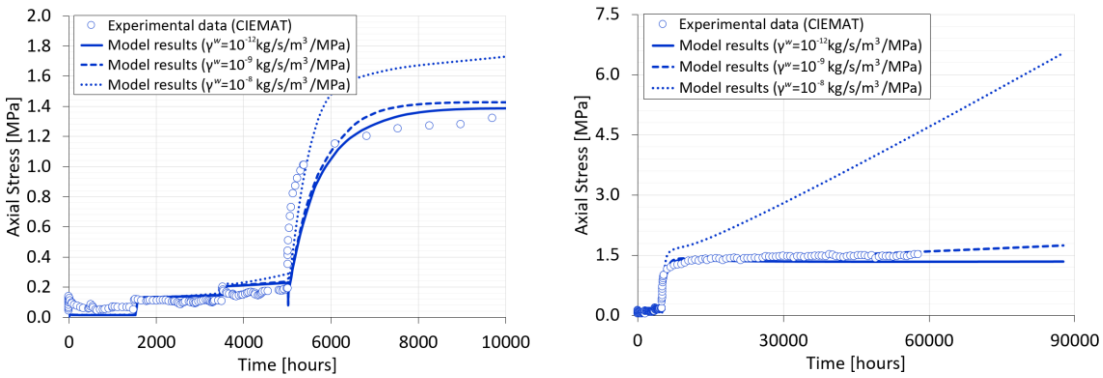

Figure 8-14: Development of axial stress at the top of Cell B for three distinct leakage coefficients. Symbols represent the axial pressure measured by CIEMAT.

As discussed in the previous chapters, a lower value of γ^w produces a delay in the re-saturation of microstructure by the local water transfer from inter-aggregate to intra-aggregate pores. However, when a higher value of this parameter is adopted, micro-pores are saturated simultaneously to the saturation of macro-pores. Consequently, the swelling response of microstructure is hindered when $\gamma^w = 10^{-12}$ kg/s/m^3/MPa and enhanced when $\gamma^w = 10^{-8}$ kg/s/m^3/MPa, which is evidenced by the development of the axial pressures predicted in both cases (see Figure 8-14). However, and from the model results shown above, it can be observed that the value of $\gamma^w = 10^{-9}$ kg/s/m^3/MPa fits better the increase in the axial stress induced by the artificial hydration of the column. This value for the leakage parameter was used in the numerical analyses whose results are discussed from now on. It is important to mention that the progressive increase in the axial stress during hydration, when $\gamma^w = 10^{-9}$ kg/s/m^3/MPa (in comparison to the case when $\gamma^w = 10^{-12}$ kg/s/m^3/MPa), is a consequence of the additional swelling of pellets as micro-pores are filled with water coming from macro-pores. In both situations, most of the macro-pores in the upper half of the column are nearly saturated with water, as confirmed by the values greater than 90% for the RH measured by the sensors located at that zone and by the model results (see Figure 8-13). As mentioned in **Section 3.9**, relative humidity is a measurement of the vapour concentration in pores and it is related to suction through the psychrometric law according to Equation (3-129). A simplified form of such an equilibrium law, relating RH to the macrostructural (matric) suction (s_M), is given as follows

$$s_M = P_{gM} - P_{lM} = -\frac{\rho_{lM} \cdot R \cdot (273.15 + T)}{M_w} ln(RH) \tag{8-1}$$

where the relative humidity variable (RH) varies between 0.0 (pores completely dried) and 1.0 (fully saturated pores). The psychrometric law was employed to plot the RH evolution provided by the numerical calculations. As suction and degree of saturation are correlated by the pore-water retention curves (see **Section 2.4.1** and **Section 3.8.2.2**), RH is considered as an indirect measurement of the saturation state of non-saturated pores (Czaikowski *et al.*, 2012).

In the following, the temporal evolution of temperature and relative humidity inside Cell B when $\gamma^w = 10^{-9}$ kg/s/m^3/MPa (the "base case" hereafter) are shown in Figure 8-15 and Figure 8-16, respectively. Longitudinal profiles of temperature and RH through the vertical axis of the bentonite column at different times are plotted in Figure 8-17 while radial profiles of such variables at four distances from the heat source are given in Figure 8-18. A first inspection of such results shows the good agreement between computed and measured temperature and relative humidity, especially for the sensors closer to the heating element. Consequently, it demonstrates the ability of the fully-coupled THM formulation implemented in the FE code to model the heating-hydration experiment in a satisfying and realistic way.

The evolution and distribution of temperature in Cell B induced by the two heating episodes is reproduced quite well by the numerical simulations. Some discrepancies between measured and numerical results were observed at 10 cm to the heater (sensor T3) immediately after the first increase of the heater temperature. In fact, model predictions at that position were around 4°C – 5°C lower than the data registered by the sensor T3 during this stage. However, such differences were reduced significantly after the improvement of the external isolation system. The numerical simulation also captured the increments in temperature due to the

reinforcement of the insulation system. After the second heating episode, the three sensors inside the column recorded temperatures slightly higher than the values obtained from the numerical modelling and such differences tended to increase as the distance to the heating face also increases. Moreover, the temperature oscillations registered by the sensors (see Figure 8-15) were associated with the changes in laboratory temperature (Villar *et al.*, 2016) and were not reproduced by the model. Actually, the changes in temperature along the column obtained from the modelling were only related to increments in temperature caused by the heating process itself or induced by the improvement of the external insulation system. The high thermal gradient imposed by the heating element at the bottom and the cooling system installed at the top of the column of MX-80 pellets (Villar *et al.*, 2012b) was also reproduced by the model results, even when the thermal restriction induced by the cooling system was not modelled explicitly. In fact, model predicts temperature values in the upper portion of the column that remain practically unchanged and equal to the average room (external) temperature, as indicated by the results in Figure 8-15 and in Figure 8-17 at distances (to the heater) greater than 40 cm. Furthermore, the thermal gradient inside the column is steeper in the 10 cm closest to the heater, which reflects the saturation state along the height of the column of pellets. Villar *et al.* (2016) reported the uniaxial pattern of temperatures inside the bentonite columns, whose spatial distribution is practically homogeneous at a given distance from the heater. Such an experimental feature is well matched by the radial profiles of temperature in Figure 8-18.

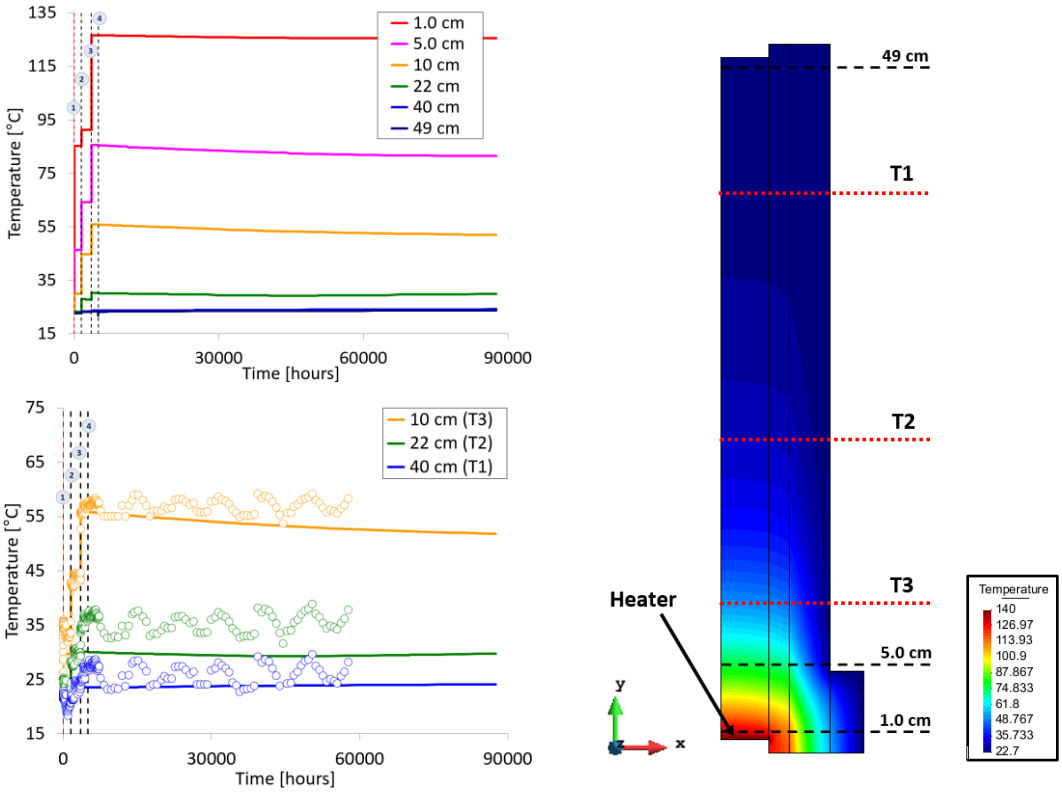

Figure 8-15: Evolution of temperature at several distances to the heater (left) and spatial distribution of temperature in Cell B at the end of calculations (right).

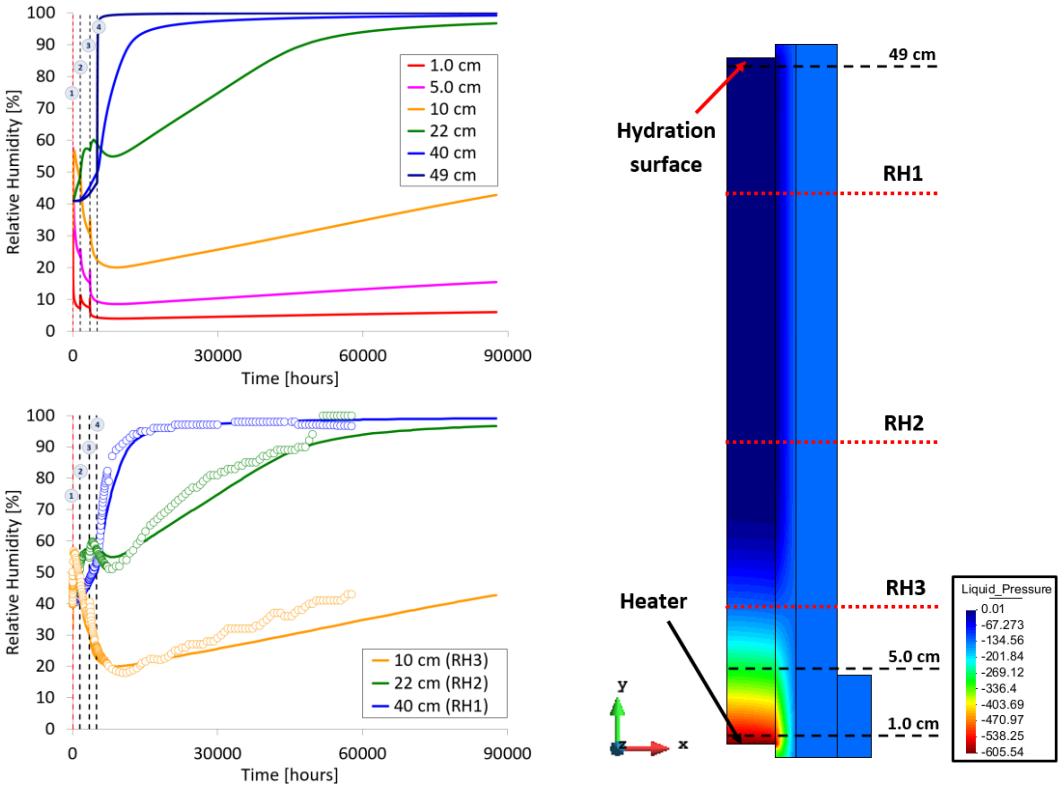

Figure 8-16: Evolution of relative humidity at several distances to the heater (left) and spatial distribution of macrostructural water pressure in Cell B at the end of calculations (right).

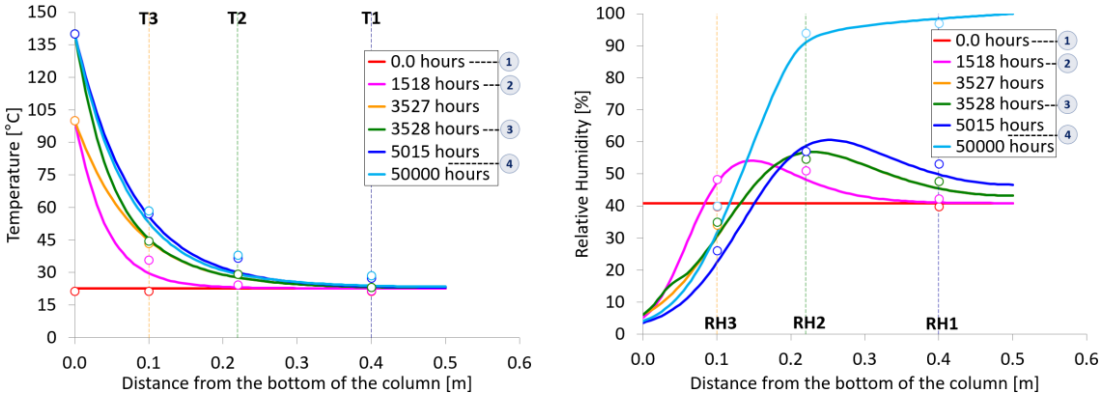

Figure 8-17: Temperature (left) and RH (right) versus distance to the heater along Cell B axis at different times. Symbols represent the experimental measurements by CIEMAT.

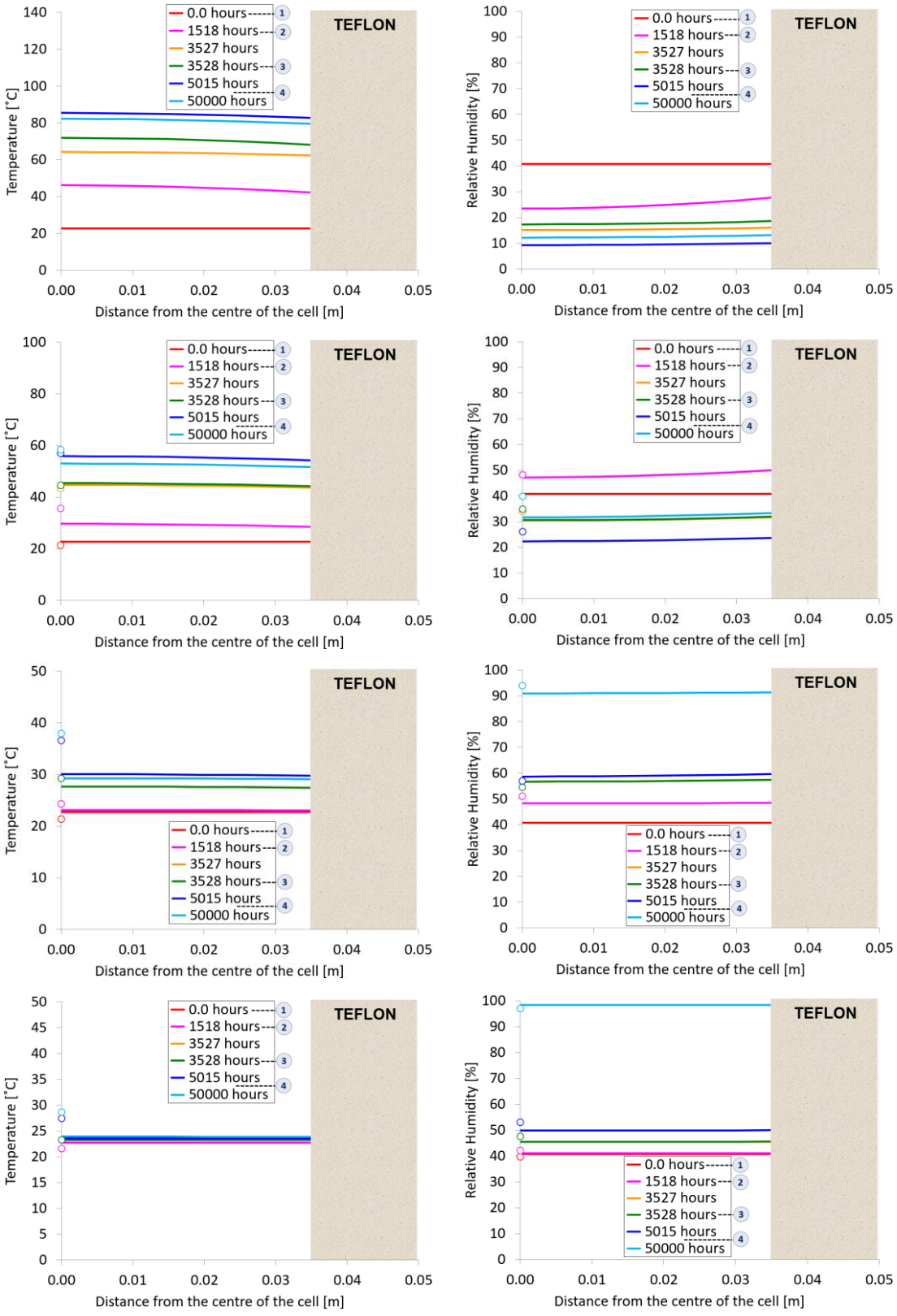

Figure 8-18: Radial profiles of temperature (left) and RH (right) at several distances to the heater (from the top to the bottom): 5.0 cm, 10 cm, 22 cm and 40 cm. Symbols represent the experimental measurements by CIEMAT.

The two heating episodes generated an initial and pronounced increase in RH at the sensor closer to the heater (sensor RH3) due to the differential expansion of macro-pore water in comparison to the thermal expansion of the solid species and the soil skeleton. Furthermore,

the magnitude of the applied thermal load was high enough to allow the generation of pore-water vapour in the lower portion of the column of pellets. In such conditions, a condensation zone developed close to the top of the bentonite cell where the water vapour (coming from the bottom of the cell by diffusion) condensates. Vapour condensation leads to an increment of the water content (and consequently, an increase of RH) at the cooler zones inside the cell, as indicated by the RH measurements and the model predictions for the two sensors farther away from the heater (see Figure 8-16). In contrast, the water content decreased near the heater during the first stages of the experiment, as registered by the sensor RH3 (see Figure 8-16). However, and after the start of the forced hydration of the heated cell, such a sensor (and the model results) registered a progressive increase in RH due to the downward flux of liquid water. At that time, the experimental and the numerical data obtained from the two sensors closer to the hydration line (RH1 and RH2) indicated an almost saturated condition (RH > 90%) of macro-pores in the upper-half portion of the bentonite column (see Figure 8-16 and Figure 8-17). The evolution of suction and degree of saturation of macro- and micro-pores predicted by the modelling performance and given in Figure 8-19 at several distances from the heater corroborates such assertions as well as the longitudinal profiles (at several times) of suction (Figure 8-20) and degree of saturation (Figure 8-21) at both structural levels.

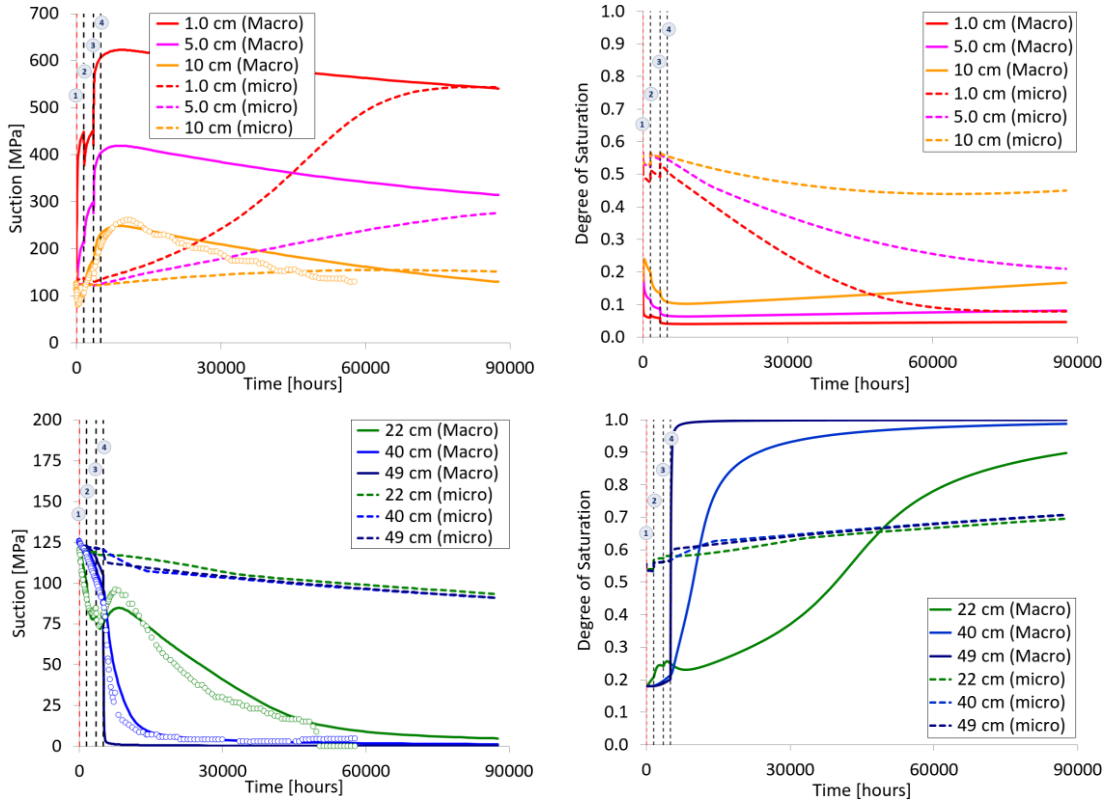

Figure 8-19: Evolution of suction (left) and degree of saturation (right) in both structural levels at points close to the heater (up) and to the hydration line (down) in Cell B. Symbols represent the suction values estimated by the psychrometric law from the experimental RH measurements by CIEMAT.

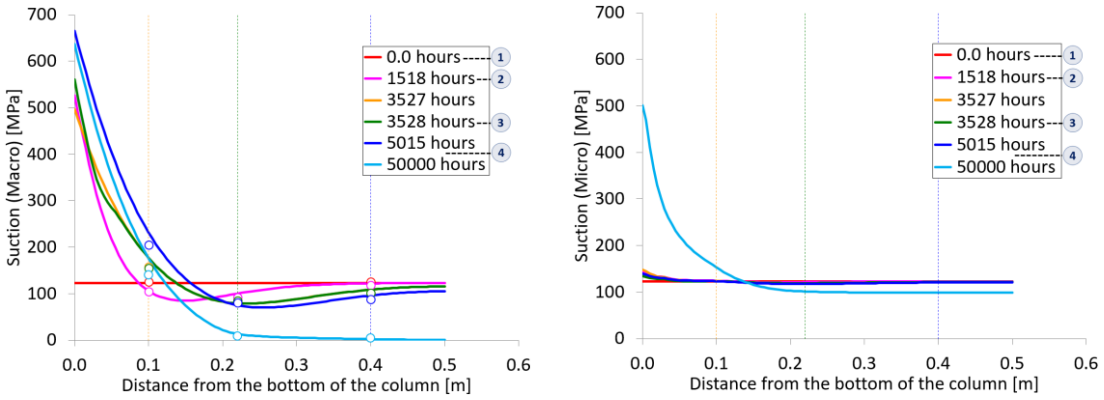

Figure 8-20: Model predictions for the macrostructural (left) and the microstructural (right) suctions versus distance to the heater along Cell B axis at different times. Symbols represent the suction values estimated by the psychrometric law from the experimental RH measurements by CIEMAT.

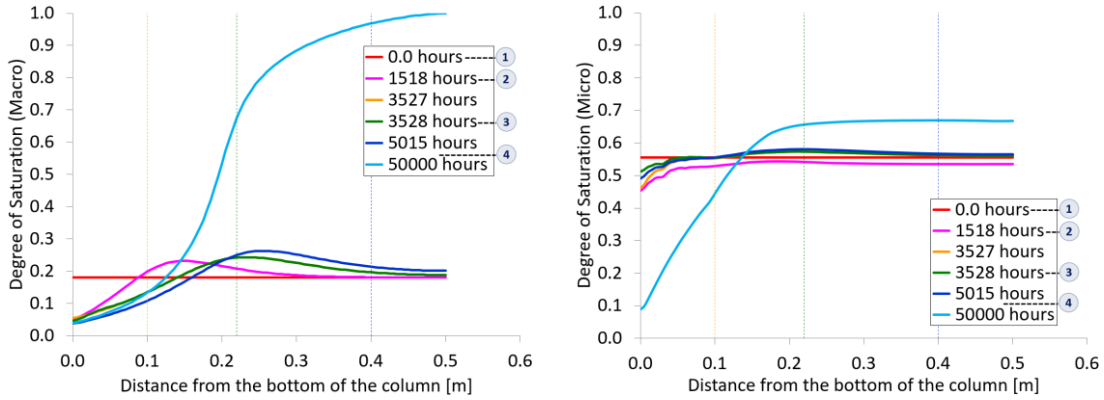

Figure 8-21: Model predictions for the macrostructural (left) and the microstructural (right) degrees of saturation versus distance to the heater along Cell B axis at different times.

From such numerical results, it can be noted that micro-pores still remain unsaturated along the 10 cm closest to the hydration surface, even when macro-pores are fully saturated in that zone. However, the local micro-macro hydraulic coupling leads to a gradual increase in the microstructural degree of saturation. In contrast, the intense thermally-induced drying of macro-pores close to the heater also promotes the drying of microstructure through the water transfer from micro- to macro-pores. Nevertheless, such a decrease in the degree of saturation of micro-pores near the heating line was also affected by the thermal expansion of micro-pores. This thermal impact on the evolution of the saturation state of micro-pores is directly related to the local increment of temperature caused by the thermal loading and diminishes as the distance to the heater increases.

The evolution of the microstructural porosity variables due to heating (and to the subsequent hydration of the column) is shown in Figure 8-22 and Figure 8-23. It can be observed from such graphs that the thermal expansion of each MX-80 pellet is the main deformation process controlling the development of micro-porosity in the vicinity of the heat source (see, for example, the model predictions for $\bar{\phi}_m$ of a point located at 1.0 cm to the heater). Immediately after the start of hydration, the model results given in Figure 8-22 and Figure 8-23 predict a trend of micro-porosity reduction at points in the upper-half portion of this bentonite column (see the results at 40 cm and 49 cm to the heater). However, such microstructural deformation

behaviour was reversed as the water saturation front advanced down the column and the local water mass transfer mechanism caused the initiation of the re-saturation of pellets. Such an increment in the microstructural water content (at low and moderate temperatures) has induced a progressive increase in the intra-aggregate porosity. Furthermore, the inter-aggregate porosity (macro-pore volume fraction) decreased close to the heater due to the thermal expansion of the MX-80 pellets, as indicated in Figure 8-24. The volumetric increment of micro-pores usually occurred at the expense of the reduction in the volume occupied by macro-pores (and vice versa) due to the deformation restrictions imposed by the body of the cell (constant volume conditions). On the other hand, the increase of the macro-pore volume fraction at the top of the column immediately after the start of hydration could be a consequence of the development of positive pore-water pressures under low confining stress conditions. However, the more significant changes in the pore structure took place close to the heater, where the thermal expansion of MX-80 pellets and water in micro- and macro-pores is the main process controlling the hydro-mechanical response. The longitudinal profiles (through the column axis) of porosity variables at several times (see Figure 8-25) illustrate such a model prediction.

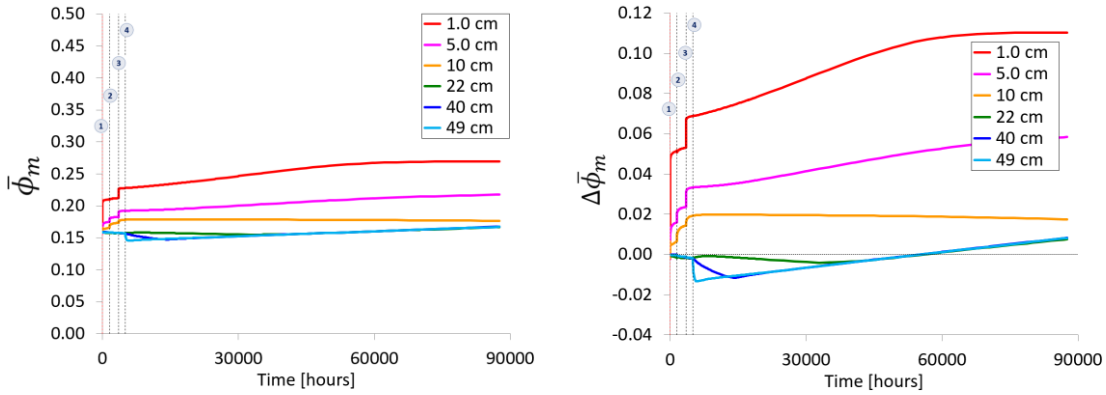

Figure 8-22: Model predictions for the evolution of the micro-pore volume fraction (left) and its variation (right) due to heating and hydration of Cell B.

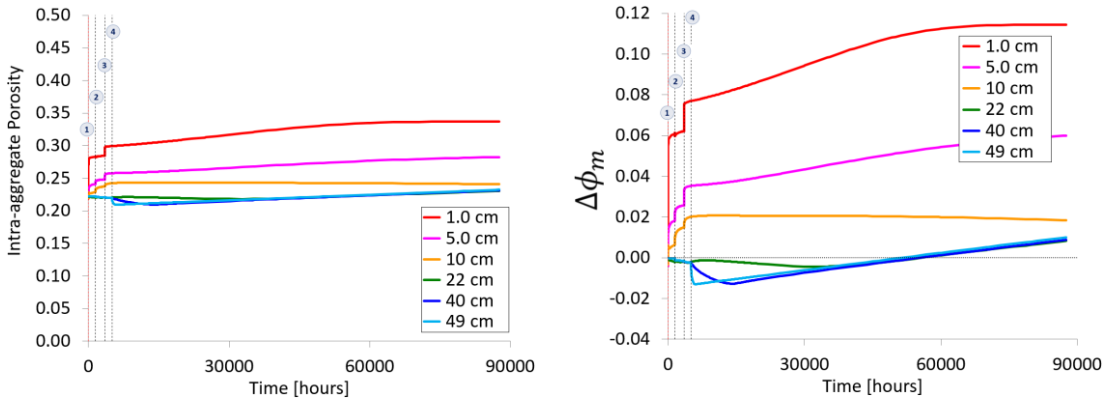

Figure 8-23: Model predictions for the evolution of the aggregate porosity (actual micro-porosity) (left) and its variation (right) due to heating and hydration of Cell B.

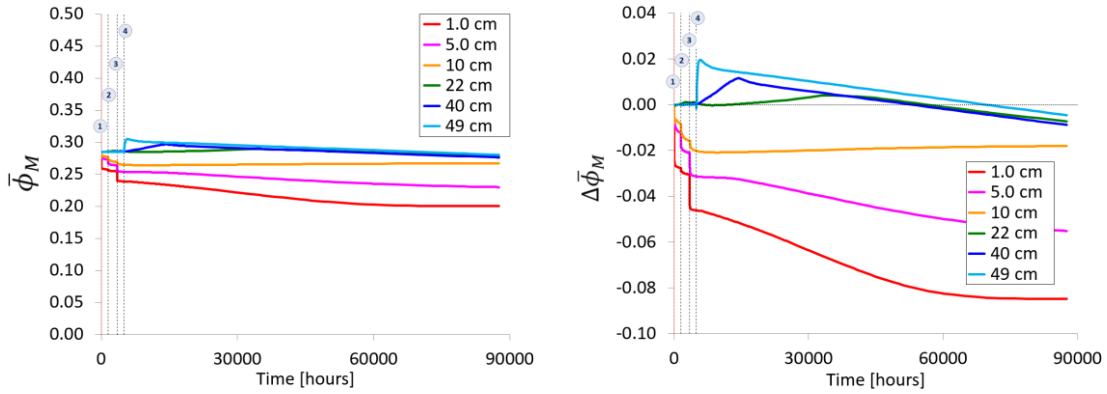

Figure 8-24: Model predictions for the evolution of the macro-pore volume fraction (left) and its variation (right) due to heating and hydration of Cell B.

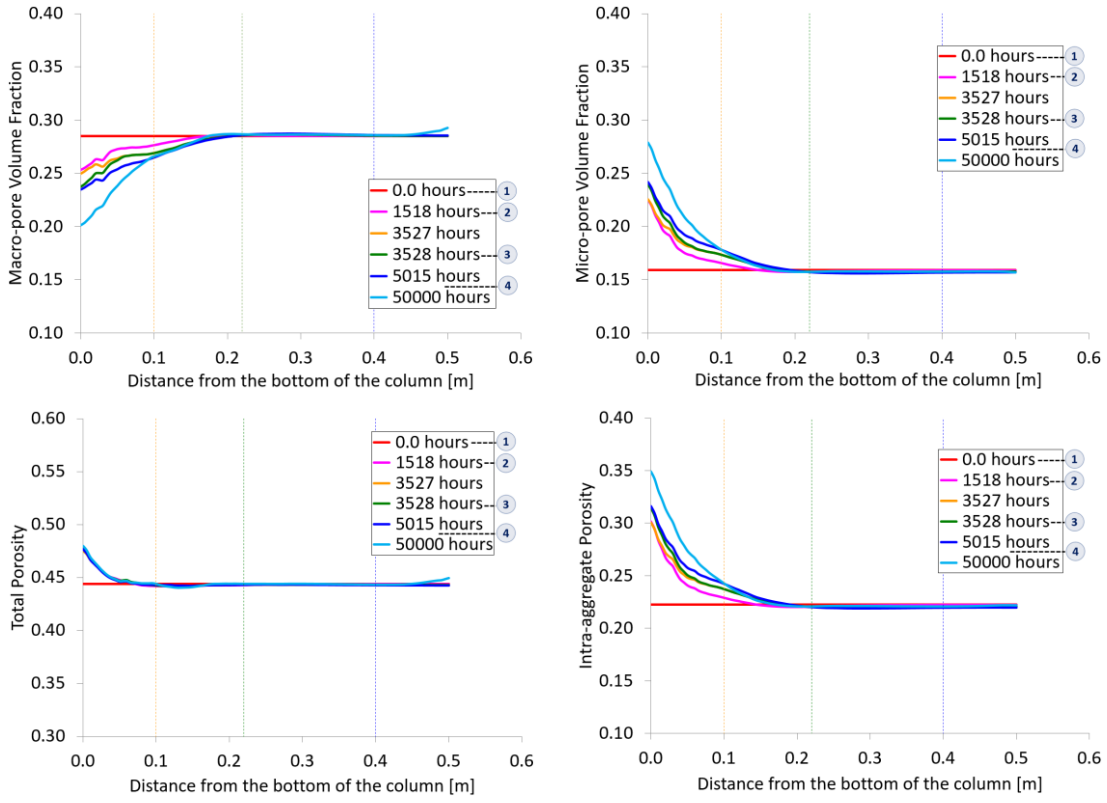

Figure 8-25: Model predictions for the macro- and micro-pore volume fractions (up), the total porosity (down, on the left) and the pellet porosity (down, on the right) versus the distance to the heater along Cell B axis at different times.

The development of axial pressures on the top of the column of pellets in response to the applied thermal and hydraulic loadings is plotted in Figure 8-26. The increase of axial pressures before the start of the artificial re-saturation of the column is associated with the considerable temperature rise in the lower portion of the column caused by the two heating episodes and the improvement of the external isolation system. It can be seen that the numerical modelling reproduces satisfactorily the increments in the axial stress generated by the thermal loading before the start of hydration. These thermally-induced stresses along Cell B arise from the lateral restrictions imposed by the body of the cell on the evolution of local thermal strains combined with the additional compression exerted by the thermal expansion of the lower layers of pellets. The evolution of the vertical (axial) and the mean stresses at several distances to the heater is

given in Figure 8-27. From such model results, it seems that the compressive stresses developed in the lower half of the column depended much more on the thermal expansion of the granulated bentonite material while the compression of the mass of pellets located in the upper half of the cell was mainly affected by the volumetric deformation of the underlying material. However, the re-saturation of the heated column led to a remarkable increment in the axial stresses at the top of the column (Figure 8-26) as well as along its full length (Figure 8-27). Such a sudden increase of the confining pressures during wetting is a result of the high swelling potential of the compacted mass of high-density pellets when macro-pores are flooded with liquid water. As mentioned previously, the progressive increment in the swelling pressure during the hydration phase (see Figure 8-26) indicates the start of the re-saturation of intra-pellet pores by the local hydraulic coupling mechanism.

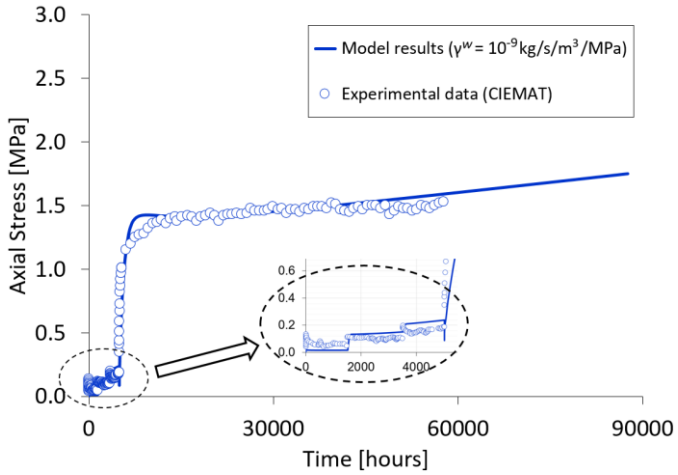

Figure 8-26: Development of the axial stress on the top of the column of pellets during the heating phase without artificial hydration (highlighted in graph) and during the re-saturation of the heated cell. Symbols represent the axial pressure measured by CIEMAT.

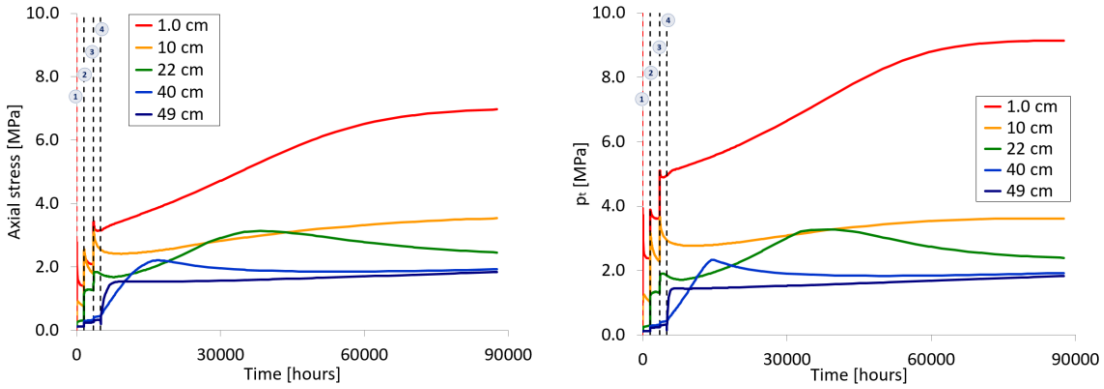

Figure 8-27: Model predictions for the development of the axial (left) and the total mean (right) stresses at several distances to the heater.

The evolution of the hardening parameter, p_0^*, and the stress paths in the p: s_M plane for points in the cell axis located at several distances to the heater are shown in Figure 8-28. It can be noted that the structural collapse of the soil skeleton induced by the thermal loading is the main strain-hardening mechanism that takes place in the bottom of Cell B. In the upper portion of the column of pellets, the main structural changes are related to the macrostructural collapse caused by the reduction of the inter-aggregate contact forces and the swelling of pellets during the hydration phase.

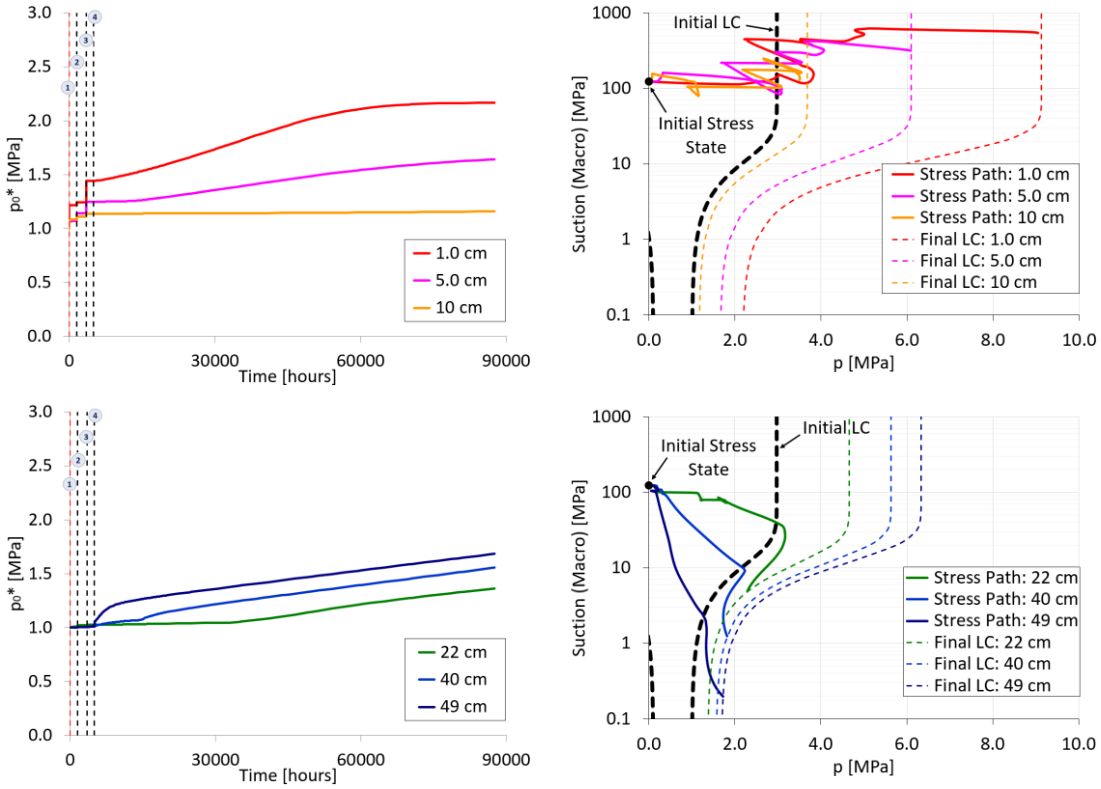

Figure 8-28: Evolution of the saturated preconsolidation pressures (left) and the stress paths in the p: s_M plane (right) during hydration under non-isothermal conditions for points close to the heater (up) and to the hydration line (down).

In the context of the double-porosity model used in the calculations, and according to the hypotheses assumed in **Section 4.2.5**, the thermally-induced macrostructural collapse was related to the intense drying (increase in macro suction) and to the increase of the confining pressures close to the heater and not necessarily to the thermal expansion of the pellets itself. As mentioned in **Section 4.4.2**, it has been assumed that the thermal expansion of microstructure does not generate permanent structural changes. However, the THM coupling of the mathematical formulation allowed the occurrence of appreciable changes in the macrostructural hydraulic variable due to the local increase of temperature. Moreover, the thermal loading under confined conditions led to the densification of the heated mass of pellets close to the heater due to the development of significant thermally-induced stresses (compare the evolution of the total mean stresses during the heating episodes in Figure 8-27 at points near and far from the heater). In other words, the zone close to the heat source experienced not only a high desaturation process but also a marked increment of the mean effective stress (p), as illustrated in Figure 8-28. Before the stress path reached the current LC, only the plastic micro-macro coupling (the plastic β-mechanism) was activated and the development of plastic strains was related to the drying process occurring at that zone. Once the current LC was intersected and moved beyond its initial position, both plastic mechanisms were activated and the irreversible structural changes were also related to the increase of the confining stresses due to heating. The evolution of the mean effective stress (p) and the preconsolidation pressures (p_0) at four points along the axis of Cell B as well as the stages of the heating-hydration test in which the numerical modelling predicted the local activation of both plastic mechanisms are shown in Figure 8-29.

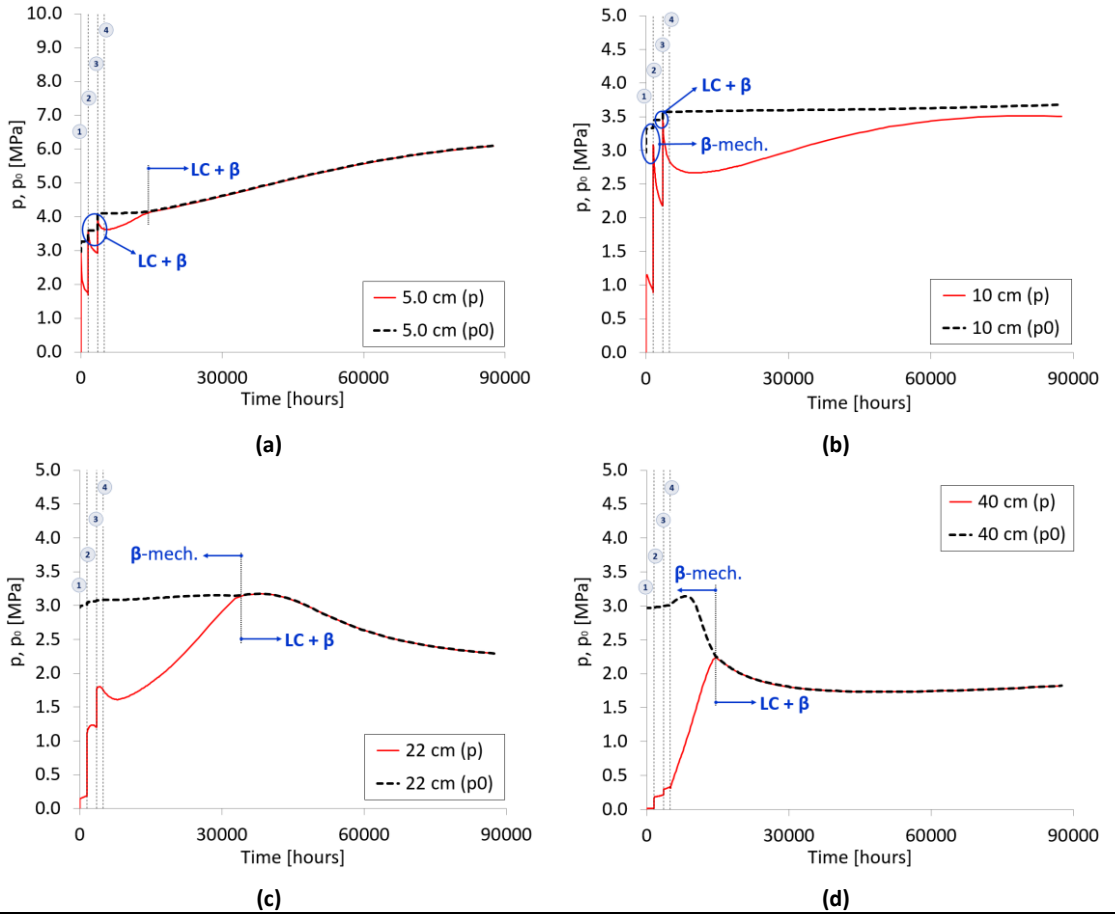

Figure 8-29: Development of the mean effective stresses (p) and the preconsolidation pressures (p_0) at distances to the heater equal to **(a)** 5.0 cm; **(b)** 10 cm; **(c)** 22 cm and **(d)** 40cm. The activation of both plastic mechanisms is also indicated. The micro-macro coupling mechanism (β-mechanism) is assumed to be always activated.

As discussed before, the thermal impact was quite limited in the upper portion of Cell B (see Figure 8-15 and the chart on the left-hand side in Figure 8-17). Therefore, the irreversible collapse of macrostructure induced by the thermal load was not relevant in that zone before the start of hydration. Due to that, the increments in the local confining stresses were not sufficient to cause the stress path to cross the current LC locus. In such conditions, the development of plastic deformations during the heating without forced hydration can be attributed to the mechanical coupling between both structural media (see Figure 8-29(c) and Figure 8-29(d)) in response to the increase in the local water content (see Figure 8-19). It is important to highlight that such a re-saturation process of the middle and the upper parts of the bentonite column is due to the condensation of water vapour coming from the zones closer to the heater. When the hydration phase started, the injection of liquid water into the cell led to a structural collapse of macro-pores due to the development of the swelling potential under confined conditions of the bentonite material in the upper-half portion of the cell. During this stage, the plastic BBM mechanism was activated when the stress path reached and moved the current LC (see the stress paths in Figure 8-28), as the saturation front advanced towards the bottom of the cell. However, a significant increment of p_0^* was estimated for points located less than 10 cm from the heater (see Figure 8-28). Although the bentonite material in that zone is still very dry, such an additional structural densification arises from the increase in the confining pressures (Figure 8-27) exerted by the swelling of the mass of pellets in the upper layers of Cell B.

8.3.5. CELL S/B

The numerical analysis of the re-saturation of the heated column of sand/MX-80 bentonite mixture carried out in the CIEMAT laboratory presented some additional model uncertainties and challenges in comparison to the modelling of the column of pellets discussed in the previous section. As the mechanical expansive response of the S/B column material to heating and forced hydration was not monitored in laboratory, the elastoplastic parameters required in the double-porosity formulation were selected from reference values reported in the literature for mixtures with a similar composition and/or a sand-bentonite proportion (see, for example, Wang *et al.*, 2013). Consequently, it was not possible to calibrate the leakage coefficient for the local water mass transfer (γ^w) by back-calculating the development of the axial pressure on the top of the large cell, as it was done in the case of the column of pellets (see Figure 8-14). Furthermore, similar (and generic) model parameters for the mechanical micro-macro coupling functions used in the modelling of Cell B were used in calculations, as indicated in Table 8-8. The hydraulic constitutive law of microstructure was modelled taking as reference the experimental water retention curves of pure MX-80 bentonite samples (Seiphoori *et al.*, 2014) as well as the corresponding curves for sand-bentonite mixtures compacted at high dry densities (Wang *et al.*, 2013; Gatabin *et al.*, 2016). However, the experimental data obtained during the dismantling of such a column (in February, 2015) provided useful information about the final state of the almost fully-saturated column. These dismantling data served to evaluate (although, in an indirect way) the model capabilities in predicting the THM response of the column as well as the accuracy of the constitutive parameters used in calculations.

The accidental flooding that took place before the initiation of the laboratory test changed the as-built profile of water content throughout the column. Due to that, the distribution of macro suction along the length of Cell S/B at the start of heating was no longer uniform, but increased from the top to the bottom. Although the accidental opening of the hydration line lasted approximately 5 minutes, the high permeability conditions of the mixture allowed the deep percolation of water into the cell, increasing the readings in all the RH sensors (Villar *et al.*, 2012b), as shown in Figure 8-30(a). The numerical modelling of this unexpected event required the adoption of a more permeable layer (with a thickness of 2.0 cm) at the top of the sand/bentonite column in order to enable the entrance of liquid water into the column. Moreover, this fast infiltration process was performed as a very slow injection of water prescribed at the top of the column, as already mentioned in **Section 8.3.2**. Such numerical strategies aim to avoid possible convergence problems caused by the development of high hydraulic gradients within the finite elements close to the hydration line. The longitudinal profiles of the calculated relative humidity before the accidental flooding (full line) and immediately before the start of heating (dashed line) together with the stabilized RH readings (symbols) after the accidental opening of the valve giving access to hydration are plotted in Figure 8-30(b). The distribution of pore-water pressure in macro-pores through the length of the column obtained from the numerical calculations at $time = 0$ (the initiation of the heating phase) is given in Figure 8-30(c). The model results in Figure 8-30(b) indicate that the material around the location of sensor RH1 (at 40 cm from the heater) was more saturated than its actual saturation state in the column. However, and according to the model findings discussed later, the full saturation condition in the vicinity of the three RH sensors during the controlled hydration process was reached earlier in the laboratory test than in the modelling predictions.

These interesting results could suggest some initial degree of heterogeneity in the S/B mixture permeability throughout the length of the cell, which is not reproduced by the numerical calculations when the bentonite column is simulated as a homogeneous material.

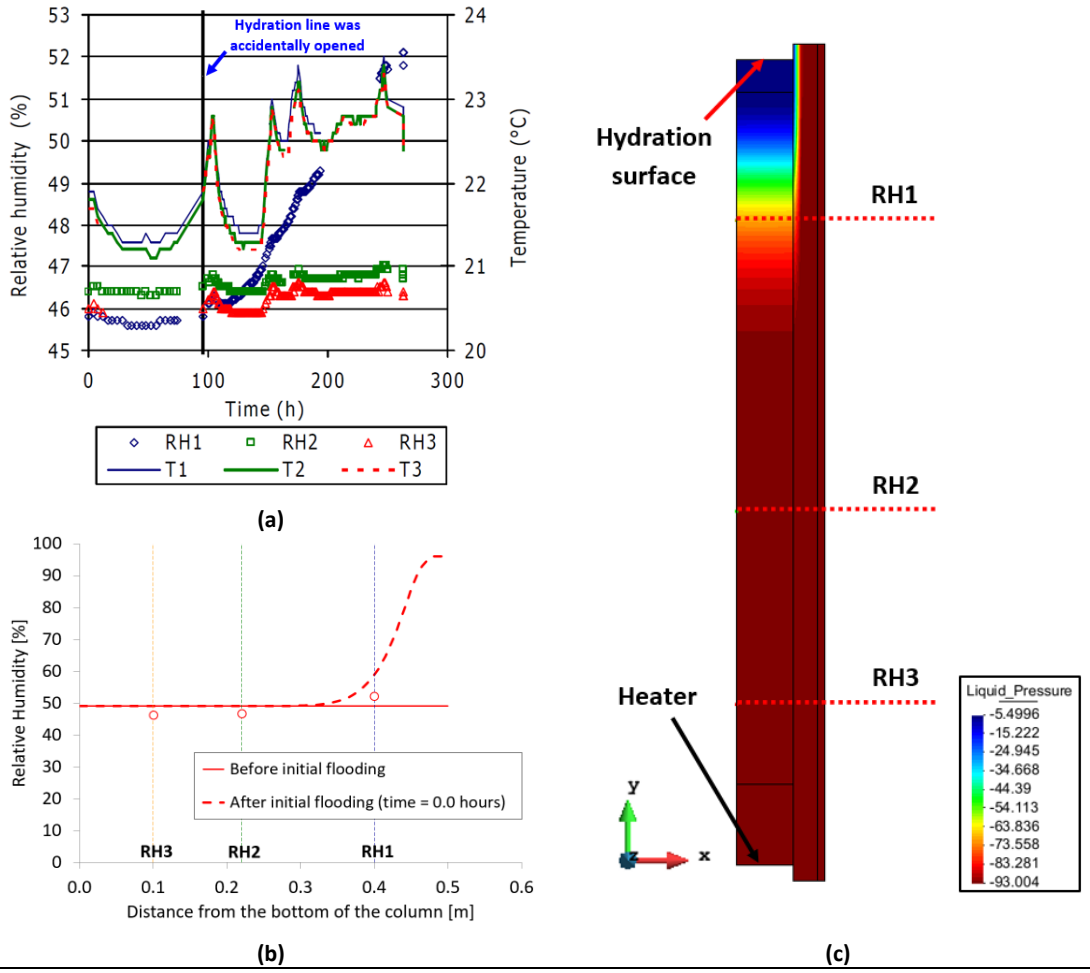

Figure 8-30: **(a)** RH and temperature readings after the accidental flooding and before the initiation of heating in Cell S/B (from Villar *et al.*, 2012b); **(b)** Longitudinal distribution of RH through the cell axis before and after the accidental flooding (symbols represent the experimental data registered by the RH sensors before the heating test initiation) and **(c)** Spatial distribution (model) of macrostructural pore-water pressure at time=0.0 hours.

Different initial micro-pore volume fractions ($\bar{\phi}_{m,0}$) were considered in the performance of the numerical calculations (see Table 8-3). Since the dry mass proportion of sand and MX-80 bentonite and the initial dry density of the mixture were kept unchanged in all the analyses, such different values of $\bar{\phi}_{m,0}$ would be related to the degree of aggregation of individual bentonite particles in the clay fraction. The elementary clay particles surrounding the non-active grains of sand can be also arranged in small bentonite granules (see Figure 8-31). In this kind of fabric, the void spaces between adjacent elementary particles give rise to a third level of structure (Gens and Alonso, 1992), characterized by the existence of inter-particle pores inside the aggregation of elementary particles (meso-pores). As mentioned before, the multi-porosity approach used in the present study only distinguishes between two pore structural levels and due to that, the micro-pore fraction includes both intra-particle pores (actual micro-pores) and inter-particle pores in clay granules (meso-pores). In that sense, the differences in $\bar{\phi}_{m,0}$ in calculations would reflect the changes in the volume occupied by the latter fraction of pores. The computed evolution of temperature and relative humidity in Cell S/B for three of such cases ($\bar{\phi}_{m,0}$ equals to 0.04, 0.06 and 0.08) together with the laboratory readings (symbols) at three

different levels (sensor positions) are shown in Figure 8-32 and Figure 8-33. These model results were obtained for a leakage coefficient of $\gamma^w = 10^{-10}$ kg/s/m^3/MPa. The comparison between the numerical and the experimental evolution of temperature and RH during the heating phase before the start of hydration in Cell S/B shows a good agreement between such results, regardless of the case considered in the calculations. However, significant differences between model results and measured data were observed after the initiation of the controlled injection of water into the column. As assumed in **Section 3.8.2.1**, the advective flux of water in a double-porosity medium develops through macro-pores. Consequently, and for a given dry density, the main effect of increasing the initial micro-pore volume fraction of the mixture is a delay in the saturation of macro-pores due to the reduction of the volume occupied by this kind of pores. Such a fact is clearly evidenced by the differences in the development of RH given by the model results in Figure 8-33, especially for the RH sensors located farther away from the hydration line (sensors RH2 and RH3).

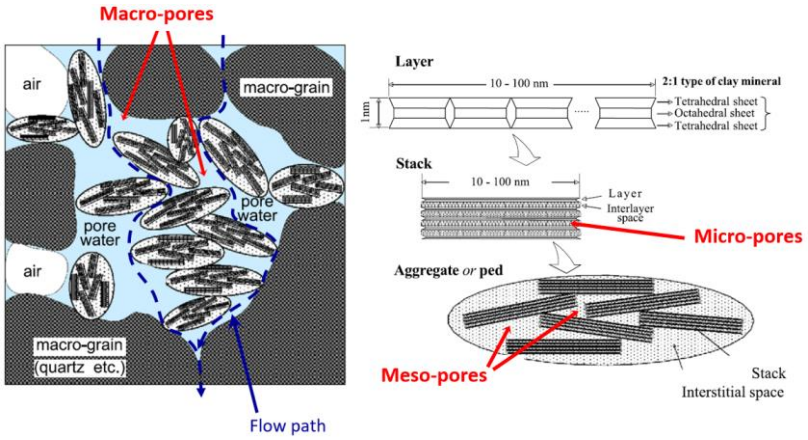

Figure 8-31: Schematic representation of the distinct pore-structure levels found in a mixture of non-active soil grains (as sand grains) and aggregation of clay particles (modified after Ichikawa *et al.*, 2004). The meso-pore fraction is also accounted for as part of the microstructural voids.

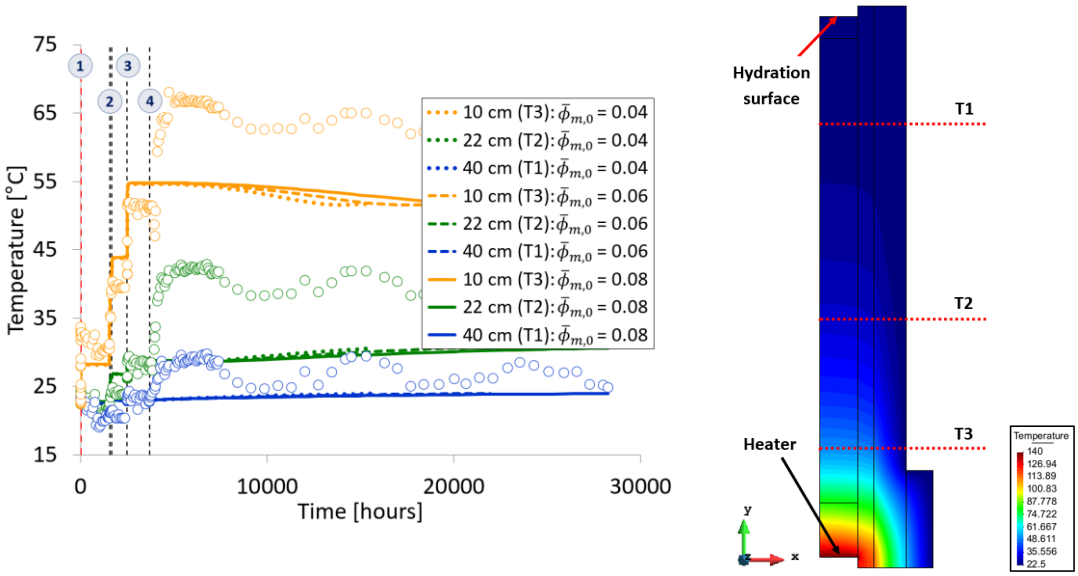

Figure 8-32: Evolution of RH at the sensor positions for three distinct values of $\bar{\phi}_{m,0}$ (left) and spatial distribution of macro water pressure in Cell S/B at the end of calculations (right). Symbols represent the RH measured by CIEMAT.

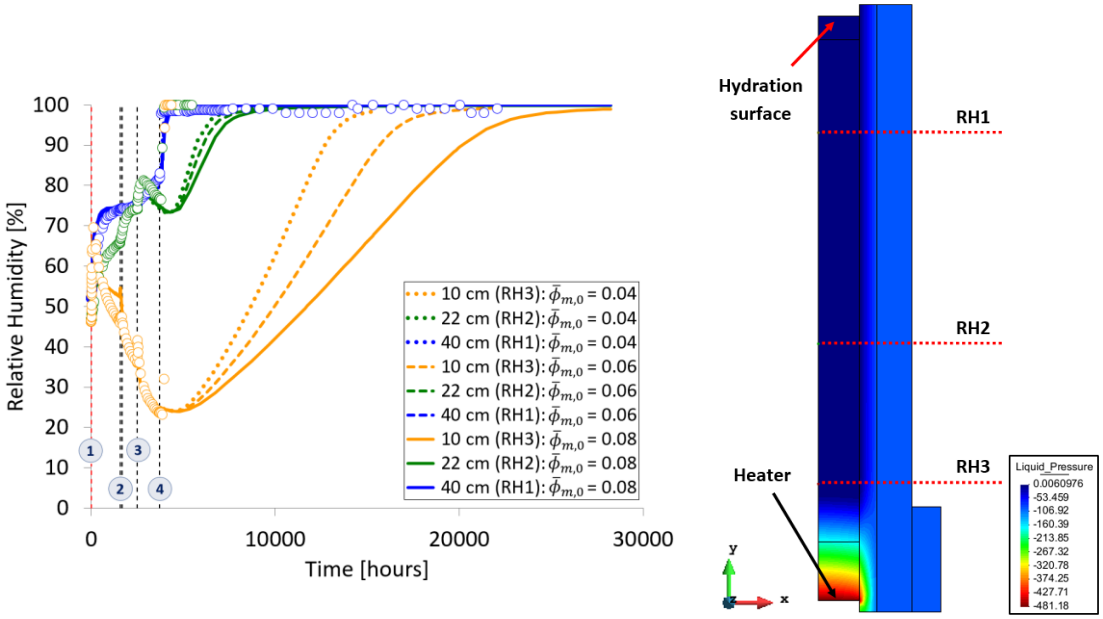

Figure 8-33: Evolution of RH at the sensor positions for three distinct values of $\bar{\phi}_{m,0}$ (left) and spatial distribution of macro water pressure in Cell S/B at the end of calculations (right). Symbols represent the RH measured by CIEMAT.

The same thermal processes that altered the distribution of pore-water along the column of pellets in the earlier stages of the heating test (as discussed in the previous section) control the changes in RH along Cell S/B: the thermal expansion of pore-water, the evaporation close to the heater and the vapour condensation in the upper-half of the column. The sudden increase of the RH readings in all the sensors after the beginning of the hydration phase is a clear evidence of the high permeability of the S/B mixture. The fast re-saturation of this column generated an increase in the thermal conductivity of the mixture, which in turn, led to the considerable and abrupt temperature increase recorded by the three sensors. Although the modelling of the hydration of the heated column also predicted the re-saturation of macro-pores (RH > 95%) at the sensor locations, such a re-saturation process was, however, slower in calculations, especially for the two sensors closer to the heater (RH2 and RH3). Due to that, the results from modelling could not reproduce the sudden increment of temperature recorded in the sensors after hydration, but rather that temperature increase was slower and minor. Furthermore, the thermal conductivity in the double-porosity formulation also depends on the saturation state of micro-pores – see Equation (3-96). Due to the low value of the micro-macro water transfer coefficient (γ^w), microstructure was still unsaturated at the end of calculations. Therefore, the hydration-induced increase in the thermal conductivity of the column between the start of the controlled re-saturation and the dismantling of the cell was hindered by the dry state of micro-pores. Such arguments are corroborated by the numerical results plotted in the following curves (from Figure 8-34 to Figure 8-38), obtained from the modelling of the case with $\bar{\phi}_{m,0} = 0.08$. In these charts, symbols represent the sensor readings taken from the laboratory heating-hydration test and the experimental data obtained after the dismantling of the cell.

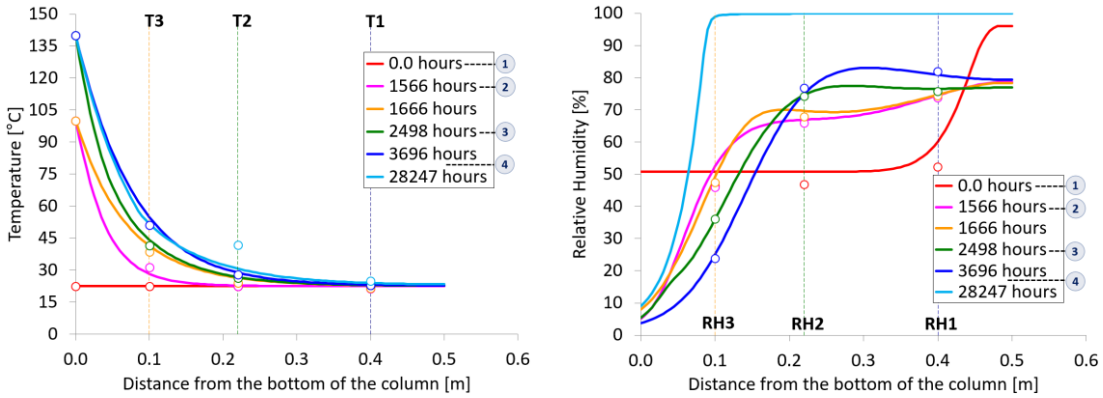

Figure 8-34: Longitudinal profiles of temperature (left) and RH (right) along Cell S/B axis at different times, when $\bar{\phi}_{m,0} = 0.08$ and $\gamma^w = 10^{-10}$ kg/s/m^3/MPa. Time = 28247 hours corresponds to the dismantling of the cell (end of calculations).

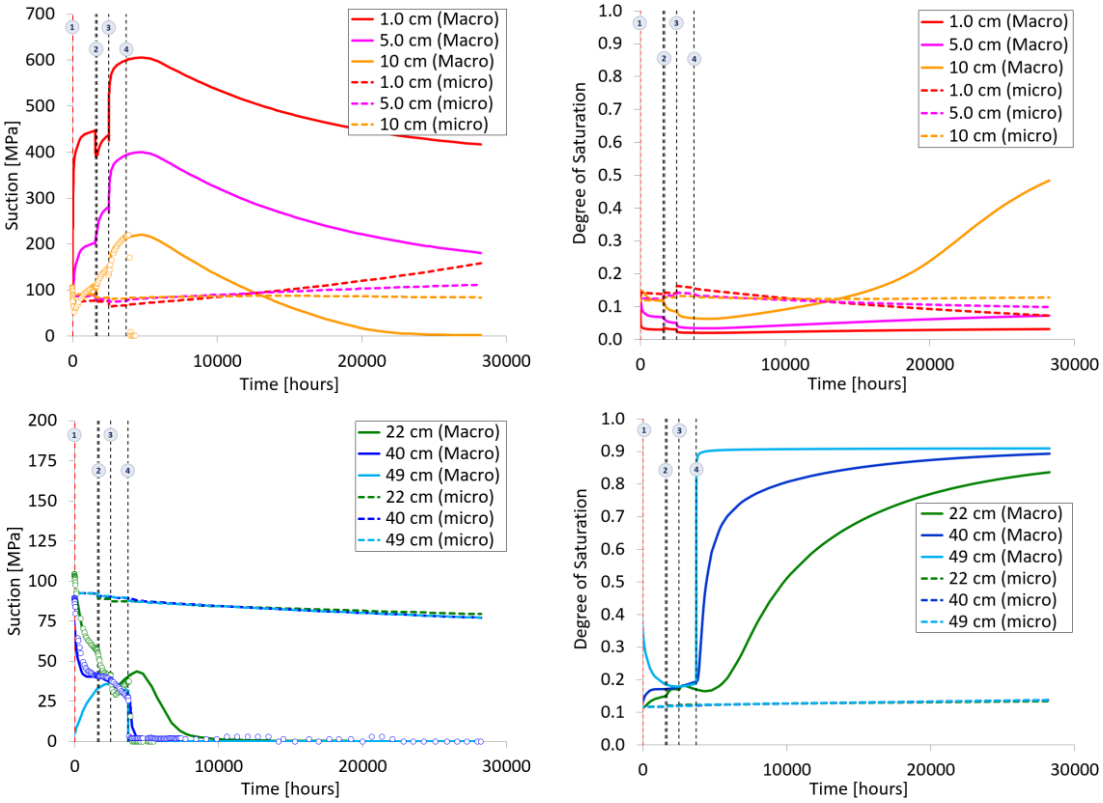

Figure 8-35: Evolution of suction (left) and degree of saturation (right) in both structural levels at points close to the heater (up) and to the hydration line (down) in Cell S/B, when $\bar{\phi}_{m,0} = 0.08$. Symbols represent the suction values estimated by the psychrometric law from the experimental RH measurements by CIEMAT.

The first heating event – when heater temperature reached 100°C – caused the thermal expansion of the mixture constituents without any significant water mass exchange between micro- and macro-pores because of the lower value of γ^w. However, the thermal expansion of microstructural water induced a "thermal wetting" of microstructure (see the longitudinal profiles of microstructural suction and degree of saturation in Figure 8-36 and Figure 8-37, respectively). The enhancement of the external insulation system and the second heating episode increased the extension of the zone affected by the thermal re-saturation of micro-pores.

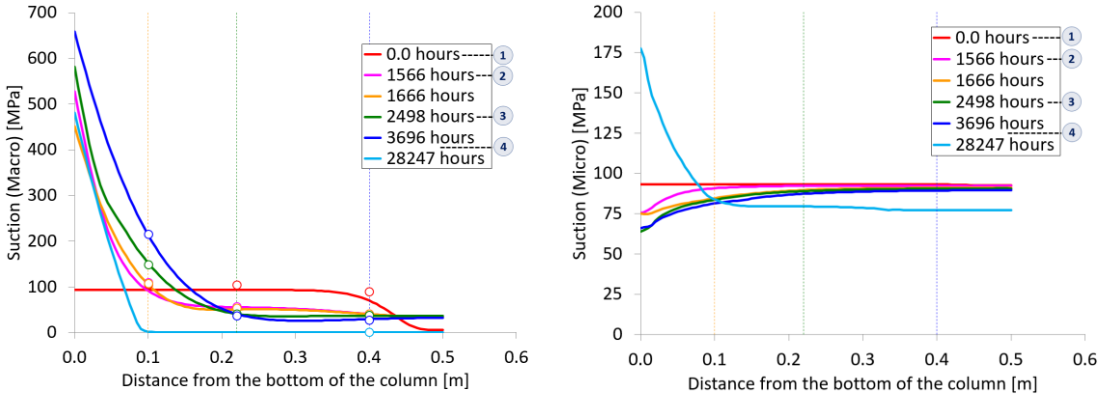

Figure 8-36: Longitudinal profiles of macrostructural (left) and the microstructural (right) suctions along Cell S/B axis at different times, when $\bar{\phi}_{m,0} = 0.08$. Time = 28247 hours corresponds to the dismantling of the cell. Symbols represent the suction values estimated by the psychrometric law from the experimental RH measurements by CIEMAT.

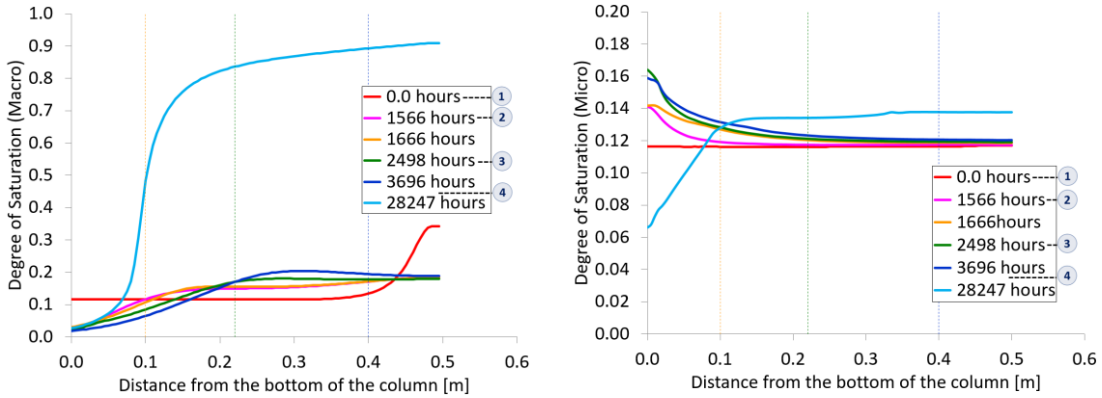

Figure 8-37: Longitudinal profiles of macrostructural (left) and the microstructural (right) degrees of saturation along Cell S/B axis at different times, when $\bar{\phi}_{m,0} = 0.08$. Time = 28247 hours corresponds to the dismantling of the cell.

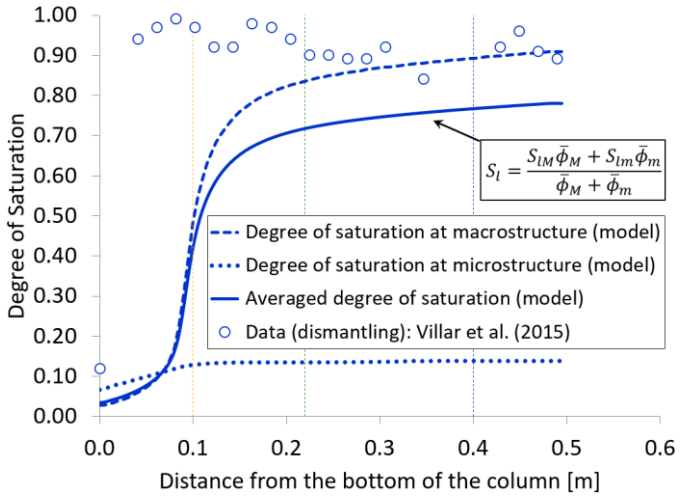

Figure 8-38: Longitudinal profiles of macro, micro and averaged degrees of saturation along Cell S/B at the start of the dismantling of the cell. Symbols represent the experimental data from the subsampling of the column after its dismantling (from Villar *et al.*, 2015b).

Porosity changes in the column of S/B mixture during the heating and the controlled hydration phases, although small in magnitude (see Figure 8-39 to Figure 8-43), can be mainly attributed to the thermal expansion of the sand and bentonite particles, the differential thermal expansion of water in micro-pores and the evaporation of water in macro-pores close to the heater. Moreover, the increment in the local confining pressures caused by the thermally-induced rise of the underneath layers also contributed to the slight changes in the micro-porosity variables (see Figure 8-39 and Figure 8-40) prior to the start of hydration in the upper portion of the column. The densification of the mixture in the lower portion of the column (reduction of the macro-pore fraction, see Figure 8-41) was related to the increase in the confining stresses induced by the thermal loading. However, the smaller changes in porosity variables predicted by the modelling performance (in comparison to the analogous results from the column of pellets) can be related to the lower content of bentonite in the mixture (35% of its dry weight). Furthermore, the low value assigned to γ^w prevented the re-saturation of micro-pores at the end of calculations and, consequently, the modelling results predicted a non-significant collapse of macrostructure induced by hydration. The evolution of the hardening parameter (p_0^*) at several distances to the heater, which is displayed in Figure 8-44, suggests that the main structural changes in Cell S/B occurred as a result of the intense heating in the lower portion of the column.

As discussed during the numerical analyses performed in the previous chapters, the main impact of increasing the micro-macro water transfer coefficient is reflected in the saturation state and the deformation response of microstructure. Thus, and for a higher value of γ^w ($\gamma^w = 10^{-9}$ kg/s/m^3/MPa), the model predicted a more saturated upper-half portion of the column as a result of the increase in the water content during hydration. Consequently, microstructural suction decreased and microstructural degree of saturation increased at the top of the column. In contrast, micro-pores suffered a desaturation process (increase of microstructural suction) in response to the intense drying of macro-pores at those points close to the heat source. Consequently, and despite the initial thermally-induced wetting of micro-pores due to the differential thermal expansion of microstructural pore-water, this class of pores exhibited a lower saturation state at the end of calculations. These comments are clearly supported by the development of suctions at four distances from the heater (Figure 8-45) and by the longitudinal profiles through the cell axis of macro and micro suctions (Figure 8-46) and degrees of saturation (Figure 8-47) for two different values of leakage parameters. The longitudinal profiles of saturation (macro, micro and average) at the end of calculations are plotted in Figure 8-48 together with the experimental data obtained from the subsampling of the dismantled column in 25 sections of approximately 2.0 cm in thickness. The increase in the rate of water mass exchange between both structural levels is expected to lead to an enhancement of the global (average) saturation condition in the upper portion of the column due to the more saturated state of micro-pores. In that sense, the experimental information on the final degree of saturation of the S/B mixture can be used to indirectly calibrate a suitable value for the leakage coefficient. However, and for the values of γ^w employed in calculations, the changes in microstructural water content along the cell axis were not significant. It is important to remark that the saturation state of macrostructure is not affected by the value of γ^w, but it mainly depends on the geotechnical properties governing the Darcy's flux of water through macro-pores. Consequently, the saturation of the S/B mixture at the end of calculations is affected by the micro-macro water mass transfer parameter, by the macrostructural permeability

properties and by the initial saturation state of macro- and micro-pores (water retention properties).

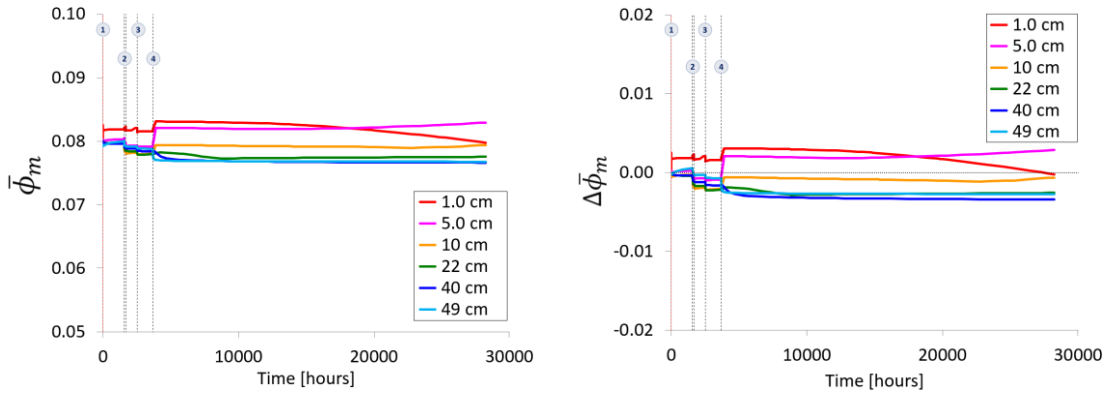

Figure 8-39: Model predictions for the evolution of micro-pore volume fraction (left) and its variation due to heating and hydration (right) in Cell S/B, when $\bar{\phi}_{m,0} = 0.08$ and $\gamma^w = 10^{-10}$ kg/s/m^3/MPa.

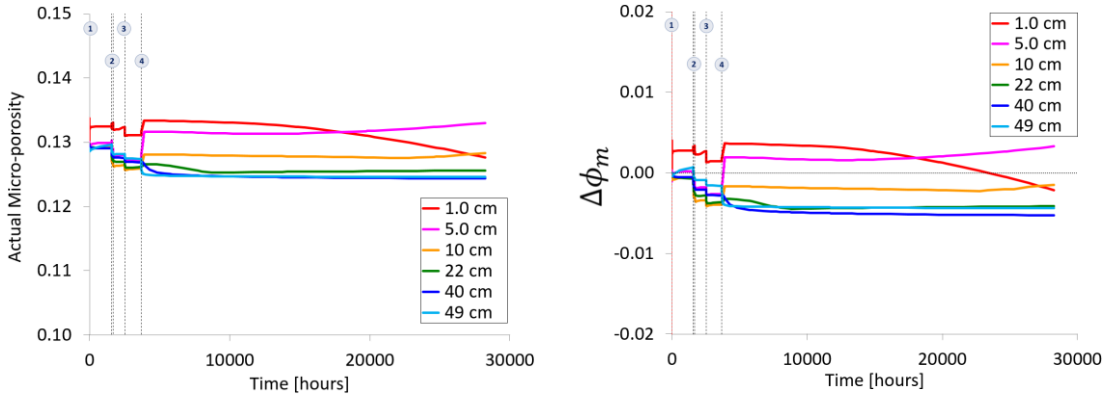

Figure 8-40: Model predictions for the evolution of the actual micro-porosity (left) and its variation due to heating and hydration (right) in Cell S/B, when $\bar{\phi}_{m,0} = 0.08$ and $\gamma^w = 10^{-10}$ kg/s/m^3/MPa.

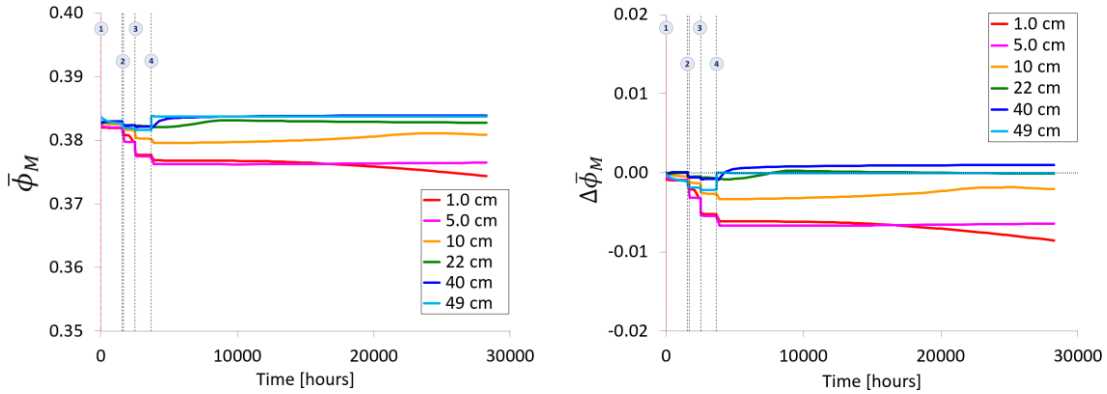

Figure 8-41: Model predictions for the evolution of macro-pore volume fraction (left) and its variation due to heating and hydration (right) in Cell S/B, when $\bar{\phi}_{m,0} = 0.08$ and $\gamma^w = 10^{-10}$ kg/s/m^3/MPa.

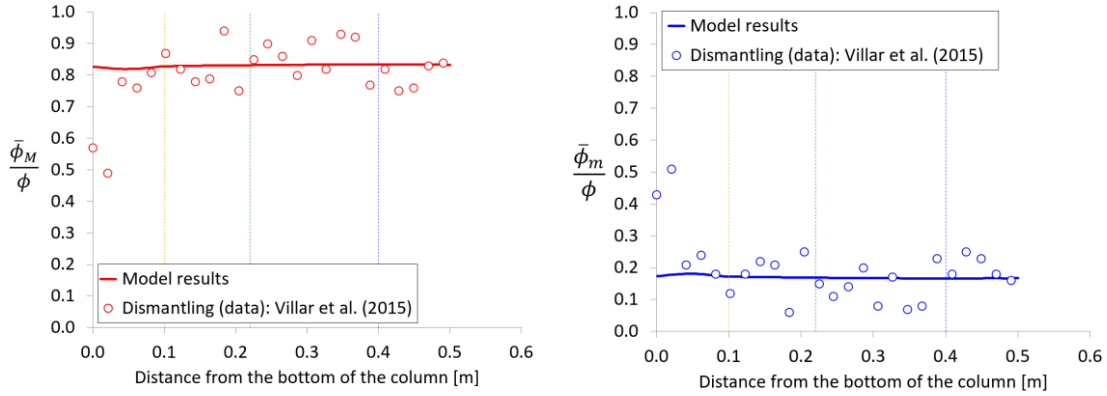

Figure 8-42: Longitudinal profiles of the proportion of macro- (left) and micro-pores (right) along Cell S/B, when $\bar{\phi}_{m,0} = 0.08$, at the beginning of the dismantling of the cell (end of calculations). Symbols represent the experimental data from the subsampling of the column after its dismantling (from Villar *et al.*, 2015b).

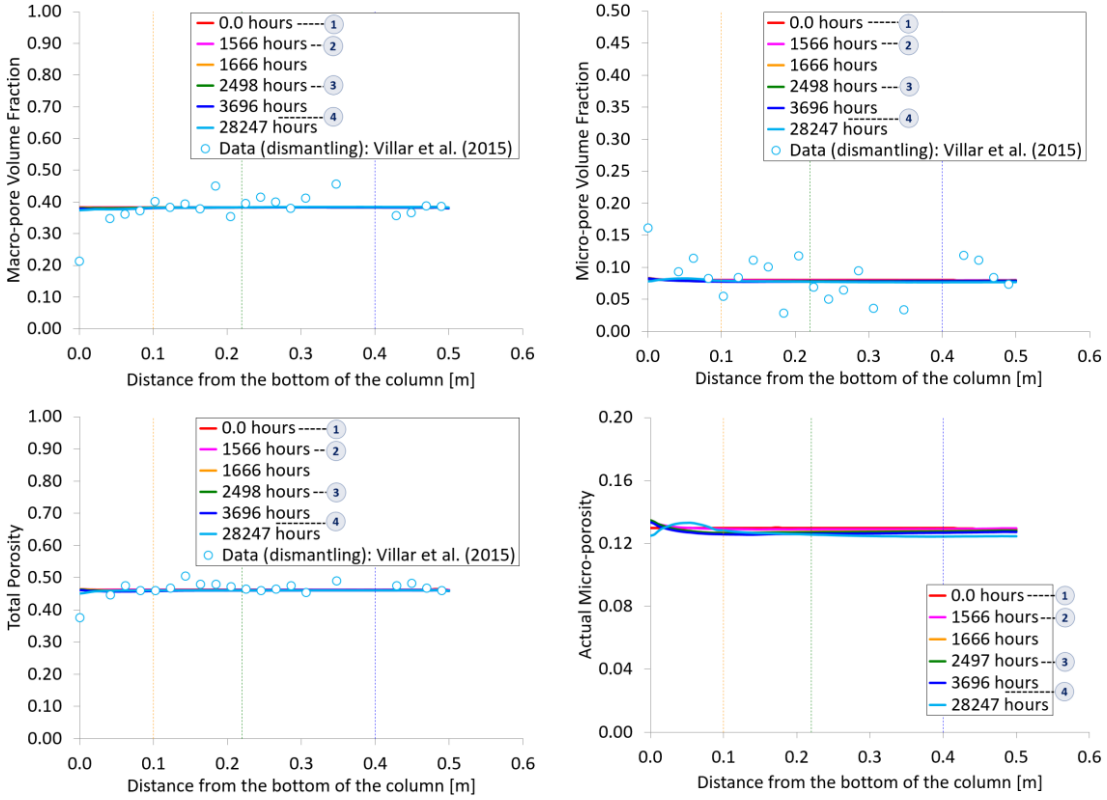

Figure 8-43: Longitudinal profiles of macro- and micro-pore volume fractions (up) and of the total and micro-porosities (down) along Cell S/B, when $\bar{\phi}_{m,0} = 0.08$, at the beginning of the dismantling of the cell. Symbols represent the experimental data from the subsampling of the column after its dismantling (from Villar *et al.*, 2015b).

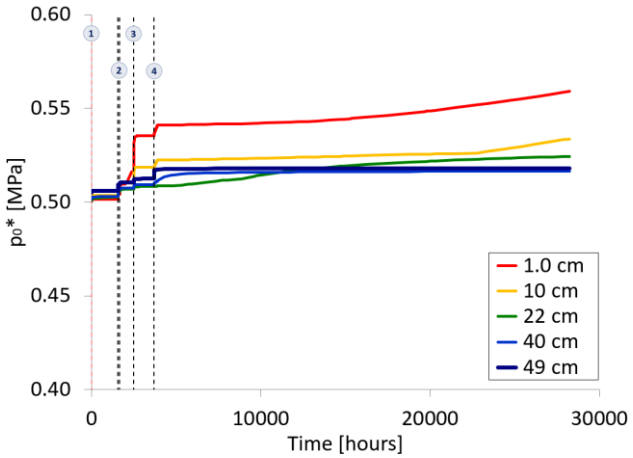

Figure 8-44: Model predictions for the development of the saturated preconsolidation pressures (right) during the heating and hydration of Cell S/B, when $\bar{\phi}_{m,0} = 0.08$ and when $\gamma^w = 10^{-10}$ kg/s/m³/MPa.

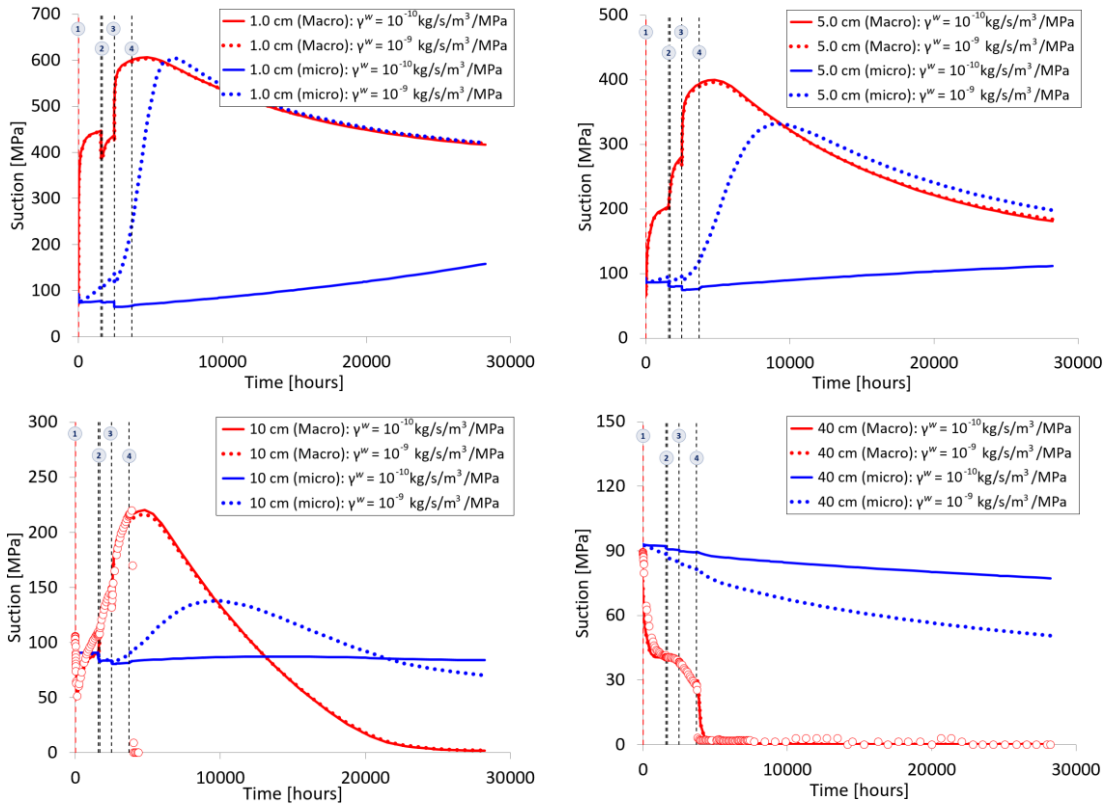

Figure 8-45: Model predictions for the evolution of suctions in both structural levels at points located at several distances to the heater (1.0 cm, 5.0 cm, 10 cm and 40 cm) inside Cell S/B, when $\bar{\phi}_{m,0} = 0.08$ and for two distinct values of γ^w. Symbols represent the suction values estimated by the psychrometric law from the experimental RH measurements by CIEMAT.

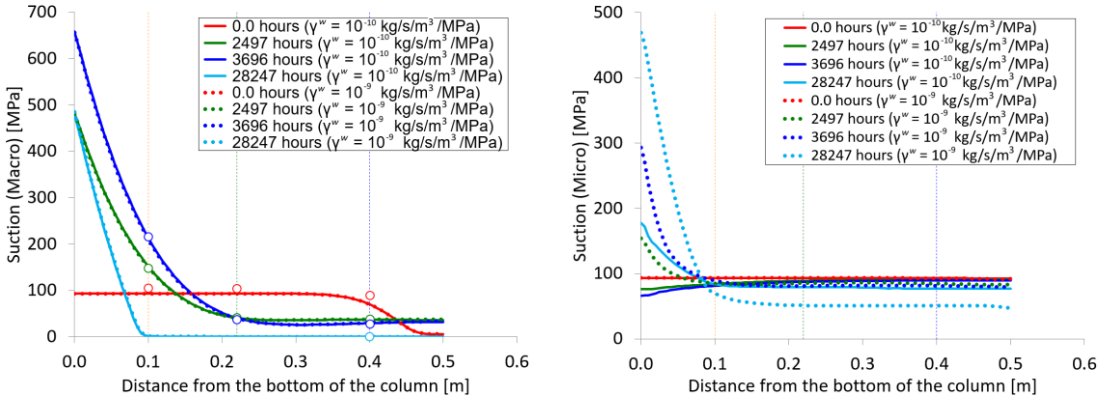

Figure 8-46: Longitudinal profiles of macrostructural (left) and the microstructural (right) suctions along Cell S/B axis at different times and for two distinct values of γ^w. Time = 28247 hours corresponds to the dismantling of the cell. Symbols represent the suction values estimated by the psychrometric law from the experimental RH measurements by CIEMAT.

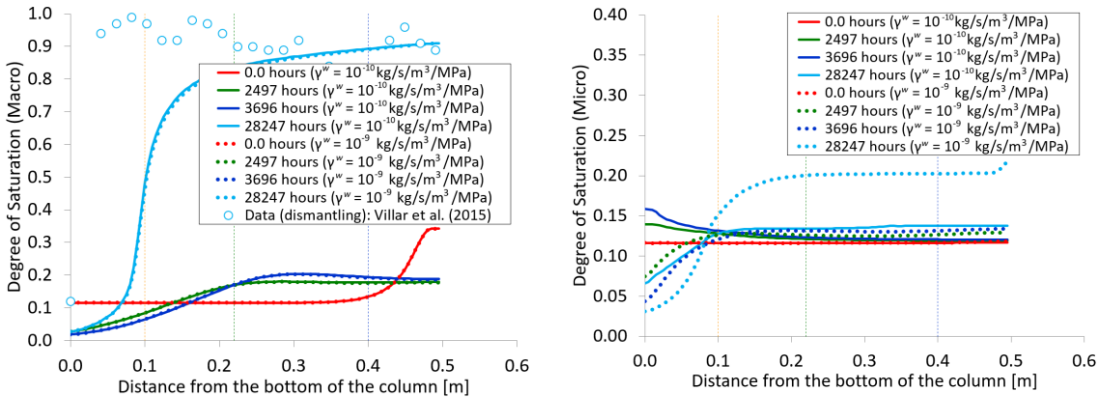

Figure 8-47: Longitudinal profiles of macrostructural (left) and the microstructural (right) degrees of saturation along Cell S/B axis at different times and for two distinct values of γ^w. Symbols represent the experimental data from the subsampling of the column (from Villar *et al.*, 2015b).

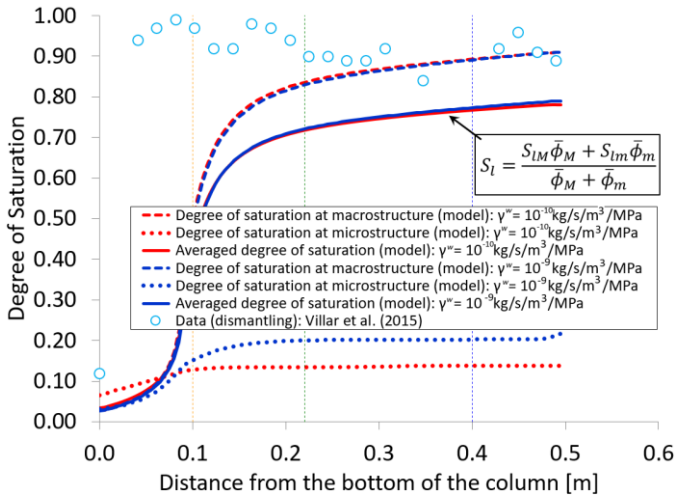

Figure 8-48: Longitudinal profiles of macro, micro and averaged degrees of saturation along Cell S/B at the end of calculations (for two values of γ^w and when $\bar{\phi}_{m,0} = 0.08$). Symbols represent the experimental data from the subsampling of the dismantled column (from Villar *et al.*, 2015b).

8.4. CONCLUDING REMARKS

The numerical modelling of the heating and forced hydration of two bentonite columns using the double-porosity model described in this document has demonstrated the ability of the proposed constitutive formulation to reproduce the main material responses observed in the measurements collected during the tests. The experimental data on the evolution of temperature and RH in both cells allowed the calibration of some input parameters related to the heat flux, the water retention capacity and the mass flow through macro-pores. The measurement of the axial stress on the top of the column of MX-80 pellets (Cell B) provided helpful information for fitting the mechanical parameters controlling the elastoplastic response of the mass of pellets under high hydro-thermal gradients. Furthermore, and since the swelling behaviour of such a bentonite material is determined by the water content of the intra-pellet voids, the vertical swelling pressure was also used to estimate a value for the leakage coefficient governing the water mass exchange between macro- and micro-pores. Due to the lack of information on the evolution of the axial stress in the column of sand/bentonite mixture (Cell S/B), such a calibration task was not possible and the mechanical parameters were taken from the literature or from previous modelling experiences. As a consequence, the micro-macro leakage parameter for the bentonite material in Cell S/B assumed similar values to the ones used in the modelling of the Cell B. The dismantling and subsampling of the Cell S/B supplied additional information on the final state of the column in terms of pore-size distribution and saturation. Further model calibrations may be required to reproduce not only the final state of such a column, but also the initial conditions of the smallest fraction of pores. The future dismantling of Cell B would provide complementary information to evaluate the model predictive capacity and the need to carry out (or not) additional adjustments in some input parameters.

Despite the difficulties outlined above, the performance of the laboratory heating-hydration tests complemented the understanding about the complex interactions between both pore-structure domains. In that sense, the evolution of the porosity variables and the water content along the columns was analysed as an extension from the local deformation and saturation responses discussed in the two previous chapters to a larger scale (laboratory-scale). In this way, it was easier to perceive the impact of the applied hydro-thermal loading on the deformation and saturation states of micro- and macro-pores.

The differential thermal expansion of the pore-water led to changes in the volumetric water content of micro- and macro-pores, but its impact was limited to the lower portion of the columns. Again, the micro-macro leakage coefficient (γ^w) plays a crucial role on the saturation conditions of micro-pores before the arrival of the downward hydration front. The generation of water vapour close to the heater (due to the intense heating and to the initial dry state of the column) and its transport by diffusion towards the top of the cells, where it condensates, determined the saturation profile within the columns before the start of the artificial wetting. However, the initiation of the controlled injection of water at the top of the heated columns altered the water content in the macro-pores and, due to the structural water mass exchange, in micro-pores as well. From that moment on, the deformation behaviour of the upper-half portion of the columns was controlled by the re-saturation of macro- and micro-pores. The high

thermal gradient close to the heater hindered the re-saturation of pores in the lower-half part of the cells. Therefore, the thermal expansion of the material constituents kept being the predominant deformation process at the bottom of the columns during the hydration phase. The thermal expansion of the confined mass of bentonite material close to the heater generated the changes in the axial stress at the top of the columns during the stage of heating without hydration. However, since the beginning of the controlled wetting, the confined swelling response of the expansive material located near the hydration surface was the dominant process in the development of the axial stress at the top of the bentonite columns.

9. SUMMARY, GENERAL CONCLUSIONS AND FUTURE RESEARCH WORKS

9.1. SUMMARY AND GENERAL CONCLUSIONS

The response of active clays submitted to changes in the environmental conditions has been investigated throughout the past century due to the high structural and economical costs caused by this type of soils in those regions where they occu. However, the potential use of bentonites in engineered barriers (EB) has contributed significantly to a deep characterization of the THM properties and behaviour of such materials under isothermal and non-isothermal scenarios. In that sense, several research projects have been carried out during the past decades, many of them including tasks of laboratory characterization, the performance and monitoring of laboratory and field prototype tests and the development of computational codes able to reproduce the main features observed experimentally. This PhD research was developed in the framework of the long-term performance of bentonite barriers for the disposal of highly radioactive waste. The general conclusions of the work carried out in this Thesis are condensed in the following sections. The most relevant aspects collected in the literature review concerning the use of bentonite barriers under isothermal and non-isothermal conditions are listed in **Section 9.1.1**. The main features related to the development and the implementation in a finite element code of a robust mathematical double-porosity formulation capable of modelling the THM response of expansive materials and its application in constitutive and in boundary value problems are summarized in **Section 9.1.2** and **Section 9.1.3**, respectively.

9.1.1. THEORETICAL ASPECTS AND PRECEDING FORMULATIONS FOR MODELLING THE RESPONSE OF EXPANSIVE CLAYS

Since the earliest research works on the particular behaviour of active clayey soils (such as bentonites), their high swelling potential has been atributted to the deformation response of the mineral-water system due to the physico-chemical phenomena occurring at particle scale. The high (total) specific surface area (SSA) of certain groups of clay minerals, such as smectites (montmorillonites), was identified as the main feature controlling the clay-ion-water interactions and, consequently, the high water retention capacity of such clays. This capacity of absorbing a large number of water molecules as those clayey soils become saturated is reflected in some engineering properties commonly used in Geotechnical Engineering, such as the liquid limit and the plastic index.

The existence of distinct pore-structure levels and water retention mechanisms is a characteristic feature of expansive clays. The pore-water retention mechanism in the smaller voids (intra-aggregate pores) is governed by electro-chemical forces, which allows the presence of considerable amount of water molecules “adhered” to the clay particles even when the expansive soil is apparently dry. In contrast, capillarity is the main water retention mechanism controlling the water content in large pores and, therefore, the water content in macro-pores is determined by the geometrical characteristics of such pores. Moreover, many experimental evidences showed that the density and mobility of microstructural water are not the same as those of the water found in macro-pores. The volumetric changes of individual active clay particles by the imbibition of water molecules (in wetting paths) or by the desiccation of the inter-layer voids (in drying paths) under unconfined conditions tends to induce, respectively, a global (and significant) swelling or shrinkage with the occurrence of some structural rearrangement of clay aggregations. The magnitude of such deformations depends on several factors, as the degree of densification of the clay fabric, the initial water content of the material and the stress path history, for instance. However, the presence of physical restraints to the free swelling leads to the development of swelling pressures, which can be notably high depending on the initial density and water content conditions of the mass of expansive clay. In both deformation scenarios (free or confined conditions), the deformation process of the expansive soil can be explained by the changes in the saturation state of the smaller and the larger pores during wetting and drying paths. In addition, the existence of an unbalanced chemical potential between microstructural and macrostructural water induces a water mass exchange between .micro- and macro-pores. The delayed deformation of active clays can be attributed to such a time-dependent mechanism, which relates the changes in the water content of the microstructure (and, consequently, its deformation response) to the changes in the water potential of the macrostructure.

These complex structural hydro-mechanical interactions between the distinct classes of pores cannot be predicted by single-porosity formulations developed to model the behaviour of unsaturated soils, as the “Barcelona Basic Model” (BBM) (Alonso *et al.*, 1990). As a consequence, several multi-porosity models have been proposed along the past three decades, as the “Barcelona Expansive Model” (BExM) (Alonso *et al.*, 1999) and the double structure model formulated in the framework of a generalized plasticity theory (Sánchez *et al.*, 2005; Ruiz, 2020).

In all the previous mentioned multi-porosity formulations, the clayey porous medium is considered as two overlapping porous media, one of them represented by the clay matrix (microstructure) and the other representing the interconnected inter-aggregate porosity (macrostructure). The coupling between these two structural levels is achieved by means of a deformation mechanism that accounts for the generation of plastic strains at macrostructure due to the elastic deformations of microstructure. In addition, the double-porosity approaches in Sánchez *et al.* (2005) and in Ruiz (2020) also consider a mass transfer process between the two pore-structure levels controlled through leakage terms. Although the double-porosity model developed in Sánchez *et al.* (2005) is able to model the response of bentonite-based materials under non-isothermal conditions, however, the mechanical coupling between the structural porous media is only partial, since the elastic behaviour of macrostructure is independent of the compressibility of microstructure. In addition, the de-saturation of micro-pores is not contemplated in such a formulation. In contrast, in the double-porosity approach in Ruiz (2020) and in this Thesis, the macrostructural compressibility is defined in terms of the compressibility of microstructure and a water retention curve is also defined for the microstructural level. However, the double-porosity formulation described in Ruiz (2020) is only able to model the swelling response of bentonite materials under isothermal conditions.

Therefore, the enhancement of the double-porosity approach by the inclusion of the thermal variable has been the main task carried out in this PhD research. In fact, the heat emission from the canister containing high-level radioactive waste to the bentonite buffer is a process expected to occur since the early post closure period of the repository system. The lower thermal conductivity of the unsaturatured buffer could lead to temperature values higher than 100°C in the vicinity of the canister. In addition to the thermal expansion of the solid and the fluid species and the water phase changes near the heat source, this non-isothermal scenario could lead to significant changes in the physico-chemical properties of water in micro- and macro-pores, to changes in the saline concentration in the soil solution and to potential changes in the clay mineralogy. Consequently, a thermal loading not only would affect the mechanical response (thermoplastic consolidation), the water retention capacity and the flux conditions in the buffer, but it could have an important impact on the swelling potential of bentonites. Therefore, the development of a double-porosity formulation capable of predicting the behaviour of expansive barriers under non-isothermal conditions, as the one proposed in this Thesis, should consider all these (or, at least, the most relevant) thermal effects in its mathematical formulation.

9.1.2. DEVELOPMENT AND IMPLEMENTATION OF AN ENHANCED DOUBLE-POROSITY FORMULATION FOR THERMO-HYDRO-MECHANICAL (THM) ANALYSES

The double-porosity model (DPM) proposed in this PhD Thesis has been developed in the framework of the generalized plasticity theory. Some of the basic theoretical and numerical features contemplated in the present formulation are similar to the ones considered in the double-structure formulation for isothermal problems described in Ruiz (2020). These common basic aspects (and assumptions) are listed below:

- Explicit consideration of two overlapping but distinct porous media. Hence, only two dominant pore levels are considered: the interconnected macro-porosity (inter-

aggregate pores) and the micro-porosity (including the actual micro-pores and the meso-pores). As a consequence, global porosities and strain components for both media are also defined.

- Definition of a water retention curve for each domain. Due to that, the unsaturation of microstructure is also taken into account.
- Hydraulic non-equilibrium between microstructural and macrostructural water potentials.
- Definition of a water mass exchange process between micro- and macro-pores controlled by a leakage term. The local hydraulic equilibrium between both media is achieved through this mass transfer mechanism.
- Local equilibrium between the gas pressure at each porous medium. As a consequence, the local water mass transfer is defined in terms of liquid pressure differences in micro- and macro-pores.
- Multiphase, non-saturated flow through the interconnected large pores. Micro-porosity does not contributed to the Darcian flow of water and air species through the porous medium.
- Different density states for the free water and the pore-water in micro-pores. A microstructural density function is included in the mathematical formulation in order to reproduce the density state of the intra-aggregate water.
- Definition of stress-small strain constitutive laws for each porous medium. It is assumed that microstructural deformations are volumetric and described by a non-linear elastic stress-strain relationship. The macrostructural behaviour is modelled in the context of classical plasticity for unsaturated soils (BBM formulation).
- Net stress for the effective stress state of the unsaturated macrostructute and Bishop's stress for the effective stress of microstructure. Consequently, the saturation-dependent effective stress parameter (Bishop's parameter), $\chi = f(S_l)$, is only defined for the microstructural medium.
- Description of the mechanical behaviour of the expansive soil in terms of the current compressibility of microstructure. A consistent relationship couples the elastic parameters of macrostructure and microstructure is defined.
- Macrostructural behaviour affected by the microstructural deformations. Elastoplastic deformations can develop in response to the volumetric deformations of the microstructure. The plastic structural interaction between both porous media is defined in terms of a pair of micro-macro coupling functions that depend on the global arrangements of clay aggregates. Nevertheless, it is assumed that macrostructural strains do not cause deformations in the microstructure.

It is important to highlight that some of the aforementioned features were already considered in the preceding double-porosity formulations developed by the UPC Geotechnical group, such as those described in Alonso *et al.* (1999) and Sánchez *et al.* (2005).

For non-isothermal problems, the main aspects (and assumptions) taken into account in the coupled THM double-porosity approach described in this Thesis are outlined as follows:

- Local thermal equilibrium between the phases and the porous media. As a consequence, the energy balance equation is solved for the whole porous medium.
- Heat propagation through the porous medium by conduction and convection.
- The more relevant THM processes that take place in a porous medium are considered in a fully-coupled way. Thus, the thermal expansion of the solid and fluid species, the differential expansion of water (in micro- and macro-pores), the water phase changes (the generation and condensation of water vapour) and other processes related to the thermal problem, as the transport of water vapour by diffusion, were already implemented in the numerical code.
- The dependence of the pore-air pressure on temperature is not considered. In addition, local equilibrium of the air pressure in micro- and macro-pores is assumed.
- The dependence of the density of microstructural water on temperature is taken into account. The thermal impact on the density and viscosity of water in macro-pores was already included in the finite element code (CODE_BRIGHT).
- The thermal impact on the water retention capacity of micro- and macro-pores is also contemplated.
- The strain components arising from the changes in temperature are assumed reversible and volumetric. Consequently, irreversible changes in the soil fabric due to the thermal loading, as the thermal collapse in open macrostructures, and the softening of the yield surface with the increase in temperature are not considered at this stage. However, the strong coupling between the thermal and the hydro-mechanical variables in the mathematical formulation allows the occurrence of some thermally-induced plastic strains.
- Irreversible structural changes of macrostructure due to the thermal expansion of microstructure are not considered. The original expression relating the plastic deformations of macrostructure to the microstructural strains through the structural coupling functions has been modified in order to discount the contribution of the thermal strain component of microstructure to the global rearrangement of aggregates.

The mathematical THM double-porosity formulation has been implemented in the finite element code CODE_BRIGHT (Olivella *et al.*, 1996). In this computational code, the general mathematical formulation is expressed in terms of balance equations, constitutive laws and equilibrium restrictions. The combination of this set of equations generates a system of partial differential equations that are solved numerically in a totally coupled way. Although the balance mass equation for the microstructural water has been defined in the mathematical formulation, such an equation is not in fact solved but the liquid pressure at microstructural level is treated as a history variable, whose values are updated during the performance of the stress integration algorithm and calculated at the constitutive integration points. Porosity variables (total porosity

and micro- and macro-pore volume fractions) are also treated as history variables. An explicit stress integration scheme with automatic sub-stepping and error controls is used to update the stress tensor and the internal variables at each Gauss point, for each iteration and for each time increment.

9.1.3. PERFORMANCE OF THE CURRENT THM DOUBLE-POROSITY FORMULATION IN MODELLING CONSTITUTIVE AND BOUNDARY VALUE PROBLEMS

The robustness and model capabilities of the double-porosity approach described in this Thesis to predict the swelling response of expansive materials (granular bentonite materials) under isothermal and non-isothermal conditions have been evaluated through the performance of constitutive and boundary value problem analyses.

The constitutive analyses consisted in submitting a small element of expansive soil to several stress paths at constant stress or constant volume conditions under constant or varying temperature. The impact of distinct initial conditions (suctions and confining pressures), the magnitude of the thermo-hydro-mechanical loadings and the sequence of application of such loadings (stress history) were investigated. In addition, some sensitivity analyses were also performed in order to determine the relationship between uncertainties in the modelling results and the uncertainties in some input parameters. In terms of the development of the swelling potential (i.e., swelling/shrinkage deformations in wetting/drying paths at unconfined conditions or swelling pressures in stress paths at isochoric conditions), the main findings obtained from these constitutive and sensitivity analyses can be summarized as follows:

- Increase of the swelling potential (strains or pressures) with the decrease in the initial water content.
- Increase of the swelling strains with the reduction of the confining pressure at which the wetting path takes place.
- Dependence of the swelling response on the sequence of operations performed between the initial and the final stress states.
- Dependence of the swelling/shrinkage response on the magnitude of the micro-macro leakage coefficient and on the period of time prescribed to hydrate/dehydrate macro-pores. The micro-macro water exchange coefficient is the model parameter governing the water mass transfer between the two structural media.
- For a certain value of the micro-macro leakage parameter, the swelling strains and stresses depend on the period of time prescribed to saturate or de-saturate the large pores.
- Thermally-induced saturation of the micro- and the macro-pores occurs due to the differential thermal expansion of pore-water with respect to the solid grains and clay fabric. The higher the magnitude of the thermal loading, the higher the thermally-

induced stresses (under confined conditions) and the "thermal" wetting of micro- and macro-pores.

- The swelling response during the hydration at high temperature is strongly dependent on the suction and stress conditions in the heated sample of soil at the beginning of the wetting path. The "initial conditions" for the re-saturation process are affected by the magnitude of the previous thermal loading and by the characteristics of the micro-macro hydraulic coupling.

The local mass transfer of water between micro- and macro-pores is the mechanism governing the saturation state of micro-pores and, consequently, the swelling response of the material under local water potential gradients. Although the results from the sensitivity analyses showed that a high micro-macro leakage parameter leads to high values of swelling strains and pressures, it is important to emphasize, however, that such a model parameter is, in fact, a material parameter related to geometric characteristics of the clay aggregates. A higher value for the leakage coefficient implies that the time required to reach the local balance between the macrostructural and microstructural water potentials is shorter in such a situation. In other words, the higher the leakage parameter, the faster the material develops its full swelling potential developing higher swelling strains or pressures during this process (for the same period of time).

THM processes expected to occur inside a bentonite barrier as heat flux by conduction and convection, water phase exchange, diffusive transport of water vapour, advective flux through macro-pores are not taken into account in a constitutive analysis. However, the numerical modelling of laboratory scale tests (boundary value problems) allows the incorporation of such coupled processes into the analysis and evaluates the model performance in reproducing accurately the response of a porous medium subjected to complex THM loadings. In that context, the artificial re-saturation of two heated bentonite columns (Cell B and Cell S/B by CIEMAT) was modelled using the THM double-porosity approach developed in this Thesis. The model performance in predicting the main features observed experimentally was checked by comparing the model results with laboratory data collected during the heating-hydration tests (temperature, relative humidity and axial stress) or after the dismantling and the sub-sampling of Cell S/B (final water content and pore size distribution). In addition, these experimental data allowed the calibration of some model parameters. The main conclusions based on the results from the modelling of the heating-hydration of the two bentonite columns are listed below:

- The differential thermal expansion of pore-water controlled the saturation state of micro- and macro-pores at the bottom of the columns during the first stages of heating and before the start of hydration.
- Water vapour is generated due to the high thermal gradient in the lower portion of the columns and is transported by diffusion towards the top of the columns, where it condensates. Such a conclusion can be evidenced by the significant de-saturation of pores close to the heater and the increase of the water content in the upper part of the columns before the start of the hydration phase.
- Thermal expansion of the mass of granular bentonite materials is the predominant deformation process at the bottom of the columns. The increase in axial stress on the

top of Cell B before the initiation of the hydration phase is a consequence of the thermal expansion of the mass of bentonite material close to the heater.

- Deformation behaviour of the upper half portion of the columns is controlled by the re-saturation of macro- and micro-pores after the beginning of the controlled injection of liquid water (at the top of the columns). Since the start of this wetting process, the swelling response of the bentonite material near the hydration surface has conditioned the evolution of the axial stress at the top of the columns.

Again, the water mass transfer mechanism seems to play a crucial role in the saturation state of micro-pores and, consequently, in the development of the local swelling response of the granular bentonite material. The micro-macro leakage coefficient for the column of bentonite pellets (Cell B) was estimated by back-analysis. Despite that, the future dismantling of this column will provide complementary information that could require the recalibration of such a model parameter. It is important to remark that the mechanical structural coupling (the β-mechanism) can also play a prominent role in the accuracy of the model predictions. Although generic coupling functions were used in calculations, it is necessary to emphasize the need of calibrating the model parameters that define such functions from experimental data on the evolution of the clay fabric in wetting and drying paths.

9.2. FUTURE RESEARCH WORKS

The first modelling tasks performed in this Thesis have shown the robustness of the double-porosity model (DPM) in reproducing the main expected and observed deformation behaviour of expansive materials under different boundary conditions and stress paths. However, in order to keep enhancing the state of the art in the THM modelling of expansive soils, further research must be performed in order to validate the current formulation and to include certain theoretical and/or numerical aspects that were not considered. In that sense, the following suggestions for future works are proposed:

- Isothermal and non-isothermal constitutive and sensitivity analyses at several stress paths in order to calibrate and evaluate the role played by some model parameters and to detect the model dependencies (and limitations) for the prescribed loading and boundary conditions. Special attention should be devoted to those model parameters and constitutive laws related to the microstructural behaviour and to the hydro-mechanical interaction between both structural media. In this context, a better understanding of the role played by the water retention curve of microstructure in the swelling response of expansive clays and its dependence on the high-density state of the microstructural water could be interesting aspects to be explored in such analyses.
- Numerical modelling of hydro-mechanical and thermo-hydro-mechanical tests at different scales. The modelling of laboratory and field tests is a required task for the verification and validation of the model assumptions and capabilities in predicting accurately the behaviour observed in laboratory and *in-situ* conditions. Moreover, this type of modelling task allows the calibration of some model parameters due to the large

amount of information provided by these experimental tests. A natural consequence of the modelling performed in **Chapter 8** would be the numerical simulation of the *in-situ* heating (HE-E) experiment (Teodori and Gaus, 2011) or the full-scale emplacement (FE) experiment (Müller *et al.*, 2017), both of them located at the Mont Terri underground laboratory (Switzerland).

- In connection with the previous point, and considering that some input parameters of the double-porosity model are calibrated indirectly (by back-analyses), it would be interesting to investigate the existence (or not) of empirical relationships or to establish a methodology to estimate those model parameters from geometrical or material characteristics or from pore structure analyses. Relevant questions are: is there any correlation between the value of the leakage parameter for the micro-macro water transfer and the size of the clay aggregates? or can the information from MIP curves be used to define the shape of the micro-macro coupling functions?

- The dependence of the pore-air pressure on temperature into the mathematical formulation. The hypothesis of constant gas pressure, although useful for introducing some simplifications into the THM formulation described in this Thesis, may not be realistic in cases where gas flow is inhibited.

- The inclusion of thermal plastic mechanisms into the present formulation. In that sense, some thermal phenomena as the thermal softening of the yield surface as temperature increases and the thermoplastic collapse in open macrostructures could be also modelled. The definition of a thermal structural coupling between micro and macro media would be necessary in order to relate the volumetric changes in microstructure to the structural rearrangement of clay aggregates. The micro-macro coupling functions should be redefined to also include the contribution of the thermal component of the microstructural deformation to the generation of plastic strains at the macrostructure

- The extension of the current double-porosity formulation to include a third pore level. In such a theoretical approach, the micro- and the meso-pore fractions would be treated separately. In the current double-porosity approach, the micro-pore fraction (intra-aggregate porosity) comprises the actual micro-pores (inter-layer pores) and meso-pores (inter-particle pores inside the clay aggregation). Although it is assumed that meso-pores do not contribute to the advective flow, this extended multi-porosity approach could consider explicitly the internal structure of the clay aggregates and distinguish the mechanisms controlling the water retention in the inter-layer and in the inter-particle voids. Consequently, it could reproduce the structural changes observed in expansive clays subjected to cycles of wetting-drying in a more realistic way. However, the insertion of a third pore level in the formulation would increase its mathematical complexity as well as the number of model parameters required for modelling the micro-meso-macro structural interactions.

10. REFERENCES

Abbo, A.J. (1997). Finite Element algorithms for elastoplasticity and consolidation. PhD Thesis. University of Newcastle, Newcastle, Australia.

Abbo, A.J. and Sloan, S.W. (1995) A smooth hyperbolic approximation to the Mohr-Coulomb Yield Criterion. Computers & Structures, 54 (3), 427-441.

Abbo, A.J. and Sloan, S.W. (1996). An automatic load stepping algorithm with error control. International Journal for Numerical Methods in Engineering, 39, 1737-1759.

Abdullah, W.S., Alshibli, K.A. and Al-Zou'bi, M.S. (1999). Influence of pore water chemistry on the swelling behavior of compacted clays. Applied Clay Sciences, 15, 447-462.

Abu-Hamdeh, N.H. (2003). Thermal properties of soils as affected by density and water content. Biosystems Engineering, 86 (1), 97-102.

Agus, S.S. (2005). An experimental study on hydro-mechanical characteristic of compacted bentonite-sand mixtures. PhD Thesis. Bauhaus-Universität Weimar, Weimar, Germany.

Aifantis, E. (1980). On the problem of diffusion in solids. Acta Mechanica, 37, 265-296.

AITEMIN (2001). The EB experiment engineered barrier emplacement in Opalinus Clay. Test Plan, version 3.0. Madrid, Spain.

AITEMIN (2012). Engineered Barrier Emplacement Experiment in Opalinus Clay: "EB" Experiment. Test Plan and sampling book. Madrid, Spain.

Akinwunmi, B., Sun, L., Hirvi, J.T., Kasa, S. and Pakkanen, T.A. (2019). Influence of temperature on the swelling pressure of bentonite clay. Chemical Physics, 516, 177-181.

Alawaji, H., Runesson , K. and Sture, S. (1992). Implicit integration in soil plasticity under mixed control for drained and undrained response. International Journal for Numerical and Analytical Methods in Geomechanics, 16, 737-756.

Al-Homoud, A.S., Basma, A.A., Malkawi, A.I. and Al Bashabsheh, M.A. (1995) Cyclic swelling behavior of clays. Journal of Geotechnical Engineering, 121 (7), 562-565.

Alonso, E.E. and Hoffmann, C. (2007). Modelling the field behaviour of a granular expansive barrier. Physics and Chemistry of the Earth, Parts A/B/C, 32 (8-14), 850-865.

Alonso, E.E. and Navarro, V. (2005). Microstructural model for delayed deformation of clay: loading history effects. Canadian Geotechnical Journal, 42, 381-392.

Alonso, E.E., Gens, A. and Gehling, W.Y.Y. (1994). Elastoplastic model for unsaturated expansive soils. In: Numerical models in geotechnical engineering. A.A. Balkema, Rotterdam, the Netherlands. 11-18.

Alonso, E.E., Gens, A. and Josa, A. (1990). A constitutive model for partially saturated soils. Géotechnique, 40 (3), 405-430.

Alonso, E.E., Romero, E. Hoffmann, C. and García-Escudero, E. (2005). Expansive bentonite-sand mixtures in cyclic controlled-suction drying and wetting. Engineering Geology, 81, 213-226.

Alonso, E.E., Vaunat, J. and Gens, A. (1999). Modelling the mechanical behaviour of expansive clays. Engineering Geology, 54, 173-183.

Alonso, E.E., Yang, D.Q., Lloret, A. and Gens, A. (1995). Experimental behaviour of highly expansive double-structure clay. In: Proceedings of the 1st International Conference on unsaturated soils (UNSAT'95), Vol. 1. September 6-8, 1995. Paris, France. 11-16.

Alther, G.R. (1987). The qualifications of bentonite as a soil sealant. Engineering Geology, 23 (3), 177-191.

Altofer, F. (2010). Geological disposal – Regulatory framework for the safety case. In: Second Training Course (TIMODAZ) – Impact of THMC Processes on Performance Assessment. January 13-15, 2010. Universitat Politècnica de Catalunya (UPC), Barcelona, Spain.

Andrade, F.A., Al-Qureshi, H.A. and Hotza, D. (2011). Measuring the plasticity of clays: A review. Applied Clay Science, 51, 1-7.

Ardani, A. (1992). Expansive soil treatment methods in Colorado. Final Report ODOT-DTD-R-92-2. Colorado Department of Transportation, Denver, Colorado, USA.

Arifin, Y.F. (2008). Thermo-hydro-mechanical behavior of compacted bentonite-sand mixtures: an experimental study. PhD Thesis. Bauhaus-University Weimar, Weimar, Germany.

Arnepalli, D.N., Shanthakumar, S., Hanumantha Rao, B. and Singh, D.N. (2008). Comparison of methods for determining specific-surface area of fine-grained soils. Geotechnical and Geological Engineering, 26, 121-132.

Arnott, R.J. (1965). Particle sizes of clay minerals by small-angle X-ray scattering. The American Mineralogist, 50 (10), 1563-1575.

Ashbaugh, H.S., Truskett, T.M. and Debenedetti, P.G. (2002). A simple molecular thermodynamic theory of hydrophobic hydration. Journal of Chemical Physics, 116 (7), 2907-2921.

Ashoka, H.G. (2006). Studies on physico-mechanical properties of the amended expansive clay solid. PhD Thesis. Kuvempu University, Karnataka, India.

ASTM D4546-08 (2008). Standard test methods for one-dimensional swell or collapse of cohesive soils. ASTM International. West Conshohocken, Pennsylvania, USA.

Atkinson, J.H. and Bransby, P.L. (1978). The Mechanics of Soils: an introduction to critical state soil mechanics. McGraw-Hill Book Co., London, UK.

Attom, M.F. (1997). The effect of compaction energy level on some engineering properties. Applied Clay Science, 12, 61-72.

Attom, M.F., Abu-Zreig, M.M. and Obaidat, M.T. (2006). Effect of remolding techniques on soil swelling and shear strength properties. In: Expansive Soils: Recent advances in characterization and treatment. Al-Rawas, A.A. and Goosen, M.F.A. (Eds.). Taylor & Francis. London, UK. 127-138.

Aylmore, L.A.G., Quirk, J.P. and Sill, I.D. (1969). Effects of heating on the swelling of clay minerals. Highway Research Board, Special Report 103. National Academy of Sciences, Washington, D.C., USA. 31-38.

Bag, R. and Rabbani, A. (2017). Effect of temperature on swelling pressure and compressibility characteristics of soil. Applied Clay Science, 136, 1-7.

Bagherieh, A.R., Khalili, N., Habibagahi, G. and Ghahramani, A. (2009). Drying response and effective stress in a double porosity aggregated soil. Engineering Geology, 105, 44-50.

Bain, J.A. (1971). A plasticity chart as an aid to the identification and assessment of industrial clays. Clay Minerals, 9, 1-17.

Baldi, G., Hueckel, T. and Pellegrini, R. (1988). Thermal volume changes of the mineral-water system in low-porosity clay soils. Canadian Geotechnical Journal, 25 (4), 807-825.

Basma, A.A, Al-Homoud, A.S. and Al-Tabari, E.Y. (1994). Effects of methods of drying on the engineering behavior of clays. Applied Clay Science, 9, 151-164.

Basma, A.A, Al-Homoud, A.S., Husein Malkawi, A.I. and Al-Bashabsheh, M.A. (1996). Swelling-shrinkage behavior of natural expansive clays. Applied Clay Science, 11, 211-227.

Bastiaens, W., Bernier, F., Buyens, M., Demarche, M., Li, X.L., Linotte, J.-M. and Verstricht, J. (2003). The extension of the HADES underground research facility at Mol, Belgium. The construction of the connecting gallery. EURIDICE Report 03-294. Mol, Belgium.

Bayesteh, H. and Mirghasemi, A.A. (2015). Numerical simulation of porosity and tortuosity effect on the permeability in clay: microstructural approach. Soils and Foundations, 55 (5), 1158-1170.

Bear, J. (1972). Dynamics of fluids in porous media. American Elsevier Publishing Company, Inc. New York, NY, USA.

Bennett, C. (2014). An experimental study on the hydraulic conductivity of compacted bentonites in geoenvironmental applications. PhD Thesis. Cardiff University, Cardiff, UK.

Bernier, F., Li, X.-L. and Bastiaens, W. (2007). Twenty-five years' geotechnical observation and testing in the Tertiary Boom Clay formation. Géotechnique, 57 (2), 229-237.

Bernier, F., Volckaert, G. and Villar, M.V. (1997). Suction controlled experiments on Boom clay. Engineering Geology, 47, 325-338.

Beziat, A., Dardaine, M. and Gabis, V. (1988). Effect of compaction pressure and water content on the thermal conductivity of some natural clays. Clays and Clay Minerals, 36 (5), 462-466.

Bishop, A.W. (1959). The principle of effective stress. Teknisk Ukeblad, 106 (39), 859-863.

Booker, J.R. and Savvidou, C. (1985). Consolidation around a point heat source. International Journal for Analytical Methods in Geomechanics, 9, 173-184.

Börgesson, L., Fredrikson, A. and Johannesson, L.-E. (1994). Heat conductivity of buffer materials. SKB Technical Report 94-29. Clay Technology AB, Lund, Sweden.

Borja, R.I. (1991). Cam-Clay plasticity, Part II: Implicit integration of constitutive equation based on a nonlinear elastic stress predictor. Computer Methods in Applied Mechanics and Engineering, 88 (2), 225-240.

Borja, R.I. and Lee, S.R. (1990). Cam-Clay plasticity, Part I: Implicit integration of elasto-plastic constitutive relations. Computer Methods in Applied Mechanics and Engineering, 78 (1), 49-72.

Brackley, I.J.A. (1975). A model of unsaturated clay structure and its application to swell behavior. In: Proceedings of the 6th Regional Conference for Africa on Soil Mechanics and Foundation Engineering. A. A. Balkema. Durban, South Africa. 65-70.

Bradbury, M.H. and Baeyens, B. (2002). Sorption of Eu on Na- and Ca-montmorillonites: Experimental investigations and modelling with cation exchange and surface complexation. Geochimica et Cosmochimica Acta, 66 (13), 2325-2334.

BRE (1993). Low-rise buildings on shrinkable clay soils. Building Research Establishment Digest 240. London, UK.

Brooks, R.H. and Corey, A.T. (1964). Hydraulic properties of porous media. Hydrology Papers, Nº 3. Colorado State University, Fort Collins, Colorado, USA.

Callister, W.D., Jr. and Rethwisch, D.G. (2008). Fundamentals of Materials – Science and Engineering. An integrated approach, 3rd Edition. John Wiley and Sons.

Campanella, R.G. and Mitchell, J.K. (1968). Influence of temperature variations on soil behavior. Journal of the Soil Mechanics and Foundations Division, ASCE (SM 3), 709-734.

Campbell, G.S. (1974). A simple method for determining unsaturated conductivity from moisture retention data. Soil Science, 117 (6), 311-314.

Caputo, H.P. (1996). Mecânica dos Solos e suas aplicações: Fundamentos. LTC Editora, 6ª Edição Revista e Ampliada. Rio de Janeiro, Brazil.

Carlsson, T. (1986). Interaction in MX-80 bentonite/water/electrolyte systems. PhD Thesis. University of Lulea, Lulea, Sweden.

Cases, J.M., Bérend, I., Besson, G., François, M., Uriot, J.P., Thomas, F. and Poirier, J.E. (1992). Mechanism of adsorption and desorption of water vapor by homoionic montmorillonite. 1. The sodium-exchanged form. Langmuir, 8, 2730-2739.

Cerato, A.B. (2001). Influence of specific surface area on Geotechnical characteristics of fine-grained soils. Master Thesis. University of Massachusetts, Massachusetts, USA.

Chandrasekharan, E.C., Boominathan, S., Sadayan, E. and Narayanaswamy Setty, K.R. (1969). Influence of heat treatment on the pulverization and stabilization characteristics of typical tropical soils. Highway Research Board, Special Report 103. National Academy of Sciences, Washington, D.C., USA. 161-172.

Charlier, R., Collin, F., Dizier, A., Fauriel, S., Gens, A., Guangjing, C., Laloui, L., Meynet, T., Pascon, F., Radu, J.-P., Van Marcke, P. and Vaunat, J. (2010). Large scale excavation and heater in-situ experiment: the PRACLAY experiment modelling. TIMODAZ Report, Deliverable D13 – Annex 6.

Chen, F.H. (1988). Foundations on Expansive Soils. Elsevier. Amsterdam, the Netherlands.

Chen, G.J. and Ledesma, A. (2009). Coupled Thermohydromechanical modeling of the Full-scale in situ Test "Prototype Repository". Journal of Geotechnical and Geoenvironmental Engineering, 135 (1), 121-132.

Cho, W.J., Lee, J.O. and Chun, K.S. (1999). The temperature effects on hydraulic conductivity of compacted bentonite. Applied Clay Science, 14, 47-58.

Cho, W.J., Lee, J.O. and Kang, C.H. (2000). Influence of temperature elevation on the sealing performance of a potential buffer material for a high-level radioactive waste repository. Annals of Nuclear Energy, 27, 1271-1284.

Clem, A.G. and Doehler, R.W. (1961). Industrial applications of bentonite. Clays and Clay Minerals, 10 (1), 272-283.

CODE_BRIGHT User's Guide (2014). UPC Geomechanical Group. Universitat Politècnica de Catalunya, Barcelona, Spain.

Colmenares, J.E. (2002). Suction and volume changes of compacted sand-bentonite mixtures. PhD Thesis. Imperial College of Science, Technnology and Medicine, London, England.

Crisfield, M.A. (1991). Non-linear Finite Element Analysis of Solid and Structures. Volume 1: Essentials. John Wiley and Sons. Chichester, England.

Cui, Y.-J. (2017). On the hydro-mechanical behaviour of MX80 bentonite-based materials. Journal of Rock Mechanics and Geotechnical Engineering, 9, 565-574.

Cui, Y.-J., Le, T.T., Tang, A.M., Delage, P. and Li, X.L. (2009). Investigating the time-dependent behaviour of Boom Clay under thermomechanical loading. Géotechinque, 59 (4), 319-329.

Cui, Y.-J., Sultan, N. and Delage, P. (2000). A thermomechanical model for saturated clays. Canadian Geotechnical Journal, 37, 607-620.

Czaikowski O., Garitte, B., Gaus, I., Gens, A., Kuhlman, U. and Wieczorek, K. (2012). Design and predictive modelling of the HE-E test. PEBS Deliverable D3.2-1. NAB 12-003. Wettingen, Switzerland.

Dakshanamurthy, V. and Raman, V. (1973). Simple method of identifying an expansive soil (Technical Note). Soil and Foundations, 13 (1), 97-104.

Daniel, D.E. (1982). Measurement of hydraulic conductivity of unsaturated soils with thermocouple psychrometers. Soil Science Society of America Journal, 46 (6), 1125-1129.

Day, R.W. (1994). Swell-shrink behaviour of compacted clay. Journal of Geotechnical Engineering (ASCE), 120 (3): 618-623.

de Jong, E., Acton, D.F. and Stonehouse, H.B. (1990). Estimating the Atterberg limits of Southern Saskatchewan soils from texture and carbon contents. Canadian Journal of Soil Science, 70 (4), 543-554.

de Jong, G.J. (1968). Consolidation models consisting of an assembly of viscous elements or a cavity channel network. Géotechnique, 18, 195-228.

Del Olmo, C., Fioravante, V., Gera, F., Hueckel, T., Mayor, J.C. and Pellegrini, R. (1996). Thermomechanical properties of deep argillaceous formations. Engineering Geology, 41, 87-101.

Delage, P., Cui, Y.-J. and Sultan, N. (2004). On the thermal consolidation of Boom Clay. In: Proceedings Eurosafe 2004 Conference. Berlin, Germany.

Delage, P., Marcial, D., Cui, Y.J. and Ruiz, X. (2006). Ageing effects in the compacted bentonite: a microstructure approach. Géotechnique, 56 (5), 291-304.

Delage, P., Sultan, N. and Cui, Y.J. (2000). On the thermal consolidation of Boom Clay. Canadian Geotechnical Journal, 37 (2), 343-354.

Della Vecchia, G., Dieudonné, A.-C., Jommi, C. and Charlier, R. (2015). Accounting for evolving pore size distribution in water retention models for compacted clays. International Journal for Numerical and Analytical Methods in Geomechanics, 39 (7), 702-723.

Demars, K.R. and Charles, R.D. (1982). Soil volume changes induced by temperature cycling. Canadian Geotechnical Journal, 19 (2), 188-194.

Dennis, J.E. and More, J. (1977). Quasi Newton methods: motivation and theory. Society for Industrial and Applied Mathematics – SIAM Review, 19 (1), 46-89.

Dereeper, B. and Volckaert, G. (2002). The RESEAL Project: A large scale shaft sealing demonstration test. In: International Meeting on Clays in Natural and Engineered Barriers for Radioactive Waste Confinement. December 9-12, 2002. Reims, France. 269-270.

Derjaguin, B.V., Karasev, V.V. and Khromova, E.N. (1986). Thermal expansion of water in fine pores. Journal of Colloid and Interface Science, 109 (2), 586-587.

Derski, W. and Kowalski, S.T. (1979). Equations of linear thermos-consolidation. Archives of Mechanics, 31 (3), 303-316.

Dieudonné, A.-C., Della Vecchia, G. and Charlier, R. (2017). A water retention model for compacted bentonites. Canadian Geotechnical Journal, 54 (7), 915-925.

Dieudonné, A.-C., Gatabin, C., Talandier, J., Collin, F. and Charlier, R. (2016). Water retention behaviour of compacted bentonites: experimental observations and constitutive model. In: The 3rd European Conference on Unsaturated Soils (E-UNSAT 2016). Delage, P., Cui, Y.-J., Ghabezloo, S., Pereira, J.M., and Tang, A.M. (Eds.). E3S Web of Conferences, Vol 9, 11012.

Dif, A.E. and Bluemel, W.F. (1991). Expansive soils under cyclic drying and wetting - Technical Note. Geotechnical Testing Journal, 14 (1), 96-102.

Ding, K.Z., Qin, Q.-H. and Cardew-Hall, M. (2005). A new integration algorithm for the finite element analysis of elasto-plastic problems. In: Proceedings of the 9th International Conference on Inspection, Appraisal, Repairs & Maintenance of Structures. October 20-21, 2005. Fuzhou, China. 209-216.

Ding, K.Z., Qin, Q.-H. and Cardew-Hall, M. (2007). Substepping algorithms with stress correction for the simulation of sheet metal forming process. International Journal of Mechanics Sciences, 49, 1289-1308.

Dixon, D., Sandén, T., Jonsson, E. and Hansen, J. (2011). Backfilling of deposition tunnels: use of bentonite pellets. Technical Report SKB P-11-44, Stockholm, Sweden.

Dixon, D.A., Gray, M.N. and Graham, J. (1996). Swelling and hydraulic properties of bentonites from Japan, Canada and USA. In: Proceedings of the 2nd International Congress on Environmental Geotechnics (ICEG: IS-Osaka'96). Osaka, Japan. November 5-8, 1996. 43-48.

Dolinar, B., Mišič, M. and Trauner, L. (2007). Correlation between surface area and Atterberg limits of fine-grained soils. Clays and Clay Minerals, 55 (5), 519-523.

Driscoll, R. and Crilly, M. (2000). Subsidence damage to domestic buildings. Lessons learned and questions remaining. Building Research Establishment. London, UK.

Duplay, J., Montes, G., Geraud, Y. and Martinez, L. (2002). Influence of interlayer cation in swelling and shrinkage of bentonite MX80. In: International Meeting on Clays in Natural and Engineered Barriers for Radioactive Waste Confinement. December 9-12, 2002. Reims, France. 293-294.

El Sayed, S.T. and Rabbaa, S.A. (1986). Factors affecting behavior of expansive soils in the laboratory and field – a review. Geotechnical Engineering, 17 (1), 89-107.

Elarabi, H. (2010). Damage mechanism of expansive soils. In: Conference of Graduate Studies and Scientific Research. February 2010. University of Khartoum, Khartoum, Sudan. 371-378.

Elsharief, A.M., Zumrawi, M.M.E. and Salam, A.M. (2014). Experimental study of some factors affecting swelling pressure. University of Khartoum Engineering Journal, 4 (2), 1-7.

ENRESA (2000). FEBEX Project: Full-scale engineered barriers experiment for a deep geological repository for high level radioactive waste in crystalline host rock. Final Report. ENRESA Technical Report 1/2000. Madrid, Spain.

Estabragh, A.R., Moghadas, M. and Javadi, A.A. (2013). Effect of different types of wetting fluids on the behaviour of expansive soil during wetting and drying. Soils and Foundations, 53 (5), 617-627.

Farouki, O.T. (1981). Thermal properties of soils. CRREL Monograph 81-1. Hanover, New Hampshire, USA.

Faust, C.R. and Mercer, J.W. (1977). Theoretical analysis of fluid flow and energy transport in hydrothermal systems. Open-file Report 77-60. Dept. of the Interior, Geological Survey, Reston, Virginia, USA.

Feng, M. and Fredlund, D.G. (1999). Hysteretic influence associated with thermal conductivity sensor measurements. In: Proceedings from Theory to the Practice of Unsaturated Soil Mechanics in Association with the 52nd Canadian Geotechnical Conference and the Unsaturated Soil Group. October 23-24, 1999. Regina, Saskatchewan, Canada 14:2:14-14:2:20.

Feng, M., Gan, J.K.-M. and Fredlund, D.G. (1998). A laboratory study of swelling pressure using various test methods. In: Proceedings of the 2nd International Conference on Unsaturated Soils, Vol 1. August 27-30, 1998. Beijing, China. 350-355.

Fernández, A.M. (2011). Determination of the specific heat capacity of materials used as confinement barrier at El Cabril. Interim Report CIEMAT/DMA/2G208/3/11. Madrid, Spain.

Fernández, A.M. and Rivas, P. (2005). Analysis and distribution of waters in the compacted FEBEX bentonite: pore water chemistry and adsorbed water properties. In: Advances in understanding engineered clay barriers. Alonso, E.E. and Ledesma, A. (Eds.). Balkema. Leiden, the Netherlands. 257-275.

Fine, R.A. and Millero, F.J. (1973). Compressibility of water as a function of temperature and pressure. The Journal of Chemical Physics, 59 (10), 5529-5536.

Forouzan, A.J. (2016). Prediction of swelling behavior of expansive soils using Modified free swell index, methylene blue and swell oedometer tests. Master Thesis. Middle East Technical University, Ankara, Turkey.

François, B. and Laloui, L. (2008). ACMEG-TS: A constitutive model for unsaturated soils under nin-isothermal conditions. International Journal for Numerical and Analytical Methods in Geomechanics, 32, 1955-1988.

François, B., Salager, S., El Youssoufi, M.S., Ubals Picanyol, D., Laloui, L. and Saix, C. (2007). Compression tests on a sandy silt at different suction and temperature levels. ASCE Geotechnical Special Publication, 157.

Fredlund, D.G. (1969). Consolidometer test procedural factors affecting swell properties. In: Proceedings of the 2nd International Conference on Expansive Clay Soils. College Station, Texas, USA. 435-456.

Fredlund, D.G. (1975). Engineering properties of expansive clays. In: Seminar on Shallow Foundations on Expansion Clays. October 27-28, 1975. Regina, Saskatchewan, Canada.

Fredlund, D.G. (1989). Discussion Leader's report on the unsaturated soils. In: Proceedings of the 12th International Conference on Soil Mechanics and Foundation Engineering. August 13-18, 1989. Rio de Janeiro, Brazil. 2861-2878

Fredlund, D.G. and Pham, H.Q. (2006). A volume-mass constitutive model for unsaturated soils in terms of two independent stress state variables. In: Proceedings of the 4th International Conference on Unsaturated Soils, ASCE, Vol. 1. Miller, G.A., Zapata, C.E., Houston, S.L. and Fredlund, D.G. (Eds.). April 2-6, 2006. Carefree, Arizona, USA. 105-134.

Fredlund, D.G. and Xing, A. (1994). Equations for the soil-water characteristic curve. Canadian Geotechnical Journal, 31, 521-532.

Fredlund, D.G., Hasan, J.U. and Filson, H. (1980). The prediction of total heave. In: Proceedings of the 4th International Conference on Expansive Soils. Denver, Colorado, USA. 1-11.

Fredlund, D.G., Rahardjo, H. and Fredlund, M.D. (2012). Unsaturated Soil Mechanics in Engineering Practice. John Wiley & Sons, Inc. Hoboken, New Jersey, USA.

Gallipoli, D., Gens, A., Sharma, R. and Vaunat, J. (2003). An elasto-plastic model for unsaturated soil incorporating the effects of suction and degree of saturation on mechanical behaviour. Géotechnique, 53 (1), 123-135.

Gao, H. and Shao, M. (2015). Effects of temperature changes on soil hydraulic properties. Soil & Tillage Research, 153, 145-154.

Garitte, B., Gens, A., Vasconcelos, R.B., Vaunat, J., Gaus, I. (2015). The HE-E experiment (Mont Terri): modelling a large in situ heating test. In: Proceedings of the 6th International Conference – Clays in Natural and Engineered Barriers for Radioactive Waste Confinement. March 23-26, 2015. Brussels, Belgium. 532-533.

Gatabin, C., Talandier, J., Collin, F., Charlier, R. and Dieudonné, A.-C. (2016). Competing effects of volume change and water uptake on the water retention behaviour of a compacted MX-80 bentonite/sand mixture. Applied Clay Science, 121-122, 57-62.

Gaus, I. (2011). Long term performance of engineered barrier systems (PEBS). Mont Terri HE-E experiment: detailed design report. NAGRA Arbeitsbericht NAB 11-01. Nagra, Wettingen, Switzerland.

Gaus, I., Garitte, B., Senger, R., Gens, A., Vasconcelos, R., Garcia-Sineriz, J.-L., Trick, T., Wieczorek, K., Czaikowski, O., Schuster, K., Mayor, J.C., Velasco, M., Kuhlmann, U. and Villar, M.V. (2014a). The HE-E Experiment: Layout, interpretation and THM modelling. NAGRA Arbeitsbericht NAB 14-53. NAGRA, Wettingen, Switzerland.

Gaus, I., Wieczorek, K., Schuster, K., Garitte, B., Senger, R., Vasconcelos, R. and Mayor, J.C. (2014b). EBS behaviour immediately after repository closure in a clay host rock: HE-E experiment (Mont Terri URL). In: Clays in Natural and Engineered Barriers for Radioactive Waste Confinement. Geological Society, London, Special Publications, 400. 71-91.

Gens, A. (1995). Constitutive Laws. In: Modern issues in non-saturated soils. Edited by A. Gens, P. Jouanna and B. Schrefler. Springer-Verlag. 129-158.

Gens, A. and Alonso, E.E. (1992). A framework for the behaviour of unsaturated expansive clays. Canadian Geotechnical Journal, 29, 1013-1032.

Gens, A. and Vasconcelos, R. (2019). HE-E Experiment: Modelling of the HE-E test. Mont Terri Project TN 2019-43. Barcelona, Spain.

Gens, A., Filippi, M., Vallejan, B., Weetjens, E., Van Geet, M., Volckaert, G. and Bastiaens, W. (2009a). RESEAL II Project: Final report on modelling (WP4). External Report SCK·CEN-ER-80. Mol, Belgium.

Gens, A., García Molina, A., Olivella, S., Alonso, E. and Huertas, F. (1998). Analysis of a full scale in-situ test simulating repository conditions. International Journal for Numerical and Analytical Methods in Geomechanics, 22, 515-548.

Gens, A., Pomaro, B., Sánchez, M. and Villar, M.V. (2018). On the hydration of unsaturated barriers of high-level nuclear waste disposal. In: The 7th International Conference on Unsaturated Soils (UNSAT2018). Hong Kong University of Science and Technology (HKUST). Hong Kong, China. 55-60.

Gens, A., Sánchez, M., Guimarães, L. do N., Alonso, E.E., Lloret, A., Olivella, S., Villar, M.V. and Huertas, F. (2009b). A full-scale in situ heating test for high-level nuclear waste disposal: observations, analysis and interpretation. Géotechnique, 59, 1-23.

Gens, A., Valleján, B., Sánchez, M., Imbert, C., Villar, M.V. and Van Geet, M. (2011). Hydromechanical behaviour of a heterogeneous compacted soil: experimental observations and modelling. Géotechnique, 61 (5), 367-386.

Geradin, M., Idelsohn, S. and Hogge, M. (1980). Non linear structural dynamics via Newton and quasi Newton methods. Nuclear Engineering Design, 58, 339-348.

Gesto, J.M. (2014). Implementation of the Barcelona Expansive Model (BExM) in CODE_BRIGHT. UPC Report. Barcelona, Spain.

Gesto, J.M., Gens, A. and Vaunat, J. (2011). Smoothing of Yield surfaces and a reformulation of multi-surface plasticity. In: Proceedings of the XI International Conference on Computational Plasticity (COMPLAS XI) – Fundamentals and Applications. September 7-9, 2011. Barcelona, Spain. 1-11.

Ghiadistri, G.M., Potts, D.M., Zdravković, L. and Tsiampousi, A. (2018). A new double structure model for expansive clays. In: Proceedings of the 7th International Conference on Unsaturated Soils (UNSAT 2018). August 3-5, 2018. Hong Kong, China.

Gorączko, A. and Olchawa, A. (2017). The amounts of water adsorbed to the surface of clay minerals at the plastic limit. Archives of Hydro-Engineering and Environmental Mechanics, 64 (3-4), 155-162.

Gran, M., Carrera, J., Olivella, S. and Saaltink, M.W. (2011). Modeling evaporation processes in a saline soil from saturation to oven dry conditions. Hydrology and Earth System Sciences, 15, 2077-2089.

Grauer, R. (1990). The chemical behaviour of montmorillonite in a repository backfill: selected aspects. Technical Report 88-24E, NAGRA. Baden, Switzerland.

Habibagahi, K. (1977). Temperature effect and the concept of effective void ratio. Indian Geotechnical Journal, 1, 14-34.

Halama, R. and Poruba, Z. (2009). Tangent modulus in numerical integration of constitutive relations and its influence on convergence of N-R Method. Applied and Computational Mechanics, 3, 27-38.

Hamby, D. M. (1994). A review of techniques for parameter sensitivity analysis of environmental models. Environmental Monitoring and Assessment, 32, 135-154.

Hamidi, A., Tourchi, S. and Kardooni, F. (2017). A critical state based thermo-elasto-plastic constitutive model for structured clays. Journal of Rock Mechanics and Geotechnical Engineering, 9, 1094-1103.

Hamidi, A., Tourchi, S. and Khazaei, C. (2015). Thermomechanical constitutive model for saturated clays based on Critical State Theory. International Journal of Geomechanics, 15 (1), 1-9.

Hashim, R. and Muntohar, A.S. (2006). Swelling rate of expansive clay soils. In: Expansive Soils: Recent advances in characterization and treatment. Al-Rawas, A.A. and Goosen, M.F.A. (Eds.). Taylor & Francis. London, UK. 141-148.

Heilman, M.D., Carter, D.L. and Gonzalez, C.L. (1965). The ethylene glycol monoethyl ether (EGME) technique for determining soil-surface area. Soil Science, 100 (6), 409-413.

Heng, L.C. and Fong, C.S. (1991). Determination of specific surface areas of clay fractions of soils under rubber by adsorption of cetyl pyridinium bromide. Journal of Natural Rubber Research, 6 (2), 127-133.

Herbert, H.-J., Kasbohm, J., Sprenger, H., Fernández, A.M. and Reichelt, C. (2008). Swelling pressures of MX-80 bentonite in solutions of different ionic strength. Physics and Chemistry of the Earth, 33, S327-S342.

Hidnert, P. and Dickson, G. (1945). Some physical properties of mica. Journal of Research of the National Bureau of Standards, 35 (4), 309-353.

Hiley, R.A. and Rouainia, M. (2008). Explicit Runge-Kutta methods for the integration of rate-type constitutive equations. Computational Mechanics, 42 (1), 53-66.

Hiraiwa, Y. and Kasubuchi, T. (2000). Temperature dependence of thermal conductivity over a wide range of temperature (5-75˚C). European Journal of Soil Science, 51, 211-218.

Hoffmann, C. (2005). Caracterización hidromecánica de mezclas de pellets de bentonite: studio experimental y constitutivo. PhD Thesis. Universitat Politècnica de Catalunya, Barcelona, Spain.

Hoffmann, C., Alonso, E.E. and Romero, E. (2007). Hydro-mechanical behaviour of bentonite pellet mixtures. Physics and Chemistry of the Earth, 32, 832-849.

Hökmark, H. (2004). Hydration of the bentonite buffer in a KBS-3 repository. Applied Clay Science, 26, 219-233.

Hökmark, H., Ledesma, A., Lassabatere, T., Fälth, B., Börgesson, L., Robinet, J.C., Sellali, N. and Sémété, P. (2007). Modelling heat and moisture transport in the ANDRA/SKB temperature buffer test. Physics and Chemistry of the Earth, 32, 753-766.

Holtz, R.D. and Kovacs, W.D. (1981). An introduction to geotechnical engineering. Prentice-Hall. New Jersey, USA.

Holtz, W.G. (1959). Expansive clays – Properties and problems. Quarterly of the Colorado School of Mines, 54 (4), 89-125.

Holtz, W.G. and Gibbs, H.J. (1956). Engineering properties of expansive clays. Transactions of the American Society of Civil Engineering (ASCE), 121 (1), 641-663.

Hopmans, J. and Dane, J.H. (1985). Effect of temperature-dependent hydraulic properties on soil water movement. Soil Science Society of America Journal, 49 (1), 51-58.

Horseman, S.T. and McEwen, T.J. (1996). Thermal constraints on disposal of heat-emitting waste in argillaceous rocks. Engineering Geology, 41, 5-16.

Houston, S.L., Dye, H.B., Zapata, C.E., Walsh, K.D. and Houston, W.N. (2011). Study of expansive soils and residential foundations on expansive soils in Arizona. Journal of Performance of Constructed Facilities, 25 (1), 31-44.

Hueckel, T. and Baldi, G. (1990). Thermoplasticity of saturated clays: experimental constitutive study. Journal of Geotechnical Engineering, 116 (12), 1778-1796.

Hueckel, T. and Borsetto, M. (1990). Thermoplasticity of saturated soils and shales: constitutive equations. Journal of Geotechnical Engineering, 116 (12), 1765-1777.

Hueckel, T. and Pellegrini, R. (1996). A note on thermomechanical anisotropy of clays. Engineering Geology, 41, 171-180.

Huertas, F., de la Cruz, B., Fuentes-Cantillana, J.L., Alonso, E., Linares, J., Samper, J., Elorza, F.-J., Svemar, C., Salo, J.-P., Muurinen, A., Pacovsky, J., Verstricht, J., Bazargan-Sabet, B., Jockwer, N., Vignal, B., Shao, H., Kickmaier, W., Baeyens, B., Börgesson, L., Rhén, I., Villieras, F., Robinet, J.C. and Gourry, J.C. (2005). Full-Scale Engineered Barriers Experiment for a deep geological repository for high-level waste in crystalline host rock – Phase II. FEBEX II Final Report. Project Report EUR 21922.

IAEA (International Atomic Energy Agency) (1984). Effects of heat from high-level waste on performance of deep geological repository components. Technical Report IAEA-TECDOC-319. Vienna, Austria.

IAEA (International Atomic Energy Agency) (1995). The Principles of Radioactive Waste Management. Safety Series No. 111-F. Vienna, Austria.

IAEA (International Atomic Energy Agency) (2003). Scientific and Technical basis for the geological disposal of radioactive wastes. Technical Reports Series No. 413. Vienna, Austria.

Ichikawa, Y., Kawamura, K., Fujii, N. and Kitayama, K. (2004). Microstructure and micro/macro-diffusion behavior of tritium in bentonite. Applied Clay Science, 26, 75-90.

Iglesias, R.J., Gutiérrez-Álvarez, C. and Villar, M.V. (2018). HE-E Experiment: Progress report of a THM cell with MX-80 pellets – Ph 23. Mont Terri Project TN 2018-04. Madrid, Spain.

Imbert, C. and Villar, M.V. (2006). Hydro-mechanical response of a bentonite pellets-powder mixture upon infiltration. Applied Clay Science, 32 (3-4), 197-209.

Inoue, A., Utada, M. and Wakita, K. (1992). Smectite-to-illite conversion in natural hydrothermal systems. Applied Clay Science, 7, 131-145.

IS 1498 (1970). Indian Standard Classification and Identification of Soils for General Engineering Purposes. Bureau of Indian Standards (BIS). New Delhi, India.

Jacinto, A.C., Villar, M.V. and Ledesma, A. (2012). Influence of water density on the water-retention curve of expansive clays. Géotechnique, 62 (8), 657-667.

Jayalath, C.P.G., Gallage, C. and Miguntanna, N.S. (2016). Factors affecting the swelling pressure measured by the oedometer method. International Journal of GEOMATE, 11 (24), 2397-2402.

Jennings, J.E. (1969). The prediction of amount and rate of heave likely to be experienced in engineering construction on expansive soils. In: Proceedings for the 2nd International Conference on Expansive Clay Soils. College Station, Texas, USA. 99-105.

Jennings, J.E. and Kerrich, J.E. (1962). The heaving of buildings and the associated economic consequences with particular reference to the Orange Free State Goldfields. Civil Engineer in South Africa, 4, 221-248.

Jennings, J.E. and Knight, K. (1957). The prediction of total heave from the double oedometer test. Transactions South African Institution of Civil Engineering, 7, 285-291.

Jennings, J.E., Firth, R.A., Ralph, T.K. and Nagar, N. (1973). An improved method for predicting heave using the oedometer test. In: Proceedings for the 3rd International Conference on Expansive Clay Soils, Vol 2. Haifa, Israel. 149-154.

Jeyapalan, J.K., Rice Jr., G.T. and Lytton, R.L. (1981). State-of-the-art review of expansive soil treatment methods: a report. Texas A&M Research Foundation, College Station, Texas, USA.

Johnson, L.D. (1969). Review of literature on expansive clay soils. U.S. Army Engineer Waterways Experiment Station, USAEWES. Miscellaneous Paper S-69-24. Vicksburg, Mississippi, USA.

Johnson, L.D. and Stroman, W.R. (1976). Analysis of behavior of expansive soil foundations. U.S. Army Engineer Waterways Experiment Station, USAEWES. Technical Report S-76-8. Vicksburg, Mississippi, USA.

Johnson, L.H., Niemeyer, M., Klubertanz, G., Siegel, P. and Gribi, P. (2002). Calculations of the temperature evolution of a repository for spent fuel, vitrified high-level waste and intermediate level waste in Opalinus Clay. NAGRA Technical Report NTB 01-04. Nagra, Wettingen, Switzerland.

Jonas, E.C. and Oliver, R.M. (1967). Size and shape of montmorillonite crystallites. Clays and Clay Minerals, 15(1), 27-33.

Jones, D.E. and Holtz, W.G. (1973). Expansive Soils – The hidden disaster. American Society of Civil Engineering Journal, 31, 87-89.

Jones, L.D. and Jefferson, I.F. (2012). Expansive soils. In: ICE Manual of Geotechnical Engineering: Volume 1 – Geotechnical engineering principles, problematics and site investigation. ICE Publishing. London, UK. 413-441.

Joshi. R.C., Achari, Gopal, Horsfield, D. and Nagaraj, T.S. (1994). Effect of heat treatment on strength of clays. Journal of Geotechnical Engineering, ASCE, 120 (6), 1080-1087.

Justo, J.L., Delgado, A. and Ruiz, J. (1984). The influence of stress path in the collapse swelling of soils in the laboratory. In: Proceedings of the 5th International Conference on Expansive Soils. May 21-23, 1984. Adelaide, Australia. 67-71.

Kabubo, C.K., Gariy, Z.A., Mwea, S.K. and Abuodha, S.O. (2017a). The effect of varying heat temperatures on the grading and the swelling behaviour of expansive clay soils. International Journal of Science and Research (IJSR), 6 (4), 2371-2377.

Kabubo, C.K., Mwea, S.K., Abuodha, S.O. and Gariy, Z.A. (2017b). The effect of heat on the properties of expansive clay soil. International Journal of Science and Research (IJSR), 6 (1), 464-469.

Kahn, A. (1963). Studies on the size and shape of clay particles in aqueous suspension. Clays and Clay Minerals, 6, 220-236.

Karnland, O. and Birgersson, M. (2006). Montmorillonite stability with respect to KBS-3 conditions. SKB Report TR-06-11. Stockholm, Sweden.

Karnland, O., Nilsson, U., Weber, H. and Wersin, P. (2008). Sealing ability of Wyoming bentonite pellets foreseen as buffer material – Laboratory results. Physics and Chemistry of the Earth, Parts A/B/C, 33, S472-S475.

Karnland, O., Pusch, R. and Sánden, T. (1992). The importance of electrolyte on the physical properties of MX-80 bentonite. SKB Report AR 92-35. Stockholm, Sweden.

Karube, D. and Kato, S. (1994). An ideal unsaturated soil and the Bishop's soil. In: Proceedings of the 13th International Conference on Soil Mechanics and Foundation Engineering, Vol. 1. New Delhi, India. 43-46.

Karube, D. and Kawai, K. (2001). The role of pore water in the mechanical behavior of unsaturated soils. Geotechnical and Geological Engineering, 19, 211-241.

Kellomäki, A., Nieminen, P. and Ritamäki, L. (1987). Sorption of ethylene glycol monoethyl ether (EGME) on homoionic montmorillonites. Clay Minerals, 22, 297-303.

Khalili, N. and Khabbaz, M.H. (1998). A unique relationship for χ for the determination of the shear strength of unsaturated soils. Géotechnique, 2, 1-7.

Khalili, N., Geiser, F. and Blight, G.E. (2004). Effective stress in unsaturated soils: review with new evidence. International Journal of Geomechanics, 2, 115-126.

Khalili, N., Uchaipichat, A. and Javadi, A.A. (2010). Skeletal thermal expansion coefficient and thermo-hydro-mechanical constitutive relations for saturated homogeneous porous media. Mechanics of Materials, 42, 593-598.

Khorshidi, M., Lu, N., Akin, I.D. and Likos, W.J. (2017). Intrinsic relationship between specific surface area and soil water retention. Journal of Geotechnical and Geoenvironmental Engineering, 143, 04016078.

Knutsson, S. (1983). On the thermal conductivity and thermal diffusivity of highly compacted bentonite. Technical Report 83-72. University of Lulea, Lulea, Sweden.

Komine, H. (2004). Simplified evaluation for swelling characteristics of bentonites. Engineering Geology, 71, 265-279.

Komine, H. and Ogata, N. (1994). Experimental study on swelling characteristics of compacted bentonite. Canadian Geotechnical Journal, 31, 478-490.

Komine, H., Yasuhara, K. and Murakami, S. (2009). Swelling characteristics of bentonites in artificial seawater. Canadian Geotechnical Journal, 46 (2), 177-189.

Krebs, R.D., Thomas, G.W. and Moore, J.E. (1960). Anion influence on some soil physical properties. Clays and Clay Minerals, 9, 260-268.

Kuligiewicz, A. and Derkowski, A. (2017). Tightly bound water in smectites. American Mineralogist, 102, 1073-1090.

Laird, D.A. (2006). Influence of layer charge on swelling of smectites. Applied Clay Science, 34, 74-87.

Laloui, L. and Cekerevac, C. (2003). Thermo-plasticity of clays: an isotropic yield mechanism. Computers and Geotechnics, 30, 649-660.

Lanyon, G.W. and Gaus, I. (2016). Main outcomes and review of the FEBEX in situ test (GTS) and mock-up after 15 years of operation. NAGRA Technical Report 15-04.

Lambe, T.W. (1958). The engineering behaviour of compacted clay. Journal of Soil Mechanics and Foundation Division, ASCE, 84 (2), 1-35.

Lambe, T.W. (1960a). The character and identification of expansive soils. Technical Report FHA-701, Federal Housing Administration. Washington D.C., USA.

Lambe, T.W. (1960b). The structure of compacted clay. Journal of the Soil Mechanics and Foundation Engineering Division, ASCE, 125, 682-706.

Lambe, T.W. and Whitman, R.V. (1979). Mecánica de Suelos. Editorial Limusa, México.

Leroueil, S. and Vaughan, P.R. (1990). The general and congruent effects of structure in natural soils and weak rocks. Géotechnique, 40 (3), 467-488.

Lipinski, M.J. and Wdowska, M.K. (2011). A stress history and strain dependent stiffness of overconsolidated cohesive soil. Annals of Warsaw University of Life Sciences – SGGW, Land Reclamation, 43 (2), 207-216.

Lloret, A. and Villar, M.V. (2007). Advances on the knowledge of the thermo-hydro-mechanical behaviour of heavily compacted "FEBEX" bentonite. Physics and Chemistry of the Earth, 32, 701-715.

Lloret, A., Romero, E. and Villar, M.V. (2004). FEBEX II Project Final report on thermo-hydro-mechanical laboratory tests. Publicación Técnica ENRESA 10/04. Madrid, Spain.

Lloret, A., Villar, M.V., Sánchez, M., Gens, A., Pintado, X. and Alonso, E.E. (2003). Mechanical behaviour of heavily compacted bentonite under high suction changes. Géotechnique, 53 (1), 27-40.

Low, P.F. (1976). Viscosity of interlayer water in montmorillonite. Soil Science Society of America Journal, 40 (4), 500-504.

Low, P.F. (1979). Nature and properties of water in montmorillonite-water system. Soil Science Society of America Journal, 43, 651-658.

Lutenegger, A.J. and Cerato, A.B. (2001). Surface area and engineering properties of fine-grained soils. In: Proceedings of the 15th International Conference on Soil Mechanics and Geotechnical Engineering, Vol 1. A. A. Balkema. August 27-31, 2001. Istanbul, Turkey. 603-606.

Macari, E.J., Weihe, S. and Arduino, P. (1997). Implicit integration of elastoplastic constitutive models for frictional materials with highly non-linear hardening functions. Mechanics of Cohesive-frictional Materials, 2, 1-29.

Macht, F., Eusterhues, K., Pronk, G.J. and Totsche, K.U. (2011). Specific surface area of clay minerals: Comparison between atomic force microscopy measurements and bulk-gas (N_2) and –liquid (EGME) adsorption methods. Applied Clay Science, 53, 20-26.

Mahiya, G. (1999). Experimental measurement of steam-water relative permeability. Master Thesis. Stanford University, Stanford, California, USA.

Malmberg, C.G. and Maryott, A.A. (1956). Dielectric constant of water from 0° to 100°C. Journal of Research of the National Bureau of Standards, 56 (1): 2641.

Manca, D. (2015). Hydro-chemo-mechanical characterisation of sand/bentonite mixtures, with a focus on the water and gas transport properties. PhD Thesis. École Polytechnique Fédérale de Lausanne, Lausanne, Switzerland.

Marjavaara, P., Holt, E. and Sjöblom, V. (2013). Customized bentonite pellets: manufacturing, performance and gap filling properties. Working Report 2012-62. POSIVA OY, Olkiluoto, Finland.

Martin, T.R. (1962). Adsorbed water on clay: a review. In: Proceedings of the 9th National Conference on Clays and Clay Minerals. Purdue University Pergamon Press. October 5-8, 1960. Lafayette, Indiana, USA. 28-70.

Mašin, D. (2011). An effective stress based model for the dependency of a water retention curve on void ratio. In: Unsaturated Soils, Vol. 2. Alonso, E. and Gens, A. (Eds.). Taylor & Francis Group, London, UK. 863-868.

Mašín, D. (2013). Double structure hydromechanical coupling formalism and a model for unsaturated expansive clays. Engineering Geology, 165, 73-88.

Mašín, D. and Khalili, N. (2012). A thermo-mechanical model for variably saturated soils based on hypoplasticity. International Journal for Numerical and Analytical Methods in Geomechanics, 36 (12), 1461-1485.

Mašín, D. and Khalili, N. (2016). Swelling phenomena and effective stress in compacted expansive clays. Canadian Geotechnical Journal, 53 (1), 134-147.

Mata, C. and Ledesma, A. (2003). Hydro-mechanical behaviour of bentonite-based mixtures in engineered barriers. In: Proceedings of the International Workshop Large Scale Field Tests in Granite. Advances in Understanding and Research Needs. November 12-14, 2003. Sitges, Spain.

Mayor, J.C. and Velasco, M. (2008). Ventilation Test (VE) Experiment: Final activity report for ENRESA, WP 4.3. The Ventilation Experiment Phase II (Synthesis report). NF-PRO Deliverable D4.3.18. Madrid, Spain.

Mayor, J.C., García-Siñeriz, J.L., Velasco, M., Gómez-Hernández, J., Lloret, A., Matray, J.M., Coste, F., Giraud, A., Rothfuchs, T., Marschall, P., Rösli, U. and Mayer, G. (2005). Ventilation experiment in Opalinus Clay for the management of radioactive waste. ENRESA Technical Report 07/2005. Madrid, Spain.

McKinstry, H.A. (1965). Thermal expansion of clay minerals. The American Mineralogist, 50, 212-222.

Megaw, H.D. (1933). The thermal expansions of certain crystals with layer lattices. In: Proceedings of the Royal Society of London, Vol 142, 198-214.

Melamed, A. and Pitkänen, P. (1996). Chemical and mineralogical aspects of water-bentonite interaction in nuclear fuel disposal conditions. Research Notes 1766. VTT Communities and Infrastructure, Meddelanden, Finland.

Mesri, G. and Olson, R.E. (1971). Mechanisms controlling the permeability of clays. Clays and Clay Minerals, 19, 151-158.

Milly, P.C.D. (1984). A mass-conservative procedure for time stepping in models of unsaturated flow. In: Proceedings of the 5th International Conference on Finite Elements in Water Resources. Springer-Verlag, New York, NY, USA. 103-112.

Mitchell, J.K. (1976). The properties of cement-stabilized soils. In: Proceeding of Residential Workshop on Materials and Methods for Low Cost Road, Rail, and Reclamation Works. University of New South Wales, Leura, Australia. 365-404.

Mitchell, J.K. (1993). Fundamentals of Soil Behavior. 2nd Edition. John Wiley & Sons Inc. New York, USA.

Mitchell, J.K. and Campanella, R.G. (1963). Creep studies on saturated clays. In: Symposium on Laboratory Shear Testing of Soils, ASTM-NRC. Special Technical Publication 361. September 1963. Ottawa, Canada.

Mitchell, J.K. and Soga, K. (2005). Fundamentals of Soil Behavior. 3rd Edition. John Wiley & Sons Inc. New York, USA.

Molinero, A., Mokni, N., Delage, P., Cui, Y.-J., Tang, A.M., Aimedieu, P., Bernier, F. and Bornert, M. (2017). In-depth characterization of a mixture composed of powder/pellets MX80 bentonite. Applied Clay Science, 135, 538-546.

Mooney, R.W., Keenan, A.G. and Wood, L.A. (1952). Adsorption of water vapor by montmorillonite. I. Heat of desorption and application of BET theory. Journal of the American Chemical Society, 74 (6), 1367-1371.

Morin, R. and Silva, A.J. (1984). The effects of high pressure and high temperature on some physical properties of ocean sediments. Journal of Geophysical Research, 89 (B1), 511-526.

Mualem, Y. and Dagan, G. (1978). Hydraulic conductivity of soils: unified approach to the statistical models. Soil Science Society of America Journal, 42, 392-395.

Mualem, Y. and Miller, E.E. (1979). A hysteresis model based on an explicit domain-dependence function. Soil Science Society of America Journal, 43, 1067-1073.

Muhunthan, B. (1991). Liquid limit and surface area of clays. Géotechnique, 41 (1), 135-138.

Mulla, D.J., Low, P.F. and Roth, C.B. (1985). Measurement of the specific surface area of clays by internal reflectance spectroscopy. Clays and Clay Minerals, 33 (5), 391-396.

Müller, H.R., Garitte, B., Vogt, T., Köhler, S., Sakaki, T., Weber, H., Spillmann, T., Hertrich, M., Becker, J.K., Giroud, N., Cloet, V., Diomidis, N. and Vietor, T. (2017). Implementation of the full-scale emplacement (FE) experiment at the Mont Terri rock laboratory. Swiss Journal of Geosciences, 110, 287-306.

Murthy, V.N.S. (2002). Geotechnical Engineering: Principles and Practices of Soil Mechanics and Foundation Engineering. CRC Press. New York, USA.

Nadeau, P.H. (1985). The physical dimensions of fundamental clay particles. Clay Minerals, 20, 499-514.

Nagaraj, H.B., Mohammed Munnas, M. and Sridharan, A. (2009). Critical evaluation of determining swelling pressure by swell-load method and constant volume method. Geotechnical Testing Journal, 32 (4), 305-314.

Navarro, V. and Alonso, E. E. (2001). Secondary compression of clays as a local dehydration process. Géotechnique, 51 (10), 859-869.

Nayak, G.C. and Zienkiewicz, O.C. (1972). Elasto-plastic analysis – a generalization for constitutive relations including strain softening. International Journal for Numerical Methods in Engineering, 5, 113-135.

NDA (2011). Nuclear Decommissinioning Authority Strategy: effective from April 2011. (http://www.officialdocuments.gov.uk/)

NDA (2014). Geological disposal: A review of the development of bentonite barriers in the KBS-3V disposal concept. NDA Technical Note 21665941. Nuclear Decommissioning Authority, UK.

NDA (2016). Geological disposal: Engineered barrier system. Status Report. NDA Report DSSC/452/01. Radioactive Waste Management, UK.

Nelson, J.D. and Miller, D.J. (1992). Expansive soils: problems and practice in foundation and pavement engineering. John Wiley & Sons, Inc. New York, USA.

Nikooee, E., Habibagahi, G. and Ghahramani, A. (2011). Determination of the effective stress parameter: A pore network study. In: Unsaturated Soils, Vol. 2. Alonso, E. and Gens, A. (Eds.). Taylor & Francis Group, London, UK. 901-905.

Nimmo, J.R. (1992). Semi-empirical model of soil water hysteresis. Soil Science Society of America Journal, 56, 1723-1730.

Nishimura, T., Hirabayashi, Y., Fredlund, D.G. and Gan, J.K-M (1999). Influence of stress history on the strength parameters of an unsaturated statically compacted soil. Canadian Geotechnical Journal, 36 (2), 251-261.

Northey, R.D. (1950). An experimental study of the structural sensitivity of clays. PhD Thesis. University of London, London, UK.

O'Connor, P. (2001). Constant-pressure measurement of steam-water relative permeability. Master Thesis. Stanford University, Stanford, California, USA.

OECD NEA (1995). The Environmental and ethical basis of geological disposal of long-lived radioactive wastes. A Collective Opinion of the Radioactive Waste Management Committee of the OECD Nuclear Energy Agency (NEA). OECD, Paris, France.

Olchawa, A. and Gorączko, A. (2012). The relationship between the liquid limit of clayey soils, external specific surface area and the composition of exchangeable cations. Journal of Water and Land Development, 17, 83-88.

Olchitzky, E. (2002). Couplage hydromécanique et perméabilité d'une argile gonflante non saturée sous sollicitations hydriques et thermiques: courbe de sorption et perméabilité à l'eau. PhD Thesis. Ecole Nationale des Ponts et Chaussées, Marne La Vallee, Paris, France.

Olivella, S. (1995). Nonisothermal multiphase flow of brine and gas through saline media. PhD Thesis. Universitat Politècnica de Catalunya, Barcelona, Spain.

Olivella, S. and Gens, A. (2000). Vapour transport in low permeability unsaturated soils with capillary effects. Transport in Porous Media, 40, 219-241.

Olivella, S., Carrera, J., Gens, A. and Alonso, E.E. (1994). Non-isothermal multiphase flow of brine and gas through saline media. Transport in Porous Media, 15, 271-293.

Olivella, S., Gens, A., Carrera, J. and Alonso, E.E. (1996). Numerical formulation for a simulator (CODE_BRIGHT) for the coupled analysis of saline media. Engineering Computations, 13 (7), 87-112.

Olivella, S., Vaunat, J. and Rodriguez-Domo, A. (eds.) (2020). CODE_BRIGHT 2020: User's Guide. UPC Geomechanical Group. Universitat Politècnica de Catalunya, Barcelona, Spain. (https://deca.upc.edu/en/projects/code_bright)

Oloo, S., Schreiner, H.D. and Burland, J.B. (1987). Identification and classification of expansive soils. In: Proceedings of the 6th International Conference on Expansive Soils. December 1987. New Delhi, India. 23-29.

Ortiz, M. and Simo, J.C. (1986). Analysis of a new class of integration algorithms for elastoplastic constitutive relations. International Journal for Numerical Methods in Engineering, 23, 356-366.

Oscarson, D.W. and Dixon, D.A. (1989). The effect of steam on montmorillonite. Applied Clay Science, 4, 279-292.

Oweis, I.S. and Khera, R.P. (1998). Geotechnology of Waste Management. PWS Publishing. Boston, USA.

Owen, D.R.J. and Hinton, E. (1980). Finite elements in Plasticity: Theory and Practice. Pineridge Press. Swansea, UK.

Paaswell, R.E. (1967). Temperature effects on clay soil consolidation. Journal of the Soil Mechanics and Foundation Engineering Division, ASCE, 93 (SM3), 9-22.

Palacios, B., Rey, M., García-Siñeriz, J.L., Villar, M.V., Mayor, J.C. and Velasco, M. (2013). Engineered Barrier Emplacement Experiment in Opalinus Clay: "EB" Experiment. As-built of dismantling operation. PEBS Deliverable nº: D2.1-4.

Palciauskas, V.V. and Domenico, P.A. (1982). Characterization of drained and undrained response of thermally loaded repository rocks. Water Resources Research, 18 (2), 281-290.

Papafotiou, A., Li, C. and Kober, F. (eds.) (2017). Pre-dismantling THM modelling of the FEBEX in situ experiment. NAGRA Arbeitsbereicht NAB 16-22. Wettingen, Switzerland.

Pedroso, D.M. and Farias, M.M. (2005). Implicit and Explicit numerical integration schemes applied to elastoplastic constitutive laws for soils. In: IWS-Fortaleza – 2nd International Workshop in Computational Geotechnics. January 2005. Fortaleza, Brazil. 13 pp.

Pereira, J.-M., Coussy, O., Alonso, E.E., Vaunat, J. and Olivella, S. (2011). Is the degree of saturation a good candidate for Bishop's χ parameter? In: Unsaturated Soils, Vol. 2. Alonso, E. and Gens, A. (Eds.). Taylor & Francis Group, London, UK. 913-919.

Perkins, W.W. (1995). Ceramic Glossary. The American Ceramic Society. Westerville, Ohio, USA.

Pham, H.Q., Fredlund, D.G. and Barbour, S.L. (2005). A study of hysteresis models for soil-water characteristic curves. Canadian Geotechnical Journal, 42, 1548-1568.

Philip, J. and de Vries, D. (1957). Moisture movement in porous materials under temperature gradients. Eos, Transactions, American Geophysical Union (AGU), 38 (2), 222-232.

Philip, J.R. (1964). Similarity hypothesis for capillary hysteresis in porous materials. Journal of Geophysical Research, 69, 1553-1562.

Pintado, X. (1999). Ensayos THM para el Proyecto FEBEX realizados por la UPC-DIT. Report 70-UPC-M-0-03. Barcelona, Spain.

Pinto, C.S. (2000). Curso básico de Mecânica dos Solos em 16 aulas. Oficina de Textos. São Paulo, Brazil.

Piquemal, J. (1994). Saturated steam relative permeabilities of unconsolidated porous media. Transport in Porous Media, 17, 105-120.

Pitzer, K.S. (1983). Dielectric constant of water at very high temperature and pressure. In: Proceedings of the National Academy of Sciences of the United States of America (PNAS), 80 (14), 4575-4576.

Plötze, M. and Weber, H.P. (2007). ESDRED: Emplacement tests with granular bentonite MX-80 – Laboratory results from ETH Zürich. NAGRA Arbeitsbericht NAB 07-24. NAGRA, Wettingen, Switzerland.

Polidori, E. (2007). Relationship between the Atterberg limits and clay content. Soils and Foundations, 47 (5), 887-896.

Post, J.L. and Paduana, J.A. (1969). Soil stabilization by incipient fusion. Highway Research Board, Special Report 103. National Academy of Sciences, Washington, D.C., USA. 243-253.

Potts, D.M. and Ganendra, D. (1994). An evaluation of substepping and implicit stress point algorithms. Computer Methods in Applied Mechanics and Engineering, 119, 341-354.

Potts, D.M. and Gens, A. (1985). A critical assessment of methods of correcting for drift from the yield surface in elasto-plastic finite element analysis. International Journal for Numerical and Analytical Methods in Geomechanics, 9, 149-159.

Potts, D.M. and Zdravković, L. (1999). Finite element analysis in geotechnical engineering: Theory. Thomas Telford Publishing. London. UK.

Pousada, E. (1984). Deformabilidad de arcillas expansivas bajo succión controlada. PhD Thesis. Universidad Politécnica de Madrid, Madrid, Spain.

Prat, P. and Gens, A. (2003). Leyes de Comportamiento de Materiales. In: Curso de Máster – Métodos Numéricos para Cálculo y Diseño en Ingeniería. Febrero 2003. Universitat Politècnica de Catalunya, Barcelona, Spain.

Pusch, R. (1982). Mineral-water interactions and their influence on the physical behaviour of highly compacted Na-bentonite. Canadian Geotechnical Journal, 19, 381-387.

Pusch, R. (2000). On the effect of hot water vapor on MX-80 clay. SKB Technical Report TR-00-16. Stockholm, Sweden.

Pusch, R. (2001a). Experimental study of the effect of high porewater salinity on the physical properties of a natural smectite clay. SKB Technical Report, TR-01-07. Stockholm, Sweden.

Pusch, R. (2001b). The microstructure of MX-80 clay with respect to its bulk physical properties under different environmental conditions. SKB Technical Report, TR-01-08. Stockholm, Sweden.

Pusch, R., Bluemling, P. and Johnson, L. (2003). Performance of strongly compressed MX-80 pellets under repository-like conditions. Applied Clay Science, 23, 239-244.

Pusch, R., Drawrite, A.B., Yong, R.N. and Nakano, N. (2010). Stiffening of smectite buffer clay by hydrothermal effects. Engineering Geology, 116, 21-31.

Pusch, R., Karnland, O. and Hokmark, H. (1990). GMM – A general microstructural model for qualitative and quantitative studies of smectite clays. SKB Technical Report 90-43. Stockholm, Sweden.

Pusch, R., Přikryl, R., Weishauptová, Z., Xiaodong, L. and Knutsson, S. (2012). Role of clay microstructure in expandable buffer clay. Journal of Purity, Utility Reaction and Environment, 1 (6), 267-292.

Pusch, R., Takase, H. and Benbow, S. (1998). Chemical processes causing cementation in heat-affected smectite – the Kinnekulle bentonite. SKB Technical Report 98-25. Stockholm, Sweden.

Pytte, A.M. and Reynolds, R.C. (1989). The thermal transformation of smectite to illite. In: Thermal History of Sedimentary Basins. Naeser, N.D. and McCulloh, T.H. (Eds.). Springer. New York, USA. 133-140.

Quigley, R.M. and Fernandez, F. (1989). Clay/organic interactions and their effect on the hydraulic conductivity of barrier clays. In: Proceedings of the International Symposium on Contaminant Transport in Groundwater. A. A. Balkema. Stuttgart, Germany. 259-266.

Ravindra Reddy, T., Kaneko, S., Endo, T. and Lakshmi Reddy, S. (2017). Spectroscopic characterization of bentonite. Journal of Lasers, Optics & Photonics, 4 (3): 171.

Reeve, M.J., Hall, D.G.M. and Bullock, P. (1980). The effect of soil composition and environmental factors on the shrinkage of some clayey British soils. Journal of Soil Science, 31, 429-442.

Reschke, A.E. and Haug, M.D. (1991). The physico-chemical properties of bentonites and the performance of sand-bentonite mixtures. In: Proceedings of the 44th Canadian Geotechnical Conference. September 29 – October 2, 1991. Calgary, Alberta, Canada. 62:1 – 62:10.

Rieke, R.D. (1982). The role of specific surface area and related index properties in the frost susceptibility of soils. Master Thesis. Oregon State University, Oregon, USA.

Rizzi, M., Seiphoori, A., Ferrari, A., Ceresetti, D. and Laloui, L. (2012). Analysis of the behaviour of granular MX-80 bentonite in THM processes. Nagra-Aktennotiz AN 12-102. Wettingen, Switzerland.

Romero, E. (1999). Characterisation and Thermo-hydro-mechanical behaviour of unsaturated Boom Clay: an experimental study. PhD Thesis. Universitat Politècnica de Catalaunya, Barcelona, Spain.

Romero, E. (2013). A microstructural insight into compacted clayey soils and their hydraulic properties. Engineering Geology, 165, 3-19.

Romero, E., Della Vecchia, G. and Jommi, C. (2011). An insight into the water retention properties of compacted clayey soils. Géotechnique, 61 (4), 313-328.

Romero, E., Gens, A. and Lloret, A. (1999). Water permeability, water retention and microstructure of unsaturated compacted Boom Clay. Engineering Geology, 54, 117-127.

Romero, E., Gens, A. and Lloret, A. (2001). Temperature effects on the hydraulic behaviour of an unsaturated clay. Geotechnical and Geological Engineering, 19, 311-332.

Romero, E., Gens, A. and Lloret, A. (2003). Suction effects on a compacted clay under non-isothermal conditions. Géotechnique, 53 (1), 65-81.

Romero, E., Villar, M.V. and Lloret, A. (2005). Thermo-hydro-mechanical behaviour of two heavily overconsolidated clays. Engineering Geology, 81, 255-268.

Ross, G.J. (1978). Relationships of specific surface area and clay content to shrink-swell potential of soils having different clay mineralogical compositions. Canadian Journal of Soil Science, 58, 159-166.

Rothfuchs, T., Czaikowski, O., Hartwig, L., Hellwald, K., Komischke, M., Miehe, R. and Zhang, C.-L. (2012). Self-sealing Barriers of sand/bentonite mixtures in a clay repository – SB-Experiment in the Mont Terri Rock Laboratory. Final Report. GRS-302, Braunschweig, Germany.

Rouainia, M. and Wood, D.M. (2001). Implicit numerical integration for a kinematic hardening soil plasticity model. International Journal for Numerical and Analytical Methods in Geomechanics, 25 (13), 1305-1325.

Rueedi, J., Marschall, P., Manca, D., Ferrari, A., Monfared, M., Laloui, L., Kulenkampff, J., Gründig, M., Lippmann-Pipke, J. and Kontar, K. (2013). FORGE (Fate of Repository Gases). Final Laboratory Report. Deliverables D3.34 and D3.36. NAGRA Arbeitsbericht NAB 12-62. NAGRA, Wettingen, Switzerland.

Ruiz, D.F. (2020). Hydro-mechanical analysis of expansive clays: Constitutive and numerical modelling. PhD Thesis. Universitat Politècnica de Catalunya, Barcelona, Spain.

Runesson, K. (1987). Implicit integration of elastoplastic relations with reference to soils. International Journal for Numerical and Analytical Methods in Geomechanics, 11 (3), 315-321.

Rutqvist, J., Zheng, L., Chen, F., Liu, H.-H. and Birkholzer, J. (2014). Modeling of coupled thermo-hydro-mechanical processes with links to Geochemistry associated with bentonite-backfilled repository tunnels in clay formations. Rock Mechanics and Rock Engineering, 47, 167-186.

Saiyouri, N., Tessier, D. and Hicher, P.Y. (2004). Experimental study of swelling in unsaturated compacted clays. Clay Minerals, 39, 469-479.

Sakaguchi, I., Momose, T. and Kasubuchi, T. (2007). Decrease in thermal conductivity with increasing temperature in nearly dry sandy soil. European Journal of Soil Science, 58, 92-97.

Salager, S., François, B., El Youssoufi, M.S., Laloui, L. and Saix, C. (2008). Experimental investigations of temperature and suction effects on compressibility and pre-consolidation pressure of a sandy silt. Soils and Foundations, 48 (4), 453-466.

Salas, J.A.J. and Serratosa, J.M. (1957). Foundations on swelling clays. In: Proceedings of the 4th International Conference on Soil Mechanics and Foundation Engineering, Vol 1. London, UK. 424-428.

Saltelli, A., Andres, T.H. and Homma, T. (1993). Sensitivity analysis of model output: An investigation of new techniques. Computational Statistics & Data Analysis, 15, 211-238.

Samper, J., Zheng, L., Montenegro, L., Fernandez, A.M. and Rivas, P. (2008). Coupled thermo-hydro-chemical models of compacted bentonite after FEBEX in situ test. Applied Geochemistry, 23, 1186-1201.

Samuels, S.G. (1950). The effect of base exchange on the engineering properties of soils. Building Research Station Note C176. Garston, Watford, Hertfordshire, England.

Sanavia, L., Bonetto, A. and Laloui, L. (2014). Multi-physics modelling of the consolidation processes in variably saturated elasto-plastic soils due to high temperature. In: 11th World Congress of Computational Mechanics WCCM 2014. July 20-25, 2014. Barcelona, Spain. 3230-3239.

Sánchez, J. and Schechter, R. (1990). Steady adiabatic, two-phase flow of steam and water through porous media. SPE Reservoir Engineering, 293-300.

Sánchez, M. (2004). Thermo-hydro-mechanical coupled analysis in low permeability media. PhD Thesis. Universitat Politècnica de Catalunya, Barcelona, Spain.

Sánchez, M. and Gens, A. (2006). FEBEX Project: Final report on thermo-hydro-mechanical modelling. ENRESA Technical Report 05-2/2006. Madrid, Spain.

Sánchez, M., Gens, A., Guimarães, L. do N. and Olivella, S. (2005). A double structure generalized plasticity model for expansive materials. International Journal for Numerical and Analytical Methods in Geomechanics, 29, 751-787.

Sánchez, M., Gens, A., Guimarães, L.N. and Olivella, S. (2008). Implementation algorithm of a generalised plasticity model for swelling clays. Computers and Geotechnics, 35, 860-871.

Santamarina, J.C., Klein, K.A., Wang, Y.H. and Prencke, E. (2002). Specific surface: determination and relevance. Canadian Geotechnical Journal, 39, 233-241.

Satik, C. (1998). A measurement of steam-water relative permeability. In: Proceedings 23rd Workshop on Geothermal Reservoir Engineering. Stanford University, Stanford, California, USA. 120-126.

Savage, D., Lind, A. and Arthur, R.C. (1999). Review of the properties and uses of bentonite as a buffer and backfill material. SKI Report 99:9. Stockholm, Sweden.

Schanz, T. and Al-Badran, Y. (2014). Swelling pressure characteristics of compacted Chinese Gaomiaozi bentonite GMZ01. Soils and Foundations, 54 (4), 748-759.

Schiffmann, R.L. (1971). A thermoelastic theory of consolidation. In: Environmental and Geophysical Heat Transfer. Cremen, C.J., Kreith, F. and Clark, J.A. (Eds.). American Society of Mechanical Engineers (ASME). New York, NY, USA. 78-84.

Schofield, A.N. and Wroth, C.P. (1968). Critical state soil mechanics. McGraw-Hill. London, UK.

Schramm, L.L. and Kwak, J.C.T. (1982). Influence of exchangeable cation composition on the size and shape of montmorillonite particles in dilute suspension. Clays and Clay Minerals, 30 (1), 40-48.

Schuster, K., Furche, M., Velasco, M., Gaus, I., Trick, T., García-Siñeriz, J.L., Rey, M., Schulte, F., Herrero, S.S., Tietz, T. and Mayor, J.C. (2014). Engineered barrier emplacement experiment in Opalinus Clay: "EB" Experiment. Horizontal borehole results (geophysics, hydro test, laboratory test). Deliverable D2.1-1. Madrid, Spain.

Sears, G.W. (1956). Determination of specific surface area of colloidal silica by titration with sodium hydroxide. Analytical Chemistry, 28 (12), 1981-1983.

Seed, H.B., Woodward, R.J. and Lundgren, R. (1962). Prediction of swelling potential for compacted clays. Journal of the Soil Mechanics and Foundations Division, ASCE, 88 (SM3), 53-87.

Seiphoori, A., Ferrari, A. and Laloui, L. (2014). Water retention behaviour and microstructural evolution of MX-80 bentonite during wetting and drying cycles. Géotechnique, 9, 721-734.

Sellin, P. and Leupin, O.X. (2013). The use of clay as an engineered barrier in radioactive-waste management – A review. Clays and Clay Minerals, 61 (6), 477-498.

Shear, D.L., Olsen, H.W. and Welson, K.R. (1992). Effect of desiccation on the hydraulic conductivity versus void relationship for a natural clay. Transportation Research Record, 1369, 130-135.

Shepard, M.D. (1998). Thermal treatment of expansive soil. Master Thesis. University of Colorado, Denver, USA.

Shetty, R., Singh, D.N. and Ferrari, A. (2019). Volume change characteristics of fine-grained soils due to sequential thermo-mechanical stresses. Engineering Geology, 253, 47-54.

Shuai, F. (1996). Simulation of swelling pressure measurements on expansive soils. PhD Thesis. University of Saskatchewan, Saskatoon, Canada.

Simmons, K.B. (1991). Limitations of residential structures on expansive soils. Journal of Performance of Constructed Facilities, 5 (4), 258-270.

Skauge, A., Fuller, N. and Hepler, L.G. (1983). Specific heats of clay minerals: sodium and calcium kaolinites, sodium and calcium montmorillonites, illite, and attapulgite. Thermochimica Acta, 61, 139-145.

Skempton, A.W. (1953). The colloidal "activity" of clays. In: Proceedings of the 3rd International Conference on Soil Mechanics and Foundation Engineering. Zurich, Switzerland. 57-61.

Sloan, S.W. (1987). Sub-stepping schemes for the numerical integration of elasto-plastic stress-strain relations. International Journal for Numerical Methods in Engineering, 24, 893-911.

Sloan, S.W. and Booker, J.R. (1986). Removal of singularities in Tresca and Mohr-Coulomb yield functions. Communications in Applied Numerical Methods, 2 (2), 173-179.

Sloan, S.W. and Booker, J.R. (1992). Integration of Tresca and Mohr-Coulomb constitutive relations in plane strain elastoplasticity. International Journal for Numerical Methods in Engineering, 33, 163-196.

Sloan, S.W. and Randolph, M.F. (1982). Numerical prediction of collapse loads using finite element methods. International Journal for Numerical and Analytical Methods in Geomechanics, 6, 47-76.

Sloan, S.W., Abbo, A.J. and Sheng, D. (2001). Refined explicit integration of elastoplastic models with automatic error control. Engineering Computations, 18, 121-154.

Smith, E.D., Szidarovszky, F., Karnavas, W.J. and Bahill, A.T. (2008). Sensitivity analysis, a powerful system validation technique. The Open Cybernetics and Systemics Journal, 2, 39-56.

Smits, K.M., Sakaki, T., Howington, S.E., Peters, J.F. and Illangasekare, T.H. (2013). Temperature dependence of thermal properties of sands across a wide range of temperatures (30-70˚C). Vadose Zone Journal, 138 (4), 2256-2265.

Snethen, D.R., Johnson, L.D. and Patrick, D.M. (1977). An evaluation of expedient methodology for identification of potentially expansive soils. U.S. Army Engineer Waterways Experiment Station, USAEWES. Report FHWA-RD-77-94. Vicksburg, Mississippi, USA.

Sołowski, W.T. and Gallipoli, D. (2006). A stress-strain integration algorithm for unsaturated soil elastoplasticity with automatic error control. Numerical Methods in Geotechnical Engineering, 113-118.

Sołowski, W.T. and Gallipoli, D. (2010). Explicit integration with error control for the Barcelona Basic Model, Part I: Algorithms formulations. Computers and Geotechnics, 37, 59-67.

Sposito, G. and Prost, R. (1982). Structure of water adsorbed on smectites. Chemical Reviews, 82 (6), 554-573.

Sridharan, A. and Prakash, K. (2000). Classification procedures for expansive soils. Proceeding of the Institution of Civil Engineers: Geotechnical Engineering, 143, 235-240.

Sridharan, A. and Rao, G.V. (1975). Mechanisms controlling the liquid limits of clays. In: Proceedings of Istanbul Conference on Soil Mechanics and Foundation Engineering, Vol 1. Istanbul, Turkey. 75-84.

Sridharan, A., Rao, A.S. and Sivapullaiah, P.V. (1986a). Swelling pressure of clays. Geotechnical Testing Journal, 9 (1), 24-33.

Sridharan, A., Rao, S.M. and Murthy, N.S. (1986b). Liquid limit of montmorillonite soils. Geotechnical Testing Journal, 9 (3), 156-159.

Stavridakis, E.I. (2006). Assessment of anisotropic behaviour of swelling soils on ground and construction work. In: Expansive Soils: Recent advances in characterization and treatment. Al-Rawas, A.A. and Goosen, M.F.A. (Eds.). Taylor & Francis. London, UK. 371-384.

Subba Kao, K.S. and Styadas, G. (1987). Swelling potential with cycles of swelling and partial shrinkage. In: Proceedings of the 6th International Conference on Expansive Clays, Vol.1. New Delhi, India. 137-142.

Sultan, N., Cui, Y.-J. and Delage, P. (2010). Yielding and plastic behaviour of Boom clay. Géotechnique, 60 (9), 657-666.

Svensson, D., Dueck, A., Lydmark, S. and Hansen, S. (2011). Alternative buffer material. Status of the ongoing laboratory investigation of reference materials and test package 1. SKB Technical Report TR-11-06. Stockholm, Sweden.

Tamagnini, C., Castellanza, R. and Nova, R. (2004). Implicit integration of constitutive equations in Computational Plasticity. In: Numerical Modelling in Geomechanics. Pastor, M. and Tamagnini, C. (Eds.). Kogan Page Science, London and Sterling, VA. London, UK. 159-175.

Tang, A.-M. and Cui, Y.J. (2005). Controlling suction by the vapor equilibrium technique at different temperatures and its application in determining the water retention properties of MX80 clay. Canadian Geotechnical Journal, 42, 287-296.

Tang, A.-M. and Cui, Y.-J. (2010). Effects of mineralogy on thermo-hydro-mechanical parameters of MX80 bentonite. Journal of Rock Mechanics and Geotechnical Engineering, 2 (1), 91-96.

Tang, A.M., Cui, Y.J., Le, T.T. (2008). A study on the thermal conductivity of compacted bentonites. Applied Clay Science, 41 (3), 181-189.

Tao, L., Xiao-Feng, T., Yu, Z. and Tao, G. (2010). Swelling of K^+, Na^+ and Ca^{2+}-montmorillonites and hydration of interlayer cations: a molecular dynamics simulation. Chinese Physical Society and IOP Publishing Ltd, 19 (10), 109101.

Teodori. S.-P. and Gaus, I. (eds.) (2011). Long term Performance of Engineered Barrier Systems (PEBS). Mont Terri HE-E experiment: as built report. NAB 11-025. NAGRA, Wettingen, Switzerland.

Terzaghi, K. (1936). The shearing resistance of saturated soils and the angle between the planes of shear. In: International Conference on Soil Mechanics and Foundation Engineering. Harvard University Press. Cambridge, Massachusetts, USA. 54-56.

Tessema, G. (1984). Foundations on expansive soils. Journal of EAEA, 6, 13-20.

Thatcher, K.E., Bond, A.E., Robinson, P., McDermott, C., Fraser Harris, A.P. and Norris, S. (2016). A new hydro-mechanical model for bentonite resaturation applied to the SEALEX experiments. Environmental Earth Sciences, 75: 974.

Thury, M. and Bossart, P. (1999). Mont Terri Rock Laboratory: Results of the hydrogeological, geochemical and geotechnical experiments performed in 1996 and 1997. SNHGS Geological Report 23.

Toprak, E., Olivella, S. and Pintado, X. (2016). Coupled THM modelling of engineered barriers for the final disposal of spent nuclear fuel isolation. In: Radioactive Waste Confinement: Clays in Natural and Engineered Barriers. Geological Society, London, Special Publications (Online), 443. 1-17.

Tourchi, S. and Hamidi, A. (2015). Thermo-mechanical constitutive modeling of unsaturated clays based on the critical state concepts. Journal of Rock Mechanics and Geotechnical Engineering, 7, 193-198.

Towhata, I., Kuntiwattanakul, P., Seko, I. and Ohishi, K. (1993). Volume change of clays induced by heating as observed in consolidation tests. Soils and Foundations, 33 (4), 170-183.

Tripathy, S., Bag, R. and Thomas, H.R. (2015). Enhanced isothermal effect on swelling pressure of compacted MX80 bentonite. Engineering Geology for Society and Territory, 6, 537-539.

van Eekelen, H.A.M. (1980). Isotropic yield surface in three dimensions for use in soil mechanics. International Journal for Numerical and Analytical Methods in Geomechanics, 4, 89-101.

Van Geet, M., Bastiaens, W., Volckaert, G., Weetjens, E., Sillen, X., Gens, A., Villar, M.V., Imbert, C., Filippi, M. and Plas, F. (2007). Installation and evaluation of a large-scale in-situ shaft seal experiment in Boom Clay – The RESEAL Project. In: International Meeting on Clays in Natural and Engineered Barriers for Radioactive Waste Confinement. September 17-18, 2007. Lille, France. 189-190.

Van Geet, M., Bastiaens, W., Volckaert, G., Weetjens, E., Sillen, X., Maes, N., Imbert, C., Billaud, P., Touzé, G., Filippi, M., Plas, F., Villar, M.V., García-Gutiérrez, M., Mingarro, M., Gens, A. and Vallejan, B. (2009). RESEAL II: A large-scale in situ demonstration test for repository sealing in an argillaceous host rock– Phase II. RESEAL II Final Report, European Commission, EUR 24161. Luxembourg.

van Genuchten, M.T. (1978). Calculating the unsaturated hydraulic conductivity with a new closed-form analytical model. Water Resources Bulletin 78-WR-08. Department of Civil Engineering, Princeton University, Princeton, New Jersey, USA.

van Genuchten, M.T. (1980). A closed-form equation for predicting the hydraulic conductivity of unsaturated soils. Soil Science Society of America Journal, 44, 892-898.

van Olphen, H. (1963a). An introduction to clay colloid chemistry: for Clay Technologists, Geologists and Soil Scientists. Wiley. New York, USA.

van Olphen, H. (1963b). Compaction of clay sediments in the range of molecular particle distances. Clays and Clay Minerals, 11, 178-187.

Vanapalli, S.K. and Lu, L. (2012). A state-of-the art review of 1-D heave prediction methods for expansive soils. International Journal of Geotechnical Engineering, 6, 15-41.

Vanapalli, S.K., Fredlund, D.G. and Pufahl, D.E. (1999). The influence of soil structure and stress history on the soil-water characteristics of a compacted till. Géotechnique, 49 (2), 143-159.

Vasconcelos, R. and Gens, A. (2015). Modelling infiltration tests on pelletized bentonite under non-isothermal conditions. In: Proceedings of the XIII International Conference on Computational Plasticity (COMPLAS XIII) – Fundamentals and Applications. September 1-3, 2015. Barcelona, Spain. 661-666.

Vasconcelos, R., Gens, A., Vaunat, J., Ruiz, D.F. and Villar, M.V. (2019). Modelling a heating-hydration bentonite-based column test using a double porosity approach. In: Proceedings of the XV International Conference on Computational Plasticity (COMPLAS XV). September 3-5, 2019. Barcelona, Spain.

Vasconcelos, R., Pinyol, N., Alonso, E.E. and Gens (2014). Modelling and interpretation of the EB experiment hydration & Interpretation of the final state of the EB experiment barrier. PEBS Deliverable D3.1-1 and D3.1-2.

(http://www.pebs-eu.de/PEBS/EN/Downloads/downloads_node_en.html)

Vermeer, P.A. (1980). Formulation and analysis of sand deformation problems. PhD Thesis. Department of Civil Engineering, Delft University of Technology, Delft, the Netherlands.

Villar, M.V. (1999). Ensayos THM para el Proyecto FEBEX. FEBEX report 70-IMA-L-0-66. Madrid, Spain.

Villar, M.V. (2002). Thermo-hydro-mechanical characterisation of a bentonite from Cabo de Gata. A study applied to the use of bentonite as sealing material in high level radioactive waste repositories. ENRESA Technical Publishing 01/2002. Madrid, Spain.

Villar, M.V. (2004). Thermo-hydro-mechanical characteristics and processes in the clay barrier of a high level radioactive waste repository. State of the Art Report. CIEMAT Technical Reports 1044. Madrid, Spain.

Villar, M.V. (2005). MX-80 bentonite. Thermo-hydro-mechanical characterisation performed at CIEMAT in the context of the Prototype Project. CIEMAT Technical Report 1053. Madrid, Spain.

Villar, M.V. (2006). FEBEX Project Final Report: Post-mortem bentonite analysis. ENRESA Technical Report 05-1/2006. Madrid, Spain.

Villar, M.V. (2013). Long-term THM tests: isothermal infiltration tests with materials from the HE-E. PEBS Deliverable 2.2-7.2. CIEMAT Technical Report CIEMAT/DMA/2G210/07/2013. Madrid, Spain.

Villar, M.V. and Lloret, A. (2001). Variation of the intrinsic permeability of expansive clays upon saturation. In: Clay Science for Engineering. Adachi, K. and Fukue, M. (Eds.). A.A. Balkema, Rotterdam, the Netherlands. 259-266.

Villar, M.V. and Lloret, A. (2004). Influence of temperature on the hydro-mechanical behaviour of a compacted bentonite. Applied Clay Science, 26 (1-4), 337-350.

Villar, M.V. and Lloret, A. (2007a). Influence of dry density and water content on the swelling of a compacted bentonite. Applied Clay Science, 39, 38-49.

Villar, M.V. and Lloret, A. (2007b). Dismantling of the first section of the FEBEX in situ test: THM laboratory tests on the bentonite blocks retrieved. Physics and Chemistry of the Earth, Parts A/B/C, 32 (8-14), 716-729.

Villar, M.V. and Lloret, A. (2008). Influence of dry density and water content on the swelling of a compacted bentonite. Applied Clay Science, 39 (1), 38-49.

Villar, M.V., Campos, R. and Gutiérrez-Nebot, L. (2014a). EB experiment: Laboratory post-mortem analyses report. PEBS Report D2.1-7. CIEMAT Technical Report CIEMAT/DMA/2G210/01/2014. Madrid, Spain.

Villar, M.V., García-Siñeriz, J.L., Bárcena, I. and Lloret, A. (2005). State of the bentonite barrier after five years operation of an in situ test simulating a high level radioactive waste repository. Engineering Geology, 80 (3-4), 175-198.

Villar, M.V., Gómez-Espina, R. and Gutiérrez-Nebot, L. (2012a). Basal spacings of smectite in compacted bentonite. Applied Clay Science, 65-66, 95-105.

Villar, M.V., Gómez-Espina, R. and Lloret, A. (2010). Experimental investigation into temperature effect on hydro-mechanical behaviours of bentonite. Journal of Rock Mechanics and Geotechnical Engineering, 2 (1), 71-78.

Villar, M.V., Iglesias, R.J. and García-Siñeriz, J.L. (2018). State of the in situ FEBEX test (GTS, Switzerland) after 18 years: a heterogeneous bentonite barrier. Environmental Geotechnics, 80 (3-4), 175-198.

Villar, M.V., Lloret, A. and Romero, E. (2003). Thermo-mechanical and geochemical effects on the permeability of high-density clays. In: Proceedings of the International Workshop Large Scale Field Tests in Granite. Advances in Understanding and Research Needs. November 12-14, 2003. Sitges, Spain.

Villar, M.V., Martín, P.L. and Romero, F.J. (2014b). THM cells for the HE-E test: update of results until February 2014. CIEMAT Technical Report CIEMAT/DMA/2G210/03/2014. Madrid, Spain.

Villar, M.V., Martín, P.L. and Romero, F.J. (2015a). HE-E Experiment: Progress report of a THM cell with MX-80 pellets. *Mont Terri Project TN 2015-44*, Madrid, Spain.

Villar, M.V., Martín, P.L., Gómez-Espina, R., Romero, F.J. and Barcala, J.M. (2012b). THM cells for the HE-E test: setup and first results. PEBS Report D2.2-7.1. CIEMAT Technical Report CIEMAT/DMA/2G210/02/2012. Madrid, Spain.

Villar, M.V., Martín, P.L., Romero, F.J., Gómez-Espina, R., Iglesias, R.J., Gutiérrez-Rodrigo, V. (2015b). HE-E Experiment: Laboratory test in a THM cell with the sand/bentonite mixture. Mont Terri Project TN 2015-43. Madrid, Spain.

Villar, M.V., Martín, P.L., Romero, F.J., Iglesias, R.J. and Gutiérrez-Rodrigo, V. (2016). Saturation of barrier materials under thermal gradient. Geomechanics for Energy and the Environment, 8, 38-51.

Volckaert, G., Dereeper, B., Put, M., Ortiz, L., Gens, A., Vaunat, J., Villar, M.V., Martin, P.L., Imbert, C., Lassabatère, T., Mouche, E., Cany, F. (2000). A large-scale in situ demonstration test for repository sealing in an argillaceous host rock. RESEAL Project – Phase I. European Commission, EUR 19612. Luxembourg.

Voss, C.I. and Provost, A.M. (2010). SUTRA: A model for saturated-unsaturated, variable-density ground-water flow with solute or energy transport. Water-Resources Investigations Report 02-4231. US Geological Survey, Reston, Virginia, USA.

Wagner, J.-F. (2013). Mechanical properties of clays and clay minerals. In: Handbook of Clay Science, Vol. 5. Bergaya, F., Theng, B.K.G. and Lagaly, G. (Eds.). 347-381.

Walsh, J.B. (1973). Theoretical bounds for thermal expansion, specific heat, strain energy due to internal stresses. Journal of Geophysical Research, 78, 7636-7647.

Walsh, K.D., Colby, C.A., Houston, W.N. and Houston, S.L. (2009). Method for evaluation of depth of wetting in residential areas. Journal of Geotechnical and Geoenvironmental engineering, 135 (2), 169-176.

Wang, G. and Wei, X. (2015). Modeling swelling-shrinkage behavior of compacted expansive soils during wetting-drying cycles. Canadian Geotechnical Journal, 52, 783-794.

Wang, M.C., Jao, O. and Ghazal, M.S. (2008). Heating effect of swelling behavior of expansive soils. Geomechanics and Geoengineering, 3 (2), 121-127.

Wang, Q., Tang, A.M., Cui, Y.-J., Barnichon, J.-D., Ye, W.-M. (2013). Investigation of the hydro-mechanical behaviour of compacted bentonite/sand mixture based on the BExM model. Computers and Geotechnics, 54, 46-52.

Wang, Q., Tang, A.M., Cui, Y.-J., Delage, P. and Gatmiri, B. (2012). Experimental study on the swelling behaviour of bentonite/claystone mixture. Engineering Geology, 124, 59-66.

Wang, X., Shao, H., Hesser, J., Zhang, C., Wang, W. and Kolditz, O. (2014). Numerical analysis of thermal impact on hydro-mechanical properties of clay. Journal of Rock Mechanics and Geotechnical Engineering, 6, 405-416.

Warkentin, B.P. (1972). Use of the liquid limit in characterizing clay soils. Canadian Journal of Soil Science, 52 (3), 457-464.

Watson, K.K. (1966). An instantaneous profile method for determining the hydraulic conductivity of unsaturated porous materials. Water Resources Research, 2 (4), 709-715.

Wayllace, A. (2008). Volume change and swelling pressure of expansive clay in the crystalline swelling regime. PhD Thesis. University of Missouri, Columbia, Missouri, USA.

Welty, J.R., Wicks, C.E., Wilson, R.E. and Rorrer, G.L. (2008). Fundamentals of Momentum, Heat and Mass Transfer, 5th ed. John Wiley and Sons, Hoboken, New Jersey, USA.

Wersin, P., Johnson, L.H. and McKinley, I.G. (2007). Performance of the bentonite barrier at temperatures beyond 100˚C: A critical review. Physics and Chemistry of the Earth, 32, 780-788.

West, W.J. (1952). Size determination of clay particles in water suspensions by use of low-angle X-ray diffraction. Journal of Colloid Science, 7 (3), 295-305.

Wheeler, S.J. and Karube, D. (1995). State of the art report: Constitutive modeling. In: Proceedings of the 1st International Conference on Unsaturated Soils (UNSAT'95), Vol. 3. September 6-8. Paris, France. 43-46.

Wheelwright, E.J., Hodges, F.N., Bray, L.A., Westsik, J.H. Jr., Lester, D.H., Nakai, T.L., Spaeth, M.E. and Stula, R.T. (1981). Development of backfill material as an engineered barrier in the waste package system. Interim topical report. Pacific Northwest Laboratory, Richland, WA, USA.

Whitney, G. (1990). Role of water in the smectite-to-illite reaction. Clays and Clay Minerals, 38 (4), 343-350.

Wiebe, B., Graham, J., Tang, X. and Dixon, D. (1998). Influence of pressure, saturation and temperature on the behaviour of unsaturated sand-bentonite. Canadian Geotechnical Journal, 35, 194-205.

Wieczorek, K., Gaus, I., Mayor, J.C., Schuster, K., García-Siñeriz, J.L. and Sakaki, T. (2017). In-situ experiments on bentonite-based buffer and sealing materials at the Mont Terri rock laboratory (Switzerland). Swiss Journal of Geosciences, 110, 253-268.

Wieczorek, K., Miehe, R. and Garitte, B. (2011). Measurement of thermal parameters of the HE-E buffer materials. PEBS Deliverable D2.2-5.

Wieczorek, K., Miehe, R. and Garitte, B. (2013). Thermal characterisation of HE-E buffer. PEBS Deliverable D2.2-9.

Wilson, J. and Bond, A. (2016). Impact of elevated temperatures on bentonite buffers. Technical Report QRS-1384Q-R3, Version 1.2. October 2016.

Wilson, R. and Aifantis, E. (1982). On the theory of consolidation with double porosity. International Journal of Engineering Science, 20 (9), 1019-1035.

Wissmann, J.W. and Hauck, C. (1983). Efficient elastic-plastic finite element analysis with higher order stress point algorithms. Computers and Structures, 17, 89-95.

Wyoming Multi-Hazard Mitigation Plan (2014). Wyoming multi-harzard mitigation plan: Comprehensive update. June 2014. Wyoming Office of Homeland Security. Cheyenne, Wyoming, USA.

Xu, Y., Sun, D., Zeng, Z. and Lv, H. (2019). Temperature dependence of apparent thermal conductivity of compacted bentonites as buffer material for high-level radioactive waste repository. Applied Clay Science, 174, 10-14.

Yahia-Aissa, M., Delage, P. and Cui, Y.J. (2001). Suction-water content relationship in swelling clays. In: Clay Science for Engineering. Adachi, K. and Fukue, M. (Eds.). Rotterdam, the Netherlands. 65-68.

Yang, D.Q., Alonso, E.E. and Rahardjo, H. (1998). Modelling the volumetric behaviour of an unsaturated expansive soil. In: Proceedings of the 2nd International Conference on Unsaturated Soils, Vol. 2. August 1998. Beijing, China. 249-254.

Ye, W.M., Cui, Y.J., Qian, L.X. and Chen, B. (2009). An experimental study of the water transfer through confined compacted GMZ bentonite. Engineering Geology, 108, 169-176.

Ye, W.M., Wan, M., Chen, B., Chen, Y.G., Cui, Y.J. and Wang, J. (2013). Temperature effects on the swelling pressure and saturated hydraulic conductivity of the compacted GMZ01 bentonite. Environmental Earth Sciences, 68, 281-288.

Ye, W.M., Zheng, Z.J., Chen, B., Chen, Y.G., Cui; Y.J. and Wang, J. (2014). Effects of pH and temperature on the swelling pressure and hydraulic conductivity of compacted GMZ01 bentonite. Applied Clay Science, 101, 192-198.

Yilmaz, I. (2006). Indirect estimation of the swelling percent and a new classification of soils depending on liquid limit and cation exchange capacity. International Journal of Geomechanics, 11 (3), 159-166.

Yong, R.N., Champ, R.K. and Warkentin, B.P. (1969). Temperature effect on water retention and swelling pressure of clay soils. Effect of Temperature and Heat on Engineering Behavior of Soils. Special Report 103. Highway Research Board (HRB). Washington D.C., USA. 132-137.

Yong, R.N., Taylor, L. and Warkentin, B.P. (1962). Swelling pressures of sodium montmorillonite at depressed temperature. In: Proceedings of the 11th National Conference on Clays and Clay Minerals, 268-281.

Yoshida, R.T., Fredlund, D.G. and Hamilton, J.J. (1983). The prediction of total heave of a slab-on-grade floor on Regina clay. Canadian Geotechnical Journal, 20 (1), 69-81.

Yukselen, Y. and Kaya, A. (2006). Comparison of methods for determining specific area of soils. Journal of Geotechnical and Geoenvironmental Engineering, 132 (7), 931-936.

Zhao, J., Sheng, D., Rouainia, M. and Sloan, S.W. (2005). Explicit stress integration of complex soil models. International Journal for Numerical and Analytical Methods in Geomechanics, 29 (12), 1209-1229.

Zienkiewicz, O.C. and Taylor, R.L. (2000a). The Finite Element Method. Volume 1: The Basis (5th Edition). Butterworth-Heinemann.

Zienkiewicz, O.C. and Taylor, R.L. (2000b). The Finite Element Method. Volume 2: Solid Mechanics (5th Edition). Butterworth-Heinemann.

APPENDIX A

THE PEGAUS ALGORITHM FOR THE INTERSECTION WITH THE YIELD SURFACE

The Pegasus scheme is able to solve the yield surface intersection problem during the performance of the trial step. Like all the bracketing methods, this algorithm is unconditionally convergent and its convergence rate is quite satisfactory (Sloan *et al.*, 2001). Unlike the Newton-Raphson scheme, the Pegasus algorithm does not require the use of derivatives. Moreover, it combines features from the bisection and the secant methods. Like the bisection method, the iteration procedure starts with two initial values $\alpha^{(0)}$ and $\alpha^{(1)}$ enclosing the intersection point with the yield surface.

Taking into account Equation (5-9) and Equation (5-10), it is assumed that $\alpha^{(0)} = \frac{\Delta\tau_{(i)}^{Peg,(0)}}{\Delta\tau_{(i)}}$ and $\alpha^{(1)} = \frac{\Delta\tau_{(i)}^{Peg,(1)}}{\Delta\tau_{(i)}}$, where $\Delta\tau_{(i)}^{Peg,(l)} = \alpha^{(l)} \cdot \Delta\tau_{(i)}$, with $\Delta\tau_{(i)}^{Peg,(0)} = 0$ and $\Delta\tau_{(i)}^{Peg,(1)} = \Delta\tau_{(i)}$. Consequently, the yield function values at those two points, $F_{LC}^{(0)} = f\left(\alpha^{(0)} \cdot \delta\boldsymbol{\varepsilon}^{g}\right) = f\left(\Delta\tau_{(i)}^{Peg,(0)} \cdot \Delta\boldsymbol{\varepsilon}^{g}\right) = F_{LC}\left(\boldsymbol{\sigma}_{n-1}, p_{0,n-1}^{*}\right)$ and $F_{LC}^{(1)} = f\left(\alpha^{(1)} \cdot \delta\boldsymbol{\varepsilon}^{g}\right) = f\left(\Delta\tau_{(i)}^{Peg,(1)} \cdot \Delta\boldsymbol{\varepsilon}^{g}\right) = F_{LC}\left(\boldsymbol{\sigma}_{n}^{trial}, p_{0,n}^{*,trial}\right)$, have opposite signs, that is, $F_{LC}^{(0)} \cdot F_{LC}^{(1)} < 0$. Assuming the continuity of the yield function F_{LC} in $\left[\tau_{(i-1)}, \tau_{(i)}\right]$, the intermediate value theorem guarantees the existence of a root for this function. At each iteration, the interval containing the intersection point with the yield surface diminishes.

At iteration l ($l \in \mathbb{N}^*$), the estimate value for the root of Equation (5-36), by the Pegasus algorithm, is computed by the following recurrence relation

$$\Delta\tau_{(i)}^{Peg,(l+1)} = \Delta\tau_{(i)}^{Peg,(l)} - \frac{F_{LC}^{(l)}}{F_{LC}^{(l)} - F_{LC}^{(l-1)}} \cdot \left(\Delta\tau_{(i)}^{Peg,(l)} - \Delta\tau_{(i)}^{Peg,(l-1)}\right) \tag{A-1}$$

or, after grouping some of these terms,

$$\Delta\tau_{(i)}^{Peg,(l+1)} = \frac{\Delta\tau_{(i)}^{Peg,(l-1)} \cdot F_{LC}^{(l)} - \Delta\tau_{(i)}^{Peg,(l)} \cdot F_{LC}^{(l-1)}}{F_{LC}^{(l)} - F_{LC}^{(l-1)}} \tag{A-2}$$

where $F_{LC}^{(l)} = f\left(\Delta\tau_{(i)}^{Peg,(l)} \cdot \Delta\boldsymbol{\varepsilon}^{g}\right)$, $F_{LC}^{(l-1)} = f\left(\Delta\tau_{(i)}^{Peg,(l-1)} \cdot \Delta\boldsymbol{\varepsilon}^{g}\right)$ and $\Delta\tau_{(i)}^{Peg,(l+1)}$ is the root of the equation for the secant line through $\left(\Delta\tau_{(i)}^{Peg,(l-1)}, F_{LC}^{(l-1)}\right)$ and $\left(\Delta\tau_{(i)}^{Peg,(l)}, F_{LC}^{(l)}\right)$. The expression in Equation (A-1) is also used for finding the root of a function by the secant method. Nevertheless, the criteria used for the choice of the initial input values ($\Delta\tau_{(i)}^{Peg,(l-1)}$ and $\Delta\tau_{(i)}^{Peg,(l)}$) at each new iteration is different in the two methods. The secant method always uses the last two computed values while in the Pegasus algorithm these values are chosen in such a way that the root of the function belongs to the interval defined by these end-points. The procedure for selecting the values bounding the crossing with the yield surface is described below.

Once the approximated solution $\Delta\tau_{(i)}^{Peg,(l+1)}$ is calculated through Equation (A-2), the stress integration algorithm is performed again and a new estimate for the yield function, $F_{LC}^{(l+1)} = f\left(\Delta\tau_{(i)}^{Peg,(l+1)} \cdot \Delta\boldsymbol{\varepsilon}^{g}\right)$, is obtained at the end of the trial step. If $F_{LC}^{(l)} \cdot F_{LC}^{(l+1)} < 0$, means that $F_{LC}^{(l+1)}$ has the same sign of $F_{LC}^{(l-1)}$, the Pegasus algorithm is reinitialized by setting as input values (for the new iteration):

$$\begin{aligned}
&\Delta\tau_{(i)}^{Peg,(l-1)} \leftarrow \Delta\tau_{(i)}^{Peg,(l)} \quad (\Delta\tau_{(i)}^{Peg,(l-1)} \textit{ “receives” } \Delta\tau_{(i)}^{Peg,(l)} \textit{ as its new value)} \\
&\Delta\tau_{(i)}^{Peg,(l)} \leftarrow \Delta\tau_{(i)}^{Peg,(l+1)} \\
&F_{LC}^{(l-1)} \leftarrow F_{LC}^{(l)} = f\left(\Delta\tau_{(i)}^{Peg,(l)} \cdot \Delta\boldsymbol{\varepsilon}^{g}\right) \\
&F_{LC}^{(l)} \leftarrow F_{LC}^{(l+1)} = f\left(\Delta\tau_{(i)}^{Peg,(l+1)} \cdot \Delta\boldsymbol{\varepsilon}^{g}\right)
\end{aligned} \tag{A-3}$$

In contrast, if $F_{LC}^{(l-1)} \cdot F_{LC}^{(l+1)} < 0$ (that is, $F_{LC}^{(l)}$ and $F_{LC}^{(l+1)}$ have the same sign), the value of $\Delta\tau_{(i)}^{Peg,(l+1)}$ is recalculated, replacing $F_{LC}^{(l-1)}$ in Equation (A-2) by a reduced value of the yield function at $\Delta\tau_{(i)}^{Peg,(l-1)}$, given by $\gamma \cdot F_{LC}^{(l-1)}$, where $\gamma = \frac{F_{LC}^{(l)}}{F_{LC}^{(l)} + F_{LC}^{(l+1)}}$. The trial step is performed again for this new estimate of $\Delta\tau_{(i)}^{Peg,(l+1)}$, that is, $\Delta\tau_{(i),rep}^{Peg,(l+1)}$

$$\Delta\tau_{(i),rep}^{Peg,(l+1)} = \frac{\Delta\tau_{(i)}^{Peg,(l-1)} \cdot F_{LC}^{(l)} - \tau_{(i)}^{Peg,(l)} \cdot \gamma \cdot F_{LC}^{(l-1)}}{F_{LC}^{(l)} - \gamma \cdot F_{LC}^{(l-1)}} \tag{A-4}$$

and a new value for the yield function, $F_{LC,rep}^{(l+1)} = f\left(\Delta\tau_{(i),rep}^{Peg,(l+1)} \cdot \Delta\boldsymbol{\varepsilon}^{g}\right)$, is obtained. If $F_{LC}^{(l)} \cdot F_{LC,rep}^{(l+1)} < 0$, a new Pegasus iteration is performed taking as starting values:

$$\begin{aligned}
&\Delta\tau_{(i)}^{Peg,(l-1)} \leftarrow \Delta\tau_{(i)}^{Peg,(l)} \\
&\Delta\tau_{(i)}^{Peg,(l)} \leftarrow \Delta\tau_{(i),rep}^{Peg,(l+1)} \\
&F_{LC}^{(l-1)} \leftarrow F_{LC}^{(l)} = f\left(\Delta\tau_{(i)}^{Peg,(l)} \cdot \Delta\boldsymbol{\varepsilon}^{g}\right) \\
&F_{LC}^{(l)} \leftarrow F_{LC,rep}^{(l+1)} = f\left(\Delta\tau_{(i),rep}^{Peg,(l+1)} \cdot \Delta\boldsymbol{\varepsilon}^{g}\right)
\end{aligned} \tag{A-5}$$

Otherwise, the iterative process is reinitialized with

$$\begin{aligned}
&\Delta\tau_{(i)}^{Peg,(l-1)} \leftarrow \Delta\tau_{(i)}^{Peg,(l-1)} \\
&\Delta\tau_{(i)}^{Peg,(l)} \leftarrow \Delta\tau_{(i),rep}^{Peg,(l+1)} \\
&F_{LC}^{(l-1)} \leftarrow F_{LC}^{(l-1)} = f\left(\Delta\tau_{(i)}^{Peg,(l-1)} \cdot \Delta\boldsymbol{\varepsilon}^{g}\right) \\
&F_{LC}^{(l)} \leftarrow F_{LC,rep}^{(l+1)} = f\left(\Delta\tau_{(i),rep}^{Peg,(l+1)} \cdot \Delta\boldsymbol{\varepsilon}^{g}\right)
\end{aligned} \tag{A-6}$$

This iterative process is repeated until the inequality $\left|F_{LC}^{(l+1)}\right| \leq FTOL$ is satisfied or until a specified (maximum) number of Pegasus iterations (defined by the user) is reached. In the latter case, the calculation process is stopped and an error message is printed. A schematic representation of the Pegasus iterative method is depicted in Figure A-1.

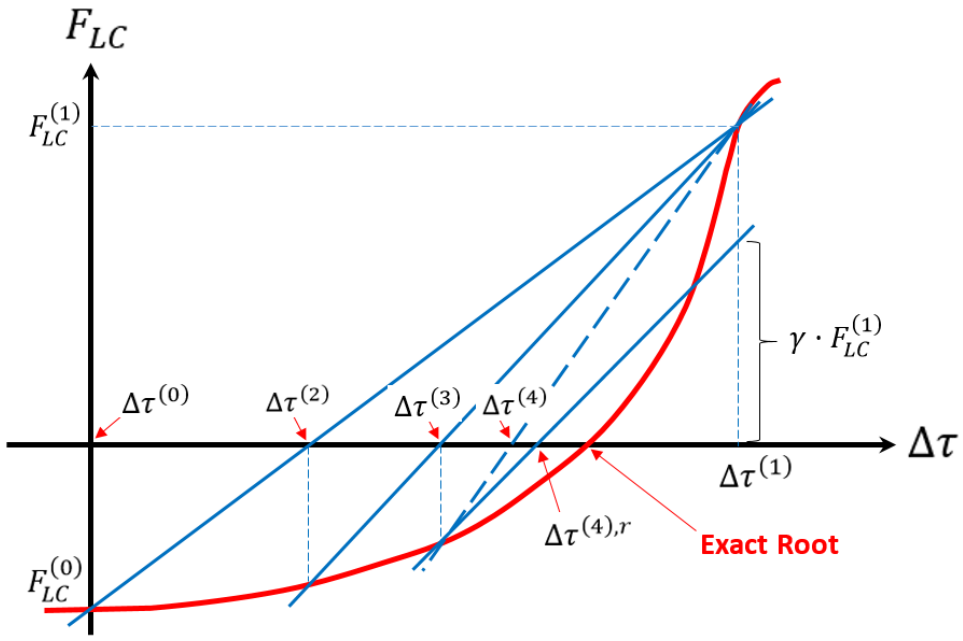

Figure A-1: Geometric interpretation of the Pegasus algorithm.

REFERENCE

Sloan, S.W., Abbo, A.J. and Sheng, D. (2001). Refined explicit integration of elastoplastic models with automatic error control. Engineering Computations, 18, 121-154.